CRANFIELD UNIVERSITY

PABLO COLADAS MATO

ADHESIVE JOINT GEOMETRY VARIATION IN NON-RIGID AIRCRAFT STRUCTURES

SCHOOL OF AEROSPACE, TRANSPORT AND MANUFACTURING

PhD in Aerospace
Academic Year: 2019 - 2020

Supervisor: Prof Phil Webb
Associate Supervisor: Dr Yigeng Xu
Industry Supervisors: Dr Dan Graham, Mr Andrew Portsmore

November 2019

CRANFIELD UNIVERSITY

SCHOOL OF AEROSPACE, TRANSPORT AND MANUFACTURING

PhD in Aerospace

Academic Year 2019 - 2020

PABLO COLADAS MATO

ADHESIVE JOINT GEOMETRY VARIATION IN NON-RIGID AIRCRAFT STRUCTURES

Supervisor: Prof. Phil Webb
Associate Supervisor: Dr. Yigeng Xu
Industry Supervisors: Dr Dan Graham, Mr Andrew Portsmore
November 2019

This thesis is submitted in fulfilment of the requirements for the degree of Doctor of Philosophy

ABSTRACT

Adhesive bonding is a proven alternative to mechanical fasteners for structural assembly, offering lighter and thus more fuel efficient aircraft and cost-effective manufacturing processes. The effective application of bonded structural assemblies is however limited by the tight fit-up requirement, which is with tolerance ranges of hundreds of microns; this can be a challenge for the industry to meet considering the variability of current part manufacturing methods and the conservative nature of the conventional tolerance stack-up analysis method. Such a (perceived) limitation can discourage effective exploitation of bonding technologies, or lead to development of overengineered solutions for assurance.

This work addresses such challenge by presenting an enhanced bondline thickness variation analysis accounting for part deflection of a bonded skin-stringer assembly representing a typical non-rigid airframe structure. A semi-analytical model accounting for unilateral contact and simplified 1D adhesive flow has been developed to predict bondline thickness variation of the assembly given the adherends' mechanical properties, adhesive rheological properties, and external assembly forces or boundary conditions. A spectral-analysis method for assembly force requirement estimation has also been tested. The bondline dimensions of several representative test articles have been interrogated, including a reconfigurable test assembly designed specifically to test the input conditions that affect bondline geometry variation. It has been demonstrated that the part deflections need to be accounted for regarding the fit-up requirement of bonded non-rigid structural assembly. The semi-analytical model has been found to more reliable and realistic prediction of bondline thickness when compared to a rigid tolerance stack-up. The analysis method presented can be a major technology enabler for faster, more economical development of the aircraft of the future, as well as of any analogue structures with high aspect ratios where weight savings and fatigue performance may be core objectives.

Keywords:

Adhesive; Aerospace; Assembly; Deflection; Deformable assemblies; Direct Linearization Method; Finite Element Analysis; Flexible assemblies; Metal-to-metal bonding; Non-rigid assemblies; Quadratic Programming; Skin; Squeeze-flow; Stringer; Unilateral contact; Viscous flow

ACKNOWLEDGEMENTS

Four years is a very long time, even if at the end of the journey it seems to have gone in a flash. I started this project clueless, penniless, struggling with a recently-acquired stutter, teetering on the edge of depression, and dangerously unfit, and seem to be stumbling out of the other end in a rather better condition (save for my slowly but inexorably receding hairline, and a worrying decline in my alcohol resistance).

As exciting as aircraft assembly is, it would be a stretch to credit that alone with my improved situation. Countless people have helped me along the way in multiple ways — for the most part, too many to name.

My dozens of once-flatmates, truly too many to name. Many have come and gone but always at some point managed to keep me entertained when things were getting dull and cheer me up when things were getting grim and (a precious few; oh, so few) wash up when the kitchen was getting grimy. Special mention to Ash who helped with the Summer 2016 Cleaning Campaign, creating a usable dining room and study space for the very first time.

The folks at the ever growing GKN research and technology teams where I was based — Filton Technology and the Composites (and) Technology Centre, too many to name. An invariably warm bunch who helped me find my way through various donkey work, kept me soaked in a rich engineering and applied science environment, and ensured I never felt alone even when working as a one-man team.

The Bonded Structures team, at one point too many to name, later too few not to overburden, who supported some of my need for data and measurement work, and endured my technical presentations without much shifting-on-seats action. Special thanks to Mark who did a fab job at documenting the curved panel tests, Jan who reviewed some of my reports in a very short timeframe and gave a load of insightful feedback, Paul who held my hand through part and assembly drawings and did a much better job at documenting test part manufacture than I ever could have, and Tsetso who liaised time and again to keep things running smoothly and made sure to poke holes in my logic at every occasion.

Other GKN Aerospace colleagues, especially Johan from Trollhattan who liaised with the Chalmers U to get the chance for a long chat and test the RDnT software and provided supportive feedback along the way, Kev from Cowes who did excellent preliminary tolerancing work and gave me some particularly valuable insights during the early stages, and Dr Fresh from Bath who provided some invaluable donkey work, data wrangling scripts, good inspection practice, and advice from a recent doctorate's perspective.

My multiple supervisors and putative research supervisors, too many to name, too few to do the work for me, who contributed in various facilities from technical review to keeping my sanity in check.

The AMRC folks who so patiently and competently helped with the multi-stringer test validation definition stage, and then did an awesome job at delivering top quality work within schedule and on a tight budget.

A few scattered people who with their comments on other aspects of the business (and life in general) ensured I was never out of inspiration and stimulation. Jose RM was particularly helpful in getting me up to speed with finite element modelling.

The people from CAV/Northern Aerospace and Metal Improvement Company, who provided a great deal of expertise in part manufacturing and supported the curved panel tests with high quality work and reporting.

The reader, for bearing with me this far.

STATEMENT OF AUTHORSHIP

The author is the sole responsible for the work presented herein, except aspects of the product design, inspection and realisation, as laid out below.

Flat test assemblies (Section 5.1) were defined entirely by colleagues in GKN Aerospace and GKN Fokker Aerostructures. The parts were manufactured, and the inspection defined and carried out by, Retrac Productions Ltd. The panels were assembled and inspected in GKN Fokker's Papendrecht (Netherlands) site, wholly by GKN Fokker personnel. All analysis and modelling presented herein were conducted by the author.

Curved test assemblies (Section 5.2) were designed by colleagues in GKN. Manufacture was carried out jointly by Northern Aerospace Ltd[i] (Consett, UK). and Curtiss-Wright Surface Technologies / Metal Improvement Company (Broughton, UK), according to their manufacturing best practice, which is held as a trade secret. The part inspection was carried out by the above following the author's specification (peer reviewed by GKN colleagues). The inspection fixture was not defined by the author, and was manufactured by Kaman Tooling. The panels were assembled and inspected in GKN Fokker's Papendrecht (Netherlands) site, with some of the tool-part gap checks performed by the author and the remaining measurements by GKN Fokker personnel. The pre-and post-cure inspection was defined by the author, in close communication with Fokker and GKN colleagues. All analysis and modelling presented herein were conducted by the author.

Multi-stringer assembly trials (Section 5.3) were devised by the author based on a design philosophy identified by the author. The final geometry was (re)defined by the author based on feedback on manufacturability from the AMRC's (Advanced Manufacturing Research Centre with Boeing) Composites and Integrated Manufacturing Groups. AMRC defined the exact machining strategy based on author indications and given dimensions; commissioned the tooling;

---

[i] Site previously owned by CAV Aerospace, and by Gardner Aerospace as of writing.

and devised the inspection method according to author-defined requirements. The detailed route cards with step by step instructions for the bonded assemblies were generated by AMRC based on the test plan and guidance documentation provided by the author. Additional manual inspection was planned and carried out entirely by the author. All analysis and modelling presented herein were conducted by the author.

Mid-scale demonstrator design for *Section 4.2* was generated entirely by the author based on a simplified representative commercial jet wing skin. The choice of area for modelling was informed by a prior GKN Aerospace study that had identified it as a source of manufacturing challenges.

The phrasing and presentation of information has also been reworked based on feedback from multiple supervisors, industry colleagues, publication peer reviewers, and associates. Most of the work is also in some way informed by the inevitable exchange of ideas that takes place in any research and engineering environment.

Any images of airplanes used in this thesis are subject to no known copyright restrictions. All were obtained through the flickr.com collection of the San Diego Air and Space Museum, except the image of a SAAB 340 which was obtained through flickr.com user 'Robert Sullivan'.

TABLE OF CONTENTS

LIST OF FIGURES

LIST OF TABLES

LIST OF EQUATIONS

LIST OF ABBREVIATIONS

1SP	Single-Side Pressure
2SP	Double-Side Pressure
AC	Autoclave Curing
AFT	Aft/aftward
AMRC	Advanced Manufacturing Research Centre [with Boeing]
CAE	Computer Aided Engineering
CAT	Computer Aided Tolerancing
CMM	Coordinate Measurement Machine
CPD	Coherent Point Drift
DFC	Datum Flow Chain
DLM	Direct Linearization Method
F&DT	Fatigue and Damage Tolerance
FEA	Finite Element Analysis
FEM	Finite Element Method
FFT	Fast Fourier Transform
FWD	Fore/forward
FSI	Fluid–Structure Interaction
GD&T	Geometric Dimensioning and Tolerancing
IBD	Inboard
MCMC	Markov Chain Monte-Carlo
MIC	Method of Influence Coefficients
OBD	Outboard
OoA	Out of Autoclave [curing]
PCFR	Position-Clamp-Fasten-Release
QP	Quadratic Programming
RBF	Radial Basis Function
RDnT	Robust Dimensioning and Tolerancing
RQ	Research Question
SF	Squeeze-Flow
SOVA	Stream of Variation

LIST OF VARIABLES

Variable name	Meaning	Units[ii]
P	Pressure applied in the course of a bonding cycle. Alternatively noted as ΔP to explicitly indicate *manometric* pressure	MPa
δ	Deviation from nominal of a stringer normal to the assembly interface, and deflection (absolute) associated with it	mm
δ_{poly}	Deviation or deflection of a stringer basd on polynomial (flexure-driven) shape	mm
$\delta^{res,k}$	Residual deviation left in step k of an iterative spectral decomposition	mm
a	Amplitude of an isolated component of the dimensional variation of a stringer	mm
f	Spatial frequency of a component of the dimensional variation of a stringer	mm^{-1}
λ	Wavelength of a component of the dimensional variation of a stringer	mm
n_{sf}	Number of frequencies used in a spectral decomposition of a component's variation	-
m_{sf}	Number of high-frequency components removed from a spectral decomposition on account of very small amplitude	-
N_L	Number of points sampled along a stringer length	-

[ii] Unless explicitly stated otherwise in the text

Variable name	Meaning	Units[ii]
E	Material elastic modulus	MPa
ν	Material Poisson's ratio	-
I	Second moment of inertia of the area of a stringer cross-section	mm^4
w	Width of a stringer foot flange, or of the associated bondline	mm
T	Tolerance related to a dimension indicated in the subscript	mm
L	Position along the length of a stringer	mm
L_{wav}	Position along a stringer length where the distance to the nominal attains a local minimum	mm
$L_{stringer}$	Length of a stringer	mm
k_{shear}	Shear factor of a cross-section (in an established direction)	-
G	Material shear modulus	MPa
A	Area of a stringer cross-section	mm^2
φ	Phase offset of a component of the dimensional variation of a stringer	rad
c	Adjustment coefficient for amplitudes of non-sinusoidal components of variation	-
x, y, z	Positional coordinates	mm

Variable name	Meaning	Units[ii]
x', y', z'	Positional coordinates in a transformed reference frame	mm
θ	Rotation used in a reference frame transformation	rad
x_{min}, x_{max}	Minimum and maximum x coordinate of a part	mm
y_{min}, y_{max}	Minimum and maximum y coordinate of a part	mm
$(\vec{X})_i$	Element i of vector $\vec{X}$	matches $\vec{X}$
$(\vec{X})^T$	Transpose of vector $\vec{X}$	matches $\vec{X}$
$\hat{n}_i$	Unit vector normal to a bonding surface (nominal)	mm
$\vec{F_i}$	Force normal to a bonding surface at node i (vector)	N
F_i	Force normal to a bonding surface at node i (modulus, scalar)	N
$\vec{F}$	Vector of forces normal to the nominal bonding surface, for a set of nodes and conditions given by the subscript/superscript	mm
$\vec{X_i}$	Geometric deviation from nominal, normal to a bonding surface at node i (vector)	mm
X_i	Geometric deviation from nominal, normal to a bonding surface at node i (modulus, scalar)	mm
$\vec{X}$	Vector of geometric deviations normal to the nominal bonding surface, for a set of nodes and state given by the subscript/superscript respectively	mm

Variable name	Meaning	Units[ii]
$\overrightarrow{X_G}$	Vector of geometric deviations normal to the nominal bonding surface, for the gap between two or more bodies	mm
ΔX_i	Deflection of node i nominal to the nominal bonding surface at its location, as a result of force application	mm
$\overrightarrow{\Delta X}$	Vector of deflections (changes in position) under external and/or internal forces, nominal to the nominal bonding surface, for a body and condition given by the subscript/superscript	mm
U_{ij}	Deflection of node i in response to a unit force on node j, both normal to the nominal bonding surface at their respective location	mm/N
$\mathbf{U}$	Compliance matrix	mm/N
$\mathbf{U_{A-B}}$	Compliance matrix of the nodes of body A that interface with (i.e. form contact pairs with) nodes of B	mm/N
$\mathbf{U_{A-B}^{C-D}}$	Compliance matrix describing the change in gaps in the contact pairs between bodies C-D, in response to contact forces in contact pairs between bodies A-B.	mm/N
b	Thickness of a single layer of adhesive as studied in a squeeze-flow problem	mm
b_{1t}	Thickness of a single layer of adhesive at time t of cure	mm
t	Time elapsed during the curing process	s
n_{film}	Number of layers of film adhesive used in bonding	-

Variable name	Meaning	Units[ii]
b_{bond}	Final bondline thickness given by squeezeflow alone	mm
$b_{0_{layer}}$	Initial thickness of adhesive in one film layer	mm
$b_{carrier}$	Thickness of the carrier in a layer of film adhesive	mm
b_0	Initial (pre-cure) thickness of a layer of adhesive within one flow domain	mm
$b_{overall}$	Overall bondline thickness in an assembly cross-section	mm
b_{obs}	Observed (measured) bondline thickness	mm
b_{sim}	Bondline thickness predicted by simulation	mm
$b^*_{verifilm}$	Measured thickness of a piece of verifilm	mm
$b_{adhesive}$	Adhesive contribution to thickness of a piece of verifilm	mm
b_{rf}	Thickness of release film in a piece of verifilm	mm
$twist$	Angle variation of the bondline thickness in a cross-section	rad
$concavity$	Bondline thickness variation due to concavity of the parts in an assembly cross-section	mm
η	Kinematic viscosity of an adhesive	mm^{2}s^{-1}
v_x, v_z	Adhesive flow velocity in a direction indicated by the subscript	mm/s
p	Pressure of the adhesive	MPa
$k_{[\mathrm{comp}]}$	Coefficient that multiplies a unit component of variation comp when generating variation with a modal approach	-

Variable name	Meaning	Units[ii]
$S_{[\mathrm{criterion}]}$	Quality loss function based on $\mathrm{criterion}$	-
$\mathrm{RMS}(\vec{X})$	Root Mean Square of the values in vector $\vec{X}$	matches $\vec{X}$
$\mathrm{STD}(\vec{X})$	Standard deviation of the values in vector $\vec{X}$	matches $\vec{X}$
$\mathrm{tol}(\mathrm{var})$	Tolerance for a variable var, used to quantify assembly quality	matches var
α, β, γ	Coefficients used in linear regression of quality loss and variation components	-
R	Radius of chordwise curvature of an airframe skin	mm
X_{Gwave}	Local maximum of a stringer-skin gap between parts within a wave (i.e. between two consecutive minima)	mm
$L_{upr,wave}$	Maximum length position of a stringer variation 'wave'	mm
$L_{lwr,wave}$	Maximum length position of a stringer variation 'wave'	mm
ψ	Ratio of maximum to minimum reaction forces given by 1D squeeze flow, when the thickness varies among cross-sections	-
ρ	Coefficient used for assembly model calibration	-
$\zeta_{BC,skin}$	Coefficient used for assembly model calibration based on skin boundary conditions	-
$\xi_{BC,strg}$	Coefficient used for assembly model calibration based on stringer boundary conditions	-

Variable name	Meaning	Units[ii]
δ_{mod}	Model inadequacy for bondline prediction	mm
$\alpha_{xsectpos}$	Model inadequacy related to bondline variations along the stringer cross-section	mm
$\beta_{contact}$	Model inadequacy related to bondline variations depending on close contact (or lack thereof) between adherends	mm
ς	General uncertainty term for the calibrated bondine model	mm
ε_{meas}	Model discrepancy with measurements due to bondline thickness measurement error	mm
μ_{burr}	Mean thickness of unremoved burr in a cut section	mm
σ	Standard deviation of the bondline thickness measurement error introduced by a source indicated in the subscript	mm
ϵ	Observation error involved in assessing bondline thickness, corresponding to a source given by the subscript	mm
μ_{rf}	Mean thickness of a layer of release film	mm
τ_{rf}	Deviation from mean thickness of any piece of release film	mm
α	Level of confidence for a confidence interval	-
$\mathrm{CI}(1-\alpha)$	Confidence interval with level of confidence α	varies
Unif	Uniform distribution	-

Variable name	Meaning	Units[ii]
N	Normal distribution	-
t	Student’s t distribution	-
Γ	Gamma distribution	-
GI	Gamma-inverse distribution	-
φ_{obs}	Angular error when measuring a bondline thickness from a cross-section	rad
θ	Generic parameter for a model calibration	
f_k^*	Spatial frequency of variation corresponding to the longest wavelength for which the cumulative assembly pressure score of an assembly improves by the pressure applied	mm^{-1}

1 INTRODUCTION

1.1 Problem statement and thesis summary

The global air transportation market has grown steadily for the past two decades, and predictions are that this trend will continue for just as long. In parallel, competition amongst airline operators and airframe manufacturing is ever fiercer, accompanied by increased environmental emission restrictions and cost of fossil fuels. These combine into a strong driver for faster manufacturing processes which deliver lighter, more aerodynamically-efficient aircraft.

Current aircraft are produced as assemblies of a large number of parts; not only is the assembly process time-consuming, but the large joints between parts add up to significant weight as they tend to involve heavy fasteners, as well as extra features such as flanges and buttstraps for attachment. Fastener-based assembly of primary structures, in particular, incurs long cycle times due to the need to drill and clean thousands of holes, and then insert rivets or bolts individually.

Figure 1-1. Some examples of bonded primary airframe structures. Original images obtained through flickr.com (Comet, TriStar and 146: San Diego Air and Space Museum; SAAB 340: Robert Sullivan).

Assembly technologies which do away with mechanical fasteners (such as adhesive bonding and welding), are therefore highly desirable due to their potential for weight and cycle time reduction. Adhesive bonding, in particular, has been used since the dawn of commercial aviation (examples in Figure 1-1) by virtue of its excellent fatigue behaviour, ability to join dissimilar materials, and lack of interference with aerodynamic surfaces.

There are, however, perceived challenges for generalised use of adhesive bonding. In part, this is due to the memory of some high-profile failures of early bonded aircraft (albeit unrelated to the bonded joints); however, there is a real technical difficulty in meeting tight bondline geometry requirements. Typical acceptable thicknesses lie in a tolerance band a hundred microns wide in the sub-millimetre range; meanwhile, variation of individual parts can easily exceed these values[iii]. This means that, according to a typical rigid tolerance stack-up, bonded aerostructures would not be viable given current manufacturing processes. Yet, as evidenced by the successful deployment of bonding, such is very much not the case in reality: many aircraft components are indeed not rigid, and can thus be pushed against each other to closely fit together.

The insight that aircraft components can be deformed to meet bonding interface requirements is not new; in fact, its active utilisation dates from (at least) the 1950s, and its effective application has been reported to be a strong determinant of tooling design and assembly strategies. It also is routinely incorporated into geometrical inspection. However, there is no well-documented method for quantifying the impact of deflections on bonded assembly variation. Such a method could have a great enabling effect on design and tolerancing methods. It would not only support trade of different options for part manufacture and assembly setups early in the design process: it also would help de-risk and accelerate exploration of innovative concepts.

This work adapts finite element-based techniques already deployed in the automotive sector, and demonstrates them in multiple structural-bonding scenarios. Applications include assembly simulation based on various types of geometric inspection data, stochastic simulation to support early design decisions, and comparison against a bespoke validation assembly. The tool

[iii] Profile tolerance values quoted in publicly available sources are often in the hundreds of microns; meanwhile, measurements in a production environment have shown deviations of several millimetres. This discrepancy is an open secret in the industry.

created has been actively used to inform demonstrator design, manufacture, and inspection decisions.

1.2 Thesis structure

This work is structured as follows:

First, within this chapter, a historical overview is presented on adhesive bonding of metal airframes. This shows the history of successful application of the technology, but also the concerns around dimensional control of the bondline, and how this issue has driven tooling design and assembly philosophy. This overview reveals the importance of considering part deformation in effective adhesive bonding.

Chapter 2 presents a literature review focussed on non-rigid considerations for geometry assurance. Non-rigidity is defined, after which an overview is provided on variation modelling and inspection approaches for non-rigid components. This is followed up by a review of the ways considerations of non-rigidity have been included in the study of assembly variation, and leads to the research questions to be answered.

Chapter 3 describes the methodology in terms of numerical tools used. Two analysis approaches are advanced which use considerations of non-rigid parts: an estimator of gap closure requirements based on spectral decomposition, and a semi-analytical bondline thickness prediction that combines numerical deflection simulation with an analytical flow equation. These have been applied to the test cases in subsequent chapters.

Chapter 4 contains two uses of the semi-analytical bondline thickness prediction. Stochastic variation analysis of an assembly is presented for a single stringer and for a mid-scale panel assembly, showing the usefulness of this model for trade of design and manufacture options. Then, an embodiment of the tool is presented which enables a quick assembly fitness study, based on ad hoc measurements taken in a production environment prior to bonding, thus de-risking assemblies.

Chapter 5 shows the diverse physical test assemblies studied, all of which focus on skin-stiffener arrangements:

– flat panels with built-in steps which test the adhesive flow condition;

– curved panels which show the manufacturing challenges, effects of various joint-formation mechanisms, and sources of inaccuracy for the models developed;

– a multi-stringer panel which demonstrates the effect of different combinations of part variation and boundary conditions.

All these are modelled using the semi-analytical model, and the modelling results are discussed.

Chapter 6 provides a summary review of the results and research achievements. The research limitations are also discussed, both in terms of scope and quantifying some of the modelling inaccuracies. The chapter concludes by summarizing the research outcomes and indicating the novel aspects of the work.

Chapter 7 summarises the work undertaken and briefly discusses future research prospects for the methods developed, both in terms of expansion and industrial integration.

The appendices provide further information on the pre- and post-processing techniques used, in terms of shape fitting, uncertainty analysis, and model regression. Detailed discussion, too lengthy for the main body of the thesis, is provided for the adhesive flow equations and spectral analysis results. Additional details are provided on the manufacturing and inspection procedures, inclusive of inspection results and curing cycle traces.

1.3 Metal-to-metal bonding: historical highlights

Bonding of metal to metal in airframe structures is recorded as far back as the 1940s, with wing skin-to-stiffener bonded joints in the deHavilland Dove, shortly followed by the Vickers Viking and Viscount, all three small propeller aircraft. The bonds were performed with simple tools, such as clamps and hard profile boards, with heat for curing applied by introducing the clamped assembly in an oven.

With the development of the larger deHavilland Comet (Figure 1-2), with bonded wings and fuselage panels (Anon, 1952; de Bruyne, 1953), specialised tooling became more practical; thus, presses with embedded heating systems were introduced. Embedded heating was achieved by either incorporating resistance heaters, or vapour circuits for the press platens (Anon, 1957). However, at the same time the limitations of such mechanical pressure application system became apparent, as bonding of larger curved components became too sensitive to tool variability. Thus, the 1950s also mark the beginning of autoclave curing as a distinctly capable technique. This can be evidenced in the Fokker F27 and F28, where the majority of structural components were bonded, though often involving metal-resin laminates (rather than purely metallic parts) or in combination with rivets (Harrison, 1967).

Figure 1-2. A deHavilland Comet-1, the first commercial jetliner, which used metal-to-metal bonding extensively in primary structures. Source: flickr.com, San Diego Air and Space Museum.

The Comet saw several high-profile structural failures with loss of life, which led to questions around the safety of bonded joints, in spite of the lack of adhesive failures in previous deHavilland models (Anon, 1954); eventually, enquiries identified fuselage fatigue as the root cause of the accidents (van der Neut, 1974;

Pethrick, 2012). However, by this point the confidence in adhesive had been substantially undermined and rivet-based solutions had become the clear dominant option.

Metal adhesive bonding did continue, in the Fokker family of regional aircraft (Fokker 27/28/50/100). Extensive use of bonding in most primary enabled these airframes to achieve substantial weight reductions and material savings: laminates permitted adding material as required in any area, rather than having to remove material from an oversize initial stock. The success of metal laminate-based solutions continues today, with Fokker produced laminated fuselage and empennage for Gulfstream and Dassault.

Interest in adhesive bonding would not reach the American manufacturers until the late 1960s, with the Lockheed L1011 TriStar wide-body jetliner (Figure 1-3) using adhesive and rivets for joining of stiffeners to fuselage panels some 11 m x 4.6 m in size. The Cessna Citation III business aircraft used structural adhesives extensively, though monolithic parts were bonded preferentially in flat or single-curved areas and often in combination with rivets (Velupillai and Hall, 1979).

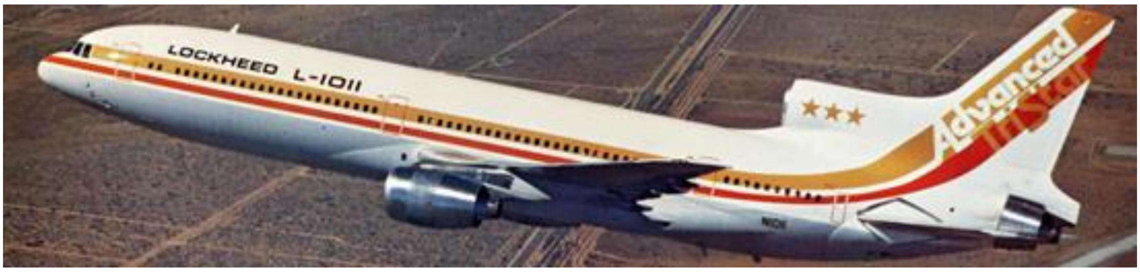

Figure 1-3. Lockheed 1011 TriStar. Source: flickr.com, San Diego Air and Space Museum.

Starting in 1975, a large scale industrial development project for solely-bonded primary structures (Primary Adhesively Bonded Structure Technology [PABST]) was carried out by McDonnell Douglas (later integrated in Boeing) in cooperation with the USA Air Force. This resulted in the most extensive piece of documented aerospace adhesive bonding work available to the public (Anon, 1976, Anon, 1977; Land and Lennert, 1979). Aluminium fuselage skin sections some 2.5m in arc were bonded to stiffeners with a film epoxy adhesive, requiring extensive use of verifilm and part rework for adhesive layer thickness control. Tooling philosophy was found instrumental to success of the bonded assembly: cradle-like ‘female’ tools were less efficient than ‘male’ formboards positioned at the stringers for shape and adhesive layer thickness control, due to the skin being more compliant than the stiffeners. Because of this, pushing the skin against located stiffeners ensured better bondline control, and subsequently the process became more tolerant of part manufacture variation: “the precision demanded for the stiffeners was relaxed considerably at the same time as the fit of the parts was being improved” (Hart-Smith, 1980). Extensive commentary was published on manufacturing considerations following the PABST development; among other conclusions, it was recommended that the assembly configuration “relies on the parts themselves to define the shape”, thus reducing the presence of rigid tooling; and the importance of integration of processes was emphasised: “it is more important to coordinate the design, tooling, and manufacturing approaches for bonded structure than for riveted structure”. Crucially, viability of a bonded structure was linked to geometric qualities which can be assessed before bonding, noting the relative futility of assessing the bondline quality after assembly: “The most practical solution [...] is not to have any faults in the bonded structure at the time of manufacture [...]. The key is the fit of the parts [...] if the parts fit together prior to bonding there is no need to inspect them after bonding whereas, if they do not fit together before bonding them, there is no point bothering to inspect them after bonding, before scrapping them”. Excess adhesive pushed from between the adherends was also key, with the presence or absence of outflowing adhesive being a key indicator of quality: “The nature of the [adhesive] fillet [at the bond edges] indicates two things: if the adhesive flowed, and if the adhesive wet the surfaces. All other inspection criteria are of lesser importance.” (Hart-Smith, 1980). An example of this adhesive excess is presented in Figure 1-4. Interestingly, no numbers were explicitly associated, in openly available reports, to part deflection nor adhesive flow (and indeed, no modelling of these manufacturing aspects is reported), even if it may be possible to reverse-engineer them from the tolerances quoted.

The insights from the PABST programme then went on to influence the tooling used for SAAB 340 and 2000 in the 1980s, with fuselage panels and single-curved wing skins (length ~9 m) bonded to stringers. The process used male locators and low-stiffness female tools (Hart-Smith and Strindberg, 1997). Thus, as recommended in the PABST report cited above, the SAAB assembly configuration “relies on the parts themselves to define the shape”).

Interestingly enough, the PABST programme was carried out as a very similar bonding process was developed for similarly-sized A300 fuselage panels in Europe. However, performance of bonded Airbus structures was reportedly unsatisfactory, in addition to exhibiting proneness to corrosion (possibly owing to the different tooling philosophy and surface treatments). This resulted in a reduction in use of adhesives within the main Airbus aircraft, either by combining it with rivets, or by totally discontinuing it from areas prone to moisture accumulation (Räckers, 2004).

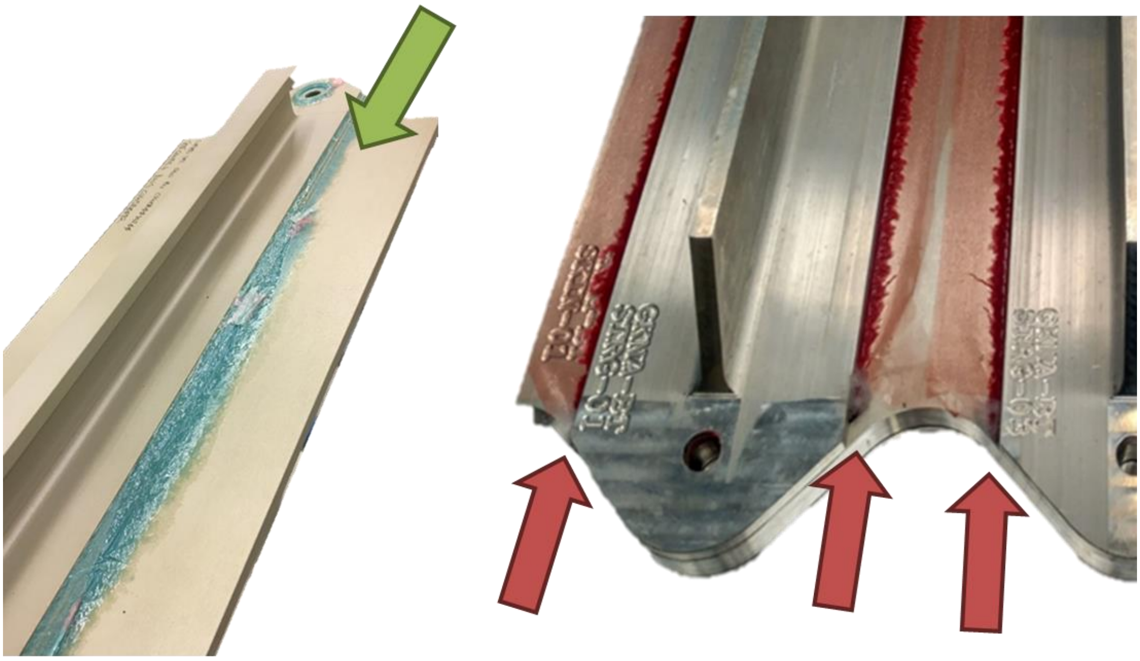

Figure 1-4. Examples of adhesive spewed, or ‘squeeze-out’, observed in tests used for this work. Absence of such feature would typically signal a poor bond.

The following decades did not see significant growth in airframe structural metal adhesive bonding, partly because of the growth of composites, which have received much attention, and partly because of reluctance due to previous experiences. A noteworthy application is production of the BAe 146 (Figure 1-5) in the 1980s, with Redux bonding of wing skins to >10m long stringers. Advances in laminates, which the development of ARALL and GLARE (which, with bonded stiffeners, has a large presence in the fuselage and upper wing skin of the A380), are of note (Higgins, 2000).

Figure 1-5. BAe 146. Source: flickr.com, San Diego Air and Space Museum.

In the last few years, the panorama of search for maximum efficiency and incremental improvements to existing aircraft models has sparked new interest in bonding of assemblies that are currently mechanically fastened. Adhesives are still used in regional and business aircraft, such as the Gulfstream G650. Smaller secondary structures, such as A380 flaps, are bonded too (Nobis et al., 2010). An additional challenge comes in the form of new materials requirements and restrictions; for example, the environment and health-driven phasing-out of surface pretreatments using hexavalent chromium, through the EU's REACh[iv] directive. This increases the pressure for bonding process improvement.

Yet at the same time, significant breakthroughs in the bonding manufacturing process, be it in the way of assembly modelling, control or implementation, seemingly have not taken place. This is illustrated in the outcomes of an extensive industry survey and workshop sessions held by the FAA[v] (Davies, 2004; Tomblin et al., 2005): the core concerns included surface treatments and bondline thickness control (Tomblin et al., 2005). Participant interventions highlighted that the methods and level of knowledge of the overall process had

[iv] Registration, Evaluation, Authorisation and restriction of Chemicals

[v] United States Federal Aviation Administration

not progressed much from the times of PABST: the process still relies on skilled manual intervention (Textron, 2004), pressure is applied mostly with vacuum bag and autoclave (Davies, 2004), goodness of a joint is proven by excess ‘squeezed-out’ adhesive (Voto, 2004), and interface gap management is summed up as “tooling must bring the surface in contact” (Abbott, 2004). Use of ‘verifilm’ where a mock assembly run is conducted prior to bonding, either with non-sticking resin or by encasing the adhesive in release film, was still frequent as a means of interface geometry verification (Davies, 2004); a clear symptom that no suitable analytical or numerical methods could readily provide the same confirmation.

Ultimately, in spite of these apparently limitations, adhesive bonding is still acknowledged by industry practitioners as a strong enabler for manufacture of more efficient and durable airframes. This technology therefore stands to deliver substantial benefits if appropriate method improvements and formal knowledge were developed to aid its swifter, more widespread industrialisation.

2 LITERATURE REVIEW

This section opens with introductory definitions, and bounding the scope of discussion. This is followed by the chapters of literature review proper.

The literature review, therefore, comprises four parts:

- What is understood as “non-rigid”, “variation”, and “tolerancing”, and how these concepts will fit in the context of airframe bonded assemblies;
- How part geometric variation is modelled, in particular for geometries found in typical aerostructural components;
- How inspection is carried out for non-rigid components;
- How assembly of non-rigid structures has been modelled to aid tolerancing and variation management activities.

2.1 Defining the scope of discussion

This subsection provides context regarding terms that will be used repeatedly throughout the thesis. These

2.1.1 Variation, tolerances and tolerancing

We understand variation in two ways:

- First, as the deviation of the properties of an entity from the nominal values. This can cover material or dimensional properties of a component such as elastic modulus and flange thickness, or process parameters such as the temperature during an adhesive curing cycle.

  In the case at hand, since the main concern is geometric variation, and bonding process parameters can be influenced directly, hereafter “variation” will be used as shorthand for “geometric variation”.
- Secondly, extending the first understanding, as the *variability* of a property or parameter; that is, as a statistical measure of the expected variation found in a type of component or process. Again, in this work only the geometry will be considered.

The concept of tolerances ties directly with that of variation:

- First, in the narrow sense, a tolerance is understood as the acceptable (or, more accurately, ‘tolerable’) variation of a property or parameter. Once it is acknowledged that no part or process will be absolutely perfect, the tolerance is a statement of what will be considered ‘close enough’. This is, depending on e.g. functional or assembly requirements, often expressed as a range around a nominal value, but also can be defined by other metrics and techniques such as spatial and temporal filters. Geometric Product Specification (GPS) norms offer an ever-expanding overview of ways to filter and encode geometries, for example in ISO 16610 (BSI, 2015).
- As an extension of the strict understanding of a tolerance, the term is also used to refer to the *expected variation* in the inputs to a modelled (sub)process. This reflects the fact that these inputs are assumed to be controlled by external procedures, such as machine calibration or subcomponent geometric inspection; therefore, the tolerances in these upstream procedures will determine the variation of the process inputs.

Tolerancing is, then, applicable in either (or both) of two ways (Stricher, 2013):

- Study of the combination of multiple sources of variation, given some tolerances, and the resulting variation of a process or product. This is also understood as “tolerance analysis” or, given the looser definition of a tolerance as input variation, “variation analysis”.
- Study of allocation of tolerances to multiple input sources, according to appropriate engineering considerations, for the purpose of meeting given tolerances in an output. This is also understood as “tolerance synthesis”.

2.1.2 Non-rigid structures

The concept of a non-rigid body is not new. Whereas a perfectly rigid body maintains all its dimensions when subjected to mechanical loads, all objects in the real macroscopic world experience some degree of deformation when loaded. Yet the concept and distinction of rigid and non-rigid objects is very much useful, as attested by the existence of items such as shock absorbers, bicycle helmet padding, and pillows (and as this work will further demonstrate).

The informal, and most often implicit, definition of non-rigidity (or alternatively, “flexibility”, “deformability” or “compliance”[vi]), which is common to all references to it, is “non-rigid enough that one needs to care about the reasonably expected changes in dimensions and stresses”.

Accepted standard definitions are in the same vein, with ISO 10579:2013 (BSI, 2013) defining “non-rigid” parts as those that

> *...when removed from their manufacturing environment, may deform significantly from their defined limits [...] the deformation is acceptable provided that the parts may be brought within the indicated tolerance by applying reasonable force*.

The amount of qualifiers in this definition (“may”; “significantly”; “reasonable”) underscores that the distinction is chiefly pragmatic, and —coincidentally— not at all rigid. This is also underscored by the content of the norm, which simply establishes the need to convey the fixturing state of a part prior to assembly or inspection, with any further details confined to the drawing notes.

In following discussion, an adaptation of a recently-proposed criterion which formalises this idea (Abenhaim, Desrochers and Tahan, 2012) will be used: a body is considered rigid if the forces it encounters during an operation (e.g. an assembly step or inspection) result in deflections that are smaller than the relevant tolerances by, at least, one order of magnitude. The original work referenced proposes a three-zone system which, depending on the exact deformation/tolerance ratio, distinguishes A “rigid”, B “non-rigid” (beams, small sheet metal) and C “highly non-rigid” (membranes, rubber, large sheet metal). This three-zone model, presented in Figure 2-1 with some examples based on the author’s experience, offers good pragmatic insight, but is not necessarily universally translatable into actionable insight: the frontier between zones B and

---

[vi] The implications and choice of terms are discussed in subsection 2.1.2.1—Alternative terminology in the literature.

C is blurry, and zone C includes a very wide array of components, from large assemblies to wires. Indeed, some of the examples of this classification presented in subsequent work by the same group (Aidibe, 2014) experience an order of magnitude increase in deflection between stress states, making the classification potentially highly process-specific.

In any case, the base formal premise in this convention — that whenever the deflection/tolerance ratio of an object is not close to zero, this object should not be considered rigid — is valid. In subsequent discussion, the term “non-rigid” will be used to refer to parts whenever they don’t belong to zone A “rigid”, regardless of whether they might fit in zones B or C. This is because the discussion is largely concerned with structural parts which can be considered rigid in at least one dimension (e.g. in-plane for skins), and because the assembly forces and tolerances may not be known.

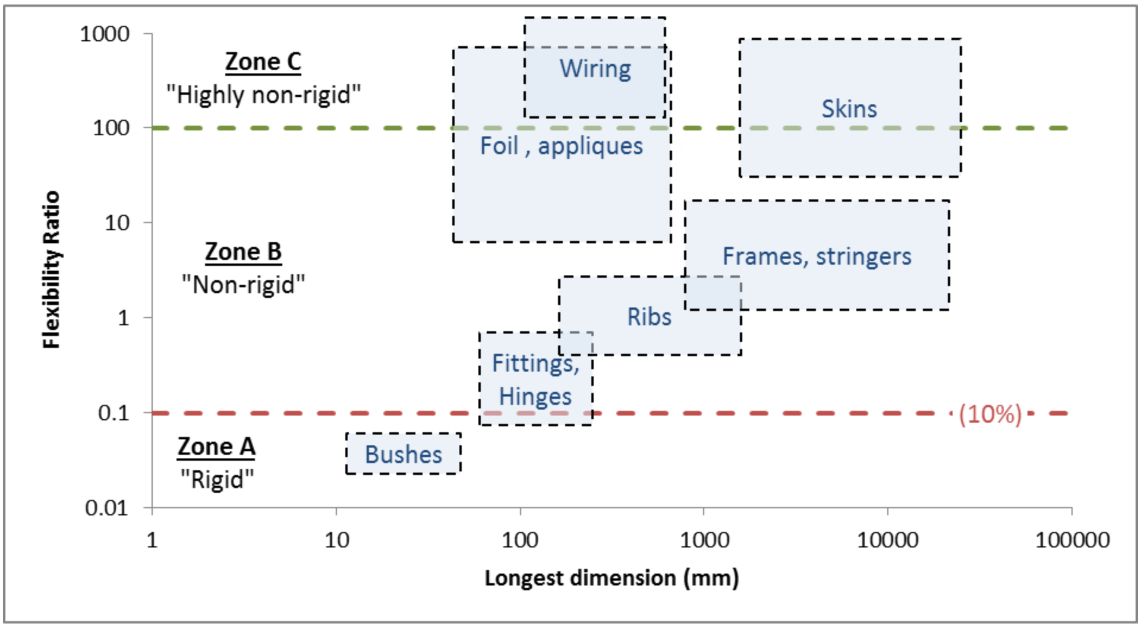

Figure 2-1. The concept of non-rigidity as a function of the relevance of expected deflections given by a “Flexibility Ratio” = (deformation/tolerance). (Generated by the author based on the approach in Aidibe, 2014). The “flexibility ratio” range for each component goes from deflection under weight alone, to the combination of weight and typical assembly forces.

This definition captures the criteria in the implicit definition:

- The expected dimensional change, depending on typical process forces, is evaluated. In this way, a component may be considered effectively rigid when it undergoes contactless inspection[vii], but as non-rigid when it is fit into an assembly by force (Samper, 2007).
- Dimensional tolerances are taken into account. This indicates whether the deformation is 'enough to care' as implied in the norm definition. By taking tolerances into account, an object can be similarly considered rigid or not depending on the particular process it is involved in. For instance, deformation of a part under its own weight may be a non-issue when applying a chemical surface treatment, but become highly problematic later during visual inspection of the treated surface due to e.g. light reflection and handling difficulties.

As this criterion is intended to be general/generalisable, it does not highlight another point which is captured in K. Merkley's concept of "material continuity" (Merkley, 1998): deformations occur locally to the forces applied. Thus boundary conditions, local contact conditions, and the range over which loads are imparted, can mark the difference between effectively rigid or not. This is explicitly captured in another common observation that some component "bends a lot over long distances, but is locally pretty stiff", and implicitly by some tolerances that state a deviation over a range (or an amplitude-wavelength pair). An example of the latter is provided in Figure 2-2; numerous bonding-specific cases are available in the reports from the PABST development (Land and Lennert, 1979).

[vii] In many cases, deflection of an object under its own weight will be enough to require taking it into account during inspection. This is immaterial to the example.

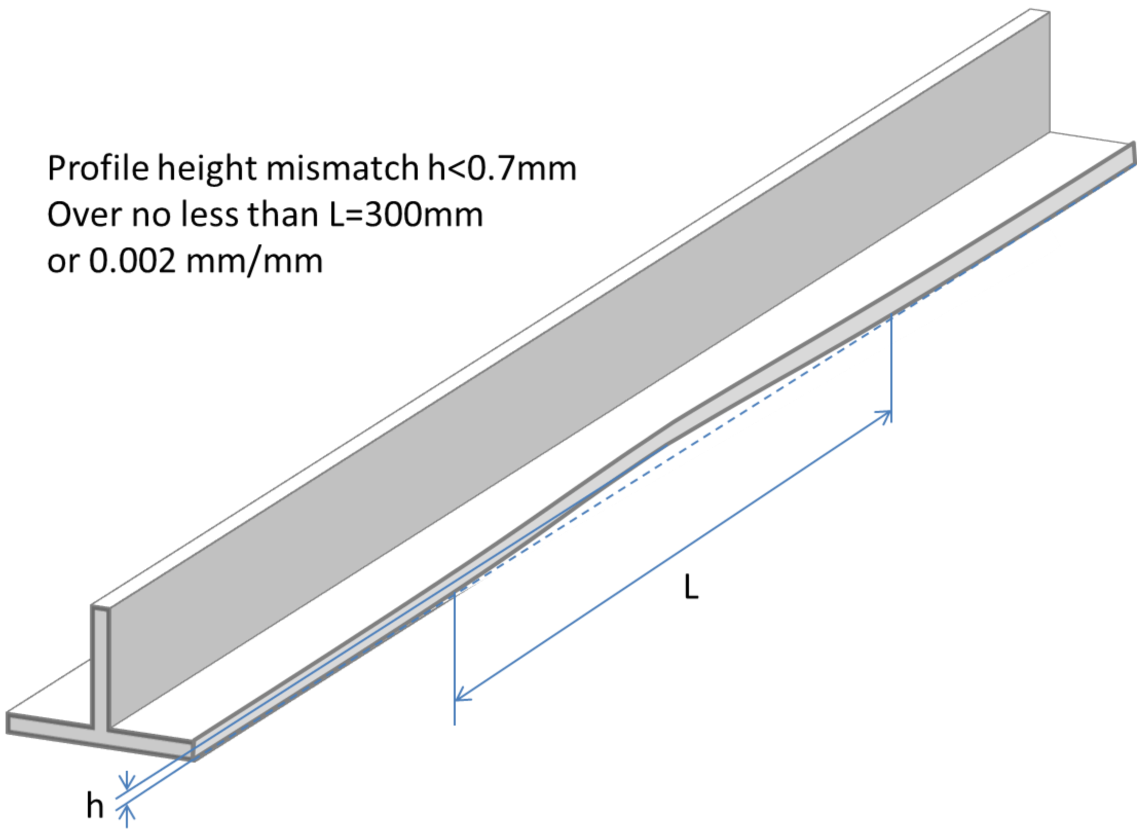

Figure 2-2. Example tolerance of a bond detail, stating a minimum range for a defect to appear.

2.1.2.1 Alternative terminology in the literature

The terms "non-rigid", "flexible", "deformable", and "compliant" tend to be used almost interchangeably when referring to the property of solids which change in dimensions when subjected to external forces. However, as explained in K. Merkley's doctoral dissertation (Merkley, 1998) following discussion among Computer Aided Tolerancing (CAT) scholars, the terms are not equal. For example, "deformable" can have negative connotations, while "flexible" can also refer to something that is not limited to one working mode, such as a "flexible manufacturing system". Merkley thus used the term "compliant". Although this word can also refer to something that "complies with" a requirement or specification, it has the advantage of linking to the *compliance matrix*, which is central to many approaches to non-rigid assembly tolerancing. For this reason, in this work, the expression "conform to" will be used instead to convey agreement with a requirement or restriction, be it a specification or a physical object. This work will routinely use the term “non-rigid”, as in the ISO 10579:2013 norm (or “nonrigid” if quoting other work). This is the least likely to lead to misunderstandings, while “compliance” will be used when referring to the opposite of “stiffness” (e.g. the compliance matrix is the inverse of the stiffness matrix). The preferred uses of compliance-related words for the purpose of this work are summarised in Table 2-1.

Table 2-1. Summary of potentially equivocal terms referring to non-rigid components

Term indicating “not rigid”	**Potential confusion**	**Preferred connotation in this work**
Nonrigid, non-rigid	None	Able to deflect significantly (relative to typical tolerances) under expected loads during a given task or process
Deformable, deformation	Negative connotation, idea of non-conformance or spuriousness	Quoted or referring to a component’s initial or an assembly’s final variation, or deflection under forces
Flexible	Able to take on diverse work, e.g. “flexible assembly system”	Quoted or referring to quickly reconfigurable tools or polyvalent systems
Compliant, compliance	Meet a requirement	Compliance matrix — gives the deflection caused by external forces
Conform	Adapt in shape to (drape over) another object	Meet a requirement/restriction

2.1.3 Aerostructure part typology

Aircraft structures are made up, generally speaking, of combinations thin plates with local stiffening reinforcements, or light cores sandwiched between thin plates. This provides mechanical and aerodynamic performance while minimising the weight of the structure. Due to manufacturing considerations, such as tool access and the drive to minimise material wastage from machining, some of these structures (mainly those including large aerodynamic surfaces) are often made up of plates (skins) and slender beams (stringers), which are manufactured separately and then assembled together into panels. These panels are joined to other, internal stiffening and load-bearing components, such as ribs and spars, which tend to be in fewer pieces. There also are a range of connecting hinges and brackets.

Panels in wings, fuselages and tail planes contain the largest structural joints in aircraft, due to their large surface area and concentration of stiffeners. Combined with the relatively simple geometry of each component, they are very good candidates for fastener reduction. The geometry is particularly amenable to bonding, as the planar, long stringer-skin interfaces naturally lend themselves to application of adhesive in tape or paste form. A representative stringer profile and component nomenclature are provided in Figure 2-3.

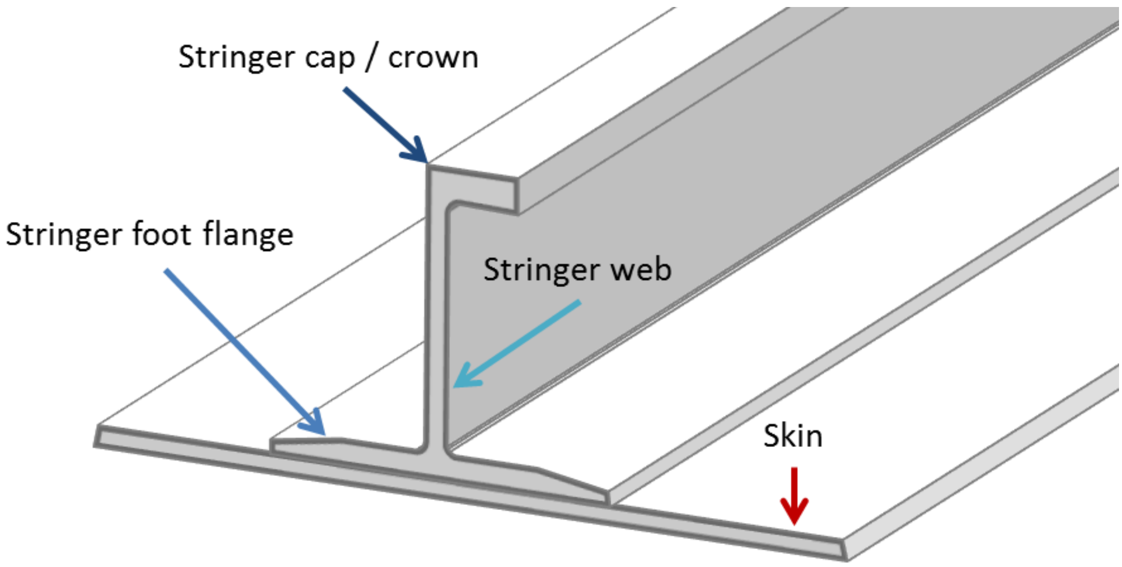

Figure 2-3. Stringer/skin arrangement and parts.

The adherends focused on are the following high-aspect-ratio parts:

- Planar skins several millimetres thick;
- Slender beams where one flange ('foot') interfaces with the joint and is generally wider than the others.

Indeed, these, along with skin 'doublers' for local reinforcement of the skin, were found to be the chief components of bonded assemblies in the FAA "Bonded Structures Industry Survey" referenced earlier, a result reproduced in Figure 2-4.

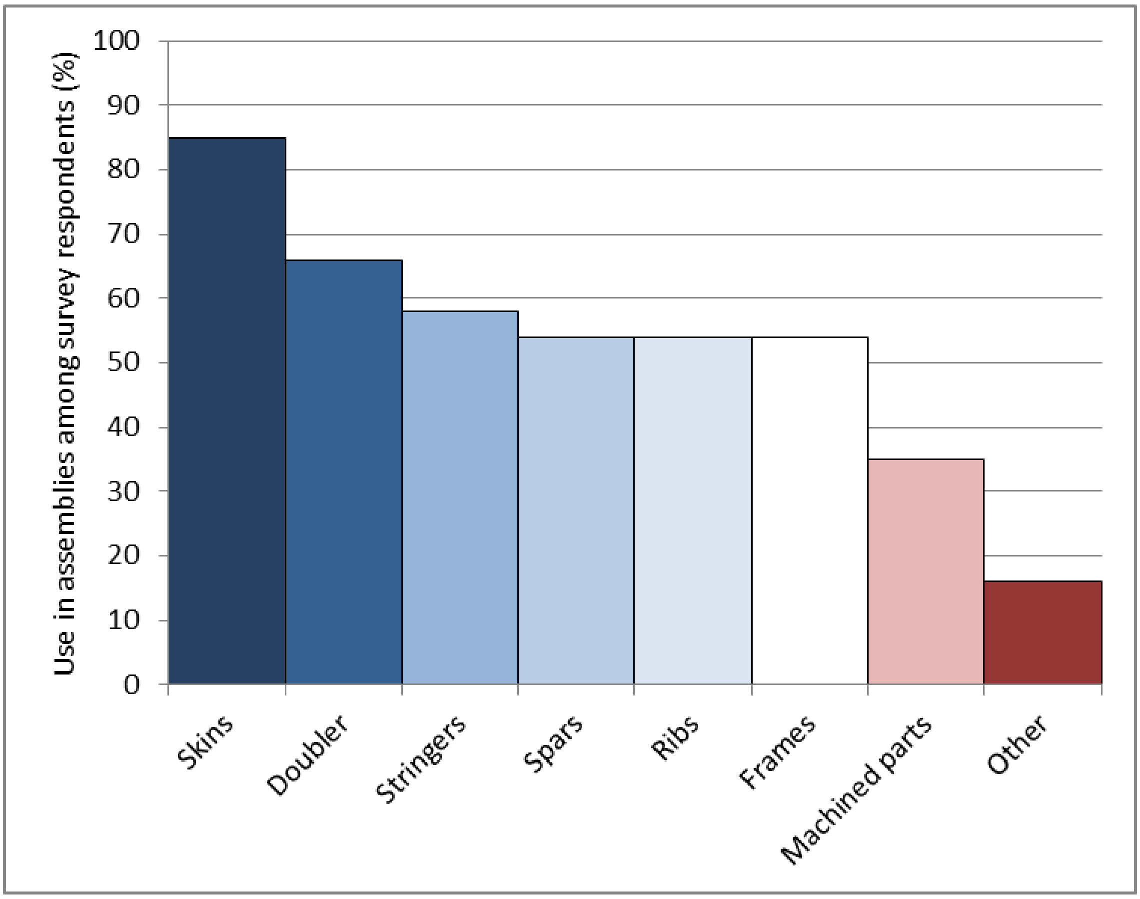

Figure 2-4. Frequency of inclusion of different parts in bonded assemblies across the aircraft industry. Chart generated by the author using the results of a 2004 FAA industry survey (Tomblin et al., 2005).

In addition, it should be noted that deflection is only considered inasmuch as it affects the bonded joint thickness; that is, out-of-plane deformation is the focus, and other deformations are only considered based on their effect on it.

2.2 Modelling part variation

Variation analysis, and more widely tolerancing, are fundamentally dependant on understanding of the input variations to the system. These are not only key determinants of the final variation, but also one of the most visible and readily-modifiable inputs that can be used to change the outputs. Indeed, the point of tolerance *synthesis* is precisely to find a suitable combination of these inputs, based on considerations such as production speed and the cost of manufacture, inspection and lack of quality. It makes sense, thus, to start the assessment of the state of the art by looking at the way incoming part variation is understood.

2.2.1 Recurrent paradigms

It is worth setting out some concepts which are referenced, implicitly or explicitly, by different authors. The scope of discussion is generally components with high aspect ratios, or with assembly interfaces which can't be modelled as a single point or node.

2.2.1.1 Skin model

In airframe assemblies, much of the interaction between parts takes place through large mating surfaces. Whenever this is the case, reducing the interfaces to simple 'feature' models with a few parameters attached may be ineffective, as such an approach fails to capture the complexity of interaction between surfaces. The concept of 'skin model' seeks to address this issue, modelling directly the interface geometries by explicitly looking at the position or deviation of individual control points (as exemplified in Thiébaut, 2016).

The points modelled in the 'skin', even if numerous, still could be collectively defined by a small number of descriptors; however, formulating them explicitly makes it straightforward to model how two surfaces will interact. Some features, such as control points or drilled holes, may still be modelled with more rigid paradigms.

It should be noted that although extensive exploitation and discussion of this paradigm for tolerancing has only taken place recently, it has been used for longer in studies of part interaction, whereby interaction of assembled parts would be studied looking at sets of nodes.

2.2.1.2 Part continuity/smoothness

The typical structural aerospace part will contain a collection of smooth, continuous-looking surfaces which interface with similarly smooth, continuous-looking surfaces in other subcomponents. However, a simple tolerance band does not quite capture this, as it does not preclude non-smooth geometries. Existing norms and GD&T conventions address this issue by adding other concepts such as spatial-frequency filters and profile tolerances over ranges. However, the underlying principle is not explicitly enunciated in these documents.

Researchers from the ADCATS[viii] group from Brigham Young University formalised the concept of node variation correlation (or covariance), whereby neighbouring points in a solid are not fully independent (Bihlmaier, 1999; Merkley, 1998). Rather, they are coupled both in their initial, as-manufactured variations ("geometric covariance", Figure 2-5) and in deformations under external and internal forces ("material covariance", Figure 2-6). Taking variation covariance into account was found to reduce the dispersion of results in assembly variation modelling; indeed, both concepts go hand in hand, with geometric covariance defining the input variability, and material covariance defining the ability to mitigate it.

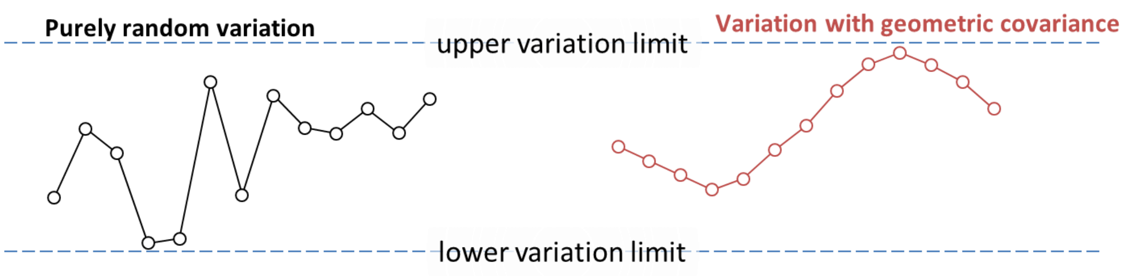

Figure 2-5. Illustration of the concept of "geometric covariance" or "surface continuity": the geometric deviation of a node is similar to that of its neighbours.

[viii] Association for the Development of Computer-Aided Tolerancing Systems

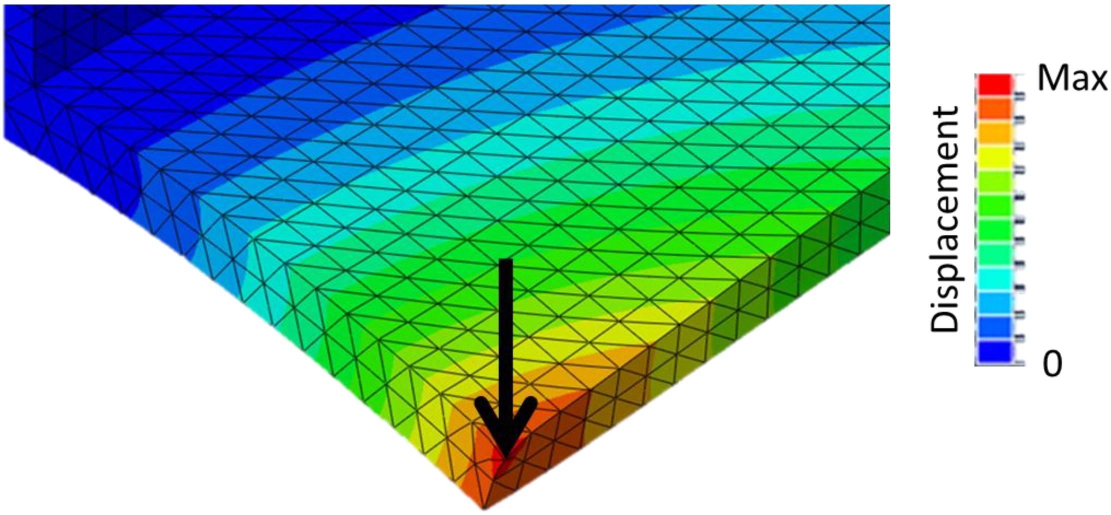

Figure 2-6. Illustration of the concept of "material covariance": when a force is applied to a body (in this case, the corner of the flange as indicated by the black arrow), the resulting deformation decays as one gets farther from the point of application.

Like for skin models, such formal definition is far preceded by the pragmatic application of the concept. For example, tolerance requirements which transpired from the PABST programme (Land and Lennert, 1979) contained multiple references to the shape and range in which variation could be allowed to occur, while Saint-Venant's principle indicates that the effect of a load has both global and local components.

2.2.2 Covariance-based dimensionality reduction

2.2.2.1 Principal Component Analysis (PCA)

In a set of part variation data in several points, for multiple instances of the same part, there usually will be some degree of correlation between variation at different points. However, it is possible to create an orthogonal base such that each variation component in the base (henceforth also referred to as "mode") is independent of the others, and the modes are not correlated. Part variation can thus be modelled as a linear combination of the modes created. In addition, a large number of points can be modelled reasonably accurately with a smaller number of nodes, thus simplifying modelling and inspection procedures substantially.

Creation of this base, dubbed Principal Component Analysis, is useful when a sufficiently-large sample of variation data is available, and the manufacturing process can be assumed homogeneous. It is limited in its ability to actually help draw *meaning* from the results, since the method is purely data-driven, with nothing informing the modes a priori. Furthermore, the need for a large and homogeneous enough sample makes it potentially risky to rely on the PCA approach for concept development or initial exploration of processes where little or partial data may be available.

2.2.2.2 Designated Component Analysis (DCA)

DCA was presented as an attempt to address perceived shortcomings of PCA (Camelio, Hu and Zhong, 2004; Liu and Hu, 2016). The principle is that *there is usually some prior knowledge about the sources of variation*, for instance, based on manufacturing processes or fixture design. Reasonably-expected modes (Designated Components) of variation are added into the variation base before analysing the part variation data. The resulting components are thus rendered more meaningful, and it is possible to diagnose the occurrence of the sources of variation modelled. However, the orthogonality (non-correlation) of the modes can be lost.

2.2.2.3 Deviation clustering

By modelling variation as a linear combination of non-correlated modes, it is possible to miss important nuances of variation. For example, part defects could come from mutually-exclusive sources (such as discrete changes to a system, like fixture resetting or different material suppliers). Clustering techniques have been presented as a further step that can be performed *on top of PCA* to enhance the understanding of variation mechanics. Work carried out within Australian National University (Matuszyk, 2008; Matuszyk, Cardew-Hall and Rolfe, 2010) showed that such approach (using, in particular, Kernel Density Estimation to generate statistical distributions around clusters) allowed to identify fixture faults and different clamping sequences in a sheet metal fabrication procedure.

2.2.3 Bézier curves

Pioneering work on deformable assemblies carried out within ADCATS explored variation modelling based on a small number of control points (Figure 2-7), while respecting the covariance considerations (Merkley, 1998). This was achieved by reducing the parts to their interfaces, and modelling these as Bézier curves (though acknowledging that similar results could be achieved with other models such as cubic splines). Variation of the control points was thus used as the system input, but still modelling a respectable number of interface points. In order to support reduction of the model to the interfaces, Merkley also presented a matricial procedure which would create a linear model based on these points from the FE model of a whole part.

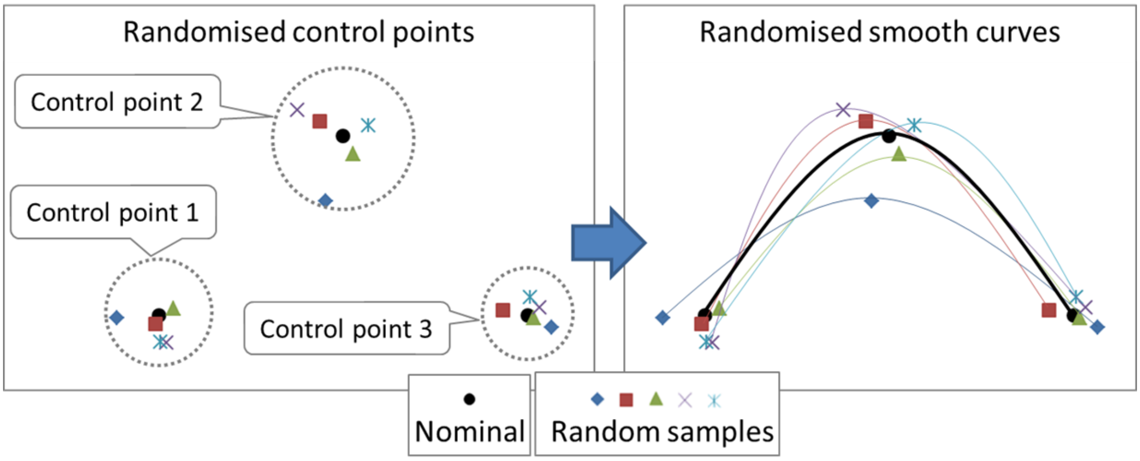

Figure 2-7. Modelling of profile with variations as a Bézier curve with randomised control points (as proposed by Merkley, 1998): a small number of control points (left) is used to generate smooth profiles which retain geometric covariance (right).

2.2.4 Spectral analysis by Fourier transform

Following Merkley's work, more ADCATS work explored modelling of variation as a linear combination of sinusoidal components (Bihlmaier, 1999). This was applied to sheet metal assembly modelling. In addition to using spectral analysis for dimensionality reduction, a covariance matrix of the amplitudes of the different modes was presented; this was applied both to the part and assembly variations, though without explicit discussion of the input variation assumptions.

2.2.5 Part vibrational modes

A body of work undertaken by the SYMME[ix] lab proposed improving mode-based variation simulation by considering intrinsic part characteristics, focusing on vibration harmonics for small, rigid machined components (Favrelière, 2009; Samper, 2009). The idea being that vibrations are key in part variation, it was found that, although modes from the lower-order harmonics were generally larger contributors to the parts studied, the relative importance of each was not totally straightforward. Within the practical application of the work cited above, the amplitude of each harmonic was not neatly correlated with its order: while some low-order harmonics contributed more variation than higher-order ones, others did not. Additional statistical treatment on part measurements, e.g. by PCA, was therefore necessary to allow realistic variation simulation.

One of the potential developments outlined within the aforementioned research was use of a modal base, created from typical failures or sources of variation within each manufacturing step, e.g. tool wear or part mispositioning; however, although a simple example was provided, there is no report of this idea being taken any further.

2.2.6 "Technological" modes

A piece of work carried out within the LURPA[x] group at École Nationale Supérieure Cachan in cooperation with EADS (now Airbus), and focussed on non-rigid assembly modelling (Stricher, 2013), used simple modes based on deformation archetypes. These were dubbed "technological modes" ["les modes technologiques"]. Two mutually-orthogonal flexure modes, plus a torsion mode, were used to describe the initial deformation of thin-section metal beams. These modes were not explicitly based on specific variation data, but rather engineering wisdom, and were used to demonstrate an assembly simulation method as well as pre- and post-processing applications. The mathematical definition of the

---

[ix] SYstème et Matériaux pour la MÉcatronique (System[s] and Materials for Mechatronics)

[x] Laboratoire Universitaire de Recherche en Production Automatisée (University Laboratory of Manufacture Automation Research)

modes, where the flexure was modelled with sines and the torsion was uniform, was not devised to reflect the mechanical behaviour of the parts either, as it did not incorporate any inertia or material qualities.

The same approach has repeatedly been employed by the ÉRICCA[xi]/LIPPS[xii] research groups in digital inspection testing, though making no formal enunciation (Karganroudi et al., 2016; Sabri et al., 2017): sheet metal components were modified by adding “torsional”, “flexural” and “bump” deviations, sometimes accompanied by “big” and “small” levels.

2.2.7 Physics- and process-based variation modes

It is acknowledged that variation assumptions based on mathematical abstractions, such as those presented above, may not be the most accurate or efficient way of modelling products with potentially complex geometries, material histories, and manufacturing processes — convenient as it is. Thus, when able, different research groups have attempted to incorporate concrete sources into their process simulations. This is the case in, for instance, demonstrations of the AnaToleFlex assembly simulation tool (Falgarone et al., 2016), sheet-metal assembly modelling with CAT software RDnT, and simulations for automotive products (Das et al., 2016). In these pieces of work, the need for simplified models (such as achievable from modal decomposition) is emphasised and justified with the computational cost of a component-manufacture simulation, which would make it prohibitive to simulate a large number of assemblies of different components. In any case, an *awareness* of the likely process-related variations is key to a successful tolerancing effort, even if process or production data may be sparse, especially at the design or pre-industrialisation stage.

2.3 Inspection of non-rigid components

High-aspect-ratio objects, such as the metal sheets and slender beams used in aircraft primary structures, deflect significantly under their own weight. Weight-

---

[xi] Équipe de Recherche en Intégration CAO-CAlcul (CAD-Calculus Integration Research Team)

[xii] Laboratoire d'Ingénierie des Produits, Procédés et Systèmes (Products, Processes, and Systems Engineering Laboratory)

induced sag and local deformations due to fixture defects have, in fact, been found to exceed measurement uncertainty from the measurement instrument itself. As a result, inspection is not trivial as it cannot be carried out in a purely stress-free state, while any fixture can also add to the problem. This means that very often the true assembly-fitness of a part or subassembly is not well known before an attempt at an assembly is made; by this point, corrective actions are costly due to lead time and material flow disruptions.

2.3.1 Functional build inspection: the legacy approach

A usual way of assessing conformance of non-rigid parts, not only in the aerospace sector, is to force them to their desired assembly state, subject to pre-defined allowable push or pull forces (Hammett, Baron and Smith, 1999). These tolerable forces are defined by stress or aesthetic considerations, or based on the assembly process (e.g. the deflection an operator could cause by hand pressure). Alternatively, the parts can be placed on a highly overconstrained fixture which simulates the stress-free state, and measured on it. Both approaches suffer from limitations:

- Acceptable forces may not be easy to define, as a part that complies with build stress requirements may still result in unacceptable loss of quality due to e.g. thermal instability or rattle;
- Usually not all mating points can be assessed, which results in non-conforming points surfacing only during assembly; this is especially critical for continuous joints like adhesive or welded lines.
- Product-specific fixtures are needed, incurring significant capital cost and a large shop footprint; alternatively, costly flexible or reconfigurable fixtures may be used instead, but requiring more frequent recalibration.
- Fixtures need to be assumed reliable. However, in industries with long parts (such as aerospace) or high throughputs (such as automotive), it is hard to consistently keep them within the tight assumed tolerances without frequent downtime for recertification or extra investment in embedded metrology solutions.

All in all, it is of interest to find ways of reducing reliance on highly specialised inspection fixtures, which are expensive and sometimes not that reliable to begin with.

The first reported study on implications of fixtures for inspection of non-rigid products was produced by the American Auto/Steel Partnership (A/SP) and focused on measurement system capability for car bodies (Hammett, Baron and Smith, 1999). Looking at inspection schemes for similar products in different manufacturers, it was concluded that adding constraints beyond kinematic to the part being measured (by clamping more than the theoretically sufficient 3 points), the *perceived* manufacturing capability increased by squashing out individual variations. However, such approach also introduced measurement biases which could become noticeable later during assembly.

The A/SP report reached the conclusion that inspection of parts in an overconstrained state is not necessarily detrimental to success of the overall manufacture, as long as it is carried out with a “functional build” design; that is, as long as the forces applied during inspection are representative of the final assembly state. The report concluded by suggesting that, based on satisfactory assembly outcomes, a functional build approach may actually be *the* preferable option: “this potential impact of measurement systems on mean dimensions further supports the implementation of a functional build strategy”.

However, as pointed out before, inspection by fully emulating the assembly state can be too complicated or time-consuming to be practicable, in addition to causing loss of potentially valuable geometric data.

2.3.2 Virtual deformation

An alternative approach to non-rigid component inspection, based on virtual assembly simulation, was applied to precision optics in the Lawrence Livermore National Laboratory (LLNL). A vision system was used to digitise a manufactured component, and the target assembly conditions were then added to the resulting finite element model (Blaedel et al., 2002). Details of the procedure were not disclosed, with the process simply schematised as per Figure 2-8. A similar strategy (Weckenmann, Gall and Gabbia, 2005) was later proposed for sheet metal, and dubbed “Virtual Deformation”. More recently, this philosophy was expanded with automated boundary condition definition and used to predict quality of assembled consumer products (Gentilini and Shimada, 2011). The main limitations of such approaches, where a scanned object is then virtually deformed to fit assembly, are that full digitisation of the object from a scan is not always feasible, and the stress conditions *during the digitisation* are not necessarily clear; further, sometimes only a limited number of critical points or features actually need to be inspected, which makes full digitisation unnecessary and potentially wasteful.

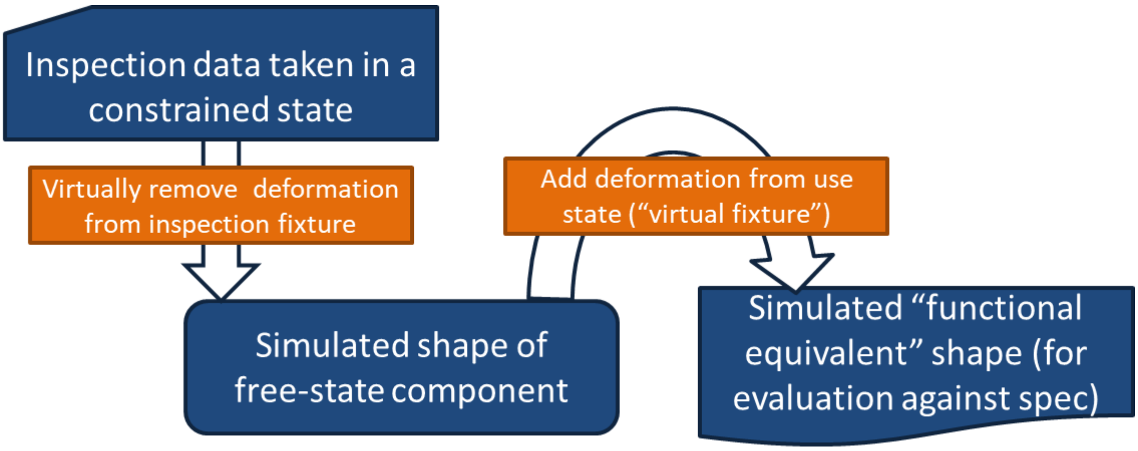

Figure 2-8. The virtual deformation approach flow, as first presented in a LLNL report (based on a figure in Blaedel et al., 2002, p.6).

The “Virtual Deformation” method was reworked soon after its first publication and dubbed “Virtual Reverse Deformation” (Weckenmann, Kraemer and Hoffmann, 2007), where a nominal model was deformed according to an assumed inspection state (which can then be imposed through a simple fixturing scheme). Measurements can be then compared to the nominal “inspection stress state” object to assess conformance to specifications. This approach has reportedly been used effectively in first article inspection to improve manufacturing of rapid-prototyped parts (Bouchenitfa et al., 2009; Boukebbab and Bouchenitfa, 2009), though without explicit reference to the prior art. It also has been refined to accommodate partial scans and allow automated boundary recognition (Jaramillo, Boulanger and Prieto, 2011; Jaramillo, Prieto and

Boulanger, 2013), although this specific application required off-line system training.

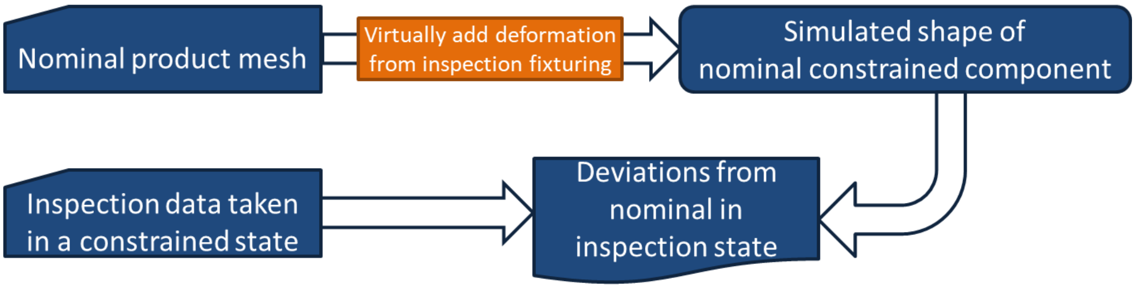

Figure 2-9. The Virtual Reverse Deformation approach (based on Weckenmann, Kraemer and Hoffmann, 2007).

Inspection based on virtual deformation is limited by the need to control the boundary conditions so that part deformation can be calculated reliably. To the best knowledge of the author of this thesis, no study has been done on how variations in the real boundary conditions translate into inaccuracies in the calculated inspection state.

2.3.3 Non-rigid registration

Following the surge in computer capacity and capabilities of optical measurement systems, a variety of algorithms for fixtureless inspection of sheet metal have been explored in works developed with Bombardier Aerospace, the ÉRICCA and LIPPS groups in Canada, and UT Dortmund in Germany. The basic idea is to deform an inspected mesh to make it fit a nominal mesh, which is normally called "non-rigid registration". These methods work based on an assumption of known, controlled thickness, which allows fully digitising an object by inspecting it in one single position with an optical scanning system. It is assumed that the parts can be flexed indefinitely, but are not subject to in-plane stretching (much like a piece of paper). This is translated into a condition of geodesic distance preservation, whereby the parts can be deformed as long as the node-to-node distance is kept invariant. (Aidibe, 2014)

The first embodiment of such an approach, called Iterative Displacement Inspection (IDI), requires a certain level of closeness between the nominal and inspected state (Abenhaim et al., 2011). The scanned and nominal meshes are first aligned roughly, and correspondences between nodes in both meshes are estimated. The nominal mesh nodes are then subjected to coherent displacements towards their counterparts in the scan, calculated in such a way that distance between them is preserved. This proposal was tried on aerospace components. An approach similar in philosophy, but different in implementation, has recently been applied to automotive stampings (Schweinoch et al., 2016); in this case, coherent deformation is achieved by first rigidly displacing whole sections of the mesh, and then re-establishing connectivity so as to minimise strain energy.

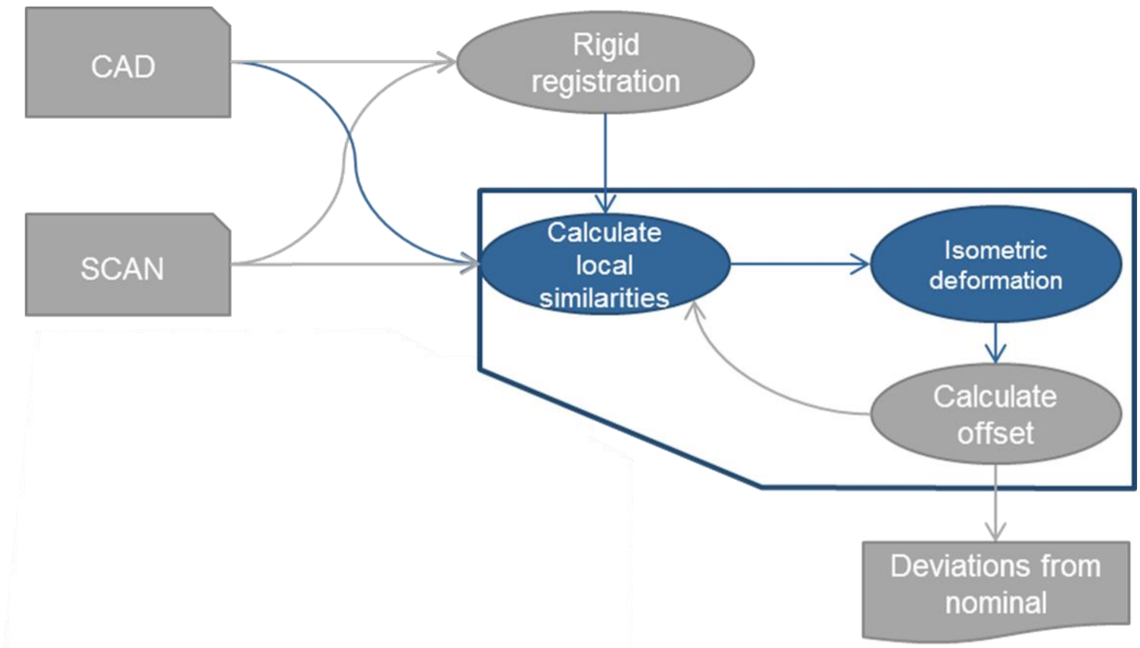

Figure 2-10. The IDI algorithm detects defects in areas where isometric transformation between the scan and nominal is not possible. (based on Aidibe, 2014)

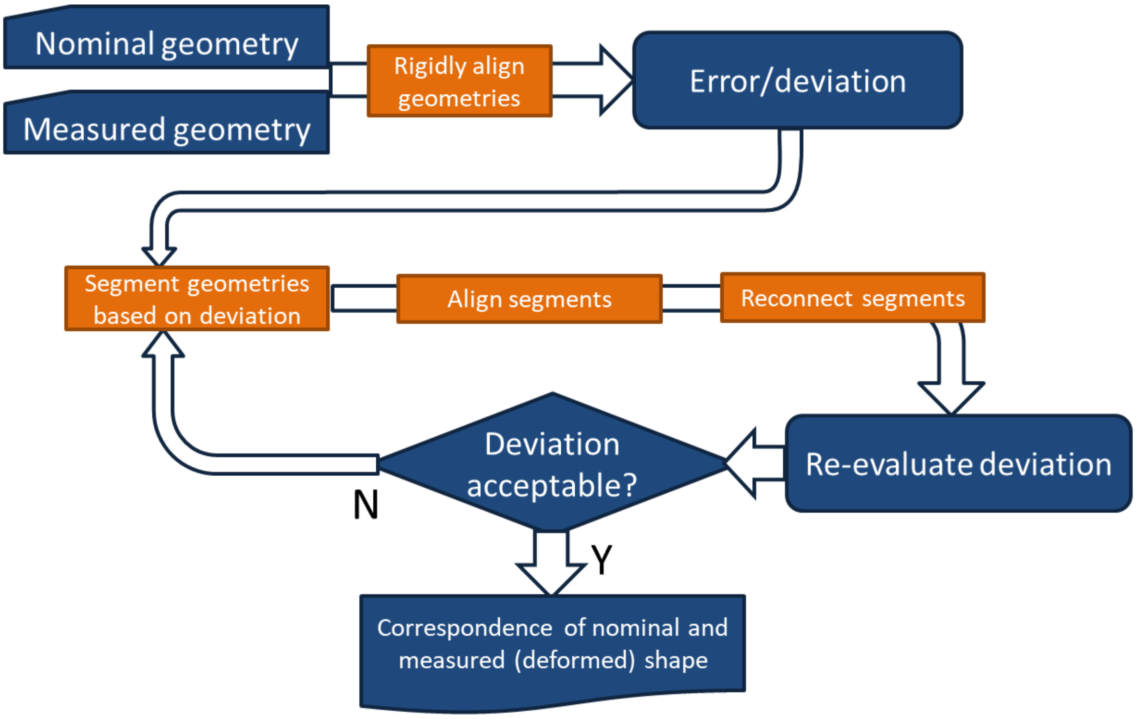

Figure 2-11. Non-rigid registration by segment rigid registration and mesh rebuilding (based on Schweinoch et al., 2016)

The Generalised Numerical Inspection Fixture (GNIF) method (Radvar-Esfahlan and Tahan, 2012) is based on enforcing isometry from the beginning. Initially, the geodesic distances between all the nodes in an object mesh are calculated; then, a dimensionality reduction algorithm is used to map the mesh to a simplified “canonical form” (Figure 2-12). Digitised parts are mapped similarly, and deviations are calculated between the simplified canonical forms. This algorithm was later improved into the Robust Numerical Inspection Fixture (RNIF) by addition of an outlier-filtering step which makes it more robust to scanning noise and large defects (Radvar-Esfahlan and Tahan, 2014). However, even with outlier filtering, it still suffers from excessive variations in the canonical form if the inspection stress state causes large local deformations in the part.

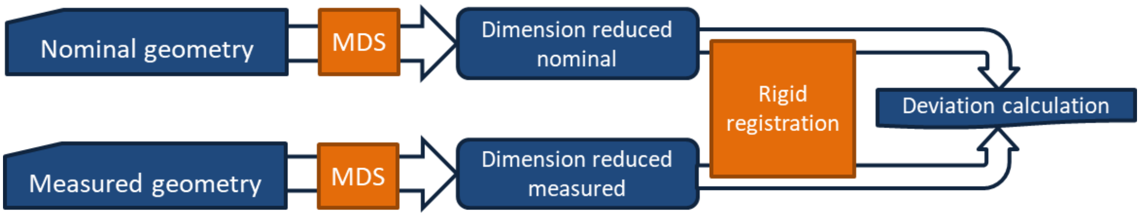

Figure 2-12. Scheme for mapping of sheet metal to a "canonical form" in GNIF. Mapping is performed with Multi-Dimensional Scaling (dimension reducing) algorithms and the canonical forms are the ones being compared. (based on Radvar-Esfahlan and Tahan, 2014)

The GNIF concept is still subject to improvements. More recent developments have focussed on mitigating measurement errors (Karganroudi et al., 2016), resulting in successive application of filtering techniques based on criteria such as local curvature fluctuations and mesh deformation stress. It has been found that the stress state cannot be readily computed from the inspected mesh, as node-based geodesic distance calculation introduces cumulative errors which can result in large in-built fictive stresses.

Another set of algorithms are built on the Coherent Point Drift (CPD) registration algorithm, initially developed for recognition of tissues and other highly non-rigid objects in medical applications (Myronenko and Song, 2010). CPD iteratively applies coherent (that is, correlated within a neighbourhood) displacements to a given pointcloud based on probabilistic estimations based on each node's position relative to the others. Because CPD allows for body stretch, it cannot be used straight away on parts which aren't non-rigid in all directions, unless the part is close to nominal in the inspection state by e.g. being relatively stiff (Ravishankar, Dutt and Gurumoorthy, 2010). The first adaptation to isometric conditions (Sacharow et al., 2011) was achieved by adding a "mesh reintegration" step where, after each iteration, the displaced mesh elements were re-connected and reoriented based on trigonometric considerations. In a later attempt by a different group (Aidibe and Tahan, 2015a, 2015b), an initial series of simulations had to be performed to tune the parameters until transformations were distance preserving within a specified tolerance. This was enforced by minimising a "stretch" objective function.

A different strategy is based on local curvature estimation (Aidibe and Tahan, 2014, 2013). A correspondence is established between the nominal and inspected meshes, and defects are identified as large local variations in estimated curvature. This means that large, long-range defects (such as a bulge in a skin) are not flagged by the algorithm, but small kinks and shape or position variations in stamped features generally are.

An obvious weakness of the non-rigid-registration based algorithms, as described above, is that no previous knowledge of where defects come from, where they may appear, or any particulars on how they are expected to look like, are considered. This is in addition to the strong assumptions which make them applicable to sheet metal only. Furthermore, a large amount of information (in the form of point clouds) is needed, and thus these algorithms rely on specific measurement systems and setups, which may not always be viable for high-rate manufacturing.

It is clear from the above that non-rigid registration techniques are not necessarily fully mature for widespread application, given the multiple sources of uncertainty both in data acquisition and in the algorithms themselves that must be overcome. However, it is their current limitation to sheet metal, as well as the radical departure from existing industrial practice, that truly make it of interest to consider other alternatives for the nearer term.

2.3.4 Virtual fixture setting

A highly interesting, though small, corpus of work has focused on the reduction of clamping in existing inspection schemes. These were based on the "functional build strategy" inspection approach, where multiple clamps and weight application are permitted for bringing the part to nominal on a highly overconstrained fixture.

One of these applications, presented by researchers affiliated with Volvo Cars and Chalmers UT (Lindau et al., 2012), involved digitisation of a carbody part in a state of reduced clamping, and using MIC to simulate the fully-clamped state under the assumption of allowable clamping forces. The fully-clamped state was well aproximated, in addition to reducing fixturing time and preserving more shape information on the part (which would otherwise have been effaced by overconstraint).

Such an approach offers clear advantages when compared with a pure virtual-deformation philosophy, as it allows adaptation of existing “functional build” inspection criteria for smaller overheads and greater access to information. Furthermore, virtual fixture setting allows partial reuse of existing tooling, while supporting insertion of alternative measurement systems as necessitated by new quality requirements. For instance, clamp removal allows improved access of optical scanners which obtain larger volumes of information with greater repeatability than manual feeler gauges. The same could be expected of the complex multi-point supports used in checking of large aircraft components.

The fact that assembly related tools have been used for inspection should not come as a surprise, as inspection involves, ultimately, temporary *assembly* of a part to a fixture, complete with application of forces from weight, contact with supports, and clamping.

Independently, a procedure similar to that outlined above, dubbed FE-BDC (Finite Element Boundary Displacement Constrained) was applied to inspection of sheet metal aerospace components (Abenhaim et al., 2015a, 2015b). In this case, due to reduced line of sight to the multi-point fixture supporting the part, the position of each support was estimated, and displacements were simulated taking into account pressure application allowables and contact with the fixture, using constrained function optimisation tools available in MATLAB. The FE-BDC method was reported to be superior to “current methods”, understanding these as virtual deformation based on assumed boundary conditions; however, a thorough description of the implementation of these was never provided in the references above. In addition, fixture defects were not explicitly addressed in the methodology, and only mentioned *a posteriori* as the likely cause of a discrepancy with the physical results.

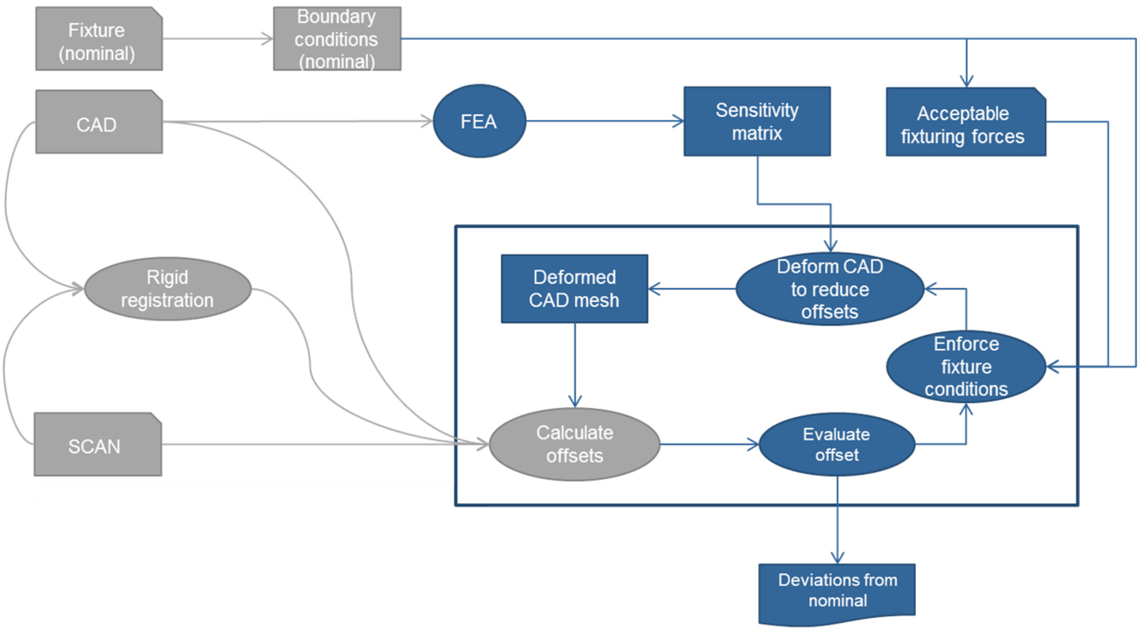

Figure 2-13. Outline of the FE-BDC virtual fixture setting method (based on Abenhaim et al., 2015a)

More recently, metrology company GOM has announced a “virtual clamping” capability to complement light scanning and computational tomography systems (GOM, 2019). This is aimed chiefly at sheet parts which would typically require clamping for inspection, such as stamped automotive components. At the time of writing, further details had yet to be disclosed to the public.

2.3.5 Virtual assembly

The current state of non-contact scanners and computational systems is such that virtual assembly could be performed for all components that go through a manufacturing system. This links directly to the much topical concept of factory and product digital twins. If this is the case and all assemblies are simulated, could quality compliance not be steered with these results? This would, after all, be no different from the pre-assembly, pre-fit or functional build approach, and indeed would offer to provide more accurate stress data too.

In fact, this concept has been advanced recently for aerospace. It has been proposed that not just quality checking, but *part matching* could be performed from digitised parts. Components with the right variations would be combined such that all the production meets stress and dimensional requirements (Thiébaut, 2016). Such production system would be able to relax dimensional requirements by enabling efficient manufacturing processes without an interchangeability requirement on components — as already demonstrated in “selective assembly” through batch matching in the automotive sector (Kern, 2003) — though potentially compromising reparability and serviceability[xiii].

2.4 Non-rigid assembly tolerancing

Formalised study of non-rigid parts may have escaped the aerospace industry for a while, but this is not the case for mass-producing sectors where one-by-one rework is not viable, and where the cost of procedure or design changes can be recovered faster owing to high production rates and lower cost of failure. These fall closer to consumer products, and especially automotive sector.

Systematic exploration of assembly tolerancing with non-rigidity considerations started with work carried out in University of Michigan, focused on the automotive sector. This work consists of two main strands: Stream of Variation (SOVA), which models propagation of locating and machining errors in multi-station manufacturing processes; and weld variation simulation.

2.4.1 Datum Flow Chain and generic deflection allowance

A feature-based approach to assembly tolerance analysis and design optimisation was developed by MIT researchers (Whitney et al., 1999). The Datum Flow Chain (DFC) method turns a complex assembly into a graph (Figure 2-14) which connects various features (nodes) with links that represent feature interaction and dimensional requirements. Each assembly link is given a weight representing the tolerance or variability of the joint, based on physical tests or engineering expertise. Different assembly paths can thus be evaluated procedurally with little effort based on a tolerance stack approach (e.g. by using

---

[xiii] The author’s experience is that the prospect of abandoning interchangeability can be quite divisive. Though critics will draw attention to the need for a stock to draw parts from, and problems generated through the product lifecycle, it is also true that many large assemblies already are not truly interchangeable — requiring match drilling or largely-manual interface management operations.

Dijkstra's algorithm). Some human intervention may be needed to assess actual viability of an optimised assembly path (due to e.g. access issues). Although initially based on rigid assumptions, DFC can be expanded to account for part deflection by adding clearance/deflection tolerances, e.g. by considering the acceptable compression of a bolt in an interference fit. DFC has been used to optimise aerospace assemblies (Naing et al., 2001). However, it offers limited potential for structural joint analysis, as the joining features themselves are the simplest elements of the graph. Large mating surfaces where gaps or clashes may appear only locally (as in a skin-stringer joint) are similarly not well characterised by this method.

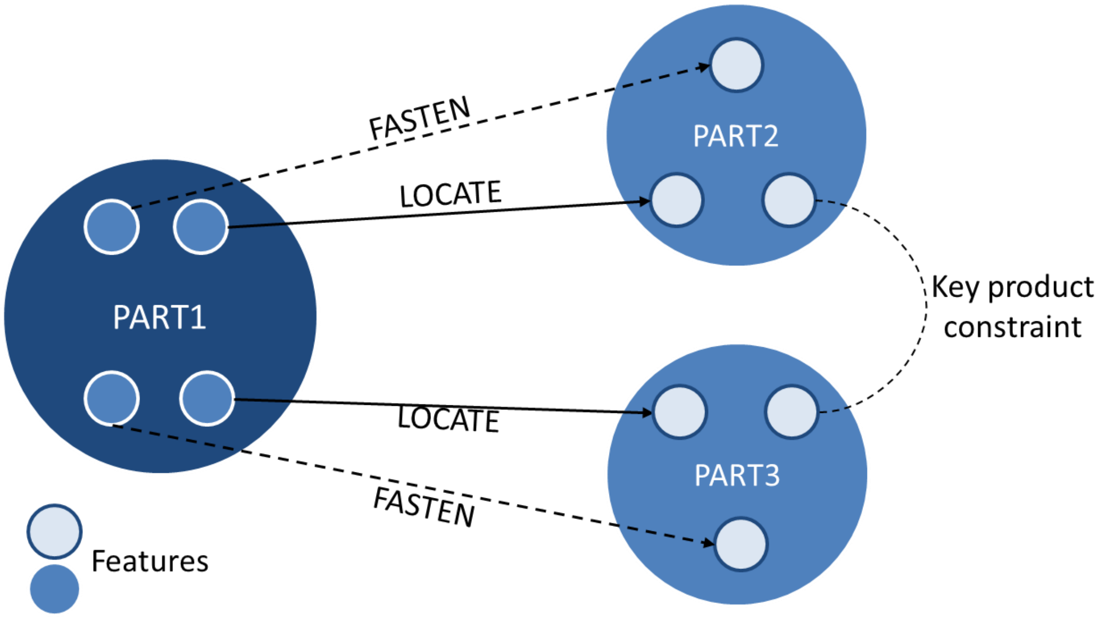

Figure 2-14. Simple example of a DFC for a subassembly, where elements display different relationships and functions. (based on Naing et al., 2001)

2.4.2 Stream-Of-VAriation (SOVA)

SOVA typically uses transformation matrices (conveying translation and rotation) to model positioning and geometrical errors from fixturing and datum schemes. The resulting matrices can be interrogated by feeding them variation distributions (for tolerance analysis) and for diagnosability of each defect. The matrix-based modelling works well with processes taking place in succession, thus forming a "stream" (Figure 2-15). An important conclusion from SOVA modelling is that non-conformance in ‘parallel’ assemblies (e.g. where components are stacked) can not be subject to full diagnosis if the individual parts are not known (Hu, 1997).

SOVA has been extensively worked on to incorporate various machining-related defects (e.g. tool wear, spindle deflection), as well as non-rigid assembly defects such as springback of the welded assembly after clamp release. The method has also been used for fixture error diagnosis and assembly inspection optimisation. It also has been integrated with process-oriented tolerance synthesis (Abellán Nebot, 2011), by incorporating cost functions for different sources of variation. However, the usefulness of SOVA for the aircraft industry is not clear due to the different characteristics of the product: it considers multi-station processes with kinematic (3-2-1) fixturing, whereas many aerospace components are placed on overconstrained (N-2-1 or N-M-O) fixtures[xiv], machined with little repositioning, and then possibly subjected to forming operations. Furthermore, SOVA considers joints given by kinematic fixturing schemes; this is not representative of many joints in aerospace products, which are highly overconstrained (Stricher, 2013).

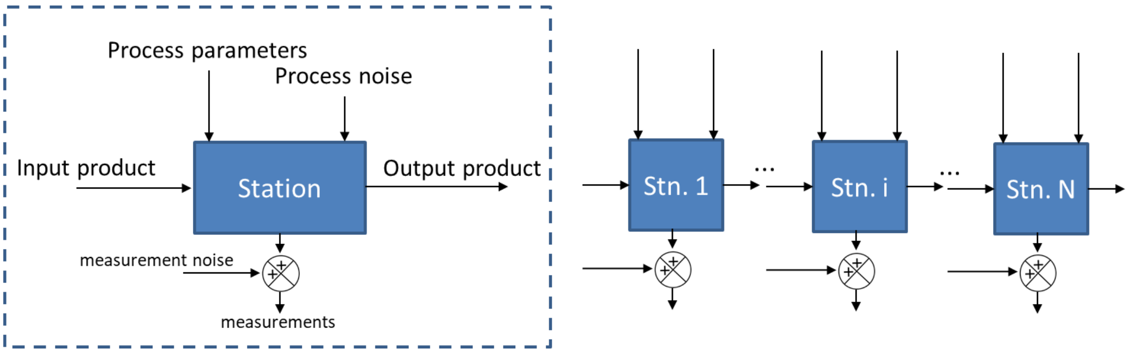

Figure 2-15. Top-level concept of SOVA, where at each station some process parameters cause a transformation in the product state, and measurements may be taken; all subject to noise. Left: single station. Right: generic serial ‘daisy chained’ station arrangement. (Huang and Kong, 2008)

2.4.3 Direct Linearization Method (DLM)

A very simple approach for non-rigid assembly modelling consists of reducing each part to a linear model comprising a subset of discrete points, and applying

[xiv] With x-y-z referring to the number of displacement constraints on each axis. A 3-2-1 fixturing arrangement is kinematic i.e. not overconstrained.

joining operations (e.g. applying a force or a displacement constraint) to matching nodes. Such application was developed within research for General Motors (Hsieh and Oh, 1997a); The implementation joined designated nodes of an assembly's subcomponents, precluding both tangential and normal relative displacements, and without contemplating contact at non-joined spots. A genetic algorithm was used to find the weld sequence that minimised a deformation score. The work was applied to a sheet metal car component, and was presented alongside a bespoke set of "coding blocks" intended to streamline industrial use (Hsieh and Oh, 1997b).

2.4.4 Method of Influence Coefficients (MIC)

The mechanistic variation model, more usually named Method of Influence Coefficients, was proposed for stochastic tolerance analysis of welded assemblies (Liu and Hu, 1997). This method consists of a direct linearisation based on finite element analysis for calculation of force responses of designated nodes, which allows quick calculation of assembly forces and springback in a typical Position-Clamp-Fasten-Release (PCFR) cycle as depicted in Figure 2-16. By linearising the response of the non-assembled and assembled state, joining elements such as spot-weld nuggets or fasteners can be accounted for. This method was later integrated in SOVA (Camelio, Hu and Ceglarek, 2003).

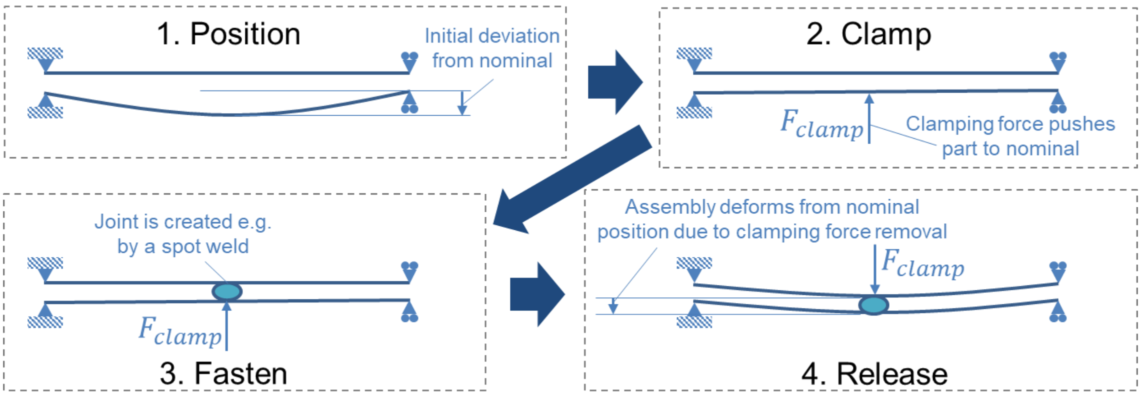

Figure 2-16. A PCFR cycle illustration (Camelio, Hu and Ceglarek, 2003). The springback is calculated by MIC considering part and assembly stiffness.

MIC (like DLM) is limited by its linearity assumption, as it requires small deformations and does not account for unilateral contact (that is, that some nodes may or may not be in touch, an interaction that can not be modelled linearly). In addition, part variation has typically been simulated with simplistic assumptions which there was no effort to justify, or even were justified as simply convenient and “of no physical significance” (Ungemach and Mantwill, 2009).

It is worth noting that MIC, though very reminiscing of a DLM procedure, enables streamlining of repeat calculations by deriving the sensitivity matrix. In addition, a stress (rather than strain) sensitivity matrix has been shown to be usable for fast calculation of assembly stresses (Lorin and Lindkvist, 2014; Söderberg, Wärmefjord and Lindkvist, 2015).

2.4.5 Node joining within ADCATS

The work carried out in the late 1990s decade by Brigham Young University’s computer-aided tolerancing research group dealt primarily with bolt-based joining of sheet metal, along relatively narrow interfaces (Bihlmaier, 1999; Merkley, 1998). As such, assembly was modelled as simultaneous joining of a set of matching nodes from FE meshes of opposing parts. By assuming no excess compressive load or residual gap was left by the clamping and fastening stage, a determinate linear system was formulated. The geometries fed into this model were informed by the concepts of variation correlation proposed by the same group.

This modelling approach is insufficient for problems where contact interaction of parts is considerable, or where assembly details are stiff enough that a residual gap may be left. However, it offers a very quick way of simulating geometries which conform to the modelling assumptions; for example, joining two fuselage panels in a fuselage section by a single row of rivets.

2.4.6 Tolerance domain and flexible tolerance domain

Some work within the SYMME research group has focused on the translation of tolerance requirements into polytopes or sets within a dimensional hyperspace, referred to as “domains”. The idea is to use set operations to build variation spaces which can then be checked against functional tolerance such as total length or play between parts. This has been extended to include “inertial tolerances" which draw from Taguchi's quadratic loss function (Adragna, 2009; Mansuy, 2012); in such case, stochastic analysis is needed (as the quadratic loss function does not support basic set operations, which are linear). Though initially aimed at small parts assumed rigid, it was found that adding allowable assembly forces expanded the tolerance domain noticeably. It must be noted that this line of work was more concerned with small, precision machined parts, such as bearings and shafts, where deformation would be compressive rather than flexural (Samper, 2009).

2.4.7 Expanding MIC

Industrial researchers from Chalmers University of Technology have worked extensively on improving the initial concept of MIC to support tolerance analysis of increasingly complex assemblies. Central to this work is the standalone software RD&T ("Robust Dimensioning and Tolerancing"), which is commercialised through a Chalmers spinoff.

Possibly the first breakthrough addition for the purpose at hand was contact considerations into MIC (Dahlström and Lindkvist, 2007). This was done by combining a contact node search function, whereby each master node interacted with three slave nodes, with an iterative contact enforcement system later dubbed Node-Based Iterative Push, or NBip (Lindau et al., 2016). Results of sheet metal welding simulation were found in much better approximation to full FE simulation than MIC without contact; in trade, however, computation times rose sharply due to the lengthy contact enforcement process. The NBip method was revised for faster computation (Lindkvist, Wärmefjord and Söderberg, 2008) by considering node-to-node contact only and automated mesh coarsening, and applied to welded assembly of two sheet metal frames based on real part measurement data. The paper did not include stochastic analysis, but rather was applied on a case-by-case basis to a set of assemblies.

Additional developments from Chalmers UT include adding clamp friction considerations (Lindau et al., 2013), integration with thermal expansion (Lorin et al., 2013) welding variation (Pahkamaa et al., 2012) and streamlined contact condition enforcement (Lindau et al., 2016). Additionally, recent developments have shifted from automotive welding to other components such as composites for aerostructures (Söderberg, Wärmefjord and Lindkvist, 2015) and aeroengine fabrication (Madrid et al., 2016).

Another stream of work, though not continued as far as public reports go, was developed in a doctorate within ENS Cachan (Stricher, 2013). In this case, MIC, plus the contact search and NBip enforcement initially proposed by Dahlström and Lindkvist in 2007, was used to model riveted assembly of typical airframe structure components such as slender beams. Stricher implemented the assembly simulation using the software CAST3M with an extension written in the programming language Gibiano, and modelled each riveted joint as a group of nodes rather than a joint in a node pair. Part variation was generated as a linear combination of “technological modes”[xv] of flexure and torsion, admittedly not based on any particular observed mechanism. The work used the method of initial deformations (assuming the parts were clamped to their nominal position on making a joint) and predicted final strains and stresses, although stress values at fastened locations were found too high to be realistic. Such unrealistic result is expected (as indicated in the thesis in question itself), given the high local stresses which are caused by fastener insertion, and the lack of plasticity considerations in the model. Joint formation mechanisms, such as local plasticity and material expansion around the rivets, were not included in the model.

In addition, Stricher investigated expansion of MIC outside small deformations by adding displacement-dependent terms to the compliant matrices. This was supported by defining compliance matrix corrections for each “technological mode”. Stochastic simulation and comparison to FEA showed that mode-based corrections to the compliance matrix did not appreciably improve the model’s accuracy, unless one variation mode was clearly predominant. It was suggested that mapping interaction of variation modes might improve the results, though risking a substantial increase of the cost of model generation. Realistic variation modes were identified as one of the desirable future developments.

[xv] This is a literal translation of the original French “modes technologiques”

2.4.8 Modelling of joint characteristics

All the work referenced is based on a premise that allows substantial simplification: any design joint results in a zero or negligible gap between parts, and the mechanics of the joint formation itself are irrelevant. Indeed, no matter the process, riveting, tacking, or spot welding, the modelling approach is the same: target nodes are joined and their displacements henceforth equated. Similar assumptions have been used in the limited work conducted specifically for clip fastening of thin sheet (Wärmefjord et al., 2016), whereby *clusters of nodes* would be held at zero normal gap but allowing tangential slip. This is still somewhat inaccurate, however, as fasteners inserted with interference fit cause expansion of the assembly details, and welds are formed with a heat input and subsequent material property change.

The node-to-node joint simplification is, in any case, not applicable to other assembly methods, such as seam welding and adhesive bonding, where the joint is continuous (rather than at discrete spots), new material is added to the joint, or material properties change (due to e.g. thermal expansion).

Variability of assemblies with continuous joints has been addressed in a limited fashion, with investigation of fillet weld variation in a T-joint (Pahkamaa et al., 2010, 2012). The simulations conducted coupled use of the softwares RDnT (for fixturing variation generation and postprocessing) and VrWeld (for generation of the weld fillet elements and heat). The weld elements were generated between mispositioned parts, thus changing the initial dimensions of the joint. In another instance, the weld elements were created from preexisting nodes in the parent material which were estimated to surpass the melting temperature (Wärmefjord et al., 2016). In both instances, for deformation purposes, all the heat input was applied at once or in few stages rather than transiently, and all associated dimensional changes were assumed elastic. Thus, by eliminating time-step calculations and linearising material behaviour, the computational cost was kept low enough for stochastic analysis to remain viable (Wärmefjord et al., 2016). Even for a simple case assembly, such as the T joint cited above, the variations caused by the welding process were found to be amplified by the fixture variation;

this was without even considering non-nominal part shapes. This result showed that simply adding the different sources of variation is not enough to predict deformations satisfactorily.

2.4.9 Applications in aerospace

Not many examples are found in the literature where real — or realistic — variation data was fed into stochastic assembly modelling. This is at least in part due to the difficulty in acquiring variation data in the first place. However, some attempts have been made at introducing real, or at least arguably representative, variations into the tolerance analyses at hand. Incidentally, this is very much the case in aerospace applications.

An interesting example is found in development of a wing demonstrator during the ALCAS[xvi] programme (Maropoulos et al., 2011). In this case, since the part was a one-off, a hybrid approach was adopted whereby some parts were measured and their real dimensions used, while other components were assumed based on specifications or prior knowledge. Monte-Carlo assembly simulation was then performed using the 3DCS workbench for CATIA, adding measurement uncertainty to the considerations. This resulted in reduced overall uncertainty. Some of the predicted variations did not match the final assembly measurements (though they were closed based on the overall variation range permitted by the component specifications); discussion of the reasons for this is not publicly available.

Another relevant example comes from studies of fastened assembly optimisation conducted within Zhejiang University in collaboration with Chengdu Aerospace Industries (Liu et al., 2014, 2015). The optimisation was developed for fuselage shells. In this case, a series of skin-stiffener gap measurements are performed on the fixtured assembly details before fastening operations begin. Temporary fastener sequences are optimised attending to considerations of predicted residual gaps and number of temporary fasteners, where deflections are calculated based on a superelement compliance matrix obtained in the fashion

---

[xvi] Advanced Low Cost Aircraft Structures

of MIC. Though initially based on measuring each fastened point at each stiffener, the method was later refined to build a randomised set of splines (much like in Merkley's approach that used B-curves) based on a small set of measurements. A single "overall best" fastening sequence was then found using a genetic algorithm. The initial iteration of the work underestimated the final gaps, possibly because it did not account for contact. In the later work, contact was integrated and a programme interface was created that lets the operator tweak optimality criteria.

Within the LoCoMACHS[xvii] programme, work was undertaken incorporating process-dependent variations, although this approach was not described with any reference to a modal base (Falgarone et al., 2016). Aerospace part variations were reported to be simulated based on small changes in process input parameters, without further detail. The assembly was simulated using the software AnaToleFlex, developed within the research programme, which uses MIC to include non-rigid considerations. Also within LoCoMACHS, a work package for affordable liquid shimming developed a system whereby part measurements and acceptable assembly forces were used to predict shim volume (Figure 2-17). The work used a specialised functionality within AnaToleFlex; publicly available reporting does not include discussion of liquid shim behaviour such as pressure required, compaction, or flow (Engström, 2015). AnaToleFlex was similarly used to support tolerance management in a composite wing cover (Figure 2-18).

[xvii] Low-Cost Manufacturing and Assembly of Composite and Hybrid Structures.

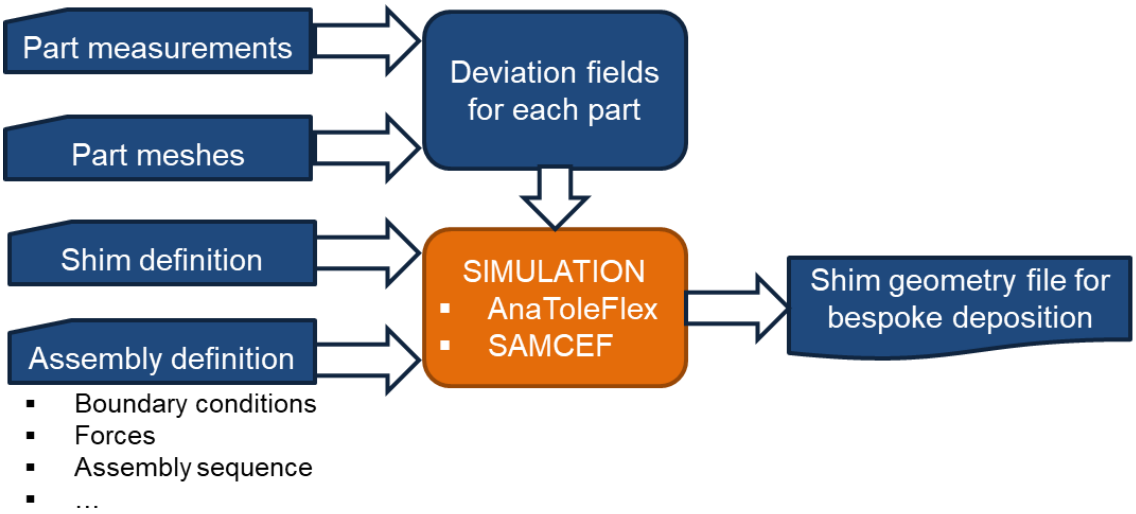

Figure 2-17. Schematic showing how part geometries, assembly sequence and process forces (but not shim properties) were accounted for in the work "Predictive gaps simulation for robotic AM shimming" (Engström, 2015, p.21).

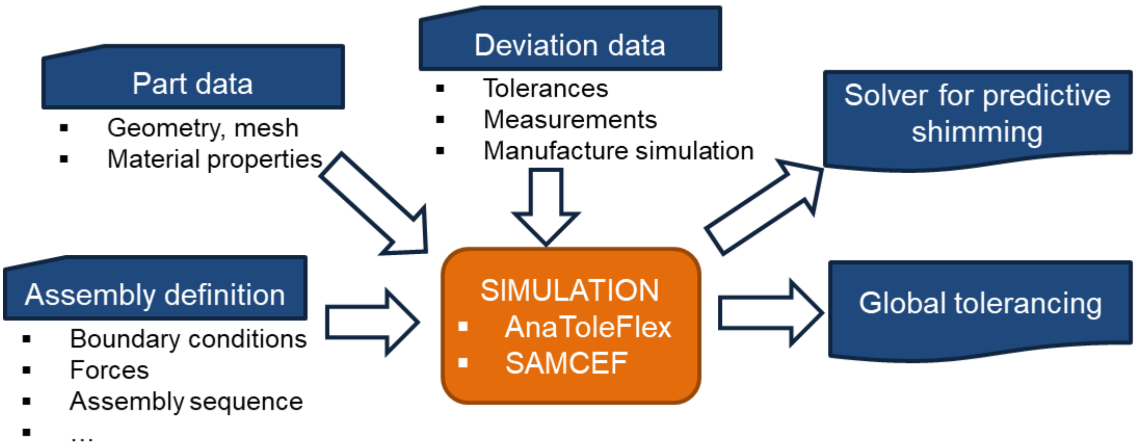

Figure 2-18. Workflow in "Flexible Tolerancing of composite structure" (Engström, 2015, p.14), with use of AnaToleFlex for a composite wing spar.

2.5 Conclusions

An analysis of prior art on non-rigid components and assemblies shows the following:

- Non-rigid part inspection and assembly are deeply interlinked through the concept of functional fit, as is explicitly recognised in the relevant norms. Therefore, deflection considerations are often embedded in inspection strategy and conformance criteria. However, there is no single agreed-upon way for this is done or expressed.

- There is no dominating paradigm in part variation modelling; due to data scarcity, options which are not necessarily fully representative, such as use of linear superposition of arbitrary modes, abound.
- To date, most variation-analysis work for non-rigid assemblies has centred on sheet parts where joints were punctual — such as in a spot-welded or riveted assembly. The joint itself is usually substantially simplified. Within the context of non-rigid assemblies and variation analysis, no evidence has been found of efforts to model adhesive joints.

2.6 Research Questions

This thesis seeks to address the following questions:

RQ1. What are the challenges for variation analysis of non-rigid assemblies for the bonded case?

RQ2. How can these challenges be addressed?

RQ3. (How) can non-rigid considerations be systematically incorporated in part/ assembly design and manufacture for bonded assemblies?

RQ4. (How) can non-rigid considerations be systematically incorporated in the quality assurance process for bonding?

RQ2 is the core question which technical solutions are developed and tested for; this has RQ1 as a necessary enabler where the areas of interest must be identified for research and modelling.

Finally, RQ3 and RQ4 are of a distinctly pragmatic nature: "how can this work support design and manufacture today and tomorrow?" (i.e. "what's in it for me?"), and will be answered through brief demonstration of applicability.

As indicated in the introduction, however, such optimisation methods are not at the core of the present work, the objective of which is, rather, to enable their use for bonded assemblies in the first place. Plenty of focussed, fully-operational applications (including non-rigid tolerancing software, like 3DCS, RDnT and AnaTole) have been developed and productionised for other technologies or manufacturing environments. Similarly, many of the enabling statistical and mathematical tools (inclusive of regression, Pareto analysis, quality loss functions, and heuristic-based optimisation) can readily be transferred to the adhesive bonding situation.

3 METHODOLOGY

3.1 Research strategy

The work undertaken seeks to answer the research questions, identifying mechanisms that determine bondline geometry, proposing analysis tools for bondline variation analysis, showing performance of these tools in practice, and providing examples where these tools generate industrially useful results.

The analysis tools proposed include a variation modal analysis, assembly simulation based on part linearisation and contact modelling, and a simplified adhesive flow model. The latter two have been used in tandem; however, their limitations are discussed separately.

The model performance verification is carried out against Finite Element Analysis (FEA) and against results from physical trials. Multiple physical tests are carried out, covering a variety of confounding factors.

Model use demonstration includes stochastic variation analysis of an assembly for a given set of part variation, and prediction of assembly fitness from measurements taken in a manufacturing environment.

3.1.1 Test assembly definitions

A variety of skin-stringer assemblies of different complexity have been studied for this work.This is partly a result of the project progress, but also intends to explore different factors of the assembly behaviour. The assemblies include:

(a) Single notional stringer bonded onto a rigid, nominal skin, both nominally flat.
(b) Multiple stringers bonded onto a skin; all with complex curvature based on representative aircraft wing cover features.
(c) Flat stringer-skin panels with in-built gaps of known size, and both stringers and skin close to nominal.
(d) Variants of a single curved stringer of the wing cover in (b), each with a different design of the stringer and skin.

(e) Flat stringer-skin panels with multiple stringers per panel, and designed-in profile variation such that the variation of adjacent stringers interacts in pre-defined ways.

3.1.2 Work alignment

The use of assemblies as outlined above is summarised in Table 3-1. In addition to analysis by the stated methods, practical limitations of each test conducted are discussed in the respective chapter section.

Based on the sheer volume of physical test results studied in this work, the order of steps has been altered slightly from the outline above. Demonstrations of model use will be shown and discuss before presenting physical results. Utility of the applications demonstrated is ultimately predicated on the adequacy of the models; however, the reader will hopefully appreciate the general usefulness of the analysis applications and discussion presented, even before showing the results of verification work.

Table 3-1. Configurations studied, their uses, and corresponding research RQs. All analysis covers RQ1 and RQ2.

		Single flat stringer	Subscale wing panel	Flat stringers and spacers	Curved stringer/skin assemblies	Multi stringer / skin
Main purpose		Basic model test/demo	Advanced model demo	Test model, dry/wet separation	Test model limitations in production scenario	Test effect of boundary conditions
Analyse	**Variation spectrum**		RQ1 | RQ2	RQ1 | RQ2	RQ1 | RQ2	RQ1 | RQ2
	Linear part + hard contact	RQ1 | RQ2	RQ1 | RQ2	RQ1 | RQ2	RQ1 | RQ2	RQ1 | RQ2
	Adhesive flow	RQ1 | RQ2	RQ1 | RQ2	RQ1 | RQ2	RQ1 | RQ2	RQ1 | RQ2
Verify	**Physical test**			RQ1 | RQ2	RQ1 | RQ2	RQ1 | RQ2
	FEA			RQ1 | RQ2		
Demonstrate	**Monte-Carlo variation analysis**	RQ3	RQ3			
	Gap health check				RQ4	

3.2 Variation-spectrum-based assembly requirement estimation

An intuitive approach put forward by researchers previously mentioned (Favrelière, 2009; Huang et al., 2014) is that, once geometrical variation is decomposed into modes, it is possible to translate these in terms of assembly requirements. The viability of such a concept has been explored for the stringer-bonding application, using spectral analysis.

This is not only of interest from an academic and theoretical standpoint: on the contrary, it is easy to imagine prescribing amplitude/range geometry requirements based directly on assembly simulation, or embedding profile variation filters into inspection procedures and manufacturing process evaluation. A simple spectral analysis also makes sense as a heuristic for diagnosis of assembly fitness.

In this case, stringers will be analysed, being generally the stiffest (and thus more potentially problematic) component. A simple Fourier decomposition of the profile deviation will be used, and an external pressure requirement will be derived for each mode.

Use of Fourier transform for closure analysis of long stringers offers two advantages:

- Simplicity and ease of understanding: a peak at one frequency can directly be translated in terms of scale, and resolution needed for inspection and manufacture.
- Homogeneity: each valley-to-valley interval within a given component is the same, which will be shown to allow each component to be translatable into a single pressure value.

The Fourier transform has previously been used for sample generation within ADCATS simulation of sheet metal joining (Bihlmaier, 1999); though in this case, the assembly was studied by means of finite element analysis, and unilateral contact was not considered.

3.2.1 Assumptions

1. Behaviour of components other than the stringer (skin and adhesive) are neglected.
2. Tangential displacements (in the plane of the assembly interface) are negligible; the only focus is out-of-plane deviation.
3. Variations across the stringer cross-section, as well as torsion, are negligible.
4. Stringers can be simplified as nominally straight, since variations occur over a short range compared to nominal curvature/twist;
5. Small displacements: part behaviour is in the elastic regime and can be linearised;
6. Effects can be superposed with a reasonably small loss of accuracy;
7. Forces are exerted only normally to the assembly interface;
8. Behaviour is constant throughout the stringer length (no changes in crossection and no noticeable impact of the boundary conditions at the stringer edges).

3.2.2 Basic derivation

Consider a nominally straight slender stringer with a uniform cross-section, exhibiting a shape defect in the form of a perfect sine wave, with a single spatial frequency $f = \lambda^{-1}$ (λ being the wavelength) and amplitude $a \ll \lambda$ (Figure 3-1). The small amplitude is necessary in order for the small displacements and pressures-normal-to-the-interface assumptions to hold, and for the stringer to be modelled as a straight beam.

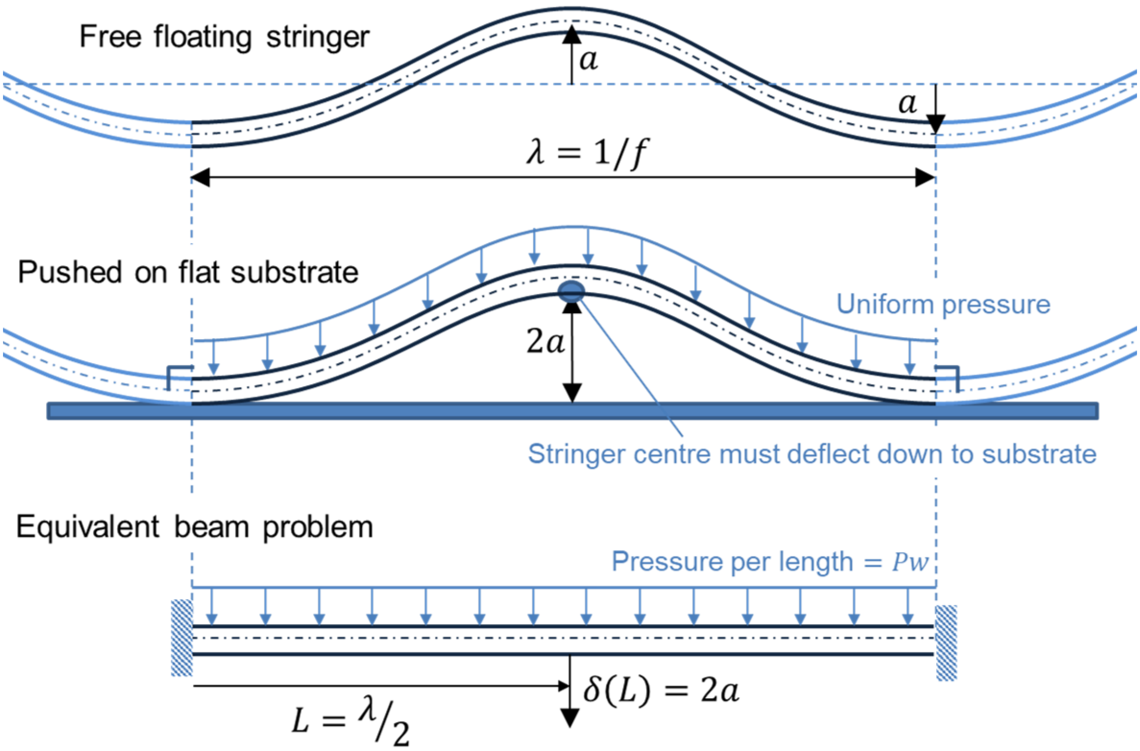

Figure 3-1. One wavelength of a component of the variation of a stringer (top); pressure and deflection considerations with symmetry to neighbouring wavelengths (middle); and resulting double-cantilevered beam model (bottom)

If such a stringer is placed on a nominally flat target skin surface, before any force is applied, the interface gap will be a sine curve offset from the skin, with value 0 at the stringer profile minima and maximal gap values $2a$. In addition, the stringer will be tangent to the skin at the initial contact points. Furthermore, if the stringer is several wavelengths long, symmetry can be assumed, with adjacent waves resisting each other's boundary displacement. Thus, one can model the problem as the deflection of a double-cantilevered beam.

For the initial naive approach, the wave closure pressure is defined as the uniformly applied downward pressure that would cause the local stringer maximum to deflect back to the target skin, without further contact considerations. Using the analytical equations for nominally straight slender beams (available in e.g. Roark's Formulas for Stress and Strain, 6th ed., Young and Budynas, 2002)[xviii], and assuming flexure only, the uniform pressure requirement is easily derived.

Maximum deflection of a uniformly loaded double-cantilevered beam occurs at the middle point along the length, $L = \lambda/2$, and (for the single-wavelength beam presented earlier) is[xix]:

$$[\text{max deflection}] = \delta(L/2) = 2a = \frac{Pw\lambda^4}{384EI} \tag{3-1}$$

where P is the uniform pressure applied, w is the flange width (therefore Pw is the load per unit length); E is the material modulus of elasticity, and I is the second moment of inertia of the area of the stringer cross-section relative to the plane perpendicular to the pressure[xx].

Solving equation (3-1) for P, and substituting $\lambda = f^{-1}$:

$$P \ = \frac{768EI}{w} af^4 \tag{3-2}$$

The modelling of variation as a sine is now extended to the full range of variation of the beam-like component, modelling it as the sum of a number of sines of spatial frequency f_j and amplitude a_j. The deviation from the 'flat' nominal, which as modelled is equated with the deflection under external pressures, is, then, expressed in line with a Fourier Transform:

$$\delta(L) = \frac{1}{2}a_0 + \sum_{j=1}^{n_{sf}} a_j \cos(2\pi f_j L + \varphi_j) = \frac{1}{2}a_0 + \sum_{j=1}^{n_{sf}} a_j \cos(2\pi \frac{L}{\lambda_j} + \varphi_j) \tag{3-3}$$

where φ_j is a phase offset, and as a result the corresponding variation component has a local minimum at position $L = \lambda_j(1/2 - \varphi_j(2\pi)^{-1})$. If the values for the

[xviii] Although the solutions to particular load cases can be found in such reference manuals, any practitioner, and many undergraduates, should be able to derive them on pen and paper from the basic equations for stress and strain, given some time, by applying basic concepts of [anti]symmetry, equilibrium of forces/moments, and polynomial integration.

[xix] As stated in footnote xviii, this can be derived from the equations for beam stress and strain using pen and paper, but is also available in manuals (e.g. Young and Budynas, 2002, p.193).

[xx] Later in this chapter, the subscript flex will be used to specify that this pressure is calculated without accounting for shear. The subscript $\mathrm{flex} + \mathrm{shear}$ will be used when shear is included.

parameters in equation (3-3) are calculated through the Fast Fourier Transform (FFT) of a number N_L of points equispaced along the length of the stringer, then the frequencies f_j and the number of frequencies n_{sf} are further subject to:

$$f_j = jL^{-1} \qquad \text{(therefore } \lambda_j = L/j\text{)}$$
$$n_{sf} = 2^{floor(\log_2 N_L)-1} \quad \text{(equals } N_L/2 \text{ if } N_L \text{ is a power of 2)} \tag{3-4}$$

The deviation corresponding to a_0 is constant along the length of the stringer; it thus can be compensated by a rigid motion and could be omitted from further analysis. Alternatively, it can be retained with $f_0 = 0$, which will equally result in no additional pressure requirement when applying equation (3-2).

When the closure pressure in (3-2) is extended to the entire spectrum under consideration as presented in (3-3), and through the assumption of linear superposition, this translates to a total pressure requirement P, which should enable pushing the stringer to the nominal profile.

$$P = \sum_{j=0}^{n_{sf}} P_j = \sum_{j=0}^{n_{sf}} \frac{768EI}{w} a_j f_j^4 \tag{3-5}$$

It becomes clear that the value P is heavily dependent on any correlation between a_j and f_j. Although intuitive expectations and observations in the literature point to a decrease in amplitude for short-range variation, that is, $da/df < 0$, the type of law that this follows (which is not clearly stated in previous work reviewed) could have a large impact on assembly feasibility.

As an example, consider the cases: $a_j \propto f_j^{-1}$ ('hyperbolic'), and $a_j \propto \exp(-f_j)$ ('exponential'), such that the sum of all components' amplitudes, $\sum_{j=1}^{n_{sf}} a_j$, is the same for both cases. The amplitude and pressure values for a range of frequencies are presented, in a generic, normalised case, in Figure 3-2 and Figure 3-3. (The parameters are genericised such that (1,1) is crossed by the 'hyperbolic' spectrum). A hyperbolic-type spectrum will result in very high closure pressures from the shorter-wavelength components; meanwhile, an exponential-type spectrum will contain variation components that become irrelevant (assembly-requirement-wise) at short enough ranges[xxi].

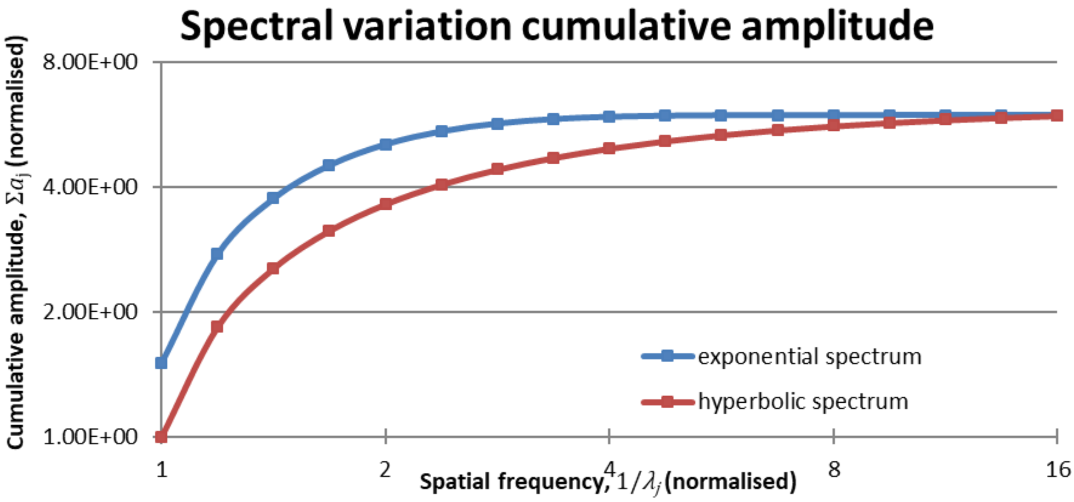

Figure 3-2. Variation amplitudes resulting from two different idealised distributions. Although the final cumulative value is the same, the 'exponential' relation is biased towards longer wavelengths (i.e. lower spatial frequencies).

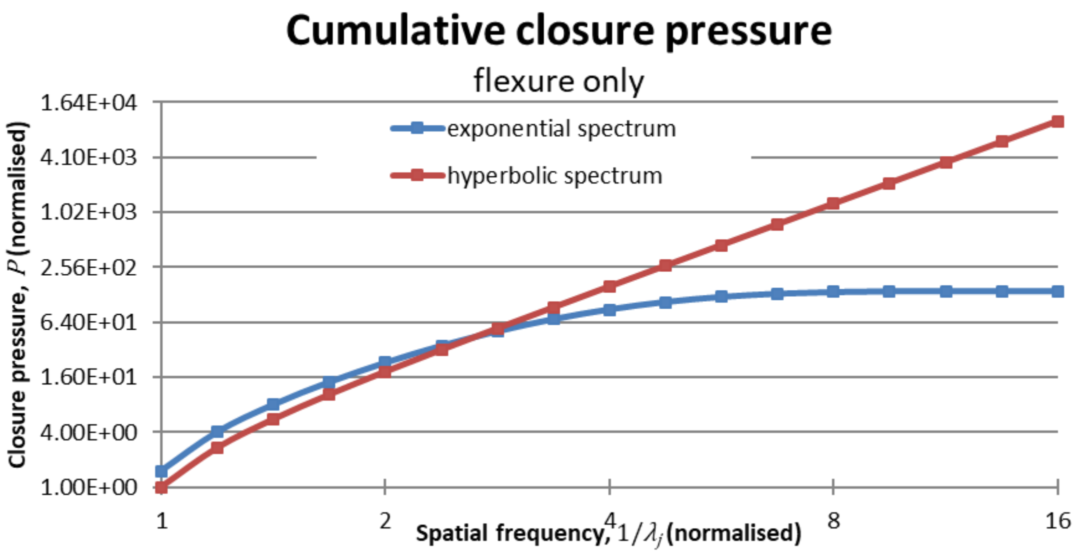

Figure 3-3. Closure pressure scores that would result from the amplitudes and frequencies in Figure 3-2. Note the logarithmic scale which allows better viewing of order-of-magnitude differences.

[xxi] For $a = a_0 exp(-\gamma f)$, where γ is a real-number coefficient, the maximum component-associated pressure P_i would occur at $= 4/\gamma$. This can be calculated by simple differentiation of (af^4).

Of course, this is not fully descriptive of the industrial reality. In practice, there will be no need to remove absolutely all the geometric variation, as all joints have *some* variation tolerance. Therefore, as long as the variation amplitude decays 'fast enough' with spatial frequency, the specific relationship with wavelength is largely non-critical.

3.2.3 Restriction of spectrum's wavelength

Given a dense point sample from stringer inspection, it would be possible to obtain a variation spectrum covering hundreds of wavelengths, down to the mm range. As pointed out above, such a level of detail is unnecessary given that these variation components will not only be very small in amplitude, but also well out of the scope of the assumptions outlined initially (the stringer will indeed not be a slender beam over such short distances). What's more, short-enough wavelengths (in the mm range) cannot realistically be expected to be inspectable with typical contact-based instruments such as gauges and touch-probe CMMs, since variation over such ranges will be filtered out as depicted in Figure 3-4 (see for example Arenhart, 2010).

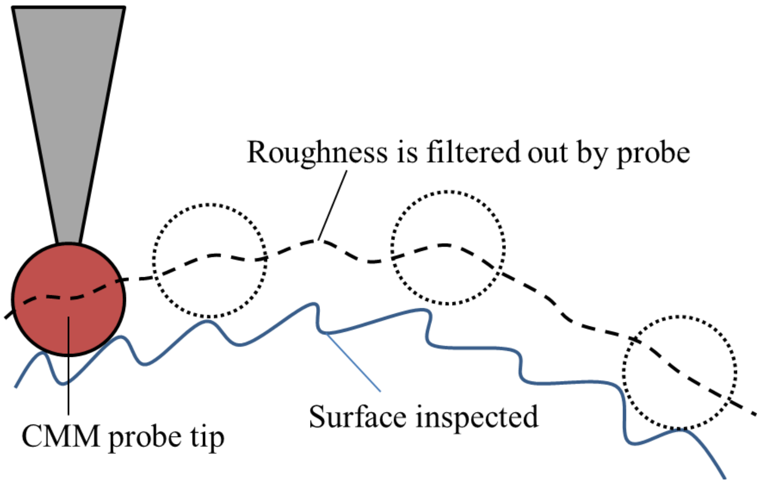

Figure 3-4. Example of short-range variation filtering by contact-based measurement.

Therefore, a number m_{sf} of wavelengths, the shortest in the initial analysis, will be left out of further steps, such that

$$\sum_{j=m_{sf}}^{n_{sf}} a_j < T_{spectrum} \ll T_{joint} \tag{3-6}$$

where T_{joint} is a design tolerance range for assembly joint variation (typically in the order of 0.05 mm to 0.10 mm), and $T_{spectrum}$ is an arbitrary small spectrum accuracy tolerance value.

For clarity, subsequent analysis in this chapter will still use the nomenclature from equation (3-3), without noting m_{sf} explicitly.

The spectral reconstruction, with increasing accuracy (but diminishing returns) as shorter frequency components are added, is illustrated in Figure 3-5.

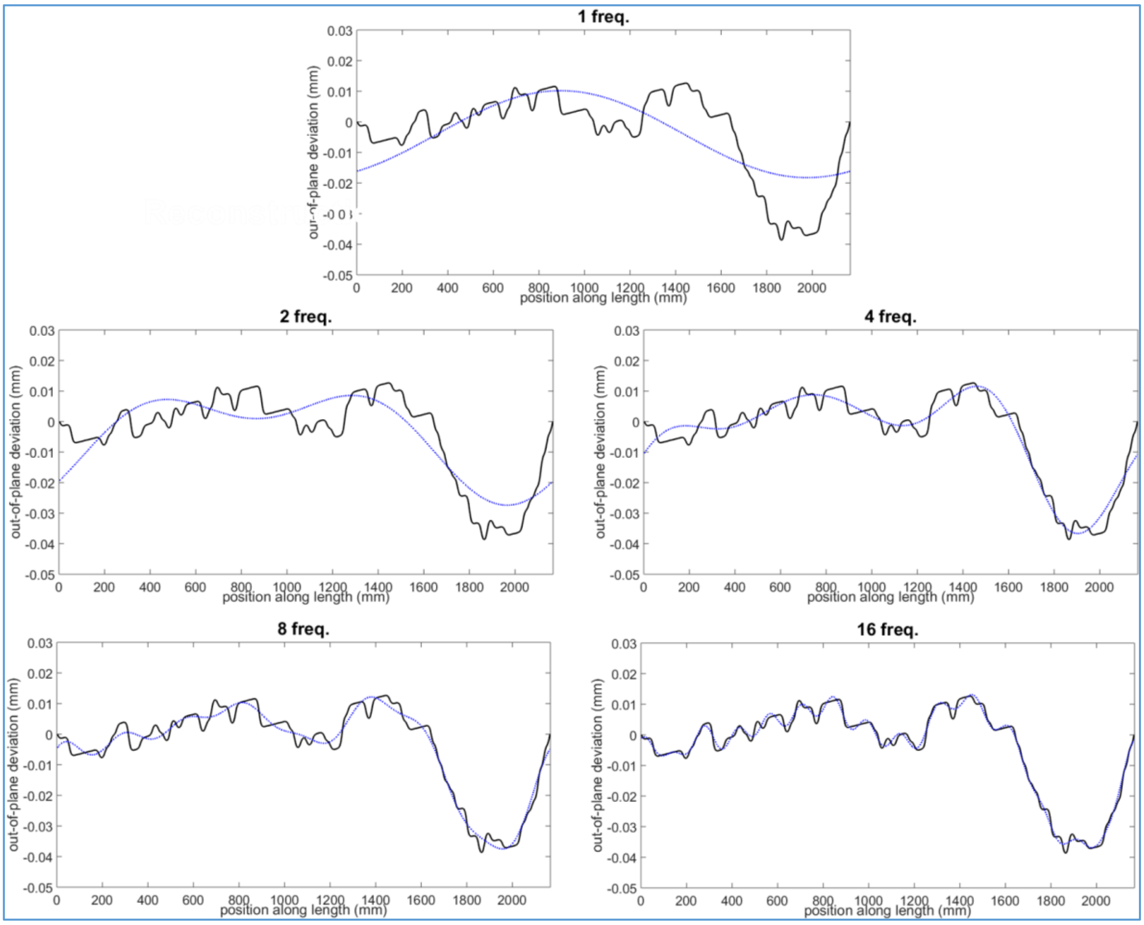

Figure 3-5. Example of stringer reconstruction accuracy gain as the number of frequencies increases. Note the diminishing returns, with the first few frequencies already achieving a fairly close (sub-0.01 mm) match.

For future uses in this work, a value of 0.01 mm will be used for $T_{spectrum}$. This value is in the order of the accuracy achievable by mid-large volume measurement instruments, such as a CMM's Maximum Permissible Error (MPE), and smaller than the typical resolution of other instruments such as slip and feeler gauges.

3.2.4 Limitations and corrections

3.2.4.1 Localised variations

The usefulness of Fourier Transform analysis is predicated on the periodicity and stationarity of the dataset provided (see, for example, Huang et al., 1998, p.905). This is a condition not necessarily met by manufactured parts, especially given how many parts are indeed not periodical or uniform in design. For instance, a stringer for a wing panel, with varying curvature through its span, may be very variable in areas that necessitate extensive forming, but achieve nominal curvature around other more flat, straight areas. This is in addition to how stringer nominal cross-sections are not necessarily constant (although, in many cases, they do vary very little).

A local deviation will express itself in the spectrum as a peak at one spatial frequency, plus multiple secondary peaks at higher-frequency (stiffer) harmonics.

3.2.4.2 Boundaries

The assumption on closure behaviour is based on local boundary conditions given by:

- Localised contact between adherends;
- Interaction of adjacent segments of stringer.

However, this is not the case where some fixturing is in place. Typically, this will occur near tooling pins, locating fingers/boards, and at the stringer ends (where, in addition, there is no such "adjacent segment of stringer" on one side).

It must be noted, further to this, that simulations for comparison with the spectral approach can become unreliable in the vicinity of boundary conditions, due to the difficulty in modelling them. For example, modelling a stringer as a simply-supported slender beam may be a reasonable analytical approach, but in reality the stringer ends will be able to move normal to the plane, resulting in considerable simulation inaccuracies whenever there is variation close to them. In this case, however, the validity of the spectral approach is not undermined, as the “float” provided by the real typical boundary conditions is actually closer to the assumptions for the proposed spectral analysis.

3.2.4.3 Variation shape

The calculation proposed does not check whether each individual component of the variation spectrum accurately describes the deflection behaviour. Sure enough, the deflection behaviour of a uniformly loaded double cantilever (as described in Figure 3-1 above) is not described by a sine, but by a polynomial.

The deflection of such a beam (of total length λ) at a length position L, accounting for flexure only, is given by equation (3-7)[xxii]:

$$\delta_{poly}(L) = Pw\frac{(L)^2(\lambda - L)^2}{24EI} = a\frac{32(L)^2(\lambda - L)^2}{\lambda^4} \qquad \textbf{(3-7)}$$

where the term to the farthest right results from substituting the value of P as in equation (3-2). This has the effect of modelling deflection at L as relative to the maximum deflection ($2a$ at $L = \lambda/2$).

The difference between the sine and polynomial cases becomes obvious when studying a simple deflection case (Figure 3-6). Under the external pressure which, according to the calculation presented above, would *just* close the gap, a stringer presenting shape variation as per the polynomial formula closes perfectly; in contrast, a stringer variation described by a sine, with the same amplitude, does not close fully[xxiii]. Rather counterintuitively given the deflection

---

[xxii] As stated earlier in note, this results directly from the basic formulas for stress and strain. A motivated highschooler with knowledge of polynomials also may obtain this expression by using the boundary conditions and conditions of maximum deflection.

[xxiii] The assembly simulation was performed using the method presented later in this chapter, subsection 3.3.3. Dry component: Linear model with contact search by quadratic programming (QP). This was done without consideration of adhesives, and using the analytical flexure equations for a slender beam to generate the part compliance model (compliance matrix).

outcome, the gap in a sine shape is actually slightly *less* deep than the polynomial; however, this makes sense when considering the closure process: as the parts are pushed together, the current effective length over which the sine-shaped gap occurs becomes shorter due to contact, thus ‘stiffening’ the gap.

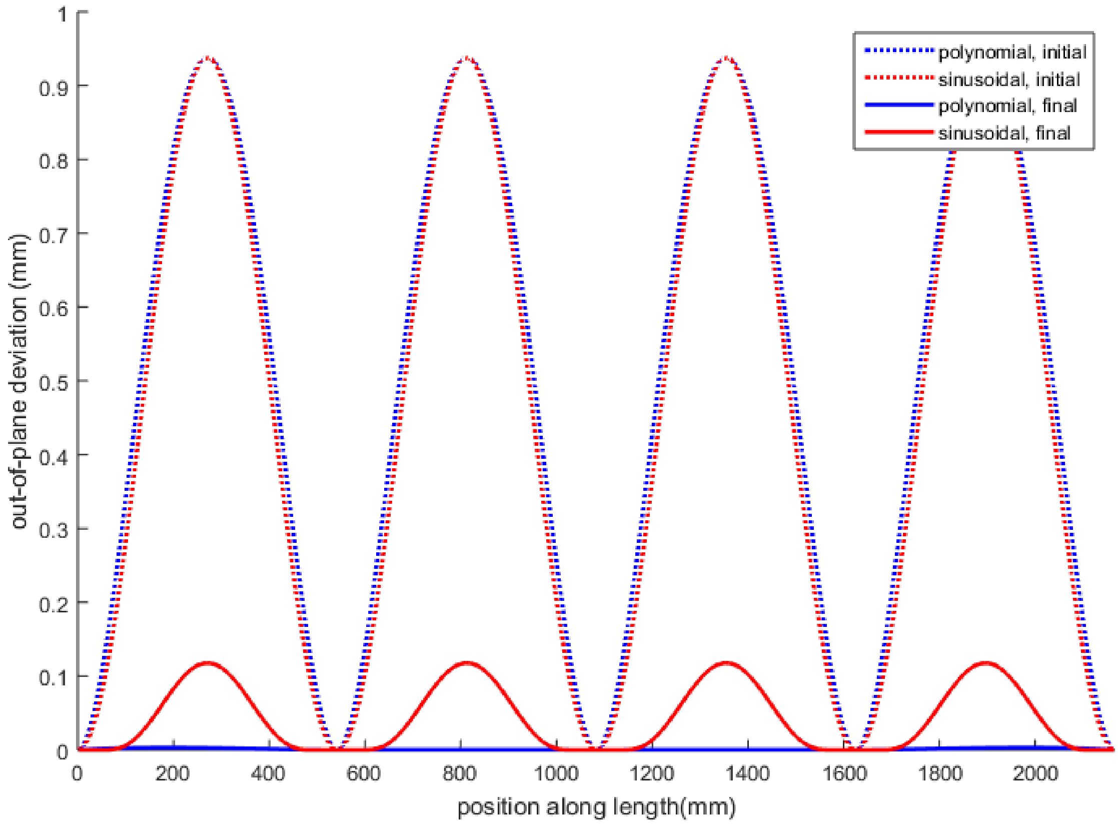

Figure 3-6. Comparison of closure (flexure only) of a truly sinusoidal beam geometry (single Fourier component) and a geometry based on beam deflection, under the same pressure of 1 MPa. Note that the slightly bigger overall gap in the polynomial geometry actually allows it to close better.

The spectral analysis for this case (Figure 3-7) illustrates the inadequacy of the purely sine-based concept: the polynomial-shaped variation is given a higher pressure score pre-deflection (i.e. is expected to be somewhat harder to push down to nominal) due to how the function generates multiple harmonics. The spectrum does correctly reflect which stringer has the larger residual gaps post-deflection, but this is because the one with polynomial shape has practically achieved zero gap.

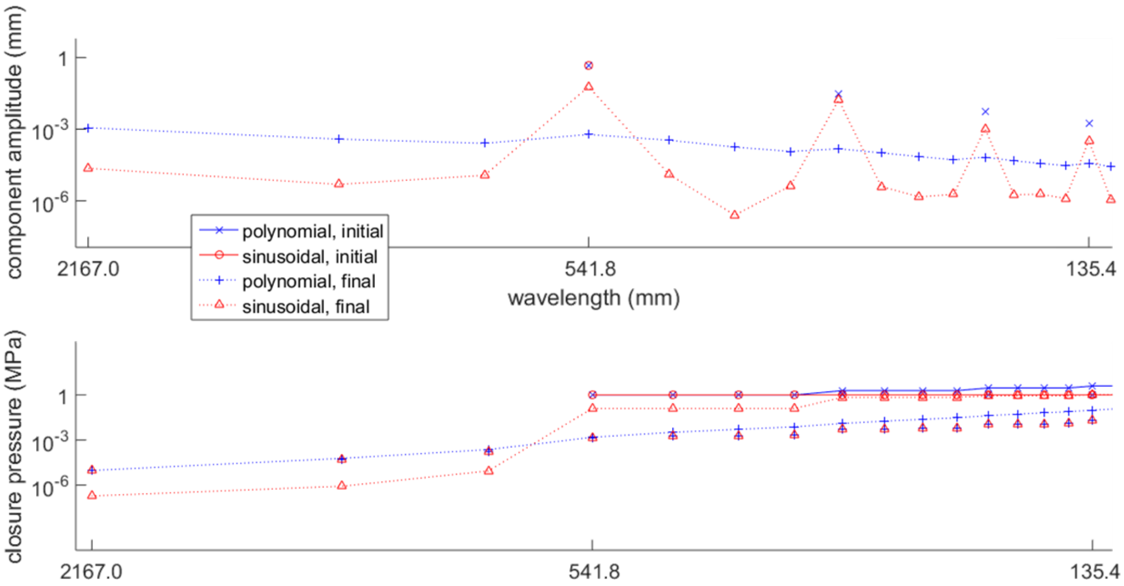

Figure 3-7. Spectral analysis (16 biggest wavelengths) of the Figure 3-6 scenario. Note the lone red circle at (541.8, 1) in the top graph, indicating the pure, one-component sine shape. Also note how the 'impure' sinusoidal is initially (wrongly) calculated as harder to close (bottom graph).

This result further emphasises the need to consider contact. An even more important lesson, however, is that there is a level of uncertainty associated to describing a gap with only two descriptors (amplitude and length). Either the shape must be captured, or uncertainty from shape considerations must be taken into account. In the example presented, the difference between the final gaps is actually smaller (in amplitude) than that between the final (pressed) gaps, although the location of such deviation is displaced.

Note that the same can be said for cases with lack of periodicity: in Figure 3-8, the same waves occurring over half the stringer are shown not to close any worse (though more irregularly), but the resulting spectrum, presented in Figure 3-9, is higher-energy than that for perfectly periodic variation shown earlier Figure 3-7.

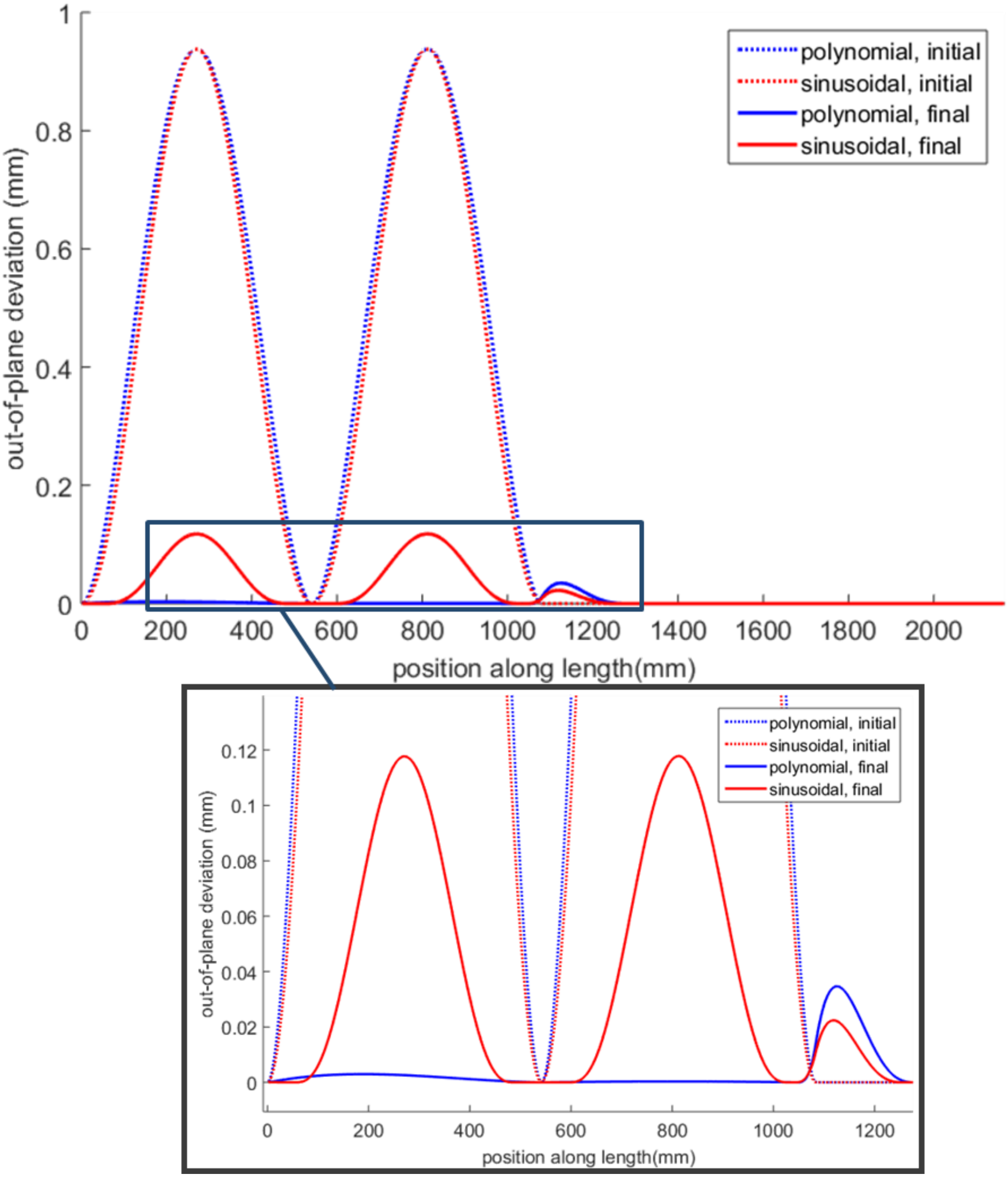

Figure 3-8. Closure issues brought about by local conditions: Note the different profile near the transition from no-gap to gap condition, where the gap is propagated to a previously gap-less area, and the slight variation in closure near the part edge due to the boundary condition allowing part rotation.

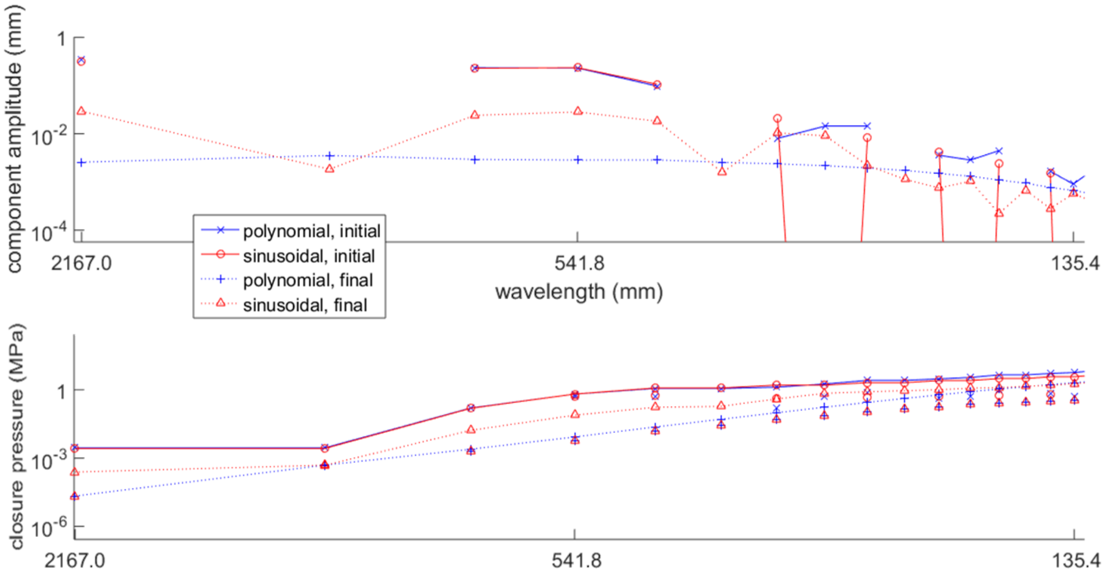

Figure 3-9. Spectra for the geometries in Figure 3-8. The spectrum is much more irregular (larger harmonics) than for the case of waves all over the part, and the estimated closure pressure is higher than in that case too.

3.2.4.4 Adapting the spectral components to flexure-based deflection

Given the mismatch between sine components and the expected behaviour of a stringer, it is useful to explore the effect of a modified spectrum on the calculated pressure requirements. This has been implemented through an iterative process which takes each component of the sine-based spectrum starting with the lowest spatial frequencies, replaces it with a polynomial of the same wavelength and amplitude, and updates the remaining (higher-frequency) components with the harmonics of the updated component. The process flow is summarised on Figure 3-10.

For the purpose of variation mode implementation, a single polynomial 'wave' may appear repeatedly, just like the periodically repeating values of a sine. The local minimum may not be at $L = 0$. Therefore, the deflection function in equation (3-7) is offset along the stringer length,

$$\delta_{poly}(L) = a\frac{32(L - L_{wav})^2(L_{wav} + \lambda - L)^2}{\lambda^4} \qquad \textbf{(3-8)}$$

with auxiliary variable L_{wav} representing the length position at which the 'wave' starts (i.e. local minimum). This variable is defined in expression (3-9):

$$L_{wav} = n_{wav}\lambda + L_{wav,0} \quad \textbf{(3-9)}$$

with n_{wav} being the number of repeat of each wave, and $L_{wav,0}$ representing the length offset for the start of the first wave. From the physical meaning of the follows that the maximum value of L_{wav} will be equal or less than the total length $L_{stringer}$ of the stringer modelled. Therefore, $n_{wav} \in [0, L_{stringer}/\lambda]$.

The value of $L_{wav,0}$ is calculated from the phase offset φ since they share their physical meaning:

$$L_{wav,0} = \lambda \times (\frac{\varphi}{2\pi} - \frac{1}{2}) \quad \textbf{(3-10)}$$

Then the polynomial expression for deformation can be made periodic, by rearranging the terms in (3-8) so that $(L - L_{wav})/\lambda$ is used as the independent variable and using an auxiliary function to implement the periodicity from (3-9):

$$\begin{aligned}
&\delta_{poly}(\lambda, a, \varphi, L) = 32a\left(L_{frac}(\lambda, \varphi, L)\right)^2\left(1 - L_{frac}(\lambda, \varphi, L)\right)^2 \quad , \\
&L_{frac}(\lambda, \varphi, L) = \mathrm{frac}\left(\frac{L}{\lambda} + \frac{\varphi}{2\pi} - 0.5\right) \\
&\mathrm{frac}(x) = x - \mathrm{floor}(x)
\end{aligned} \quad \textbf{(3-11)}$$

It is now possible to iteratively convert the variation spectrum from a Fourier transform, into one that reflects the beam deflection shape[xxiv]. The process is summarised in the flowchart in Figure 3-10:

1. The regular Fast Fourier Transform is calculated for the stringer profile variation $\delta(L)$, yielding a spectrum with parameters $\{\lambda_j, a_j, \varphi_j\}, j = 0 \ldots n_{sf}$ in accordance with eqs. (3-3), (3-4).
2. Each mode k with nonzero frequency ($k \geq 1$) will be adjusted sequentially, starting with the longer wavelengths (that is, from $k = 1$ until $k = n_{sf}$). Because as and when the new modes are generated, they are subtracted from the variation; the use of this residual variation (which changes at each step k) will be denoted by applying the superscript res, k, to δ and to λ_j, a_j,

[xxiv] In the context of this algorithm, the left pointing arrow ← represents a value assignment.

φ_j. Furthermore, the residual variation is initialised as $\delta^{res,0}(L) \leftarrow \delta(L)$ before starting the iteration $k = 1$.

a. A new component is generated based on the polynomial behaviour of the stringer, such that the wavelength and phase offset are the same as for the sine-shaped original component $j = k$. For clarity, the subscript $j = k$ will be used instead of j to identify the parameters used.
   i. The amplitude $a_{j=k}^{res,k}$ is adjusted to account for harmonics, so that the sine variation component k is fully removed from subsequent steps. The adjusted value is equal to $a_{j=k}^{res,k}/c$, where c is the amplitude of the first non-constant Fourier component of the polynomial component. For the polynomial component as presented in (3-7), it was found that $c \approx 0.9855$.
   ii. The new component $\delta_{poly,k}$ is generated using the expression from (3-11) and the adjusted amplitude as per step i above: $\delta_{poly,k} \leftarrow \delta_{poly}\left(\lambda_{j=k}^{res,k}, a_{j=k}^{res,k}/c, \varphi_{j=k}^{res,k}, L\right)$.
b. The new component is subtracted from the stringer (residual) variation, obtaining an (updated) residual variation, $\delta^{res,k} \leftarrow \delta^{res,k-1} - \delta_{poly,k}$.
c. The regular Fourier transform is calculated for the newly-obtained residual, resulting in a new set of values $\{\lambda_j^{res,k}, a_j^{res,k}, \varphi_j^{res,k}\}$ and the process is repeated for the next k.

3. The zero-frequency component, corresponding to $k = 0$, is calculated from the final residual deviation value, $\delta_{poly,0} \leftarrow \delta^{res,n_{sf}}$. This component is overlooked in the spectral closure analysis, and thus the method tolerates the variation that was flushed into the $k = 0$ component due to lack of antisymmetry of the new modes.
4. The variation can now be expressed as the summation of the modes calculated, as per (3-12):

$$\begin{aligned} &\delta(L) = \delta_{poly,0} + \textstyle\sum_{k=1}^{n_{sf}} \delta_{poly,k}(L) \\ &\delta_{poly,0} + \textstyle\sum_{k=1}^{n_{sf}} \delta_{poly}(\lambda_k^{res,k}, a_k^{res,k}/c, \varphi_k^{res,k}, L) \quad ,c = 0.9855 \end{aligned} \tag{3-12}$$

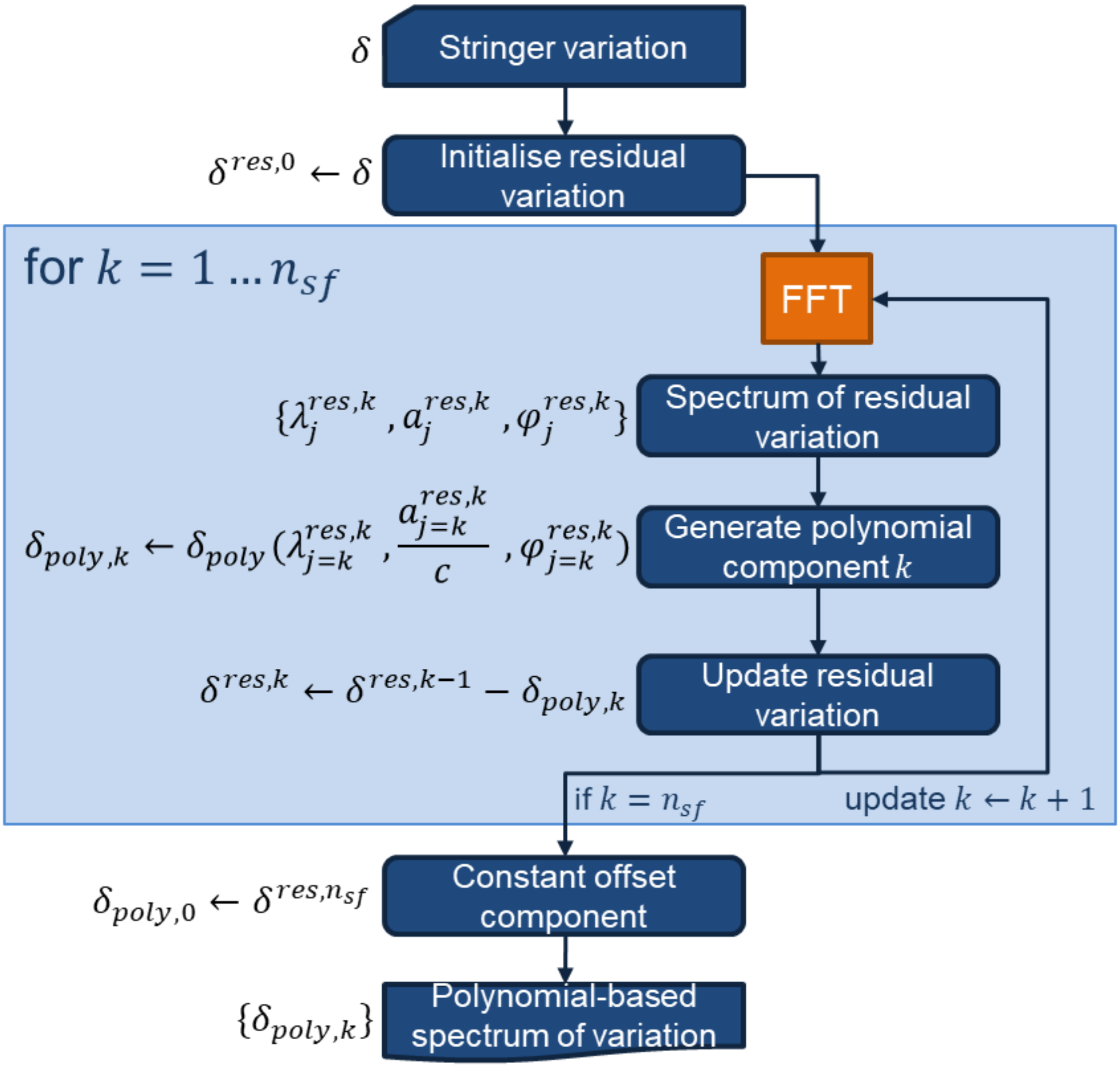

Figure 3-10. Procedure for adapting the Fourier transform of stringer variation to shapes based on flexural-deflection.

The impact of this reconstruction will be seen in the comparative studies between spectral analysis approaches, in Appendix I— Test of the spectral pressure score.

3.2.4.5 Incorporating shear

Due to the way beam stiffness scales with length, variation appearing over a shorter range is worth special attention as more difficult to mitigate. On the other hand, shorter lengths of beam should not be modelled as flexure-only, with shear becoming a bigger contributor to the deflection behaviour.

Without considering any shape effects and using the same closure requirement as for flexure-only (midpoint of the wave pushed without contact), the pressure inclusive of shear, ($P_{\text{flex+shear}}$) can be formulated just like it was done for the pressure considering flexure only, P_{flex}, as presented in earlier in equation (3-2).

Returning to the expression for maximum deflection of a double-cantilevered beam under a uniformly distributed load (equation (3-1)), and including shear[xxv]:

$$[\text{max deflection}] = \delta(\lambda/2) = 2a = \frac{Pw\lambda^4}{384EI} + \frac{Pw\lambda^2}{8k_{shear}GA} \tag{3-13}$$

where k_{shear} is the cross-section's shear factor[xxvi] relevant to the direction of deflection, G is the material shear modulus, and A is the area of the stringer cross-section.

Solving for the pressure again (this time noted as $\mathrm{P}_{\text{flex+shear}}$)

$$P_{\text{flex+shear}} = \frac{768EI}{w\left(1 + \frac{48EI}{k_{shear}GA} f^2\right)} af^4 = P_{flex} \frac{1}{1 + \frac{48EI}{k_{shear}GA} f^2} \tag{3-14}$$

The difference comes, thus, from the $\frac{48EI}{k_{shear}GA} f^2$ term added to the divisor. Interpretation of this term's implications are fairly intuitive: shear becomes more relevant as a contributor to stringer deflection as the spatial frequency f increases. For large enough values of f (that is, over short enough lengths), the pressure requirement will be substantially reduced compared to that calculated from flexure alone.

One can easily estimate the variation wavelength at which shear becomes relevant, based on the denominator $(1 + \frac{48EI}{k_{shear}GA} f^2)$. For this work, an arbitrary criterion will be used that shear is negligible when $\frac{48EI}{k_{shear}GA} f^2 \leq 0.1 \ll 1$, and that it dominates (flexure is negligible) when $\frac{48EI}{k_{shear}GA} f^2 \geq 10 \gg 1$. In the case of

[xxv] The deflection due to shear can be calculated trivially by integrating the pressure load over half the double-cantilevered beam length (see, for example, Young and Budynas, 2002, p.166).

[xxvi] For the cases studied, the shear factor will be approximated as the ratio of the area of the cross-section of the web to the total area of the cross-section; this is typical engineering practice (see, for example, Young and Budynas, 2002, p.166).

shear-dominated deflection, the pressure requirement from eq. (3-8) would be simplified, scaling with the 2nd power of the spatial frequency (instead of the 4th):

$$P_{\text{shear}} = \frac{16 k_{shear} GA}{w} a f^2 \tag{3-15}$$

The impact of considering shear, and the three modes (flexure-dominated, mixed, and shear-dominated) are illustrated in Figure 3-11. The figure is based on genericised values such that the flexure-only score P_j is 1 when λ_j is 1, and a value $\frac{48EI}{k_{shear}GA} = 0.05$ is used so that the changing impact of shear is visible. The vertical dashed lines mark the domain where both flexure and shear have a noticeable impact (the arbitrarily defined $0.1 < \frac{48EI}{k_{shear}GA}\lambda_i^{-2} < 10$).

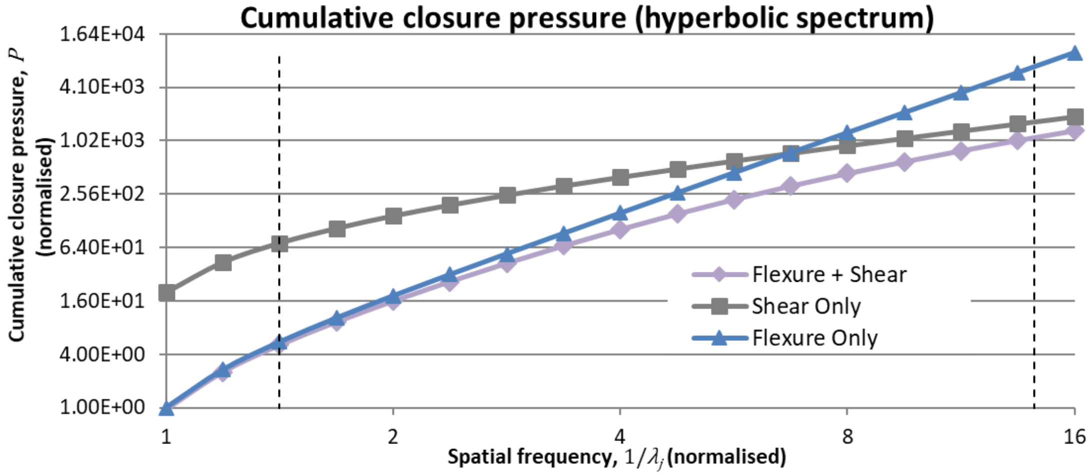

Figure 3-11. Illustrative closure pressure scores for a hyperbolic spectrum (amplitude proportional to wavelength). Accounting for shear reduces the scores for higher frequencies.

For the cross-sections and materials studied in this work, the value of $\frac{48EI}{k_{shear}GA}$ has been found to be between 0.4×10^4 and 1.2×10^4. Thus, the spatial frequency interval where both flexure and shear are relevant is approximately between 0.001 mm^{-1} and 0.01 mm^{-1} (wavelengths between 600~1000 mm and 60~100 mm, depending on the specific cross-section). The higher-frequency end of the interval is small enough that the slender beam consideration is not valid anymore, and typical variation amplitudes will be very small anyway. The upper end at 600~1000 mm wavelengths, however, is relevant: typical sources of variation, e.g. forming processes and inspection fixtures, will introduce variability at or below this scale. Therefore, limiting the assumption to stringer flexure will also limit the accuracy of the model, by overstating stiffness noticeably and oversimplifying shorter-range (stiffer) variation components.

3.2.5 Conclusions

The spectrum-based approach presented in this chapter is, in principle, a tempting solution for lightweight diagnosis of assembly fitness. On the other hand, it suffers from obvious limitations due to the number of simplifications used, including neglect of part inhomogeneity and local deviations and difficulty in incorporating realistic part behaviour, as well as disregarding parts in the assembly other than each individual stringer in isolation. In addition, it offers no predictions of what the final assembly will actually look like. The lack of meaning of the analysis is illustrated through a deep dive into the simulation and physical test results, provided in Appendix I — Test of the spectral pressure score.

In spite of these objections, however, the modal decomposition approach stands to offer a 'quick and dirty' verdict on individual parts given enough inspection data, or alternatively, given sufficient background investigation, could support definition of acceptance heuristics beyond a 'maximum-gap-to-tool' policy. If found sufficiently capable, thus, spectral analysis could provide a very low-cost solution to quality control based on process parameters.

3.3 **Semi-analytical model**

Note: prior publication

Parts of the methodology description and discussion in this subsection has been published in the paper by this thesis' author and co-supervisors:

Coladas Mato, P., Webb, P., Xu, Y., Graham, D., Portsmore, A. and Preston, E. (2019) 'Enhanced bondline thickness analysis for non-rigid airframe structural assemblies', *Aerospace Science and Technology*, 91, Elsevier, pp. 434–441. (DOI: 10.1016/j.ast.2019.05.024)

This subsection provides further discussion on compliance matrix derivation, adhesive flow modelling, and model integration, while leaving out the prior art discussion (which has been covered in the literature review).

3.3.1 Assembly model summary

The assembly setup, as found during the adhesive bonding process, is made up of the following elements:

- Adherends (the solid parts being joined);
- Hard tooling such as 'female' outer mould tools or bonding tables;
- Pressure application medium (in this work, a vacuum bag and a pressure differential will typically be assumed);
- Bonding consumables such as breather fabric and flash breaker tape;
- Bondline with uncured adhesive.

These are modelled in the following way:

- The mechanical behaviour is of each separate adherend is linearised, and their interaction is simplified as taking place through direct hard contact;
- Hard tooling is modelled as any other solid parts;
- The pressure application media are simplified as a uniformly applied pressure. No phenomena like bag wrinkling or bridging, nor the effect of pressure-redistributing tooling like pressure intensifiers, have been considered in this application;
- Additional bonding consumables are disregarded, both in terms of mechanical loads (weight and pressure redistribution effects) and of impact on bond

quality due to e.g. volatile gas evacuation or adhesive flow obstruction/facilitation;

- The bondline dimensional change ('squeeze') due to bonding pressure is modelled separately from the solid parts, using a simple analytical flow model. The final bondline thickness is added to the gap between the adherends which has been calculated separately.

Through these modelling simplifications, the system can be formulated as the combination of a contact problem solved by Quadratic Programming (QP),which will be presented in section 3.3.3; and a flow problem approximately solvable with a closed-form expression, which will be presented in section 3.3.4. The different components of the model and their integration are summarised in Figure 3-12.

The separation of the aspects of assembly into 'dry' (part deflection and interaction) and 'wet' (adhesive flow) is a key simplification which enables the simple simulation, as it reduces the problem into a static optimisation and a closed form dynamic equation, thus limiting need for iterations and removing the need to consider timesteps. It also allows model accuracy verifications via FEA to be performed much more straightforwardly, since no fluid-structure interaction (FSI) is needed. The potential limitations of the dry/wet separation are discussed in Section 6.2 Research limitations**.**

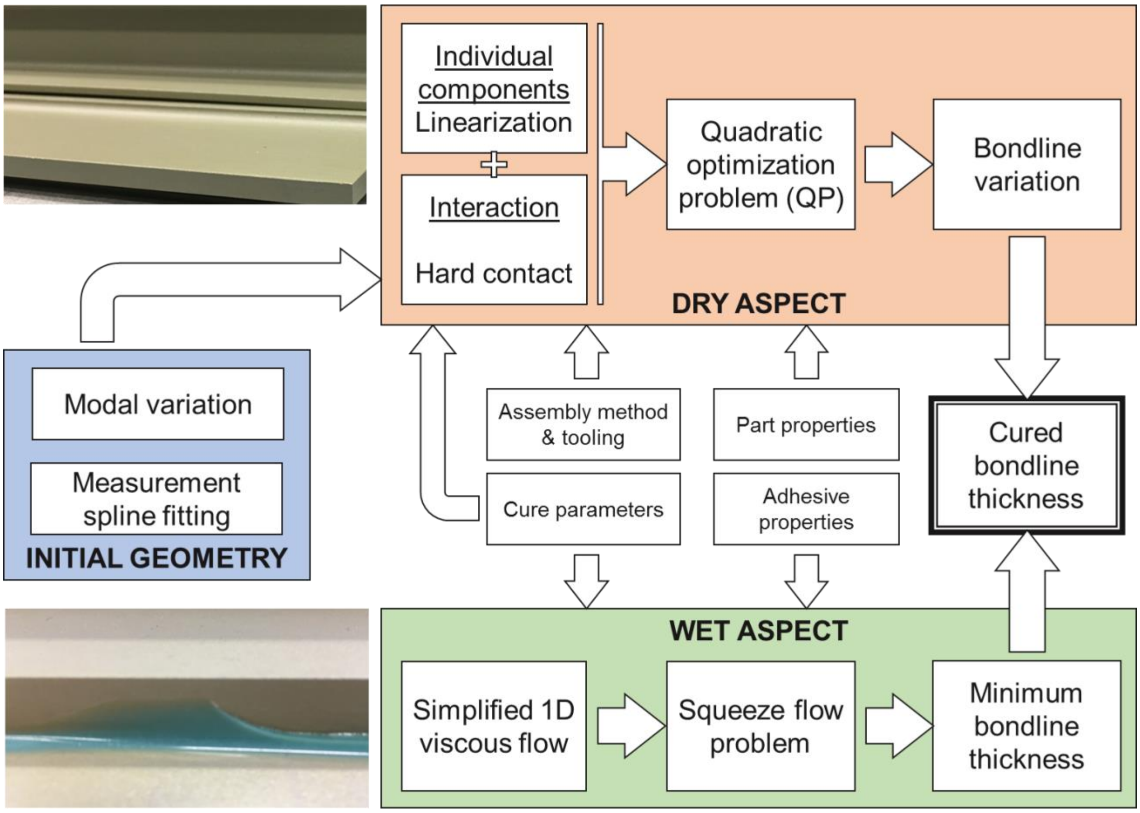

Figure 3-12. Top-level summary of the assembly modelling approach

3.3.2 Assembly interactions separation

Figure 3-13 illustrates the composition of the thickness of the uncured bonded joint. The bondline thickness of the joint will be determined by two separate mechanisms: the ability of adhesive to flow, and the deflection of the adherends; both of which are driven by the external pressure. By basic fluid dynamics (and as explicitly formulated later in Section 3.3.4 and Appendix A) the resistance to flow of the adhesive will increase as the bondline becomes thinner; therefore, the external pressure will be reacted where the adherends are brought closest together. Thus, the bondline thickness is separated into two components: a wet component for minimum bondline thickness, and a dry component for adherend separation left after discounting the wet component.

The interaction between adherends prior to the formation of the bonded joint, which consists of the transmission of pressure through the uncured adhesive, is approximated as a contact interaction at the regions of lowest adhesive thickness, since these are where the adhesive resists flow the most and becomes highly pressurised. Thus, the ‘dry’ component is approximated as the clearance between the adherends when pushed against each other as shown in Figure 3-13.

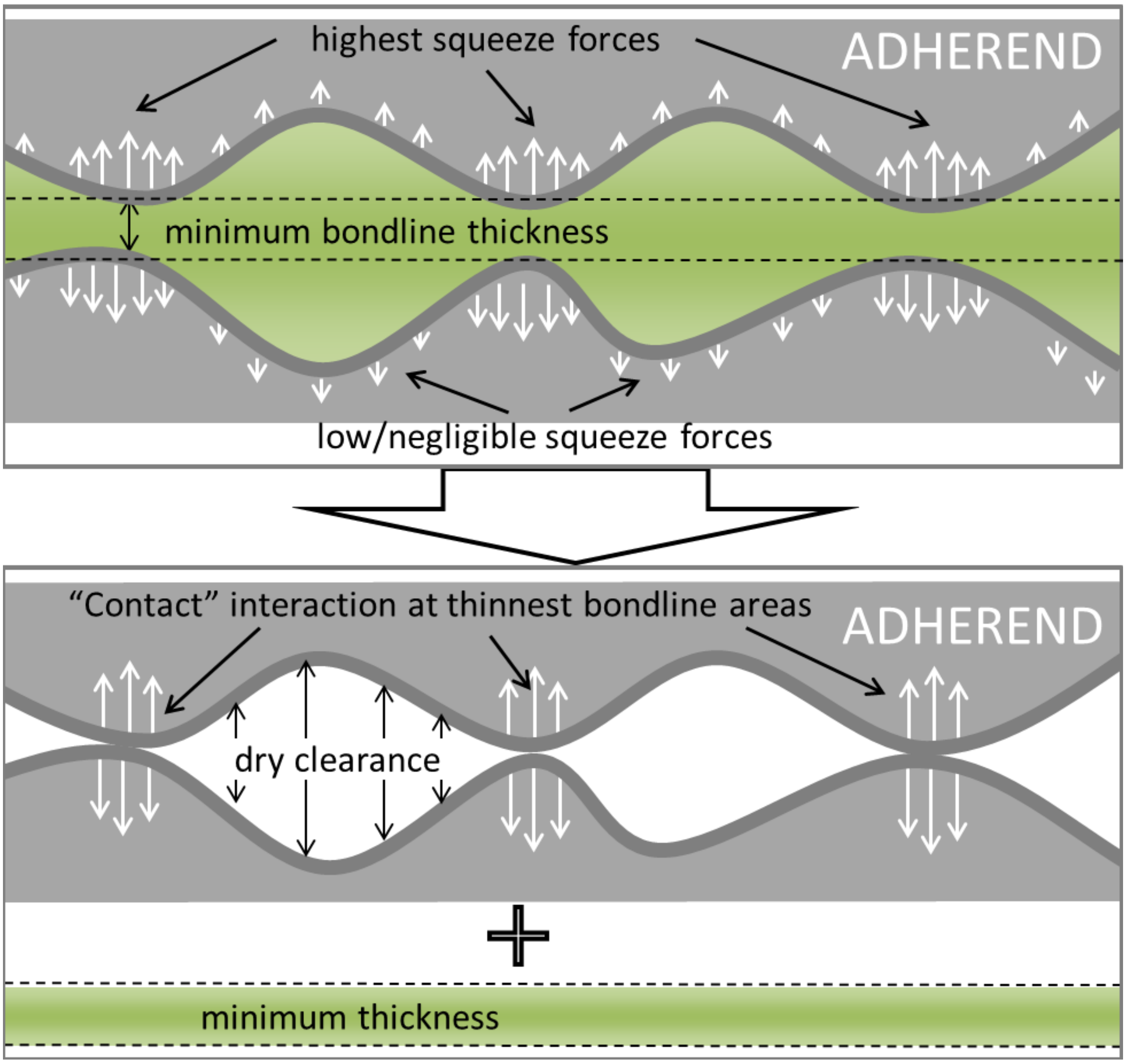

Figure 3-13. Separation of the uncured bonded joint into dry and wet components. (Pictorial representation not reflective of scales or likely variation modes.)

3.3.3 Dry component: Linear model with contact search by quadratic programming (QP)

The dry assembly has been modelled by part linearisation and modelling of the hard contact into a quadratic equation. The contact solution follows prior art applied to automotive sheet metal (Lindau et al., 2016), with the node interactions reframed to better reflect the assumptions of the bonding problem. The solution is reformulated below for the benefit of the reader. Solution of the contact problem starts with the following simplifications:

1. The individual assembly parts satisfy the small deformations hypothesis, which justifies the application of the principle of superposition and hence linearisation;
2. External forces are applied normal to the nominal surface at each position[xxvii];
3. Adhesive behaviour has been accounted for in the wet component (as presented in Figure 3-13) and will be ignored for the determination of the dry component of the bondline thickness. The adhesive will, however, transmit the reaction forces and act as a lubricant which eliminates any friction between parts from tangential displacements.

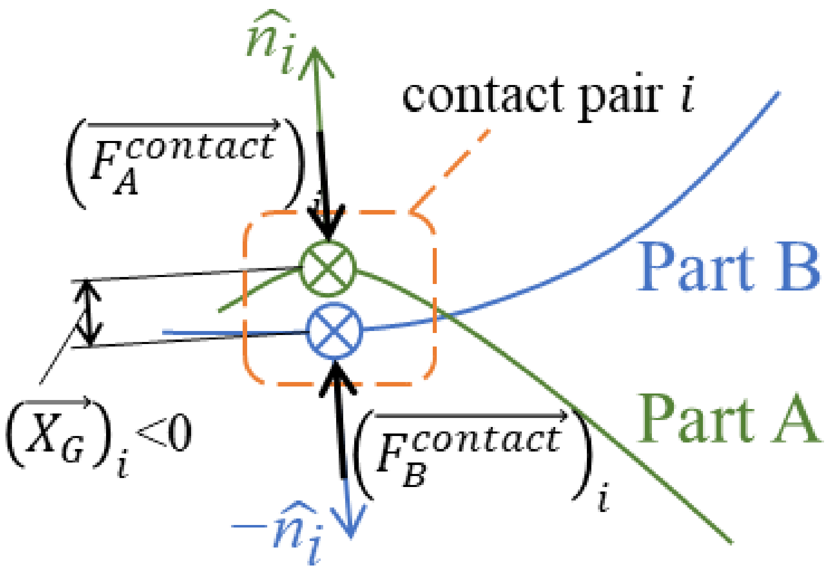

Figure 3-14. Part interaction based on node pairs with normal reactions only. The negative gap presented in the illustration signifies part penetration.

Through assumptions 1 and 2, only the interactions normal to the nominal mating surface (that is, only normal forces and displacements) are considered, as represented in Figure 3-14. Thus at node i, the force $\vec{F_i}$ is parallel to the vector normal to the surface $\hat{n}_i$; and similarly, the position $\vec{X_i}$ is a deviation from nominal that occurs normal to the surface only as per equations (3-16) and (3-17).

[xxvii] Alternatively: the effect of any forces not normal to the nominal interface surface is negligible.

$$\vec{F_i} = F_i\hat{n}_i = (F_{i,x}, F_{i,y}, F_{i,z}) \quad \textbf{(3-16)}$$

$$\vec{X_i} = X_i\hat{n}_i = (X_{i,x}, X_{i,y}, X_{i,z}) \quad \textbf{(3-17)}$$

where the subscript i denotes the node in question, and subscripts x, y, z mark each cartesian component of the force or displacement.

A linear model for any change in the positions of a part's nodes, $\overrightarrow{\Delta X}$, under external forces $\vec{F}$ (all normal to the nominal surface) is constructed based on the compliance matrix $\mathbf{U}$:

$$\overrightarrow{\Delta X} = \begin{bmatrix} \Delta X_1 \\ \vdots \\ \Delta X_N \end{bmatrix} = \begin{bmatrix} U_1 & \cdots & U_{1N} \\ \vdots & \ddots & \vdots \\ U_{N1} & \cdots & U_{NN} \end{bmatrix} \begin{bmatrix} F_1 \\ \vdots \\ F_N \end{bmatrix} = \mathbf{U}\,\vec{F} \quad \textbf{(3-18)}$$

This is achieved by extracting the compliance matrix from a subset of N nodes in a finite element mesh, which is the usual procedure when using the Method of Influence Coefficients (MIC) and similar to the superelement-based procedures developed within ADCATS work (Bihlmaier, 1999; Merkley, 1998).

The contact problem is formulated by considering the points interfacing between two linearised bodies A, B. The gap between them is also linearised, and a single normal $\hat{n}_i$ is picked at each contact pair i, such that the scalar value of the gap is positive, $\left(\overrightarrow{X_G}\right)_i = \left(\overrightarrow{X_{B-A}} - \overrightarrow{X_{A-B}}\right)_i > 0$, when there is clearance. With this, the change in the gap, $\overrightarrow{\Delta X_G}$, as a result of applied forces $\overrightarrow{F_A}$, $\overrightarrow{F_B}$ is:

$$\overrightarrow{\Delta X_G} = \overrightarrow{\Delta X_{B-A}} - \overrightarrow{\Delta X_{A-B}} = \mathbf{U_{B-A}}\overrightarrow{F_B} - \mathbf{U_{A-B}}\overrightarrow{F_A} \quad \textbf{(3-19)}$$

where the first term of the subscript indicates the part studied, and the second term is the part it interfaces with; therefore for example, $\mathbf{U_{B-A}}$ is the compliance matrix of the nodes of B that form a contact pair with nodes in part A.

The forces at work in the assembly are either external forces $\overrightarrow{F^{ext}}$, or internal forces which (given assumptions 2 and 3 above) are solely from contact. Thus

$$\vec{F} = \overrightarrow{F^{ext}} + \overrightarrow{F^{contact}} \quad \textbf{(3-20)}$$

Consider deflection due to internal forces $\overrightarrow{F^{contact}}$ that arise due to contact. These will be applied on both parts, due to action-reaction. Thus at each contact pair i:

$$\left(\overrightarrow{F_B^{contact}}\right)_{\mathrm{i}} = -\left(\overrightarrow{F_A^{contact}}\right)_{\mathrm{i}} = \overrightarrow{F_i^{contact}}\hat{n}_i \qquad \textbf{(3-21)}$$

And the vector of gap dimensional change is expressed as:

$$\begin{aligned} \overrightarrow{\Delta X_G} &= \overrightarrow{\Delta X_{B-A}^A} - \overrightarrow{\Delta X_{A-B}^B} \\ \overrightarrow{\Delta X_G} &= \mathbf{U_{B-A}}\overrightarrow{F_B^{ext}} - \mathbf{U_{A-B}}\overrightarrow{F_A^{ext}} + (\mathbf{U_{B-A}} + \mathbf{U_{A-B}})\overrightarrow{F^{contact}} \end{aligned} \qquad \textbf{(3-22)}$$

When looking at the above with algorithmic implementation in mind, this effectively means that the forces are being applied sequentially, as $\overrightarrow{F^{contact}}$ is initially unknown:

$$\begin{aligned} \overrightarrow{X_G^{final}} &= \left[\left(\overrightarrow{X_B^{init}} - \overrightarrow{X_A^{init}}\right) + \mathbf{U_{B-A}}\overrightarrow{F_B^{ext}} - \mathbf{U_{A-B}}\overrightarrow{F_A^{ext}}\right] + \\ &\qquad + (\mathbf{U_{B-A}} + \mathbf{U_{A-B}})\overrightarrow{F^{contact}} \\ \overrightarrow{X_G^{final}} &= \overrightarrow{X_G^{no\ contact}} + \mathbf{U_G}\overrightarrow{F^{contact}} \end{aligned} \qquad \textbf{(3-23)}$$

The simplified version of equation (3-23) uses an interim value for the gaps $\overrightarrow{X_G^{no\ contact}}$, which only accounts for the external forces. It also consolidates the compliance of multiple parts into a single compliance matrix $\mathbf{U_G}$:

$$\overrightarrow{X_G^{no\ contact}} = [\left(\overrightarrow{X_B^{init}} - \overrightarrow{X_A^{init}}\right) + \mathbf{U_{B-A}}\overrightarrow{F_B^{ext}} - \mathbf{U_{A-B}}\overrightarrow{F_A^{ext}}] \qquad \textbf{(3-24)}$$

$$\mathbf{U_G} = (\mathbf{U_{B-A}} + \mathbf{U_{A-B}}) \qquad \textbf{(3-25)}$$

The unilateral contact condition is enforced by quadratic programming (QP), by solving a problem resulting from the Hertz-Signorini-Moureau criteria (Lindau et al., 2016; Wriggers, 2006, p. 71)

1. $(\overrightarrow{X_G})_i \geq 0,\ \forall i$ — no penetration **(3-26)**

2. $(\overrightarrow{F^{contact}})_i \geq 0,\ \forall i$ — no “pull” reaction during cure **(3-27)**

From inequations (3-26), (3-27) and as $\overrightarrow{X_G}$, $\overrightarrow{F^{contact}}$ are column vectors of positive values,

$$\left(\overrightarrow{X_G}\right)^{\mathrm{T}}\overrightarrow{F^{contact}} \geq 0 \qquad \textbf{(3-28)}$$

The definition of $\overrightarrow{X_G}$ in Eq. (3-23) is substituted in Eq.(3-28):

$$\left(\overrightarrow{X_G^{no\ contact}}\right)^T \overrightarrow{F^{contact}} + \left(\overrightarrow{F^{contact}}\right)^T \mathbf{U_G}\overrightarrow{F^{contact}} \geq 0 \tag{3-29}$$

Further, either the contact force or the gap will be zero at each contact pair, which is expressed by the third Hertz-Signorini-Moureau criterion:

$$3.\ (\overrightarrow{X_G})_{\mathrm{i}}(\overrightarrow{F_{contact}})_i = 0,\ \forall \mathrm{i} \tag{3-30}$$

Thus, the quadratic inequation (3-29) can be turned into a convex minimisation problem which looks for

$$\begin{gathered}\overrightarrow{F^{contact}} = \operatorname{argmin}(func),\\ func = \left(\overrightarrow{X_G^{no\ contact}}\right)^T \overrightarrow{F^{contact}} + \left(\overrightarrow{F^{contact}}\right)^T \mathbf{U_G}\overrightarrow{F^{contact}}\end{gathered} \tag{3-31}$$

with $\overrightarrow{F^{contact}}$ as the independent N-dimensional variable.

In this implementation, the problem has been solved with quadratic programming (QP) using MATLAB's `quadprog` function, which offers pre- and post-processing, algorithm selection and convergence parameter control with little user effort.

The problem is reformulated for input to the function as

$$\begin{gathered}\mathrm{func} = \frac{1}{2}\left(\overrightarrow{F^{contact}}\right)^T (2\mathbf{U_G})\overrightarrow{F^{contact}} + \overrightarrow{X_G^{no\ contact}}\overrightarrow{F^{contact}},\\ \text{subject to}\begin{cases}-\mathbf{U_G}\overrightarrow{F^{contact}} \leq \overrightarrow{X_G^{no\ contact}}\\ \overrightarrow{(0)}_{Nx1} \leq \overrightarrow{F^{contact}}\end{cases}\end{gathered} \tag{3-32}$$

and the input to MATLAB is (with each variable/ parameter appearing in the same order):

```
F_contact = quadprog(2*U_G, X_G_nocontact, -U_G, X_G_nocontact,
[],[],zeros(N,1),[])
```

with the `[]` empty square brackets denoting the absence of equality constraints or upper bounds for $\overrightarrow{F^{contact}}$.

The algorithm used to determine the contact force of the problem was `quadprog`'s default interior-point convex optimisation algorithm.

From the resulting value of $\overrightarrow{F^{contact}}$, it is then straightforward to use the linear models in (3-18) and (3-19) to calculate the individual part positions, as well as $\overrightarrow{X_G}$ which is the parameter of most interest in this study.

It must be noted that the formulation presented herein, and applied throughout this work, requires matching superelement meshes at both sides of an interface, such that contact pairs are clearly defined. This is similar to the work developed in ADCATS (Bihlmaier, 1999; Merkley, 1998); later research by the Chalmers group addressed this by implementing automated contact pair search methods (Lindkvist, Wärmefjord and Söderberg, 2008). For the purpose of this thesis, all meshes have indeed been built with matching nodes.

3.3.4 Wet component: Minimum bondline thickness by squeeze-flow

Though it may be tempting to assume hot-setting adhesives flow freely and fully accommodate any part deflection, this is not strictly true. This is for two reasons: first, adhesives will usually contain a medium, such as a carrier film or glass beads, which effectively behaves as incompressible and limits the minimum interface gap achievable (Figure 3-15); secondly, viscous resistance to flow increases sharply as the adhesive layer is squeezed and becomes thinner, increasing the tendency to have *some* adhesive left, even under large pressures, by the time cure is complete.

Squeeze flow modelling in planar bondlines has not been widely documented. After all, the bondline geometry and process window tend to be simple enough to characterise the behaviour empirically (as indicated, for instance, remarks in the introduction to Hubert and Poursartip, 1998). There is no clearly established consensus on how to characterise the flow properties of an adhesive, if at all. Further, the magnitudes of interest change from application to application, with porosity and ability to apply the adhesive receiving more attention than the evolution of bondline dimensions. Two examples of empirical flow characterisation for commercial use products are the “area increase” used by 3M (3M, 2009) and some final bond thickness assessments presented by Henkel

(Henkel, 2005). In both cases, the planar dimensions of the initial bond (which equation (3-33) farther below will show to be highly influential) were not disclosed.

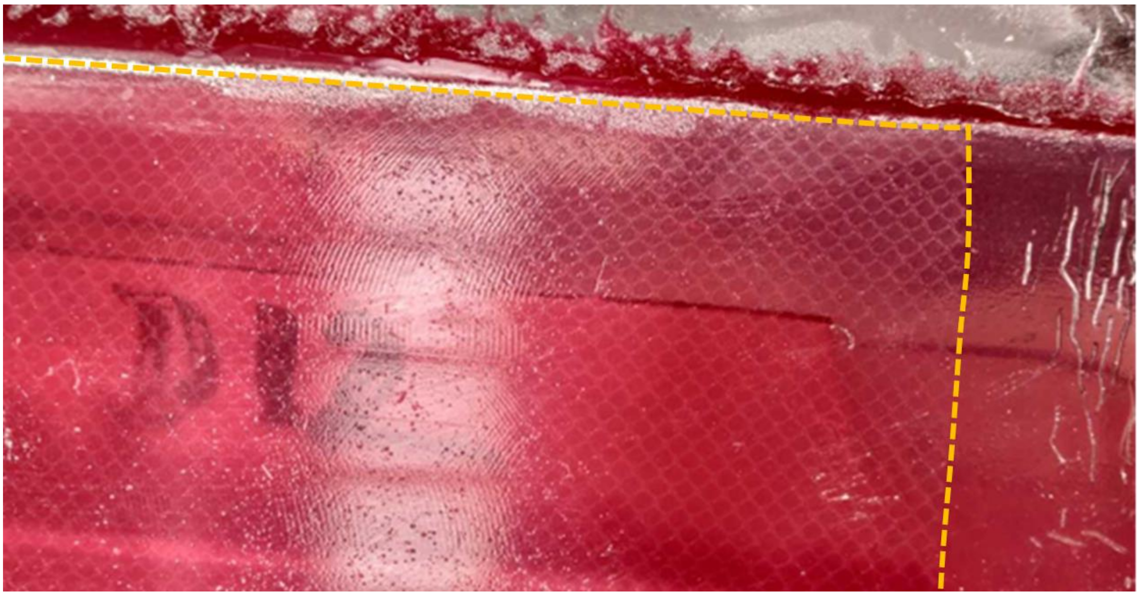

Figure 3-15. Close-up of a bondline (3M AF163-0.6K) released from the adherends, resulting from tests carried out within this work. The knit carrier is only visible within the original uncured area (marked by the dashed line).

However, there have been some more detailed efforts to model such flow in dominantly-viscous materials (Smiley, Chao and Gillespie Jr, 1991) including cases where the focus was not bondline thickness, but other quality criteria such as porosity (Chester and Roberts, 1989). The packaging industry has seen more recent study to support process parameter optimisation for adhesive dosage control (Morris and Scherer, 2016).

The flow was modelled as described in the references in the paragraph above.

The basic assumptions are:

(a) The uncured adhesive behaves as an incompressible, purely-viscous Newtonian fluid;

(b) Each layer of carrier fabric acts as a solid boundary and the layers of adhesive under and above it act as different flow domains;

(c) Both adherends can be approximated as flat and parallel for flow purposes;

(d) The problem is quasi-steady, and dominated by viscous forces with a very low Reynolds number; thus, effects of inertia and accelerations are negligible (quasi-static force equilibrium applies);

(e) Flow only takes place in the cross-section plane without any longitudinal component;
(f) Adhesive flows freely once squeezed out from between adherends.

The general concept and dimensions are captured in Figure 3-16. Thickness of a single squeezed bondline at a time t, thus, can be idealised as

$$b_{1t}(t, b_0) = \frac{1}{\sqrt{\left(\int_0^t \eta^{-1} dt\right) \frac{2P}{w^2} + \frac{1}{b_0^2}}} \tag{3-33}$$

where η is the adhesive kinematic viscosity, $P = P_{external} - P_0$ is the manometric pressure applied, $b_0 = b_{1t}(t = 0)$ is the initial bondline thickness, and w is the bond width. The width of the bondline is assumed to remain constant and equal to a starting value w (which is given by the adherend width, i.e. the stringer foot flange) at all times. For the benefit of the reader, the step by step derivation of this closed-form solution is presented in Appendix A — Derivation of the 1D squeeze-flow closed-form solution.

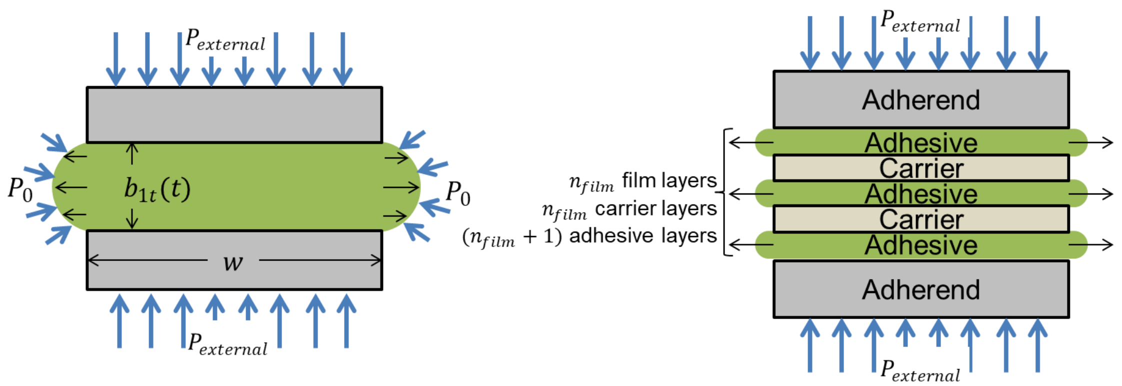

Figure 3-16. Squeeze-flow with a single domain (left) and multiple domains (right)

An additional result of interest comes from the pressure distribution along the cross-section (with x representing the distance to the centre of the cross-section):

$$p(x) = P_0 + 6\eta\left(\frac{-\dot{b}_{1t}}{b_{1t}^3}\right) w^2 \left(1 - \left(\frac{x}{w/2}\right)^2\right) \tag{3-34}$$

This result implies that (a) there is no meaningful adhesive flow unless external pressure is successfully applied; (b) the adhesive pressure which reacts the external loads is not homogeneous, and therefore is not necessarily equivalent to contact within each cross-section.

The total bondline thickness for n_{film} layers of film adhesive with carrier will thus be, as per Figure 3-16,

$$b_{bond} = \sum_{j=1}^{n_{film}+1} b_{1t}\left(t, b_{0_j}\right) + \sum_{k=1}^{n_{film}} b_{carrier_k} \tag{3-35}$$

Note that since the adhesive is assumed to be distributed evenly at both sides of the carrier in each film layer, not all flow domains will have the same starting thickness. Domains adjacent to an adherend will contain adhesive from a single film layer, while domains between layers of carrier will be initially twice as thick.

$$b_{0_j} = \begin{cases} b_{0_{layer}} & \text{if } j \in \{1, n_{film}+1\} \\ 2b_{0_{layer}} & \text{otherwise} \end{cases} \tag{3-36}$$

with $b_{0_{layer}}$ representing the initial thickness of adhesive on each side of a film layer's carrier. The carrier thickness $b_{carrier}$, initial adhesive thickness $b_{0_{layer}}$, and nominal thickness of an adhesive film layer as-applied $b_{bond}(n_{film} = 1, t = 0)$ are thus related:

$$b_{bond}(n_{film} = 1, t = 0) = 2b_{0_{layer}} + b_{carrier} \tag{3-37}$$

so for a typical 0.25 mm thick film adhesive layer, where the thickness of the carrier, $b_{carrier}$, is 0.05 mm, the value of $b_{0_{layer}}$ will be 0.01 mm.

The only term dependent on the adhesive properties, as seen in equation (3-33), is $(\int_0^t \eta^{-1} dt)$ which is a function of the rheology curve for the specific temperature cycle encountered. The evolution of the viscosity with time is highly dependent on the heat rate (Préau and Hubert, 2016), which can be difficult to predict and control for industrial equipment and large assemblies, and even idealised test data is not always provided by suppliers. For the current study, this information is estimated based on the data in literature and experimentally observed minimum bond thickness.

3.3.4.1 Integration with the calculated dry gap

The estimated value $b_{bond}(n_{film}, t)$ of the minimum bondline thickness is incorporated to the interface gap as extra thickness on one of the adherends for the purpose of modelling. This is done in one of two ways, depending on the boundary conditions (Figure 3-17):

a) If the parts are free to float to each other, the minimum bondline thickness value is calculated from the mean contact pressure from the dry step, and added uniformly to the gap once the deflection due to external and contact forces has been calculated.
b) If distance between the parts is controlled by non-adhesive features (such as tooling, spacers, or part features directly in contact), the bondline thickness is subtracted from the gap prior to solving the dry contact problem; it is then updated based on the average contact pressure from the dry contact, and added back. This may need iterative adjustment (Figure 3-18).

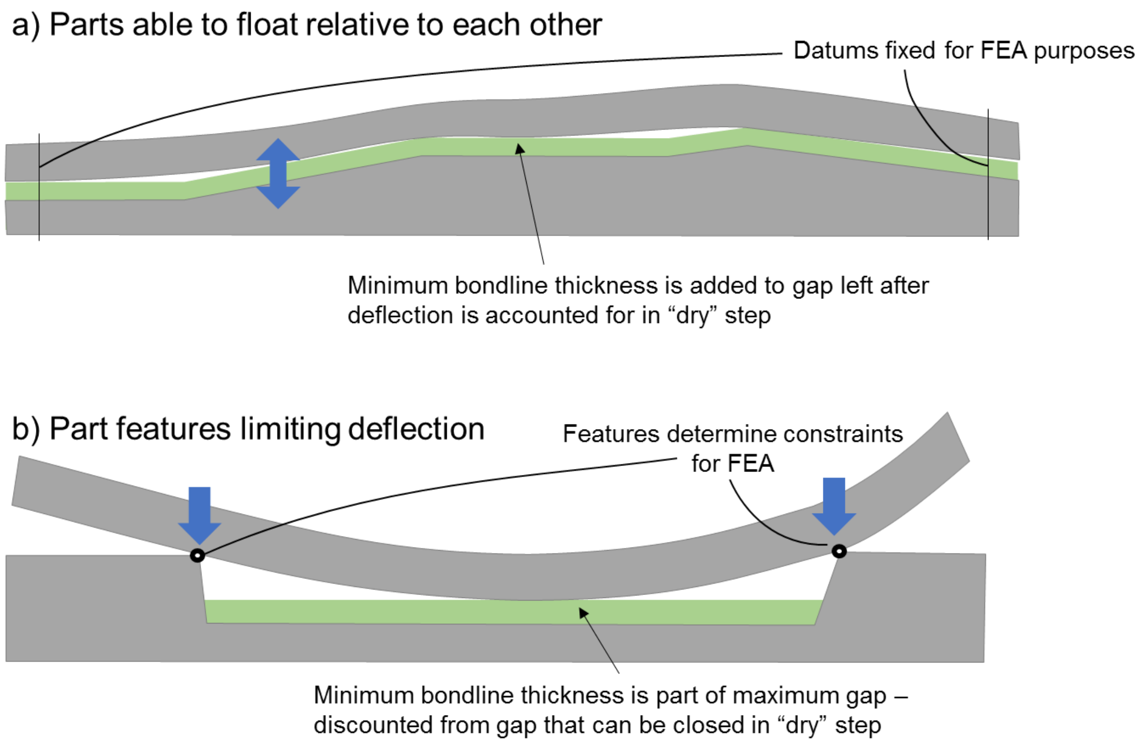

Figure 3-17. Dry/wet separation based on simplified boundary conditions.

Although the iterative solution for case b) might seem unwieldy, the one assembly modelled that fell under this type converged within 0.01 mm in a single step (that is, the QP dry assembly had to be performed only once). This may be due to the high external pressure applied, which meant the bondline thickness was insensitive to variations in the cure parameters.

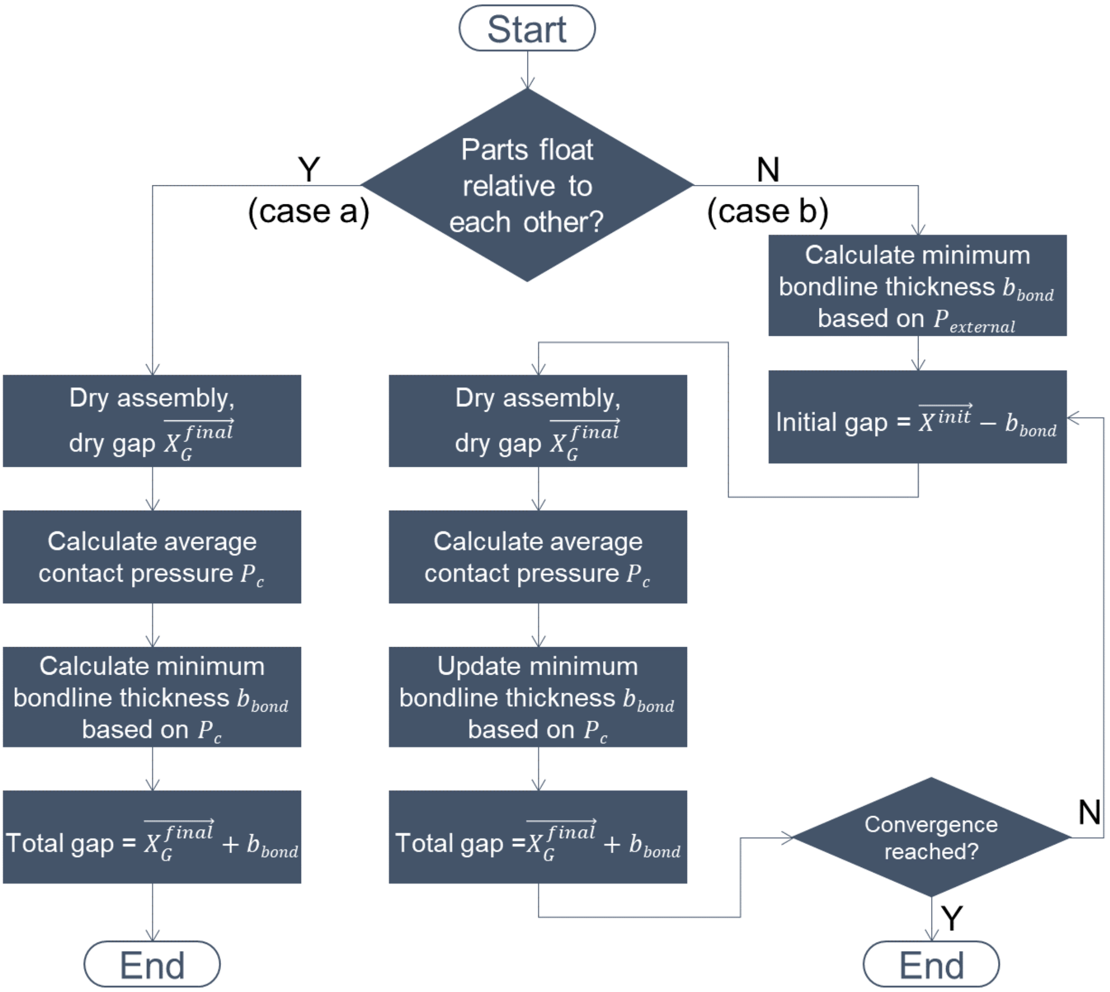

Figure 3-18. Integrating the dry and wet bondline thickness contributors based on boundary conditions.

3.4 Chapter summary

This chapter presents the two methods proposed for non-rigid bond variation analysis: an estimator of assembly pressure requirements based on Fourier Transform, and a semi-analytical model that accounts for part deflections and adhesive flow.

These two methods offer different values:

- The spectral analysis works towards dimensionality reduction, with the possibility of translating any given stiffener into one numerical value with physical meaning.
    - Such simplification is not without shortcomings, which are discussed in detail, and tentative solutions developed.
- The semi-analytical model combines non-rigid part deflection with adhesive flow for the first time to the best of the author's knowledge; indeed, as shown by the literature review, this is also one of the few instances in which an assembly model is created that accounts for the mechanics of joint formation at all.
    - The model combines methods developed for spot weld modelling, where each part in the non-rigid assembly is linearised and their interaction turned into a computer-friendly optimisation problem; and the adhesive flow is approximated with a closed-form solution to a planar case.
    - Both 'building blocks' are linked by equating hard contact reaction forces with the pressure within the adhesive associated to squeeze-flow.

The semi-analytical model will be applied to a series of panel assemblies, where long, slender stiffening elements are bonded to skins. As a supplement to this, detailed application of the spectral analysis to these assemblies can be found in Appendix I — Test of the spectral pressure score.

4 METHOD DEMONSTRATION

4.1 Monte-Carlo assembly simulation for a simple scenario

A simple demonstration of the concept of assembly simulation for tolerancing has been developed, using simplified geometries and variation profiles.

The following elements are illustrated: generation of virtual parts based on (arbitrary) variation data; virtual assembly of said parts; diagnosis of conformance based on the virtual assembly results; and analysis to link the conformance/non-conformance to the presence of certain modes of variation. The relationship between these is summarised in Figure 4-1. (Tolerance synthesis, already present in the literature, is not included in the demonstration.)

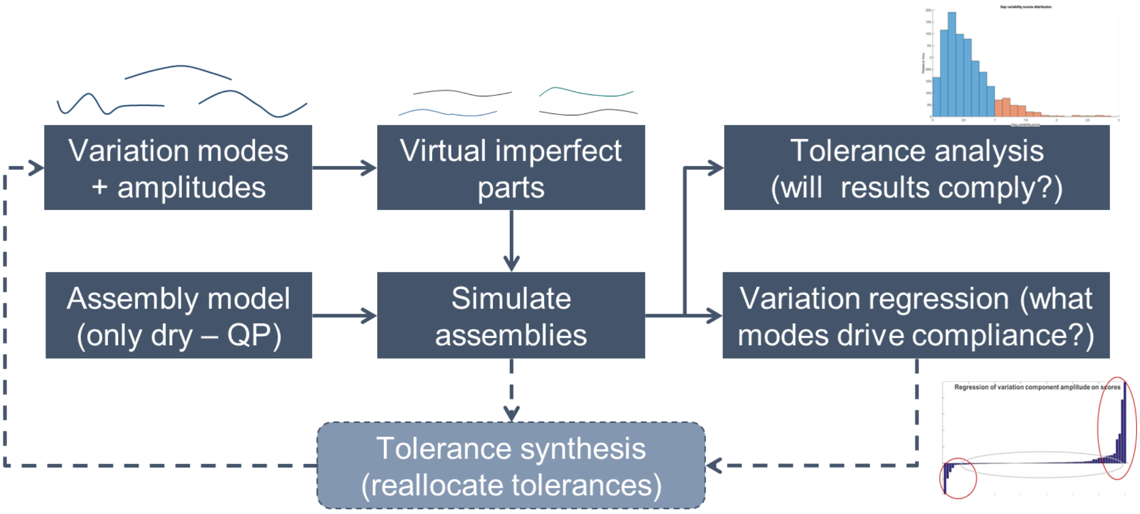

Figure 4-1. Process flow for the generic demonstration.

4.1.1 Setup

A stringer is pressed on to a stiff, nominally flat skin. The stringer is pinned on tooling lugs (non-structural) situated at both ends and is assumed to behave as a simply-supported beam. In all cases, a single layer of adhesive film has been assumed, 0.250 mm thick before cure, with 0.050 mm carrier thickness, average viscosity during cure 50 Pa·s, and 1200 s cure time.

Part variation is modelled as a linear combination of three modes: a whole-length warp, mid-range waves, and shorter-range waviness, with fixed phase (Figure 4-2). Variation amplitude was modelled as uniformly distributed for each mode, with a maximum value inversely proportional to the spatial frequency (longer range waves result in bigger deviations); that is,

$$\delta(L) = \sum_{n=1,2,7} \frac{a_0}{n} sin(2\pi \frac{n}{2L_{stringer}} L) \cdot k_n; \quad k_n \sim \text{Unif}(-1,1) \tag{4-1}$$

With a value of the maximum amplitude, a_0, of 1 mm, the maximum variation amplitudes $^{a_0}/_{n}$ for modes $n = 1$, $n = 2$, $n = 7$ are, respectively, 1.000 mm, 0.500 mm, and 0.146 mm.

(Note that the power law $a_n \propto 1/n$ matches general observations from literature, as well as in-house measurements which showed approximately $a_n \propto 1/n^{\gamma}$, with $\gamma \in \ (0.7, 1.3)$.)

The stringer modelled was based on the 'Thick' stringer from the flat test panels, with length $L_{stringer}$ 2167 mm, inertia I 274000 mm^4, and 512 equidistant nodes under the cross-section symmetry plane. The bonding pressures considered ranged from 0.01 MPa to 0.5 MPa; this goes from a representative large external-weight pressure to mid-low autoclave pressure (5 bar).

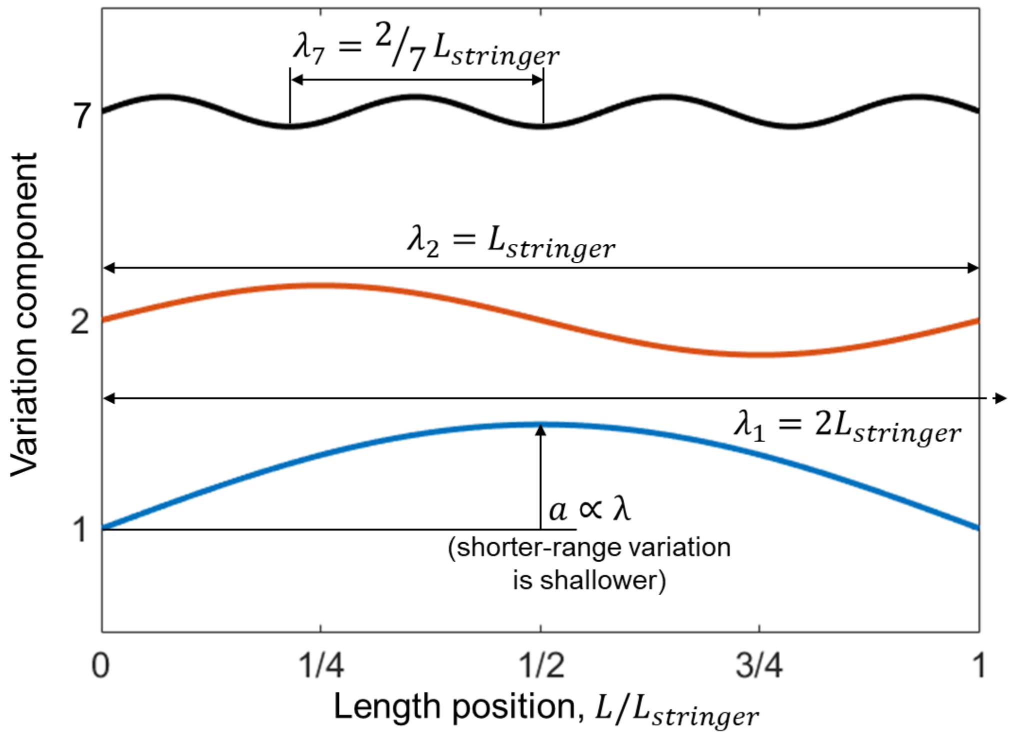

Figure 4-2. Variation components for a generic case as per expression (4-1).

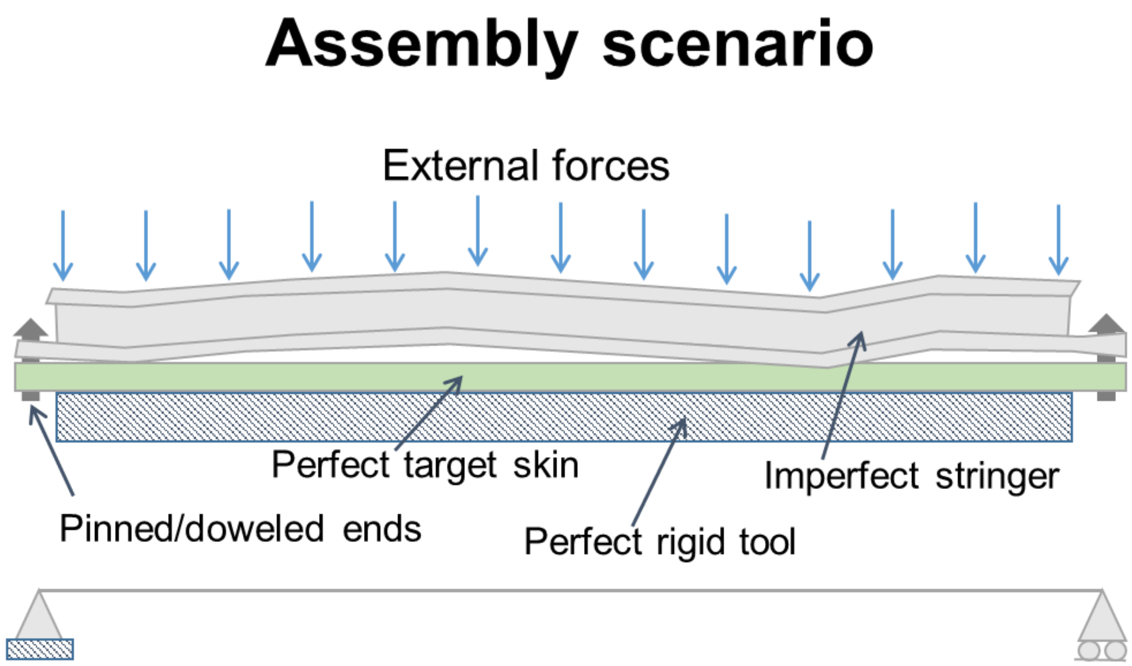

Figure 4-3. Scenario for the assembly, with the stringer approximated as simply supported (pictured).

4.1.2 Analysis

A test group of 1000 imperfect stringers were randomly generated (Figure 4-4 shows representative examples) and virtually bonded to the stiff plate, using an array of representative external downward pressures. The lowest pressure used was 0.01 MPa (corresponding to application of substantial weight e.g. by stacking bags of shot adding up to about 400 lb [180 kg]); the highest pressure was 0.5 MPa [5 bar], representative of an autoclave cycle. Figure 4-5 illustrates the evolution of the final geometries of the same examples as the pressure increased. The example stringers are the same as in Figure 4-4; it can be seen that the red stringer (which exhibited substantial maximum profile variation, but with long wavelengths) resulted in a much flatter bondline compared to the other examples, even under the lowest pressure case.

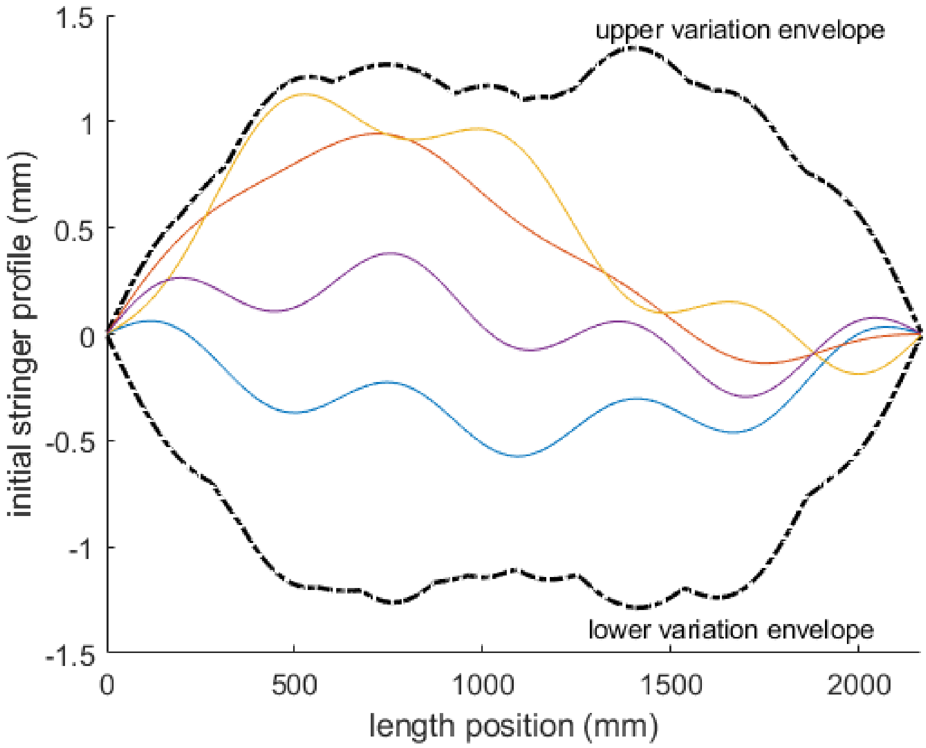

Figure 4-4. Samples and extremes of the stringer profiles generated.

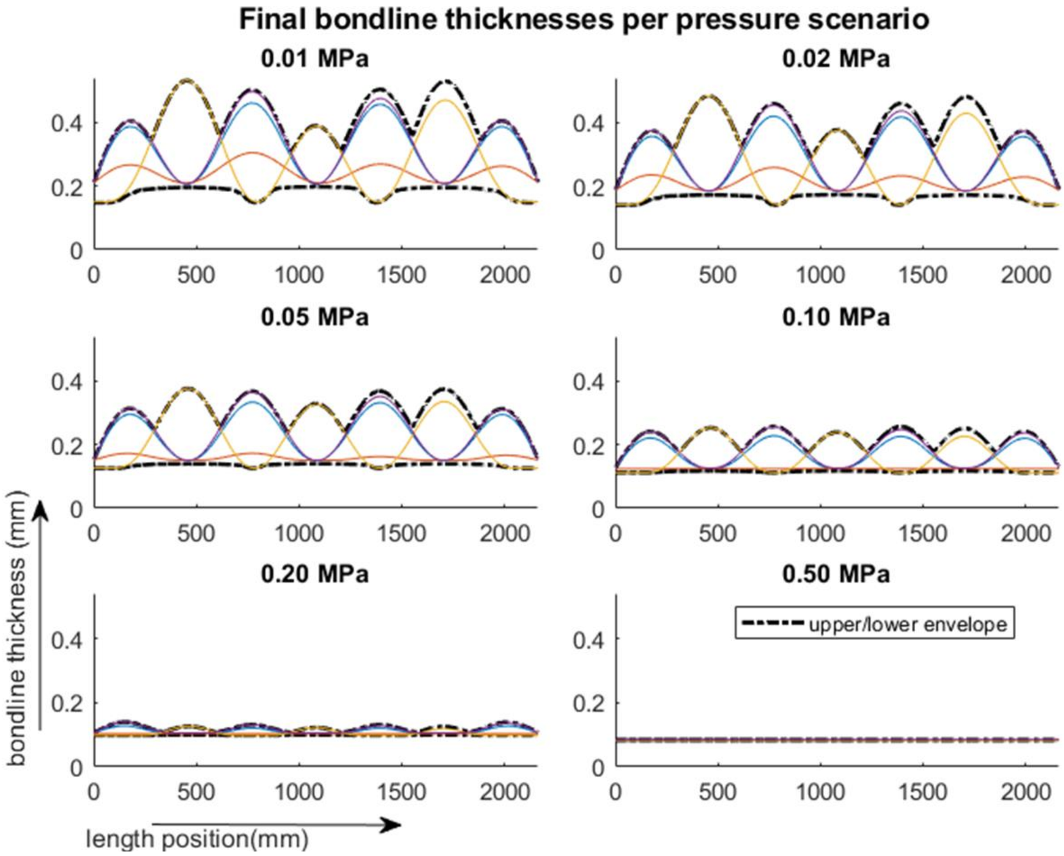

Figure 4-5. Final joint geometries: extremes and examples. The example colours correspond to the example initial variations in Figure 4-4.

The resulting interface geometries were evaluated using two scores based on a quadratic loss function: $S_{avg\ gap}$ evaluating the average final gap depth (Eq. (4-2)), and $S_{gap\ var}$ evaluating the gap depth standard deviation (Eq. (4-3)). An optimal bondline, in this case, will be as thin and uniform as possible, with no other considerations e.g. build stresses.

For ease of interpretation, both loss-of-quality scores are calculated such that, for a value of 1, the Root Mean Square (RMS) value of the respective metric (gap depth or gap depth variation) exceeds a typical allowable $\mathrm{tol}([metric])$; that is, the condition $S_{[criterion]} > 1$ implies nonconformance. When deviation from mean is considered, this is the same as evaluating the standard deviation (STD).

$$S_{avg\ gap} = \left(\frac{\mathrm{RMS}\left(\overrightarrow{X_G}\right)}{\mathrm{tol}(X_G)}\right)^2 ;\ \mathrm{tol}(X_G) = 500\ \mu\mathrm{m} \qquad \textbf{(4-2)}$$

$$S_{avg\ gap} = \left(\frac{\mathrm{STD}\left(\overrightarrow{X_G}\right)}{\mathrm{tol}(\mathrm{var}X_G)}\right)^2 ;\ \mathrm{tol}(\mathrm{var}X_G) = 50\ \mu\mathrm{m} \qquad \textbf{(4-3)}$$

As a supplement to the soft loss functions, an additional criterion has been used based on the rigid interpretation of tolerances: a rejection score $S_{max\ gap}$ which takes a value 1 (‘reject’) if the interface gap exceeds $\mathrm{tol}(X_G)$ in any spot, and 0 (‘accept’) otherwise. This results in a step function

$$S_{max\ gap} = \begin{cases} 1 & \text{if} \quad \max\left(\overrightarrow{X_G}\right) > \mathrm{tol}(X_G) \\ 0 & \text{otherwise} \end{cases} \qquad \textbf{(4-4)}$$

Given a characterisation of part variability, then, it is possible to use the stochastic simulation to identify the technical risk (in this case, understood as the probability of rejection) associated to each assembly process. Histograms for the scores $S_{avg\ gap}$ and $S_{gap\ var}$ of the simulation results in one of the assembly cases are presented in Figure 4-6, showing the expected fraction and reason for rejection.

In addition, the quality loss scores offer simple dependent variables to support linear regression based on contribution from each source of variation (or, in this case, each variation mode). This supports root cause analysis for quality loss.

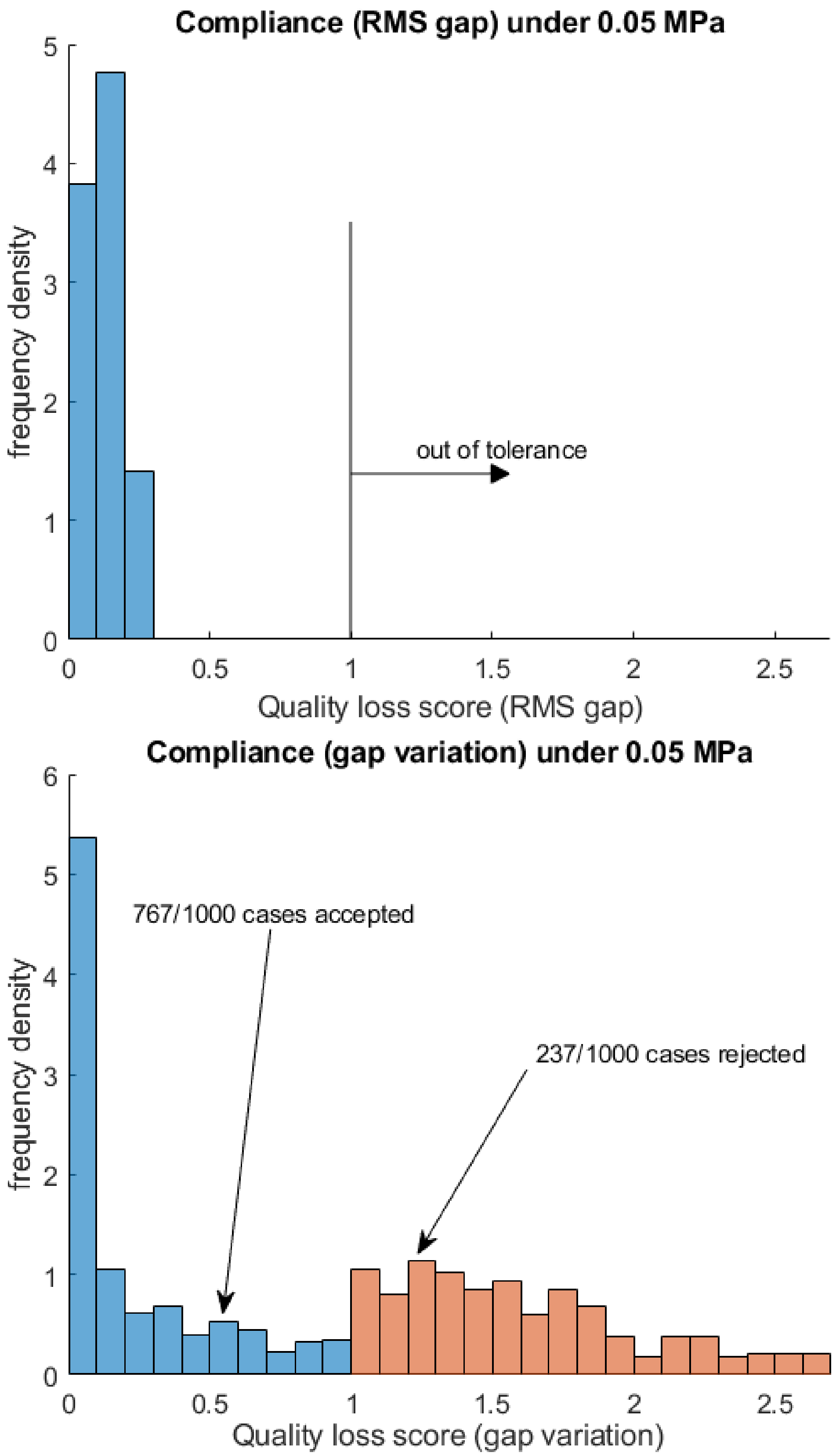

Figure 4-6. Histogram of the Taguchi-type scores for 1000 simulated cases. Note the fat tail of the distribution for the variation score $S_{gap\ var}$.

As an example, a linear fit with second-order components was conducted, using the simulation results. The model is presented in eq. (4-5), and includes linear and quadratic terms including interference of the modes. The resulting coefficients from a least-squares regression are presented in Figure 4-7 for $S_{gap\ var}$, which is the score leading to noncompliance. Among all mode-related parameters, the highest values are by far those of $\gamma_{7,7}$, corresponding to the (squared) third, short-wavelength component; this highlights that the longer waves are largely non-critical. Thus, the quality assurance requirements could be relaxed for these, while profile tolerances over a short range need further attention. This must be accounted for in design of the conformance checking process; in this case, for instance, clamping forces would be permissible and strongly bear into the final joint geometry.

$$S_{criterion} = \alpha + \left(\sum_{n=1,2,7} \beta_n k_n \right) + \left(\sum_{\substack{n=1,2,7 \\ m=1,2,7}} \gamma_{m,n} k_m k_n \right) \tag{4-5}$$

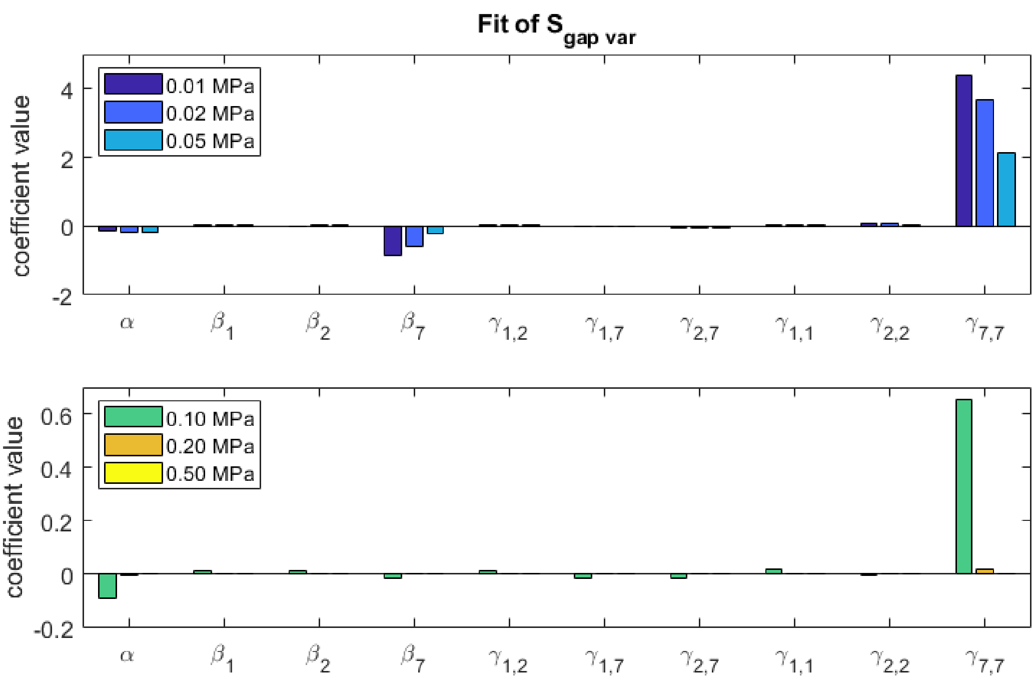

Figure 4-7. Regression coefficients for the variation components considered, against the gap variation score. The high and low pressure results are separated for visibility (note the difference in scale between both graphs).

In addition, the evaluation can be extended to different assembly conditions. This is demonstrated in Figure 4-8, where the evolution of quality metrics against external pressure is presented; in this case, a form of diminishing returns can be observed, whereby the already-compliant assemblies (i.e. the lower percentiles of quality loss) don't become significantly more compliant through further pressure increases.

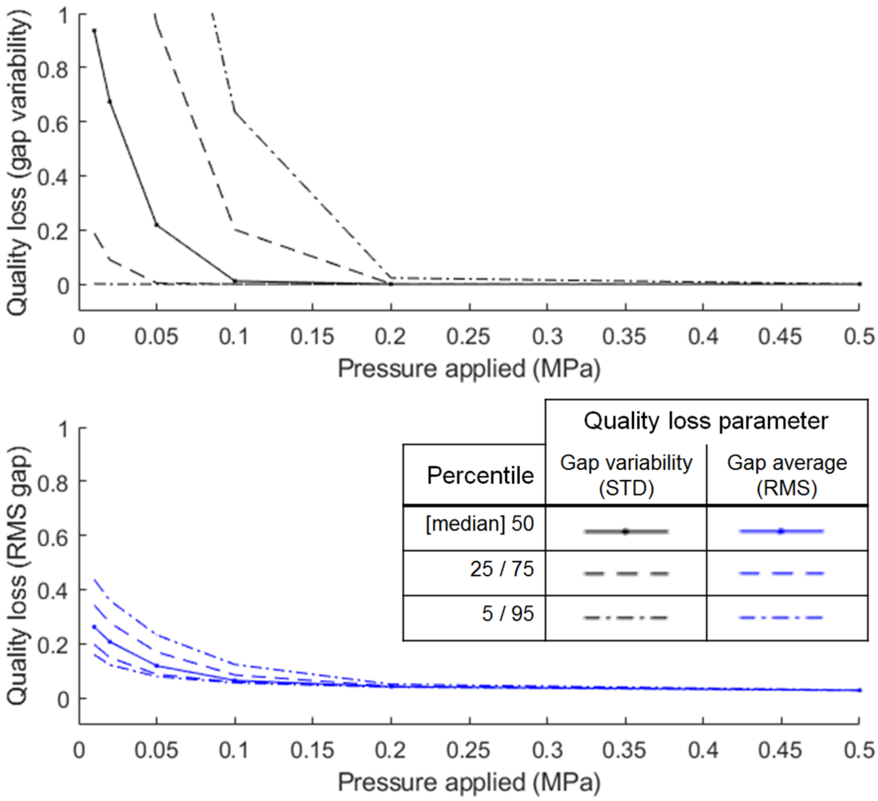

Figure 4-8. Evolution of quality loss scores as external forces increase.

4.1.3 Practical prospects

Though this is a simple example, there is nothing preventing this approach from being applied to larger problems. It is possible to use other input variables, e.g. multiple process parameters affecting variation; other evaluation approaches, e.g. go/no-go or unprocessed geometrical outcomes; and other analysis approaches, e.g. ANOVA or Bayesian modelling. Indeed, there are plenty of analysis tools commercially available which can support such statistical treatment, even if there is no commercial integrated package (as far as the author knows) which would support pre- and post-processing of the scenarios considered herein, with tolerancing based on variation modes. (Research applications, however, have been reported; additionally, study of some other assembly inputs, such as weld spot sequence, is well supported in some commercial packages.)

4.2 Mid-scale demonstrator simulation

As a supplement to small-scale physical demonstrators, a larger assembly, representative of a mid-scale wing panel demonstrator (as seen in Figure 4-11), also has been simulated. The geometry is based on a simplified section of a commercial narrowbody aircraft wing (Figure 4-9).

Figure 4-9. Example narrowbody passenger jet; the wing panel segment modelled is highlighted. Source for original: flickr.com, San Diego Air and Space Museum.

The analysis focusses on the impact of different assembly pressures and boundary conditions (single- or double-side pressure application) on the resulting bondline thicknesses and associated quality.

4.2.1 Geometry overview and modelling

4.2.1.1 Components

The panel corresponds to the forward (leading edge), inboard (wing-root adjacent) section of a lower wing cover panel. The segment covers six rib bays and thus seven rib planes have been considered; these have been simplified as parallel and equidistant. Six equidistant, constant-section stringers are considered, with a cross-section simplified as constant based on averaged values from a typical passenger jet. The material properties used are those of a generic aerospace alloy, $E = 70$ GPa, $\nu = 0.33$.

4.2.1.1.1 Stringers

The stringer cross-section geometry and separation (Figure 4-10) were generated to be representative of the ranges found in commercial aviation. The stringer separation was designed as measured over the skin surface, i.e. it is a geodesic and not a linear distance. Note that real stringers would rarely be constant in cross-sections; it is more likely that they would include grow-outs (local foot flange widening) to accommodate installation of ribs, as well as local thickening of one side of the web which tunes the panel's torsional response.

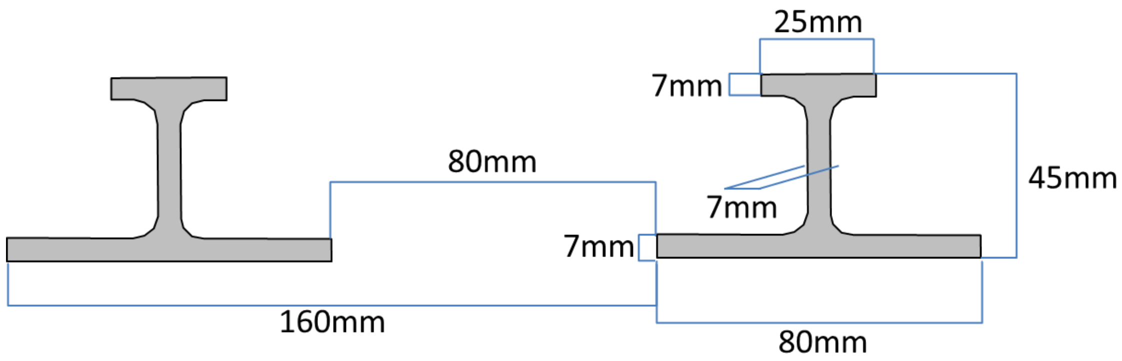

Figure 4-10. Generic stringer dimensions used. The skin curvature is omitted.

The properties of the stringer geometry are collected in Table 4-1.

Table 4-1. Properties of the cross-section of the mid-scale demonstrator stringer.

Second moment of inertia of the area of the cross-section, $I/1000$ [mm^4]	235
Area cross-section, A [mm^2]	973
Foot flange width, w [mm]	80
Cross-section shear factor, k_{shear}	0.324

4.2.1.1.2 Skin

The skin has double curvature with through-span variation. For simplicity, constant curvature is assumed at each rib plane (enforced through use of a "loft" shell creation tool) and three tangent, constant-curvature segments make up the aft edge of the panel. These reflect the almost single-curved stretch at the very root of the wing, as well as the aggressive curvature in the first few inboard rib bays. These control segments were designed such that the arc-length between accommodated stringers would correspond to the stringer separation in Figure 4-10.

The forward (leading edge) area has been widened to reflect attachment of the front wing spar. This area is not too critical to the analysis at hand, given how no stringers attach to it. In practice, a productionised wing panel would have to be attached to the front wing spar; this may require further consideration of variation of the leading-edge surfaces.

The wing thickness has been simplified as a uniform 10 mm. In a real scenario, local thickening would be expected around spar and engine attachments. In such an event, thickness transitions may result in profile variations in the skin bonding interface that are too steep for the stringer to be formed to match; this would result in in-built gaps.

4.2.2 Modelling assumptions

Given the large size of the assembly, a reduced mesh density has been used for this application. The generic nature of the design justifies the lack of highly detailed modelling: this application should yield mostly qualitative insights, rather than specific quantitative ones.

Roughly equally-spaced nodes were used, with one node at each stringer cross-section and similarly one skin node between nodes in neighbouring stringers (Figure 4-11). Control segments on the CAE model itself were procedurally queried, using a custom script to calculate the dimensions of the patch represented by each node.

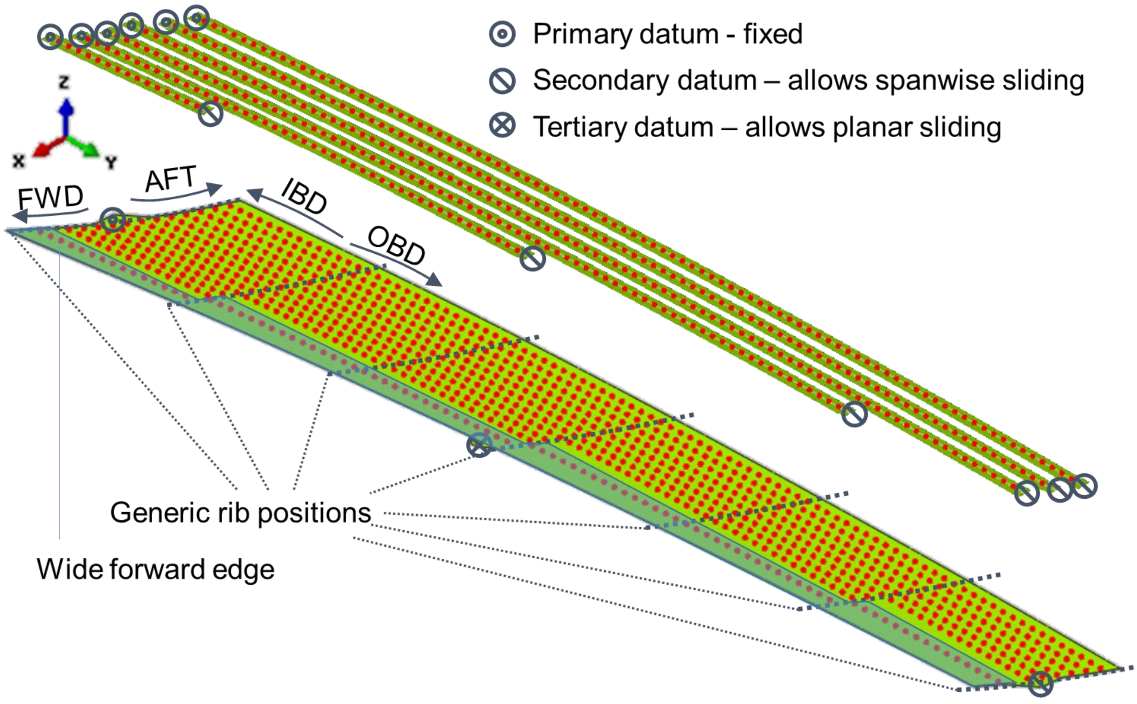

Figure 4-11. Assembly points of interest and boundary conditions. Directions are indicated: fore/aft (FWD/AFT), inboard/outboard (IBD/OBD). Stringers are numbered FWD-AFT, ribs IBD-OBD.

The interaction, as with all other scenarios, was modelled only normal to the nominal interface surface. Due to the high aspect ratio, it would always be a reasonable simplification to assume that the stringer-skin (IML) and tool-skin (OML) interfaces are the same surface; any profile mismatches, even ones due to nominal thickness transitions, would simply be washed into the initial gap values. In this case, no nominal profile mismatch has been assumed.

The stringers were modelled with a single compliance matrix (which is fairly sparse since pushing one stringer does not directly cause another one to deflect). Each stringer was modelled with 15 nodes per rib bay, all in a single row coinciding with the middle of the cross-section; therefore, stringers 1-3 had 90 nodes each, while much-shorter stringer 6 had only 15 nodes. The skin was modelled with a total of 900 nodes, of which the first 405 matched the stringer node locations; the remaining 495 only interfaced with the bonding tool (which is approximated as perfectly rigid and therefore required no model generation) on the other side. The distribution of the points used to generate the data for these nodes is presented, on top of renderings of the FEA models in Figure 4-12.

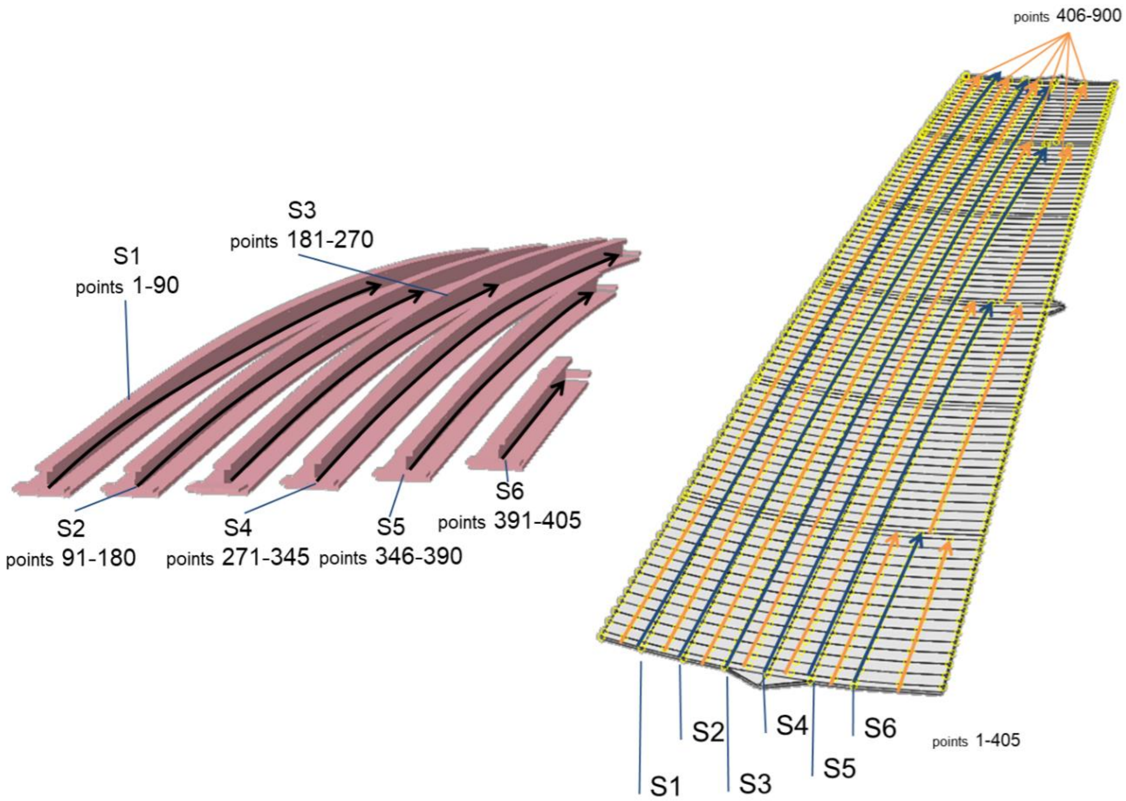

Figure 4-12. Node numbering sequence for mid-scale assembly compliance matrix generation. S1...S6 designates each stringer and the associated interfacing nodes.

The FE model required to generate the compliance matrix used beam elements B31, with approximate length 60 mm. The FE model for the skin used quad shell elements S4R, with typical size about 40 mm × 60 mm. The skin mesh can be seen in Figure 4-12. Both for the stringers and for the skin, the boundary conditions were as given by the datum feature structure presented in Figure 4-11.

The compliance matrices of the skin and all joint stringers are represented in Figure 4-13 and Figure 4-14 respectively, with the node numbering following the sequence presented two paragraphs above and in Figure 4-12. It is easy to note (1) the matrix symmetry; (2) the generally higher compliance of the skin; (3) the material continuity, expressed as smoothness where nodes are spatially close; (4) the low maximum compliance of the shorter stringers. In reality, the higher compliance of long stringers is not real once the nature of the assembly, based on local interactions, comes into play; instead, each of multiple sub-waves, as given by the interface gap geometries, would be concerned.

It should be noted that, due to the simplified modelling of the stringers (with only one, centred node at each cross-section), the impact of skin deflection is likely to be overestimated by the model. This is because the chordwise distance for the skin to deflect will always be modelled as between web positions. If, on the contrary, there was any consideration for foot flange nodes, the effective distance between unrestrained (contact-free) skin nodes would be reduced; in this case, the ability of the skin to deflect would be diminished, much like in the multi-stringer flat panel trials presented later in Section 5.3 Multi-stringer assembly trials.

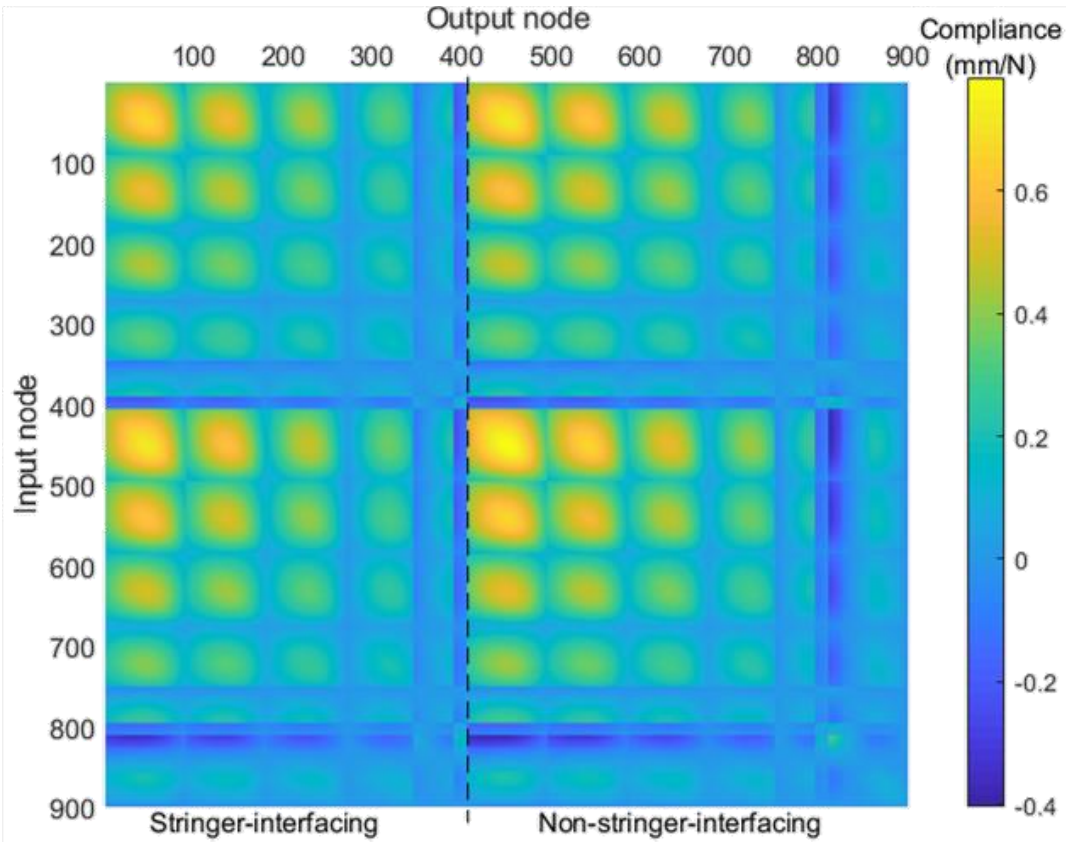

Figure 4-13. Compliance matric for the mid-scale demonstrator skin.

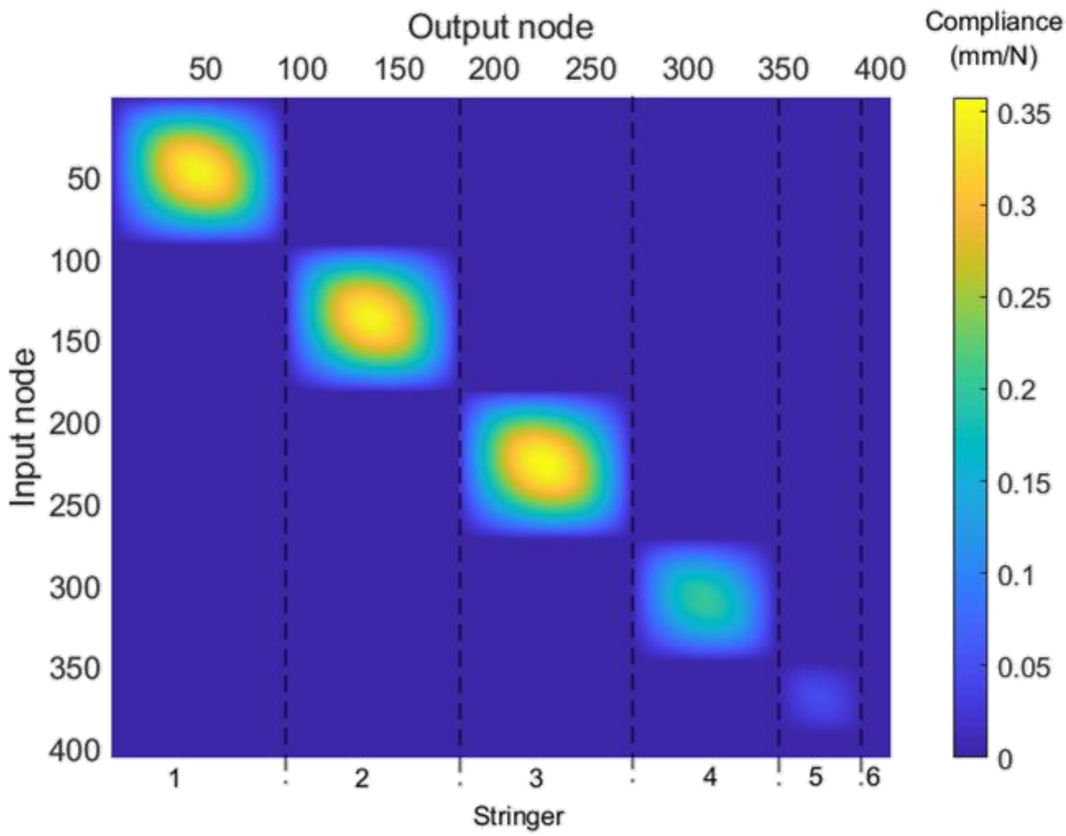

Figure 4-14. Compliance matrix for the mid-scale demonstrator stringers.

4.2.3 Variation generation

4.2.3.1 Stringers

Variation was generated modally based on a generic distance between press-forming and contact inspection points, in addition to shorter-range components. There is little point in modelling very long-range variation components, as those have been shown to be corrected with minimal external forces (including the part's own weight — so that such variation would not even be inspectable to begin with). Each stringer was given only two generic variation modes with maximum amplitude 1 mm: $k\cos[2\pi(y - y_{min})\lambda^{-1}]$, with wavelengths λ_1, λ_2 such that for stringer i of length $L_{stringer,i}$:

$$\lambda_{1,i} = \max\left(\left\{ 800\,mm\,,\ {}^{L_{stringer,i}}\!/_{6} \right\} \right);$$
$$\lambda_{2,i} = {}^{\lambda_{1,i}}\!/_{6}\ ; \qquad \textbf{(4-6)}$$
$$k_{1,i}, k_{2,i} \sim \mathrm{Unif}(-1, +1)$$

Note that the definition of the amplitude means that the phase of each mode may be reversed; beyond this, however, there are no further phase variables. The relative simplicity of the variation design is intended to avoid an explosion in the number of combinations variables, which would in turn necessitate a very large number of assembly simulations for the design space to be well explored. Even so, there are 12 variables (one per amplitude per stringer) for the stringers alone, which would result in 2^{12} = 4096 two-level combinations and 3^{12} = 531441 three-level combinations; this makes it seemingly impractical to prepare an analysis over the whole design space.

4.2.3.2 Skin

The skin was deformed in a slightly more complex way, given its 2D nature (as opposed to the 1D stringers) and more detailed knowledge of the inspection process. Skins are typically inspected while constrained by placing weights on top of them, and residual deformation is not recorded (provided it does not exceed given allowables) since the checking process is manual and operator-intensive. Thus, a hybrid mode+load approach was used, with neither the residual variation nor the highly-multivariate load data being recorded for further analysis:

1. Create a random distribution of weights, based on representative limits of 120 lb·f per weighted spot and a set of designated weight-bearing positions;
2. Deform the skin according to the weight distribution, as per its calculated compliance matrix;
3. Apply a mode-based variation.

The residual variation was generated by linear combination of three longitudinal flexure modes and two torsional modes, all modes exhibiting a random, uniformly-distributed amplitude $k \sim \mathrm{Unif}(-1, +1)$ [mm], independent of all others. The definitions are provided in Table 4-2.

Table 4-2. Residual variation modes for skins.

Mode	**Expression**	**Wavelength(s)** λ
Longitudinal flexure (1)	$k \sin[2\pi(y - y_{min})\lambda^{-1}]$	$(y_{max} - y_{min})$
Longitudinal flexure (2)	$k \cos[2\pi(y - y_{min})\lambda^{-1}]$	$(y_{max} - y_{min})$; $(y_{max} - y_{min})/2$
Longitudinal torsion	$k \dfrac{x - x_{min}}{x_{max}/x_{min}} \sin[2\pi(y - y_{min})\lambda^{-1}]$	$(y_{max} - y_{min})$; $(y_{max} - y_{min})/2$

4.2.3.3 Fixturing after deformation

A rigid fixturing step was added after the shape deformation, so as to ensure the datum points (which have compliance 0 in this model) did not need to deflect. This fixturing step was based on the simplification of the skin as contained in the horizontal XY plane, and any in-plane deviation of the datum points as negligible[xxviii].

For this simplified geometry, the fixturing was implemented as follows:

1. Primary datum to nominal (translation);
2. Secondary datum to nominal (rotation);
3. Tertiary datum to nominal (rotation — skin only).

This is implemented with the routine (4-6), where the datum points are designated A, B, C respectively, and using an auxiliary reference frame (x', y', z) resulting from rotating the original (x, y, z) about the vertical axis and based on the nomenclature in Figure 4-15.

Within the procedure in (4-7), the subscripts (A), (A,B), (A,B,C) indicate the datum points that have been fixed (and thus the part coordinates have been updated for); p represents any point in the part (inclusive of datum points); and the left pointing arrow ← indicates value assignation within the algorithmic implementation.

[xxviii] Recall that the deviations are assumed to be small, and normal to the interface surfaces only.

0. transform coordinates: $\theta = \text{atan}(\frac{y(\text{B})-x(\text{A})}{x(\text{B})-x(\text{A})})$;

$$x'(\text{p}) = x\cos\theta + y\sin\theta$$

$$y'(\text{p}) = -x\sin\theta + y\cos\theta$$

1. offset for A: $z_{\text{A}}(\text{p}) \leftarrow z(\text{p}) - z(\text{A})$ **(4-7)**

2. offset for B: $z_{\text{A,B}}(\text{p}) \leftarrow z_{\text{A}}(\text{p}) - z_{\text{A}}(\text{B}) * {}^{x'(\text{p})}\!/_{x'(\text{B})}$

3. offset for C: $z_{\text{A,B,C}}(\text{p}) \leftarrow z_{\text{A,B}}(\text{p}) - z_{\text{A,B}}(\text{C}) * {}^{y'(\text{p})}\!/_{y'(\text{C})}$

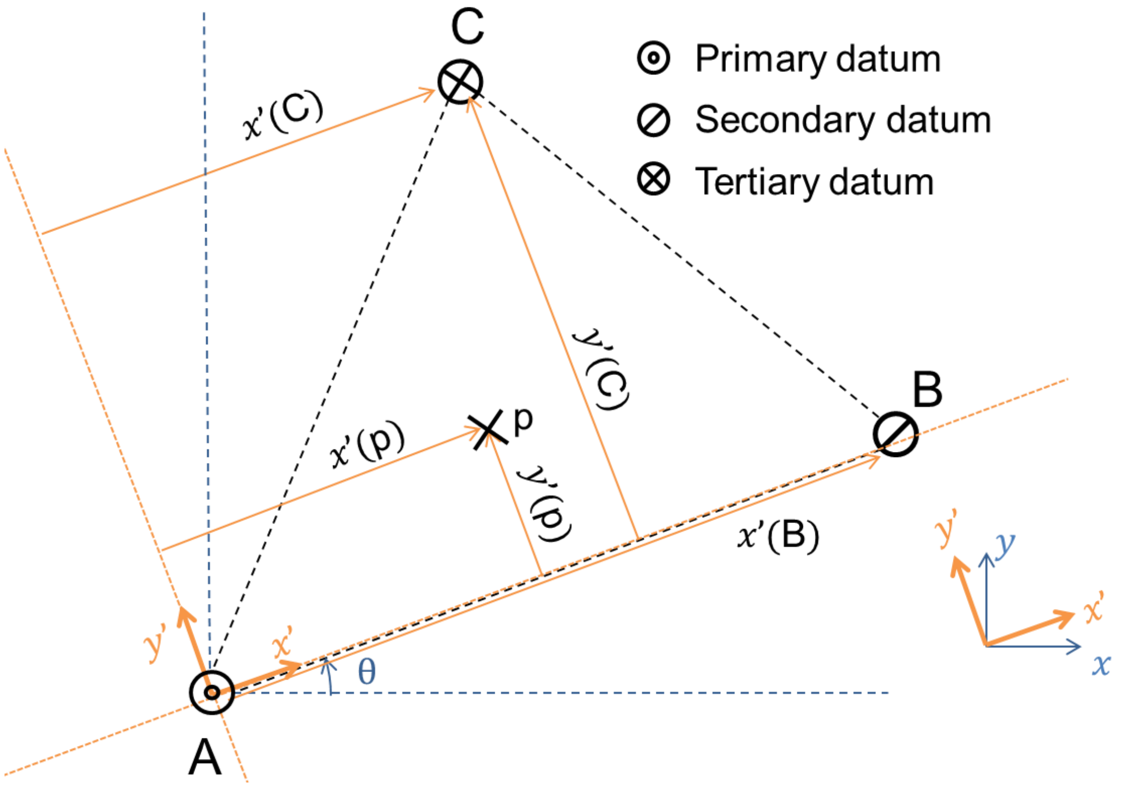

Figure 4-15. References for fixing the midscale assembly skin datums to nominal.

4.2.4 Assembly scenarios

As indicated in section 4.2.3 Variation generation, it is impractical to generate a comprehensive set of variable combinations. Typical alternatives would include conducting a pre-screening experiment to rule out interactions, followed up with a fractional factorial design; as well as a Latin Hypercube Sampling (LHS) which ensures all potential levels are sampled uniformly. For a large number of variables though, it must be accepted that a certain level of loss of confidence in the results is inevitable. An experiment by LURPA researchers on regression of assembly quality (Andolfatto et al., 2013) found that there was a minimal difference in performance between LHS and random uniform sampling. In the case referenced, a 17-input-variable neural network (11 location variables and 6 shape variables) was trained based on 10000 cases.

Given the similar number of variables in the case at hand, and in conjunction with pragmatic consideration of computing time, as well as the fact that no specific quantitative recommendations will be supported, it was decided for 10000 geometry combinations to be generated. Each of these geometry combinations would be virtually assembled in 4 situations, using two different pressure levels (representative out-of-autoclave and mid-pressure autoclave) and boundary conditions (typical single-side pressure bagged against female tool, and two-side envelope-bagged). The values are summarised on Table 4-3. In all cases, the parts are considered restrained at the designated datum points. This situation is not fully realistic and is discussed among the model limitations.

Table 4-3. Assembly conditions for all part combinations

	'Low' level	**'High' level**
Pressure	0.8 bar	3.0 bar
Boundary condition	Bagged to female OML tool, pressure on IML side only	Envelope bagged, resting on female OML tool, pressure on both sides

4.2.5 Results

The maximum bondline thickness values are presented in Figure 4-16. As the phase of the modal variation components was left invariant (beyond a π radians shift when the amplitude was negative), the values of quantiles of variation at neighbouring locations remain highly correlated; for this reason, the overall spatial distribution of the maximum thickness values retains much of the initial sinusoidal shape.

A clear shift can be seen in the behaviour of stringers 2 and 3 in 2SP (especially under out-of-autoclave [OoA] pressure), past a certain length position. Similarly, stringer 6 benefits from 2SP much more than stringers 4 and 5 (which are otherwise very similar). This corresponds to a situation of interference between adjacent stringers, which will be explored more in detail in Section 5.3: when a stringer is placed between two others, the variation of these neighbouring stringers tends to prevent the skin from deflecting under the central stringer to close the interface gaps. In contrast, where stringers 2 and 3 have no adjacent stringer (because stringers 1 and 2, respectively, are shorter), the skin becomes much freer to deflect, immediately increasing the benefit from a 2SP concept. Likewise, stringers 1 and 6 always benefit from a 2SP condition because it is on one edge of the skin.

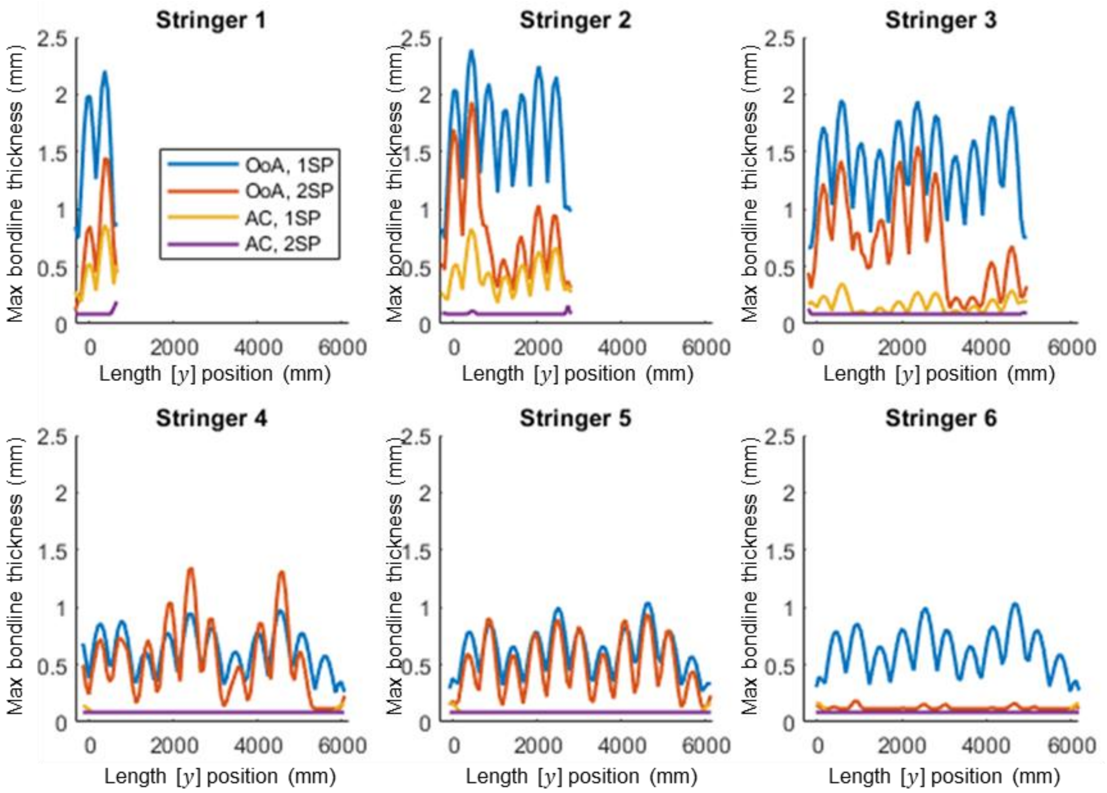

Figure 4-16. Maximum bondline thicknesses across all simulated cases per stringer, pressure and boundary conditions, and length position.

In a fashion similar to the initial notional experiment presented earlier in Section 4.1, assembly fitness was evaluated using a generic, Taguchi-inspired loss function. In this case, the evaluation was performed globally as well as piecewise per stringer; with soft tolerances[xxix] as follows:

$$\mathrm{tol}(\mathrm{X_G}) = 500\ \mu\mathrm{m}$$
$$\mathrm{tol}(\mathrm{var}X_G) = 100\ \mu\mathrm{m} \tag{4-8}$$

Since the shape of the residual gap is highly consistent, and as no consideration is made for adhesive thickness, there is a very strong direct correlation between high loss $S_{avg\ gap}$ and high loss $S_{gap\ var}$ as evidenced in Figure 4-17. The figure also evidences the beneficial quality impact of pressure increase (AC) or two-side-pressure bonding (2SP). A real scenario with richer modes of variation, including localised effects, can be expected to show less correlated values, while still maintaining the quality gains from pressure and boundary condition changes.

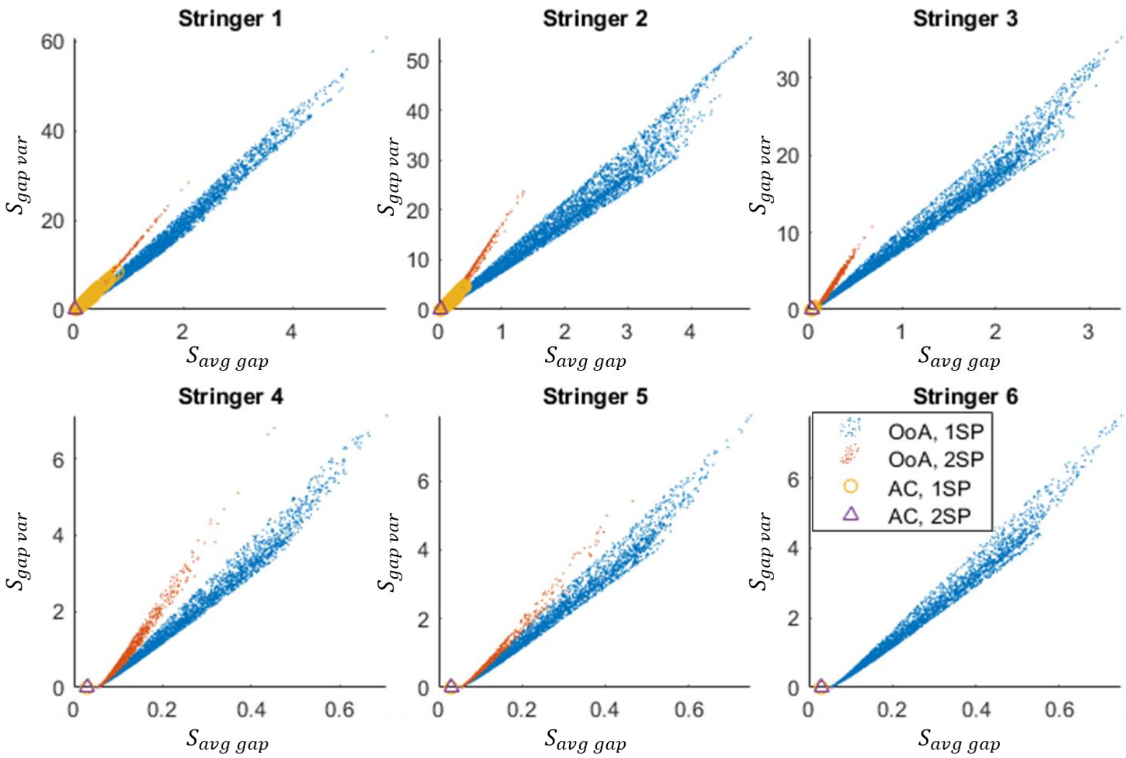

Figure 4-17. Scatter plot of the two continuous quality loss criteria for each stringer, clearly showing the strong correlation.

[xxix] As defined when first introducing this set of loss functions, a value of $S_{[criterion]}$ above 1 would mean rejection of the assembly; the difference with a hard tolerance is that there is a quality loss even when within tolerance.

This is much stricter than the $S_{avg\ gap}$ criterion, where local high values are partially compensated by the lower ones elsewhere. The fact that the hard criterion is stricter than the others can be further seen comparing Figure 4-18 and Figure 4-19, especially looking at the rejection of full panels: while over 90% of the panels in the worst-performing assembly condition (OoA, 1SP) exceed the tolerances *somewhere*, leading to rejection according to $S_{max\ gap}$, a mere 17 out of 10000 simulated panels are globally unfit by the $S_{avg\ gap}$ criterion — even as stringers 1, 2 and 3 still show substantial noncompliance rates. Such a difference highlights how specific engineering criteria must be weighed carefully for high-value products such as the panels modelled here. In this case, for instance, a locally thicker-than-desirable bondline could still be permissible if the load could be expected to be partially redistributed to neighbouring stringers — as indeed is the case with bonded structures.

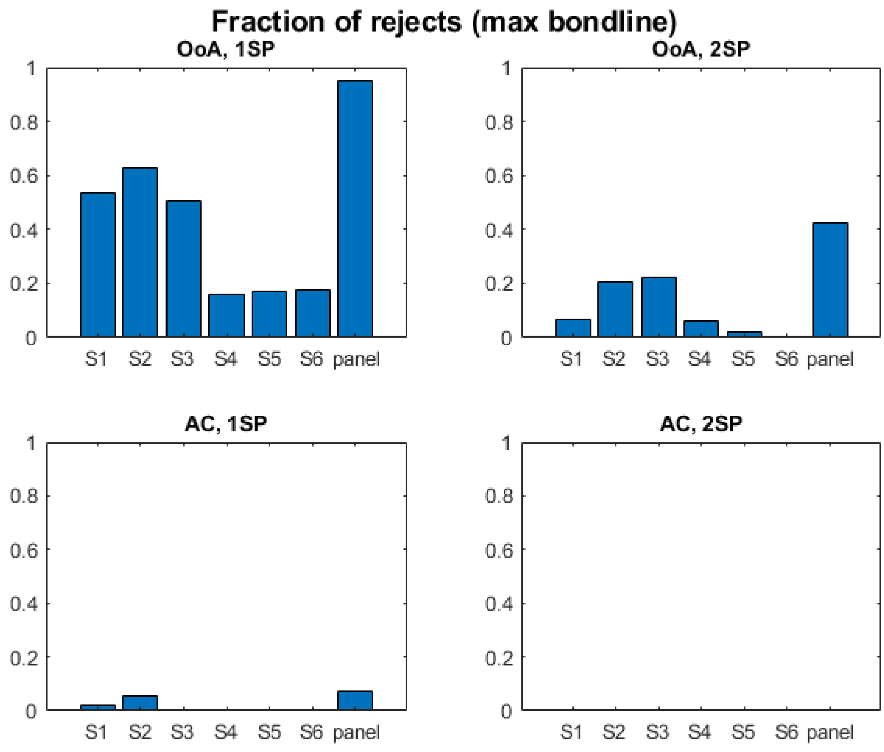

Figure 4-18. Rate of rejection by the $S_{max\ gap}$ criterion for each stringer and the complete panel.

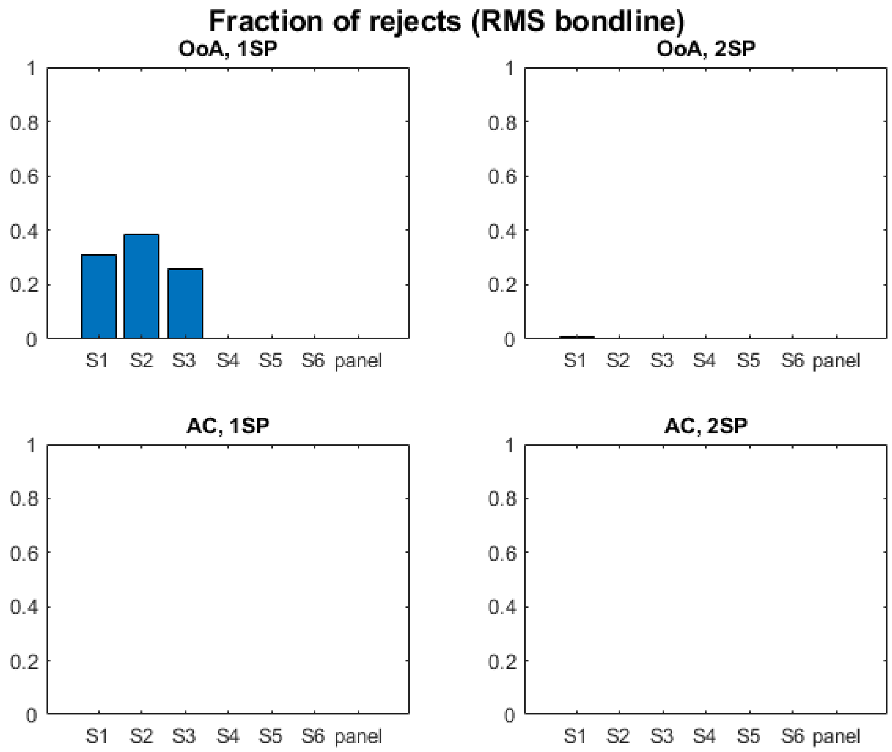

Figure 4-19. Rate of rejection by the $S_{avg\ gap}$ criterion for each stringer and the complete panel.

4.2.5.1 Effect of the different assembly conditions

Further to the compliance rates, thanks to the use of loss functions, it is possible to study how the different conditions change the distribution of quality, with much-reduced dimensions compared to the whole geometry. In this case, the effect of any change is obvious from Figure 4-20. By examining global quality indicators under different scenarios, the non-linear mechanics of the assembly problem become obvious: as the gap-closing capability is increased (be it through higher bonding pressures or more efficient boundary conditions), the distribution of quality loss becomes denser towards 0 values, as well as increasingly truncated. In the extreme case of single-side, low pressure, a barely-truncated distribution, very close to a normal (as it is given by the combination the uniformly distributed random variation for six stringers) is still recognisable. Meanwhile, in the opposite extreme case of two-side high pressure, all assemblies have reached near-zero loss and the histogram turns into a single spike[xxx].

The rejection rate and quality loss distributions allow at-a-glance diagnosis of the benefit of a 2SP assembly setup: though not quite as effective as a substantial increase in bonding pressure (0.3/0.08 = 3.75, almost four-fold), it succeeds in limiting notional rejection rates and quality loss to a large extent. When weighing these and other manufacturing options in a cost model, the value of discrete manufacturing solutions, such as geometry control improvement targeted at specific stringers, or use of local pressure intensifying equipment, can be better ascertained.

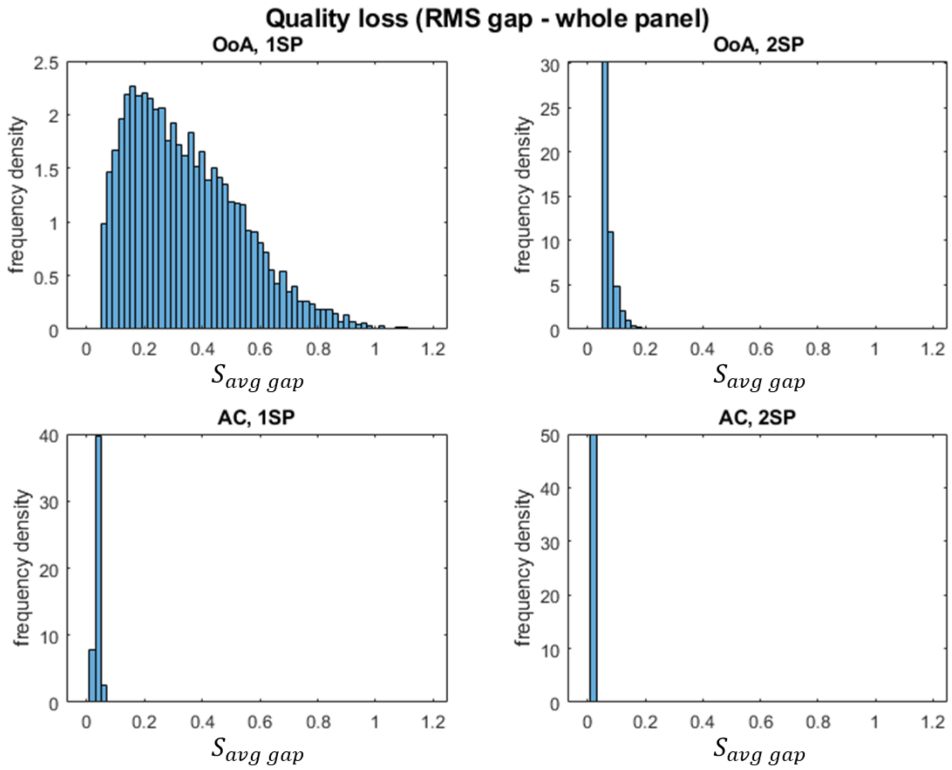

Figure 4-20. Distribution of the values of quality loss $S_{avg\ gap}$ by RMS gap, for the entire bonded panel in each condition. Note the differences in vertical axis scales.

[xxx] Two caveats are in order here. First, most loss values are still non-zero (though very small) and the histogram shape is determined by a prescribed fixed bin size for easy comparison between plots. Second, and more importantly, it must be recalled that the adhesive viscosity will, contrary to the simplified modelling assumptions, partially oppose stringer deflection when gap closure is in such an advanced state; thus, slightly more spread should be expected in a real assembly.

4.3 Interface gap health check on-the-fly

In an ideal world, all parts fed into a process would be such that compliance is ensured, and part geometry would be known prior to starting any assembly process. However, due to imperfect processes and controls for manufacturing, the current situation can diverge considerably from this ideal scenario. Indeed, assembly interface management often necessitates corrective action by shimming and fettling (adding packers or trimming material). This is often deployed on a trial-and-error basis, or alternatively resorting to on-the-spot measurement (Maropoulos et al., 2013).

Because of this, pre-assembly fit measurements can be necessary to obtain confidence of the result, or to tune the input parameters (e.g. shim thickness). However, due to the combination of large assembly forces and variable gap range, a mere dry fit under hand pressure (or otherwise under substantially less than assembly forces) can spectacularly fail to capture the final assembly unless further processing, via heuristics or calculation, is incorporated. Meanwhile, emulation of actual assembly forces may obscure valuable geometric data (Hammett, Baron and Smith, 1999; Lindau et al., 2012), or simply be impractical.

During manufacture of the curved test panels presented later in Section 5.2 Curved test assemblies, a pre-assembly fit was performed. The fit involved measuring the stringer-skin gaps in two different states: unloaded stringers, and lightly loaded (20 kg) stringers. In both cases, tooling pins were in place, and the skin was constrained to the bonding tool by vacuum.

Figure 4-21. Skin and stringer, weighted down onto the bonding tool during the dry fit. Note the tooling pins.

4.3.1 Gap check and diagnosis workflow

The overall flow of information is presented in Figure 4-22.

1. Place the parts on the bonding tool; apply the tooling pins and position the weights.
2. Perform gap measurements at selected positions, using a manual gauge; log these in an excel sheet in a predefined structure. The number of points and gauge resolution should be such that the process does not become too onerous for shop operation.
3. A custom MatLab script reads the gap values and uses them as geometry inputs for an assembly simulation (including data fit with thin plate splines).
4. The results for the assembly simulation are plotted, allowing straightforward comparison with established tolerance bands.

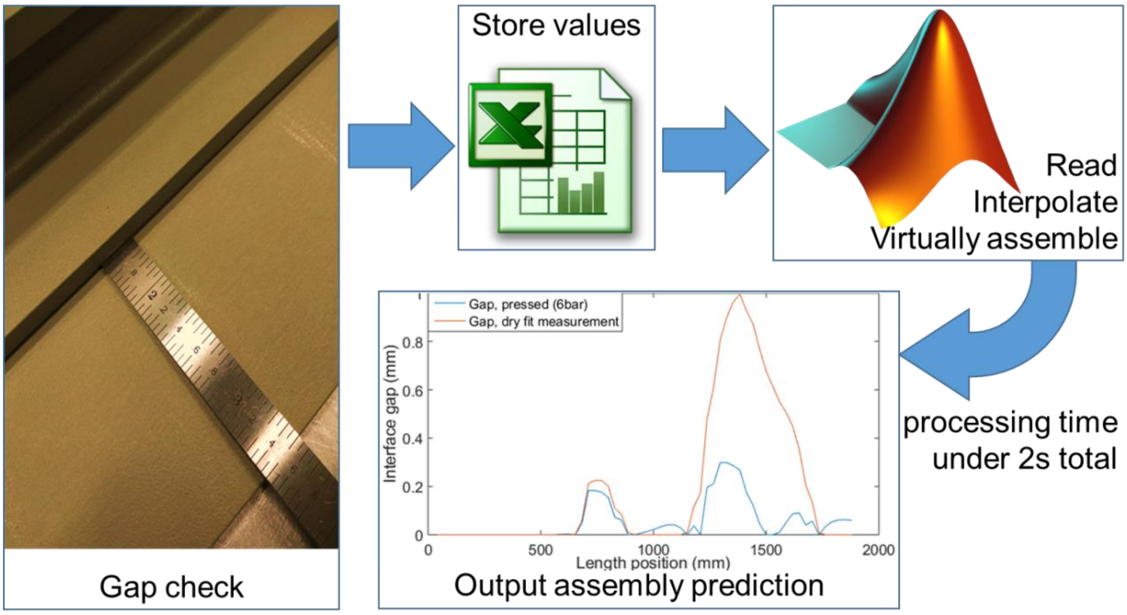

Figure 4-22. Gap prediction process. Measurements fed into a spreadsheet are quickly processed by a MatLab script which in this case outputs a simple graph.

Steps 3 and 4 were implemented reactively when initial measurements yielded gap values an order of magnitude larger than notional tolerances. This initially triggered study of different mitigation approaches, including application of additional layers of adhesive tape, increase of bonding pressure, and running a verifilm cycle ahead of bonded assembly. The assembly simulation results provided reassurance that the original assembly plan would yield a satisfactory bond.

4.3.2 Results

In all five cases studied, the simulation results confirmed that the planned externally applied pressure of 6 bar would satisfactorily reduce variation such that a single layer of adhesive could provide for the volume of the whole bondline. Local thickness maxima, all within acceptable bounds, were also highlighted. Results for an illustrative case are presented in Figure 4-23. These are both for an artificially dense (interpolated, points) and originally sparse measurement data (solid line).

In order to enhance insights into bonding capability, a hypothetical “out of autoclave” option (0.8 bar) was included in the simulation. The results for both this reduced pressure and the actual 6 bar pressure are included in the Figure 4-23 example, this clearly conveys the phenomenon of ‘diminishing returns’ whereby a substantial increase in pressure (7.5-fold, from 0.8 to 6 bar) does not result in a proportional increase in deflection — despite the fact that the bondline has not been completely flattened.

By virtue of the very short cycle time for these coarse simulations, there is no practical limit to the combinations of pressures and adhesive layers (within the bounds of a typical manufacturing process) that could be evaluated in a quick environment. Provided the right material and process qualification are in place, it would be perfectly feasible to use the data fit to select the combination of parameters that minimises bonding cycle time/cost while maintaining suitable geometric control.

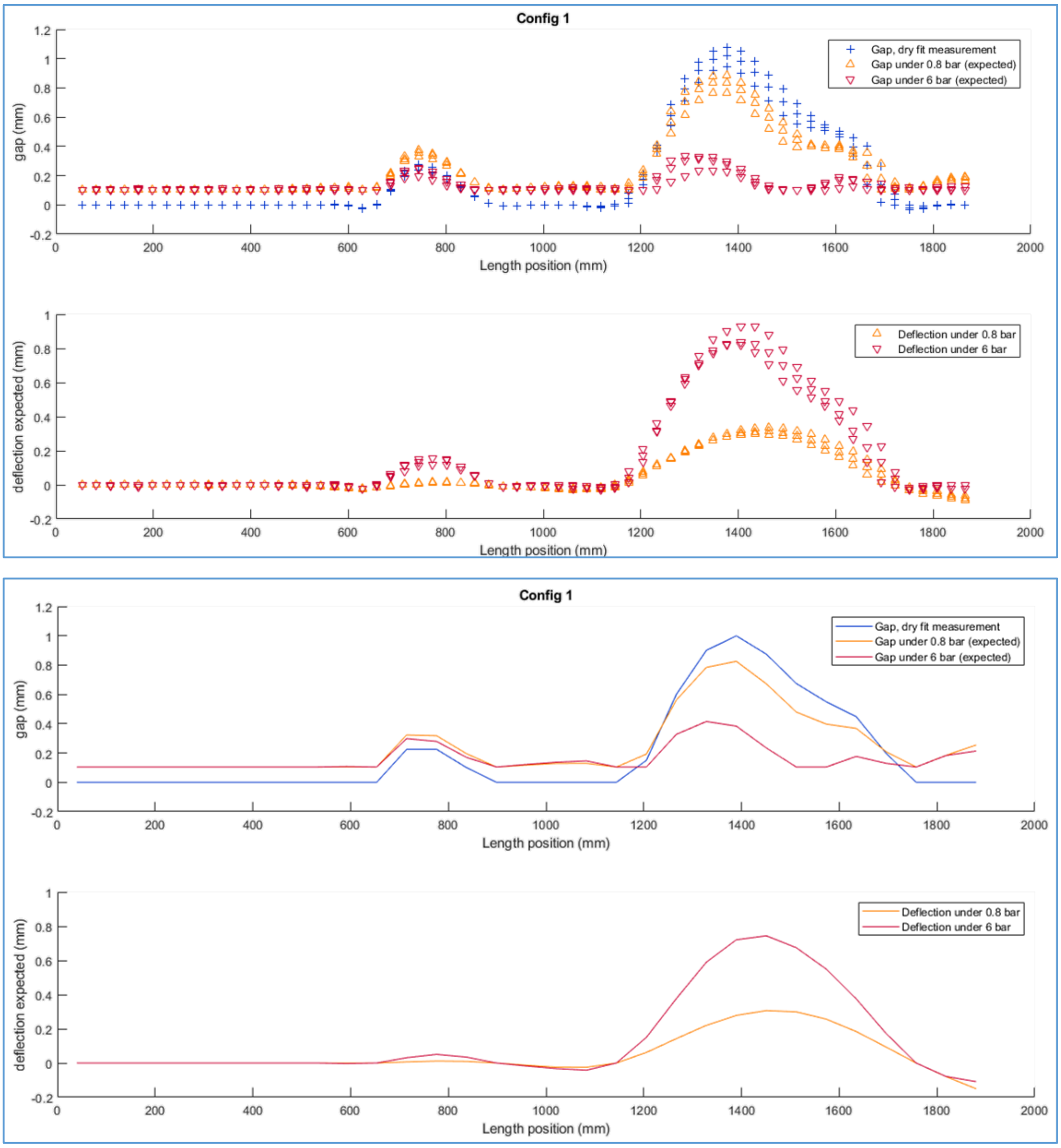

Figure 4-23. Plots of pre-assembly measured and post-assembly predicted interface gaps and of predicted stringer deflection. The red plot corresponds to the pressure actually used and brings bondline thickness under 0.5 mm everywhere. The deflection graphs highlight the smoothness of the deflection (material continuity) and the diminishing returns of a pressure increase.

4.3.3 Practical limitations

The shortcomings of the particular application case are worth highlighting. These are representative of a real manufacturing scenario, and to some degree intrinsical to the situation of use.

- *Inspection capability*: gap checks only reach the edge of the stringer, and thus risk missing variation across the stringer cross-section.
- *Inspection resolution*: the instrument used had a rather coarse resolution of 0.05 mm, and a high minimum measured value of 0.20 mm. This resulted in short-range irregularities (visible as a "jagged" profile in the predictions) and also in perceived shorter ranges for gaps, which thus increased the effective stiffness. This can be avoided in production in the event that a more automated system be implemented (using embedded metrology, fast contactless measurement systems, or feeding inspection data from previous steps).
- *Modelling limitations*: the modelling boundary conditions overestimate the constraint placed near the part ends (the pins were applied by hand pressure and thus hardly a 'pin' condition, as seen in Figure 4-24); as a result, the model risks yielding highly unrealistic results close to the datum areas. This is especially the case in the event of encountering substantial deformation next to the tooling hole areas (which was not the case in the practical example). Simplified boundary conditions restricting 6 degrees of freedom are, however, necessary for the linear model.

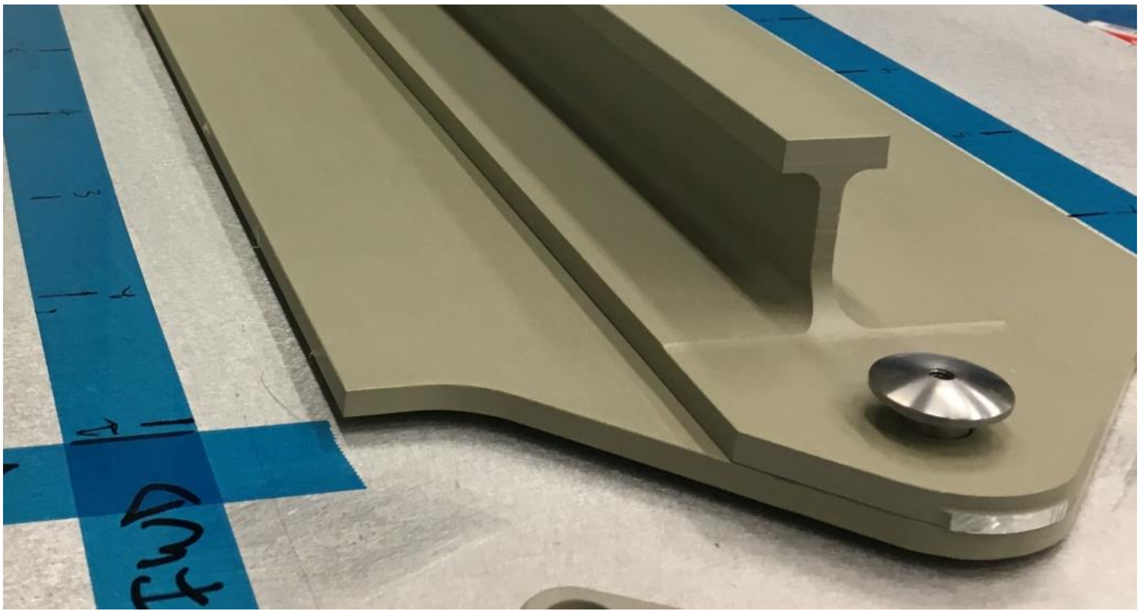

Figure 4-24. Closeup of the main datum hole location during prefit, with skin and stringer clearly sticking out away from the target position.

5 PHYSICAL DEMONSTRATORS

5.1 Flat test assemblies

Note: prior publication

Analysis and discussion pertaining to this test have been partly published in the paper by this thesis' author and co-supervisors:

Coladas Mato, P., Webb, P., Xu, Y., Graham, D., Portsmore, A. and Preston, E. (2019) 'Enhanced bondline thickness analysis for non-rigid airframe structural assemblies', *Aerospace Science and Technology*, 91, Elsevier, pp. 434–441. (DOI: 10.1016/j.ast.2019.05.024)

This subsection provides further discussion on inspected part geometry, as well as violations of the adhesive flow assumptions and lessons learned, while omitting the model enunciation (which has been provided earlier).

As a first verification of model validity, results from a bonding development test assembly were used. This assembly consists of very simple geometries and boundary conditions, which are not quite representative of a real production scenario but are easy to control and model. This case assembly was used to verify functionality of the simplified dry contact model compared to FEA, as well as test the validity of the adhesive flow assumptions.

5.1.1 Stringer-skin assembly for model validation

The dry model presented previously will first be validated against the FEA results of a stringer-skin assembly. A bonding scenario with variation occurring over multiple ranges has been used for validation. This consists of a thin (5 mm) flat skin plate, and flat stringers bonded on top of it. Stringer profile variation was emulated by introducing shims of controlled thickness at variable intervals (Figure 5-1).

A physical assembly demonstrator was manufactured which supports this study. The skin plates were gap checked against the table prior to bonding using a 0.05 mm feeler gauge, with no gaps detected. Given the skin flatness and high stiffness of the bonding table used, the skin was modelled as an encastred plate, and the shims as pad-ups integral to it — that is, no relative displacement of the shims and skin, and no flow of adhesive below or above the shims either.

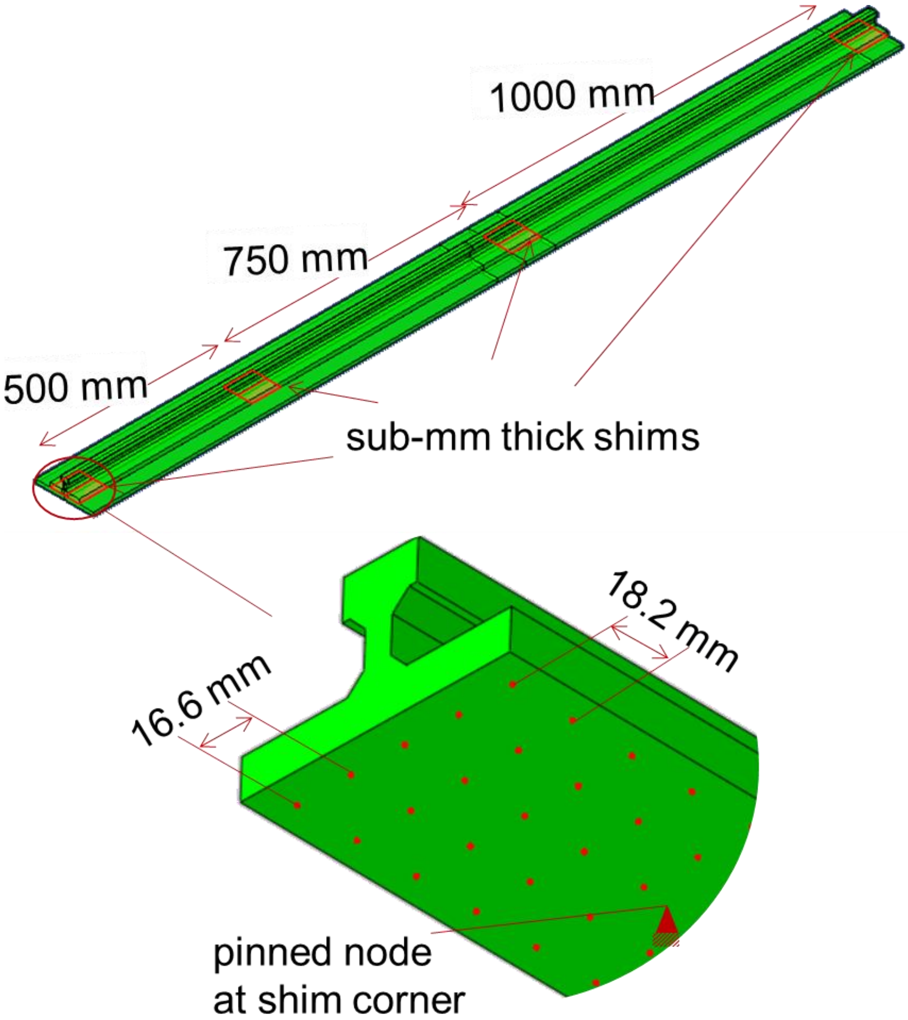

Figure 5-1. Assembly and subset of nodes considered for verification against FEA

Each stringer is of a constant cross-section and both parts were made of representative aerospace aluminium alloy. Two cross-sections were considered: ‘Thick’ (with a 12 mm-thick foot flange) and ‘Thin’ (with a 4 mm-thick foot flange)[xxxi]. These two cross-sections represent extremes of the stiffener dimensions (and compliance) in a representative target structure. The

[xxxi] The cross-sections differed also in other dimensions, with the ‘Thick’ section being overall taller and thicker. However, foot thickness becomes particularly relevant later in the analysis.

mechanical properties of both stringer variants, also used for the spectral analysis, are summarised in Table 5-1.

Table 5-1. Nominal mechanical properties for each stringer type.

Stringer series	**A 'Thick'**	**B 'Thin'**
Second moment of inertia of the area of the cross-section, $I/1000$ [mm^4]	274	122
Area cross-section, A [mm^2]	1470	590
Foot flange width, w [mm]	83	83
Foot flange thickness	12	4
Cross-section shear factor, k_{shear}	0.254	0.205
Material modulus of elasticity, E [GPa]	72	72
Material shear modulus, G [GPa]	27	27
Material Poisson's ratio, ν	0.3	0.3

In total, for the physically realised assemblies, four different shim thicknesses were used, creating a 4 × 3 × 2 (gap depth[xxxii] × wavelength × stiffness) experiment matrix (Table 5-2). This would support a study of geometrical shape variation criticality based on two descriptors: depth and span (length). This study does not consider twist or in-plane deviations.

The pressure used for the physical assemblies was 6 bar applied through vacuum bagging and autoclave cure.

[xxxii] Although a different number of adhesive film thicknesses was used across tests, this matched the shim thickness based on the nominal thickness of 0.125 mm for a single cured film layer.

Table 5-2. Experiment matrix corresponding to the initial assembly trials. Note there is mechanical interference between gaps within the same gap depth.

Cross-section	Gap span (mm)	Gap depth (mm)	Number of adhesive film layers
A (‘Thick’)	Short (417)	0.20	1
A (‘Thick’)	Mid (667)	0.20	1
A (‘Thick’)	Long (917)	0.20	1
A (‘Thick’)	Short (417)	0.30	2
A (‘Thick’)	Mid (667)	0.30	2
A (‘Thick’)	Long (917)	0.30	2
A (‘Thick’)	Short (417)	0.40	3
A (‘Thick’)	Mid (667)	0.40	3
A (‘Thick’)	Long (917)	0.40	3
A (‘Thick’)	Short (417)	0.50	4
A (‘Thick’)	Mid (667)	0.50	4
A (‘Thick’)	Long (917)	0.50	4
B (‘Thin’)	Short (417)	0.20	1
B (‘Thin’)	Mid (667)	0.20	1
B (‘Thin’)	Long (917)	0.20	1
B (‘Thin’)	Short (417)	0.30	2
B (‘Thin’)	Mid (667)	0.30	2
B (‘Thin’)	Long (917)	0.30	2
B (‘Thin’)	Short (417)	0.40	3
B (‘Thin’)	Mid (667)	0.40	3
B (‘Thin’)	Long (917)	0.40	3
B (‘Thin’)	Short (417)	0.50	4
B (‘Thin’)	Mid (667)	0.50	4
B (‘Thin’)	Long (917)	0.50	4

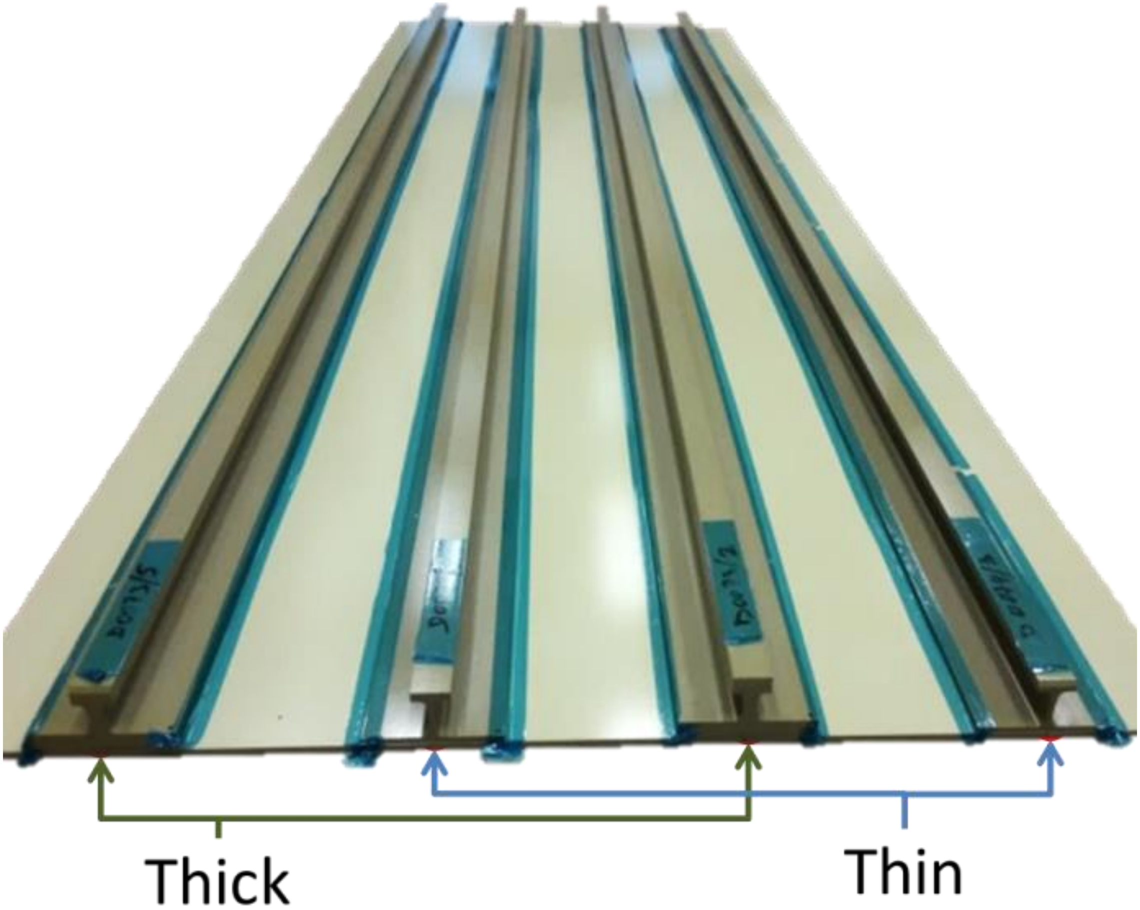

Figure 5-2. Test panel with both 'Thick' and 'Thin' stringers.

5.1.2 Dry model validation against FEA results

As a first verification of the semi-analytical model, comparison was established with results from conventional Finite Element Analysis (FEA) with Abaqus. No adhesive was considered in this case as the focus of the verification was on part deflection and contact enforcement (dry part). This also had the effect of increasing the maximum deflection achievable, and thus improving detectability of deviations.

Results for deflection were obtained for two models in each case: FEA with a fine solid mesh (C3D8 elements), and the proposed QP-based method using a stringer compliance matrix obtained from the same mesh. The boundary conditions for the stringers were set by limiting displacement in three nodes, such that a total of six degrees of freedom would be restricted before accounting for contact. Two of the pinned nodes coincided with the middle of the inner edge of the outermost shims; the approach can be seen in For the FEA simulation in Abaqus, the interaction between the stringer and skin/shims was modelled as hard contact with no friction. A typical element size of 3 mm was used, but this was made smaller at the bonding interfaces in order to accommodate multiple elements through the foot flange thickness. The shims similarly called for smaller elements. Details of the meshes can be seen in Figure 5-4.

Figure 5-3. Boundary conditions applied to three nodes on the stringer symmetry plane (lateral view). The nodes are offset from the stringer ends by one shim width.

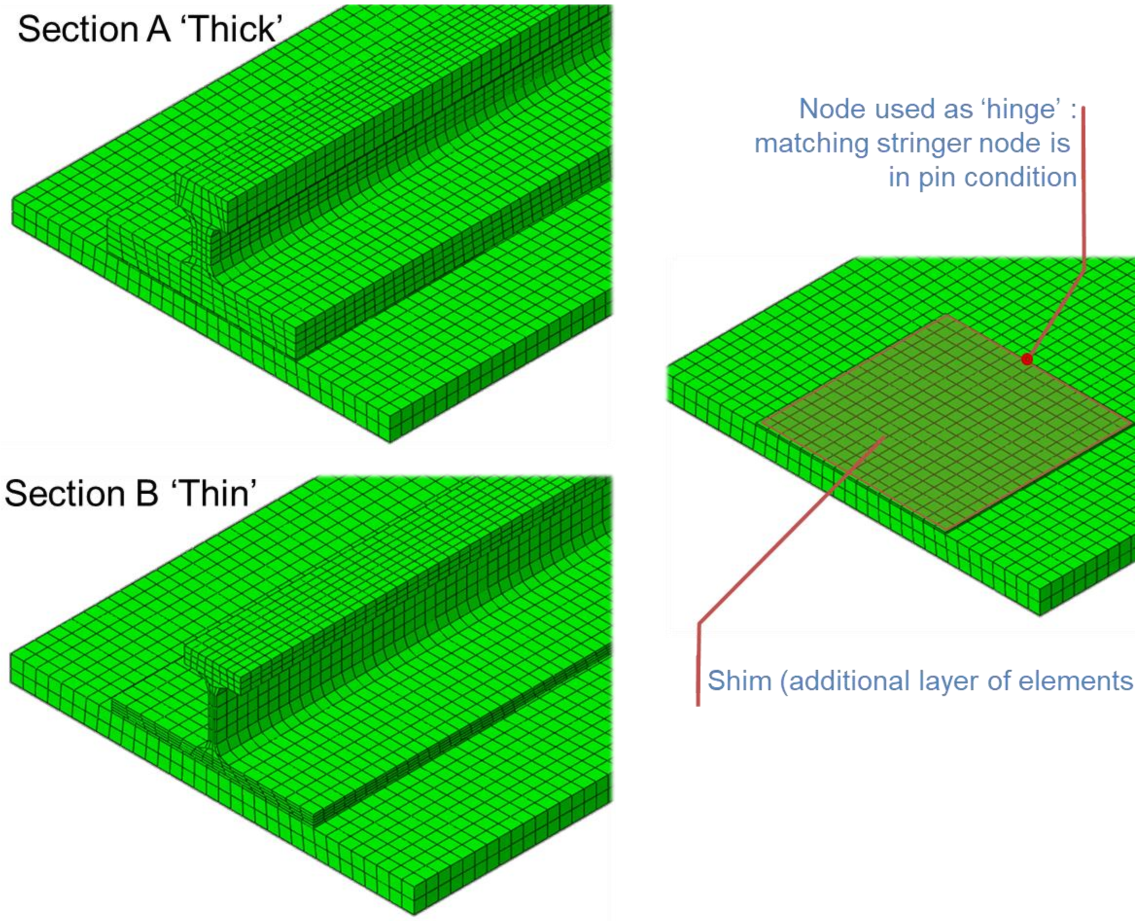

Figure 5-4. Details of the stringer and base plate with shims.

For the QP model, each stringer was reduced to (128 x 5) = 640 nodes equidistant on the foot (Figure 5-1), with matching nodes on the skin and shims. By assuming the skin panel to be perfectly flat and the table infinitely stiff, the need to model the assembly jointly (including skin-tool contact and impact of one stringer on the rest of the panel) was effectively removed. Thus, each stringer's deflection was modelled separately. This resulted in much smaller matrices and faster calculation times.

The results were extracted for nodes at two positions on the stringer foot flange: middle, and matching the node closest to the edge in the simplified model. A small subset of the results (0.5 mm shim with the highest and lowest pressures) is shown in Figure 5-5; there is very good agreement between the FEA and QP results (solid and dashed lines), except for moderate deviations in the deflection achieved where there is no adherend contact in a span between shims, as well as for the foot flange edge (red lines) of the 'Thin' stringers.

The root-mean-square (RMS) difference between the QP and FEA results generally stay below 5% of the initial gap as shown in Figure 5-2. The only substantial divergence was when dealing with a thin foot flange; in this case, the failure of the coarse node grid to properly account for the stringer edges resulted in inaccurate modelling of the contact interactions, and flange deflection was overestimated ("edge" red lines in Figure 5-6). This can be easily improved by adding more nodes in the width of the stringer flange, demonstrating the validity of the proposed semi-analytical model.

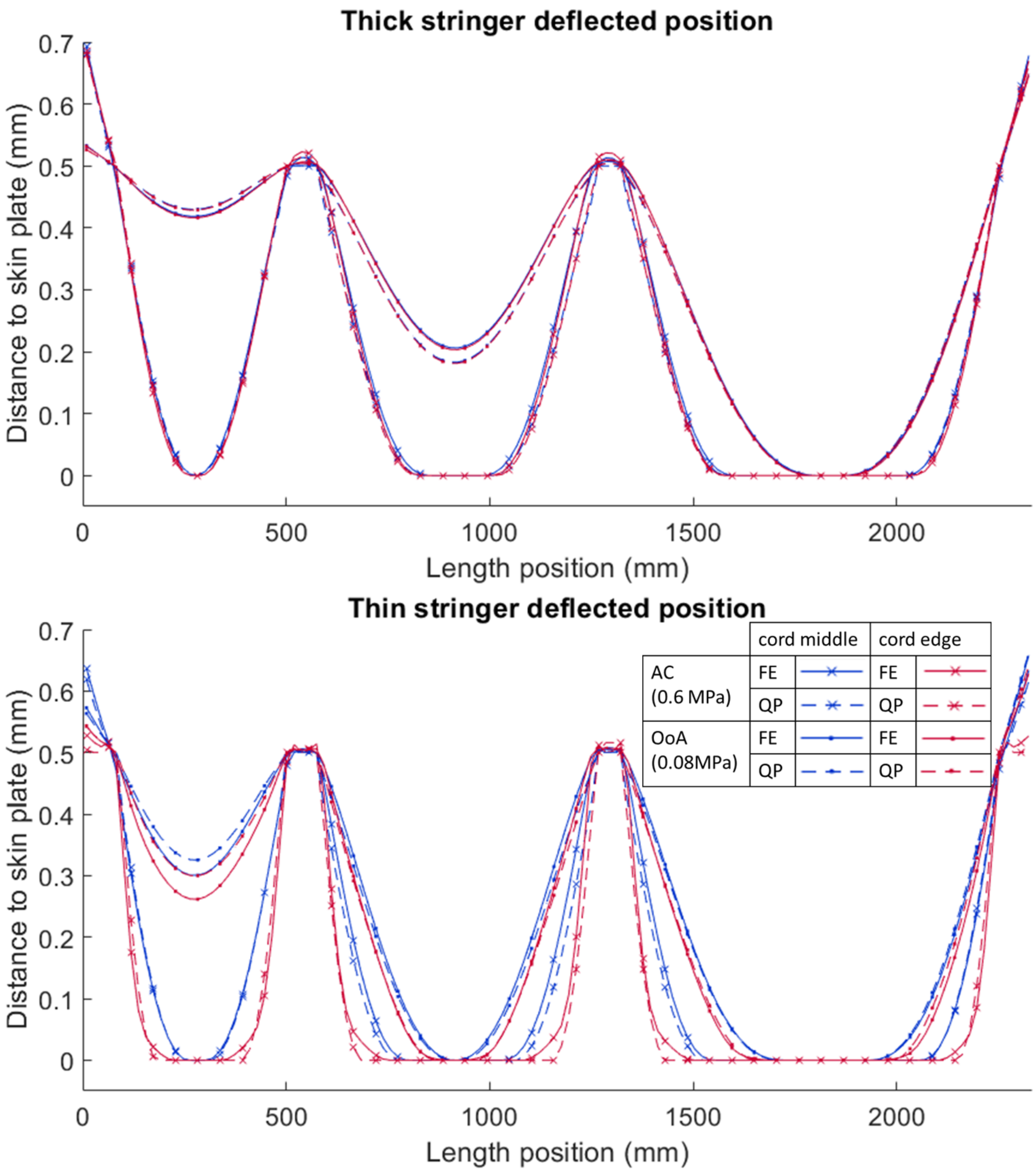

Figure 5-5. Part deflections as obtained by FEA and by the proposed method, for 0.5 mm gaps with no adhesive, under the maximum and minimum pressures considered.

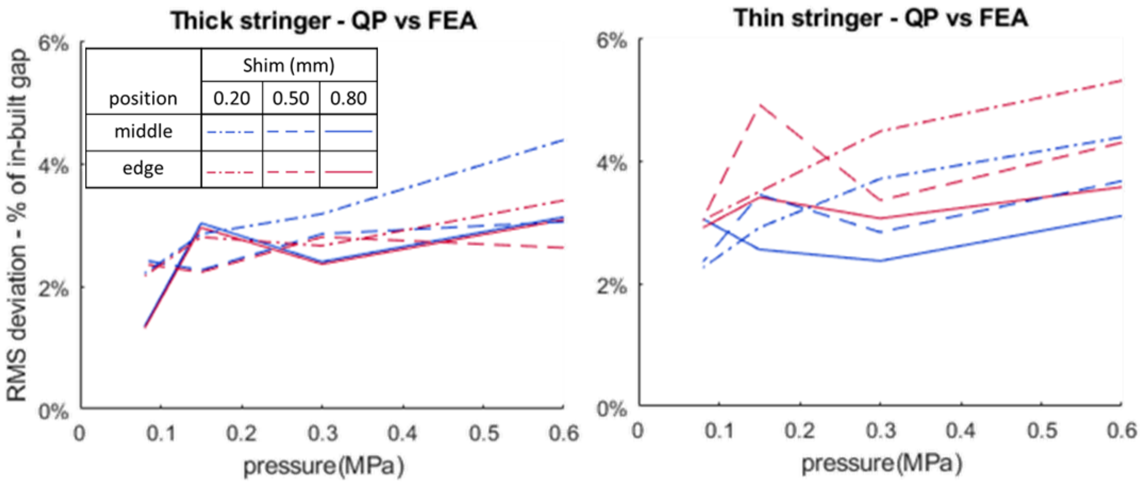

Figure 5-6. RMS deviation between all QP and FEA simulations performed (dry component only)

5.1.3 Physical test results and reliability of flow modelling assumption

The dry component simulation of the proposed model has shown good agreement with FEA results. The remaining work is to verify that the adhesive flow assumptions hold satisfactorily, to be tested with the physical assembly demonstrator shown in Figure 5-2. The intention of this test is not to verify the exact minimum-bondline-thickness achieved. Rather, the objective is to validate the model simplification of the dry/wet separation, where adhesive behaviour is only relevant for calculation of a minimum bondline thickness (wet component). If this is the case, it is reasonable to use 1DSF, and $(\int_0^t \eta^{-1} dt)$, along with the other film parameters, can then be calculated through material characterisation (e.g. using a rheometer as in (Préau and Hubert, 2016)), or the expected minimum-bondline-thickness can be determined though process-specific tests that replicate the pressure and thermal cycle. In either case, one should confirm the actual thermal cycle in the joint, especially in large assemblies where the part and tooling's thermal mass may result in large deviations across the structure and from the nominal. Usual industry practice includes attachment of multiple thermocouples to ensure the structure has undergone the correct treatment. Closer scrutiny of the adhesive model and properties may be in order if other outcomes, such as spew fillet volume and void formation, are also of concern.

The tests used the same skin-shims-stringers arrangement presented above, but incorporating adhesive outside the shimmed areas. Trials were conducted with 1, 2, 3, or 4 adhesive film layers. The number of layers is the maximum that would not overfill the artificial gaps according to manufacturing best practice, based on a nominal cured layer thickness of 0.125 mm. Two panels were manufactured using the same process and different shim thickness.

The first panel comprised a skin plate with two 'thick' and two 'thin' stringers, one of each with 0.2 mm shims (1 film layer) and other with 0.3 mm shims (2 film layers). The parts were bonded using an epoxy adhesive with scrim carrier (Cytec FM94-0.06K). The assembly was encapsulated in a vacuum bag and cured at a representative autoclave pressure of 0.6 MPa. The heat cycle comprised heating at a 2°C/min rate, holding at 120°C for an hour.

The second panel was the same as the first, but with 0.4 mm and 0.5 mm thick shims (3 and 4 adhesive film layers, respectively). Because of the large amount of adhesive in this panel, and because flash-breaking tape had been applied at the stringer edges, this panel yielded geometry results clearly in violation of the adhesive flow assumption; these will be briefly discussed below, but comparison with the simulation results is not presented.

The bonded assemblies were simulated with the QP model as described above. For the minimum bondline thickness, constant viscosity η=50 Pa·s, total squeeze time t=1200 s, initial per-layer thickness b_0=0.10mm, and carrier thickness $b_{carrier}$=0.05 mm was assumed. With w=83 mm, this results in minimum thickness values of 0.081 mm and 0.146 mm for 1 and 2 layers, respectively.

There were concerns about tracing each individually numbered stringer to a particular assembly. However, the stringers had been machined to a tight profile tolerance of 0.2 mm in the bonding surface; simulation of assembly for parts with such small variation were found yield minimal (<25 μm) deviations from nominal. This was further confirmed by a batch of simulations using the geometry values from post-machining inspection (Figure 5-7) of the stringer foot. Because of this, the results from assembly simulation of nominally-flat stringers are considered just as valid for the purpose of model validity verification.

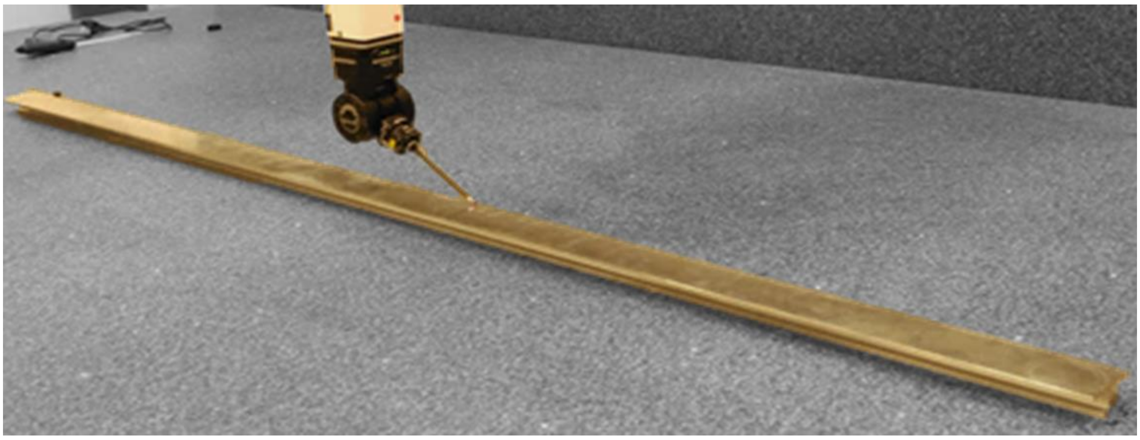

Figure 5-7. CMM inspection of one of the stringers, ahead of surface treatment and bonded assembly.

The cured assemblies were sectioned into ~200 mm segments at regular intervals between the shims, at locations adjacent to the shims and where minimum bondline thickness was expected. The bondline thickness was assessed via optical microscopy, with three spots measured at each cross-section (Figure 5-8). For the 0.2 mm and 0.3 mm shims, the longitudinal section distribution is presented in Figure 5-9 and Figure 5-10 for the 'Thick' and 'Thin' stringers, respectively; along with example results (simulated and measured).

The results show consistent behaviour of the adhesive under each stringer at high pressures, with small variability among the measured thicknesses, with standard deviations below 0.020 mm and numerical results in the range of the 1DSF preliminary sizing (Table 5-3). However, there exist divergences between stringers which are likely not fully explained by slight differences in effective heat rates, with the thin stringers obtaining more variable bondlines.

Table 5-3. Measured minimum bondline thicknesses: standard deviation (STD) and root mean square (RMS) difference to the 1DSF prediction.

	'Thick' stringer		'Thin' stringer	
Adhesive layers [Shim (mm)]	STD (mm)	RMS (mm)	STD (mm)	RMS (mm)
1 [0.2]	0.007	0.008	0.012	0.024
2 [0.3]	0.012	0.016	0.018	0.023

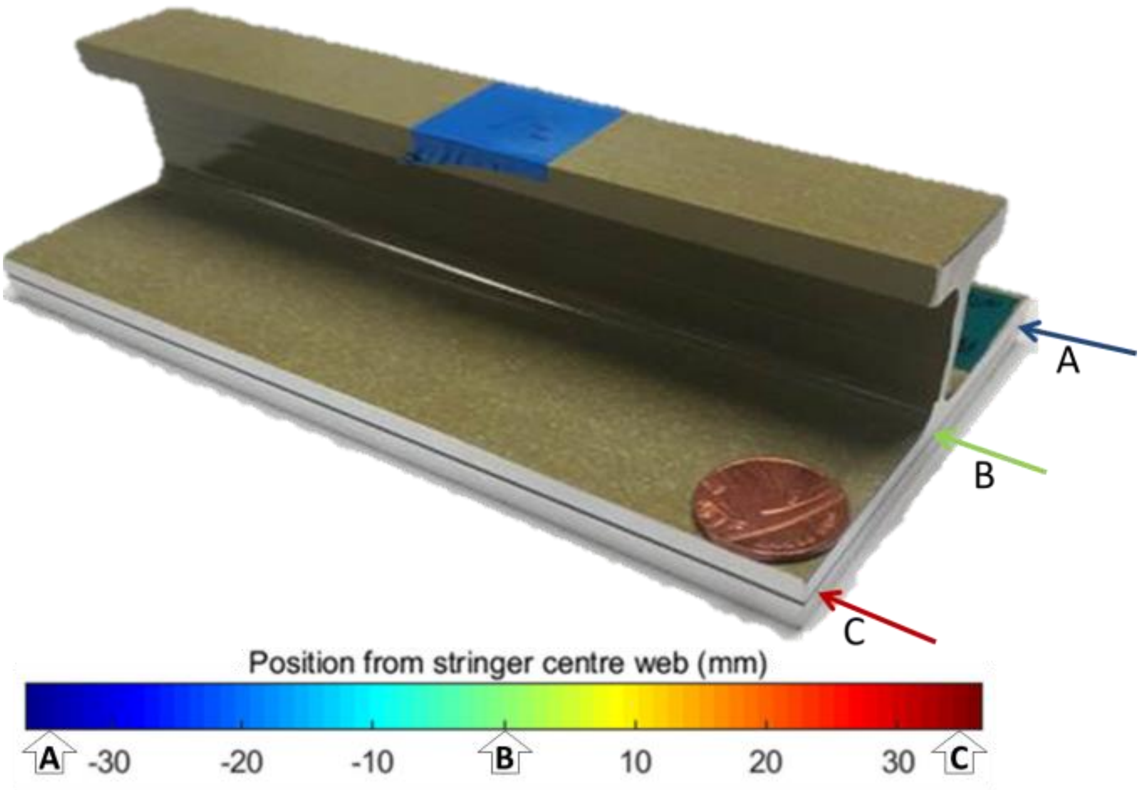

Figure 5-8. Section taken from a 'Thin' stringer, with microscopy locations marked and a penny for scale.

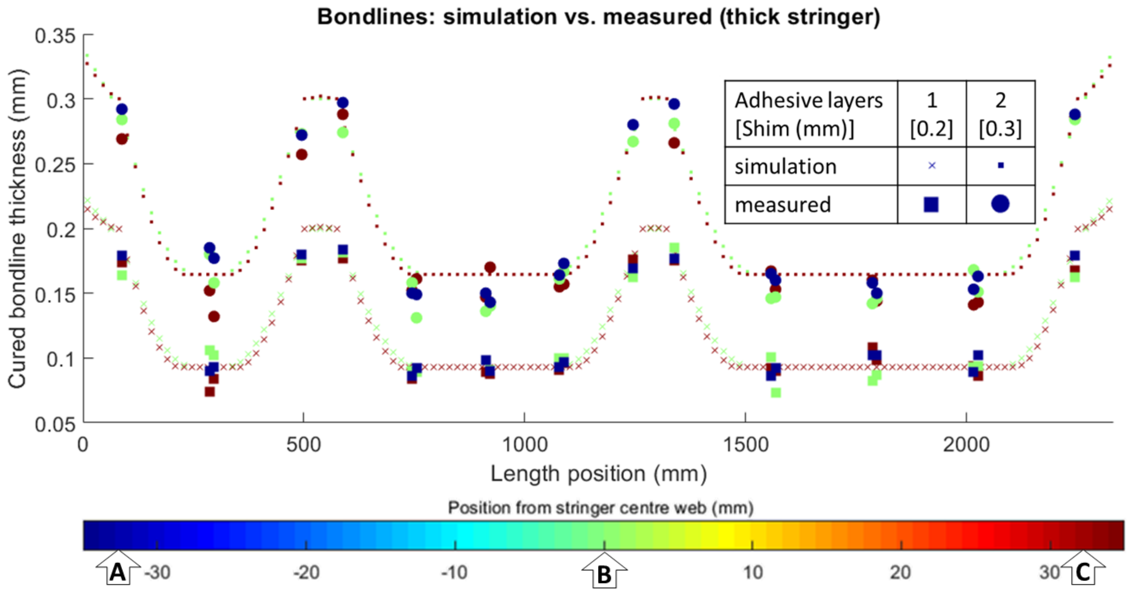

Figure 5-9. Bondline thicknesses predicted by QP+1DSF and measured (small and large markers, respectively) for the 'Thick' stringers under 0.6 MPa, using the thinner shims.

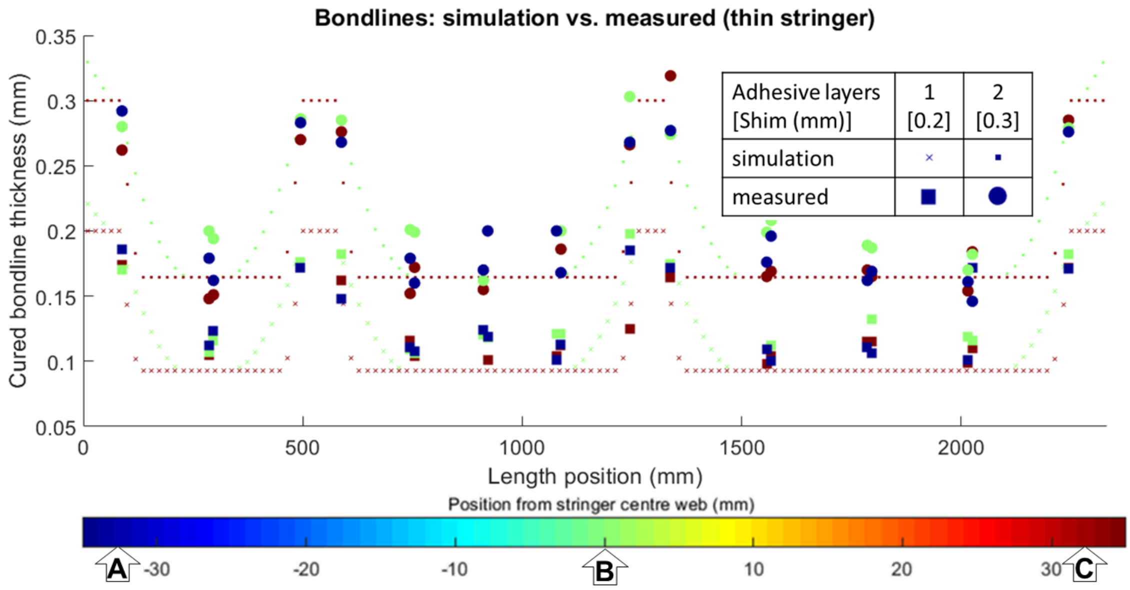

Figure 5-10. Bondline thicknesses predicted by QP+1DSF and measured (small and large markers, respectively) for the 'Thin' stringers under 0.6 MPa, using the thinner shims.

Meanwhile, the second panel with thicker shims resulted in bondline thicknesses which are totally inconsistent with the model and with initial expectations; the cured bondlines were largely thicker than the shims used, and in some cases a large amount of stringer twist appeared which had not been present before cure (Figure 5-11).

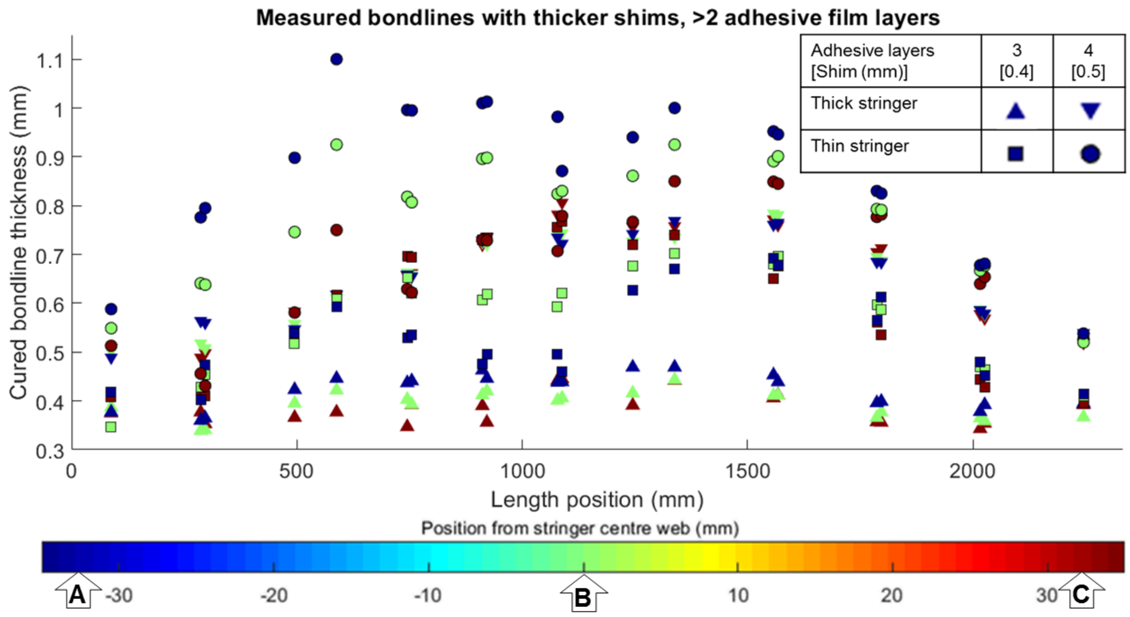

Figure 5-11. Bondline thicknesses obtained when applying too much adhesive. The artificial gaps are unrecognisable and substantial variation is generated in the bondline.

5.1.4 Main outcomes

The flat panels confirmed that the general behaviour of the stringers in a bonding application is as modelled. The tests also provided confirmation of how and when the adhesive behaviour is captured by the modelling approach.

The sparse demonstrator measurements don't allow one to draw conclusions on the accuracy of the stringer deflection model. However, the FEA simulations carried out provide suitable confidence in the accuracy of the linearisation for simulating the dry assembly problem.

The minimum adhesive thickness for the thinner shims show the merit of the minimum adhesive thickness and dry/wet separation assumptions. In addition, the slightly different results for the thick and thin stringers are consistent with the limitations of the adhesive flow model. The results for the thicker shims, which were completely unrelated to the simulation outcomes, indicate the risks associated to overfill of the bonded joint.

These tests are limited in scope, not only because of the gap geometries considered but also because of the simple geometry and boundary conditions (which essentially resulted in no appreciable skin deflection and no interaction between stringers).

5.2 Curved test assemblies

Further trials were conducted which aimed at de-risking mid-complexity structural components. These were based on the same wing archetype as Section 4.2, coupling skin thickness transitions with a combination of curvature and twist in the parts (Figure 5-12). Variations on the original design would serve to test the boundaries of model validity (as well as the overall behaviour of the adhesive joint), covering the following aspects:

- Shape variation in the skin in addition to the stiffener;
- Different stiffener cross-sections (and especially different foot flange thicknesses);
- Realistic manufacturing variation (e.g. from imperfect forming processes);
- Geometries with and without nominal in-built interface gaps/steps.

The tested designs include:

1. Legacy design with stepped interfaces;
2. Reworked legacy design with a smooth curved interface;
3. Reworked legacy design with some stringer foot thickness transferred to the skin;
4. Reworked legacy design with some stringer foot thickness transferred to doublers;
5. Reworked legacy design with a high-stiffness stringer.

The assembly combinations and part descriptors, inclusive of stringer section properties are provided in Table 5-4 to Table 5-7. In order to preserve sponsor proprietary information, only basic geometry values are provided. The analysis is based on the properties of an aerospace alloy, $E = 72$ GPa , $\nu = 0.33$.

The manufacturing and inspection processes for the parts involved are detailed in Appendix C — Curved assembly trial component manufacture.

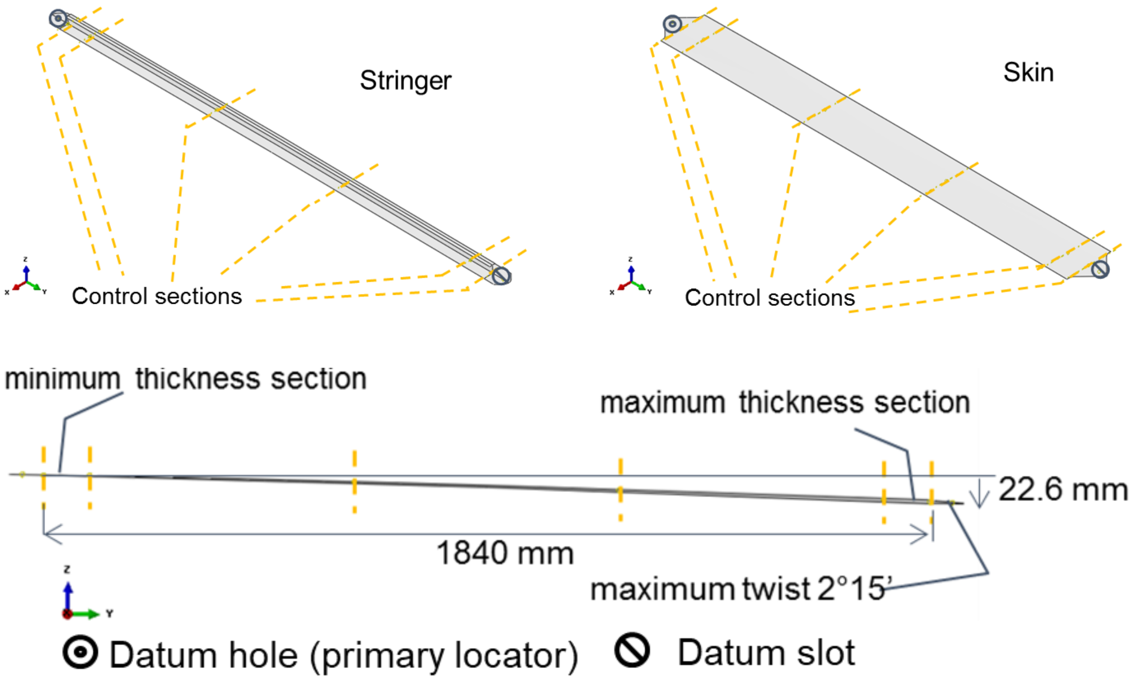

Figure 5-12. Curved bonded parts' overview (top) and general length dimensions of the skin (bottom). Shell-based models; thickness is not rendered. The doubler was modelled as the foot flange of a stringer.

Table 5-4. Reference of curved skin-stringer combinations.

Case	Description	Stringer	Skin
1	Legacy, faceted inner surface	A (Legacy, standard)	a (Faceted)
2	Smoothly curved inner surface	A (Legacy, standard)	b (Smooth curvature)
3	Smoothly curved inner surface, skin reinforced with a pad-up	B (Thin foot flange)	c (Smooth curvature, thickened under stringer)
4	Smoothly curved inner surface, doublers	B (Thin foot flange)	b (Smooth curvature) Adds 3 doublers, each 1.2 mm thick
5	Smoothly curved inner surface, stiffer stringer	C (Stiffest representative profile)	b (Smooth curvature)

Table 5-5. Test matrix of curved skin-stringer combinations. *≡includes doublers

Stringer / Skin	A standard	B thin foot	C stiffest
a - faceted	1		
b - smooth	2	4*	5
c - padup		3	

Table 5-6. Curved stringer types assembled and their section properties.

Stringer	Description	Foot thickness	2^{nd} moment of area of the cross-section, I	Area of the cross-section, A	Shear factor, $\mathrm{k}_{\mathrm{shear}}$
A	Average representative cross-section	7 mm	2.17×10^5 mm^4	878 mm^2	0.256
B	Thinned foot flange	3 mm	1.43×10^5 mm^4	574 mm^2	0.392
C	High stiffness section	12 mm	2.74×10^5 mm^4	1469 mm^2	0.254

Table 5-7. Skin types assembled.

Skin	Description	Minimum thickness	Maximum thickness
a	Representative faceted profile	6 mm	10.5 mm
b	Smooth curved profile based on a	6.5 mm	10.5 mm
c	Smooth curved profile based on a, with pad-up under stringer	6 mm (10 mm under stringer)	10.5 mm (14.5 under stringer)

5.2.1 Assembly

The parts were pre-assembled in a dry-fit operation as presented in Section 4.3 (Figure 5-13); once the pre-fit was used to de-risk the assembly, they were adhesively bonded with a single layer of adhesive (which from the prior experience, presented in Section 5.1 Flat test assemblies was expected to provide sufficient bondline filling), under 6 bar [0.6 MPa] of autoclave pressure. The reduction in mating gaps from even the light loading of the pre-fit was substantial, with widespread reduction as can be seen on Figure 5-14 and Figure 5-15. The heat cycle was the same as for the initial flat panels.

Figure 5-13. Wedge-shaped slipgauge used for dry-fit gap measurements.

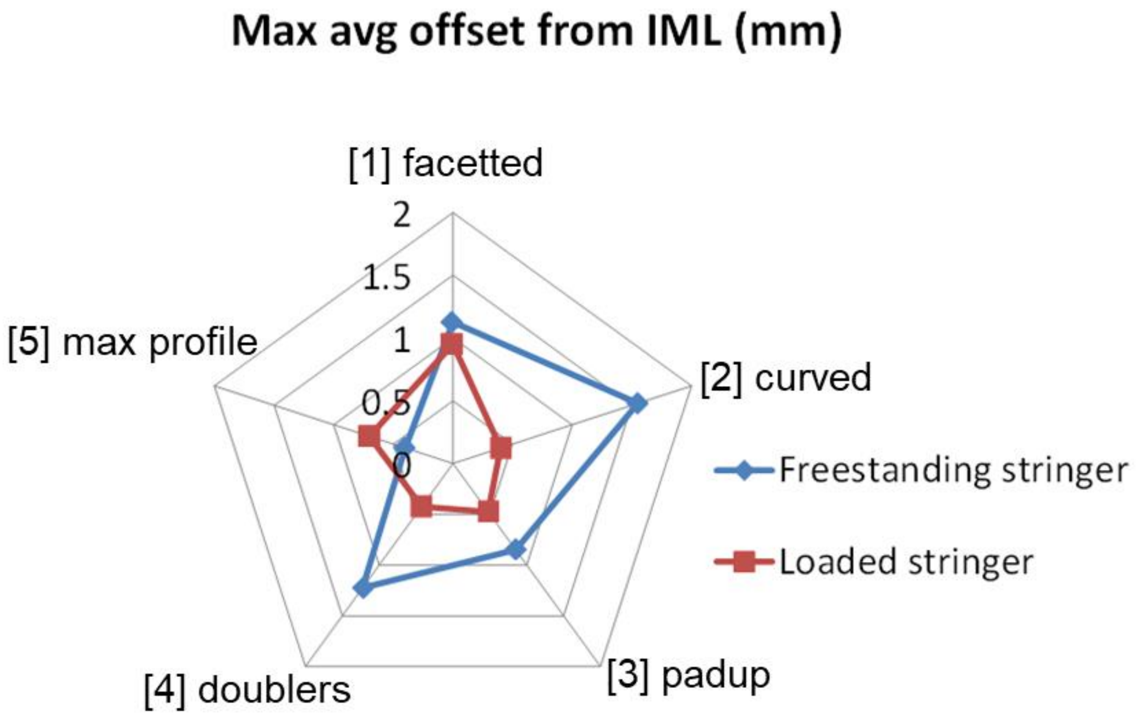

Figure 5-14. Evolution of skin-stringer gap before and after loading during dry-fit.

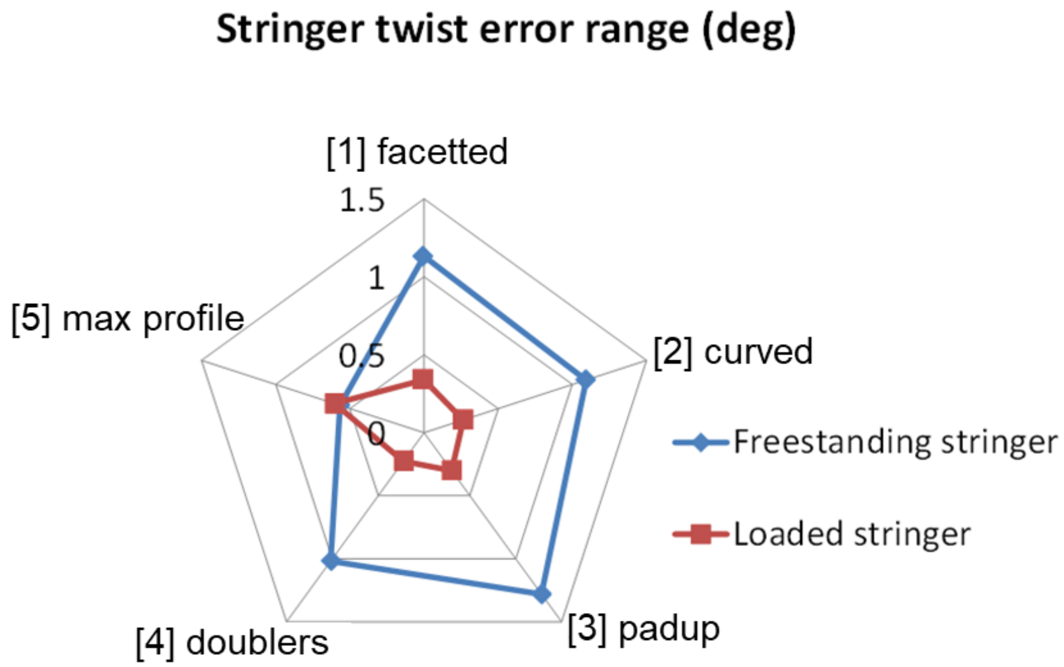

Figure 5-15. Evolution of the skin-stringer relative twist before and after loading during dry fit.

5.2.2 Model generation

Only interactions normal to the nominal interfaces were modelled, in line with the simplification presented in the methodology in section 3.3.3. Although the nominal stringer and skin bonding surfaces are not exactly the same (especially so in the case of assembly 1 with the faceted skin), the normals were simplified as being parallel between stringer and skin at each point. The stringers and doublers were simplified as 64 length positions, with 3 nodes equidistant at each cord (for a total of 192 nodes); the skins were simplified as nodes matching the stringer mesh, plus 4 extra nodes at each chord position (for a total of 448 nodes). When accounting for skin-tool interaction, this results in a total number of contact pairs (and therefore, number of tows/columns of the gap compliance matrices) of (192+448) = 640 for the skin-stringer assemblies, and in (192*4+448) = 1216 contact pairs for the skin-doublers-stringer assembly.

For the purpose of determining the compliance matrix, the parts were modelled as quad shell elements (S4R) of approximate size 30mm × 30mm in all cases, with constant thickness sections for the stringers and doubler(s); thicknesses were spatially mapped for the skins based on the nominal design. The compliance matrices are represented as surfaces in Figure 5-18; which highlights the differences in stiffness across different part designs, as well as the disparity in compliance of the different component types (with the stringers being upwards of an order of magnitude stiffer than the skins). For all part meshes, the boundary conditions reflected the datum features: the main datum hole was modelled as pinned with no rotation around the length axis, and the slot was allowed to move tangent to the bonding surface in the length direction, as well as rotate around any axis. The mesh and boundary conditions used for compliance matrix generation are illustrated in Figure 5-16 and Figure 5-17.

The assembly simulations were carried then out with the following simplifications:

- Pressure for adhesive flow calculation was modelled uniformly as the average contact pressure (even squeeze throughout the bondline[s] for each assembly);

- Part deviation was generated as the combination of the CMM results in the flat state, and the gap values on the profile checking tools in the formed state. The procedure is described in Appendix B — Approaches to data fit.
- Pressure and interaction at the tooling lugs was neglected; in fact they were not even included in the linear model. This is accordance with the considerations around the locally unrealistic nature of the boundary conditions.

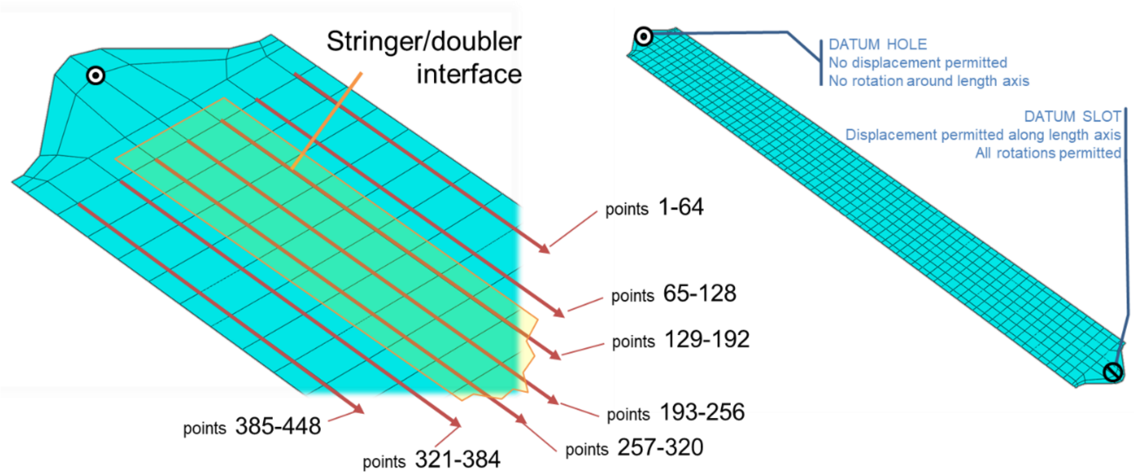

Figure 5-16. Mesh, boundary conditions, and location of linear model nodes in curved assembly skins.

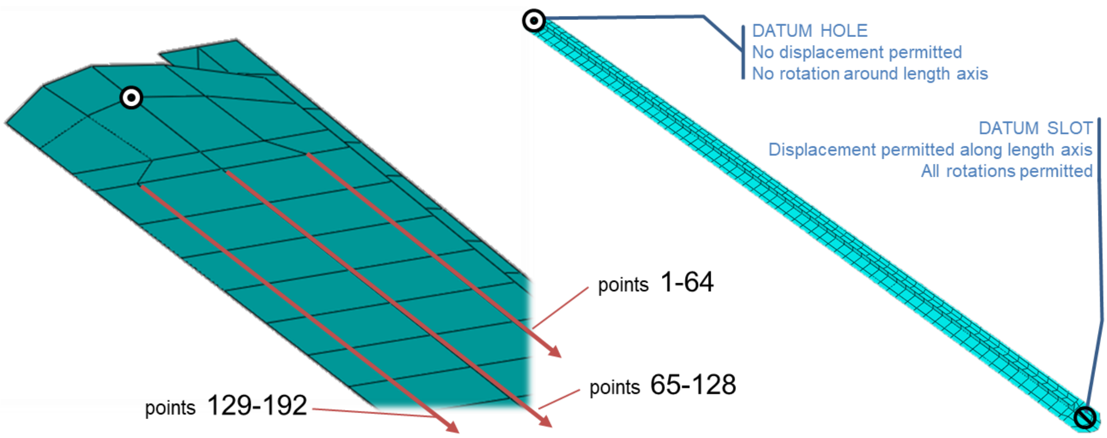

Figure 5-17. Mesh, boundary conditions, and location of linear model nodes in curved assembly stringers.

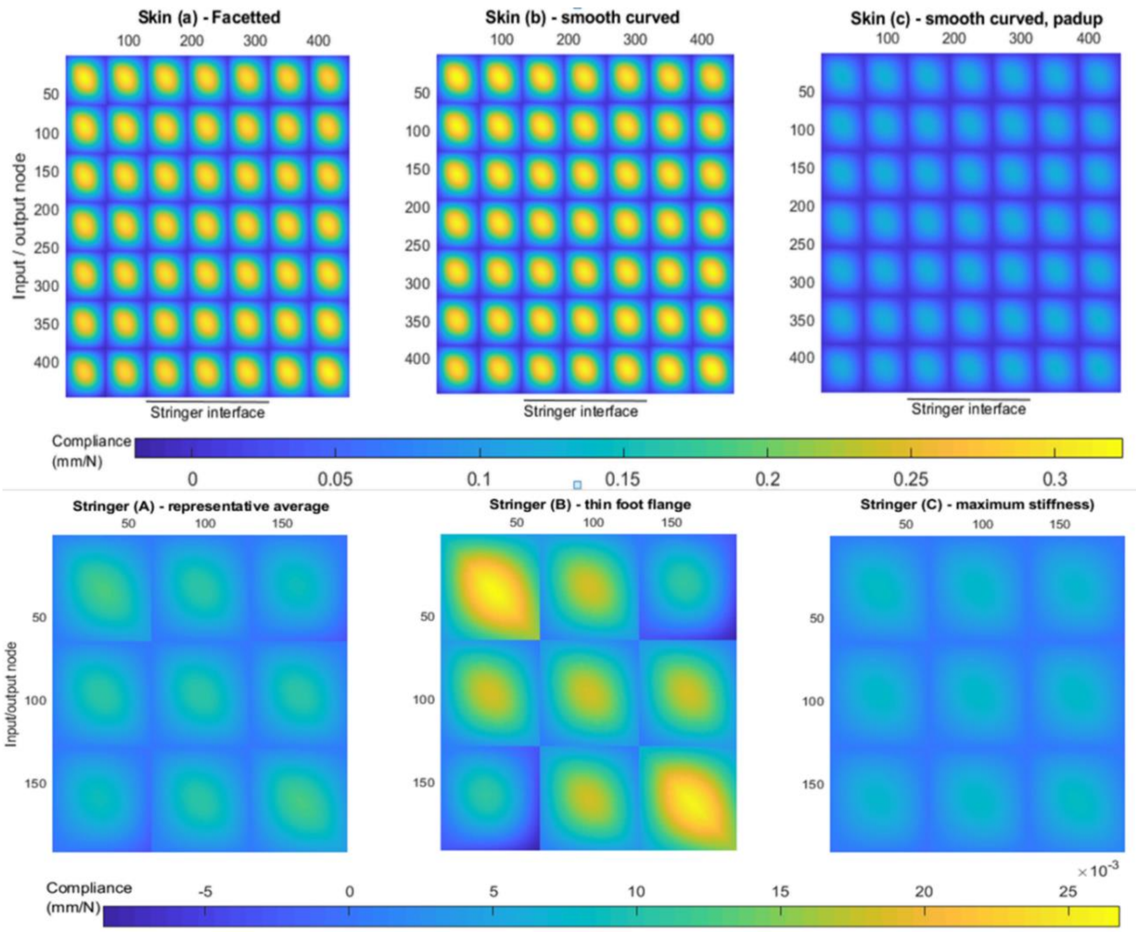

Figure 5-18. Compliance matrices for skins (top) and stringers (bottom): note the order-of-magnitude higher compliance of the skins, and the substantial variation within both part groups.

5.2.3 Results

Given the unique opportunity to test the health-check tool presented by this set of assemblies, the analysis diverges from the other tests. In the case of the aforementioned health checks, it makes little sense to attempt a detail quantification of error given the limitations of the shopfloor-based dry fit checks (rather, it is the location of maxima, and the rough height thereof, that is relevant):

- Rather poor resolution in the measurement (0.05 mm gauge graduations — with a minimum graduated value of 0.20 mm, and anything less being recorded as zero);

- Uncertainty due to the heavily manual component, with plenty of user ability to wiggle/squeeze the wedge-shaped slipgauge further in or out of the gap while maintaining full contact between the gauge and adherends;

- It is further acknowledged that any deviations/gaps away from the part edge can in no way be detected by filler or slip-gauges. As such, a decision was made to neglect the part curvature (in the pressed skin or bonding tool), resulting in an underestimation of the initial stringer-skin gap of around 50 μm under the stringer middle. The curvature *was* accounted for in the nominal bonding tool geometry, according to the principle shown in Figure 5-19 and equation (5-1), and quantified in Figure 5-20.

The prediction errors are summarised in Figure 5-21. The simulations proved less than capable for this set of tests, with RMS errors and standard deviations generally above 50 μm and thus hardly usable for the sub-mm tolerances required. In general, disagreement between both simulations was considerable, with the one that used gap checks as inputs generally exhibiting more error. However, there was good agreement between simulations, prominently, in the case of the legacy 'faceted' assembly[xxxiii] where the nominal geometry mismatch dominated the fit-up gap.

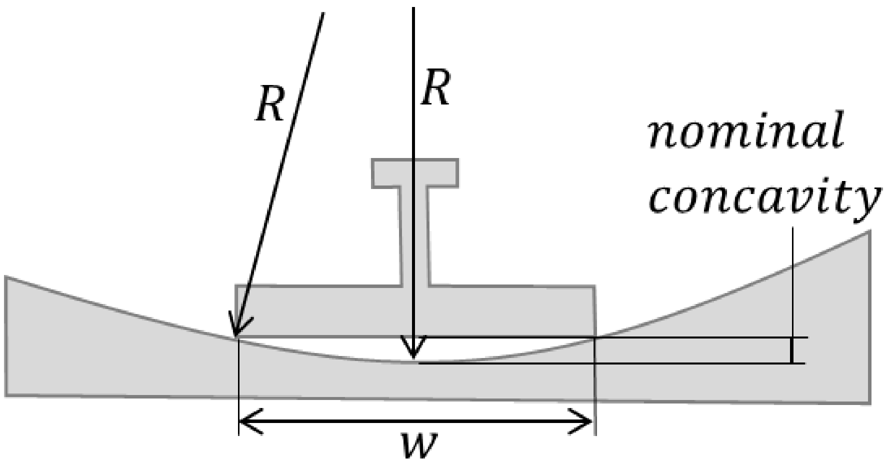

Figure 5-19. Convex skin-stringer interface due to wing curvature.

[xxxiii] Simulations of the assembly with doublers also agreed, but only because both expected highly uniform final bondlines (Figure 5-36).

Assuming a constant radius of curvature R in the bonding tool and/or skin, and given foot flange width w, the maximum mismatch between the foot and skin bonding surfaces due to concavity can be shown to be, by basic trigonometry,

$$nominal\ concavity = R - \sqrt{R^2 - (w/2)^2} \quad \textbf{(5-1)}$$

typical values of which are presented in Figure 5-20.

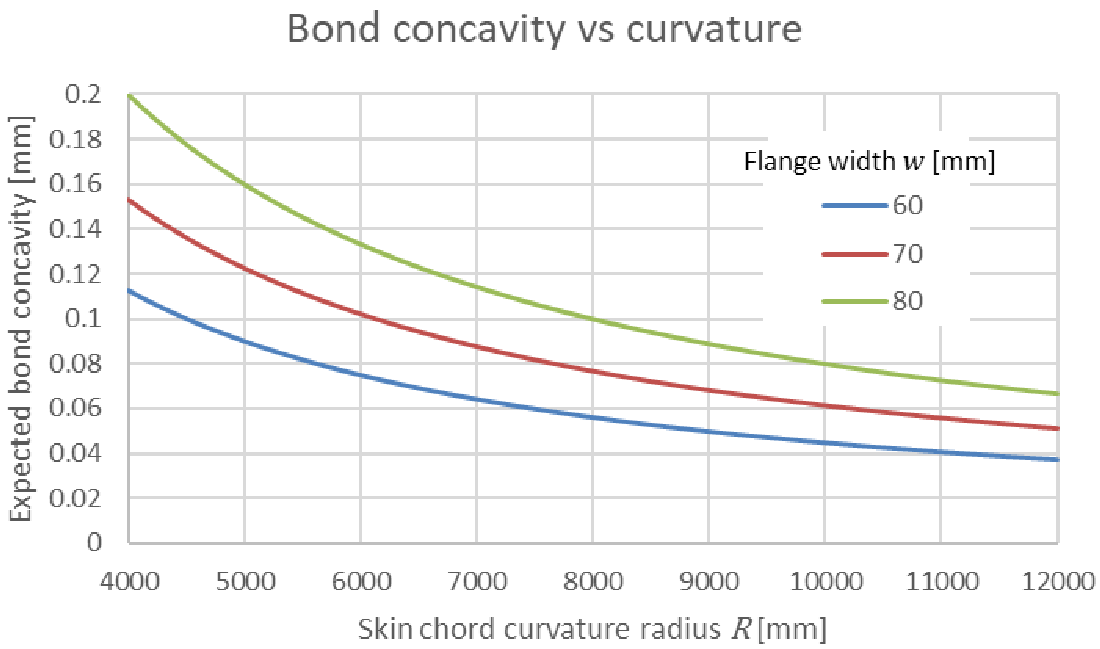

Figure 5-20. Effect of skin curvature on bondline geometry against stringers of nominally straight cross-section.

Note that even though the spatial density of the dry fit measurements was higher than for the forming process, the latter can be considered to be more reliable as they were carried with more time and higher-resolution tools, outside a production environment.

The resulting bondline thicknesses were assessed, as for the initial flat trials, via microscopy of sections. The section positions along the cross-section are provided in Figure 5-22.

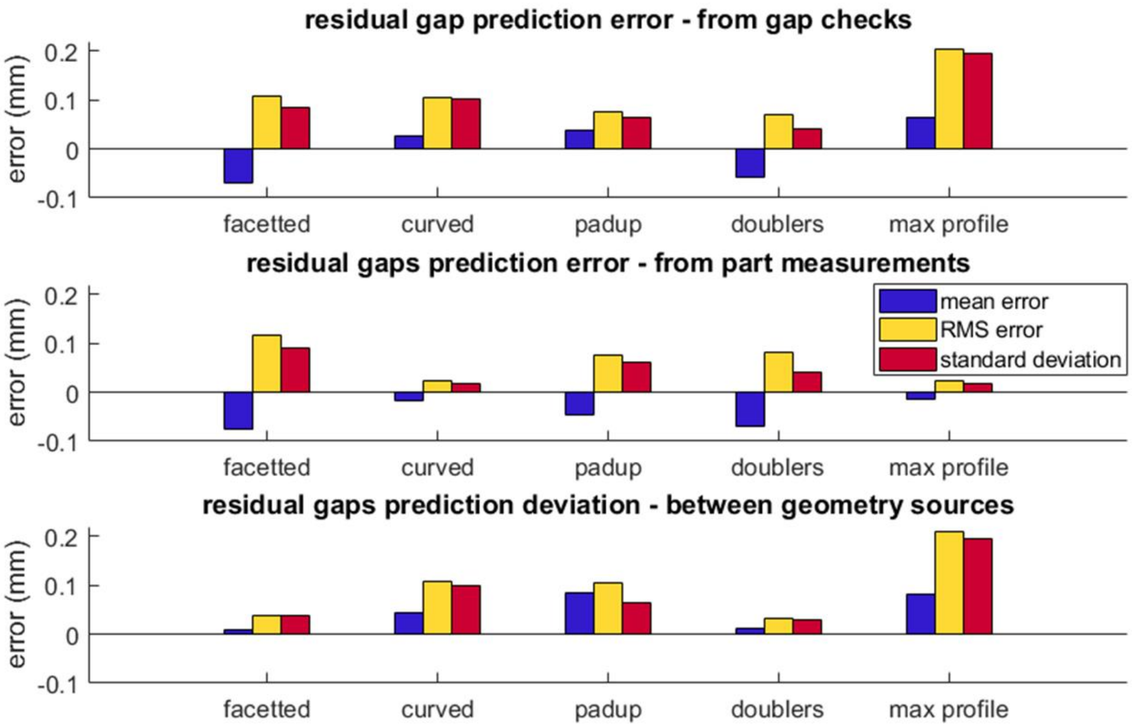

Figure 5-21. Errors in prediction of the residual gaps. The bottom graph compares both simulations (from gap checks and part measurements).

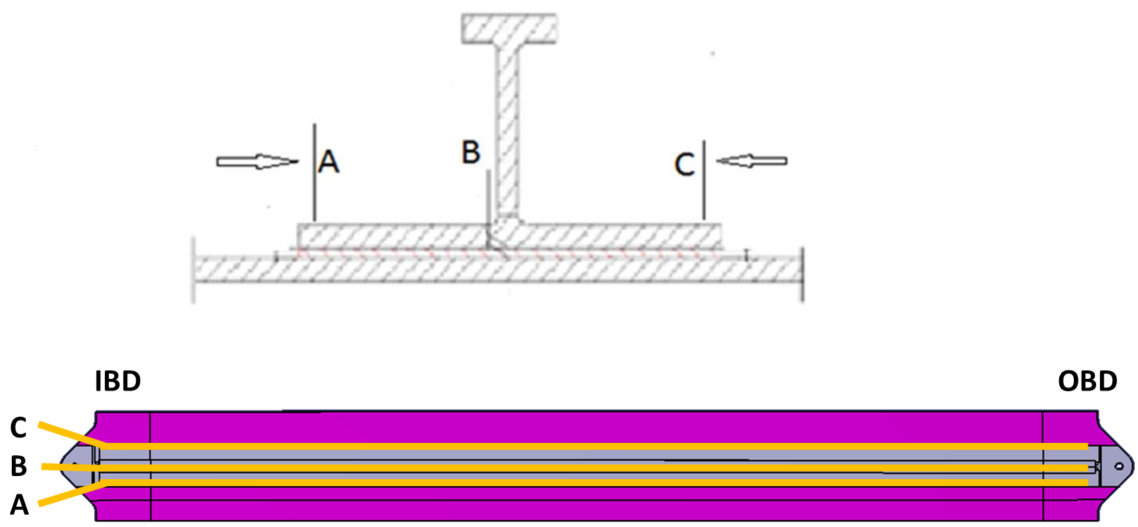

Figure 5-22. Cut locations: naming convention through each cross-section.

The section-based thickness measurement is at the root of suspected errors in assessment of the legacy ‘faceted’ assembly, due to the different section plan: given the higher expected variability of the bondline, a specific, more ambitious section plan was used. This plan, in addition to cross-sectional sections, also contemplated a number of lengthwise cuts (Figure 5-23) with denser microscopy measurements. Some of these measurements were taken at the very edge of the foot flange, with the unwanted effect that a small remainder of the naturally occurring corner radius was also measured. This had the effect of inflating the edge bondline measurements (Figure 5-24). The suspect measurements are indicated with empty markers in Figure 5-26. Subsequent project prioritisations precluded remeasurement or rework of the sections, preventing improvement of this dataset.

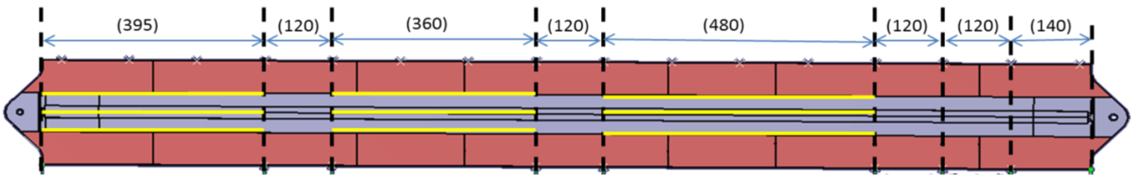

Figure 5-23. Longitudinal cuts in the 'faceted' assembly. All distances in brackets are approximate, in mm.

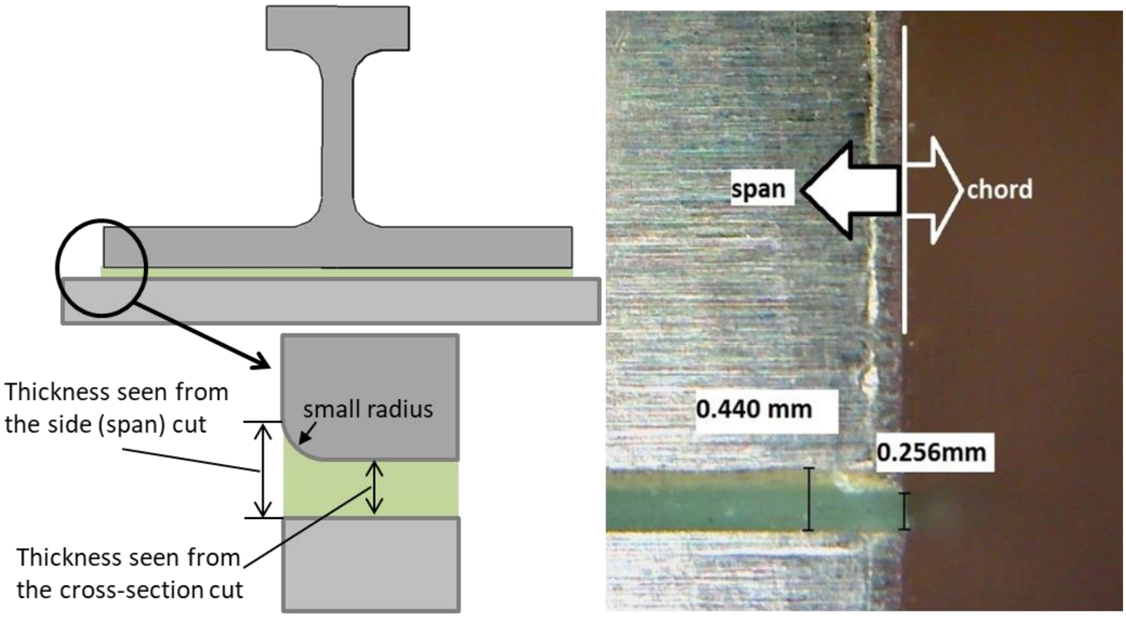

Figure 5-24. Error incurred when measuring bondlines from an edge section left: schematic; right: example macrograph). The bondline thickness as viewed from the side (span) is inflated compared to that from the cross-section (chord) due to the slightly rounded corner in the adherend.

For the purpose of description in this case, and as the interpretation needs to be at least partially qualitative due to the sparsity of the results, the measured bondline thicknesses have been characterised in terms of ‘overall thickness’, ‘twist’, and ‘convexity’ as per Figure 5-25 and the equation triad (5-2). Note that the ‘overall thickness’ and ‘twist’ can also be estimated in the pre-assembly state from dry-fit measurements alone, since they are given solely by b_A, b_C, and w.

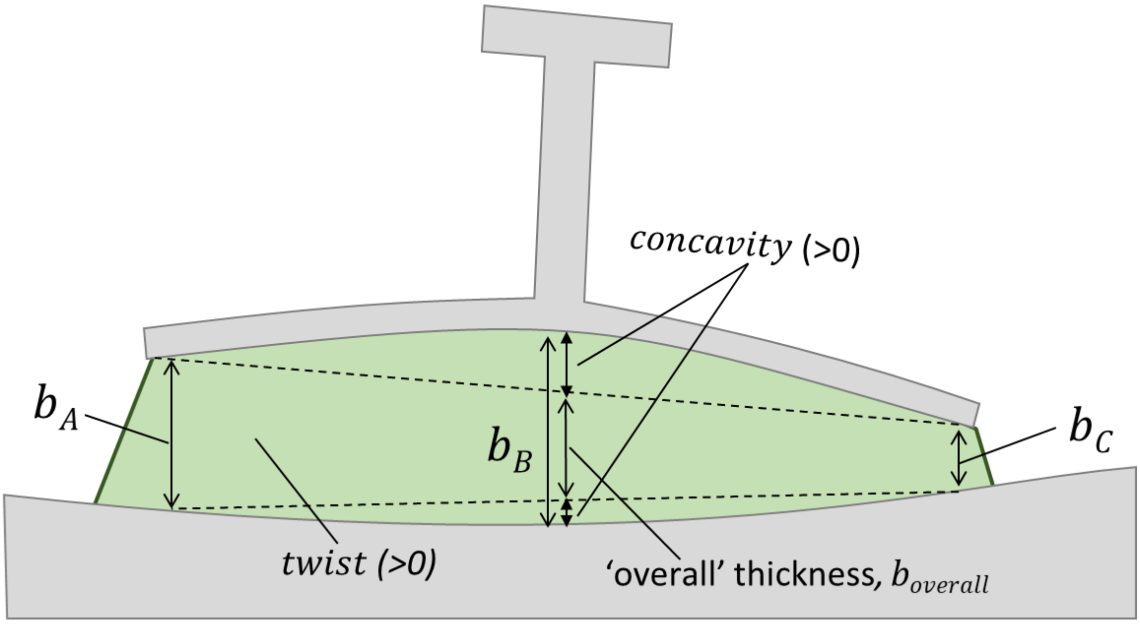

Figure 5-25. Geometric variables used to ease representation.

$$
\begin{aligned}
&b_{overall} = (b_A + b_C)/2 \\
&twist = (b_A - b_C)/w \\
&concavity = b_B - b_{overall} = b_B - (b_A + b_C)/2
\end{aligned}
\qquad \textbf{(5-2)}
$$

The results are now presented for each assembly archetype:

5.2.3.1 Assembly 1: Legacy — faceted interface

The baseline skin option yielded, as predicted by both simulations and basic (rigid) analysis of the interface, the largest residual gap. Both the coarse gap check- and detailed measurement-based simulation located the highest gap in the same area, coinciding with the vicinity of one of the facets. The results of both simulations (Figure 5-27) show fairly good agreement in the position and magnitude of residual gaps. The results also are consistent (all limitations considered) with the measured bondline thickness, as seen in Figure 5-26.

However, the minimum bondline thickness *was* overestimated by the simulations. Causes for this are discussed through the section.

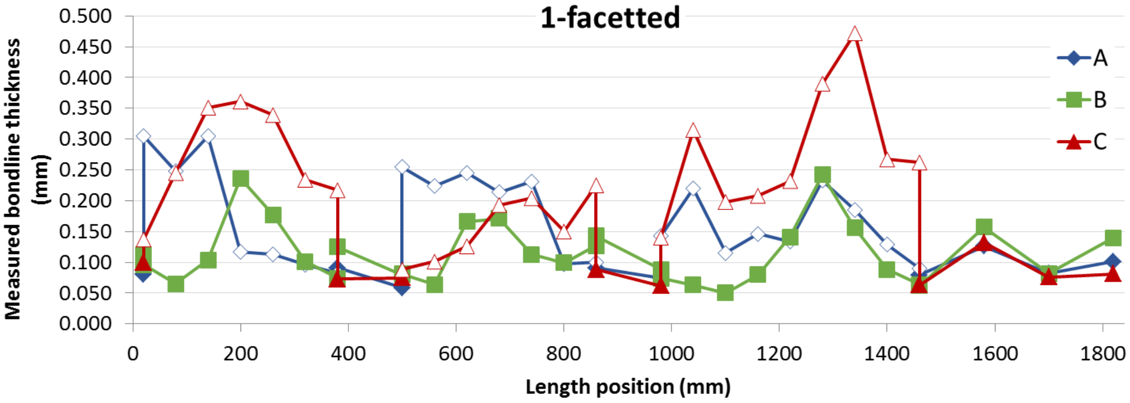

Figure 5-26. Measured bondline thicknesses for the legacy geometry assembly. Empty markers (for the A and C lines) correspond to values that are suspect due to lateral measurement as per Figure 5-24.

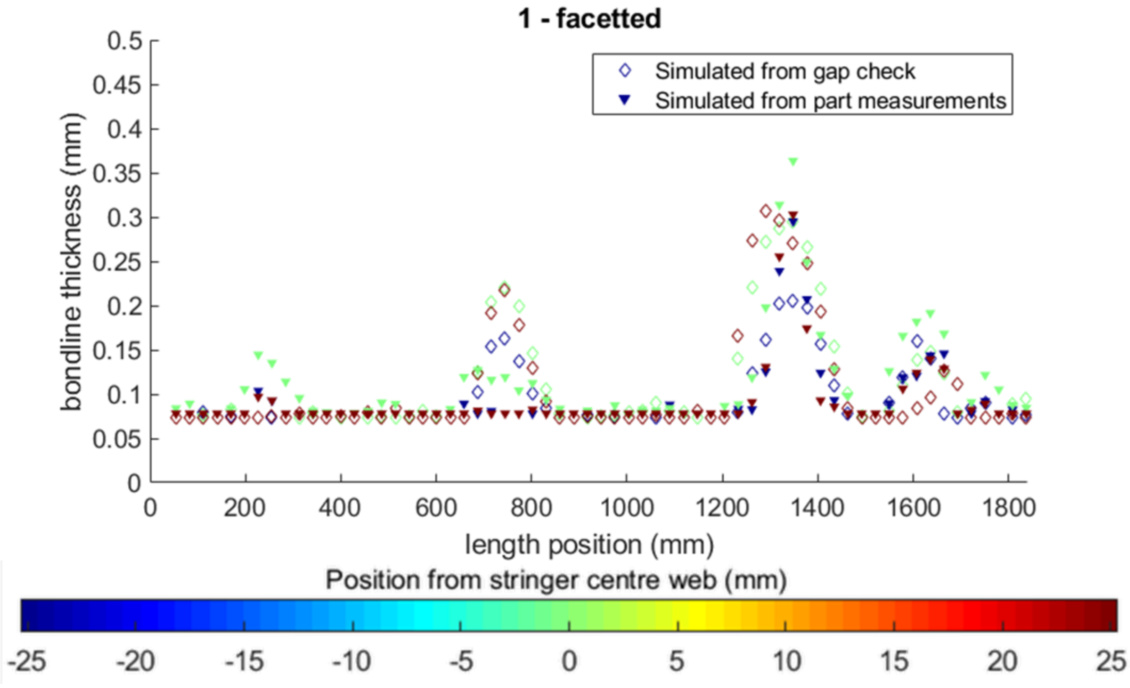

Figure 5-27. Simulation results for the legacy geometry assembly. The main peaks at length positions 200 mm, 750 mm, 1300 mm and 1600 mm are captured, though slightly overestimated.

5.2.3.2 Assembly 2: Curved interface

In spite of the similar initial variation in the stringer, and the superficially comparable dry-fit gap compared to the previous assembly, the final result was very different — reflecting the match between the nominal interface geometries. This was generally well captured by both the coarse and detailed simulations.

A discrepancy arises, however, in the form of sharply increased bondline thickness towards one of the longitudinal ends, which is predicted by the simulation but never encountered in the real case. The likely explanation for this is the unrealistic boundary condition, already discussed earlier, whereby datums are very constrained in order to enable the compliance matrix to be generated. This effects manifested themselves often enough (though always confined to a small area) that it will not be explicitly mentioned henceforth.

Greater-than-modelled complexity of the adhesive flow is also revealed in the through-section bondline thickness variation; thickness measured under the foot flange edges is greater than at the middle, but by less than 50 μm. This means that:

- There wasn't a unitary 'minimum' bondline thickness;
- Although the stringer cross-section was able to deform to partially adopt the curvature of the skin and tool underneath, it was prevented from fully doing so (even though in a dry state it should have been more than capable of achieving the full chordwise deformation).

In this case, due to the thickness bondline under the centre web, the expected effect is the following: pressure loss is lower under the stringer centre, and as a consequence more adhesive squeeze-out would occur for the quasi-steady condition to be fulfilled and force equilibrium to be retained. This again agrees with the differences between 'thick' and 'thin' stringers observed in the initial flat panel tests.

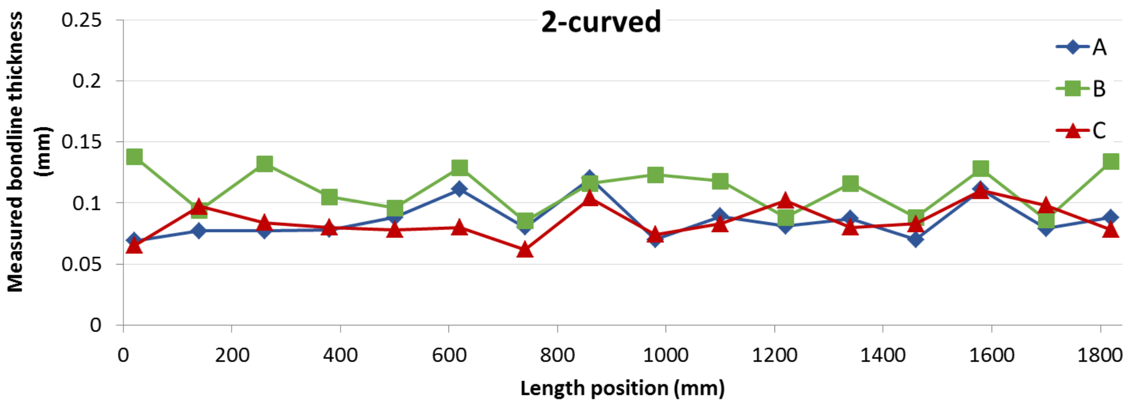

Figure 5-28. Measured bondline thicknesses for the curved-interface assembly.

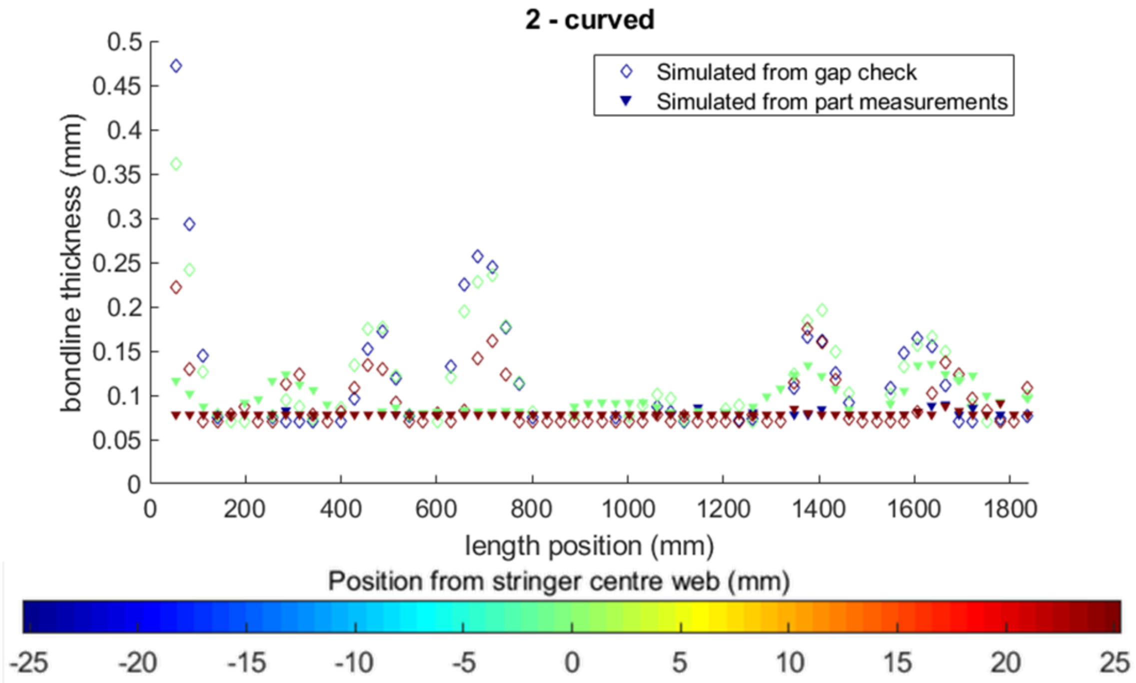

Figure 5-29. Simulation results for the curved-interface assembly. The gap-check simulation is inaccurate due to local measurement inaccuracy, while the one from part measurements results in a "flat" bondline.

5.2.3.3 Assembly 3: Pad-up and thin flanged stringer

As expected intuitively, and as foreseen by the simulations, the thinner stringer enabled manufacture of a smoother adhesive joint according to the bondline measurements. However, there was a substantial divergence towards the very inboard and outboard stringer ends: the bondline is much thicker right under the web area, but substantially thinner elsewhere. This is explained by a local convex dish or ‘bump’ caused by the press-forming process (Figure 5-32), and undetected by the gap checks confined to the edges; the adhesive was easily squeezed into such a large gap, leading to underfill in the vicinity. The principle is outlined in Figure 5-33.

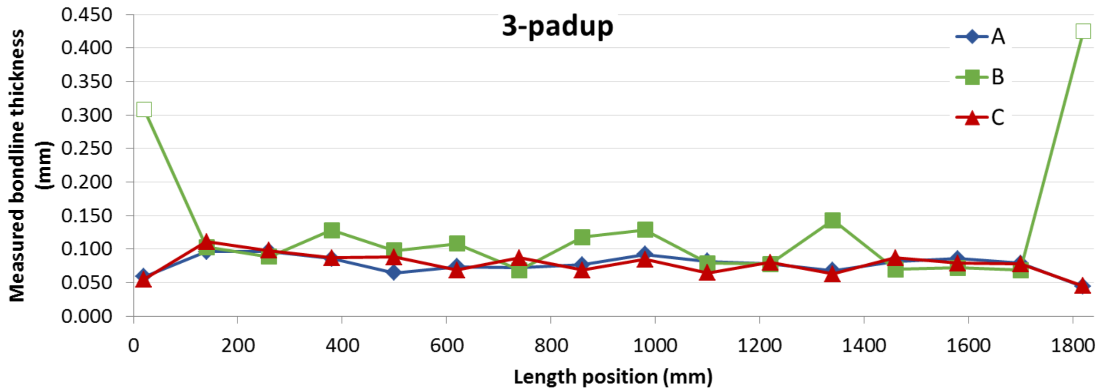

Figure 5-30. Measured bondline thicknesses for the pad-up-and-thin-stringer assembly. Empty markers at the edges (line B) are values attributed to local stringer defects.

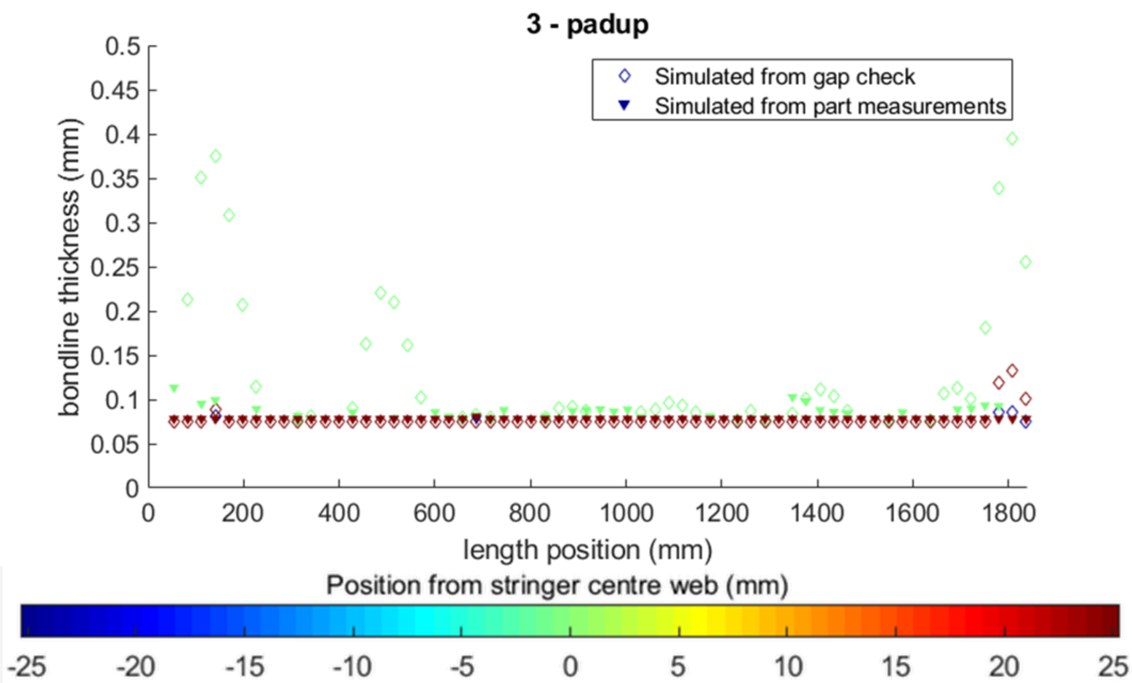

Figure 5-31. Simulation results for the pad-up-and-thin-stringer assembly. Both the large residual gaps from gap checks, and the artificially flat minimum bondline, are present.

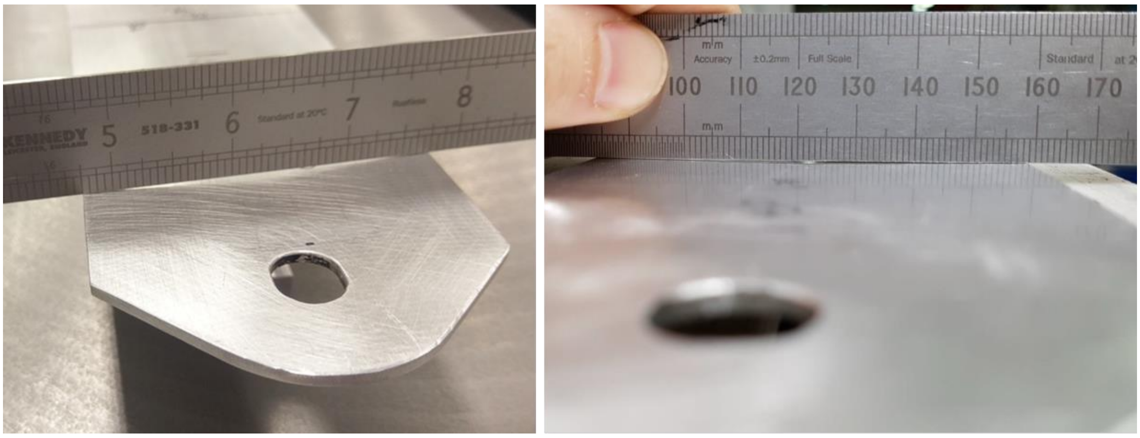

Figure 5-32. Manufacturing defect at the end of thin-flanged stringers, introducing during forming.

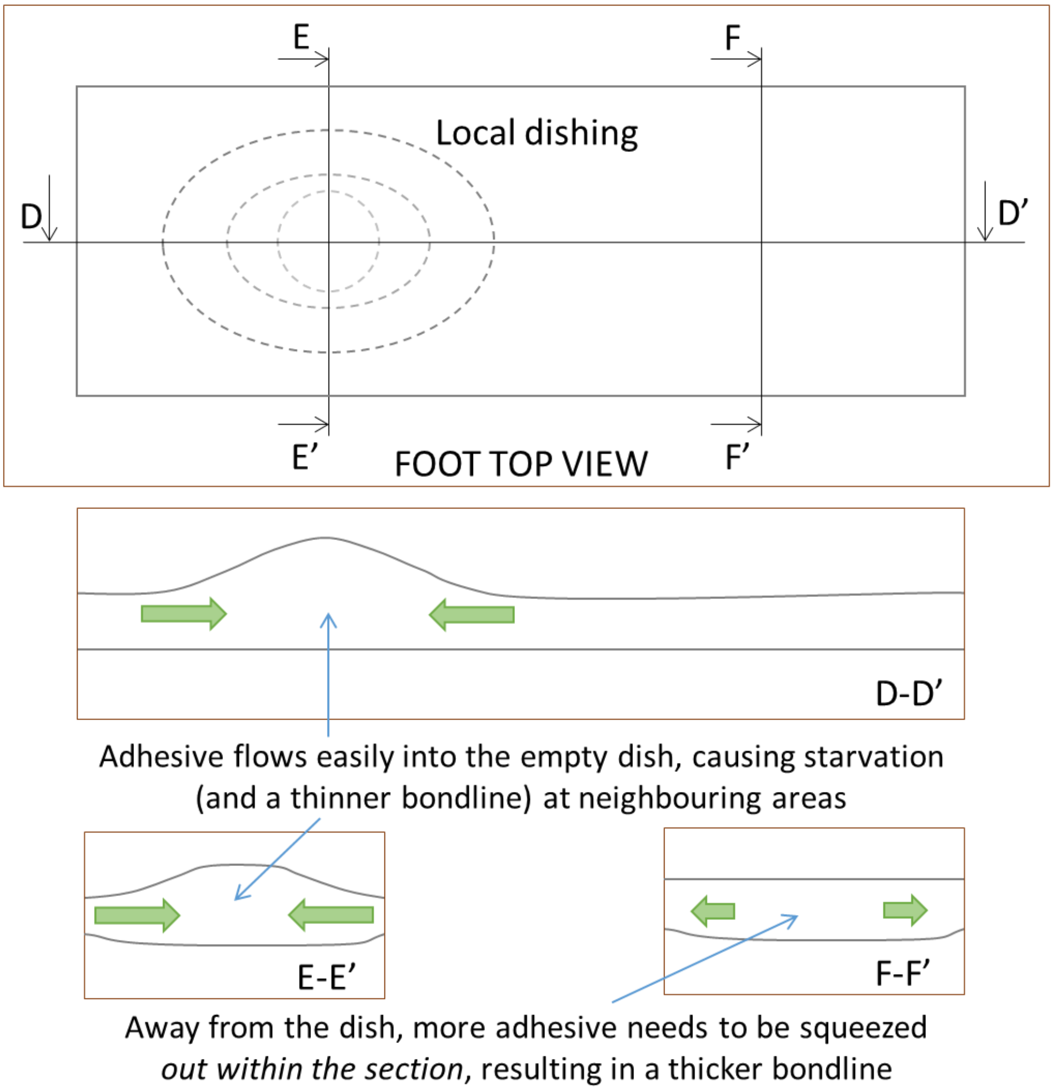

Figure 5-33. Flow of adhesive through the bondline length due to local defects.

5.2.3.4 Assembly 4: Doublers and thin flanged stringer

The outcome of this test was much in line with the previous iteration, achieving much smoothness of the bondline thanks to the use of multiple highly-compliant parts instead of monolithic components.

In addition, the test presented an interesting opportunity to confirm the pressure-driven nature of the adherend interaction, as multiple bondlines had to cope with localised curvature (in the form of 'bump' stringer form defects on one side, and tool/skin curvature on the other). Both these variations, rather than just resulting in a local gap/increased thickness in the immediately interfacing bond, actually propagated through the whole stack of components (note the range in the values in Figure 5-35). Thus:

- All bondlines at the stringer ends are substantially thicker under the stringer middle, and thinner at the edges, which is consistent with the effect on flow of the local dishing as described in Figure 5-33;
- All bondlines, not just the lowest doubler-skin one, consistently exhibit higher thickness at the middle than at the edges. Interestingly, the compounded value of this convexity effect is about 100 µm — in contrast with the expected 50 µm from the skin/tool curvature alone. A possible explanation is that, in addition to the rigid convexity from the tool, deflection of the stringer flanges may have resulted in extra convexity; this would be consistent with the results for the 'thin' stringer in the initial flat panels.

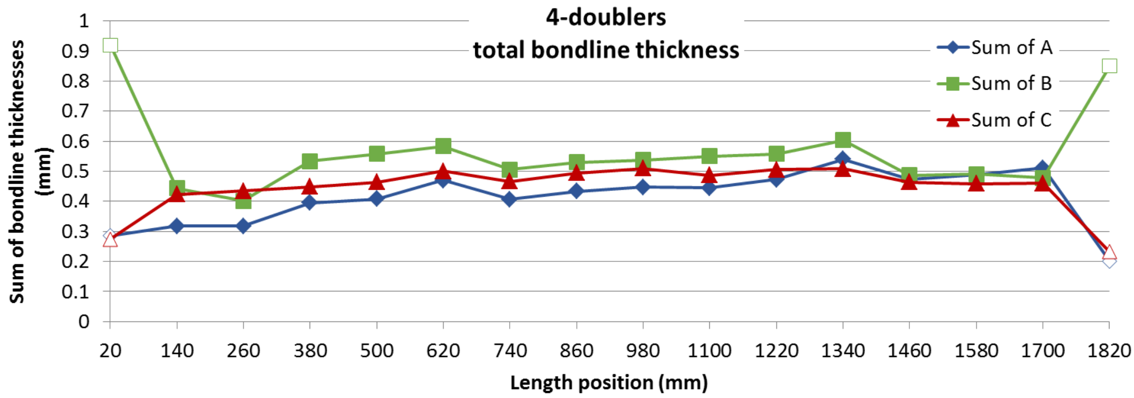

Figure 5-34. Measured bondline thicknesses for the doublers-and-thin-stringer assembly. Different interfaces are not differentiated as values are generally similar. Empty markers at the edges (series B) are for the bondline between the stringer and the topmost doubler at the edge defect location.

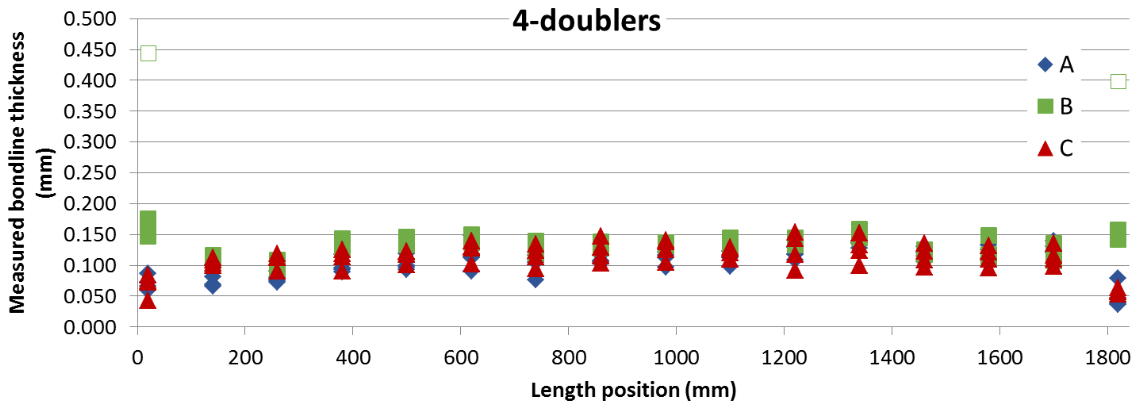

Figure 5-35. Sum of measured bondline thicknesses at each cross-section location for the doublers-and-thin-stringer assembly. Empty markers at the edges are for the edge defect location.

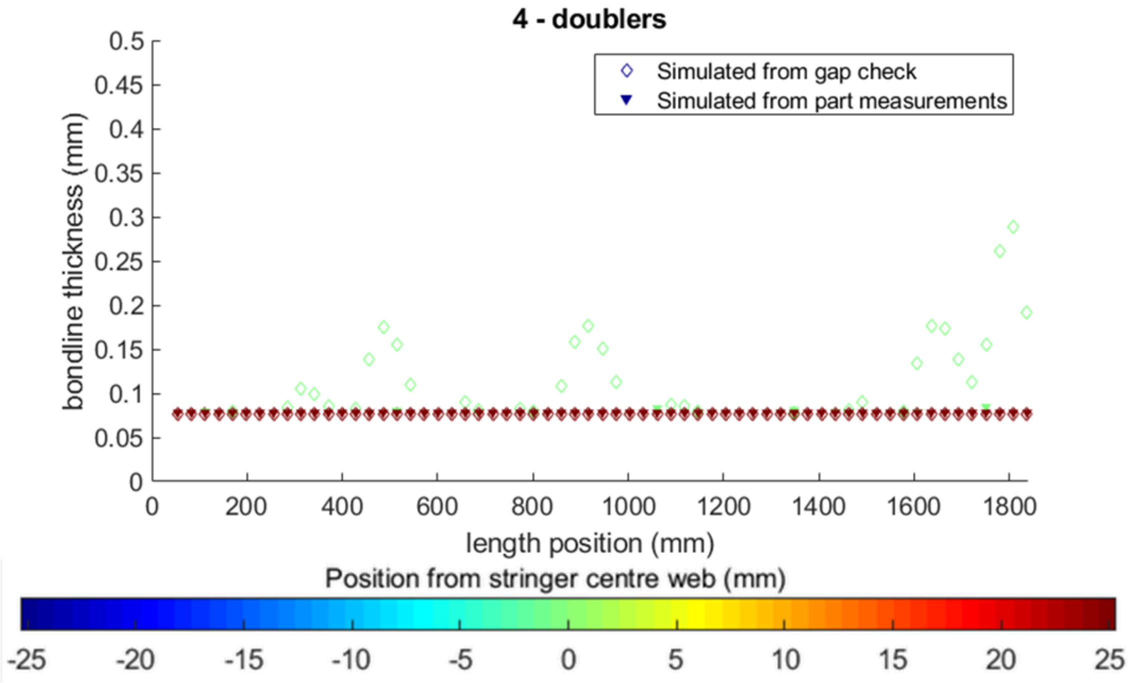

Figure 5-36. Simulation results for the doublers-and-thin-stringer assembly. Different interfaces are not differentiated as values are generally similar. Note limitations as in Figure 5-31.

5.2.3.5 Assembly 5: Curved interface - Thick stringer

In spite of the substantial increase in stiffness associated with the thickest cross-section, this test yielded results similar to the second one by virtue of the nominal match between interfaces. This is again a result reflected by the simulations. (It is worth recalling that as these tests used carefully reworked components, the manufacturing accuracy was better than what one might reasonably expect in a busy production environment; it would be a mistake to take this result as a blanket demonstration of manufacturing capability.)

More important, however, is how the stiffness of the foot flange bore on the interaction with the adhesive and bondline convexity. As the foot flange of this stringer is too thick to experience any significant deformation,

- Its cross-section remains unchanged and provides no reduction in the convexity of the interface gap; consequently, the middle-edge difference in bondline is greater than for the cases with baseline stringers;

▪ As a result, owing to the lower pressure loss near the stringer middle, the squeeze is accelerated, causing the final bondline to be thinner than for the case with curved skin interface and baseline stringer.

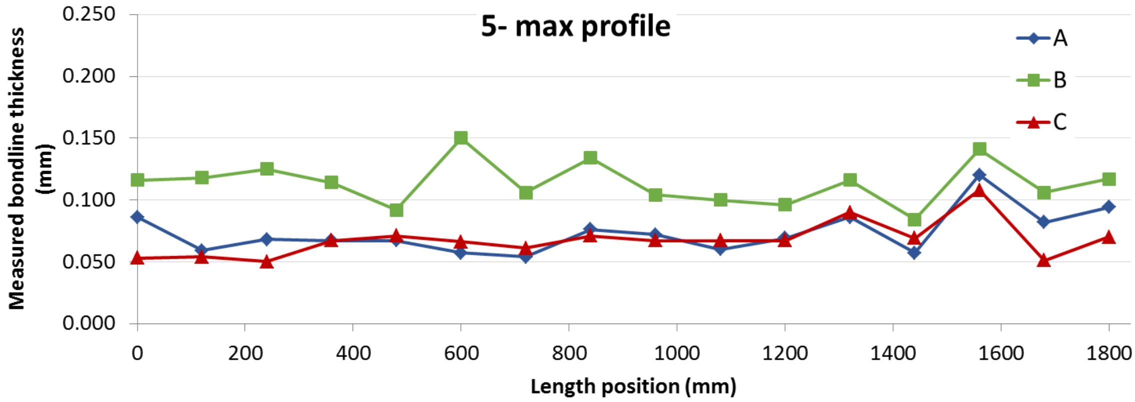

Figure 5-37. Measured bondline thicknesses for the thick stringer assembly. Note the consistent convexity.

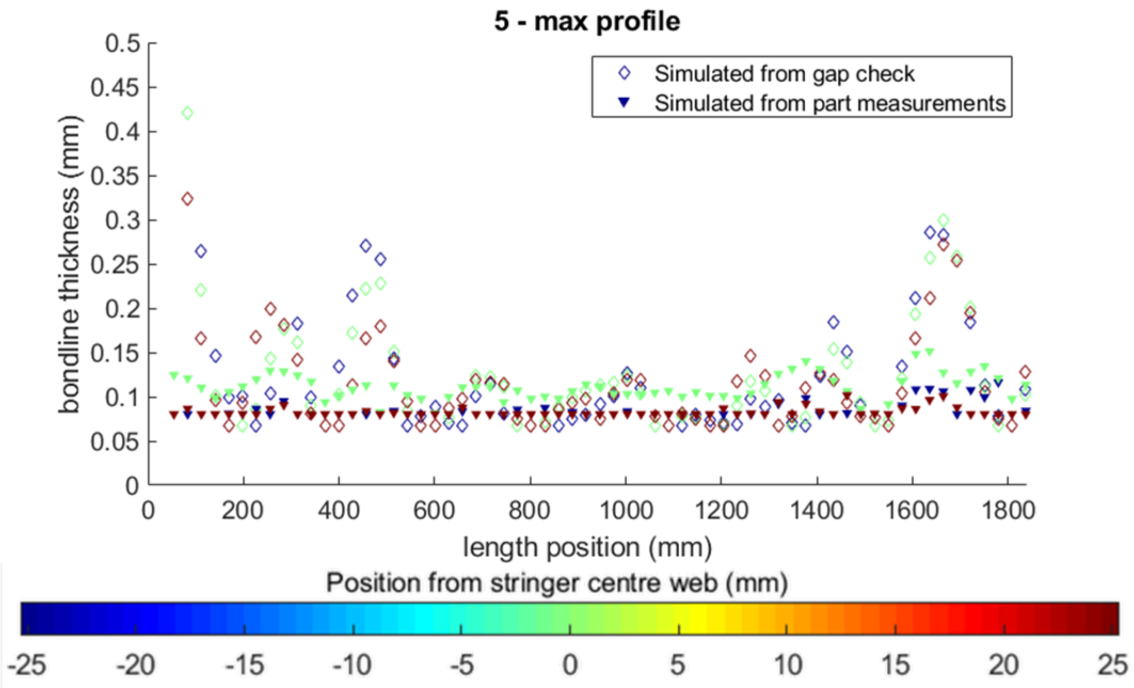

Figure 5-38. Simulation results for the thick stringer assembly.

5.2.3.6 Comparative summary

A summary of bondline overall thickness, twist and concavity is displayed for all assemblies in Figure 5-39 to Figure 5-44. This provides an opportunity for at-a-glance appraisal of each concept's ability to mitigate part variation. The impact of design decisions regarding matching surfaces is also very visible: by removing nominal steps from the bonded details, substantial reductions in the peak bondline thickness were achieved (see ‘1-faceted’ peaks in Figure 5-39 and Figure 5-41).

Once the nominal interface surfaces were in agreement, the changes in gap closing capability (due to different stringer cross-section) seemingly had a much lesser effect (see ‘2-curved’, ‘3-padup’, ‘5-max profile’); however, this can be safely attributed to the detailed work done in this case to generate good quality parts. Parts manufactured to loose tolerances are likely to behave differently. This may be traded with the fact that it is generally easier to reliably form stiffer parts.

Finally, although a laminate concept did not fail to keep bondline thicknesses relatively in control, it fared the worst of all non-faceted concepts (see ‘4-doublers’); this can be attributed to how individual bondlines still suffer from boundary condition effects, while additionally stacking up the variation across all layers. As a result, the top surface of the stringer foot (which would usually interface with other stiffening elements in a real component) exhibited substantial misalignment from the skin, and varied in height substantially.

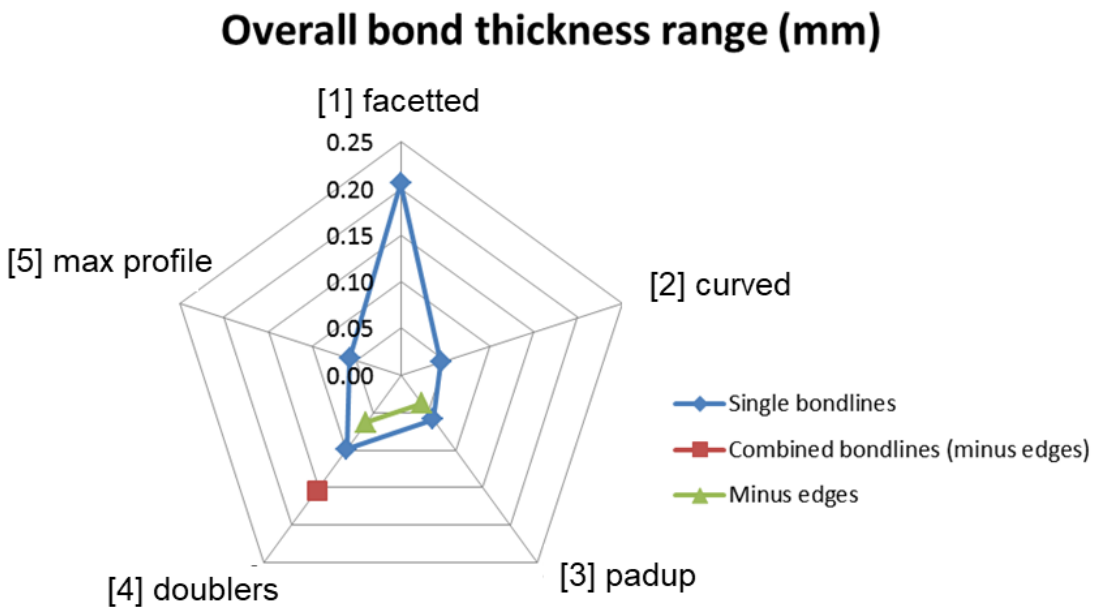

Figure 5-39. Final bond thickness range for the curved test assemblies.

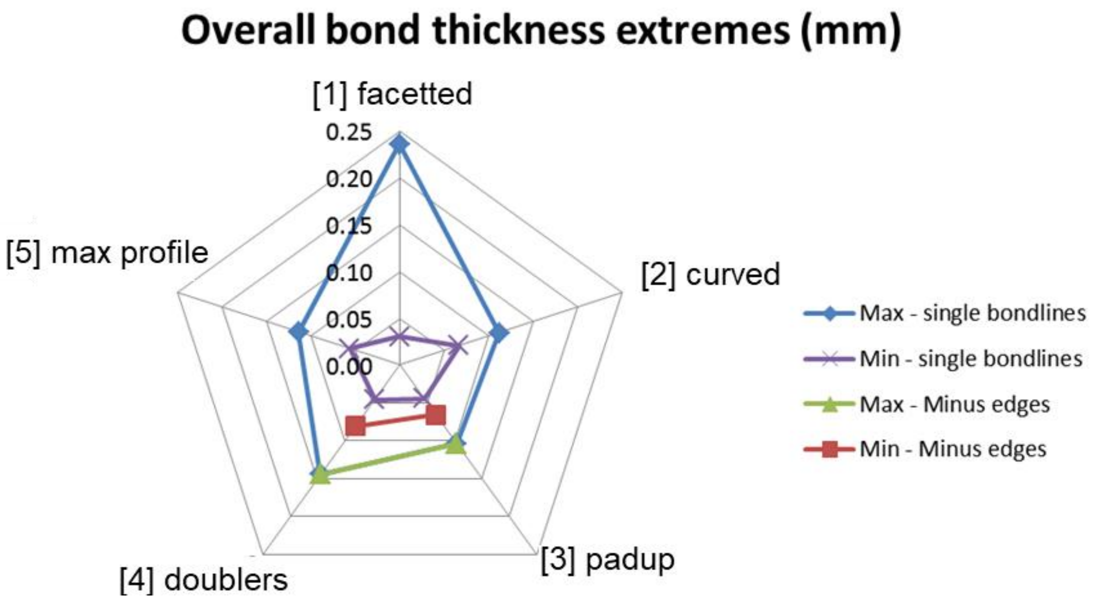

Figure 5-40. Final bond thickness extremes for the curved test assemblies.

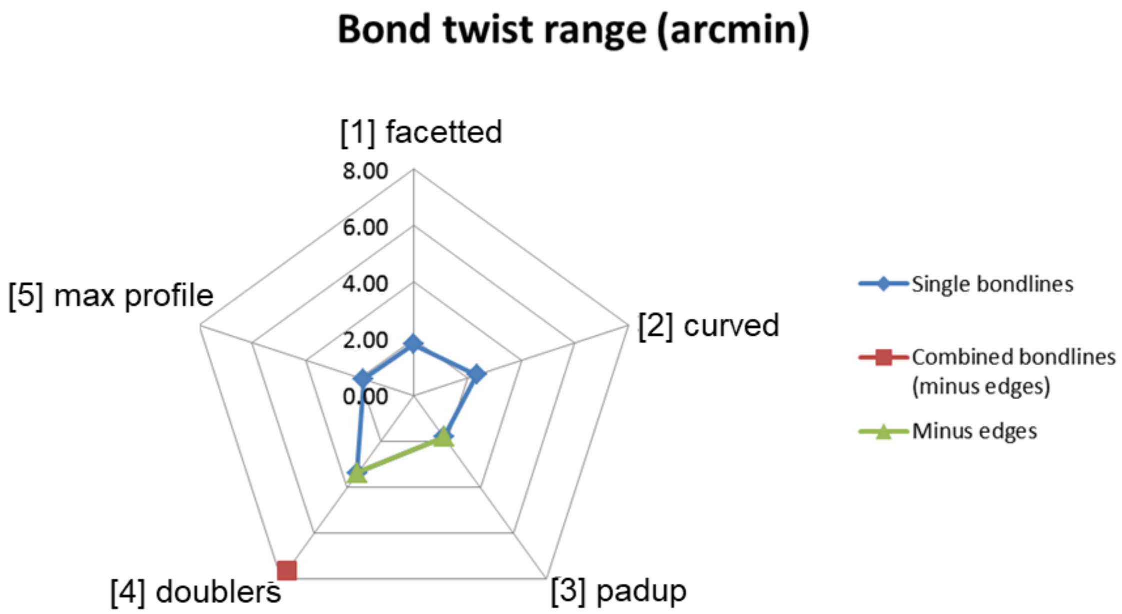

Figure 5-41. Final bond twist range for the curved test assemblies.

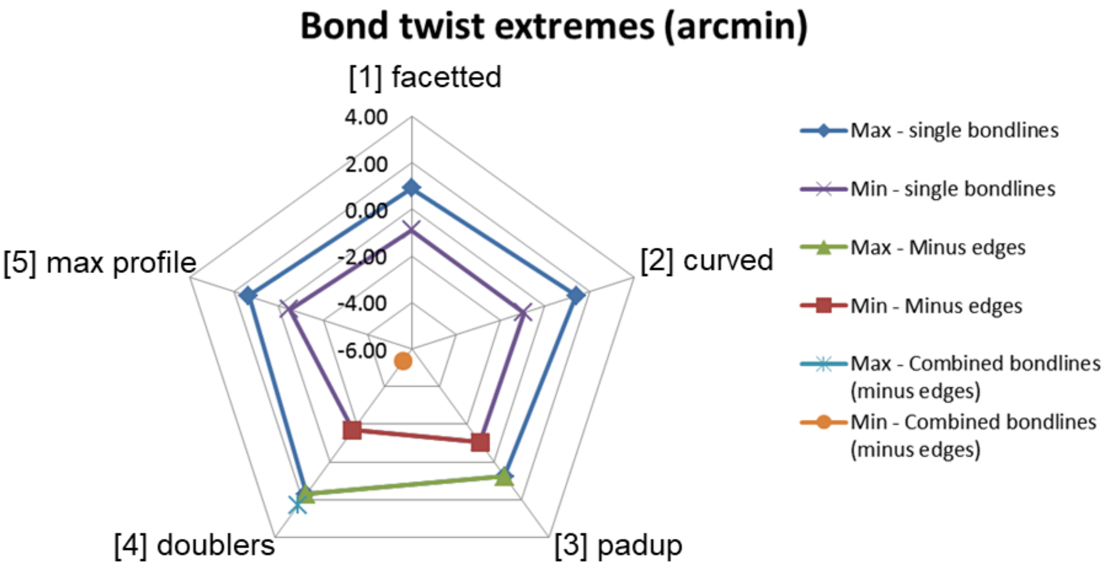

Figure 5-42. Final bond twist extremes for the curved test assemblies.

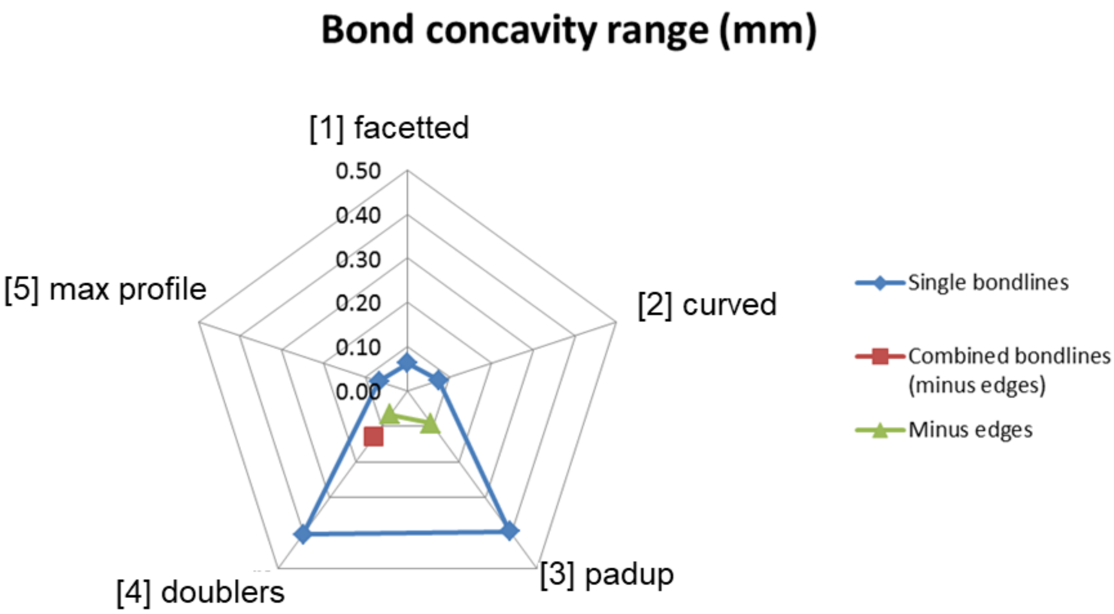

Figure 5-43. Final bond concavity range for the curved test assemblies.

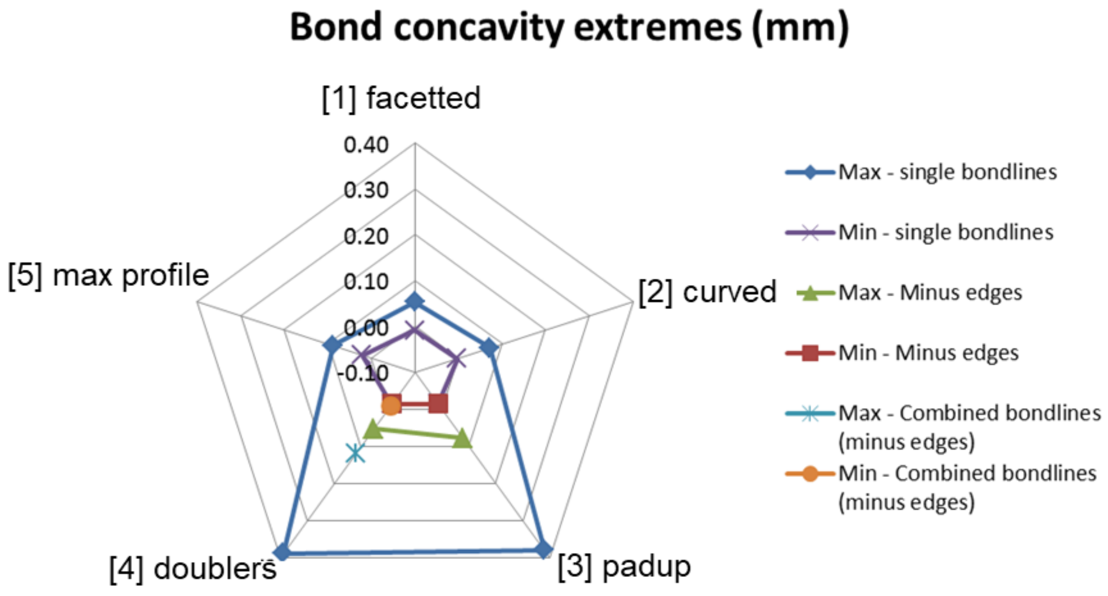

Figure 5-44. Final bond concavity extremes for the curved test assemblies.

5.2.4 Main outcomes of the curved assembly test

The results for thin or multiple adherends confirm the prominent role of adhesive-borne and -transmitted pressure in determining the geometry of bonded joints. This goes beyond the basic concern of *delivering* pressure and also affects the *distribution* thereof.

The bondline results provide further confirmation of the increased complexity of squeeze-flow for cases where cross-sections are not flat and parallel, including global curvature, cross-section deformation, and local shape defects. In all cases, the effect is consistent with the adhesive flow mechanisms at the foundation of the model.

The tests were successfully used as the testbed for a quick health-check tool fed with easily-retrievable manual check data from a pre-fit operation. Qualitative results of the coarser simulation match the results, though they also confirm limitations linked to boundary condition assumptions and measurement resolution.

Finally, trouble experienced throughout assembly realisation emphasise the need for tight control of the manufacture and inspection process, inclusive of never-removed part identity markers, unified reference frames, first-article-inspection, and first-inspection-evaluation (i.e. signing off the inspection procedure, and redesigning it if necessary, based on the outcomes from the first attempt).

5.3 Multi-stringer assembly trials

An extra set of tests was commissioned with the Advanced Manufacturing Research Centre with Boeing (AMRC). The tests seek to cover the factors not involved in previous project-aligned tests (Table 5-8): the effect of different boundary conditions, and the impact of stringer variation on skin deflection.

The tests consist of bonded assembly trials of nominally flat stringers on skins. The manufacture of these skins is purposefully varied by tampering with the machining clamping scheme, so as to obtain localised variation. Assemblies are bonded with two different boundary conditions: bagging the panel on to a thick metallic plate, and envelope bagging (similar to the double-pressure assembly concept successfully tested within the PABST programme and further in SAAB development).

Lessons learned from the prior demonstrators are applied in the work definition, including indelible marking of parts (rather than labels), first article inspection, strict definition of metrology output formats, and explicit requirement for thorough documentary evidence of each manufacture and inspection step to enable traceability.

Given the limitations of prior tests, the two distinctive requirements are:

1. The setup must permit use of different boundary conditions, and it should be possible to replicate the same distribution of geometric variation in different boundary conditions.

2. The setup must contain multiple stringers, with control over the distribution of part variations, such that effect of stringer interaction on skin deflection can be observed.

Table 5-8. Assembly aspects addressed by previous tests. The shading indicates whether prior tests addressed each element, and the text describes how.

Factor	Flat assembly tests	Curved assembly tests
Impact of part cross-section stiffness	2 cross-sections	3 cross-sections
Impact of stringer flange stiffness	2 flange geometries	3 flange geometries
Defect (unloaded gap) depths	Controlled through built-in defect	Observed, uncontrolled
Defect (unloaded gap) spans	Controlled through built-in defect	Observed, uncontrolled
Adhesive flow behaviour	Impact observed, uncontrolled	Controlled regime assured
Designed-in gaps	Built-in defects	Setup with machined stepped interface
Naturally-occurring gaps	Flat parts, tight tolerances	Variation from forming
Different boundary conditions	Rigid skin tool, single-side pressure	Rigid skin tool, single-side pressure
Multi-part assembly (series)	Flat skin and underlying tool contribute minimally to variation	Curved stringer-skin-tool stack One setup with doublers
Multi-part assembly (parallel)	Flat skin conforms to underlying tool, minimises stringer interaction	Single stringer
Key		
Satisfactorily addressed	Observed but uncontrolled	Not addressed earlier
Series assembly: stack of parts transmitting pressure Parallel assembly: multiple stringers transmitting same side pressure on skin		

Furthermore, the usual representative assembly parameters and part geometries were been desensitised and simplified to enable economical manufacture by third parties without confidentiality concerns. This includes:

- Change of adhesive (using available stock of aerospace-use film; a roll of 3M AF163-0.6K from an old project was used)
- Reduction in pressure (mitigating any potential hard-to-characterise tooling deformations, and further demonstrating OoA curing with later developments in mind)
- Constant T-section stringers, producible from standard extrusions of 6000-series aluminium alloy (this results in a section less stiff than the stiffeners studied previously)

In addition, a set of verifilm trials (non-adhering bonding mockup) was performed prior to actual bonding trials. The non-adhesion was achieved by sandwiching each layer of adhesive tape between two layers of unperforated nylon release film. Such process, as presented earlier at the end of Section 1.3, allows easy assessment of bond quality by contact-based measurement or visual examination of the cured adhesive. It also makes it possible to reuse parts for assembly tests with minimal need for cleanup. The verifilm process was instrumental to generating like-for-like assembly data for different boundary conditions and equal input geometrical variations, as well as increasing the volume of assembly data without prohibitive part manufacture costs.

5.3.1 Trial structure

5.3.1.1 Part manufacture and measurement

Stringers and matching skins were machined from near-final shape stock material, and subjected to highly accurate (probe CMM) measurement. An irregular clamping scheme plus overclamping was used with stringers so as to add controlled profile variation (Figure 5-47).

A detailed description of the manufacturing and inspection carried out is presented in Appendix D — Multi-stringer assembly manufacture.

5.3.1.2 Verifilm trials

Bonded assemblies were carried out with a layer of non-adhering release film between the adhesive and adherends, thus preventing actual bonding. The cured bondline thickness was measured. By repeating this with different boundary conditions, the effect of a double-side-pressure concept can be captured.

5.3.1.3 Bonding trials

Bonding proper was carried out after the verifilm trials, repeating a selection of verifilmed configurations. The bonded assemblies were sectioned at multiple locations along the cross-section, for microscopy-based measurement of the cured bondline thickness.

5.3.2 Assembly definition

5.3.2.1 Assembly concept

The assembly consists of 3 stringers bonded onto a skin, as presented in Figure 5-45 and Figure 5-46, for two purposes:

- Addressing the effect of stringer variations' interaction.
- Economy of assembling multiple stringers on one skin plate, and reducing the plate manufacturing steps.

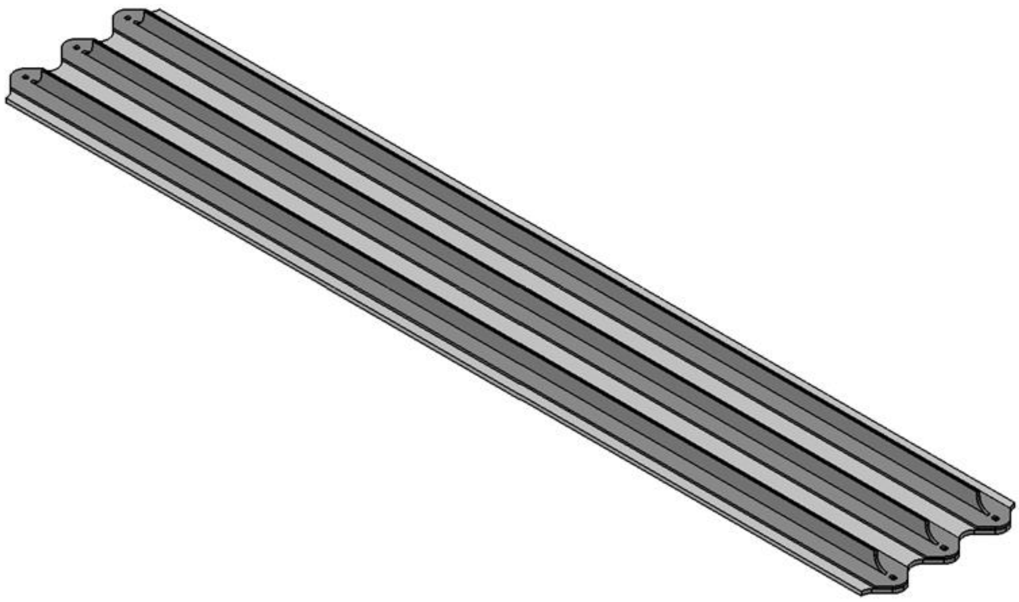

Figure 5-45. Multi-stringer panel concept: isometric view.

The assembly components were made from a 6000-series alloy ($E = 70$ GPa, $\nu = 0.33$), which offered low cost and short procurement lead time. Because the tests do not involve service loads but rather much lower ones, the validity of the results is not jeopardised by this material change.

5.3.2.2 Part geometry

Skin: uniform thickness based on representative wing cover skin. Width based on representative wing cover stringer separation.

Stringer: T section based on a baseline from a representative wing cover. Crown cap is removed and the mid web shortened, and the web widened, resulting in:

- Reduced stiffness (40% relative to baseline);
- Increased stability of the part in the bonding process;
- Highly economical manufacture, as the revised geometry can be machined from standard extrusions with a minimal number of operations.

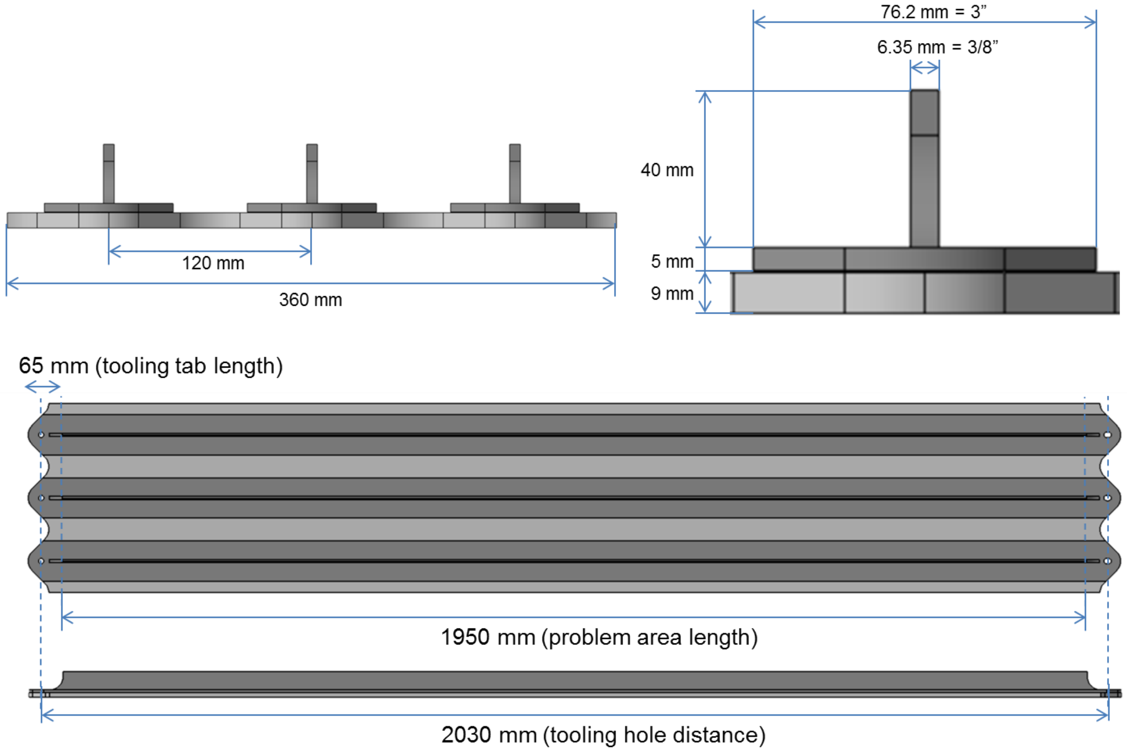

- **Figure 5-46. Multi-stringer assembly part dimensions.**

The cross-section properties of this stringer design are summarised in Table 5-9.

Table 5-9. Stringer cross-section properties for the multi-stringer assembly.

Second moment of inertia of the area of the cross-section, $I/1000$ [mm^4]	80
Area cross-section, A [mm^2]	614
Foot flange width, w [mm]	76.2
Cross-section shear factor, k_{shear}	0.414

5.3.2.3 Variation dimensioning

Variation has been incorporated through uneven fixturing and clamping of the stringer extrusions during foot machining, resulting in localised, differently-spaced hotspots of variation (Figure 5-47, Figure 5-48).

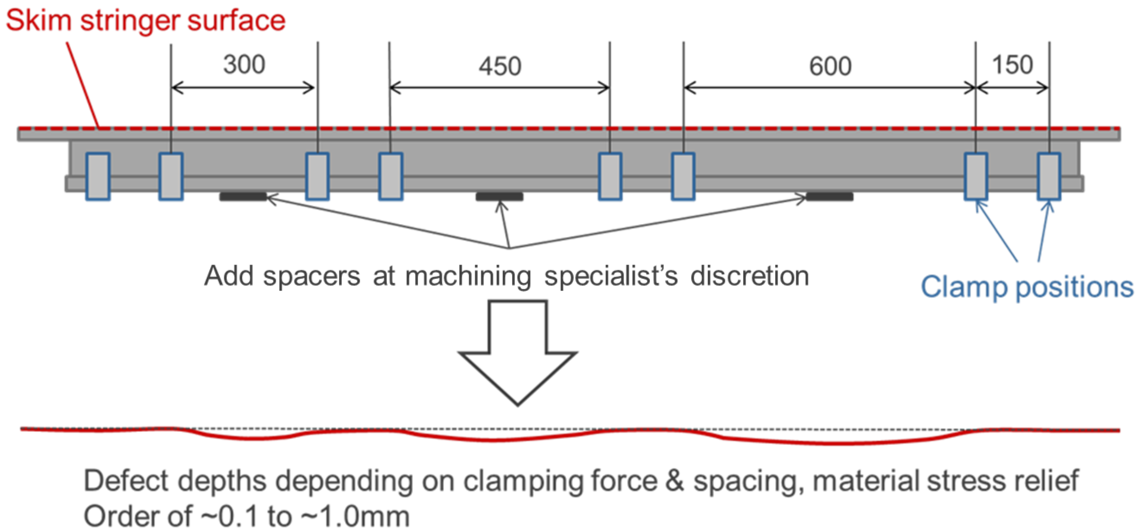

Figure 5-47. Schematic of added-variability part manufacture. Distances are in mm.

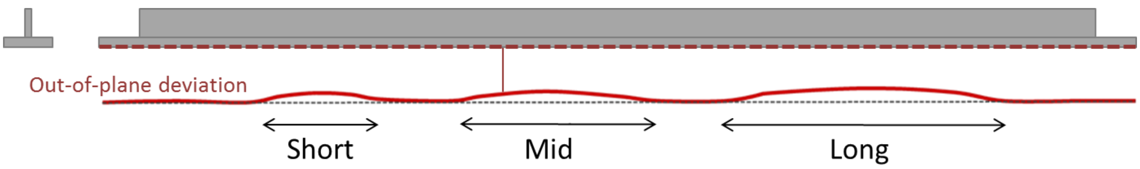

Figure 5-48. Variation ranges in the stringer profile.

Variation was added such that gaps appeared at varying pitches, representative of the typical capability of legacy inspection methods, as well as of distances between transversal stiffeners (e.g. wing ribs). Incidentally, this distribution is such that inverting the orientation of a stringer will bring the zones with lack of material neatly out of phase with a non-inverted stringer. The implications and usefulness of this phase mismatch for testing are discussed farther below.

For stringer deflection sizing, a half-stringer was simulated (minus tooling tabs) with symmetry condition in the web mid plane. The mesh was made of tetrahedral C3D10 elements, of approximate size 3mm x 3mm x 3mm. The minimum expected restriction to displacement was applied at discrete points of the foot bottom, under the mid web at the length positions corresponding to 'wave' beginning and end. These were fixed, leaving the rest of the flange free to deflect. The load consisted of 0.1MPa pressure (corresponding to the maximum 1 atmosphere achievable by vacuum bagging) applied to the surfaces of the web and foot flange top. The arrangement and a snapshot of the results are shown in Figure 5-49 and Figure 5-50, respectively. The resulting deflections are included, alongside the other stringer sizing considerations, in Table 5-10.

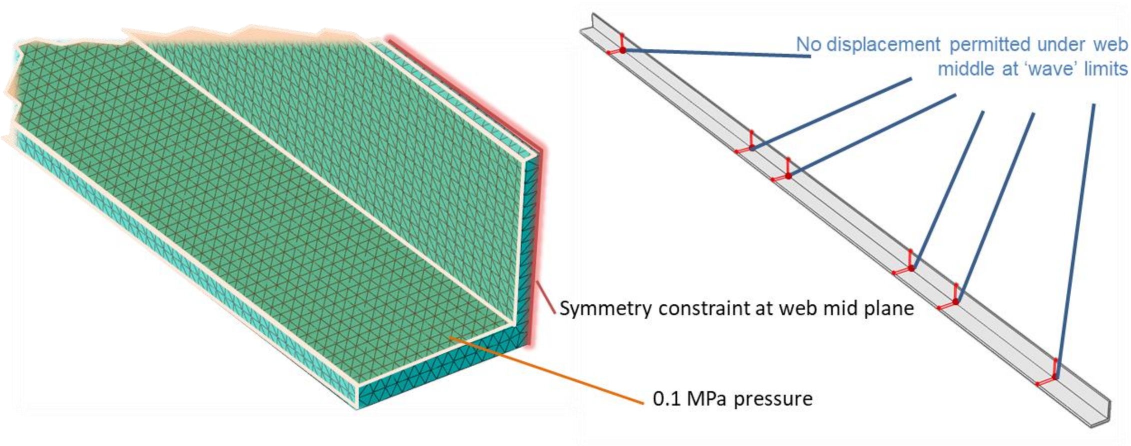

Figure 5-49. FEA model used for stringer variation sizing.

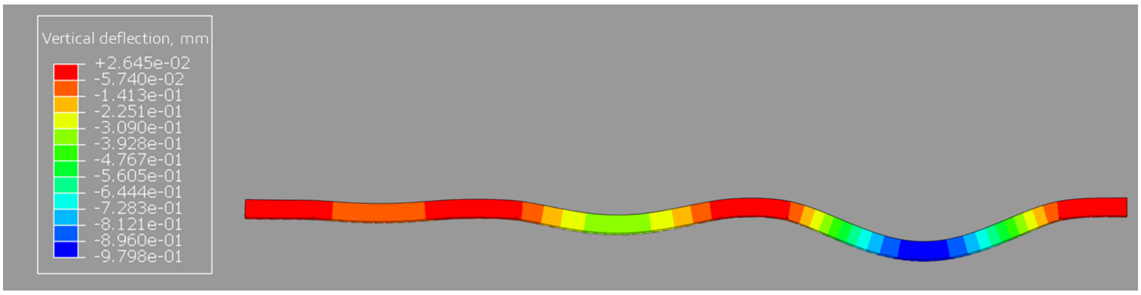

Figure 5-50. Deflection (×100) of the nominal stringer design from a starting flat condition, based on contact at the segments between local waves.

Table 5-10. Summary of initial target stringer variation wavelengths.

Variation size	**Short**	**Mid**	**Long**
Wavelength	300 mm	450 mm	600 mm
Practical significance of wavelength	Resolution of inspection during forming	Lower-bound distance between aircraft ribs	Impact of local failure of a typical forming inspection fixture
Maximum deflection of stringer mid web under 0.1 MPa	0.08 mm	0.31 mm	0.90 mm

The gap depth will be formulated in terms of inspectability and model representativity:

1. It must be observable, which in this case means gaps must be large enough that deflection can be detected by industrial-use measurement equipment.

2. It must be such that part deflection is smaller than or comparable to gap magnitude. If a gap is too small compared to the maximum deflection achievable, the gap will be fully closed by a fraction of the total load applied, and inspection will yield little useful information for the purpose of model validation.

3. It should be small enough that the hypothesis of small deformations still holds.

By changing the stringer orientation, it is possible to have adjacent stringers generate different boundary conditions for skin deflection. Generally, if for a given length position there is a skin-stringer gap at one stringer only, the skin will be effectively stiffer. If, on the other hand, all stringers are not in contact with the skin at the same length position, the skin can easily deflect and close the existing gap by single-curvature bending. Stringer orientation is subsequently noted as (-) and

(+), with (+) indicating a match between the skin and stringer holes and slots (the datum hole is always closest to the short gap)[xxxiv].

The possible stringer gap distributions (illustrated in Figure 5-51) are, thus:

- No interference — Stringer variations in phase with each other through the length;
- Slight interference — One stringer at the side having variation out of phase with the other two;
- Maximum interference — Stringer at the middle out of phase with the other two, resulting in double-curvature deflection of the skin at every gap.

These three setups cover the whole 2 × 2 × 2 (left × middle × right) test cube of stringer orientations, once symmetries are taken into account (Figure 5-52).

Maximum skin deflection for double-side-pressure bonding in the cases with interference (slight or maximum) was initially estimated with a FE model of the skin (minus tooling tab area). The mesh was made of quad shell (S4R) elements, of approximate size 20 mm × 20 mm. Similar to the approach taken for the stringer deflection, the points corresponding to the edges of each stringer flange at wave beginning and end were prevented from moving normal to the bonding surface. The location of these points changes depending on the stringer layout; shows the mesh and point distribution for the slight-interference case (one side stringer flipped). The external load consisted of 0.1MPa which, in accordance with the double-sided pressure scenario, was only applied to areas of the skin that may interface with a stringer with no contact – that is, within the area of each wave only, since the pressure would come from both sides of the skin everywhere else. The results of this deflection simulation are shown in Figure 5-54 and Figure 5-55 for the scenarios where there is some interference between stringers.

[xxxiv] A special case (0), introduced further below, had no pre-deformation added to the stringer. The machined (0) stringers still had local variation due to the clamping scheme, but much smaller than in the pre-deformed stringers.

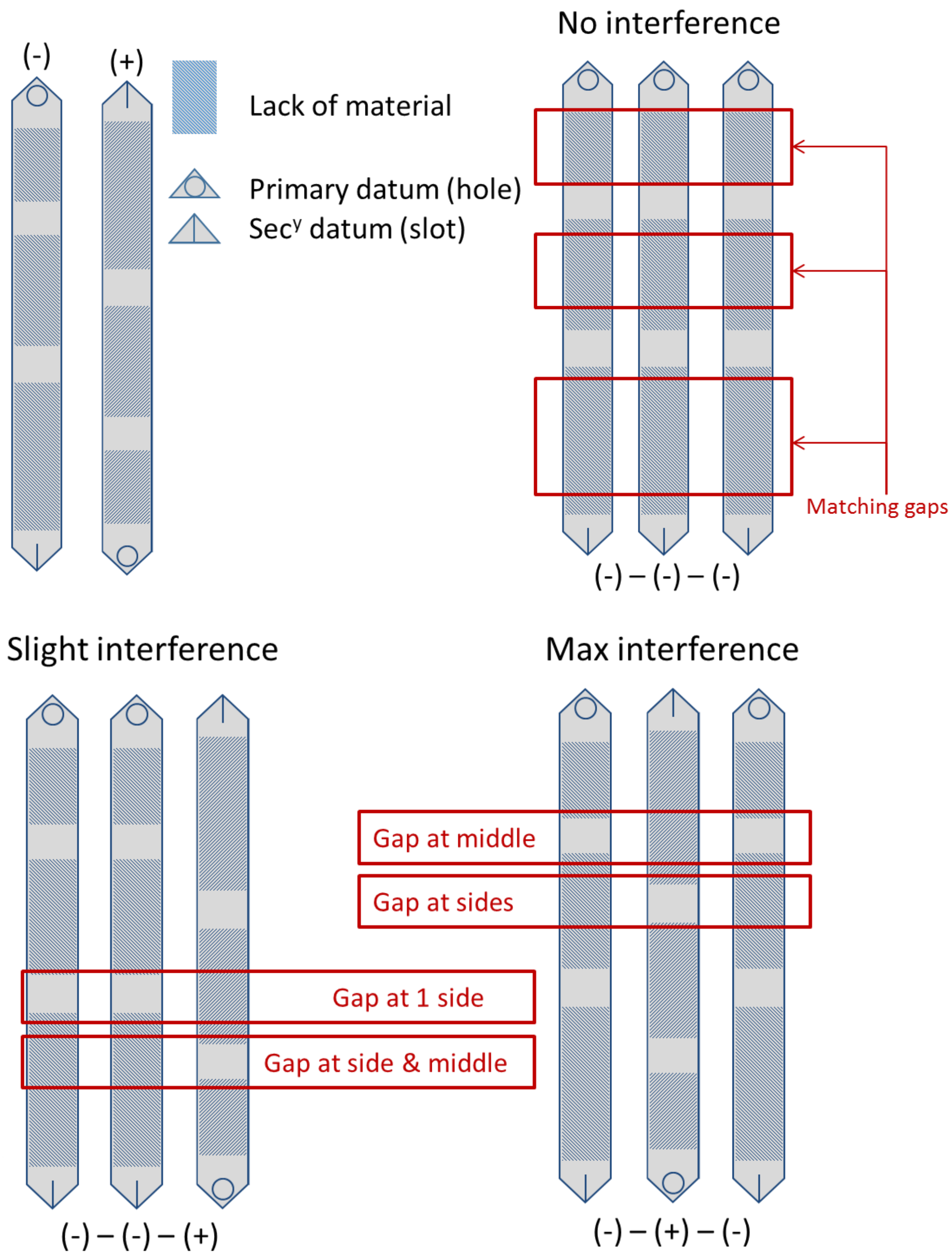

Figure 5-51. Embodiment of the different layouts and resulting feature combinations.

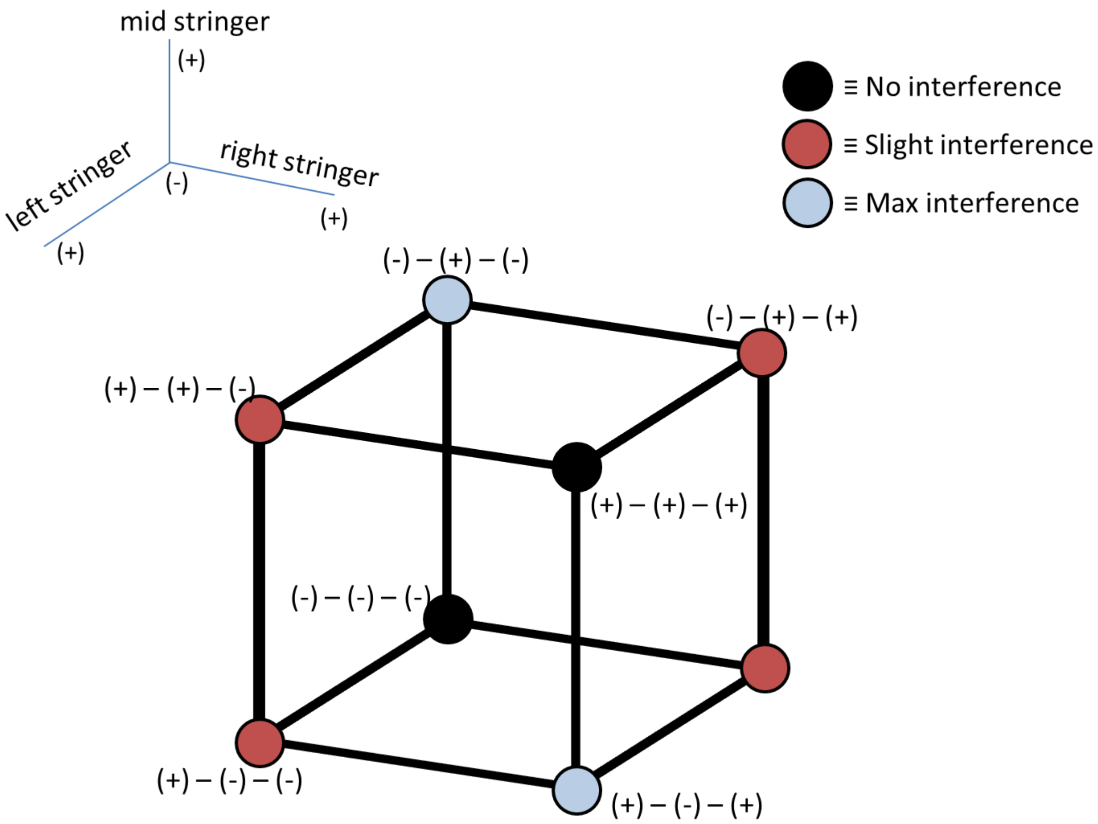

Figure 5-52. Test cube for stringer layout, based on a constant distribution of geometrical variation.

The gap depth needed, then, would result from adding the maximum expected stringer deflection and (if viable) a value larger than the either the slight-interference or maximum-interference skin deflection. This allows observing the impact of different variation scenarios that could happen in practice. (There is no point in performing tests in different conditions if the outcomes will be identical due to ‘overkill’ or overengineered external forces.)

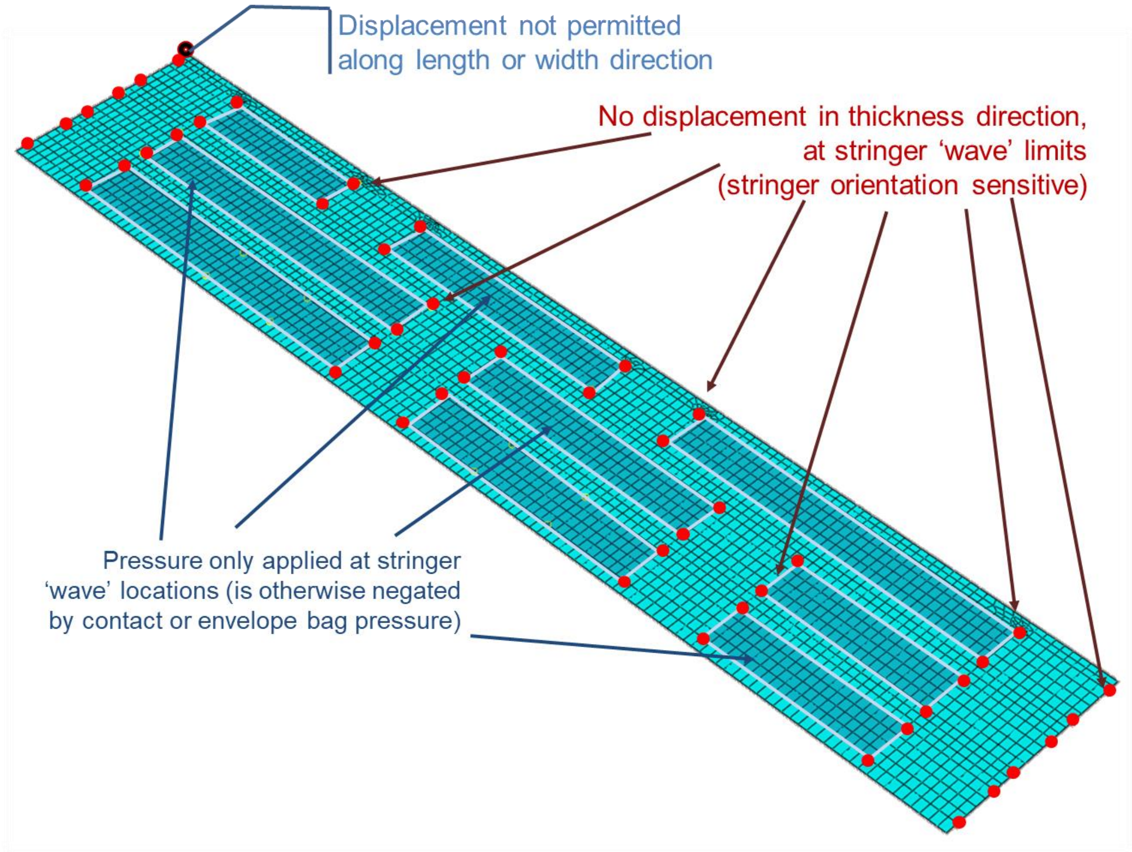

Figure 5-53. FEA model setup used for skin deflection sizing. Pictured: slight-interference scenario (-)–(-)–(+).

The built-in gaps, then, can be of five types (summarised in Table 5-11):

1. Always closed under pressure;
2. Closed under pressure in any envelope-bagged configuration (but not otherwise);
3. Closed under pressure, only when envelope bagged and not in the max-interference configuration;
4. Closed under pressure, only when envelope bagged in the no-interference configuration;
5. Never fully closed under pressure.

Clearly the most interesting are types 2 to 5, as they will show different behaviour in different configurations. In addition, type 5 is probably not necessary, as type 4 will also behave differently in all configurations. However, the representative skin displays such a large deflection, when subjected to the typical loads, that the no-interference and slight-interference setups would close gaps much larger than any representative geometric error. Thus, the desirable *and* viable options for geometrical variation are reduced to types 2 and 3.

Once the skin and stringer deflections are compounded, it becomes clear that most gaps need to fall under 2 due to the sheer scale of the combined gap closure. This is, however, not the case for the mid and long gaps, which can be dimensioned to be type 3 when placed in the middle of a skin.

This, then, gives a rationale for the target geometrical variation (or built-in assembly gaps):

- Short gap of type 2 (full closure whenever envelope bagged)
- Mid and long gap of type 3 (no full closure in one high-interference envelope-bagged scenario)

- **Table 5-11. Correspondence of gap types by closure, used to downselect geometric variations acceptable. Limited gap closure (empty cell) is preferrable. Thick solid line marks types finally downselected.**

	Achieves closure under under boundary condition... (EB ≡ envelope bagged)			
Gap type	Bagged to table	EB max interference	EB slight interference	EB no interference
1	X	X	X	X
2		**X**	**X**	**X**
3			**X**	**X**
4				X
5				

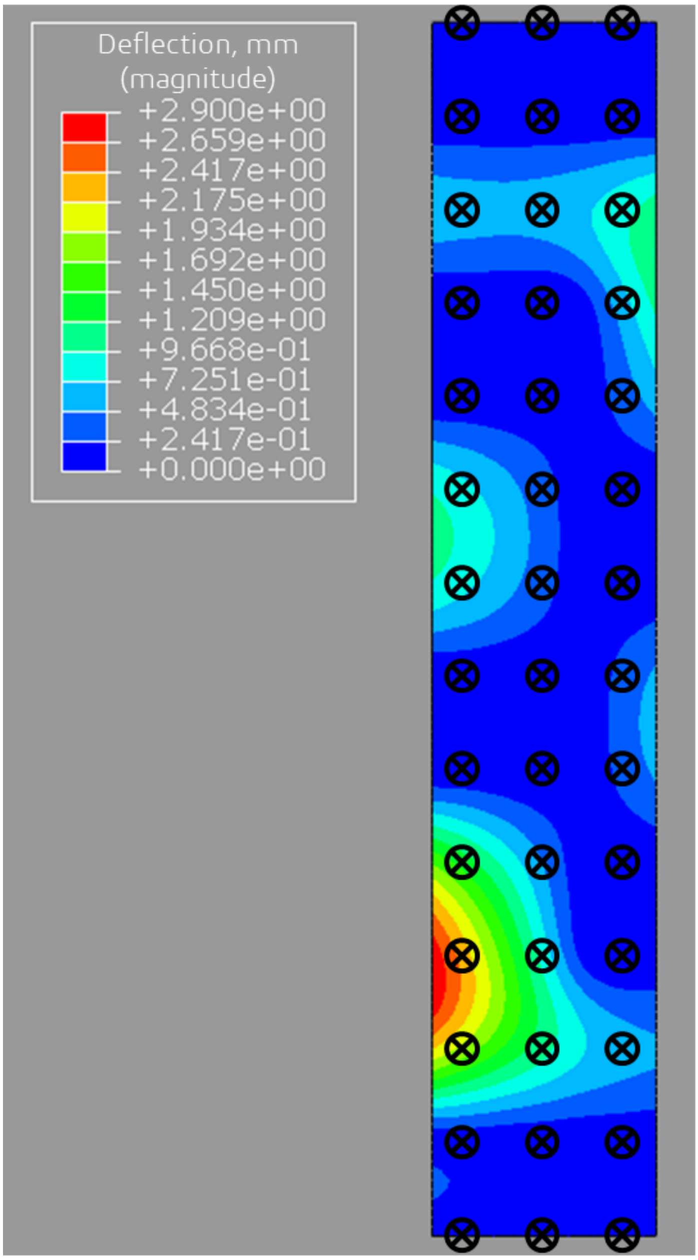

Skin deflection with slight interference (mm)		
0.00	0.00	0.00
0.01	0.01	0.01
0.55	**0.57**	**0.89**
0.02	0.03	**0.58**
0.02	0.02	**0.32**
0.76	**0.32**	0.02
0.77	**0.32**	0.01
0.01	0.01	**0.29**
0.02	0.01	**0.29**
1.29	**0.46**	0.29
2.20	**0.85**	0.04
1.78	**1.04**	**0.58**
0.02	0.01	0.01
0.00	0.01	0.00

Figure 5-54. Sample of skin deflections (FEA results) for the slight interference scenario (-)–(-)–(+). Greyed-out, not bolded readings are for non-gap areas.

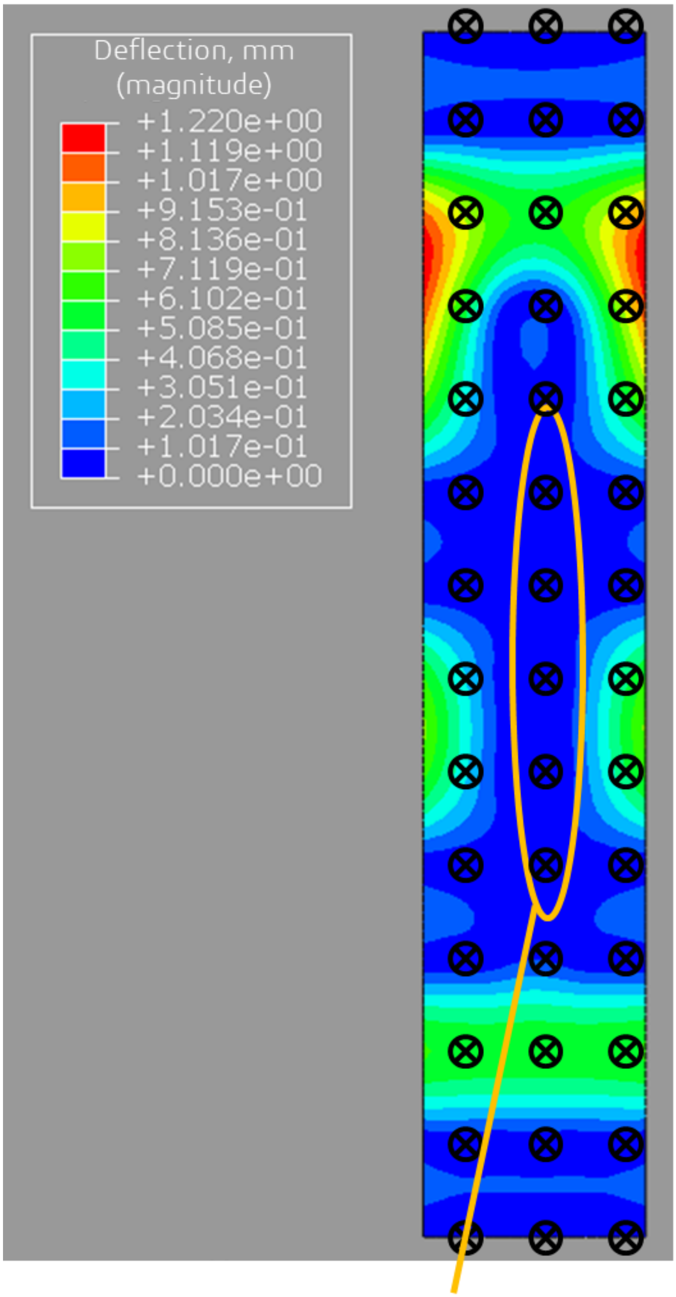

Skin deflection with maximum interference (mm)		
0.00	0.01	0.00
0.01	0.01	0.01
0.84	**0.58**	**0.84**
0.61	0.07	**0.61**
0.38	0.04	**0.38**
0.00	**0.04**	0.00
0.00	**0.03**	0.00
0.35	0.04	**0.35**
0.36	0.04	**0.36**
0.00	**0.02**	0.00
0.00	**0.10**	0.00
0.59	**0.58**	**0.59**
0.01	0.01	0.01
0.00	0.00	0.00

Figure 5-55. Sample of skin deflections (FEA results) for the max-interference scenario (-)–(+)–(-). Greyed-out, not bolded readings are for non-gap areas.

Table 5-12. Overall dimensions of controlled gaps.

Variation size	**Short**	**Mid**	**Long**
Wavelength	300 mm	450 mm	600 mm
Gap type (as per Table 5-11)	2	3	3
Target size of local gap	0.10 mm	0.50 mm	1.50 mm

In addition to the study of interference situation, it is desirable to add an extra case where only one part is substantially deformed, while the others are close to nominal. This represents a scenario where a stringer clamp would be misplaced, causing a mismatch between the stringer and skin in an otherwise accurately-machined product.

Thus, in addition to the stringers with profile variation, some parts without *intentional* variation (denoted "(0)") were manufactured and included in the assembly tests. This serves three purposes pertaining to the activities outlined above:

- To have some control parts to ascertain the extent to which profile variation is actually controlled (quantifying machining variation and inspection noise);
- To have some controlled, 'flat' parts for assembly (quantifying bond variation and inspection noise);
- To allow replication of some assembly scenarios where a single substantially deformed part is placed between much-less-deformed ones.

The preliminary set of arrangements is summarised in Table 5-13. The parts required are summarised in Table 5-14. In total, 12 stringers and 4 skins are required, corresponding to a set of 1 skin and 3 stringers per bond trial. All bonded assemblies are a repeat of a verifilm test. This provides a reference of the error (if any) that the verifilm approach may yield as compared to the conventional (and more wasteful due to the one-time use of parts) bonding approach. The extreme interference cases (maximum [+-+] and none [+++] receive more attention than the medium interference case [++-]; the one-bad-stringer case [0+0] is the one that covers most cases due to part usage considerations, but also because it provides a reference of bonding capability for a near-nominal component.

Table 5-13. Summary bonding scenarios. The letters are unique assembly identifiers.

	Bagged to table (1SP)	**Envelope bagged (2SP)**
One bad stringer (0) – (+) – (0)	[A] Verifilm [H] Bond	[E] Verifilm [L] Bond
No interference (+) – (+) – (+)	[B] Verifilm [J] Bond	[F] Verifilm
Slight interference (+) – (+) – (-)	[I] Verifilm	[D] Verifilm
Max interference (+) – (-) – (+)	[C] Verifilm	[G] Verifilm [K] Bond
Total	Verifilm x4 Bond x2	Verifilm x4 Bond x2

Table 5-14. Summary of parts manufactured for test.

	Shape & Amount	**Numbers (identifiers)**
Stringers	Nominally flat, (0) x4 Intentional variation, (+)/(-) x8	01, 02, 04, 05 03, 06, 07, 08, 09, 10, 11, 12
Skins	All same, nominally flat x4	01, 02, 03, 04

With the nominal geometries, stringer defect sizes, and number of parts required finally established, the components were manufactured and inspected, and the assembly work was carried out. This is documented in Appendix D— Multi-stringer assembly manufacture.

Table 5-15. Characteristics of each test assembly.

	Stringer arrangement				Boundary condition		Cure type
	0+0	+++	++-	+-+	1SP	2SP	
A	✔				✔		Verifilm
B		✔			✔		Verifilm
C				✔	✔		Verifilm
D			✔			✔	Verifilm
E	✔					✔	Verifilm
F		✔				✔	Verifilm
G				✔		✔	Verifilm
H	✔				✔		Bond
I			✔		✔		Verifilm
J		✔			✔		Bond
K				✔		✔	Bond
L	✔					✔	Bond
Total	4	3	2	3	6	6	

5.3.3 Model generation

The compliance matrices for the linear models were generated from shell meshes of the parts. Quad elements (S4R) of approximate size 20 mm ×30 mm were used. The boundary conditions were minimally applied to restrict six degrees of freedom without overconstraints, and coincided with the parts' tooling datum holes.

- <u>Stringers</u>: the datum hole was pinned and prevented from rotating along the length axis, while the slot was allowed to rotate freely and also slide along the length direction. Each stringer was modelled as a total of 192 nodes, with three longitudinal rows of 64 equispaced nodes each, distributed along the cross-section (one row under the web middle and the two others, $w/10$ away from the flange edge). Presented in Figure 5-56.

- Skins: like for the stringer, the datum hole was pinned and prevented from rotating along the length axis, while the slot was allowed to rotate freely and also slide along the length direction. The other non-reference holes (though still used to attach stringers) were allowed to deflect during compliance matrix generation. The nodes in the areas of the skin that interface with the stringer feet (S1, S2, S3) matched the stringer nodes. The skin was modelled with a total of 960 nodes, of which 576 interfaced with a stringer on one side and the bonding tool on the other. Presented in Figure 5-57.
- Bonding table: though initially modelled as a thicker version of the skin for sizing during the design stage, the table finally used for manufacture was more complex to allow manipulation. It consists of a fabricated steel frame with a relatively thin steel plate bonded on top and is addressed more in detail in subsection 5.3.3.1 Bonding table compliance.

The gap matrix was then defined as

$$\mathbf{U_G} = \begin{bmatrix} \mathbf{U}^{\mathbf{Strgrs-Skin}}_{\mathbf{Strgrs-Skin}} & \mathbf{U}^{\mathbf{Skin-Table}}_{\mathbf{Strgrs-Skin}} \\ \mathbf{U}^{\mathbf{Strgrs-Skin}}_{\mathbf{Skin-Table}} & \mathbf{U}^{\mathbf{Skin-Table}}_{\mathbf{Skin-Table}} \end{bmatrix} \tag{5-3}$$

with the submatrices $\mathbf{U}^{\mathbf{Strgrs-Skin}}_{\mathbf{Strgrs-Skin}}$, $\mathbf{U}^{\mathbf{Skin-Table}}_{\mathbf{Skin-Table}}$, $\mathbf{U}^{\mathbf{Skin-Table}}_{\mathbf{Strgrs-Skin}}$ capturing, respectively, the compliance of the gaps between stringer-skin contact pairs, the compliance of the gaps between skin-table contact pairs, and the change in gaps between stringer-skin contact pairs as a response to forces in skin-table contact pairs.

$$\mathbf{U}^{\mathbf{Strgrs-Skin}}_{\mathbf{Strgrs-Skin}} = \begin{bmatrix} \mathbf{U_{Strgr1}} + \mathbf{U^{S1}_{S1}} & \mathbf{U^{S2}_{S1}} & \mathbf{U^{S3}_{S1}} \\ \mathbf{U^{S1}_{S2}} & \mathbf{U_{Strgr2}} + \mathbf{U^{S2}_{S2}} & \mathbf{U^{S3}_{S2}} \\ \mathbf{U^{S1}_{S3}} & \mathbf{U^{S2}_{S3}} & \mathbf{U_{Strgr3}} + \mathbf{U^{S3}_{S3}} \end{bmatrix} \tag{5-4}$$

$$\mathbf{U}^{\mathbf{Skin-Table}}_{\mathbf{Strgrs-Skin}} = \left[\mathbf{U}^{\mathbf{Strgrs-Skin}}_{\mathbf{Skin-Table}}\right]^{\mathrm{T}} = -\mathbf{U}^{\mathbf{Skin}}_{\mathbf{S1,S2,S3}} \tag{5-5}$$

$$\mathbf{U}^{\mathbf{Skin-Table}}_{\mathbf{Skin-Table}} = \left[\mathbf{U_{Skin}} + \mathbf{U_{Table}}\right] \tag{5-6}$$

Here, S1, S2, S3 in represent the areas of skin which lay under, and interact directly with, each stringer, as presented in Figure 5-57. $\mathbf{U}_{\mathbf{S1,S2,S3}}^{\mathbf{Skin}}$ is obtained trivially from $\mathbf{U}_{\mathbf{Skin}}$, by taking the values corresponding to input nodes 1-576 and output nodes 577-960.

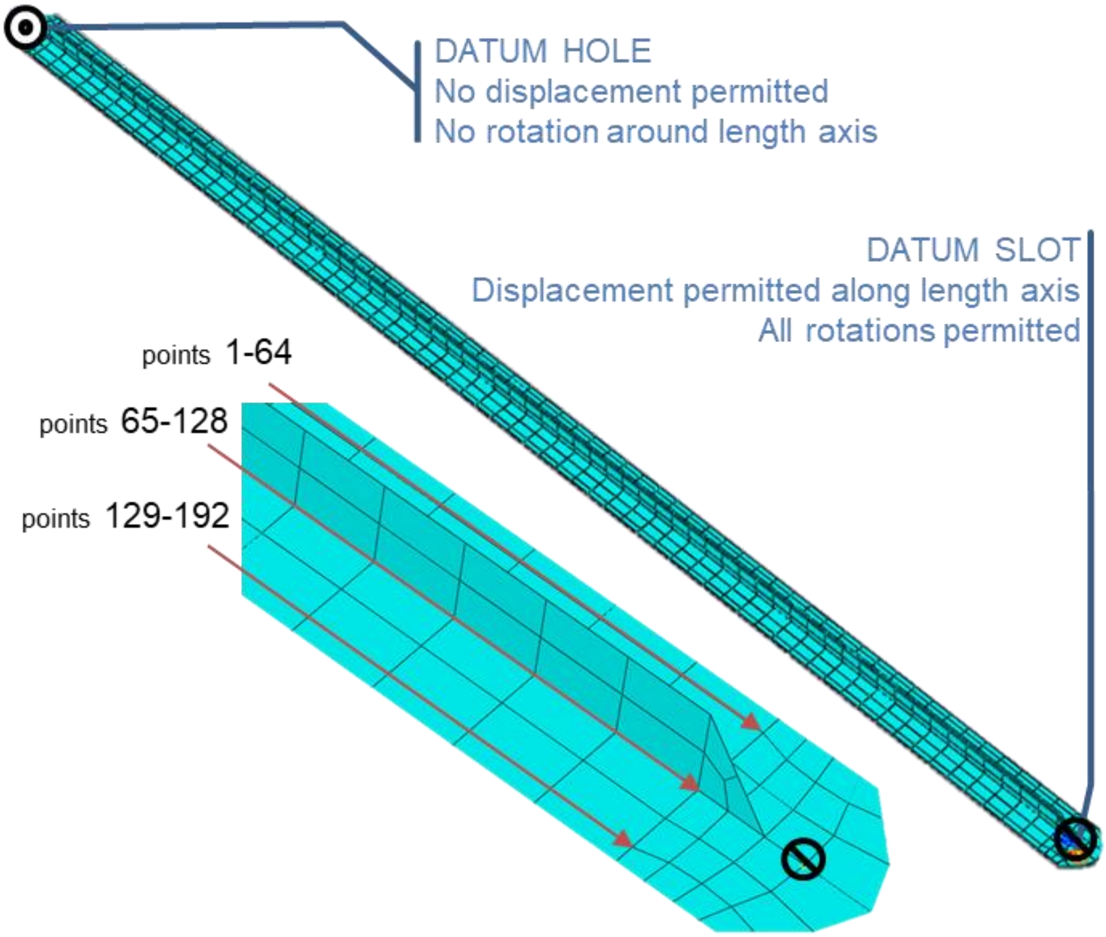

Figure 5-56. FEA mesh, boundary conditions and point location for stringer compliance matrix generation.

As the stringers have 192 nodes and the skin and table have 960 nodes, the gap consists of a total of (192×3 + 960) = 1536 nodes; consequently, the gap depth is a (1536×1) vector; $\mathbf{U_G}$ is a (1536×1536) matrix, and the part interaction forces, which is the unknown of the contact problem solved by QP, is a (1536×1) vector. An example of $\mathbf{U_G}$ is represented in Figure 5-62.

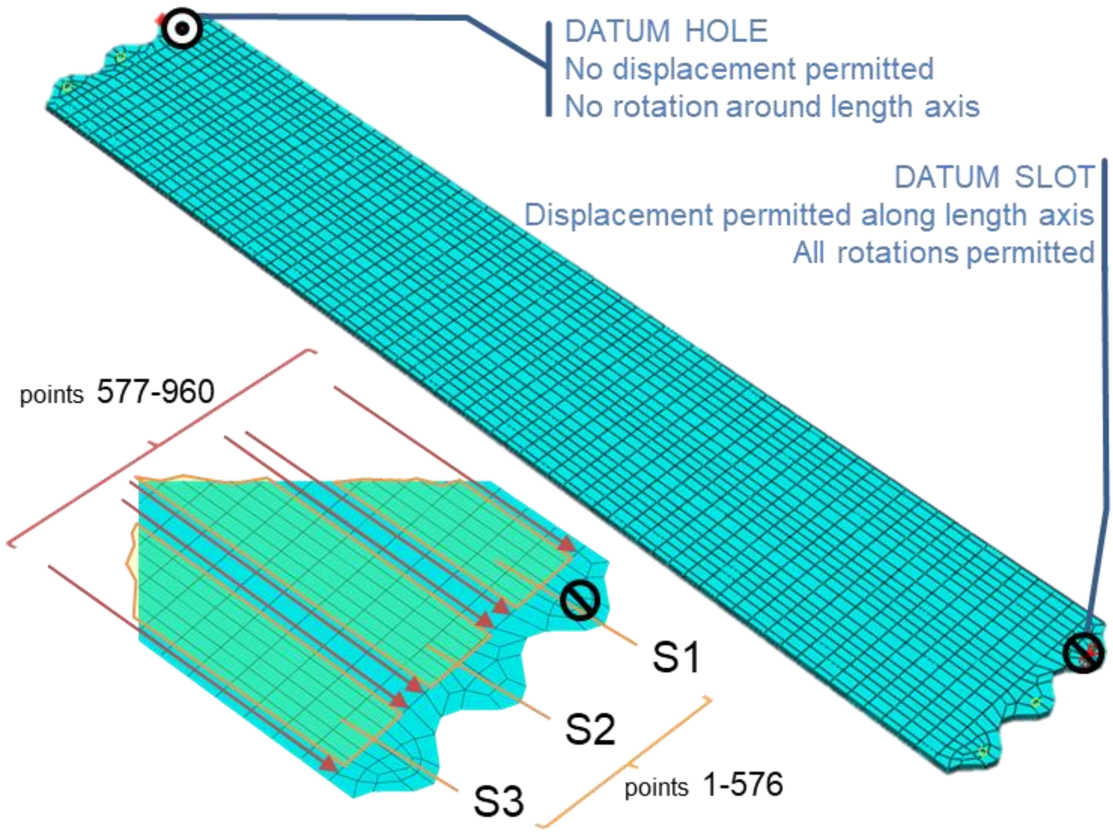

Figure 5-57. FEA mesh, boundary conditions and point location for skin compliance matrix generation. S1, S2, S3 mark the stringer interfacing areas.

5.3.3.1 Bonding table compliance

The bonding table is wide enough to fit three skins in the course of any cure cycle; thus, three different areas with different compliance matrices need to be modelled; in practice, the two lateral areas are a mirror of each other, so only two FEA models were required.

The table was meshed to match the skin nodes, with fifteen longitudinal rows of 64 equispaced nodes each, distributed along the cross-section. The mesh was allowed to be coarser and less structured away from the skin locations, since it was only the local behaviour that was of interest (Figure 5-59).

The material is a generic steel (E=200 GPa, ν=0.3); the whole table (Figure 5-58) features 3 longitudinal and 5 transversal stiffeners, each with a box-girder section (45 mm x 45 mm, 6 mm thickness) and a top plate 6 mm thick. The boundary conditions were set by modelling these stiffeners (integrated as 'stringer' engineering features) as fixed, but permitting rotation (Figure 5-60).

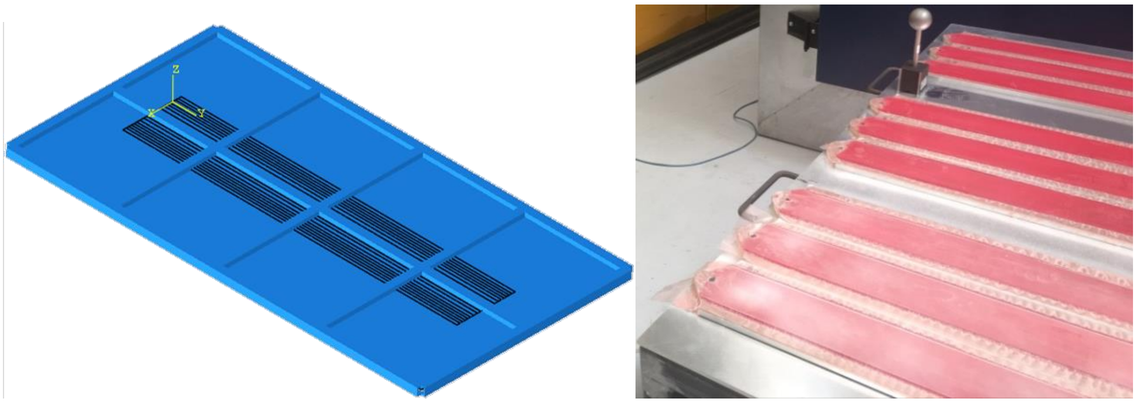

Figure 5-58. Left: Bonding table's CAE model (Abaqus) with the plate modelled as a shell and the top of the box beam frame (bonded to the plate) as 'stringer' features. The hatched area illustrates the position and area of a centered assembly. Right: position of three assemblies on top of the table.

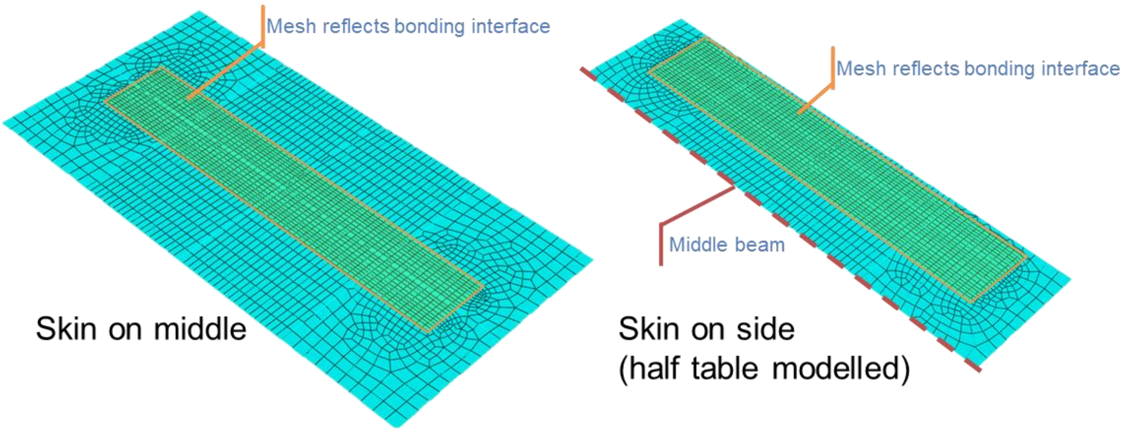

Figure 5-59. FEA meshes for the compliance matrix of the bonding table at two skin positions.

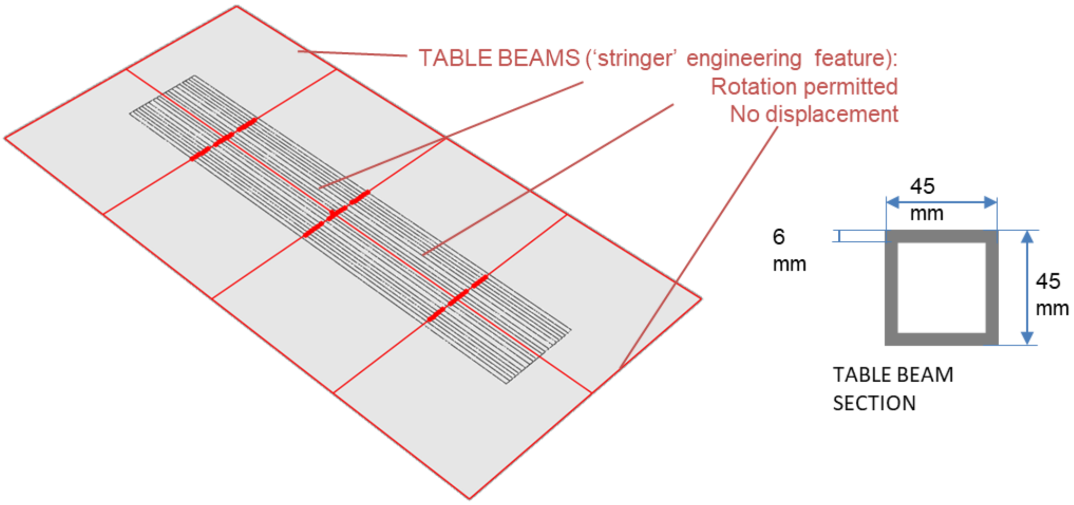

Figure 5-60. Boundary conditions and box beam section for the bonding table.

The resulting compliance matrices (Figure 5-61) reflect the effect of table stiffener distribution: the table is much stiffer right in the middle than at lateral positions. This will result in a 1SP condition that is not quite single-sided pressure, as the table does not act quite as a rigid substrate, and instead can be expected to transmit pressure to the skin (much like in a 2SP scenario, but to a lesser degree).

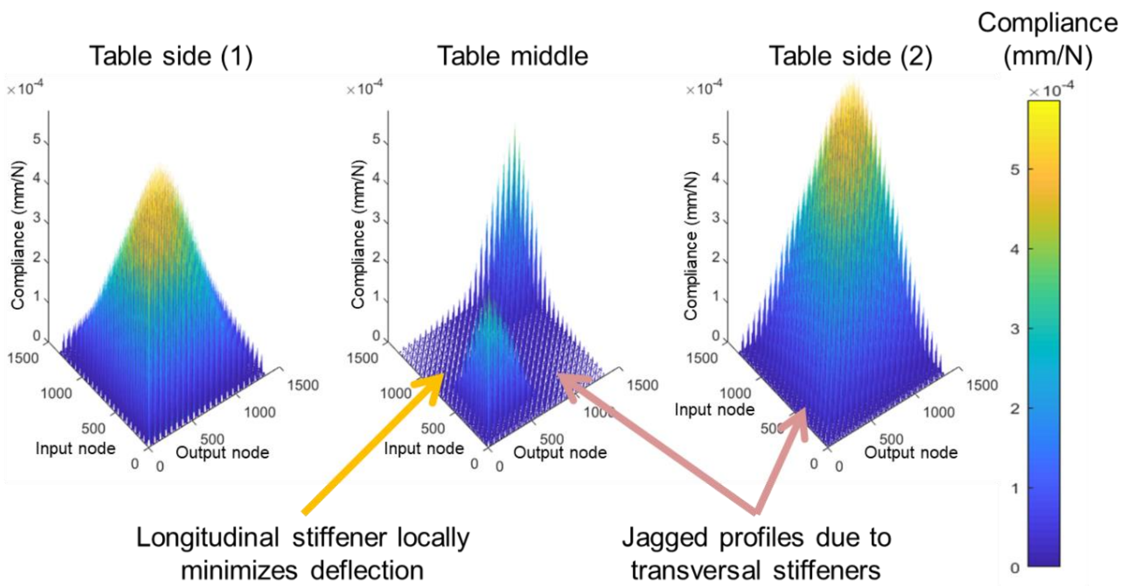

Figure 5-61. Compliance matrices of the three areas in the bonding table used. The horizontal axes indicate the node positions.

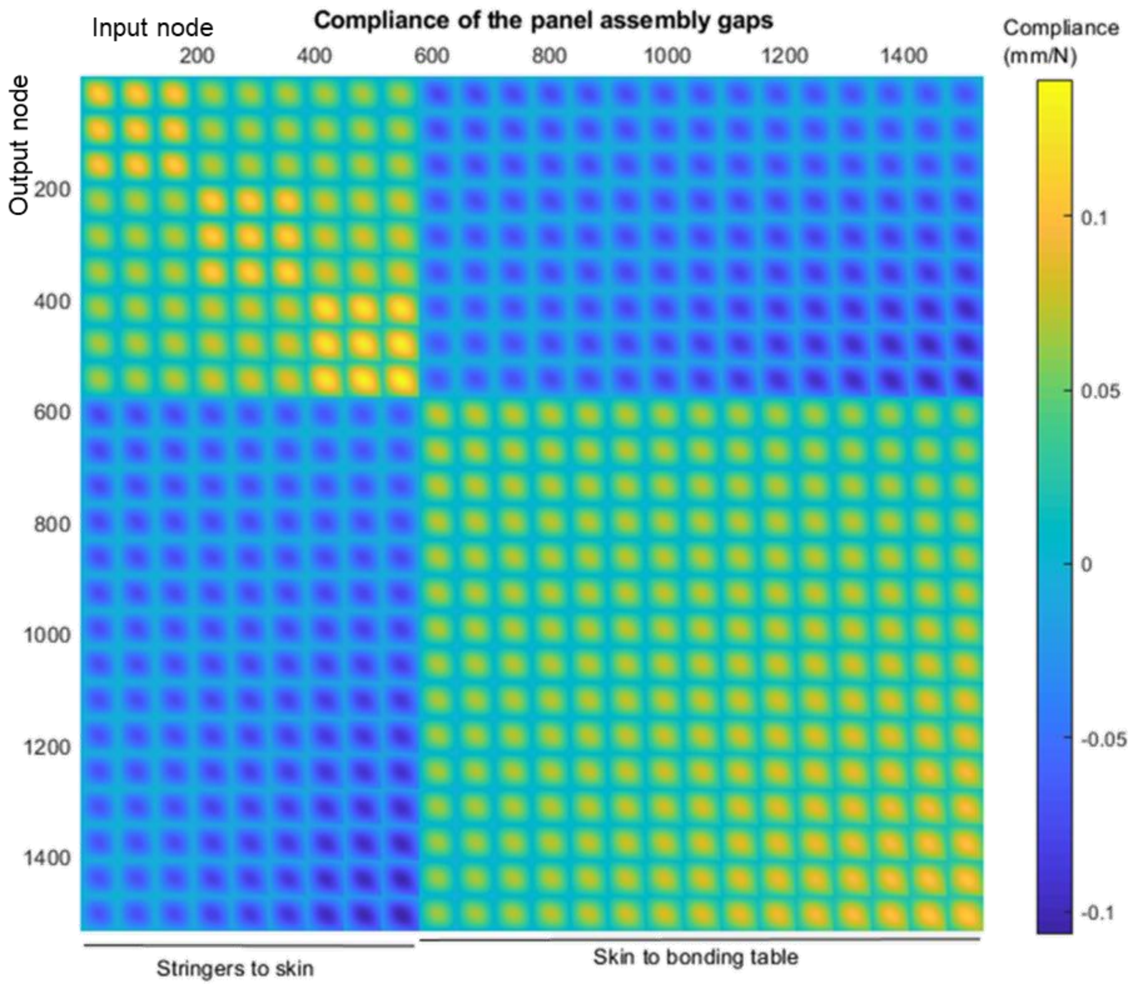

Figure 5-62. Example gap compliance for a three-stringer panel on rigid table. The compliance matrix of the table has, globally, small enough values that the visualization would be the same when using actual values for $\mathbf{U}_{\mathbf{Table}}$.

5.3.3.2 Compliance matrix corrected for variation

Because the material missing from the stringer foot was not a negligible amount (roughly up to 1.5 mm from a 5 mm initial value), there was a concern that the stiffness matrix of a nominal stringer may fail to adequately capture the actual stiffness of the deformed stringers. To this effect, an updated stringer compliance matrix was generated by mapping a deformed stringer's foot thickness to the mesh. The increase in compliance was found to be generally at or below 10% (humps at height ~0.1 as seen in Figure 5-63), save for peaks near the stringer ends; this approximately matches the decrease in I from removing 1.5 mm from the foot. Simulations were carried out with and without the updated matrix, showing the expected loss of accuracy one may expect from worst case profile variations[xxxv].

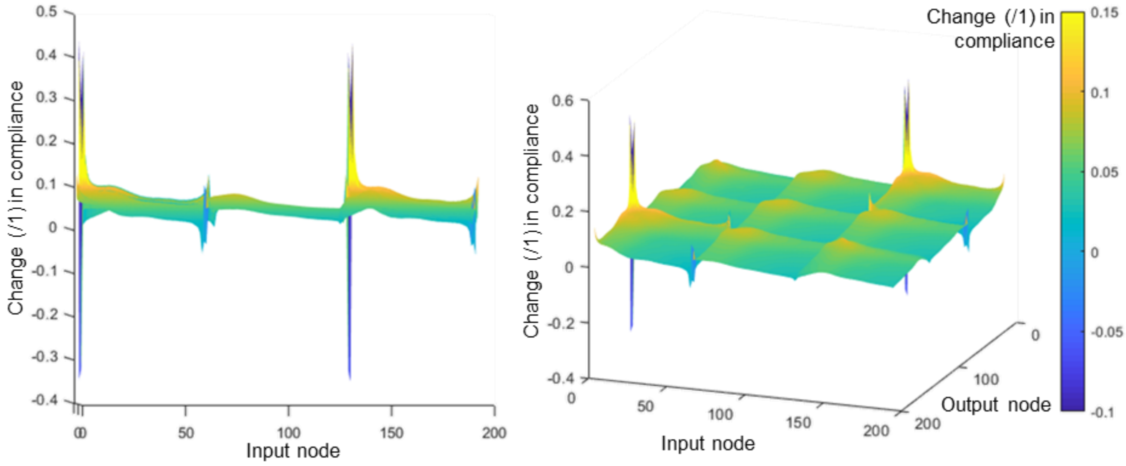

Figure 5-63. Relative increase in compliance from the nominal to the warped (selectively machined foot) stringer. The colour scale saturates below -0.1 and above 0.15 to enable visualizing the majority of the data.

5.3.4 Simulation results

Based on average results for the vacuum pressure achieved as recorded by the oven used in curing, a uniform pressure value ΔP of 0.087 MPa was used (in the one- and two-side pressure configurations) for the assembly simulations. These have been performed using uniformly the compliance matrix corresponding to nominal dimensions (Figure 5-64), as well as the one accounting for loss of material (Figure 5-65).

Although the results are qualitatively similar between the nominal-$\mathbf{U}$ and deformed-$\mathbf{U}$ simulations, there are noticeable quantitative differences with extra deflection in the deformed-$\mathbf{U}$ simulations, up to 50 μm in magnitude. This is especially noticeable in the foot flanges in the larger gap area. Note that, although the difference in compliance was up to 10%, the final deflection of the stringer with the deformed-$\mathbf{U}$ consideration was not 10% larger. This is because the skin

[xxxv] This is very much a worst case scenario and hardly relevant for production purposes of this kind of geometry, given that sub-mm machining tolerances are the norm. It would, however, be plausible to encounter a combination of manufacturing deviations which amount to a similar fluctuation in mechanical behaviour. Some prior work referenced (Stricher, 2013) addresses some of the issues pertaining to accounting for part variation in assembly mechanics modelling.

(and table) also contribute to gap closure, and because the unilateral contact condition adds a self-limiting aspect to part deflection.

For all following discussion, the simulation results used are from the second case (modified stringer compliance matrix). The results are identified by the assembly letter as presented in Table 5-13 and With the nominal geometries, stringer defect sizes, and number of parts required finally established, the components were manufactured and inspected, and the assembly work was carried out. This is documented in Appendix D— Multi-stringer assembly manufacture.

Table 5-15.

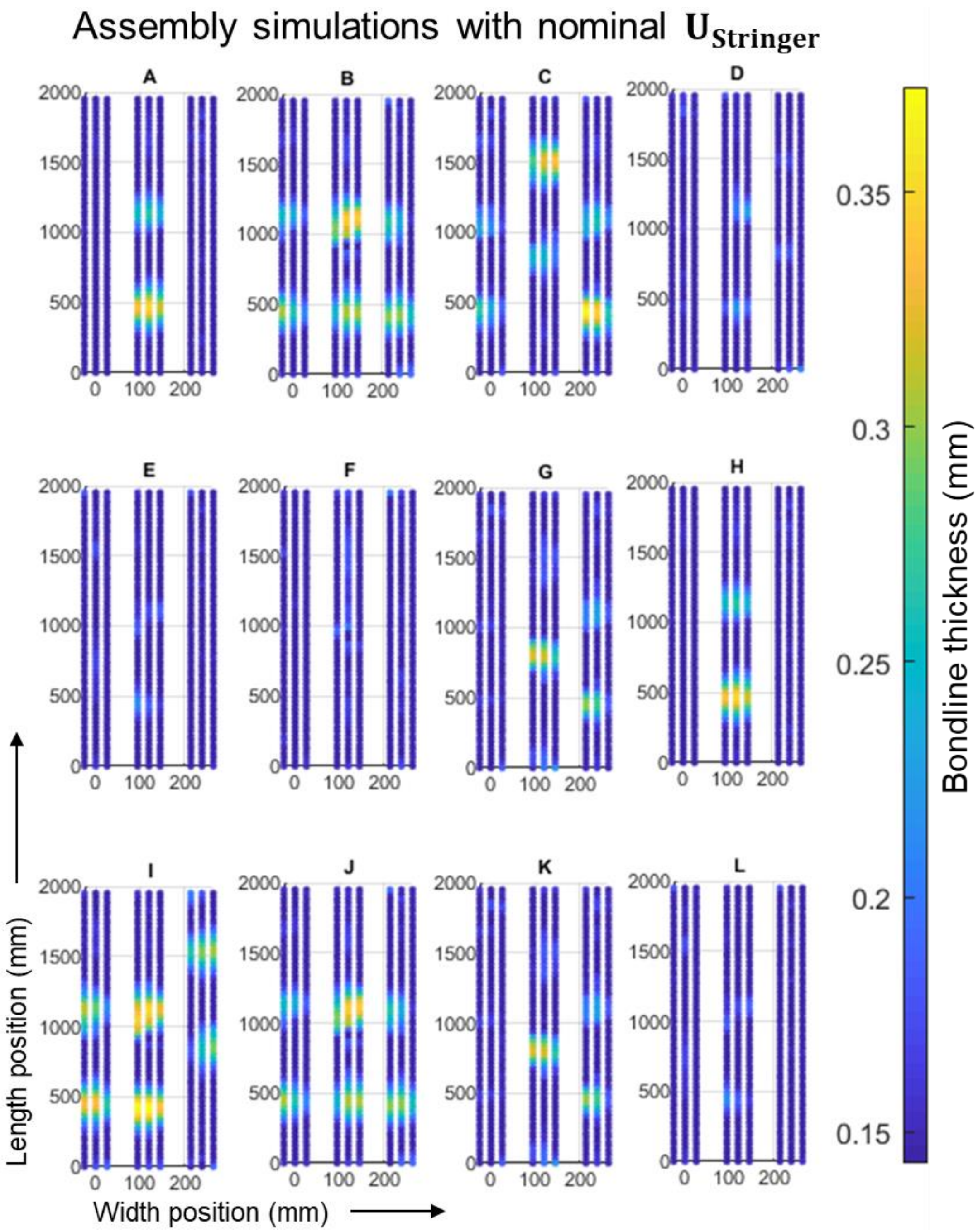

Figure 5-64. Final expected bondline thickness for all assemblies (indicated with their letter identifier A-L), with nominal compliance matrix for all stringers.

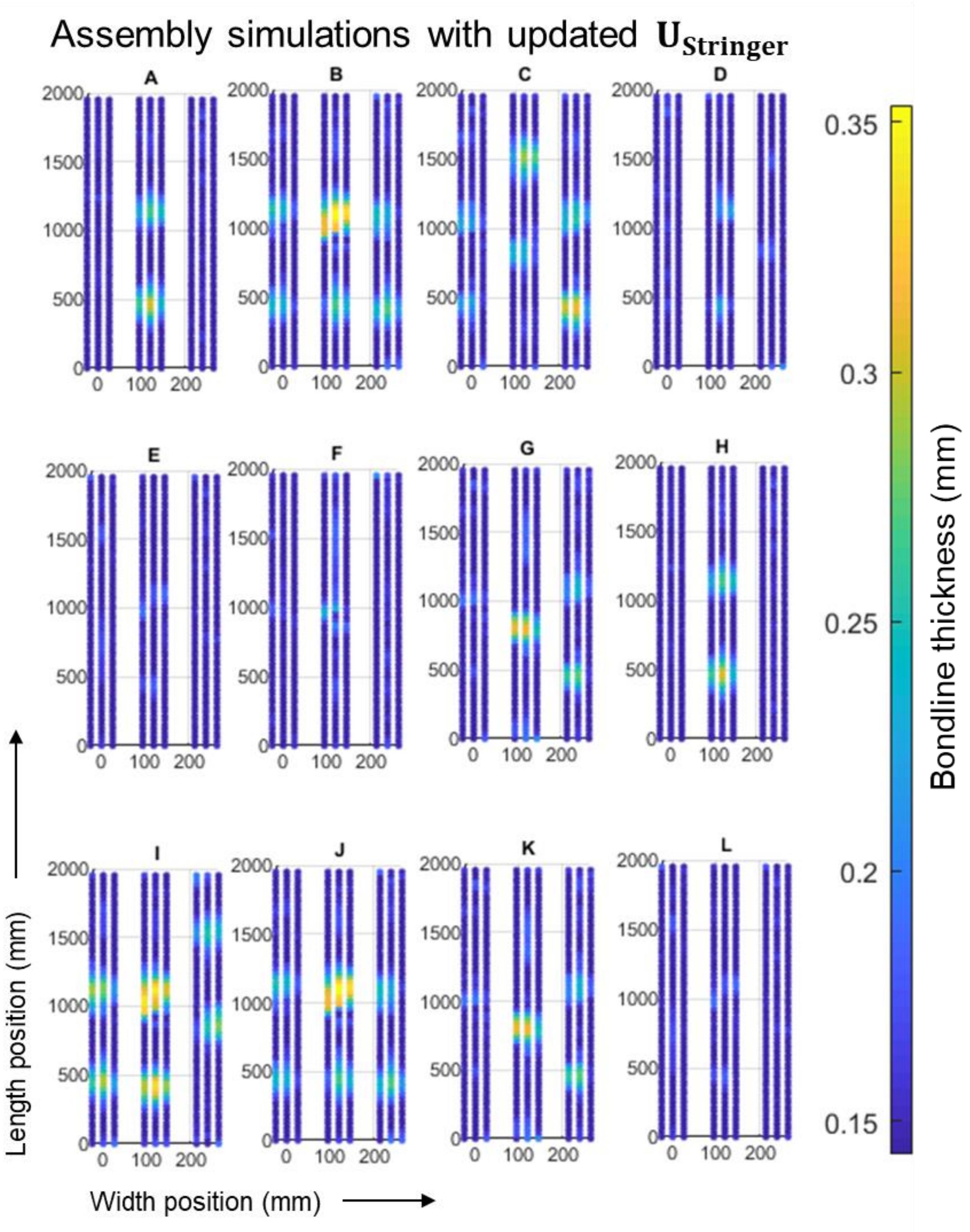

Figure 5-65. Final expected bondline thickness for all assemblies (indicated with their letter identifier A-L), where the stringers with machined-in profile variation have an updated compliance matrix.

5.3.5 Data fit and results comparison

In each case, the measurement results were used to fit a surface using a thin plate spline (no smoothing) with a centre at each measured point. The values at the simulated nodes were calculated by interpolation on these surfaces. In order to account for model inadequacy (chiefly from the modelling limitations enunciated in Section 6.2.1 Violation of assumptions and general limitations, in addition to straight up comparison of the simulation and measured values, a Bayesian Markov Chain Monte Carlo correlation was performed, and is presented at the end of this subsection (5.3.5.3.2 Regression accounting for categorical variables). (The justification and procedure for this are laid out in Appendix H — Model calibration). Such correlation showed that deviations present were consistent with the adhesive-modelling limitations highlighted, and that spread was satisfactorily small once sources of uncertainty were numerically accounted for.

5.3.5.1 Bondlines (verifilm — contact measurements)

The results extracted from the verifilm trials were qualitatively in good agreement with the simulations (i.e. the thickest-bondline areas were where expected, and reacted to boundary conditions as expected though with varying proportionality). The comparison of the simulations with the final bonded geometries yields very similar results as for verifilm. The results are not identical, which can be at least partially attributed to the difference in measurement technique. Nevertheless, the same conclusions apply: modelling the adhesive flow as quasisteady and confined to each cross-section results in both local and global errors.

An issue found was that the final gap variation under each stringer was higher than expected; this misprediction is consistent with the limitations of the quasi-steady 2D adhesive flow assumption (as the not-fully flattened stringer areas were actually subject to hydrostatic pressure from the adhesive, rather than zero pressure as presumed by the dry contact problem). Equally consistent with adhesive modelling limitations is the fact that the minimum observed adhesive thickness exhibited variation across samples, with the nominally flat stringers (serial numbers 01, 02, 04, 05) ostensibly yielding higher minimum thicknesses. This is related to how the adhesive was able to flow in multiple directions (not just within the cord cross-section) under the purposefully warped stringers, thus becoming much thinner at areas of concentrated pressure.

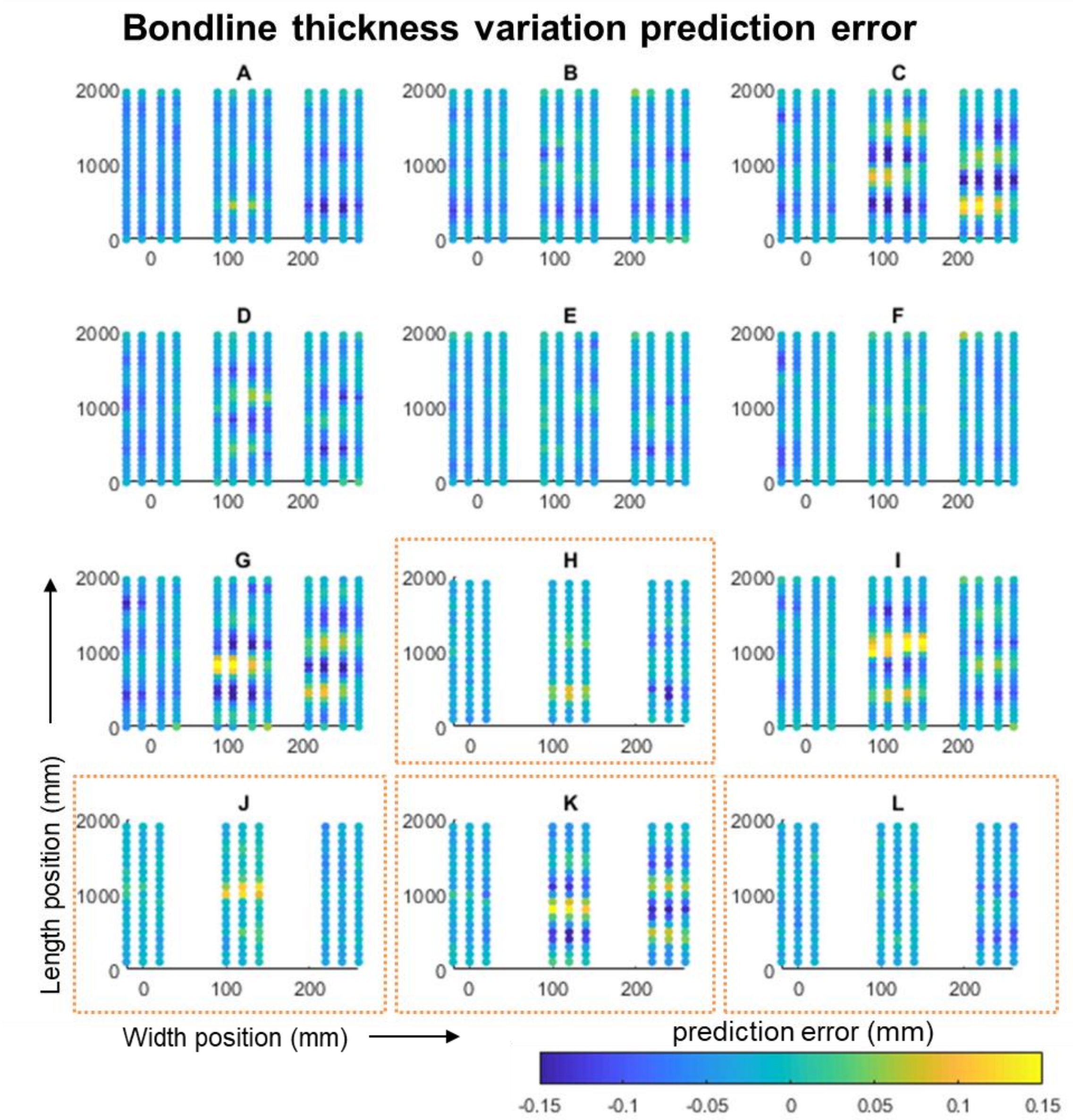

Figure 5-66. Heatmap of prediction error for the bondline variation. Plots enclosed in rectangles correspond to the bonded assemblies (H, J, K, L), the rest to verifilm.

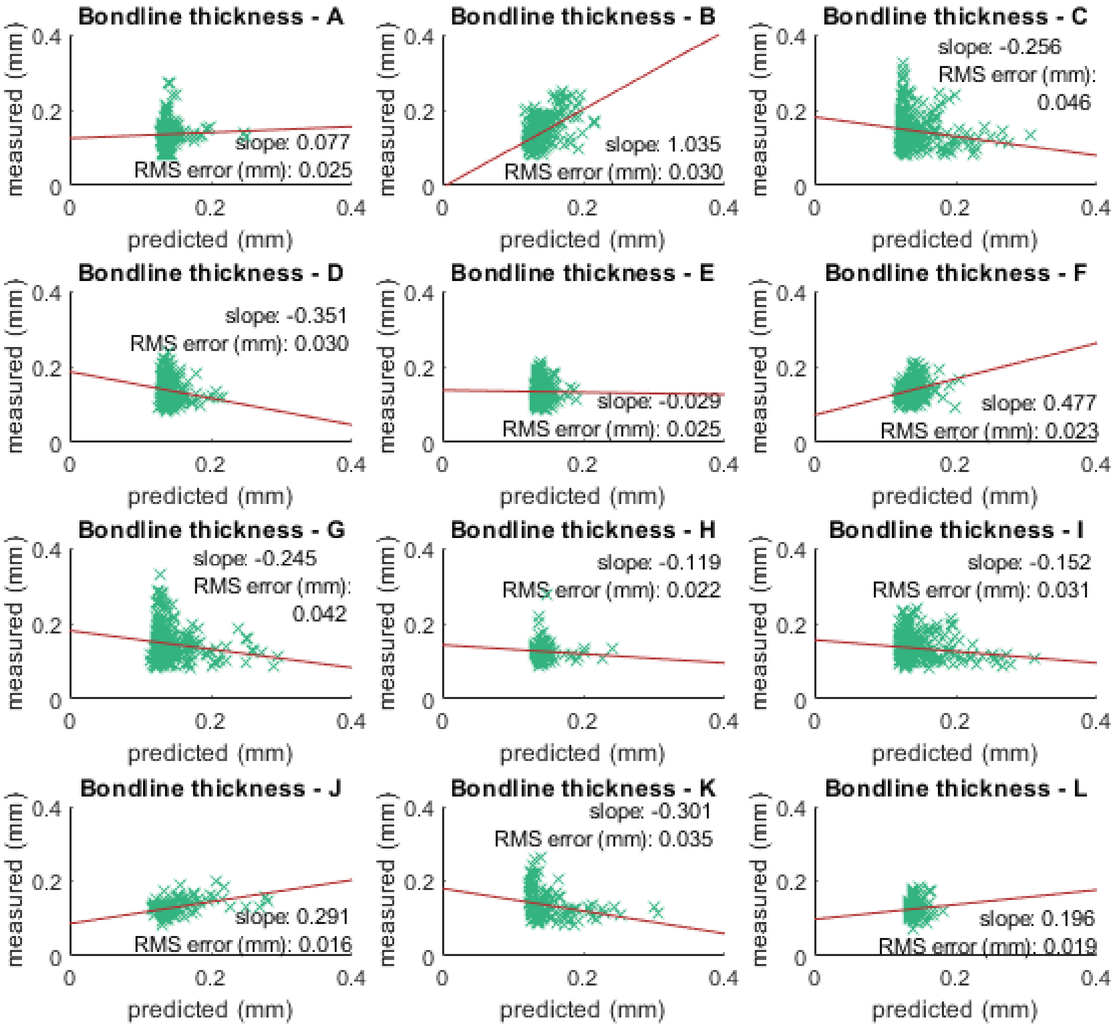

Figure 5-67. Bondline thickness: simulation prediction against values derived from measurement. The red line is a least-squares linear regression.

An important fact to be borne in mind when examining these results is that the final range of thicknesses is rather small; this makes any discrepancy between the measurement and the simulation look disproportionally large. In reality, these differences (even when unexplained by known model limitations) are fairly small compared to the initial fit-up gaps.

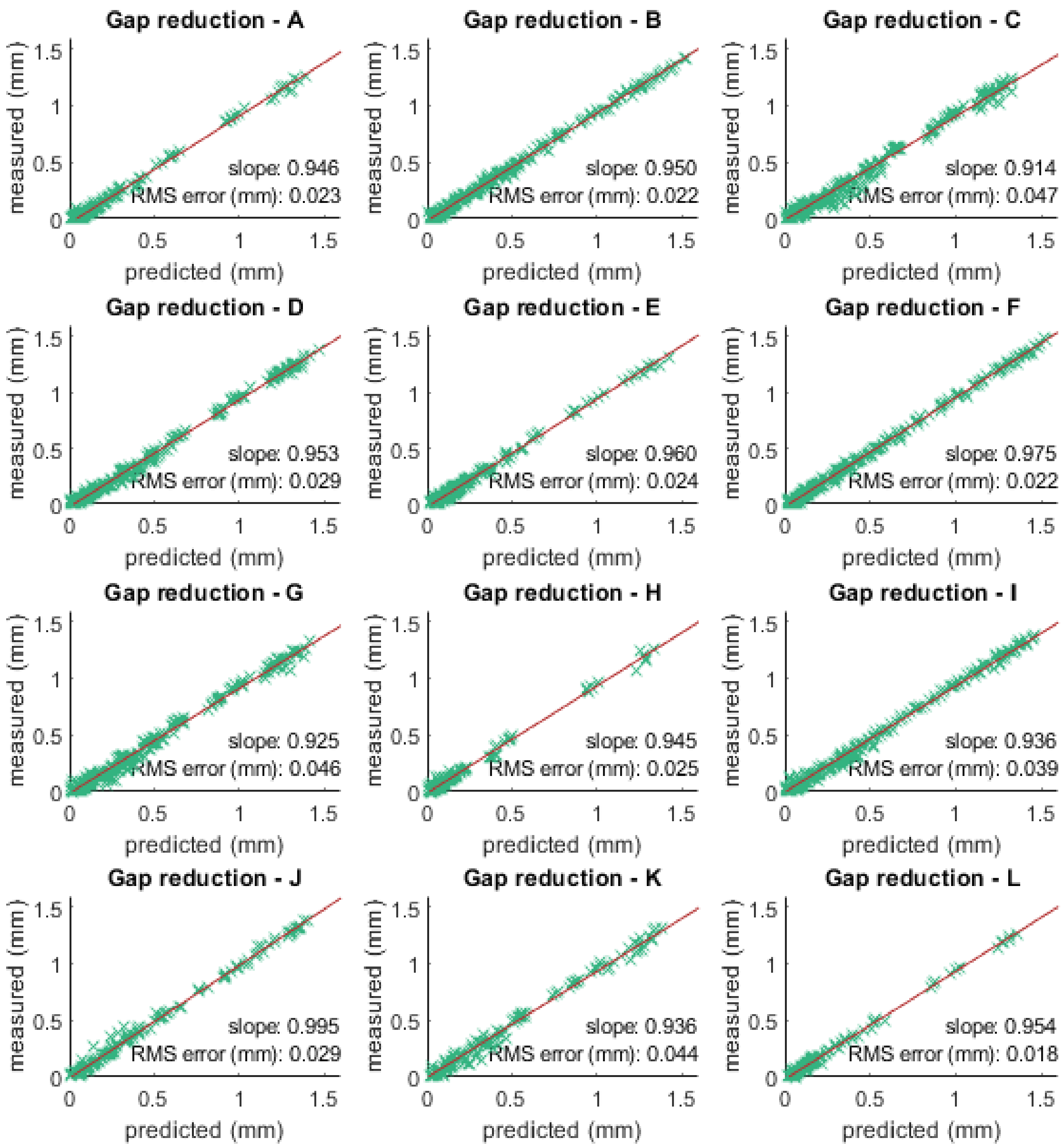

Figure 5-68. Gap reduction: simulation prediction against values derived from measurement. The red line is a least-squares linear regression.

A potentially better way of presenting the results, then, is to look at *how well the simulation predicted gap closure*. A side-by-side example of both comparisons is presented in Figure 5-69: although the magnitude of the scatter is similar, the gap reduction shows much better correlation than the bondline thickness, since the variation takes place over a longer range.

This approach would, however, potentially be too flattering against very large gaps which are closed by low pressures[xxxvi]. For this reason, it will only be presented as a supplementary analysis in a later subsection (5.3.5.3.1 Maximum gap height).

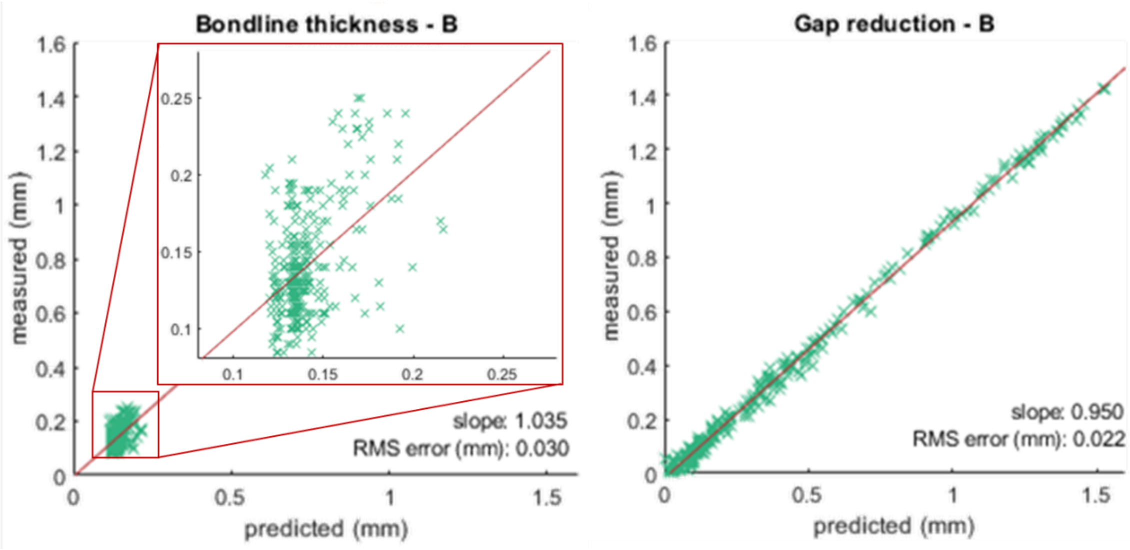

Figure 5-69. Linear regression of simulations against measurements for the same assembly, in terms of final gap (left) and gap reduction (right).

5.3.5.2 Difference between contact and optical measurements

As outlined in the test design section, four of the assembly arrangements were carried out both in the verifilm and actual bonding condition. One would have expected the results in both conditions to be closely aligned in each arrangement, especially given how verifilm is a commonplace geometric verification technique for bonded structures.

However, some differences are observable. Most prominently, thickness measurements from micrographs occasionally display local, spurious dips or rises — ostensibly due to plasticised metal being smudged over or back from the adhesive. Bondline thicknesses measured from micrographs were also, on average, less than the values resulting from the verifilm phase. Prominently, the morphology of the bondline peaks changes: sharp local increases in the verifilm

[xxxvi] Recall that generally there is little merit in simply predicting that two parts will be pushed together, as was indicated during test assembly design. It is predicting residual gaps that can be hard (and valuable).

thickness (measured by micrometre) are replaced by shallower, often more rounded maxima in the micrographs of bonded sections. Three hypotheses are advanced to explain this pervasive discrepancy:

(a) There is an unremoved metal burr from sectioning that is not only generally repeatable, but also (positively) correlates in size with bond thickness, thus deflating the peak height measured from bonded sections;

(b) Despite the care placed in manual measurement of the verifilm strips, creases of the release film found at the thickest areas (propitiated by the formation of voids, as visible in Figure 5-70) inflated the micrometre measurements.

(c) The verifilm/bonding process suffers from a degree of inherent geometric variability —from minute changes in part pose and layup, or due to thermal cycling of the parts and tooling — which only becomes apparent upon close, thorough, precise inspection; the effect would be small enough to raise no industrial concerns until the limits of the process were tested in this work.

In this particular case, the verifilm results always overestimated the peak thickness. With the main worry being *excessive* bondline thicknesses, the test would still have served its purpose of flagging up “bad” assemblies prior to permanent bonding — albeit potentially with some false positives.

Figure 5-70. Top view of a cured adhesive strip in a low adhesive pressure area. The image was sharpened to highlight the voids and wrinkles in the release film.

5.3.5.3 Overall simulation–measurement comparison

5.3.5.3.1 Maximum gap height

Given the core industrial concern around excessive bondline thickness and/or excessive bondline variation, a key question for the assembly simulation to answer is: how thick does the bondline get over a given distance? As long as this is answered in a satisfactorily accurate manner, a good understanding of the assembly quality (in a geometric sense) can be formed. From this point of view, the exact shape and thickness distribution is not critical.

With this in mind, an analysis of the reduction in height of each profile wave has been conducted. The waves are the long-, mid-, and short-range variations introduced in the test design and manufacture chapters. Within each stringer and wave, the gap height (pre- and post-assembly) was calculated as

$$X_{Gwave} = \left[\max\left(\overrightarrow{X_G^{final}}\right) - \min\left(\overrightarrow{X_G^{final}}\right)\right], \quad \text{to } L \in (L_{lwr,wave}, L_{upr,wave}) \tag{5-7}$$

where $L_{lwr,wave}$ and $L_{upr,wave}$ are (respectively) the lower and upper length position boundaries of each wave, as given by Table 5-16 and Figure 5-71. Note that the wave lengths considered for maximum height calculations are 150 mm wider than the nominals set for manufacture (as marked in Figure 5-71 for reference); this is because the initial nominal values referred to *inter-clamp distance* for manufacturing purposes.

Note that the definition in (5-7) will effectively discount whatever minimum bondline thickness has been achieved, and thus this gap height metric ignores the result of quasisteady 2-D adhesive flow. It still will be affected by adhesive model inaccuracies related to adhesive pressure redistribution.

Table 5-16. Limits for each stringer profile wave.

Wave	$L_{lwr,wave}$ **(mm)**	$L_{upr,wave}$ **(mm)**	**Total length (mm)**
Long	75	825	750
Mid	825	1425	600
Short	1425	1875	450

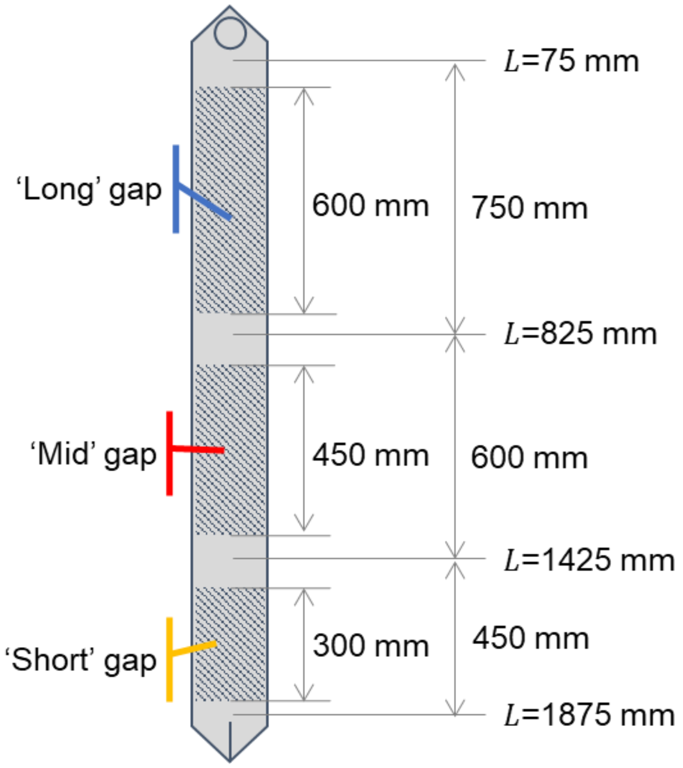

Figure 5-71. Stringer profile gap locations and lengths (mm). "O" and "I" indicate primary and secondary datums respectively. Shaded areas mark each segment deformed during manufacture, while the wider distances correspond to the lengths counted as each 'gap' for gap height calculation purposes.

Figure 5-72 and Figure 5-73 give a view of the sheer scale of the deflections achieved relative to the initial gaps. The general behaviour is the same between the simulations and physical tests. However, the residual (sub)gap heights achieved do not quite match the simulated values; this is patent in Figure 5-74, where deflection prediction errors are shown (with positive errors meaning a higher-than-predicted gap). Although the prediction error is kept mostly below 0.100 mm (which is a typical manual gauge resolution), this nevertheless results in large *relative* errors. Particularly large relative errors are encountered under nominally flat stringers (left/right in assemblies A, E, H, L) which exhibited fairly shallow profile variation to begin with; and in the ‘Short’ gaps (which are always the shallowest in a stringer).

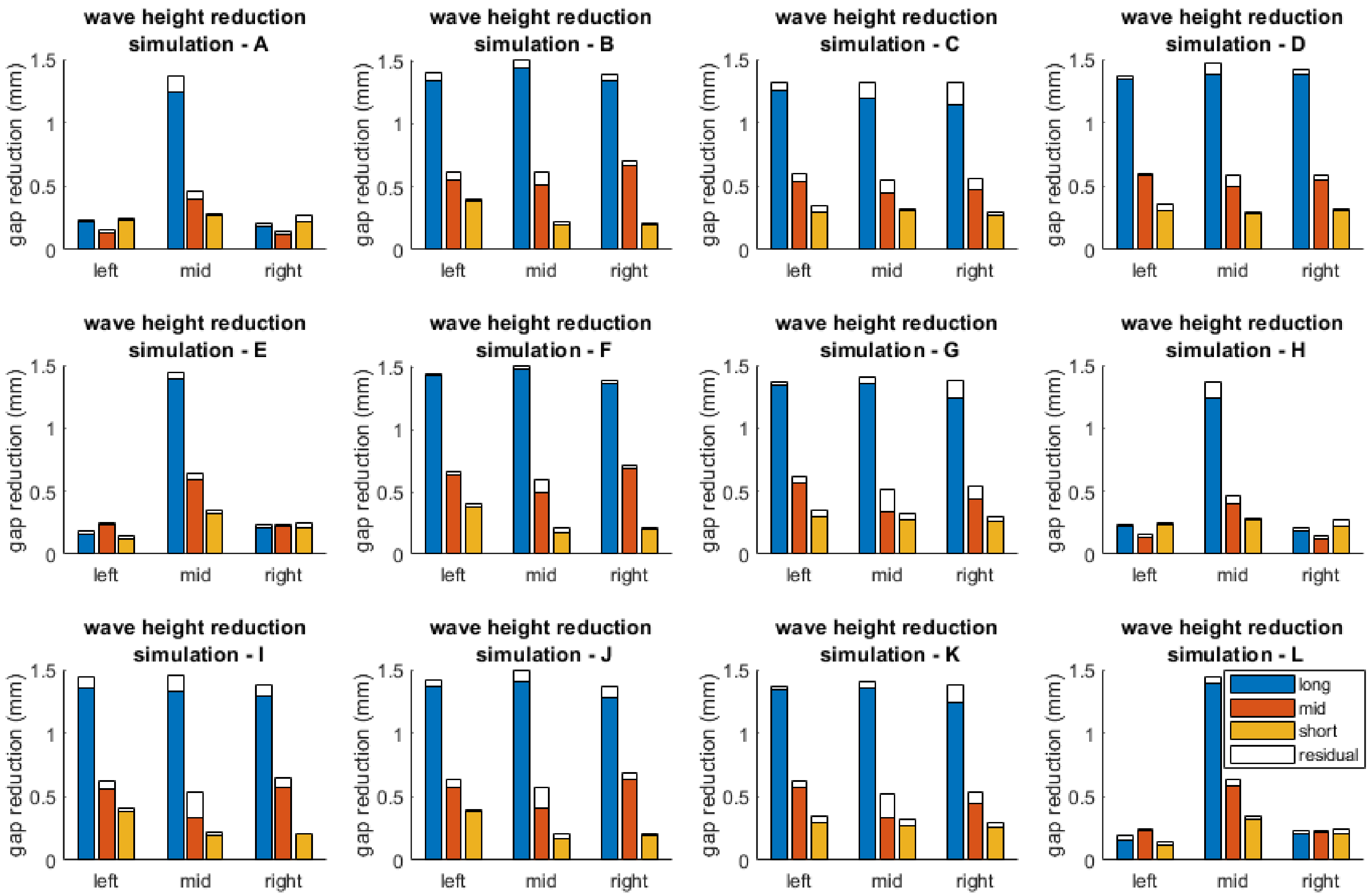

Figure 5-72. Predicted changes in wave height under each stringer. Total bar height equals the initial (unpressed) gap height. The white segment corresponds to the final gap. The colour bar is the height reduction.

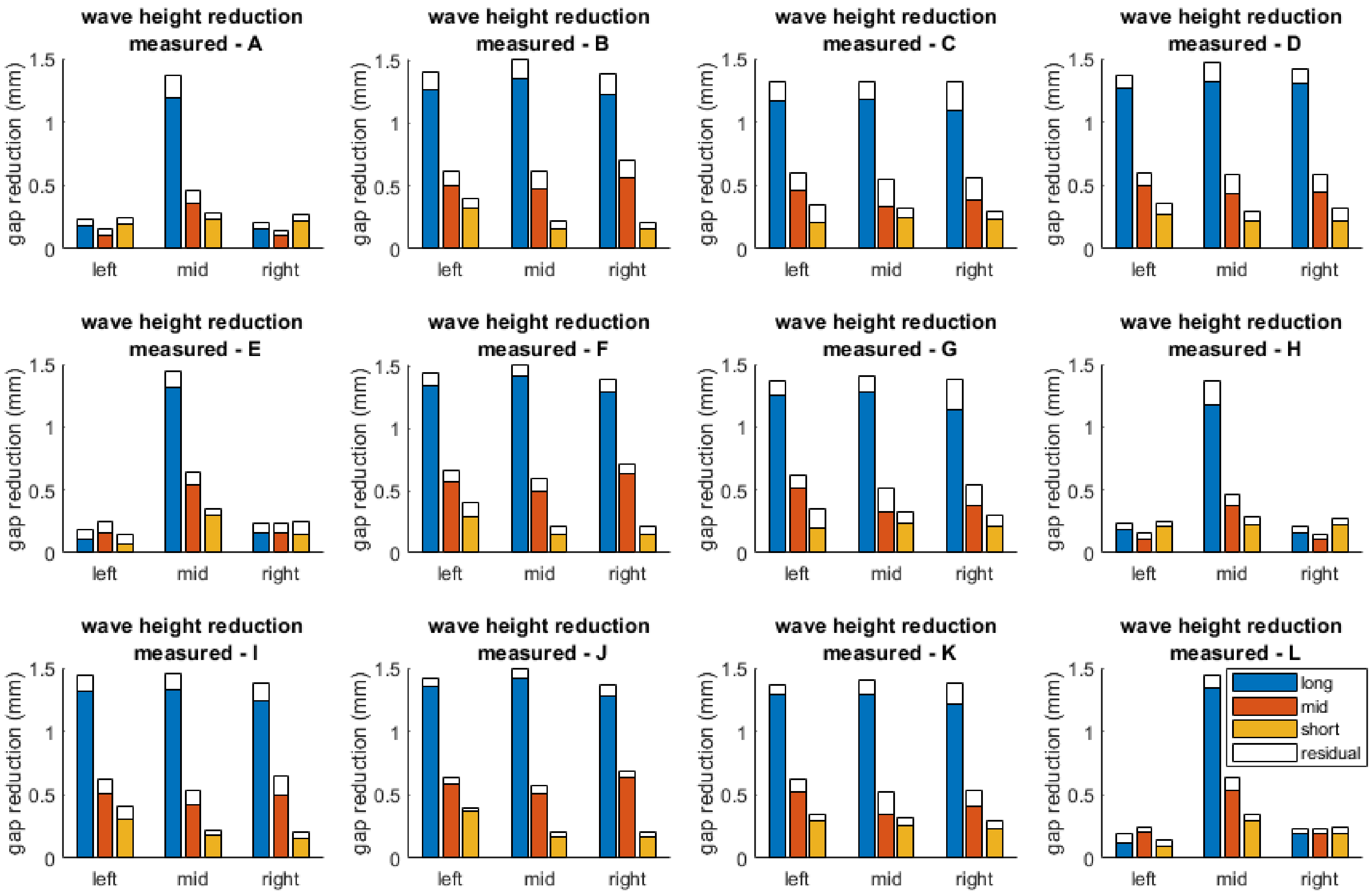

Figure 5-73. Measured changes in wave height under each stringer. Total bar height equals the initial (unpressed) gap height. The white segment corresponds to the final gap. The colour bar is the height reduction.

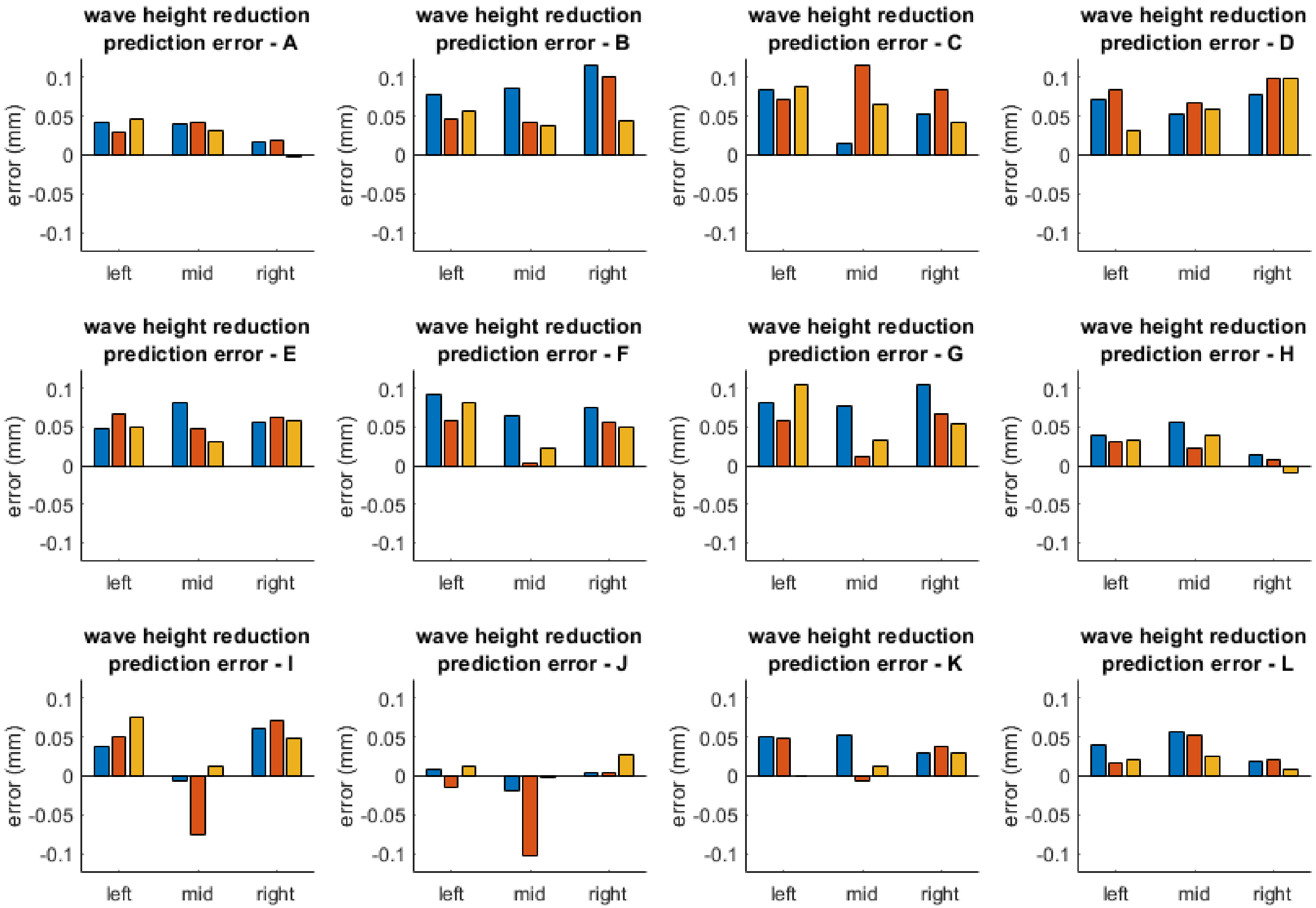

Figure 5-74. Absolute error in gap reduction prediction, by stringer and assembly. A positive value means the deflection was overestimated; that is, the measured gap height was larger than expected.

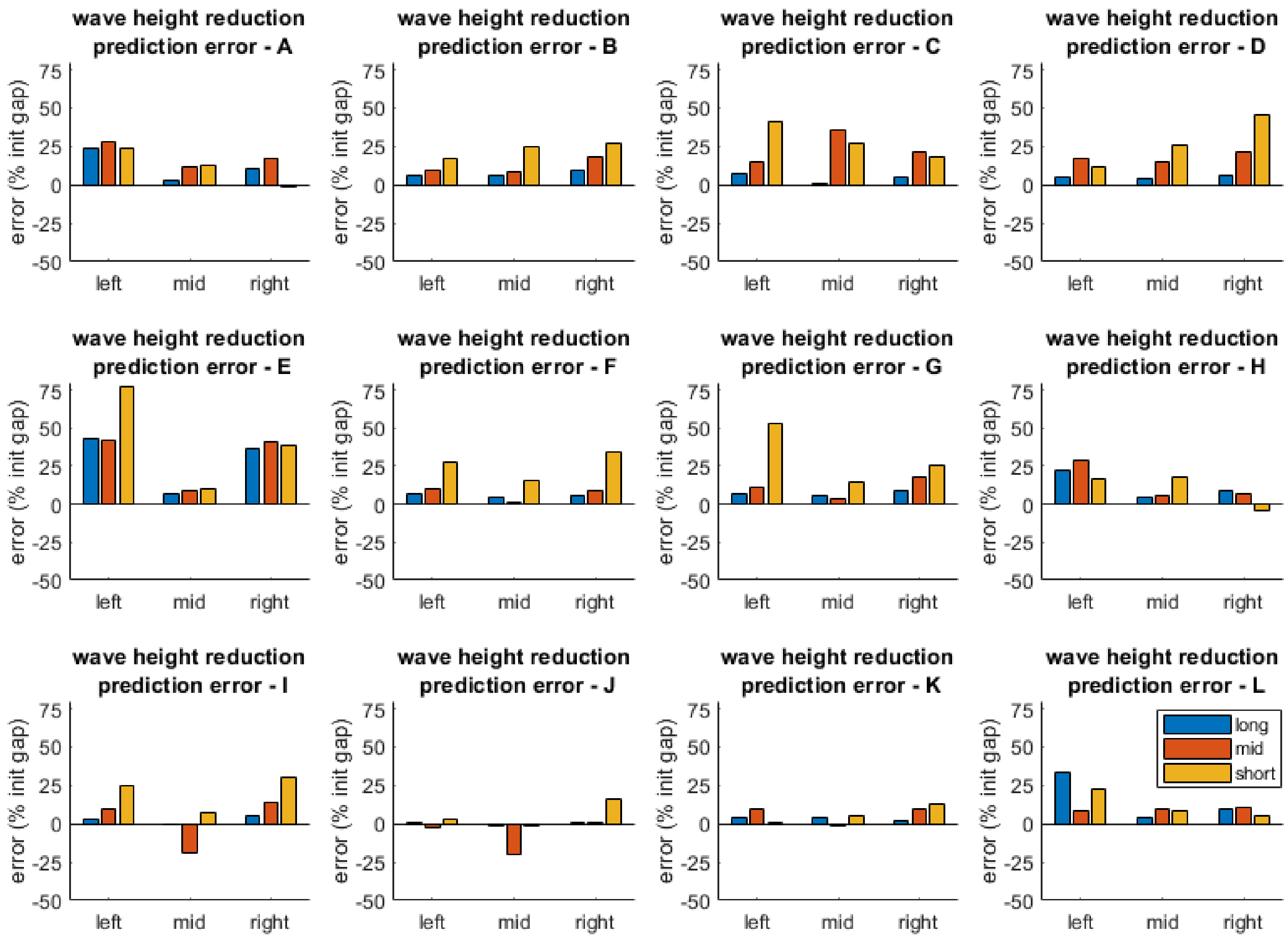

Figure 5-75. Error in the predicted deflection, relative to the initial gap height. Note the higher scale in A and E side stringers is due to the much shallower initial gaps (as they were not pre-deformed during manufacture).

5.3.5.3.2 Regression accounting for categorical variables

The theoretical-practical justification, as well as the specifics of the method, are addressed in Appendix H — Model calibration. The detailed tabulated results are also presented in the appendix.

The process is as follows (Figure 5-76):

1. Specify a probabilistic model linking the observations (demonstrator measurements) with the prediction inputs: these include the simulation results, and additional variables such as node location and assembly type, which can be categorical. The link includes uncertain parameters (i.e. variables which are modelled according to a random distribution). These are the values that will be fit to the model using observational data.
2. Generate an initial ‘guess’ as to the values of the uncertain parameters.
3. Perform a random walk through the (highly-multivariate) parameter space whereby, for each parameter.
    a. a new value is generated according to a specified prior[xxxvii];
    b. the likelihood of the observed data given the parameters is calculated;
    c. the new parameter value is accepted randomly, with a chance determined by whether it improves the likelihood of the observed data relative to the previous iteration (thus the process is a Markov chain)
4. After a large number of iterations, once the random walk has converged, all the values traversed for each parameter form a distribution for its respective value.
5. The mean of each distribution is the expected value for its corresponding parameter; meanwhile, inferences on the confidence in the value can be made based on the dispersion of the distribution.

[xxxvii] The priors used are non-informative, i.e. they are chosen so that their dispersion is high (reflecting little initial knowledge) so as not to bias the model results.

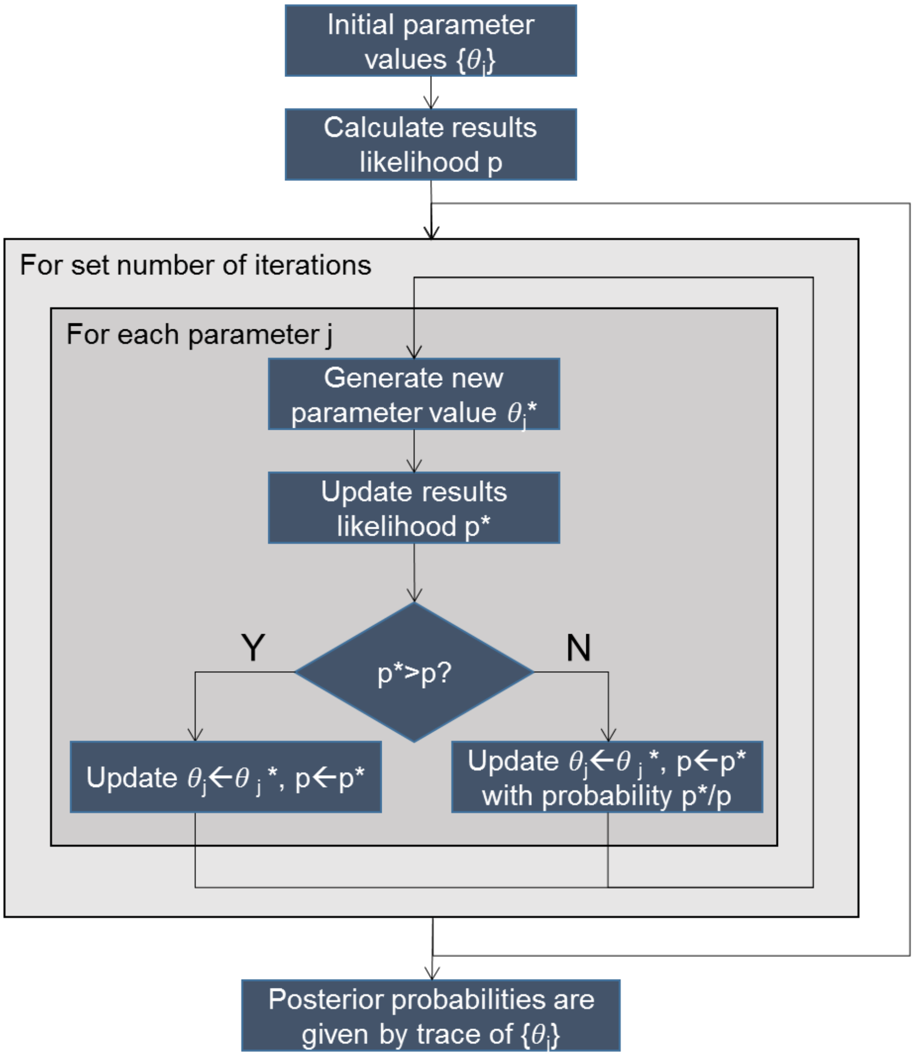

Figure 5-76. General flow of the Bayesian Markov Chain Monte-Carlo approach.

The regression conducted accounted for the following aspects:

- Bondline measurement uncertainty (including bias due to release film in the verifilm strips and unremoved metal burr in the bond sections);
- Location of the bondline under an area of initial stringer-skin contact, as well as location along the stringer cross-section (edge or middle);
- Bonding condition (Single- or double-side pressure);
- Stringer position with regards to stringer interference.

These were incorporated into the regression model as

$$b_{obs} = b_{sim} \times \rho_{boundary\ conditions} + \delta_{stringer\ location} + \varepsilon_{measurement\ error} \tag{5-8}$$

which thus links the observed (measured) bondline thicknesses b_{obs} to the values predicted by the simulation, b_{sim}. Details of the definition and calculation of the values of each parameter $\rho, \delta, \varepsilon$ are, for the reader's convenience, provided in Appendix H — Model calibration.

The regression indicated the following:

- The generic section burr thickness that best explains the verifilm-bond discrepancy reduces the visible bond thickness by 36 μm (with a 5 μm wide 95% confidence interval).
- In relation to adhesive flow modelling simplifications, the bondline thickness away from the highest pressure areas (where there is contact between substrates already when building up the assemblies) is on average thicker than explained by the simulation, by at least 19 μm, with 97.5% confidence. However, the extra deflection at the stringer edges is better accounted for by the simulation, and a correction of 8 μm or less (with 97.5% confidence) is sufficient.
- The bondline thickness is generally overpredicted by the simulation. The overprediction was proportionally most dramatic for the middle stringer in the slight-interference assembly; this was to be expected given the complex skin-stringer-adhesive interaction.
- Once this overprediction is scaled for and corrections for boundary conditions are included, the residual normally-distributed prediction error has a most likely standard deviation of no more than 24 μm (97.5% confidence). This is a reasonable uncertainty given typical part manufacturing capabilities, with feasible tolerance ranges in the hundreds of microns.

5.3.1 Main outcomes of the multi-stringer test

An innovative test assembly design has been developed which allows testing of bonding in different boundary conditions by "letting the part become the fixture", achieved through permuting variation and orientation of multiple stringers on a skin they are bonded to. The multi-stringer assembly helps cover the hitherto-unaddressed variation aspects of stringer-skin variation:

- Different boundary conditions;
- Variation of parts (stringers) interacting with each other via a common element (skin) in a parallel assembly;
- Baseline nominal[xxxviii] vs. non-nominal initial interface gap geometries.

This provides confirmation, via both physical demonstrator and simulation, of the following:

- It is possible to markedly increase bonding capability by choosing boundary conditions such that all elements are free to deflect — in agreement with the prior art on bonding for fuselage (Land and Lennert, 1979) and wing covers (Hart-Smith and Strindberg, 1997).
- The bonding capability derived from skin deflection is heavily dependent on the local boundary conditions conducive to adherend proximity/contact. Interface gap combinations requiring deflection with a double curvature, or over a very short range, may still be not possible to mitigate even if the skin is allowed to deform.

A statistical model fit shows that the systematic discrepancy between the simulated and measured results is consistent with the limitations of the adhesive flow model.

[xxxviii] This needs a qualifier: "as close to nominal as reasonably practical"

6 RESULTS DISCUSSION

6.1 Research achievements

6.1.1 Performance against FEA (dry component)

Preliminary verification of the dry aspect of the model against a commercial software package (Abaqus) showed close agreement, except in the extreme case of a thin flange modelled too coarsely (section 5.1). It was shown that, by refining the model to better capture the full dimension of the flange, agreement was improved in this extreme case as well.

6.1.2 Performance of the adhesive modelling (wet component)

The ability to predict minimum bondline thickness is less promising. However, this was expected from the beginning; it is acknowledged that only preliminary sizing can be supported by the simplified adhesive modelling approach. The two primary reasons are presented below.

6.1.2.1 Rheological property knowledge

The term $(\int_0^{t_{cure}} \eta^{-1} dt)$ is the only one, in the 1-dimensional squeeze-flow equation (3-33), that is not directly controlled/known through the input geometry and controlled assembly conditions. However, this actually comprises multiple factors in the form of multi-parametric curing dynamics and rheology, in addition to the temperature throughout the curing process. While the adhesive properties need dedicated testing to ascertain, the temperature is not easy to log and control in the oven- or autoclave-based cure processes; adherends and tooling act as heat sinks, while bonding consumables act as insulators and the sheer part sizes and geometries make it difficult to obtain completely homogeneous heat transfer.

6.1.2.2 Oversimplified flow conditions

As addressed in the analyses of physical demonstrators in Section 5, the flow of adhesive between adherends is not the simple symmetrical, one-dimensional case modelled. In reality, the flow is not only different across different cross-sections, but also is not confined to each cross-section; rather, adhesive flows from fully- to partially-filled interface gaps (explaining the thickness beyond uncured film dimensions at some areas) in response to pressure differences (as evidenced by local porosity). The impact of these effects is well observable in the physical bondlines obtained from the bespoke assembly tests.

Furthermore, the adherends, contrary to the modelling assumptions, are neither completely flat nor parallel to each other; this was observed in all physical tests. The limitation is intrinsic to the simplified modelling approach, which stops short of performing any Fluid-Structure Interaction (instead, the contact pressures from the dry assembly are fed into the flow model, but without any iteration or local reformulation).

6.1.3 Practical use/application

Three uses have been shown, spanning the whole development cycle:

6.1.3.1 Preliminary design tolerancing

Both a small-scale and representative near-full-scale case have been studied and analysed to estimate rates, and detect sources, of non-conformance, for notional values of variation and tolerances. Such analysis supports initial tolerance definition and manufacture process selection / requirement definition before any component needs to be fully designed and the procurement process started.

6.1.3.2 Assembly concept trade study

Medium- and representative near-full-scale demonstrators have been evaluated (along with physical replications for one of them) showing the implications of different assembly conditions for joint geometry variation control. The predictions are soundly in line with the qualitative expectations from reports in the literature. Thus, this application directly informs assembly design and process requirement, supporting trades such as higher part quality for gentler assembly conditions and vice-versa.

6.1.3.3 On-the-fly virtual dry fit

Product realisation has also been addressed by simulating assembly (or rather, a dry fit check under full bonding pressure) based on measurements taken on the shopfloor, and input through a simple spreadsheet interface. It would be a small leap to integrate this in production using automated measurements (or even quick manual measurements, as it was the case here, provided the manufacture rate is low enough). This has the three beneficial effects of increasing overall confidence in the final result, snagging rejects that may have slipped through previous quality checks, and (not demonstrated here due to low manufacture volume and tight schedules) allowing individual tuning of assembly conditions (e.g. by detecting critical spots that may require extra adhesive or pressure-intensifying tooling).

6.1.4 Systematic test assembly

An important step in testing the validity of the modelling approach followed, is the deliberate inclusion of part interactions (or "stringer interference" as it has been referred to in this work) into test design. This has been achieved by a natural extension of typical 'small variation'/'large variation' design criteria for assembly and inspection problems, where:

1. Individual parts contain different variation sizes;
2. Interference is generated by interaction of the variation different parts through the common part in a serial assembly;
3. The interference itself is also encoded in terms of different 'sizes' or magnitudes.

6.1.5 Model calibration

The model limitations and general inadequacy[xxxix], as well as the uncertainty due to measurement, have been incorporated into the final model assessment through a hierarchical model fit (performed by Bayesian Markov Chain Monte Carlo). This fit is a departure from usual model comparisons, which rarely stray from zero-order deviation measures (e.g. RMS error, bias, or rate of false rejections). Here, quantitative assessments of the impact of different sources of uncertainty are provided. These uncertainties come from

---

[xxxix] This is not to qualify the model as inadequate. Here "inadequacy" refers to inaccuracy of the model associated to simplifications and unknowns; the term is presented in appendix subsection H.1 The model calibration paradigm.

- Specific modelling inadequacies identified;
- Generic modelling inadequacies;
- Measurement uncertainties identified;
- Unidentified sources of uncertainty.

In particular, adhesive modelling inadequacy has been found to have an impact which agrees with the expectation based on study of the boundary condition violations. Likewise, reference measurement data, as well as measured data broadly speaking, show the measurement uncertainties to be well understood and small compared to the geometry variation range.

Lastly, unexplained model inadequacy is small, translating into a standard deviation of only tens of microns.

6.2 Research limitations

The work and results presented are encouraging and represent a step change in terms of understanding of bondline geometry. However, there are a few caveats to application of the methods developed.

Although these should be apparent from the modelling assumptions and from the problems encountered during physical testing, it is worth re-stating the limitations to applicability explicitly.

6.2.1 Violation of assumptions and general limitations

The boundary conditions for adhesive flow have been found to be critical in fidelity of the squeeze-flow model:

- <u>2D flow</u>: Bondline thickness prediction will become less accurate close to big interface gaps and part edges, where the 1D assumption is overly conservative. In these areas, the bondline will be thinner than predicted, as the adhesive is able to flow more easily than in the 1D scenario.
- <u>Restricted squeeze-out</u>: If very large amounts of adhesive are applied, or if adhesive outflow is restricted e.g. by applying flash breaker tape to part corners, the assumption that squeezed-out adhesive does not interact with the bondline will be violated. If this is the case, not only will the bondline become thicker: pressure will be redistributed between the adherends, and the "dry" modelling of adherend interaction will no longer be a reasonable approximation.

The linearity assumption can be violated in more than one way, in which case local or global inaccuracies will appear:

- <u>Plastic deformation</u>: in some cases when there is actual hard contact (without adhesive mediating) between adhesive layers, the contact pressures may far exceed the yield strength of the material. This would result in additional deflection, dimensional changes of the part, and a redistribution of contact pressures. The dimensional impact of such a situation, however, would be very small and local. It must be noted that the meshes demonstrated in this work are likely too coarse to properly reflect such high stress concentrations in the first place.

- Finite (not small) deformation: in some cases, it is possible that large-amplitude, long range variation can be encountered, which does not respect the hypothesis of small deformations, resulting in calculated deflections which do not correspond to reality. The loss of accuracy from violation of the small deformations hypothesis, and the acceptable limits, have not been assessed. As a mitigation, it is recommended that any part measurements not be conducted in a free-state configuration, but under limited loads (e.g. 1% of the expected assembly loads), thus eliminating the longest-range deformations. Incidentally, this aligns quite closely with current industrial practice.

6.2.1.1 Estimating inaccuracies in adhesive modelling

The wet/dry model separation disregards the effect that adhesive flow may have in the areas of parts which may not be coming down to the minimum bondline thickness. In practice, although the resistance to flow may be comparatively little in the areas when there’s a larger interface gap, it is not zero, especially once all the interface gap has been filled by squeezed adhesive. Indeed, all the test assemblies examined showed *some* squeeze-out in the vicinity of the thickest bondline areas; the adhesive thus expelled from between the parts here, even if not much, must have exerted some resistance.

An exercise estimating the minimum reaction pressure in gap areas (which would be out of contact in the ‘dry’ assembly model) is presented below.

The geometry changes leading up to the final cured geometry (prior to pressure release) can be traced more in detail as the following steps, which are depicted in Figure 6-1:

0. The adherends and adhesive are located in a ‘stress-free’ state (weight loads only).

1. Pressure is applied quickly, leading to elastic deformations in the part which lead to a static equilibrium. The adhesive is too viscous to exhibit significant dimensional changes at the end of the stage. This can be modelled as the 'dry' assembly, with the adhesive transmitting the calculated contact reaction forces.
2. Adhesive starts flowing in the 'dry' contact areas; it gets both squeezed out and into gap areas. Thus, gaps start getting filled. Squeeze-flow pressure outside contact area from the previous step is disregarded for now.
3. All bonding interfaces are now wet with adhesive. With no gaps left to fill, adhesive is squeezed out throughout the bondline. As the adhesive is now pressurised everywhere and not just in the minimum-gap areas, the reaction forces no longer correspond to the 'dry' case. Adherends' deflection thus varies to accommodate the new reaction forces.

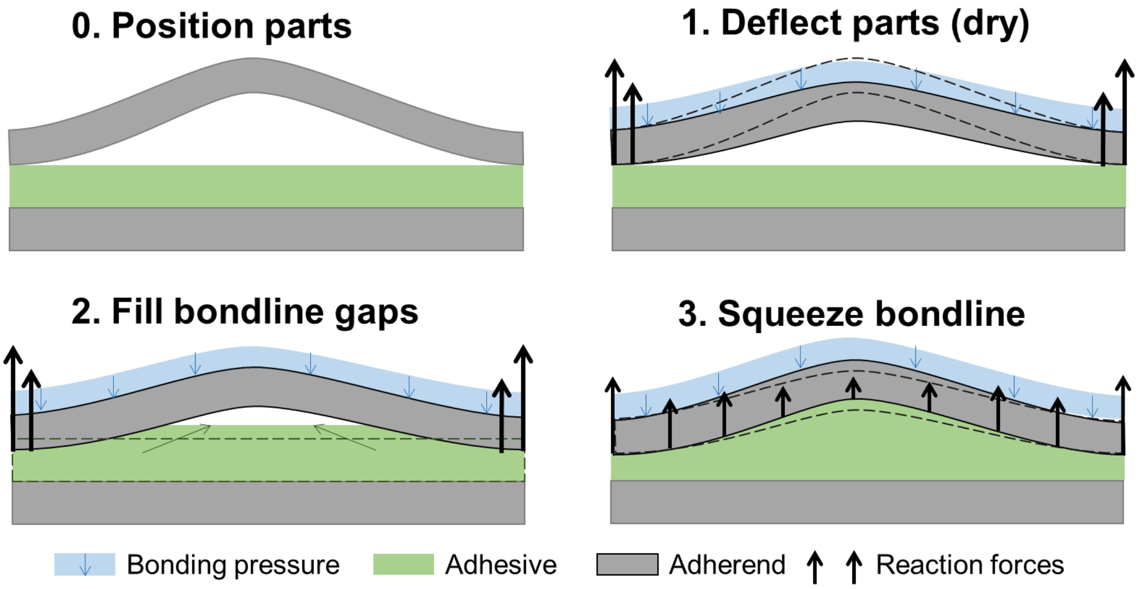

Figure 6-1. Steps leading to the final bondline geometry (side view of a simplified bondline). Deflection in one adherend only is depicted.

Consider a snapshot of the start of step 3. Initially, according to the simplification of step 2, the reactions on the substrates are dictated only by the squeeze of the thinnest areas of the bondline, which reached equilibrium at step 1; thus, thickness change rate $\dot{b}$ is (at least momentarily) uniform at each interface.

Disregarding geometry variations across each cross-section of the bonded area, the total pressure force (per length) over each cross-section is (Morris and Scherer, 2016)

$$\frac{dF}{dL} = \frac{w^3 \eta \dot{b}}{4b^3} \tag{6-1}$$

Consider a simple bond geometry of constant width w, and that the heating is homogeneous such that the viscosity η is also the same throughout the bond. According to (6-1), and given the assumption that squeeze rate $\dot{b}$ is (as stated above) uniform at the beginning of step 3, the force per length at each cross-section will be inversely proportional to the cubed thickness of the flow domain:

$$\frac{dF}{dL} \propto \frac{1}{b^3} \tag{6-2}$$

The minimum bondline thicknesses encountered in this work have fluctuated between some 80 μm and 170 μm (for a single layer of film adhesive). After discounting 50 μm corresponding to knit carrier, this makes for a flow domain thicknesses in the 30~120 μm range. A representative maximum expected/permissible deviation in bondline thickness, Δb (associated to a typical tolerance range — or, indeed, to some of the variation ranges seen in this work) would be in the order of 100~150 μm. Thus, the maximum acceptable bondline thicknesses observed could be 100~150 μm more than the minimum[xl].

It is then possible to estimate the ratio of the maximum to minimum squeeze reactions, which will be referred to as ψ:

$$\psi = \frac{\min\left(^{dF}/_{dL}\right)}{\max\left(^{dF}/_{dL}\right)} = \left(\frac{\min(b)}{\min(b) + \max(\Delta b)}\right)^3 \tag{6-3}$$

Some ratios of minimum-to-maximum squeeze forces are presented in Table 6-1 and Figure 6-2. In general, the ratio ψ presented in (6-3) can be kept below 10%, unless there is a generally thick bondline with small variation (in the cases

[xl] Note that the individual flow domains will be a fraction of the total adhesive thickness; however, proportionality of the ensuing discussion still holds if considering a single flow domain.

tabulated, this would correspond to $\min(b)$ = 120 μm, $\max(\Delta b)$ = 100 μm). More generally, if a maximum acceptable ratio ψ_{max} is defined, and directly as a consequence of expression (6-3), a minimum acceptable geometric ratio is defined:

$$\frac{\max(\Delta b)}{\min(b)} \geq \psi_{max}^{1/3} - 1 \tag{6-4}$$

If $\psi_{max} = 10\%$, this yields $\frac{\max(\Delta b)}{\min(b)} \geq 1.154$. This is represented in Figure 6-2.

Table 6-1. Some representative ratios ψ of squeeze forces as given by equation (6-3) depending on minimum flow domain thickness and maximum variation.

$\min(b)$ \ $\max(\Delta b)$	**30 μm**	**75 μm**	**120 μm**
150 μm	$\left(\frac{30}{30+150}\right)^3$ =0.005	$\left(\frac{75}{75+150}\right)^3$ =0.037	$\left(\frac{120}{120+150}\right)^3$ =0.088
100 μm	$\left(\frac{30}{30+100}\right)^3$ =0.012	$\left(\frac{75}{75+100}\right)^3$ =0.079	$\left(\frac{120}{120+100}\right)^3$ =0.162

These results highlight the kind of case where the dry/wet separation may be grossly inappropriate. A larger minimum bondline thickness will normally result from:

- Relatively low bonding pressure ΔP (e.g. OoA);
- Short cure times;
- High adhesive viscosity η (e.g. paste adhesive);
- High bond width w (e.g. with laminate skins).

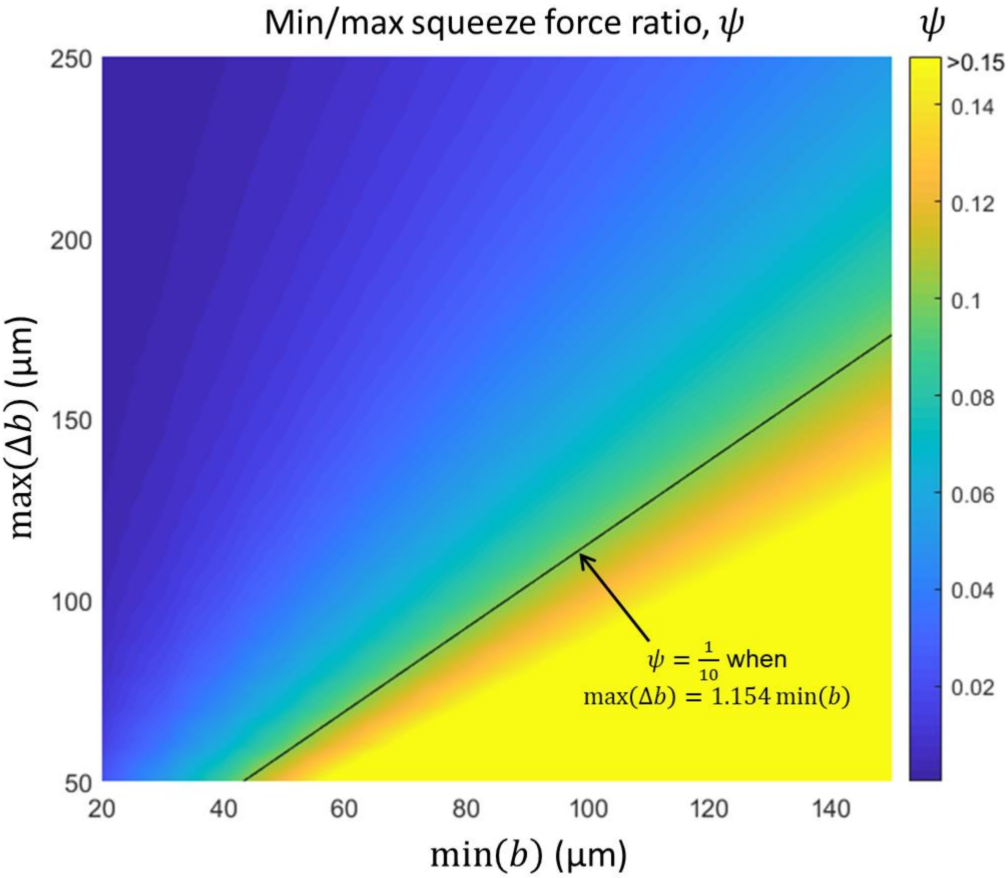

Figure 6-2. Squeeze force ratios ψ for a bondline thickness minimum/range space. Note even though the colourscale plateaus (from 0.15 onwards) under the solid black line, the monochrome area under the line actually contains growing values; it reaches an extreme value of 0.42, at the (150, 50) lower right corner.

Lower bondline variability can result from substrates which are thin (and thus of reduced stiffness, so they can be pressed into shape easily) or manufactured to a high precision; or from high bonding pressures.

When the adhesive reaction forces away from the minimum thickness are sufficiently large, a significant fraction of the force which the dry/wet model concentrates in bondline thickness minima will actually shift to thicker-bondline areas. This will have the effect of undoing some of the adherend deflection, and enlarging the interface gaps. As a result, dry/wet separation will not be realistic when modelling a bondline that is overall thick, but requires tight control of variation. Careful consideration of the particular assembly characteristics should be exerted before modelling any scenarios which risks a substantial redistribution of contact pressure due to adhesive flow.

A perk of the nature of the inaccuracies expected from dry/wet separation is that there is a negative feedback effect with gap closure: for large gap variations, the model holds thanks to the small ψ values; as the variation becomes smaller, the model becomes less accurate and the real variation can be expected to be larger than calculated. From a quality assurance standpoint, in the case where a pass/fail approach is involved, this fact would only be a minor nuisance: it would be possible to estimate the value of ψ for the limit case of a narrow fail (or narrow pass), and use it as a quantifier of model reliability.

6.2.2 Scope limitations

The focus of this work is assembly of non-rigid (also termed flexible, compliant, or deformable) components. Rigid motion considerations have been given minimal thought. Therefore, other methods may be better suited when considering bonding of structures where all parts do not match the definition of “non-rigid” used here; that is, if the deformation of all parts under reasonably expected assembly loads is negligible compared with the tolerances encountered.

The applications shown focussed on the bondline thickness calculation. Little effort has been put in extending the simulation to calculate springback. This is because, unlike in prior art where the final shape was the main variable of interest, here we are most concerned about geometry of the joint. It would be relatively simple to perform such extension, by reversing the external force application and adding the equations for elastic deformation of the bondline. However, the boundary conditions assumed are at risk of yielding unrealistic results when global shape is concerned.

Modelling of the adhesive comes with some strong assumptions:

- Fluid behaviour: only a viscous, Newtonian fluid scenario has been captured. Although analytical solutions have been developed for other cases, the validity of these has not been tested in the present work.
- Boundary conditions: in addition to the case of excess adhesive restricting outflow, it is also possible that the assumption of parallel flat plates be violated. This will occur, for example, in the event of stringer twist, or when bonding thin adherends (which can deflect at the edges where adhesive pressure drops). In both cases, pressure in the adhesive will be redistributed, increasing under the areas of the adherend that are closest, and working to restore the flat/parallel situation. However, the degree to which this will occur has not been assessed and is indeed not accounted for anywhere in the 1D model.
- Adhesive flow properties: it must be noted that only generic datasheet rheology data has been used, further supported by empirical results in a limited set of conditions. If adhesive contribution to thickness is actively incorporated in the design space (i.e. if the designer is given freedom to tweak the heat/pressure cycle to tune geometric and mechanical performance outcomes), the model would benefit from crisper data obtained from dedicated tests.

Boundary conditions as modelled (with displacements set to 0 at datum points) are not realistic, even if they are a necessary simplification for the purpose of obtaining a linear model. Indeed, the tooling lugs which were assumed pinned were actually relatively free to float, and were observed to float during pre-fit of the curved panel tests. In practice, for large parts, the impact of this is negligible (as part interaction and bonding pressure provide the dominant boundary condition). However, values near part edges should not be assumed to be as accurate as the rest.

Pressure application has been assumed to be uniform and normal to the parts' external surfaces, without any consideration of local tooling application (e.g. clamps, pressure intensifiers) or manufacture errors such as a bag being too tight. The accuracy of the simulation when these conditions are present has thus not been assessed. In particular, no methods have been studied to quantify the contribution of bag tension (which would result in tangential forces).

Thermal expansion/contraction has been assumed to play a negligible role. This may not be a reasonable assumption in the event that materials with very different coefficients of thermal expansion be bonded (for example, aluminium and CFRP). This will often not be the case, as it would result in unacceptable build stresses and assembly deformation.

6.3 Further work

A number of technical/practical shortfalls have been highlighted, which, though not precluding usefulness or completely undermining the results' validity, do reduce reliability and narrow the scope of application.

6.3.1 Boundary conditions and adaptable offset

The assemblies simulated did not incorporate any clamped or otherwise highly-restrained datum; as such, part interaction was the main (indeed, the only) driver of shape change. Some DoF had to be restrained at discrete datum locations to obtain a suitable linear model; however, this results in unrealistic modelling near said datums (as, in reality, the datums *were* free to move). The effects of the inaccuracy will remain local, as long as there are not high reaction forces in the area resulting from initial interference of the profiles.

A potential fix for the cases in which the boundary conditions result in large modelling inaccuracies would be to iteratively update the datum positions through an offset normal to the bond interface. This step could be performed based on the (fictive) reaction forces and torques at the boundaries, until such reactions are smaller than an arbitrary tolerance.

6.3.2 Enhanced adhesive modelling

One of the sources of discrepancy between the model and physical results is the substantially simplified adhesive behaviour. Simplification *is* needed for the simulation to be over after a single instance of the iterative contact solution; however, this comes at the cost of overlooking complex bondline geometries.

A suitable approach is needed to generate smooth minimum-thickness distributions accommodating local conditions, including tailored adhesive volume (be it custom paste dispensing or varying number of adhesive film layers; in this work, each assembly has used the same number of film layers throughout). Further, it would be possible to build up a more detailed model based on a few inputs and an array of different models or a database of representative fluid dynamics simulations, accounting for factors such as dry-fit reaction forces, shape of the deformed dry gap at each cord, and geometry at adjacent cord positions.

Similarly, additional adhesive considerations may be integrated; for example, bondline thickness distributions and reaction forces could be used to predict void formation, which was observed in some of the tests at spots with large separation of the adherends.

6.3.3 Automated model generation

The current solution involved manual coding of each simulation and adaptation of some common functions for part model generation from a FE mesh. However, better integration with CAE environment would be possible, utilising mesh interrogation and manipulation capabilities; the following aspects could be added:

- Automated generation of matching meshes (or near-matching nodesets from fine-enough initial meshes);
- Automatic nodeset decimation to achieve a user-requested problem size;
- Automatic generation of the linear gap compliance matrix based on user-input or auto-generated assembly chains;
- Allocation of surface area values to each modelled node, be it based on secondary geometric references (as in the work undertaken) or on computational geometry techniques such as a Voronoi tessellation.

7 CONCLUDING REMARKS

7.1 Summary of the work

Adhesive bonding is a highly capable technology for joining aerospace structures. Control of the thickness of bonded joints is critical to mechanical performance and manufacturability; however, current understanding of it is limited and empirical.

This work presents what is, to the author’s knowledge, the first attempt at variation analysis of joint geometry in bonded assembly of nonrigid skin-stiffener structures:

- A method based on spectral analysis, which has been found to offer limited information due to multiple limitations.
- A semi-analytical method based on numerical calculation of part deflection with contact enforcement, coupled with analytical estimation of the minimum adhesive bondline thickness.

Bondline geometries have been studied for several representative skin-stiffener physical tests with a variety of assembly conditions and part geometries. This includes design and realisation of a cost-effective assembly arrangement, comprised of three stiffeners on a skin, which supports systematic investigation of bonding capability in multiple boundary conditions.

The variation analysis methods proposed have been compared qualitatively and quantitatively with the measured results.

- It has been found that deviations are largely consistent with the major simplifications in modelling of the adhesive flow under conditions of part cross-section deformation or local over/under-fill of the gap at the beginning of the bonding cycle.
- Principles of the adhesive modelling inaccuracy have been presented, and preliminary quantitative bounding of the model applicability shown.

The analysis methods have been further applied to notional assemblies for stochastic variation; as well as for health checking small assemblies based on ad hoc interface gap measurements during pre-fit.

Practical and model limitations of the work have also been presented, inclusive of the underlying mechanics and estimated quantitative implications.

7.2 Future research prospects

7.2.1 Expansion for springback

The simulations have shown good agreement with practical results for calculation of the joint geometry. Although bondline thickness is the critical characteristic studied, it is only logical to expand the quality prediction to the next step, either simply by releasing the pressure and evaluating the stress-free resulting geometry, or applying the same functional-fit approach which has informed this work.

The choice of boundary conditions is a challenge for this application: with the adherends not floating relative to each other anymore, any mismatch next to a datum is likely to result in a substantial loss of accuracy. It may well be that a linearised model, as used for assembly simulation, does not perform adequately. However, a full FEA procedure may incur satisfactorily short computation times for springback calculation, since there will be few or no non-linearities stemming from contact between parts.

7.2.2 Expansion and integration with stress / F&DT analysis

The joint geometry prediction effort stemmed from concerns around mechanical performance. It is a small leap to use it to also inform the stress criteria and analysis of the bonded structure. The avenues for this are twofold:

- Use of predicted geometries to generate likely scenarios to evaluate the impact of bondline variability; given known or reasonably-assumed part variation, the study variable space (in terms of amplitude, range and shape) would thus be reduced, and analysis and coupon testing would better capture the performance of assemblies expected from manufacture.

- Residual stresses would result directly from a springback calculation; though coarse, these values would directly support stress analysis by indicating what fraction of the total joint or adherend strength is used up by the assembly.

7.2.3 Developing readiness for industrial use

A fundamental limitation of the work developed so far is lack of automation. Each assembly studied was modelled and coded manually, and given a few 'dials and buttons' and a common structure to support experimentation and interrogation. Also crucially, inputs were generated in a way that facilitated academic discussion, but not necessarily the most convenient for industrial practice. For instance, deviation modes on their own may mean little, whereas variability of manufacturing steps is easier to grasp, and more straightforward to control. Thus, better adaptation for, and integration with, the actual industrial process, are needed.

7.2.3.1 Integration with design

The design-support applications have been demonstrated successfully, but are currently only modifiable through code or (large, and thus hardly manually fillable) input tables. A fundamental step change would be to package these into an easily-redeployed application. This could be done by:

- <u>Creating a standalone app of limited scope</u> (which is supported by numerous existing computer-programming tools), probably using a small number of pre-generated models. This stands to offer a quick solution for an industry user, allowing for cheap, widespread deployment, as well as fuller intellectual property ownership.
- <u>Integrating the algorithms developed in an existing CAT suite</u> that already supports part deflections, such as RDnT, 3DCS or AnaTole/AnaToleFlex. Aspects likely to require incorporation are area-based assembly forces, input of shape or spatially-mapped deviation; and creation of a non-zero-size joint (corresponding to the bondline). Alternatively, an add-on could be created for a FEA/CAE suite.

- Creating a dedicated CAT programme from scratch, ensuring the appropriate capabilities are supported. For this option to be viable at all, substantial industry demand would need to be confirmed.

7.2.3.2 Integration with production

A small-scale, reduced-scope demonstration has been presented of how assembly simulation can use coarse measurement data, taken in a shop environment, to support quality assurance. The application was based on manual gap measurements and the decision supported was just “go ahead with no process changes”. However, some adaptations and advancements can easily result in the transition to a fully industrialised system, achieving powerful synergies within the context and philosophy of digitisation and Industry 4.0:

- Automated simulation workflow, comprising the use of inputs from measurement data, be it from part measurement or in-process gap measurements (e.g. from embedded sensors or noncontact pre-fit measurements) as well as postprocessing;
- Use of the simulation results to guide assembly decisions, such as part matching, customised adhesive dispensing, and positioning of pressure-intensifying tooling, be it in a completely automated way or providing advice to specialists through a user-friendly interface;
- Passing the simulation results downstream to support other processes, such as complementing NDT results, gap management (through adaptive shimming, trimming, or part matching) for later assembly steps, and for further data processing (such as generation of neural-network-based predictive models, or customised stress analysis in the event that extraordinary circumstances demand it).

7.3 Concluding remarks

This work presents an effort to enhance design and manufacturing wisdom in aerospace bonding, by adapting analytical tools from other fields. This is complemented by a detailed look at the joint formation mechanics, which both informs analysis of the model limitations, and provides a better insight into the physical results observed.

It is hoped that this will be only one of many ongoing and upcoming attempts to generate a new, deeper understanding of the airframe adhesive bonding process. This is a very capable assembly technique which has hitherto been marred by a largely empirical, 'just works' knowledge and process generation, with development cycles that are lengthy and costly as a result. Yet the operational and environmental benefits offered by bonding are too good to forgo without a serious attempt at addressing the development limitations. It is expected that by implementing suitable analytical methods, which can support both the design and manufacturing stages, it will be possible to make the benefits of adhesive bonding more readily accessible to airframe platforms and manufacturers of all sizes.

REFERENCES

3M (2009) *Technical Datasheet: Scotch-weld Structural Adhesive Film AF163-2*

Abbott, R. (2004) *Abbott Aerospace* Seattle

Abellán Nebot, J.V. (2011) *Prediction and improvement of part quality in multi-station machining systems applying the Stream of Variation model, PhD Thesis*. Universitat Jaume I.

Abenhaim, G.N., Desrochers, A. and Tahan, A. (2012) 'Nonrigid parts ' specification and inspection methods : notions , challenges , and recent advancements', *International Journal of Advanced Manufacturing Technology*, 63, pp. 741–752.

Abenhaim, G.N., Desrochers, A., Tahan, A.S. and Bigeon, J. (2015a) 'A virtual fixture using a FE-based transformation model embedded into a constrained optimization for the dimensional inspection of nonrigid parts', *CAD Computer Aided Design*, 62 Elsevier Ltd, pp. 248–258.

Abenhaim, G.N., Desrochers, A., Tahan, A.S. and Bigeon, J. (2015b) 'A Finite-Element Boundary Condition Setting Method for the Virtual Mounting of Compliant Components', *Journal of Computing and Information Science in Engineering*, 15(December)

Abenhaim, G.N., Tahan, A.S., Desrochers, A. and Maranzana, R. (2011) 'A Novel Approach for the Inspection of Flexible Parts Without the Use of Special Fixtures', *Journal of Manufacturing Science and Engineering*, 133(February)

Adragna, P.-A. (2009) *Tolérancement des Systèmes Assemblés, une approche par le Tolérancement Inertiel et Modal*. Université de Savoie.

Aidibe, A. (2014) *Inspection des pièces flexibles sans gabarit de conformation*. École de Technologie Supérieure, Montréal.

Aidibe, A. and Tahan, A. (2015a) 'Adapting the coherent point drift algorithm to the fixtureless dimensional inspection of compliant parts', *International Journal of Advanced Manufacturing Technology*, 79, pp. 831–841.

Aidibe, A. and Tahan, A. (2015b) 'The coherent point drift algorithm adapted for fixtureless metrology of non-rigid parts', *Procedia CIRP*. Elsevier B.V., Vol.27, pp. 84–89.

Aidibe, A. and Tahan, A. (2014) 'The inspection of deformable bodies using curvature estimation and Thompson-Biweight test', *International Journal of Advanced Manufacturing Technology*, 71, pp. 1733–1747.

Aidibe, A. and Tahan, S.-A. (2013) 'Curvature estimation for metrology of non-rigid parts', *Proceedings of the ASME 2013 International Manufacturing Science and Engineering Conference, MSEC2013*., pp. 1–6.

Andolfatto, L., Thiébaut, F., Douilly, M. and Lartigue, C. (2013) 'On neural networks' ability to approximate geometrical variation propagation in assembly', *Procedia CIRP*, 10 Elsevier B.V., pp. 224–232.

Andrieu, C., de Freitas, N., Doucet, A. and Jordan, M.I. (2003) 'An Introduction to MCMC for Machine Learning', *Machine Learning*, 50(5), pp. 5–43.

Anon (1952) Plastics in aircraft. Recent Progress in the Development of Major Components and Structures, (23 May), p. 626.

Anon (1957) 'Conference on Bonded Aircraft Structures', *Aircraft Engineering and Aerospace Technology*, 29(5), pp. 139–142.

Anon (1954) Comet inquiry: the fourth week, (19 November), pp. 731-732. 740-742.

Anon (1976) *Primary Adhesively Bonded Structure Technology (PABST). Phase Ib: Preliminary Design*.

Anon (1977) *Primary Adhesively Bonded Structure Technology (PABST). Phase II: Detail Design*.

Arendt, P.D., Apley, D.W. and Chen, W. (2012) 'Quantification of Model Uncertainty : Calibration , Model Discrepancy , and Identifiability', *Journal of Mechanical Design*, 134(10)

Arenhart, F.A. (2010) *PLANEJAMENTO E MELHORIA DE PROCESSOS DE*

MEDIÇÃO DE FORMA POR SCANNING EM MÁQUINAS DE MEDIR POR COORDENADAS. Florianópolis: Universidade Federal de Santa Catarina.

Arenhart, F.A. (2009) *Avaliação do Desempenho Metrológico de Processos de Medição de Forma por Scanning com Base na Incerteza de Medição, MSc Thesis*. Florianópolis.

Bihlmaier, B.F. (1999) *Tolerance analysis of flexible assemblies using finite element and spectral analysis, MSc Thesis*. Brigham Young University.

Blaedel, K., Swift, B., Claudet, A., Kasper, E. and Petterson, S. (2002) *Metrology of Non-Rigid Objects*.

Bouchenitfa, H., Boukebbab, S., Linares, J.M. and Sprauel, J.M. (2009) *Compensation relative deviations in the STL model using the FEM method: Application at the rapid prototyping technology. Conference paper*

Boukebbab, S. and Bouchenitfa, H. (2009) *Development of a mathematical procedure for modelling and inspecting complex surfaces for measurement process*

de Bruyne, N.A. (1953) Structural adhesives for metal aircraft, *Flight International*, (2 October), p. 490.

BSI (2015) *BS EN ISO 16610-1:2015 Geometrical product specifications (GPS) — Filtration Part 1: Overview and basic concepts* British Standards Institute (BSI), London

BSI (2013) *BS EN ISO 10579:2013 Geometrical product specifications (GPS) — Geometrical tolerancing — Tolerances of form , orientation , location and and tolerancing — Non-rigid parts* British Standards Institute (BSI), London

Camelio, J., Hu, S.J. and Ceglarek, D. (2003) ‘Modeling Variation Propagation of Multi-Station Assembly Systems with Compliant Parts’, *Journal of Mechanical Design*, 125(December), pp. 673–681.

Camelio, J., Hu, S.J. and Zhong, W. (2004) ‘Diagnosis of Multiple Fixture Faults in Machining Processes Using Designated Component Analysis’, *Journal of*

Manufacturing Systems, 23(4), pp. 309–315.

Chester, R.J. and Roberts, J.D. (1989) ‘Void minimization in adhesive joints’, *International Journal of Adhesion and Adhesives*, 9(3), pp. 129–138.

Dahlström, S. and Lindkvist, L. (2007) ‘Variation Simulation of Sheet Metal Assemblies Using the Method of Influence Coefficients With Contact Modeling’, *Journal of Manufacturing Science and Engineering*, 129, pp. 615–622.

Das, A., Franciosa, P., Williams, D. and Ceglarek, D. (2016) ‘Physics-driven Shape Variation Modelling at Early Design Stage’, *Procedia CIRP*., Vol.41, pp. 1072–1077.

Davies, C. (2004) *Bonded Structures Industry Survey*. Sussex: FAA Technical Center. Available at: https://www.niar.wichita.edu/niarworkshops/Portals/0/Oct26_0900_Survey_CurtD.pdf (Accessed: 8 April 2016).

Engström, M. (2015) *LoCoMACHS Project*

Falgarone, H., Thiébaut, F., Coloos, J. and Mathieu, L. (2016) ‘Variation simulation during assembly of non-rigid components. Realistic assembly simulation with ANATOLEFLEX software’, *Procedia CIRP*, 43 Elsevier B.V., pp. 202–207.

Favrelière, H. (2009) *Tolérancement Modal: De la Métrologie vers les Spécifications*. Université de Savoie.

Gentilini, I. and Shimada, K. (2011) ‘Computer-Aided Design Predicting and evaluating the post-assembly shape of thin-walled components via 3D laser digitization and FEA simulation of the assembly process’, *Computer-Aided Design*, 43(3) Elsevier Ltd, pp. 316–328.

GOM (2019) *Virtual Part Clamping - A Quantum Leap Forward (trade magazine article).*, *Metrology News* Available at: https://metrology.news/virtual-part-clamping-a-quantum-leap-forward/ (Accessed: 11 May 2019).

Hammett, P., Baron, J. and Smith, D. (1999) *Automotive Body Measurement*

System Capability. Auto/Steel Partnership report. Southfield. Available at: http://www-personal.umich.edu/~phammett/Papers/asp-meas-rept.PDF (Accessed: 5 May 2016).

Harrison, N. (1967) Fokker fellowship, *Flight International*, (15 June), pp. 977–984.

Hart-Smith, L.J. (1980) ‘Adhesive Bonding of Aircraft Primary Structures’, *SAE Transactions*, 89, pp. 3718–3782.

Hart-Smith, L.J. and Strindberg, G. (1997) ‘Developments in adhesively bonding the wings of the SAAB 340 and 2000 aircraft’, *Proceedings of the Institution of Mechanical Engineers, Part G: Journal of Aerospace Engineering*, 211, pp. 133–156.

Henkel (2005) *Hysol EA 9380 Assembly Paste Product Guide*. Available at: http://associatedindustriesinc.com/documents/henkel/adhesives-composite/Hysol EA9380 Guide.pdf (Accessed: 2 August 2018).

Higgins, A. (2000) ‘Adhesive bonding of aircraft structures’, *International Journal of Adhesion and Adhesives*, 20, pp. 367–376.

Hsieh, C.C. and Oh, K.P. (1997a) ‘Simulation and optimization of assembly processes involving flexible parts’, *International Journal of Vehicle Design*, 18(5), pp. 455–465.

Hsieh, C.C. and Oh, K.P. (1997b) ‘A framework for modelling variation in vehicle assembly processes’, *International Journal of Vehicle Design*, 18(5), pp. 466–473.

Hu, S.J. (1997) ‘Stream-of-Variation Theory for Automotive Body Assembly’, *Annals of the CIRP*, 46(1)

Huang, N.E., Shen, Z., Long, S.R., Wu, M.C., Shih, H.H., Zheng, Q., Yen, N.-C., Tung, C.C. and Liu, H.H. (1998) ‘The Empirical Mode Decomposition and the Hilbert Spectrum for Nonlinear and Non-Stationary Time Series Analysis’, *Proceedings of the Royal Society of London A*., pp. 903–995.

Huang, W. and Kong, Z. (2008) ‘Simulation and integration of geometric and rigid body kinematics errors for assembly variation analysis’, *Journal of Manufacturing Systems*, 27(1) The Society of Manufacturing Engineers, pp. 36–44.

Huang, W., Liu, J., Chalivendra, V., Ceglarek, D., Kong, Z. and Zhou, Y. (2014) ‘Statistical modal analysis for variation characterization and application in manufacturing quality control’, *IIE Transactions*, 46(5)

Hubert, P. and Poursartip, A. (1998) ‘A Review of Flow and Compaction Modelling Relevant to Thermoset Matrix Laminate Processing’, *Journal of Reinforced Plastics and Composites*, 17(4), pp. 286–318.

Jaramillo, A.E., Boulanger, P. and Prieto, F. (2011) ‘On-line 3-D system for the inspection of deformable parts’, *International Journal of Advanced Manufacturing Technology*, (57), pp. 1053–1063.

Jaramillo, A.E., Prieto, F. and Boulanger, P. (2013) ‘Fixtureless Inspection of Deformable Parts Using Partial Captures’, *International Journal of Precision Engineering and Manufacturing*, 14(1), pp. 77–83.

Karganroudi, S.S., Cuillière, J.-C., Francois, V. and Tahan, S.-A. (2016) ‘Automatic fixtureless inspection of non-rigid parts based on filtering registration points’, *International Journal of Advanced Manufacturing Technology*

Kennedy, M.C. and O’Hagan, A. (2001) ‘Bayesian calibration of computer models’, *Journal of the Royal Statistical Society B*, 63(3), pp. 425–464.

Kern, D.C. (2003) *Forecasting Manufacturing Variation Using Historical Process Capability Data: Applications for Random Assembly, Selective Assembly, and Serial Processing*. Massachusetts Institute of Technology.

Land, K.L. and Lennert, F.B. (1979) *Primary Adhesively Bonded Structure Technology (PABST). Phase III: Tooling, Fabrication and Quality Assurance. USAF report AFFDL-TR-79-3154*.

Lindau, B., Andersson, A., Lindkvist, L. and Söderberg, R. (2012) ‘Body in white geometry measurements of non-rigid components: A virtual perspective’, *Proceedings of the ASME 2012 International Design Engineering Technical Conferences & Computers and Information in Engineering Conference*. Chicago, IL, USA.

Lindau, B., Lorin, S., Lindkvist, L. and Söderberg, R. (2016) 'Efficient Contact Modeling in Nonrigid Variation Simulation', *Journal of Computing and Information Science in Engineering*, 16(March), pp. 1–7.

Lindau, B., Wärmefjord, K., Lindkvist, L. and Söderberg, R. (2013) 'Aspects of fixture clamp modeling in non-rigid variation simulation of sheet metal assemblies', *Proceedings of the ASME 2013 International Mechanical Engineering Congress and Exposition*. San Diego, California, USA.

Lindkvist, L., Wärmefjord, K. and Söderberg, R. (2008) 'Tolerance simulation of compliant sheet metal assemblies using automatic node-based contact detection', *Proceedings of IMECE2008 2008 ASME International Mechanical Engineering Congress and Exposition October 31-November 6, 2008, Boston, Massachusetts, USA*.

Liu, G., Tang, W., Ke, Y.-L., Chen, Q.-L. and Bi, Y. (2014) 'Modeling of fast pre-joining processes optimization for skin-stringer panels', *Assembly Automation*, 34(4), pp. 323–332.

Liu, G., Tang, W., Ke, Y., Chen, Q. and Chen, X. (2015) 'Pre-joining process planning model for a batch of skin – stringer panels based on statistical clearances', *International Journal of Advanced Manufacturing Technology*, 78, pp. 41–51.

Liu, S.C. and Hu, S.J. (1997) 'Variation Simulation for Deformable Sheet Metal Assemblies Using Finite Element Methods', *Journal of Manufacturing Science and Engineering*, 119(3), pp. 368–374.

Liu, Y.G. and Hu, S.J. (2016) 'Assembly Fixture Fault Diagnosis Using Designated Component Analysis', *Journal of Manufacturing Science and Engineering*, 127, pp. 358–368.

Lorin, S. and Lindkvist, L. (2014) 'Variation Simulation of Stresses Using the

Method of Influence Coefficients', *Journal of Computing and Information Science in Engineering*, 14(March)

Lorin, S., Lindkvist, L., Söderberg, R. and Sandboge, R. (2013) 'Combining Variation Simulation With Thermal Expansion Simulation for Geometry Assurance', *Journal of Computing and Information Science in Engineering*, 13

Madrid, J., Vallhagen, J., Söderberg, R. and Wärmefjord, K. (2016) 'Enabling reuse of inspection data to support robust design : a case in the aerospace industry', *Procedia CIRP*, 43 Elsevier B.V., pp. 41–46.

Mansuy, M. (2012) *Aide au tolérancement tridimensionnel: modèle des domaines*. Université Grenoble Alpes.

Maropoulos, P.G., Muelaner, J.E., Summers, M.D. and Martin, O.C. (2013) 'A new paradigm in large-scale assembly—research priorities in measurement assisted assembly', *The International Journal of Advanced Manufacturing Technology*, 70(1–4), pp. 621–633.

Maropoulos, P.G., Vichare, P., Martin, O., Muelaner, J., Summers, M.D. and Kayani, A. (2011) 'Early design verification of complex assembly variability using a Hybrid – Model Based and Physical Testing – Methodology', *CIRP Annals - Manufacturing Technology*, 60, pp. 207–210.

Matuszyk, T.I. (2008) *Shape Characterisation of Sheet Metal Assembly Variation with a View to Quality Assessment and Dimensional Control*. Australian National University.

Matuszyk, T.I., Cardew-Hall, M.J. and Rolfe, B.F. (2010) 'The kernel density estimate/point distribution model (KDE-PDM) for statistical shape modeling of automotive stampings and assemblies', *Robotics and Computer Integrated Manufacturing*, 26 Elsevier, pp. 370–380.

Merkley, K.G. (1998) *Tolerance analysis of compliant assemblies, PhD Thesis*. Brigham Young University.

Morris, B.A. and Scherer, J.M. (2016) 'Modeling and experimental analysis of squeeze flow of sealant during hot bar sealing and methods of preventing squeeze-out', *Journal of Plastic Film & Sheeting*, 32(1), pp. 34–55.

Myronenko, A. and Song, X. (2010) 'Point Set Registration : Coherent Point Drift', *IEEE Transactions on pattern analysis and machine intellicence*, 32(12), pp. 2262–2275.

Naing, S., Burley, G., Odi, R. and Corbett, J. (2001) 'Design for jigless assembly - Case study of a civil airliner fixed leading edge', *42nd AIAA/ASME/ASCE/AHS/ASC Structures, Structural Dynamics, and Materials Conference and Exhibit*. Seattle: AIAA.

van der Neut, A. (1974) 'Some experiences in aircraft structures', *Engineering Fracture Mechanics*, 6, pp. 609–617.

Nobis, H., Roeglin, W., Bischoff, O. and Schroeder, A. (2010) *Method for autoclave-free adhesive bonding of components for aircraft. Patent EP1984241 (B1)*.

Pahkamaa, A., Wärmefjord, K., Karlsson, L., Söderberg, R. and Goldak, J. (2012) 'Combining Variation Simulation With Welding Simulation for Prediction of Deformation and Variation of a Final Assembly', *Journal of Computing and Information Science in Engineering*, 12(June 2012), pp. 1–6.

Pahkamaa, A., Wärmefjord, K., Karlsson, L., Söderberg, R. and Goldak, J. (2010) 'Combining Variation Simulation with Welding Simulation for Prediction of Deformation', *Proceedings of the ASME 2010 International Mechanical Engineering Congress & Exposition*. Vancouver: ASME, pp. 1–7.

Pethrick, R.A. (2012) 'Welding and Joining of Aerospace Materials', in *Welding and Joining of Aerospace Materials*. Elsevier, pp. 288–319. Available at: 10.1533/9780857095169.2.288 (Accessed: 12 November 2015).

Préau, M. and Hubert, P. (2016) 'Bonded Repairs of Composite Structures : Void Formation Mechanisms in an Adhesive Film', *17th European Conference on Composite Materials*. Munich, pp. 26–30.

Qian, Z. and Wu, J. (2008) ‘Bayesian Hierarchical Modeling for Integrating Low-accuracy and High-accuracy Experiments’, *Technometrics*, 50(2), pp. 192–204.

Räckers, B. (2004) *Bonding Processes at Airbus*

Radvar-Esfahlan, H. and Tahan, S.-A. (2012) ‘Nonrigid geometric metrology using generalized numerical inspection fixtures’, *Precision Engineering*, 36 Elsevier Inc., pp. 1–9.

Radvar-Esfahlan, H. and Tahan, S.-A. (2014) ‘Robust generalized numerical inspection fixture for the metrology of compliant mechanical parts’, *International Journal of Advanced Manufacturing Technology*, 70, pp. 1101–1112.

Ravishankar, S., Dutt, H.N. V and Gurumoorthy, B. (2010) ‘Automated inspection of aircraft parts using a modified ICP algorithm’, *International Journal of Advanced Manufacturing Technology*, 46, pp. 227–236.

Sabri, V., Sattarpanah, S., Tahan, S.A., Cuillière, J.C., François, V. and Pham, X.T. (2017) ‘A robust and automated FE-based method for fixtureless dimensional metrology of non-rigid parts using an improved numerical inspection fixture’, *International Journal of Advanced Manufacturing Technology*, 92 The International Journal of Advanced Manufacturing Technology, pp. 2411–2423.

Sacharow, A., Balzer, J., Biermann, D. and Surmann, T. (2011) ‘Non-rigid isometric ICP: A practical registration method for the analysis and compensation of form errors in production engineering’, *Computer Aided Design*, 43 Elsevier Ltd, pp. 1758–1768.

Samper, S. (2007) *Tolérancement et analyse des structures au service des systèmes souples et du défaut de forme*.

Samper, S. (2009) *Monographie sur le tolérancement modal*.

Schweinoch, M., Schäfer, R., Sacharow, A., Biermann, D. and Buchheim, C. (2016) ‘A non-rigid registration method for the efficient analysis of shape deviations in production engineering applications’, *Production Engineering*, 10, pp. 137–146.

Smiley, A.J., Chao, M. and Gillespie Jr, J.W. (1991) ‘Influence and control of bondline thickness in fusion bonded joints of thermoplastic composites’, *Composite Structures*, 2(3/4), pp. 223–232.

Söderberg, R., Wärmefjord, K. and Lindkvist, L. (2015) ‘Variation simulation of stress during assembly of composite parts’, *CIRP Annal*, 64, pp. 17–20.

Stricher, A. (2013) *Tolérancement flexible d’assemblages de grandes structures aéronautiques, PhD Thesis*. École normale supérieure de Cachan.

Textron (2004) *Structural Metal Bonding At Cessna Aircraft*

Thiébaut, F. (2016) *Vers une prise en compte de la géométrie des composants déformables durant l’assemblage*. Cachan, France.

Tomblin, J., Strole, K., Dodosh, G. and Ilcewicz, L. (2005) *Assessment of Industry Practices for Aircraft Bonded Joints and Structures. FAA report DOT/FAA/AR-05/13*. Available at: http://www.tc.faa.gov/its/worldpac/techrpt/ar0513.pdf (Accessed: 2 March 2016).

Ungemach, G. and Mantwill, F. (2009) ‘Efficient Consideration of Contact in Compliant Assembly Variation’, *Journal of Manufacturing Science and Engineering*, 131(February)

Velupillai, D. and Hall, T. (1979) Citation III: technical description, *Flight International*, (24 November), pp. 1761–1766.

Voto, C. (2004) *Alenia Experience in Metal Bonding*

Wärmefjord, K., Söderberg, R., Lindau, B., Lindkvist, L. and Lorin, S. (2016) ‘Joining in Nonrigid Variation Simulation’, in Udroiu, R. (ed.) *Computer-aided Technologies - Applications in Engineering and Medicine*. IntechOpen, pp. 41–68.

Weckenmann, A., Gall, P. and Gabbia, A. (2005) ‘3D surface coordinate inspection of formed sheet material parts using optical measurement systems and virtual distortion compensation’, *Proceedings of SPIE*., Vol.5776, pp. 640–647.

Weckenmann, A., Kraemer, P. and Hoffmann, J. (2007) 'MANUFACTURING METROLOGY – STATE OF THE ART AND PROSPECTS', *9th International Symposium on Measurement and Quality Control*.

Whitney, D.E., Mantripragada, R., Adams, J.D. and Rhee, S.J. (1999) 'Designing Assemblies', *Research in Engineering Design*, 11(4), pp. 229–253.

Wriggers, P. (2006) *Computational Contact Mechanics*.Second Ed. Heidelberg: Springer-Verlag.

Young, W.C. and Budynas, R.G. (2002) *Roark's Formulas for Stress and Strain*.Seventh Ed.Hager, L. (ed.) New York: McGraw-Hill.

APPENDICES

Appendix A — Derivation of the 1D squeeze-flow closed-form solution

The following is adapted from the thorough explanation of the initial model setup in two of the references used (Morris and Scherer, 2016; Smiley, Chao and Gillespie Jr, 1991). The literature surveyed did not spell out the path from the fundamental equations to the final result; thus, the intermediate steps have been traced and are laid out in this appendix for the reader's benefit. Each individual step is not carried out in detail, but all combinations of boundary conditions and equations are made explicit.

A.1 Assumptions

The assumptions are as laid out in the section in the main body of the thesis:

(a) The uncured adhesive behaves as an incompressible, purely-viscous Newtonian fluid.
(b) Each layer of carrier fabric acts as a solid boundary and the layers of adhesive under and above it act as different flow domains.
(c) Both adherends can be approximated as flat and parallel for flow purposes.
(d) The problem is quasi-steady, and dominated by viscous forces with a very low Reynolds number; thus, effects of inertia and accelerations are negligible (quasi-static force equilibrium applies).
(e) Flow only takes place in the cross-section plane without any longitudinal component.
(f) Adhesive flows freely once squeezed out from between adherends.

(Assumption (e) is reasonable only if the length range λ over which gap variations appear is much greater than the cross-section flow domain width w; that is, $\lambda \gg w$. As seen in the experimental section of the thesis, this is not always true, which will result in a more complex flow pattern.)

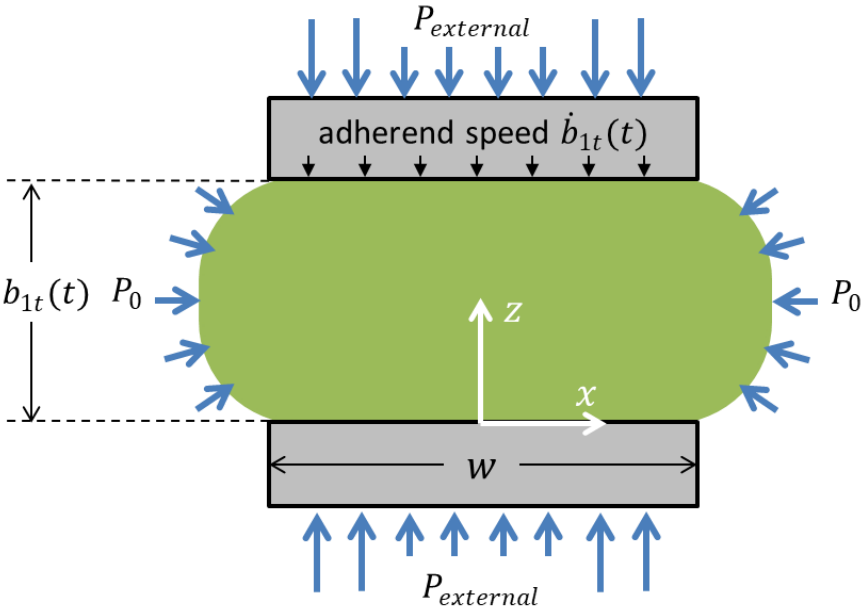

Figure A-1. Flow dimensions, loads and reference frame (thickness b_{t1} exaggerated for clarity).

A.2 Starting equations

From the assumptions above and applying continuity (conservation of mass and momentum):

$$\int_0^{b_{1t}} v_x(x,z)\,dz \;=\; \dot{b_{1t}}\;x \quad \forall x \in (-w/2, +w/2) \tag{A-1}$$

$$\frac{\partial v_x}{\partial x} + \frac{dv_z}{dz} = 0 \tag{A-2}$$

$$-\frac{dp}{dx} + \eta\,\frac{\partial^2 v_x}{\partial z^2} = 0 \tag{A-3}$$

$$-\frac{\partial p}{\partial z} = 0 \tag{A-4}$$

with the following boundary conditions:

$$\frac{\partial v_x}{dz}(z = b_{1t}) \;=\; 0 \tag{A-5}$$

$$v_x(z=0) = v_x(z = b_{1t}) \;=\; 0 \tag{A-6}$$

$$p(x = \pm w/2) = P_0 \tag{A-7}$$

$$v_z(z = b_{1t}) = \dot{b_{1t}} \;\; ; \quad v_z(z = 0) = 0 \qquad \textbf{(A-8)}$$

$$b_{1t}(t = 0) = b_0 \qquad \textbf{(A-9)}$$

in addition to symmetry around $x = 0$.

Additionally, by force equilibrium (given the quasi-steady, low-inertia assumption), the external and internal forces on each cross-section[xli] are balanced such that

$$\int_{-w/2}^{w/2} p \, dx = P_{external} \, w \qquad \textbf{(A-10)}$$

Equation (A-1) is especially worth highlighting, as it is marks the difference with a Hagen–Poiseuille flow (which is pressure-driven through a channel with time-independent cross-section). The equation is linked to how the fluid is displaced along the x direction and out of the flow domain by the downward displacement of the top boundary. This means that the volumetric flow is not uniform at each x section (as it would in a textbook Hagen-Poiseuille), but rather increases constantly, from no flow at $x = 0$, to maxima at $x = \pm w/2$.

Further to the above, it is worth noting that w is constant and equal to the smallest adherend's width; $P_{external}$, P_0 are assumed constant in time and space (which does not necessarily reflect all bonding cycles and tooling); and b_{1t} is constant over x owing to the assumption of flat parallel plates.

A.3 Deriving the bondline evolution

The equations in the prior section will allow solution of the squeeze-flow problem for viscous flow between flat parallel boundaries within each slender 2D cross-section.

First, by integrating (A-3) and applying the boundary conditions in (A-6):

$$v_x = \frac{-1}{2\eta} \frac{\partial p}{\partial x} z \, (b_{1t} - z) \qquad \textbf{(A-11)}$$

[xli] It is evident that due to the existence of adherend deflections, there will also be forces transmitted between neighbouring cross-sections. These are neglected in the flow modelling — a necessary assumption for reaching a closed-form solution without needing fluid-structure interaction (FSI).

Combining (A-11) with the flow due to squeeze (A-1) yields the pressure head:

$$\frac{\partial p}{\partial x} = 12\eta \, \frac{\dot{b_{1t}}}{b_{1t}^3} \, x \qquad \textbf{(A-12)}$$

By integrating the pressure head from (A-12) and with boundary condition (A-7), the pressure at an x position is obtained:

$$p - P_0 = 6\eta \, \frac{\dot{b_{1t}}}{b_{1t}^3} \left(x^2 - \left(\frac{w}{2}\right)^2 \right) \qquad \textbf{(A-13)}$$

The velocity profile can be cleared by substituting the pressure head from (A-12) into (A-11), although this is not a necessary step for bondline calculation:

$$v_x = 6 \, \frac{-\dot{b_{1t}}}{b_{1t}^3} \, z \, (b_{1t} - z) \, x \qquad \textbf{(A-14)}$$

With (A-13) and force equilibrium (A-10), the instantaneous gap closure rate is cleared:

$$\dot{b_{1t}} = \frac{-\,(P_{external} - P_0)}{\eta} \, \frac{b_{1t}^3}{w^2} \qquad \textbf{(A-15)}$$

Finally, integrating (A-15) and with the starting thickness boundary condition (A-9), the closed-form solution is reached:

$$b_{1t}(t) = \left(\frac{2(P_{external} - P_0)}{w^2} \int_0^t \eta^{-1} dt + \frac{1}{b_0^2} \right)^{-1/2} \qquad \textbf{(A-16)}$$

A.4 Useful results of pressure and velocity distribution

By substituting the instantaneous gap closure rate from (A-15), some of the other variables can be made time-independent. Thus, the pressure distribution (A-13) becomes

$$p = P_0 + \frac{3}{2}(P_{external} - P_0)\left(1 - \left(\frac{x}{w/2}\right)^2\right) \qquad \textbf{(A-17)}$$

and the maximum pressure in the bondline, at $x = 0$, is $P_0 + 3/2\ (P_{external} - P_0)$.

Similarly, the x-velocity profile (A-14) becomes

$$v_x = -6\frac{(P_{external} - P_0)}{\eta}\frac{z\,(b_{1t} - z)}{w^2}x \qquad \textbf{(A-18)}$$

which, through conservation of mass (A-2) and boundary condition (A-6), gives the z-velocity

$$v_z \;=\; -\,6\,\frac{(P_{external} - P_0)}{\eta\,w^2}\,z^2\left(\frac{1}{2}b_{1t} - \frac{1}{3}z\right) \qquad \textbf{(A-19)}$$

The pressure and velocity are represented in Figure A-2.

Since $P_{external}$ and P_0 do not change during the curing cycle, (A-17) means that the pressure distribution will remain constant throughout the process until gelation is complete, with the rate of thickness reduction $\dot{b}_{1t}$ evolving to adjust. Thinner bondlines offer rapidly increasing flow resistance (note the cubic term in (A-15)), therefore the bondline thickness exhibits markedly asymptotic behaviour as cure time increases.

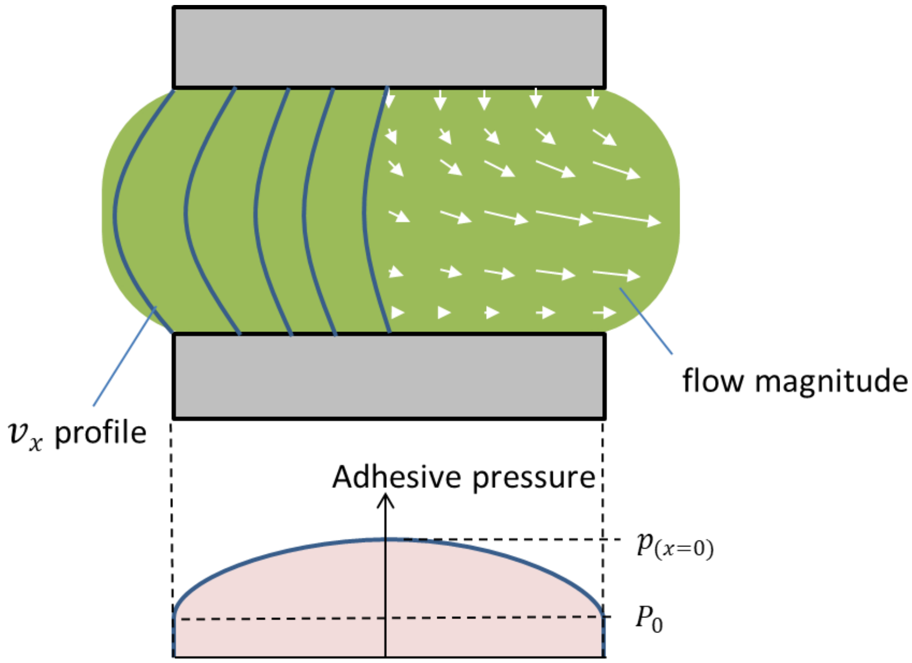

Figure A-2. 1D flow regimen in a single domain (thickness b_{t1} exaggerated for visibility).

Appendix B — Approaches to data fit

Very often, geometry data does not become available in a format that exactly accommodates pre-prepared meshes. This can be caused by procedure limitations (e.g. need for part fixturing which prevents inspection of some points), capability limitations (e.g. imperfect accuracy of measurement instrument positioning), or other practical considerations such as need to reuse sparse measurement data for dense mesh simulation.

When this was the case, geometries have been interpolated (and occasionally extrapolated at part edges) through numerical techniques which respect the consideration of geometric continuity. Incidentally, this is not the first thesis work that addresses the issue of data fit, and in this case the solutions used have been almost the same (Matuszyk, 2008), though in this case smoothing has been used.

B.1 1-D cubic spline

For cases where a single node was considered at each part length position (rather than modelling several points across the cord), a cubic spline was used. By definition, the spline satisfies the consideration of continuity and smoothness and follows all the inspected points. Cubic splines have been found to be robust to profile measurement error (Arenhart, 2009) and provide better (in this context, smoother) interpolation when compared to other options such as Gaussian filters.

The spline fit was carried out through the `spline` function in Matlab.

B.2 2-D thin-plate spline

To fit points scattered along more than one dimension on a surface, the fit was carried out using the `tpaps([x;y],z,1)` function in Matlab. This generates a surface through a linear combination of radial basis functions (RBF) $\phi(x, y)$ such that for a function centred around (x_j, y_j):

$$\phi_j(x,y) = \begin{cases} r_j^2 \log r_j & \text{if} \quad r_j > 0 \\ 0 & \text{if} \quad r_j = 0 \end{cases} \tag{B-1}$$

with $r_j^2 = (x - x_j)^2 + (y - y_j)^2$; the value of ϕ associated to $(0,0)$ is displayed in Figure B-1.

The surface is expressed as

$$z^{fit}(x,y) = \beta_0 + \beta_1 x + \beta_2 y + \sum \alpha_j \phi_j(x,y) \tag{B-2}$$

and the function minimises the deformation energy function $\mathrm{R}(z^{fit})$, while passing the control points exactly:

$$\mathrm{R}(z^{fit}) = \int\int \left[\left(\frac{\partial^2 z^{fit}}{\partial x^2} \right) + 2 \left(\frac{\partial^2 z^{fit}}{\partial xy} \right) + \left(\frac{\partial^2 z^{fit}}{\partial y^2} \right) \right] dxdy \tag{B-3}$$

This energy consideration being the reason for the name “thin plate”, which refers to the mechanical behaviour of a plate held at the knots $\{(x_j, y_j)\}$.

The coefficients are determined by solving the linear system

$$\begin{bmatrix} \mathbf{K} & \mathbf{P}^{\mathrm{T}} \\ \mathbf{P} & \mathbf{0} \end{bmatrix} \begin{pmatrix} \vec{\alpha} \\ \vec{\beta} \end{pmatrix} = \begin{pmatrix} \vec{z} \\ 0_{3\times 1} \end{pmatrix} \tag{B-4}$$

with

$$K_{i,j} = \phi_i(x_j, y_j) \quad ;$$

$$\mathbf{P} = \begin{bmatrix} 1 & 1 & \cdots & 1 \\ x_1 & x_2 & \cdots & x_N \\ y_1 & y_2 & \cdots & y_N \end{bmatrix} \tag{B-5}$$

B.2.1 Additional smoothing

In one case, it was known that inspection data had been rounded prior to reporting, thus generating an artificially jagged dataset. In this case, the third parameter was changed and `tpaps([x;y],z,p_smooth)` with $p_{smooth} \in (0,1)$ was used instead. This yields an approximate fit which does not necessarily pass through the knots, and minimises the function

$$\mathrm{H}(z^{fit}) = p_{smooth}\mathrm{E}(z^{fit}) + (1 - p_{smooth})\mathrm{R}(z^{fit}) \quad \textbf{(B-6)}$$

$\mathrm{R}(z^{fit})$ is the energy function in (B-3) above, and $\mathrm{E}(z^{fit})$ is an error measure

$$\mathrm{E}(z^{fit}) = \frac{1}{N}\sum_{j}^{j=N}\left[z_j^{fit} - z(x_j, y_j)\right]^2 \quad \textbf{(B-7)}$$

Therefore, p_{smooth} acts as a weighting factor where ($p_{smooth} = 1$) results in pure interpolation and ($p_{smooth} = 0$) yields a linear least-squares fit. The solution would be obtained by modifying the non-smoothing case (note that by increasing the diagonal of the matrix $\mathbf{K}$, a value $p_{smooth} < 1$ tends to help with ill-posed problems from noisy data):

$$\begin{bmatrix} \mathbf{K} + \dfrac{1 - p_{smooth}}{p_{smooth}}\mathbf{Id} & \mathbf{P}^{\mathrm{T}} \\ \mathbf{P} & \mathbf{0} \end{bmatrix} \begin{pmatrix} \vec{\alpha} \\ \vec{\beta} \end{pmatrix} = \begin{pmatrix} \vec{z} \\ 0_{3\times1} \end{pmatrix} \quad \textbf{(B-8)}$$

where $\mathbf{Id}$ is the identity matrix of the same size as $\mathbf{K}$.

In this case, only very local smoothing was required. The value of p_{smooth} used was in the [0.9, 1) range, such that the maximum of the absolute interpolation error at inspected points $\left|z_j^{fit} - z(x_j, y_j)\right|$ was less than the expected rounding error.

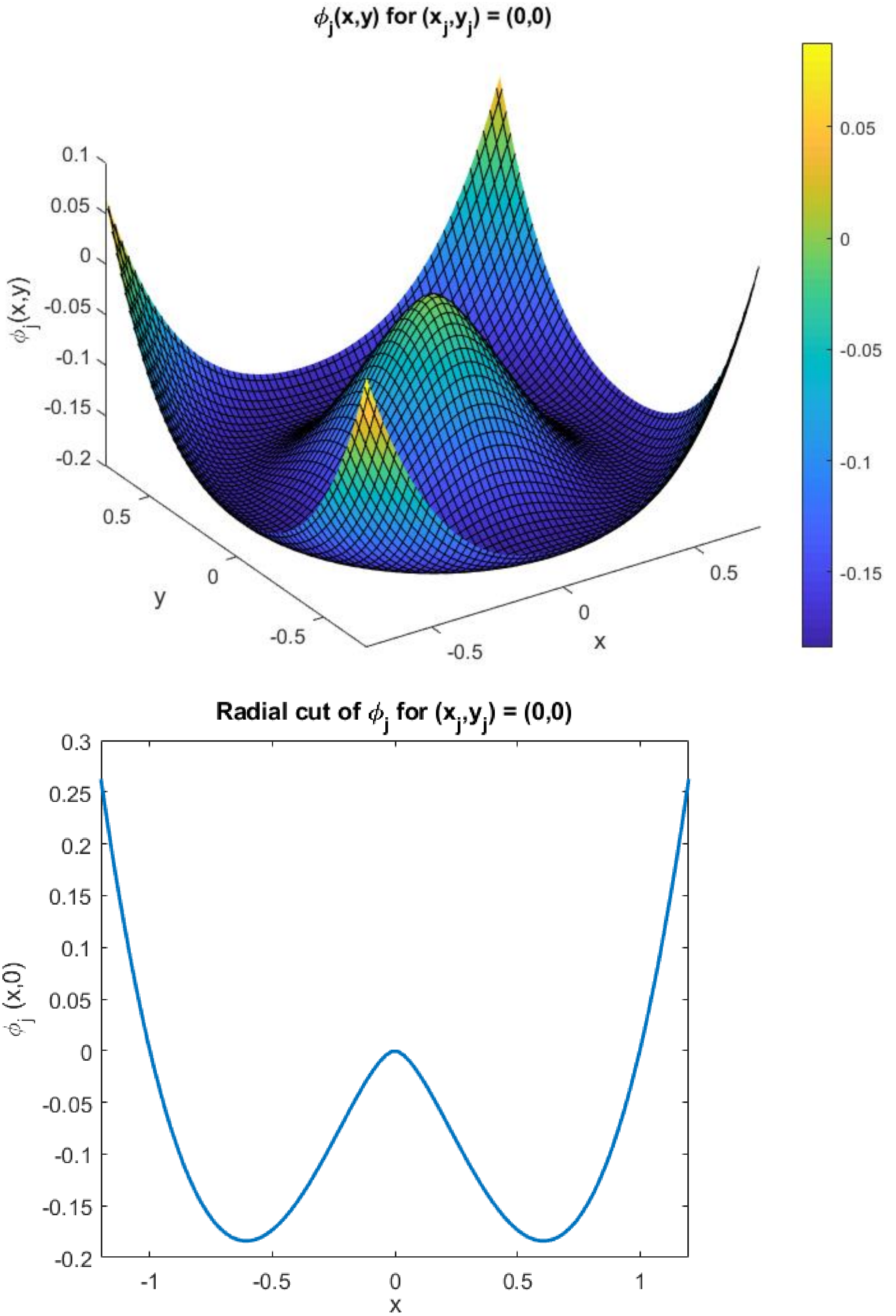

Figure B-1. Thin plate spline RBF with knots (0, 0) in three- and two-dimensional form. Note the quick growth as the radius increases.

B.3 Fitting measurements in multiple states

In the case of the curved test assemblies studied in Section 5.2 Curved test assemblies, parts were measured both after flat-state machining and after forming. The measurements were performed with different resolution and accuracy, and at the end of very different processes.

In order to capitalise on the higher-quality (denser and more precise) data from the unformed parts, which had been measured in a CMM, both sets of measurements were joined. The following steps, illustrated in Figure B-2, were followed:

1. Fit a “flat” thin plate spline through the unformed-state CMM-inspected interface points.
2. In the surface created, calculate the position of the points which would later be inspected after forming.
3. Calculate the displacement caused by forming, in the points measured after this step. These values will be the new form data.
4. Create another “form” thin plate spline using the deformations measured.
5. Add the “form” spline to the “flat” spline.

Thus

$$z_{flat}(x\,,y) = \mathrm{p_{flat}}(x\,,y), \qquad \mathrm{p_{flat}} = \mathrm{tpsfit}\left(X_{flat}\,,Y_{flat}\,,Z_{flat}\right) \tag{B-9}$$

$$\mathrm{p_{form}} = \mathrm{tpsfit}\left(X_{formed}\,,Y_{formed}\,,Z_{formed} - z_{flat}(X_{formed}\,,Y_{formed})\right) \tag{B-10}$$

$$z_{formed}(x\,,y) = \mathrm{p_{flat}}(x\,,y) + \mathrm{p_{form}}(x\,,y) \tag{B-11}$$

Where (X, Y, Z) are the coordinates of a measured point, (x, y, z) are the coordinates of a point fitted to the data, the subscript denotes the part state or process, and $\mathrm{tpsfit}(X, Y, Z)$ denotes the thin plate spline fit.

Two simplifications are made:

A. Assume the forming process does not modify any cross-section of the part; rather, the profile is deformed smoothly, and with a minimum wavelength that is much greater that the distance between form check points.

B. Measurement uncertainty is not evaluated in the procedure itself. It would be straightforward to incorporate into simulations by stochastic means.

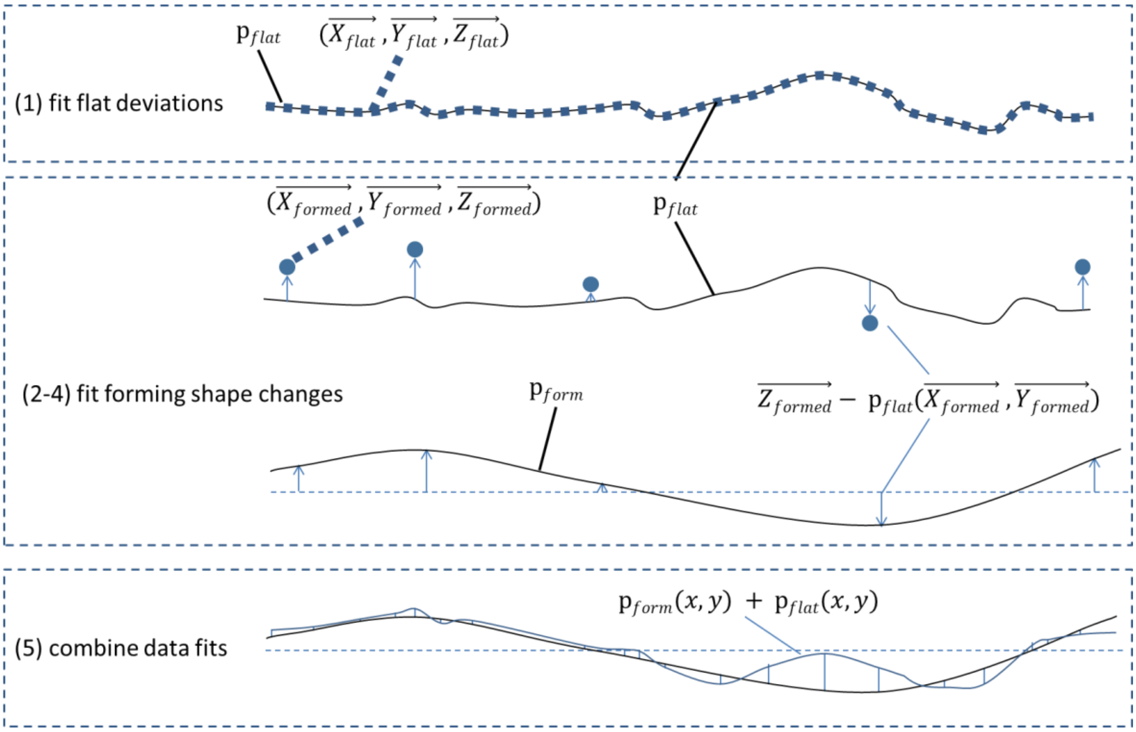

Figure B-2. Joining fine flat-profile and coarse formed-profile geometry data.

Appendix C — Curved assembly trial component manufacture

The exact manufacturing route, as well as details of the techniques used, cannot be disclosed as they include partner proprietary information. A general process flow is provided in Figure C-1, noting the inspection steps.

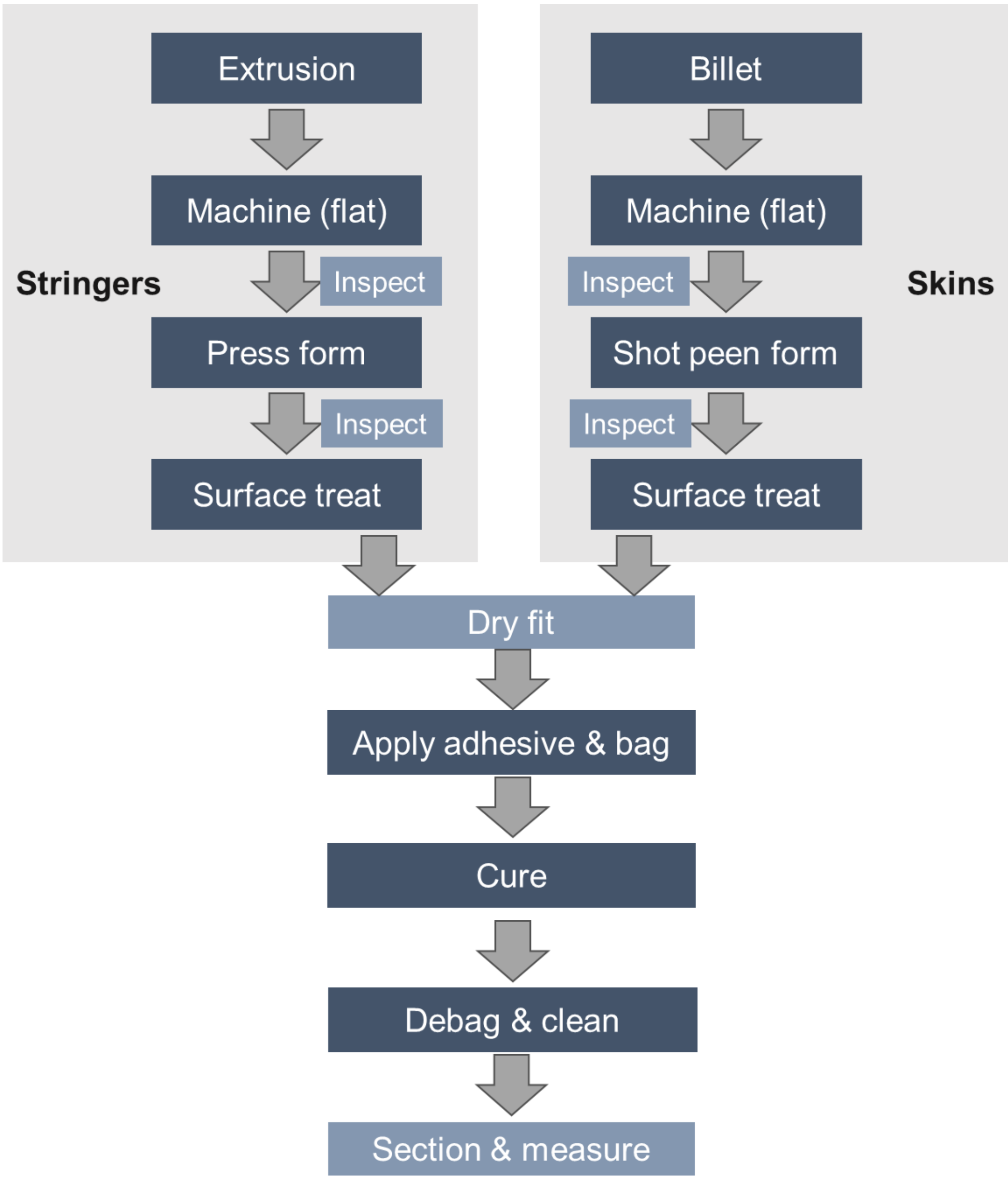

Figure C-1. General manufacturing flow for the curved assembly test articles.

C.1 Flat component inspection

Flat-machined parts were probed with a dense grid on a stationary CMM (Figure C-2). The maximum point spacing was 40 mm, which is less than 1/2 the shortest wavelength previously retained in part reconstruction from spectral components (for flat parts). The parts were fixtured lightly, supported on calibrated tooling blocks with clamping at the long edges.

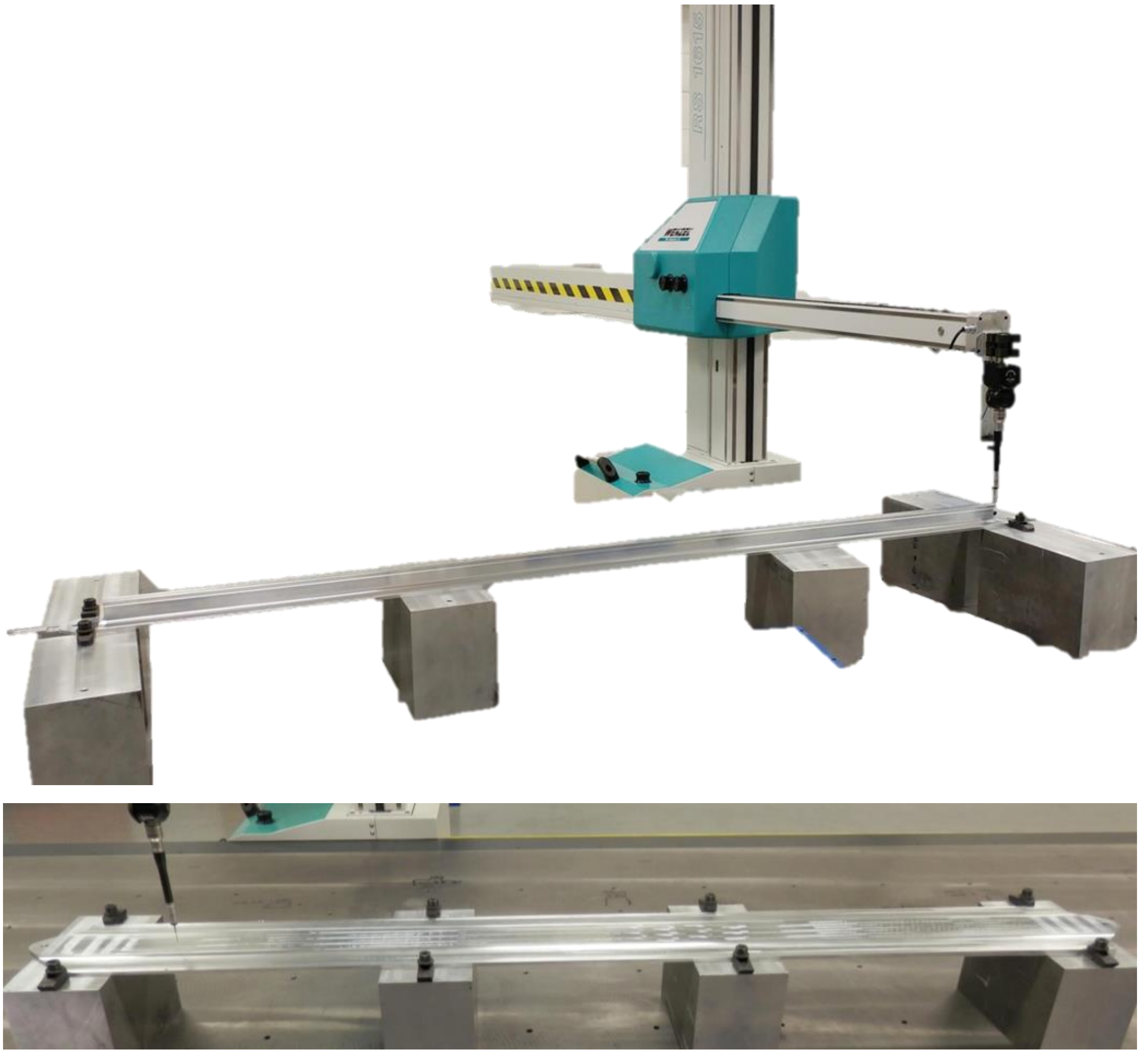

Figure C-2. CMM inspection of a flat (unformed) stringer (top) and skin (bottom). Note the skins required extra clamping to remain stable during inspection.

The stringers were inspected in two separate setups (for the top/bottom), while the skins were only inspected on the top (stringer-interfacing) surface. As the in-plane cross-section variation was found to be very small, further modelling of both parts assumed that the cross-section is invariable, and that the bond-interface deviation offers a sufficient descriptor of the profile variation. The points were fitted through an interpolating (non-smoothing) thin plate spline for further treatment; this also was used to estimate (by interpolation) the position of points at some locations which had been blocked by the clamping scheme.

C.2 Formed component inspection

Formed parts were placed on bespoke fixtures (Figure C-3), where the elements interfacing with the parts were machined to tight tolerances (<0.30 mm deviation range); their geometry was assessed by use of feeler gauges with a resolution of 0.05 mm. In the case of the stringers, measurement was performed with and without support boards in the length direction, and with and without external application of weight (Figure C-4).

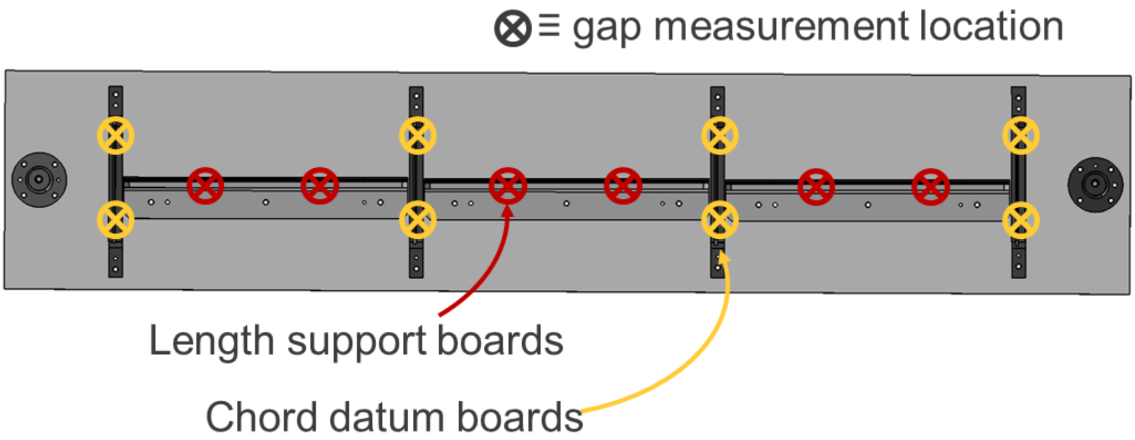

Figure C-3. Top view of the profile checking tool. Measurements were performed always using the chord boards (CB), and with and without length support boards.

Figure C-4. Formed part on a profile checking tool. Note the weights used to push the part onto the tool.

The effects observed, even without any treatment (Figure C-5), underscore two critical factors:

<u>Relevance of contact interaction with the inspection tool</u>: the tool-part gaps became smaller at the inspected locations when only chord support boards were used. The length-wise boards effectively ‘propped up’ the part. The effect was significant compared to the drawing tolerances, even though the development parts are simpler and shorter than anything full scale. On the other hand, sometimes parts were locally *overformed* to closely match profile errors in the tool. This highlights the dangers of overinspecting if tool quality is not tightly controlled; in this case, limiting the number of inspection points to a few, tightly controlled spots may have prevented misguided corrective action.

<u>Impact of external force application</u>: deviations from nominal before and after application of typical external forces through bags of weights —equivalent to less than 1% of a typical bonding pressure— were reduced by up to 0.10 mm, which is significant compared to the tolerance range. Twist error was also reduced substantially.
This outcome highlights the impact that a well-implemented ‘functional build’-type inspection can have on quality data and, by extension, manufacturability. Similarly, it shows that the forces applied need to be considered carefully when developing manufacture to tight dimensional requirements.

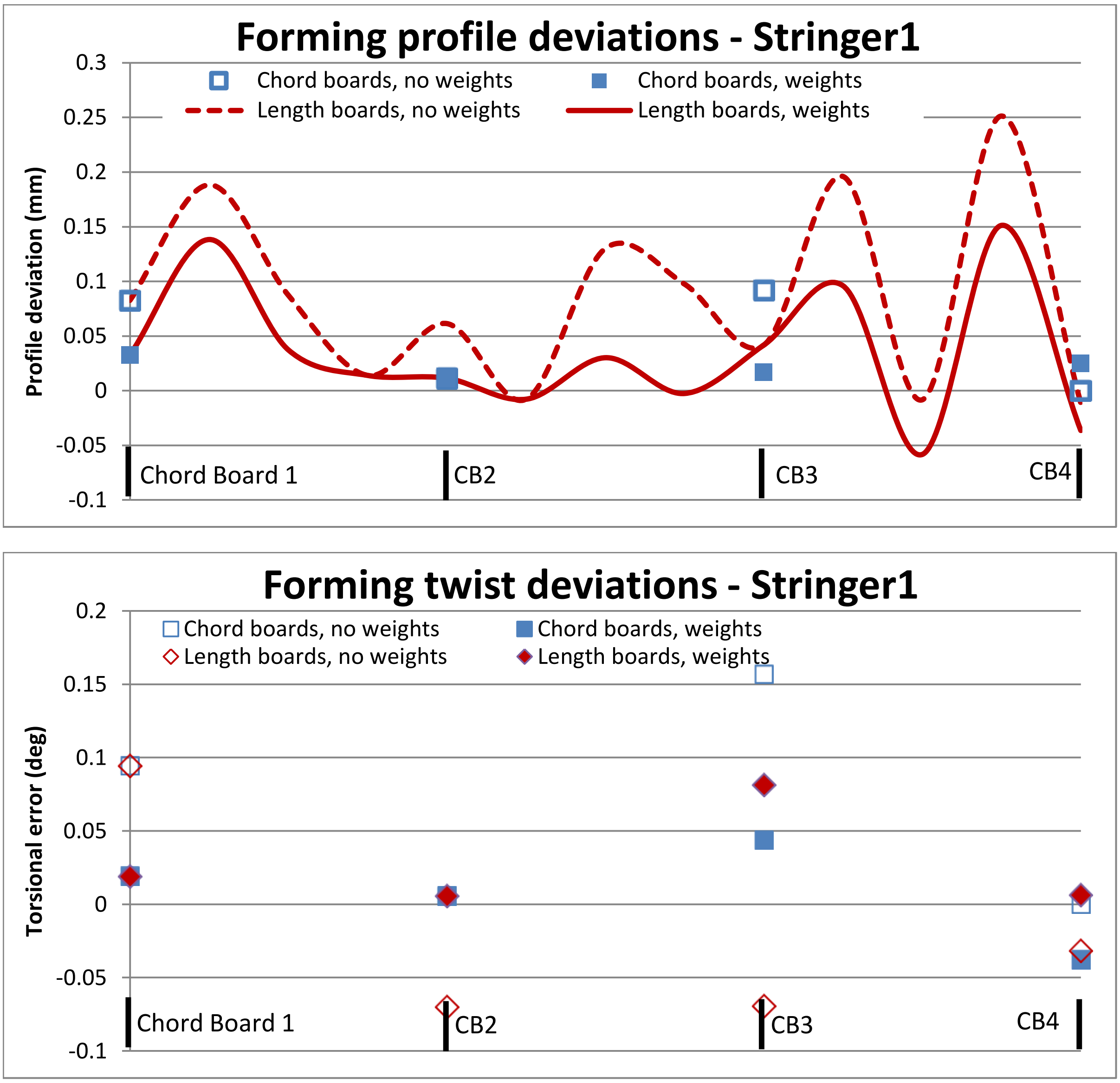

Figure C-5. Plot of measured deviations for the same formed stringer, with different boundary conditions. Note how adding contact through the length boards (red) tends to increase perceived deviations, whereas adding weights (solid) causes them to decrease.

Appendix D — Multi-stringer assembly manufacture

D.1 Parts manufacture

The stringers were manufactured from slightly over size off-the-shelf extrusions, requiring only three machining operations: removal of excess web height; machining of the tooling lug geometry and holes; and removal of excess material from the bottom of the (pre-deformed) foot flange (Figure D-1). All parts were scribed next to the datum hole for unequivocal identification (Figure D-2).

The proposed profile variation generation approach was realised through use of two sets of clamps: pre-machining deformation was introduced by pressing the stringer with finger clamps after placing prescribed spacers under the web (Figure D-3). The stringer was then held in place and its deformation was maintained by side clamps (upon which the finger clamps were retracted prior to machining). The side clamps pushed an auxiliary metal prism to hold the stringer in place (Figure D-4) to get around access limitations; as a result, the boundary conditions were not completely symmetric during machining of the bonding surface.

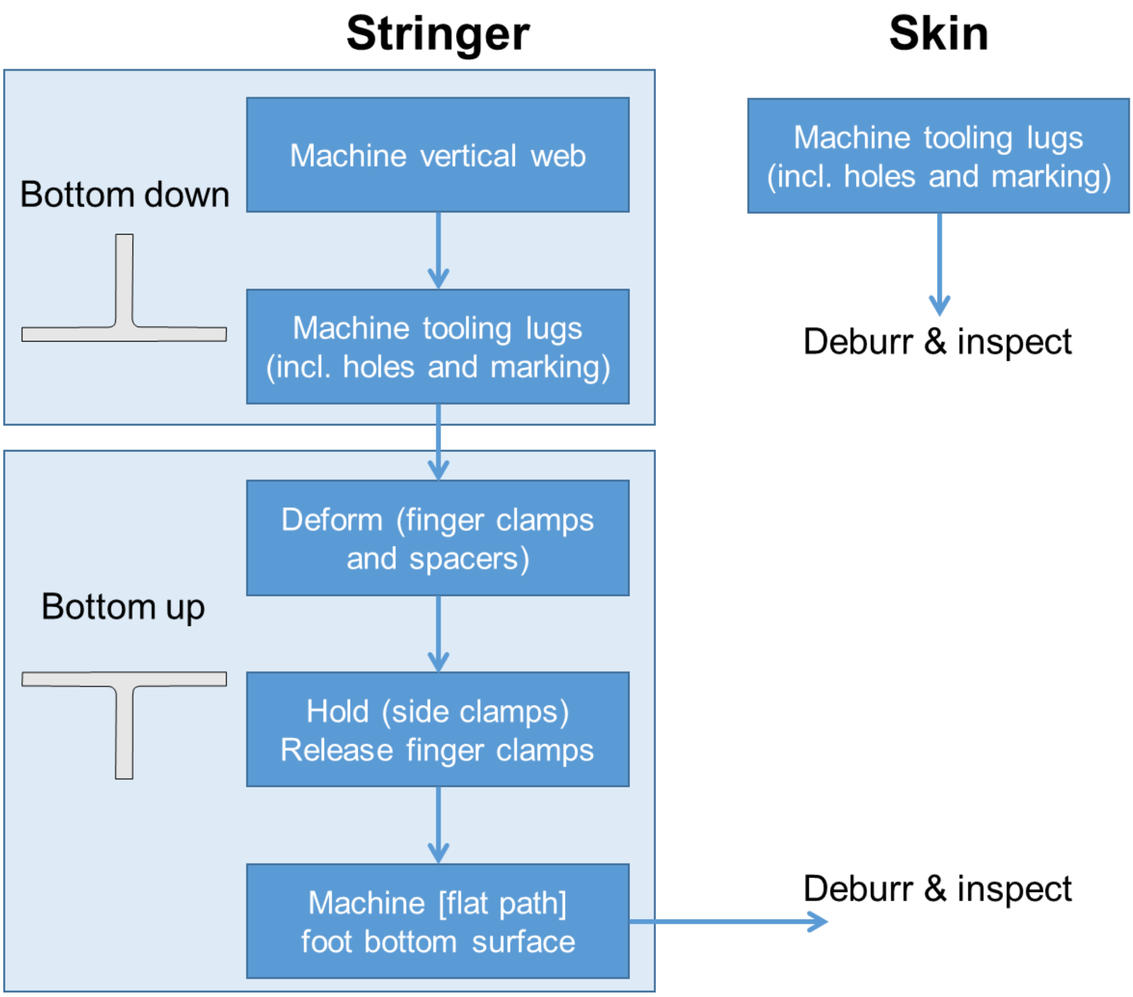

Figure D-1. Machining operations for the stringers and skin. The stringer deforming step was skipped for 4 stringers, providing a baseline of the untampered flat geometry.

The deform-machine-release approach proved capable, with results initially verified by calliper measurement of the foot thickness and visual inspection against a flat surface (Figure D-5), and later confirmed during CMM inspection.

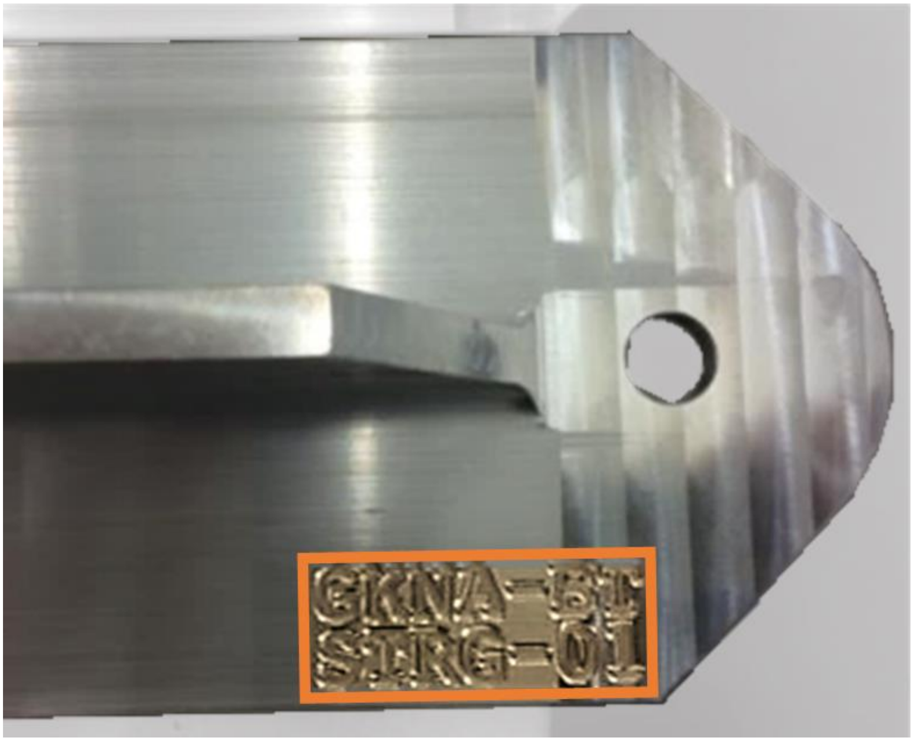

Figure D-2. Close-up of stringer datum hole with indelible labelling visible.

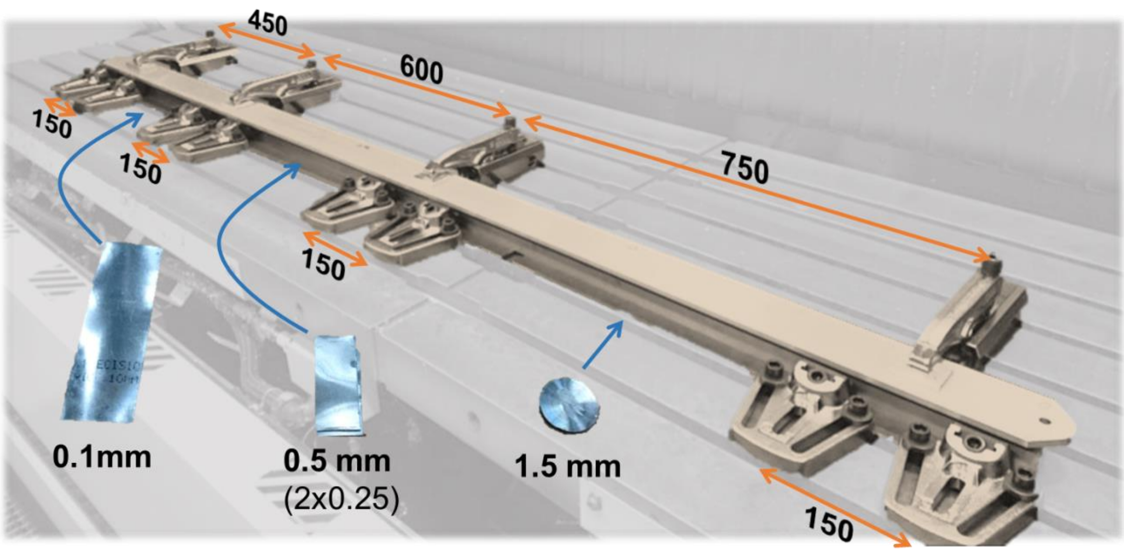

Figure D-3. Clamping scheme used to obtain localised variation. The stringers were deformed with the finger clamps, and then held in position with the side clamps during flat path machining. All separations are in mm.

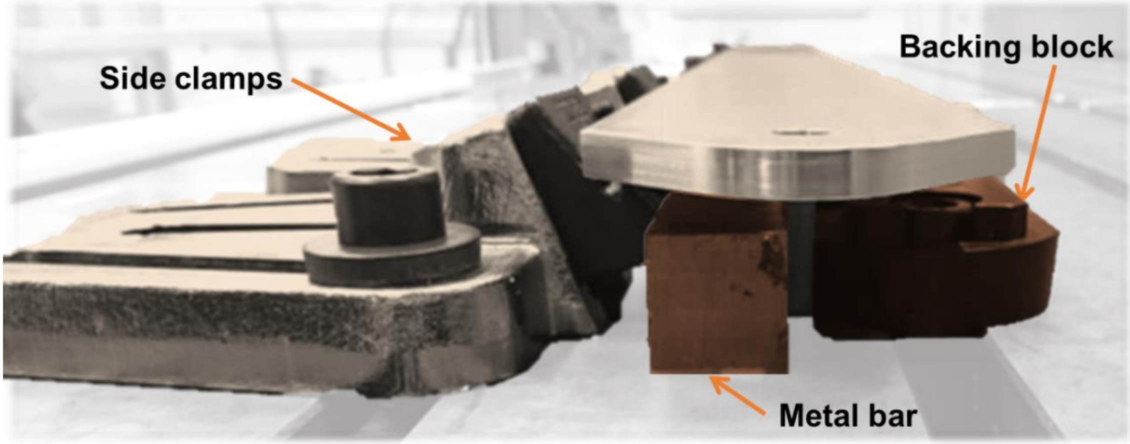

Figure D-4. Side view of the profile machining arrangement, with side clamps positioned to keep the deformed extrusion in place through an auxiliary metal prism. (Illustrative picture taken prior to clamping and machining of the foot surface.)

Figure D-5.The profile variation becomes evident when a deformed and non-deformed stringer are laid on a flat table (gap indicated by arrow).

Meanwhile, the skins required very limited machining from the stock rolled plates: the planar surfaces were left in the initial material condition and only the ends were machined to produce suitable tooling and identification features. The plate thickness deviated substantially from the 9 mm nominal, and was around 10.4 mm instead. As the thicker skin would lead to understated (rather than ‘overkill’) deflection, the impact was not expected to be detrimental to the trials. Thus, the new dimension was simply accepted without any additional material removal, and the model was updated accordingly.

D.2 Parts inspection

The dimensions were confirmed by CMM inspection in a minimally constrained state allowing single-setup inspection (Figure D-6), showing great repeatability of the stringer cross-section dimensions even if the gravity-deflected values fluctuated noticeably. The foot profile is not completely symmetrical (as apparent in the illustrative plot in Figure D-9) because the side clamps used during machining were all positioned on one side of the part for access reasons.

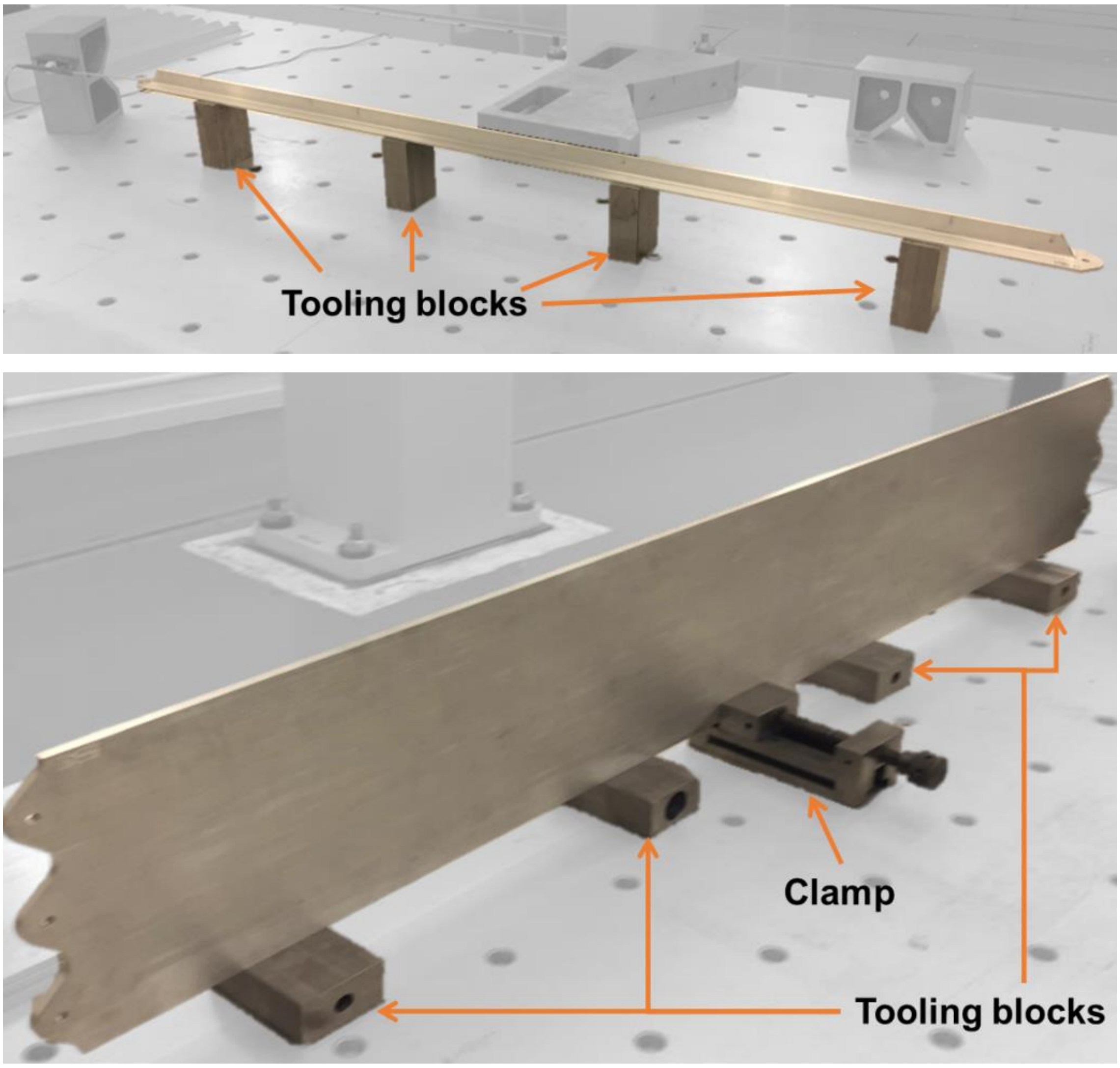

Figure D-6. Measurement setup for single-setup measurement of the stringers (top) and skins (bottom).

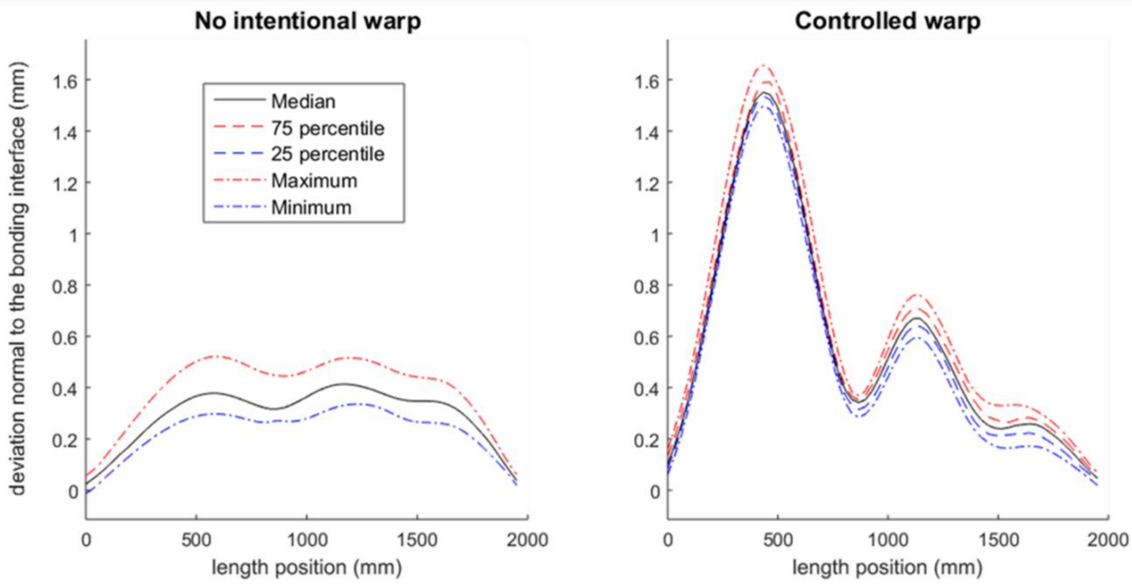

Figure D-7. Stringer foot bottom profile variation (as-inspected), for stringers with and without added deformation. There are no 1st/3rd quartile for the ones without since only four (4) such stringers were made.

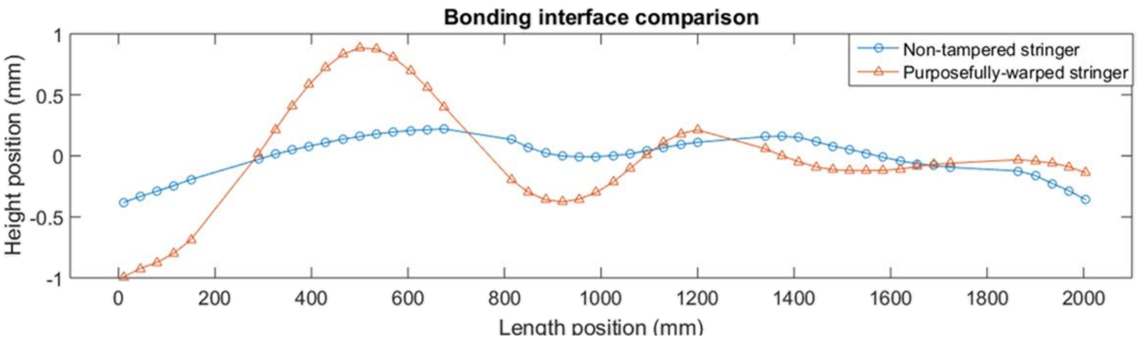

Figure D-8. CMM results for the bonding surface geometry (right below the web, width position =0) of a stringer with and without pre-machining deformation (stringer numbers 01 and 03, respectively). Missing points correspond to support blocks' positions, and were subsequently estimated by interpolation.

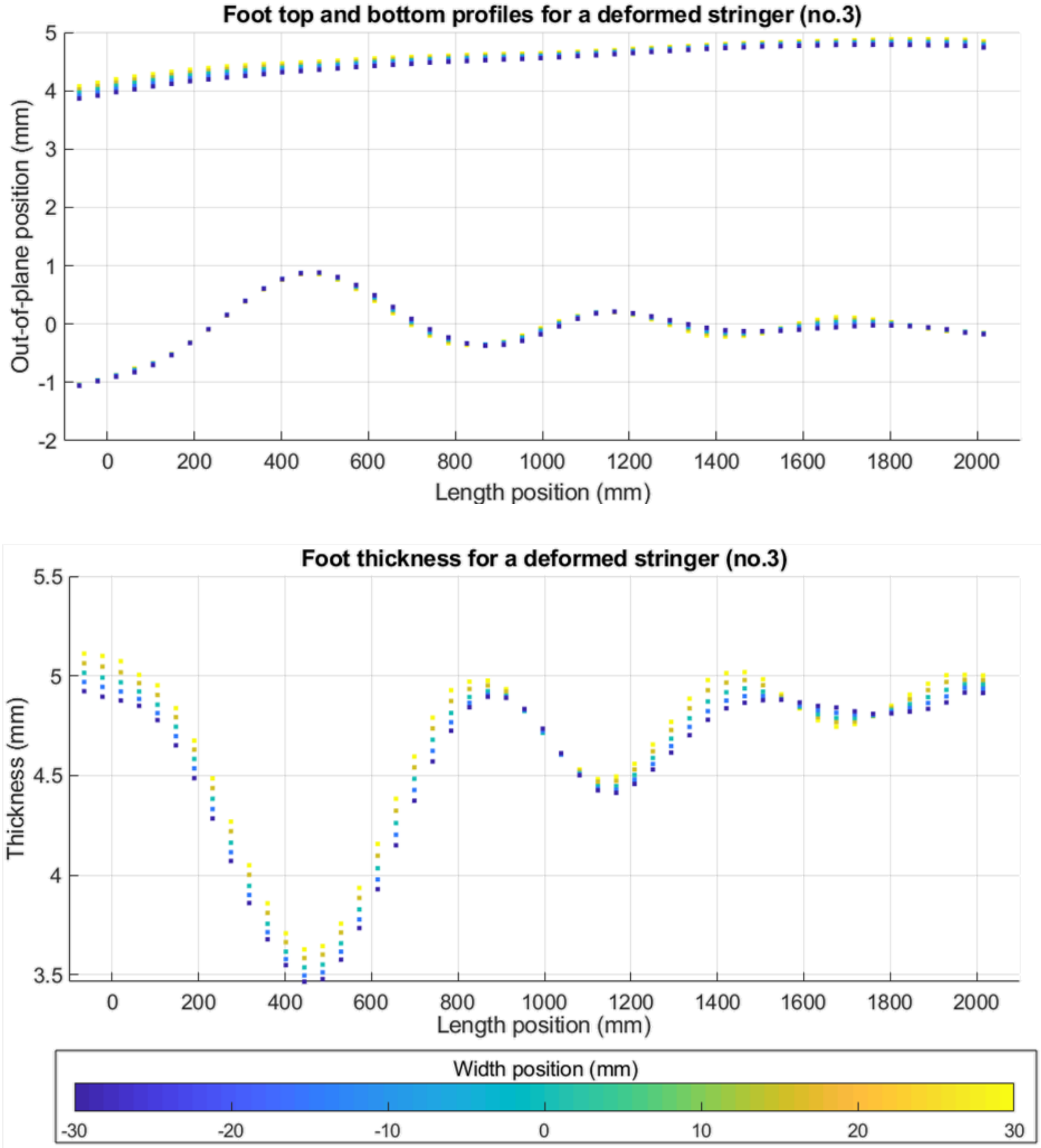

Figure D-9. Top: Foot profile (reconstructed for top and bottom) of one deformed stringer. Bottom: calculated foot thickness. The profile is flat enough in the cord direction that some points overlap in both plots.

D.3 Assembly realisation

The test assemblies were realised using an industrial oven based at the Composites Press Building of the AMRC in Sheffield. The schedule was completed as per Table D-1 through July 2018. The layup structure is schematised in Figure D-10, and representative photographs of the bagged assemblies are provided in Figure D-11. The heating cycle was based on a ramp of 2°C/min up to 120°C, followed by a 1 h plateau and subsequent cooldown (uncontrolled but still monitored). The assemblies were removed from the oven (still on the bonding table) once the temperature readings reached around 70°C during cooling; this allowed out-of-oven overnight cooling while accommodating shop hours.

Table D-1. Cure planning — note slight change in the order (relative to straight alphabetical) to facilitate grouping of batches during production.

Cure batch/date	Assy #	Skin	Stringers			Type	Boundary condition	Position on table
1 / 2018.07.05	A	1	1	3	2	Verifilm	1SP	Side – right
2 / 2018.07.10	B	3	7	8	9	Verifilm	1SP	Side – right
	C	4	10	11*	12	Verifilm	1SP	Middle
	E	2	4	6	5	Verifilm	2SP	Side – left
3 / 2018.07.12	D	1	10	11	12*	Verifilm	2SP	Side – right
	I	2	7	8	9*	Verifilm	1SP	Middle
4 / 2018.07.17	F	3	7	8	9	Verifilm	2SP	Middle
	G	4	10	11*	12	Verifilm	2SP	Side – left
	H	1	1	3	2	Bond	1SP	Side – right
5 / 2018.07.24	J	3	7	8	9	Bond	1SP	Middle
	L	2	4	6	5	Bond	2SP	Side – right
	K	4	10	11*	12	Bond	2SP	Side – left

***** ≡ stringer is flipped

The initial verifilm trial showed squeeze flow took place in the longitudinal direction next to the stringer edges (indicated in Figure D-12), going past the release film and causing local adhesion. This was avoided in subsequent tests, where the whole stringer-skin interface was covered in release film. This longitudinal flow, which was observed throughout the trials, is in violation of the

1D flow assumption. The implications are discussed in Section 6.2 Research limitations.

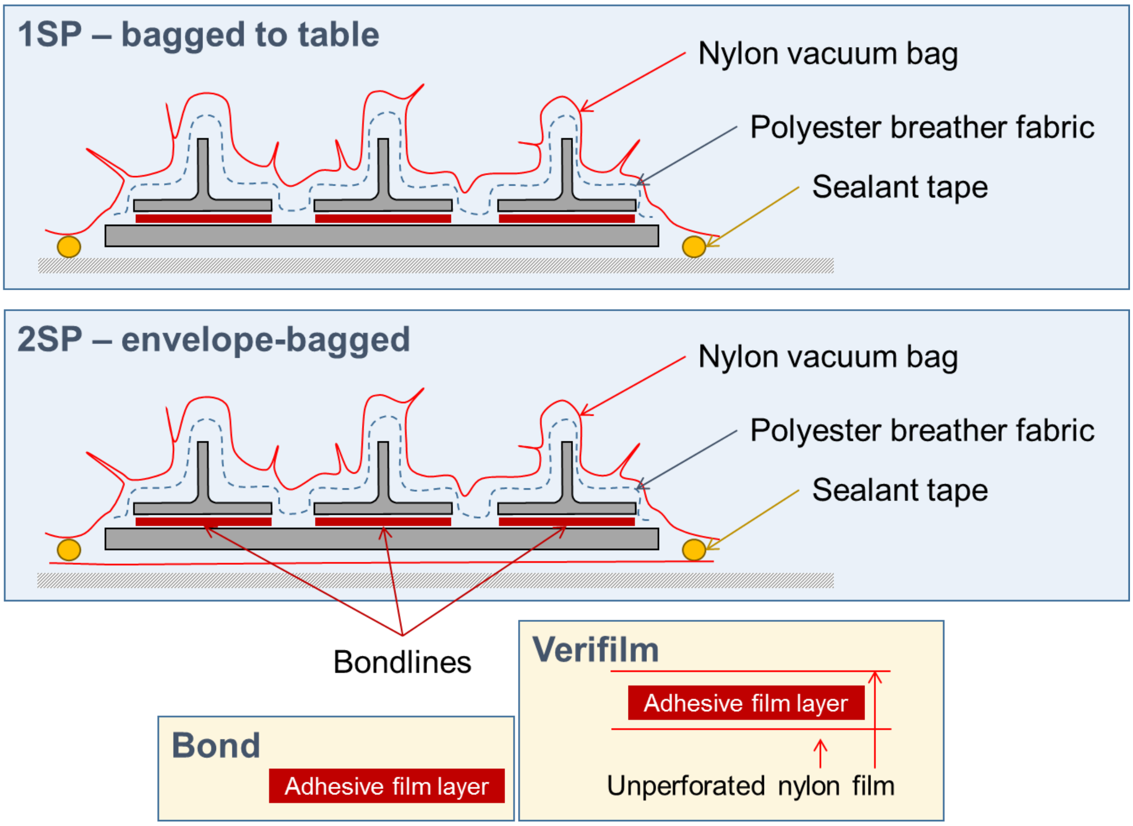

Figure D-10. Bonding arrangements employed for the different boundary conditions and cure types.

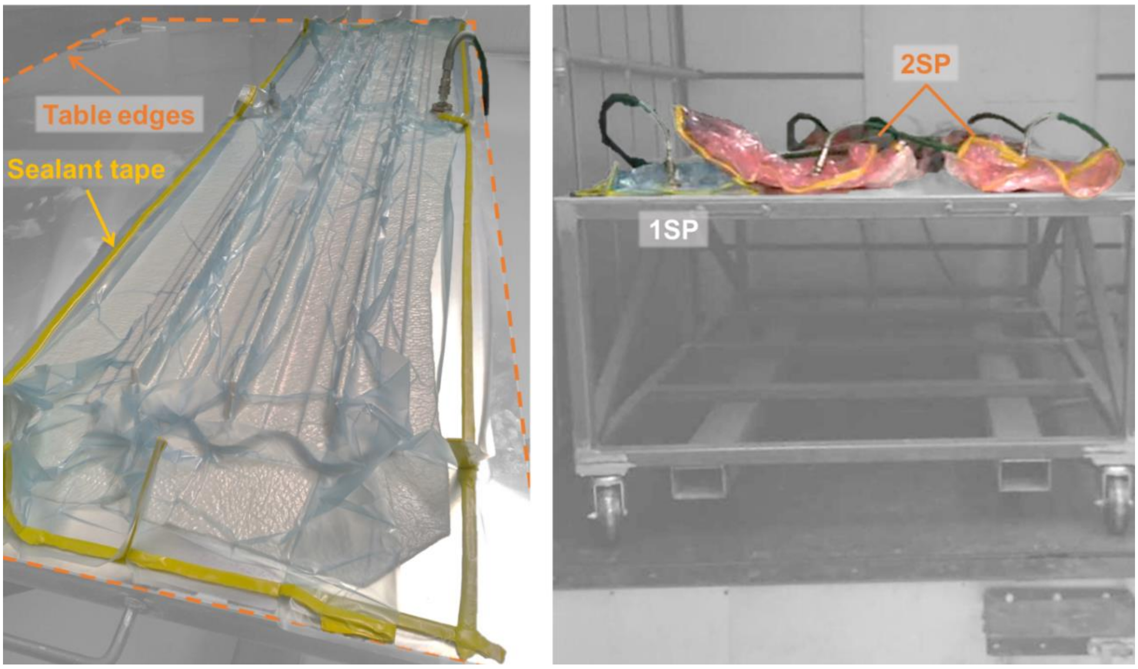

Figure D-11. Left: the first verifilm panel, bagged onto the flat bonding table and with one of the vacuum ports connected. Right: three panels (left one bagged against the table [1SP], the other two envelope bagged [2SP]) inside the oven used, ready for cure.

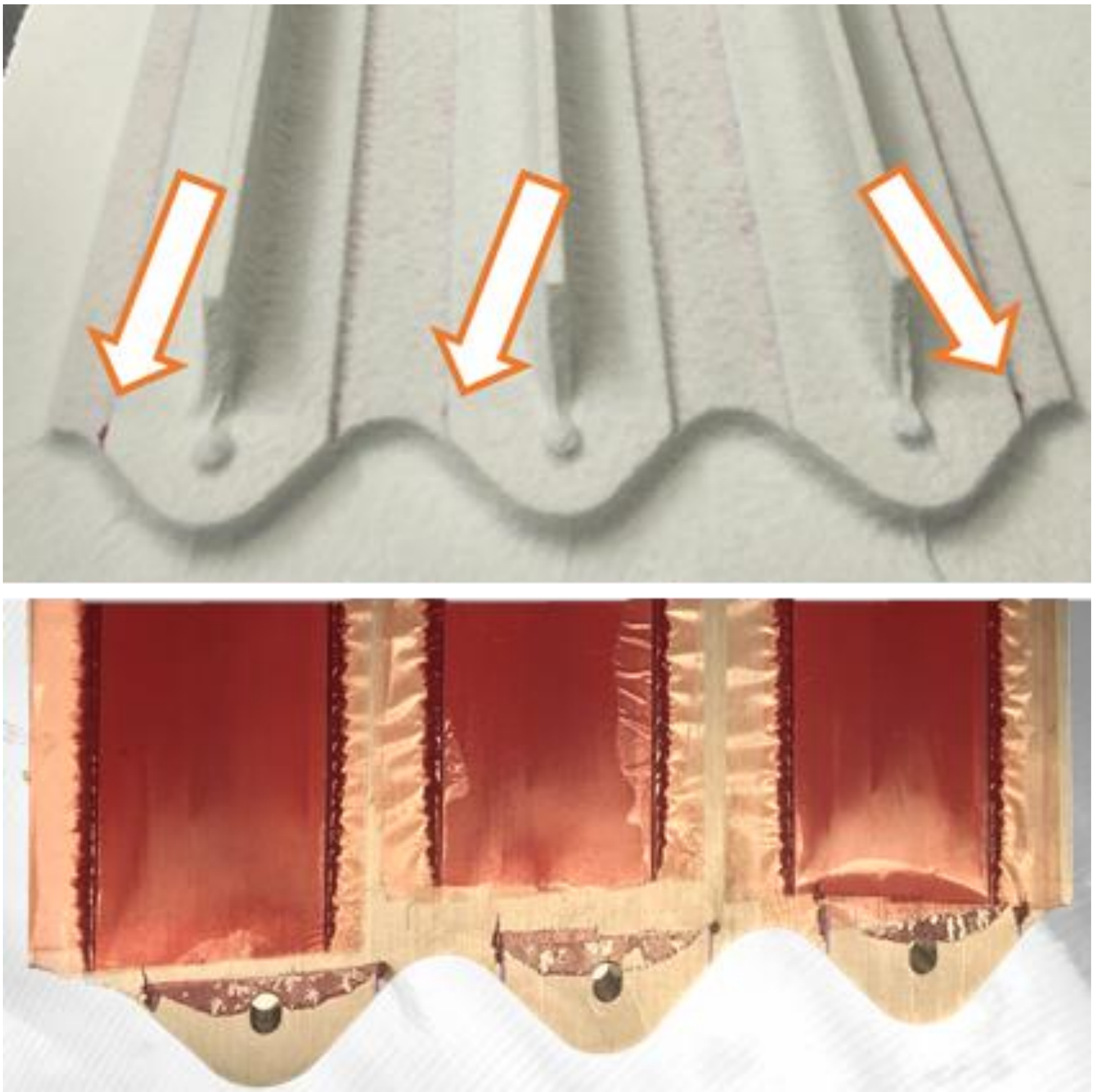

Figure D-12. The first verifilmed panel, before (top) and after (bottom) removal of the breather fabric and stringers. Longitudinal flow is apparent from bleed in the fabric (top, marked with arrows) and a spew residue on the tooling lugs (bottom). The bottom picture also illustrates how the verifilm strips tended to become misaligned upon assembly breakup.

D.4 Initial visual assessment

Mere visual inspection showed that the initial interface gaps (caused by stringer variability) had been closed under pressure, but not to the same degree as the rest of the bondline. This was evidenced by the existence of a spew fillet all along the stringer foot edges which became thinner (but did not disappear) next to the stringer-skin gaps. This is visible in Figure D-13.

In addition, upon removal of the stringers it became apparent that the pressure had been lower at these thicker bondline areas, resulting in localised porosity (Figure D-14). This phenomenon matches the initial assumption of localised adhesive pressurisation presented in the methodology in Section 3.3.2 Assembly interactions separation.

Figure D-13. Detail of the first verifilmed panel, prior to stringer removal. Note the spew fillet becomes thinner under the middle stringer (a deformed one), indicating a locally thicker bondline.

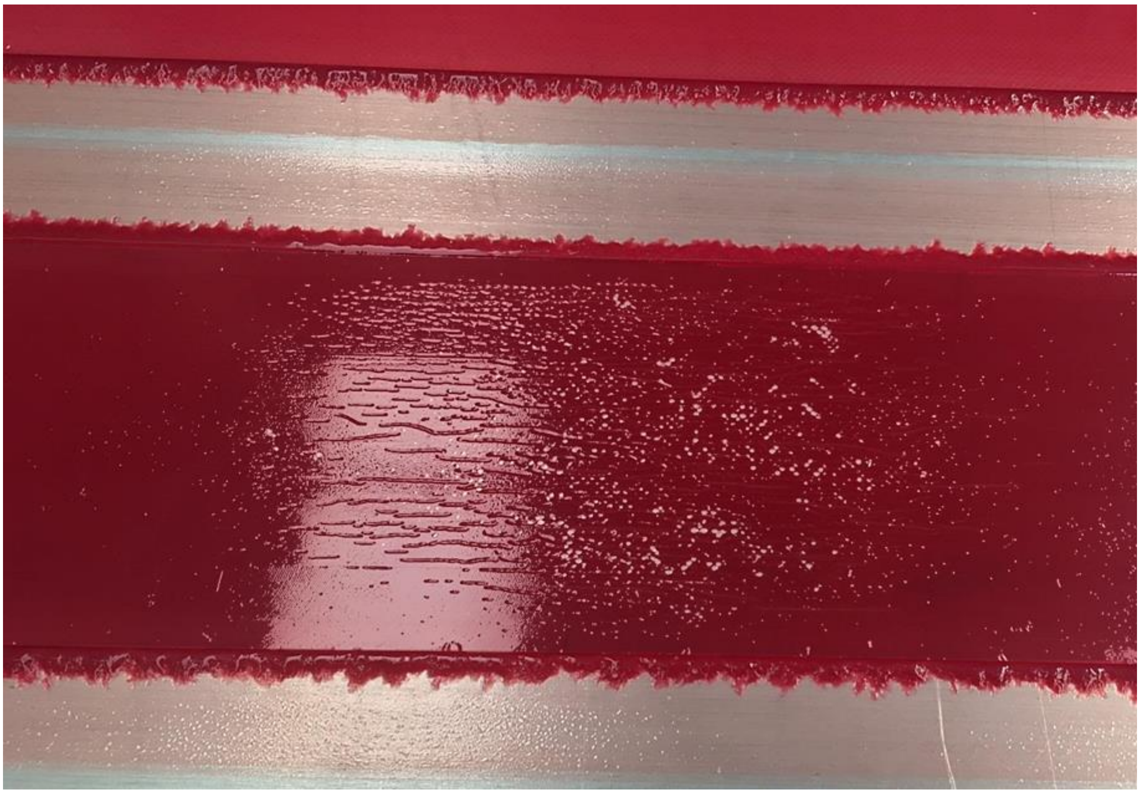

Figure D-14. Top view close-up of the bondline cured adhesive from a verifilm run under the deformed stringer's larger stringer defect (initial interface gap). Note the presence of voids, as well as wrinkles in the release film, consistent with a drop in pressure due to reduced squeeze.

D.5 Bondline measurement

D.5.1 Non-contact measurement test

Verifilm bondline scans (non-disruptive, contactless measurement) were carried out in situ, after allowing the panels to go back to room temperature overnight outside the oven.

Indirect thickness measurement was carried out using a Leica T-Scan 5 and Absolute Tracker AT960, in three stages as per Figure D-15:

1. Remove stringers without disturbing the cured glue lines. Scan the skin with the cured adhesive layers (inclusive of release film) on top.
2. Remove the cured adhesive layers (including all release film). Scan the skin top surface alone.
3. The bondline thickness is calculated as the distance between both resulting point clouds. For processing a subsample is obtained by creating a coarse grid of points (<30 mm spacing) and averaging the thickness 12.5 mm around each point.

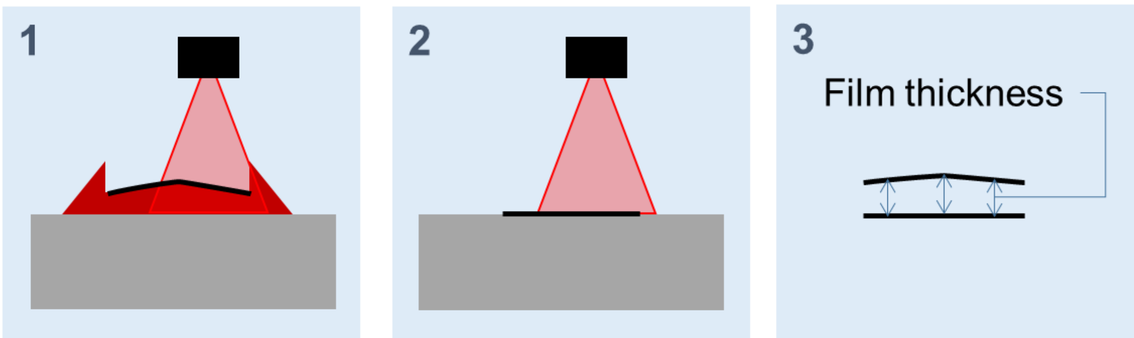

Figure D-15. Indirect non-contact measurement of the verifilm thickness.

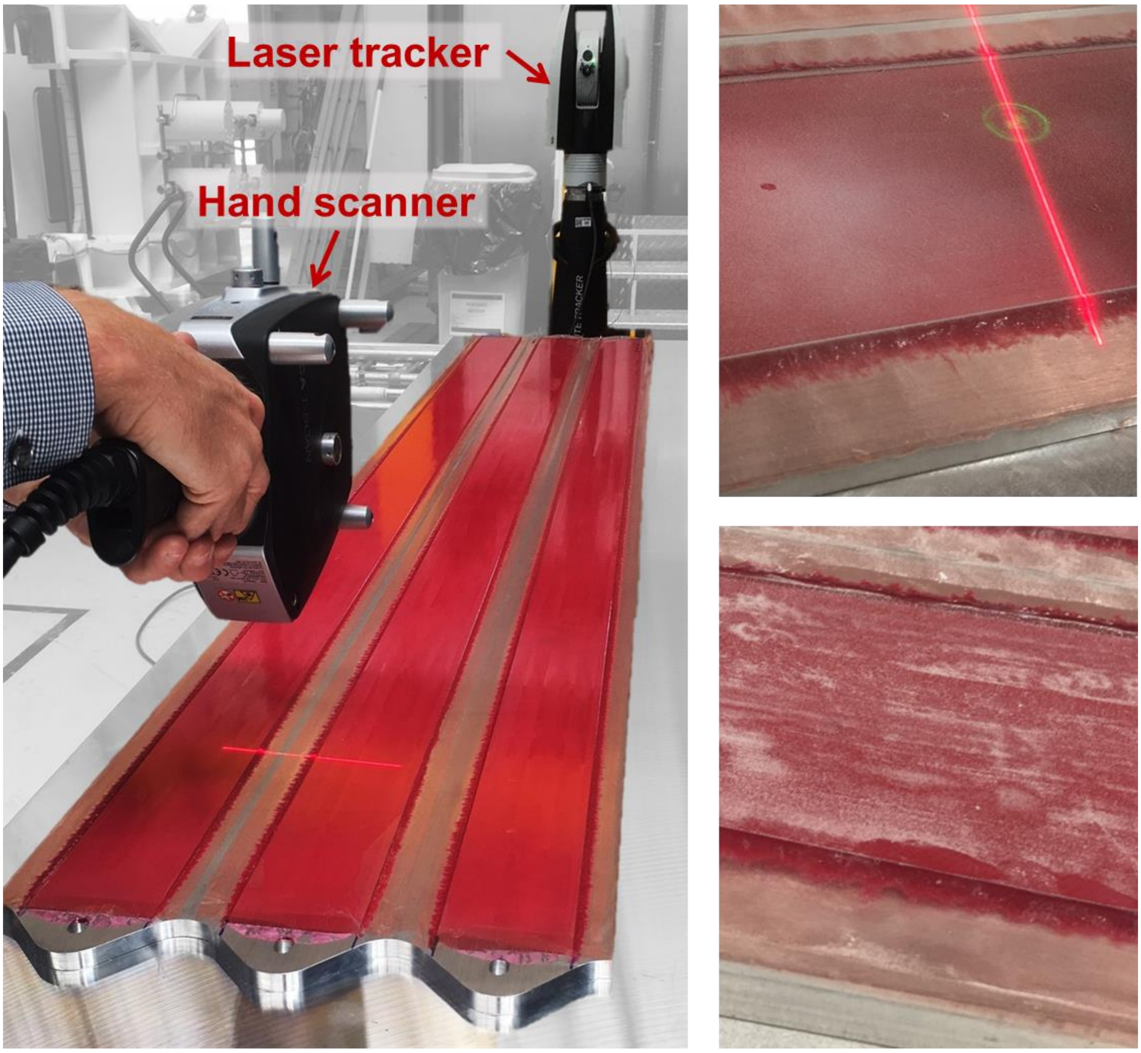

Figure D-16. Left: laser scanning the bondlines cured adhesive layers without any surface treatment. Right: closeups of sprayed bondlines, making the insufficient surface control apparent.

Laser scanning was initially carried out without any kind of surface preparation (Figure D-16, left), but this proved inappropriate as the bondlines were translucent (Figure D-17). Use of developer spray (Figure D-16, right) substantially improved the results by giving the surfaces an opaque, matte finish. However, being a manual process, the effect was not well controlled and offered uneven results. Comparison of the calculated thicknesses in Figure D-18 and Figure D-19 provides an idea of the effect of manually applied developer spray on optical measurements.

A further problem for contactless inspection was that some areas of a strip of cured adhesive would (sometimes visibly) spring up from the skin upon releasing pressure; thus, the indirectly-measured thickness was inflated. This effect (pictured in Figure D-20) became even more pronounced if the bondlines were ever moved, thus complicating remeasurement.

Given the practical impossibility of obtaining reliable thickness measurements from laser scans alone, a decision was made to re-measure all the cured adhesive strips from verifilm, using manual contact methods.

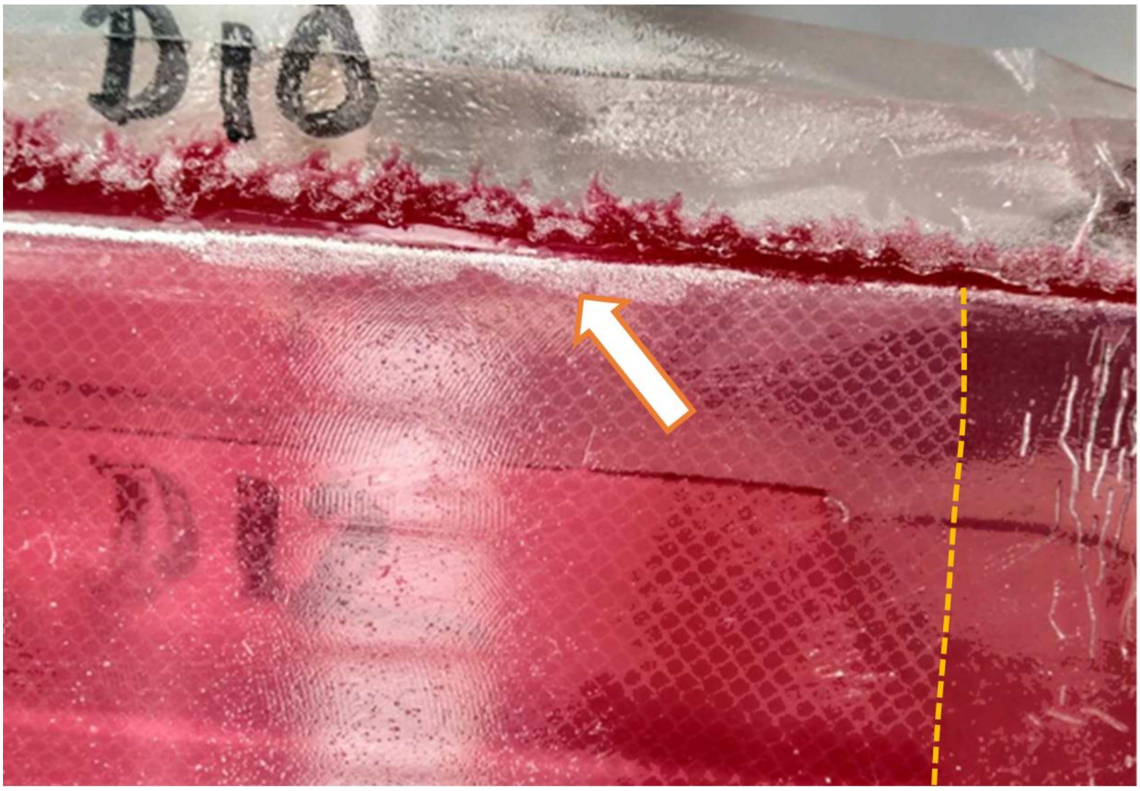

Figure D-17. Close-up of a stack of bondlines, which evidences their translucent and partially reflective nature. A residue of opaque developer spray is indicated by an arrow. Note the adhesive beyond the edge of the knit carrier (yellow dashed line) which evidence longitudinal flow. Image treated for enhanced carried visibility.

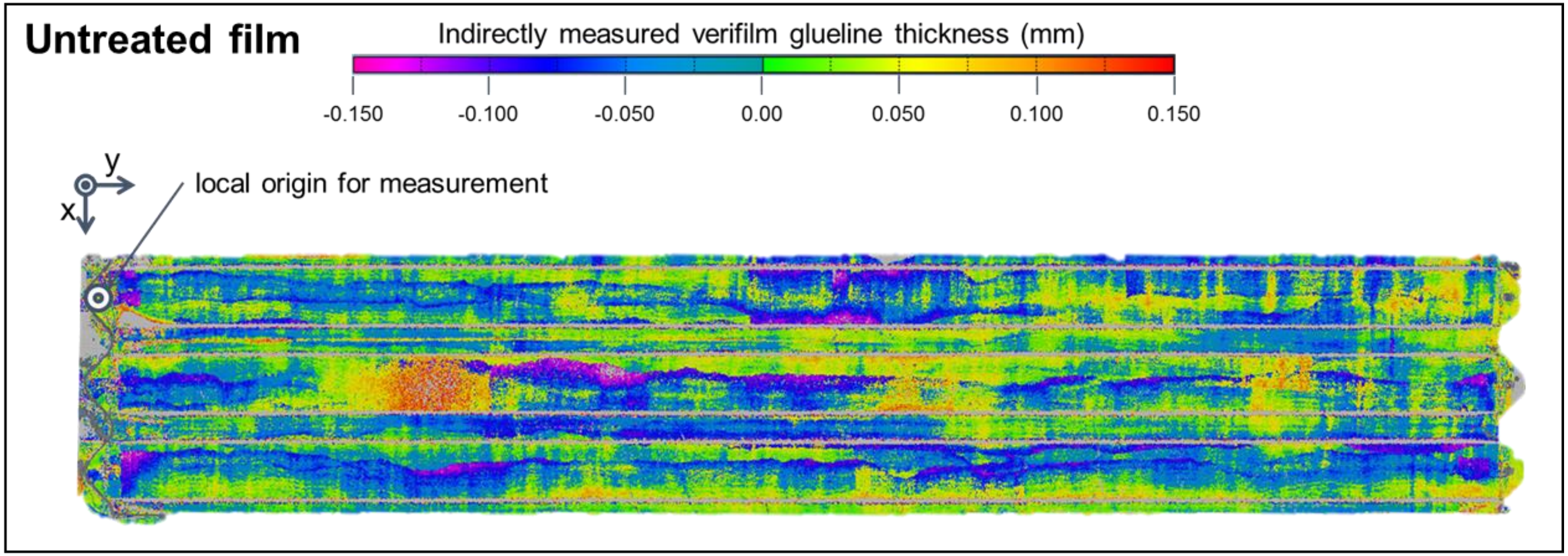

Figure D-18. Scan results example without applying surface treatment for appropriate optical properties. The untreated film yields plenty of artefacts and negative-thickness areas.

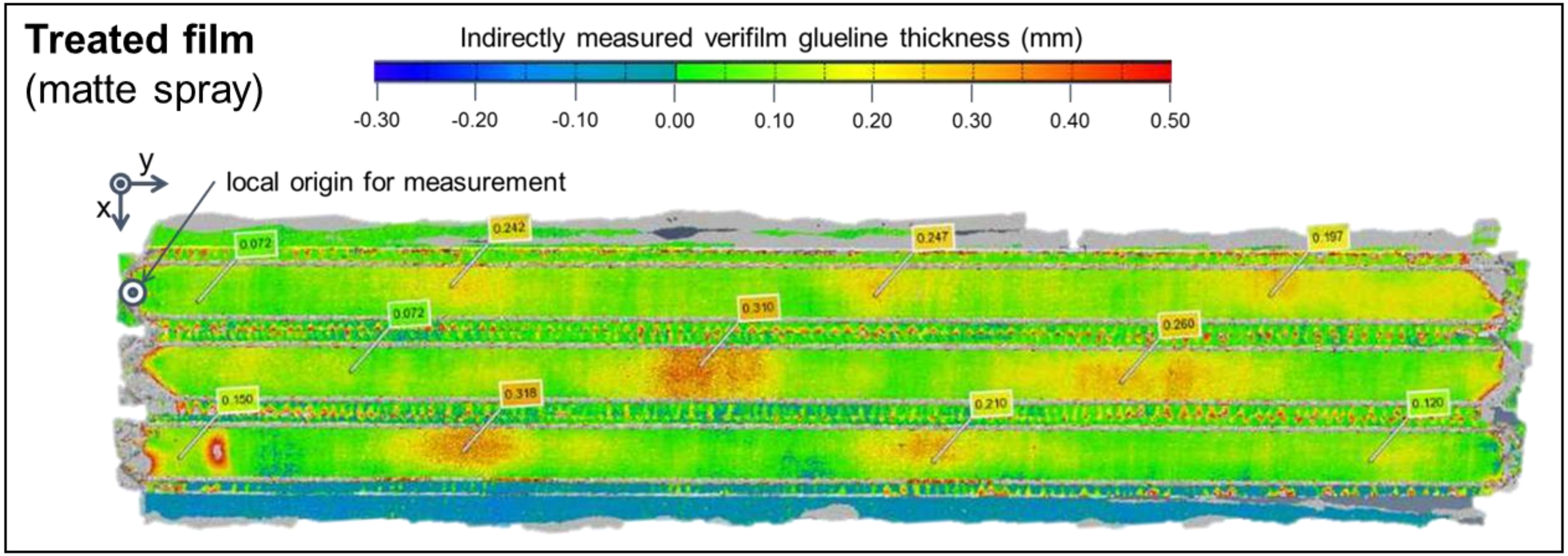

Figure D-19. Scan results example after applying surface treatment for appropriate optical properties. The treated film scans were approximately truthful but still contained negative-thickness areas and spurious bumps.

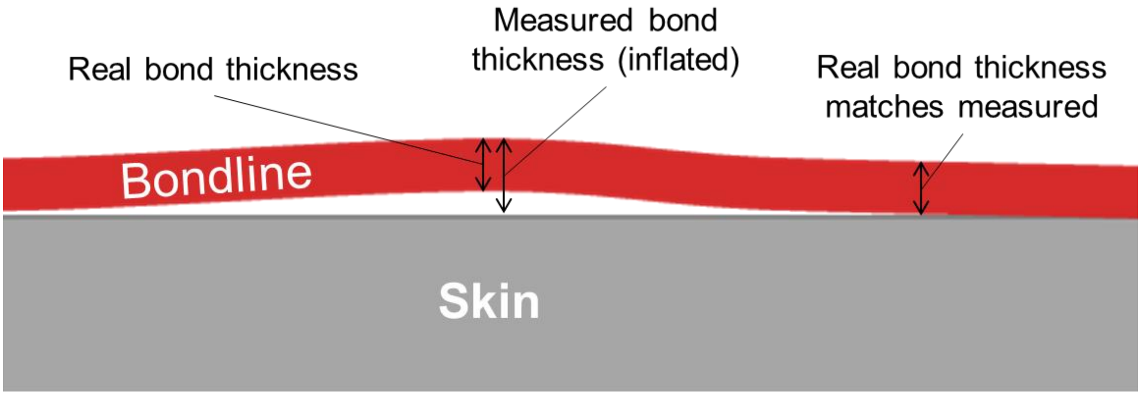

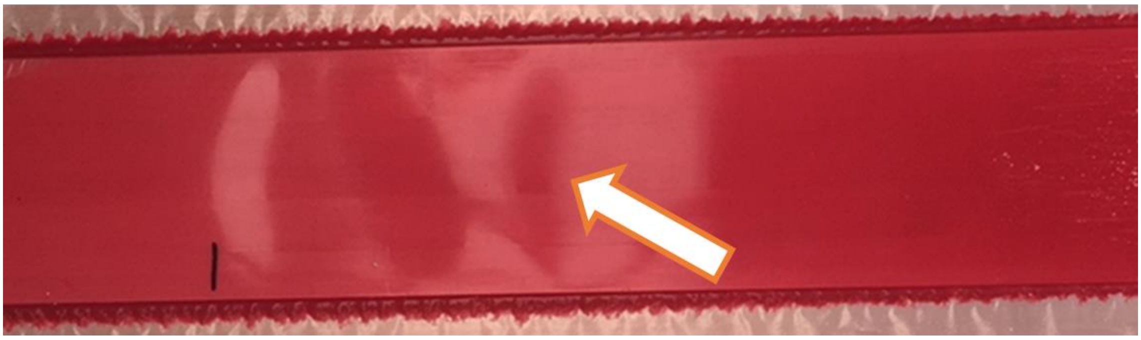

Figure D-20. Increased measured thickness caused by deformation of the layer of cured adhesive from verifilming. Top: schematic. Bottom: example where the deformation created a visible bump.

D.5.2 Verifilm contact measurement

The cured adhesive was re-measured at marked locations using an analogue micrometre with 10 µm nominal resolution. Measurements were recorded with 5 µm resolution (which is typical procedure for analogue instruments). In order to preserve the adhesive integrity, as well as all prior markings, the strips were measured with the nylon release film still attached. The entire mass of cured adhesive strips can be seen in Figure D-21.

An additional set of measurements comprised the release film alone. The resulting mean thickness of the two nylon film layers was found to be 50.9 µm (consistent with a nominal 25 µm single-layer thickness). The total uncertainty from nylon film variability plus the micrometre and appraiser uncertainty were estimated at ±10.2 µm with 99% confidence (details of the calculation are in Appendix F).

Figure D-21. Heap of cured adhesive (with the release film attached) resulting from the verifilm trials. The chair and laptop at the back give an idea of the scale.

D.5.3 Bonded panels micrograph-based measurement

The bonded panels were cross-sectioned at 100 mm length intervals using a drop saw. These were then inspected using a Keyence VK-X260K microscope. (From each 100 mm section, a 25 mm section had to be taken with another cut in order for the microscope to accommodate the samples.)

Three locations were inspected at each stringer cross-section, under the web and 20 mm away from the web to each side (just over halfway into the foot flange). A representative section is shown in Figure D-22, along with the inspection locations.

At each location, the visible bond thickness was measured at three points to provide reasonable robustness against measurement uncertainty (from human user error as well as any metal burrs from sectioning). A single user carried out all the microscope work.

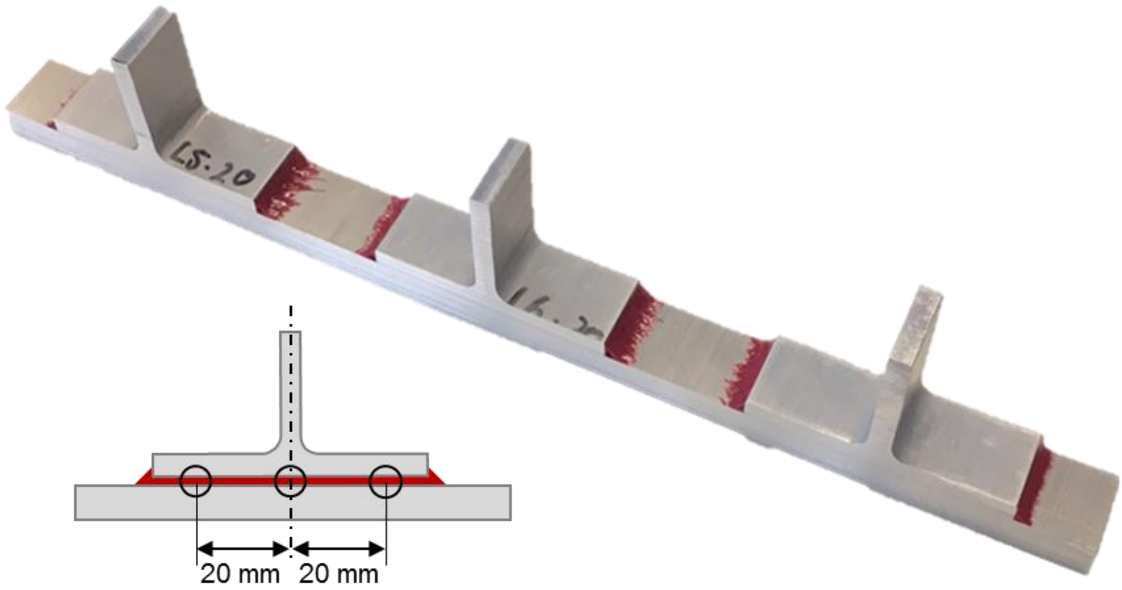

Figure D-22. Bonded panel section (25 mm depth) and inspection locations. Note the ink markings indicating assembly code, stringer, and section position.

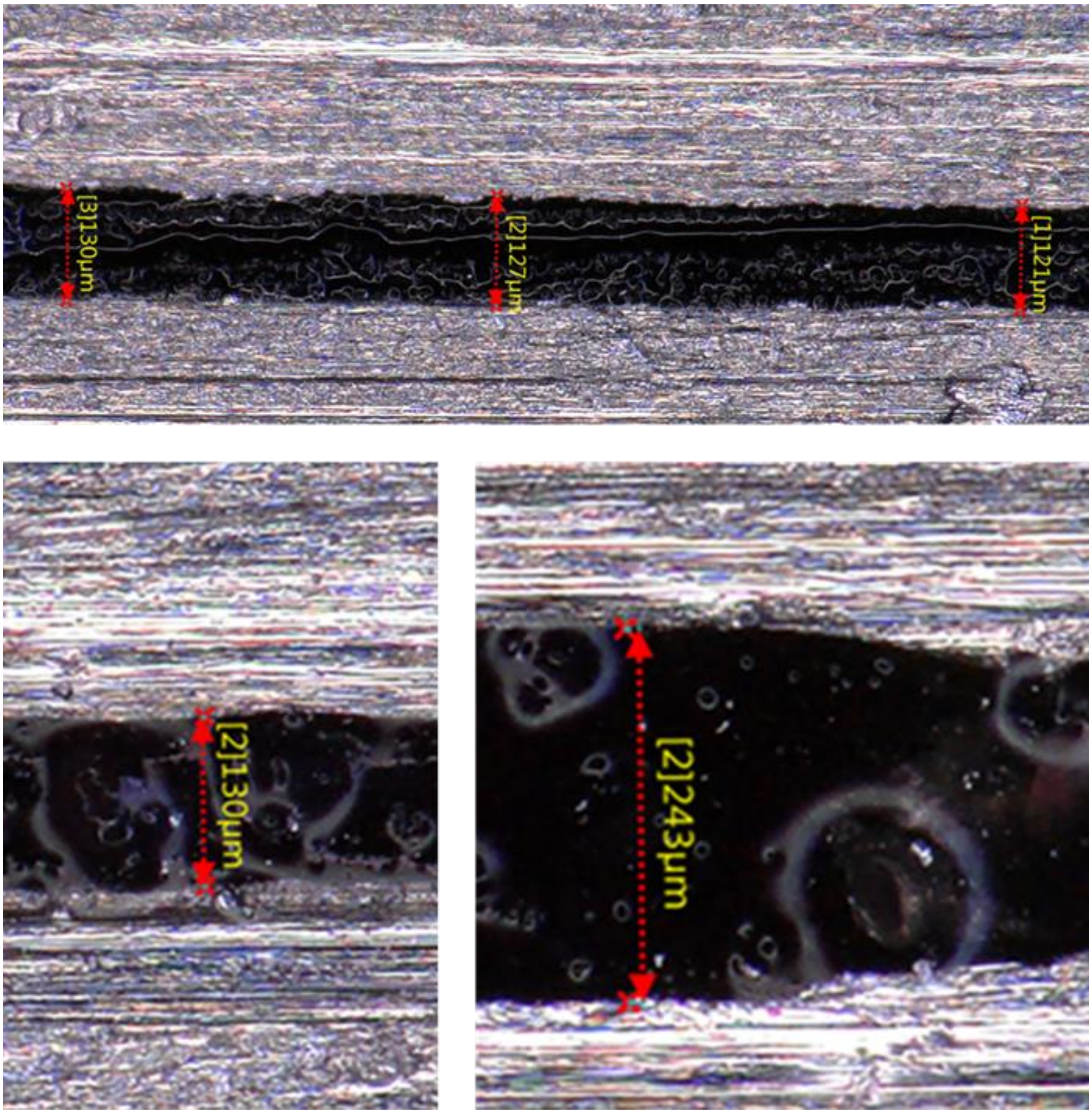

Figure D-23. Example photomicrographs. Top: array of three measurements at one location. Bottom: details at different thickness areas.

Appendix E — Cure process traceability

Temperature readings from the oven controls and additional thermocouples, as well as pressure readings from the vacuum lines, were also recorded. Examples of both readings, corresponding to the first assembly realised, are presented in Figure E-1.

The temperature plots (Figure E-1 top — the “Policeman” line is a monitor thermocouple outside the assembly) show the need to raise the overall oven temperature above that recorded in the assembly itself in order to meet the cure cycle requirements, achieving a peak of 140°C in the case of the first assembly. A sharp temperature ramp-down in the cool-down phase corresponds to the assembly being taken out of the oven as it got cool enough for manual handling (and also matches a drop in the vacuum pressure recorded as the assembly was debagged).

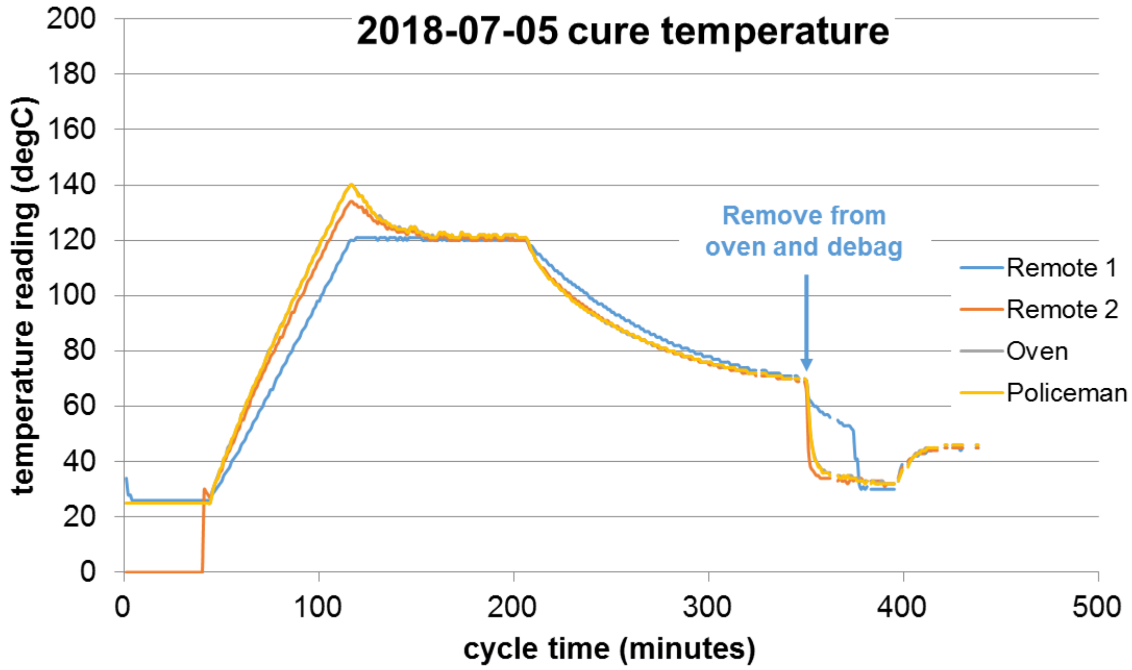

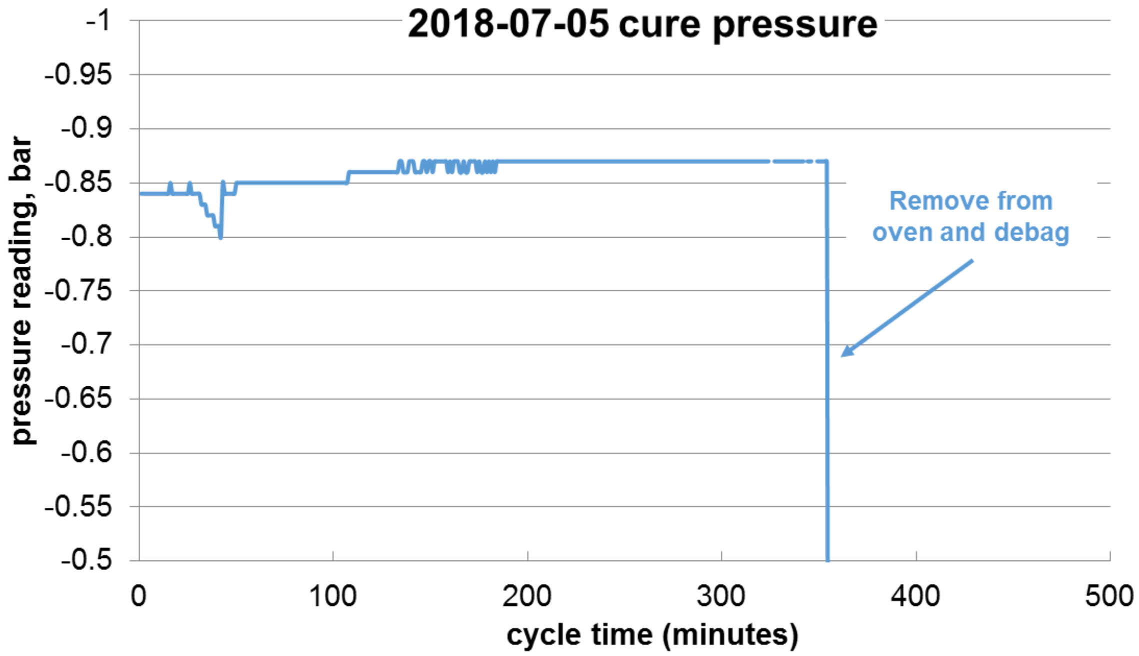

Figure E-1. Cure trace for the first test assembly (verifilm) realised.

Appendix F — Estimation of measurement uncertainty: the case of verifilm thickness

Given the large number of manual measurements of the verifilm bond thicknesses, there is a strong case for a quantified assessment of the uncertainty or expected measurement error. These measurements stand to benefit from uncertainty quantification the most because of how manual they are: no digital trace such as a log or micrograph image file was generated; there were no suitable calibration artefacts for the specific measurement at hand; and the measurements were sparse and variegated, making it hard to detect outliers in the data itself. (By contrast, the part measurements concerned repeats of the same manufacturing process, and laser scans provide a very high point density which allows making estimates based on local variation.)

F.1 Sources of uncertainty

The thickness measurements taken correspond to the layer of adhesive sandwiched between two layers of nylon release film, *inclusive of the latter*. This means that the actual thickness of adhesive is obscured by the release film thickness, including the variability thereof.

The measured verifilm thickness $b^*_{verifilm}$ (with * denoting the value observed) is

$$b^*_{verifilm} = b_{adhesive} + b_{rf} + \epsilon_{micrometre} \tag{F-1}$$

with $\epsilon_{micrometre}$ being the measurement error of the micrometre, encompassing all errors from the instrument and operator (since in this case a single user — the author — took all the measurements). $\epsilon_{micrometre}$ is assumed to follow a random, independent distribution with density symmetrical around 0, with no correlation between measurements. In this case, it is assumed that the linearity error is negligible; that is, the micrometre measurement error follows the same distribution regardless of the real value. This is reasonable as all measured thicknesses were in the 40 μm – 380 μm range, which is under 1.5% of the instrument's total measurement range.

The release film thickness in each instance corresponds to two layers of film:

$$b_{rf} = 2\mu_{rf} + \tau_{rf,1} + \tau_{rf,2} \quad \textbf{(F-2)}$$

where μ_{rf} is the mean thickness of a single release film layer, and $\tau_{rf,i}$ is the deviation from the mean value for each piece of film (including manufacturing variability, dimensional changes during cure, and any unremoved dirt).

As with $\epsilon_{micrometre}$, we assume $\tau_{rf,i}$ to follow a probability random, independent distribution with density symmetrical around 0.

Therefore, the adhesive thickness is calculated from measurements as

$$b_{adhesive} = b^{*}_{verifilm} - 2\mu_{rf} + \left(-\tau_{rf,1} - \tau_{rf,2} + \epsilon_{micrometre}\right) \quad \textbf{(F-3)}$$

As $\tau_{rf,i}$ and $\epsilon_{micrometre}$ follow symmetrical distributions with mean 0, and they are uncorrelated, one can change their signs and consolidate them into a single random uncertainty variable, also uncorrelated and symmetrical around 0.

$$\tau_{rf,1} + \tau_{rf,2} + \epsilon_{micrometre} = \epsilon_{rf} \quad \textbf{(F-4)}$$

μ_{rf} and ϵ_{rf} can be estimated empirically by measuring release film alone; indeed, the measured thickness of the double layer of release film, in an adhesive-less area, would be

$$t^{*}_{rf} = 2\mu_{rf} + \tau_{rf,1} + \tau_{rf,2} + \epsilon_{micrometre} = 2\mu_{rf} + \epsilon_{rf} \quad \textbf{(F-5)}$$

F.2 Uncertainty model

The release-film and measurement uncertainty will be assumed to follow a normal distribution,

$$\epsilon_{rf} \sim N(0, \sigma^2) \quad \textbf{(F-6)}$$

Basic practice would consist of estimating the value of $(2\mu_{rf})$ and σ^2 from a set of n_s sample measurements $\{ b^*_{rf} \}$, and using these values to generate a confidence interval (CI) based on a suitable α level:

$$\mathrm{CI}(1-\alpha) = (\widehat{m} - z_{\alpha/2} \cdot \hat{s}\,, \qquad \widehat{m} + z_{1-\alpha/2} \cdot \hat{s}) \quad \textbf{(F-7)}$$

where $(1-\alpha)$ is the level of confidence;

$\widehat{m} = \frac{1}{n}\sum b^*_{rf}$ is the sample mean $(2 \cdot \mu_{rf})$;

$\hat{s}^2 = \frac{1}{n-1}\sum\left(\widehat{m} - b^*_{rf}\right)^2$ is the sample variance,

and z_p is the z-level for cumulative probability p from the normal distribution $\mathrm{N}(0,1)$.

In this case, for the sake of completeness and because of the relatively alien nature of the measurements, uncertainties have been assumed for both $2\mu_{rf}$ and σ^2 following typical Bayesian posteriors:

$$\frac{\left(2 \cdot \mu_{rf}\right) - \widehat{m}}{\hat{s}/\sqrt{\nu_t}} \sim \mathrm{t}(\nu_t) \quad \textbf{(F-8)}$$

$$\sigma^2 \sim \mathrm{GI}\left(\frac{\nu_t}{2}\;, \qquad \frac{1}{2}\sum\left(\widehat{m} - b^*_{rf}\right)^2\right) \quad \textbf{(F-9)}$$

where $\nu_t = n_s - 1$ is the degrees of freedom, $\mathrm{t}(\nu_t)$ is the Student's t distribution with ν_t degrees of freedom, and $\mathrm{GI}(\alpha, \beta)$ is the inverse-gamma distribution with scale α and rate β. For somewhat large samples $(n_s > 30)$, there is a minimal difference between the t-distribution and the normal distribution $\mathrm{N}(0,1)$.

While the simpler solution presented in (F-7) has a very simple solution using well-established tables and available functions, the second approach, with a probability distribution for each parameter, has no straightforward analytical solution. Rather, it requires either numerical integration or stochastic estimation. Both solutions were implemented in Matlab, obtaining similar results.

F.3 Value estimation

The release-film double layer was measured at a total of 48 locations (2 per stringer verifilm strip: once near the tooling lug, once by the middle of the foot flange). The results are scattered around 50 µm (Figure F-1), consistent with a single-layer thickness of 25 µm, and a measurement range of (60-45) = 15 µm which is encouragingly low. The mean measured thickness is $\hat{m}$ is 50.94 µm, and the sample standard deviation $\hat{s}$ is 3.67 µm.

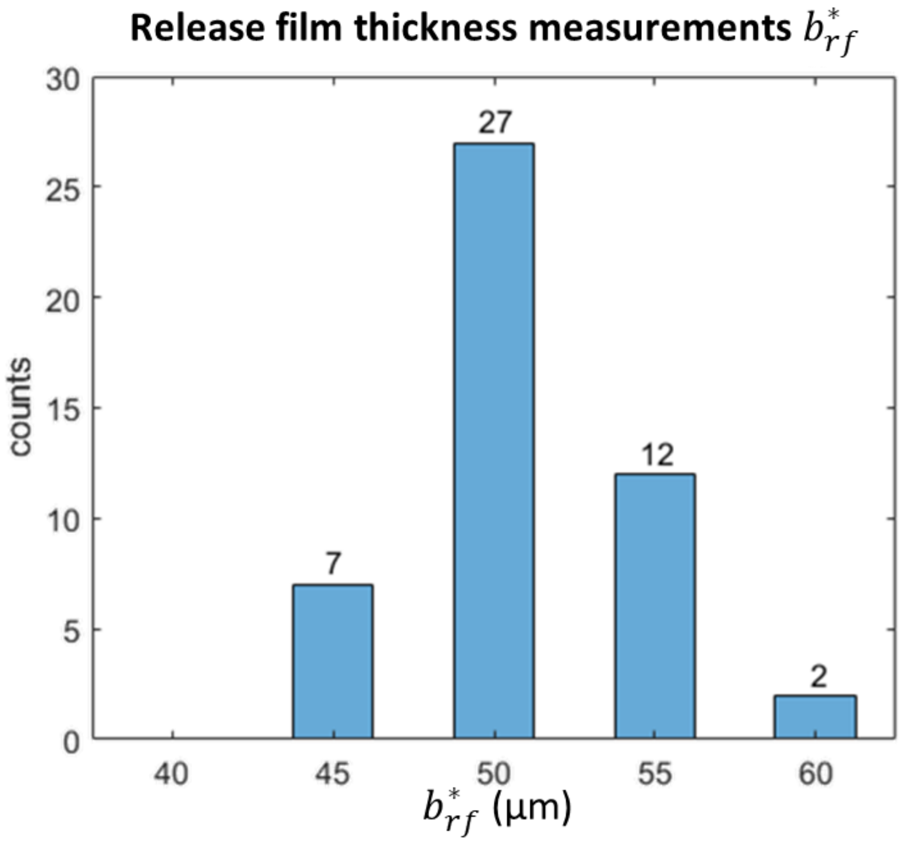

Figure F-1. Histogram of release film thickness measurements (numbers above the bars indicate measurement count).

Based on these values, the distributions for $2\mu_{rf}$ and σ were derived (presented in Figure F-3 and Figure F-3 respectively); from these, the distribution for the value of $(b_{rf} + \epsilon_{micrometre})$ can be derived (Figure F-4). The width of a CI for $(b_{rf} + \epsilon_{micrometre})$ is the same as for all the uncertainty/error components, ϵ_{rf}.

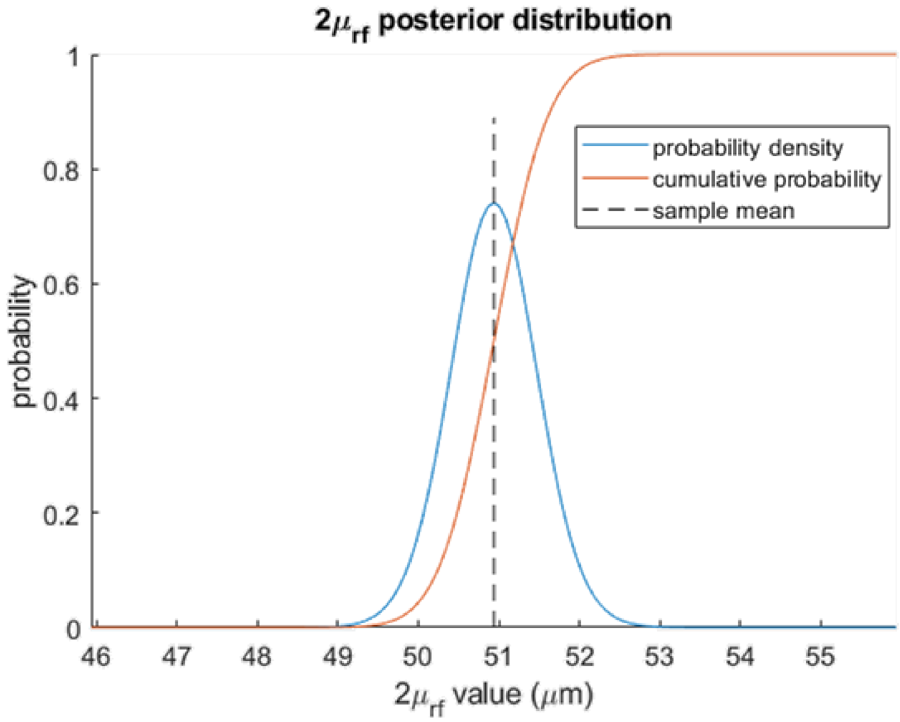

Figure F-2. Posterior distributions for the two-layer release film thickness mean value.

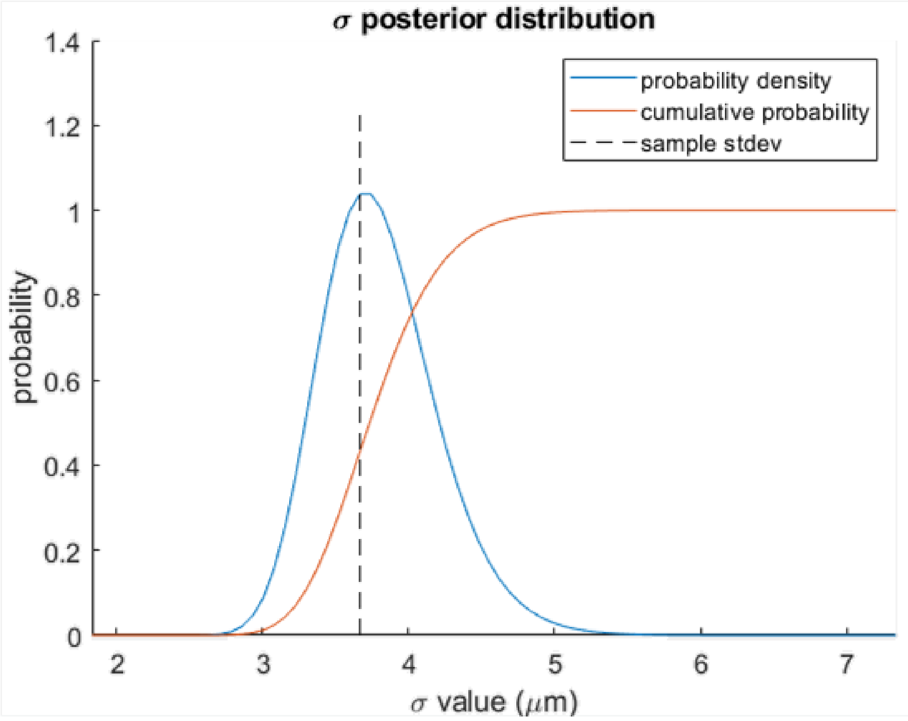

Figure F-3. Posterior distributions for the two-layer release film thickness standard deviation.

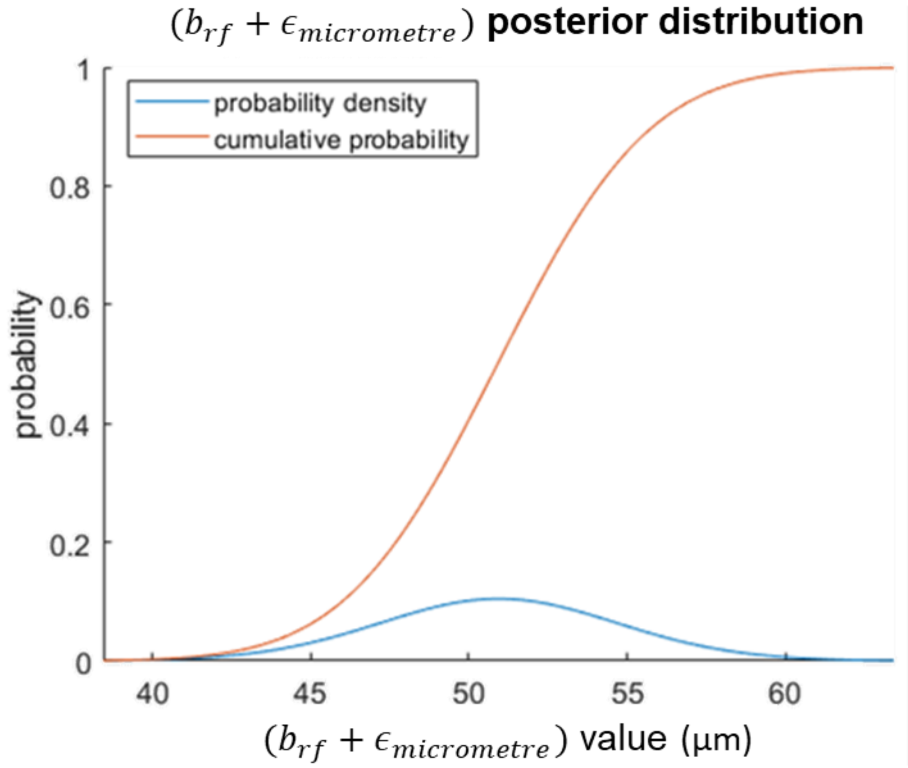

Figure F-4. Posterior distribution for the measured release film thickness, including all uncertainties.

The CI widths for different levels of confidence, both by the naïve method in (F-7) and Bayesian approach, are presented in Table F-1. At a glance, it is evident that, thanks to the relatively large sample size and small measurement dispersion, there is no substantial difference.

Note that the CI width is distributed symmetrically around the measured value; thus, a $\mathrm{CI}(99\%)$ of 20.40 μm would correspond to a confidence interval (in μm) of (-10.20, +10.20).

Table F-1. Confidence interval widths for the measured bondline thicknesses, for representative confidence levels and two calculation approaches

confidence level / **method**	**90%** (**α = 0.1**)	**95%** (**α = 0.05**)	**99%** (**α = 0.01**)	**99.73%** (**α = 0.0026**)
Normal z-values	12.07 μm	14.38 μm	18.90 μm	22.02 μm
Bayesian	12.77 μm	15.34 μm	20.40 μm	24.00 μm

Appendix G — Measurement uncertainty from micrographs

All measurements conducted on micrographs employed a 1 μm resolution; thus, resolution error is minuscule in comparison with other sources of error, as it will be seen below. Two sources of measurement error have been considered:

- Human error given by visual accuracy (as all points for measurement were defined manually);
  - Inaccurate location of the adhesive-adherend interfaces;
  - Misalignment of the measurement points at both sides of the bondline, resulting in a non-perpendicular thickness measurement.
- Cross-section cut defects in the form of a plasticised metal burr.

Measurement locations are marked by crosshairs (Figure G-1), such that one side of each marking should be on the adhesive (off-black dark in the micrographs) and the other on the adherend (grey with shiny bands). This would make for a ±(crosshairs width)/2 uncertainty at each marked position, or ±(crosshairs width) in total for each length measurement. As each crosshairs is 13 pixels wide, and the micrographs had a correspondence of 1.1μm/pixel, the uncertainty from measurement location is up to ±(13×1.1) = ±14.3 μm.

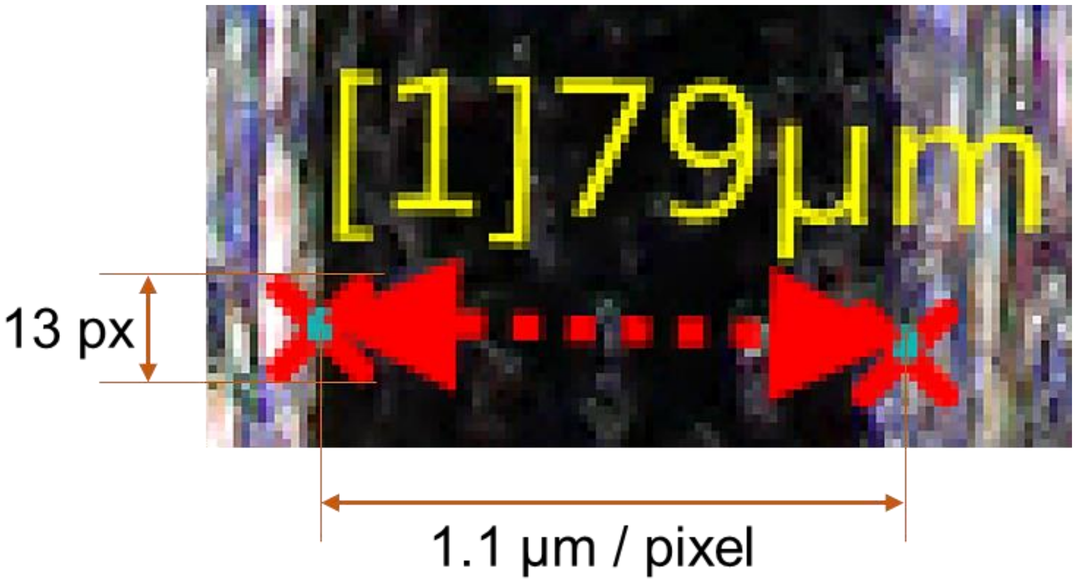

Figure G-1. Closeup of a micrograph image with digital markings for the bondline thickness measurement, along with the pixel dimensions.

If the marked positions are not perfectly aligned for the thickness to be measured perpendicular to the bondline[xlii], the value recorded will be higher than the actual thickness (Figure G-2). Given a misalignment at a small angle φ_{obs}, and an inflated thickness b^*, the real thickness is $b = b^* \, cos(\varphi_{obs}) \approx b^*(1 - \frac{\varphi_{obs}^2}{2})$, and thus the associated uncertainty is $\pm(b^*\varphi_{obs}^2)/2$. For a pessimistic maximum misalignment of 10°=π/18 rad, this translates to a maximum misalignment-associated uncertainty $+0/-(0.015b^*)$. This can be of some, but limited, significance: for a measured bondline thickness value of 300 μm (which is an upper bound to the values actually measured in sections), the error would be only (+0 / – 4.5) μm.

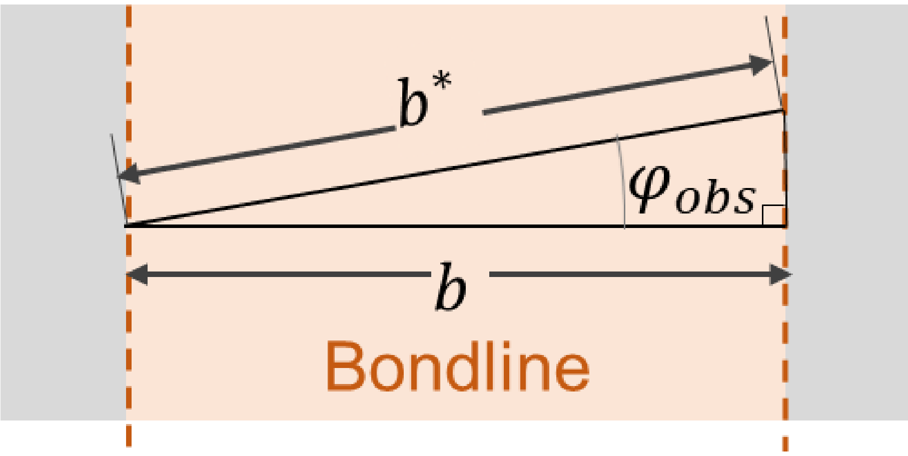

Figure G-2. Effect of a misalignment on the thickness measurement: instead of the real thickness b, a higher value b^* is observed. The value of the angle φ_{obs} in the figure is 10°, easily ascertained by a human.

The final, harder-to-quantify contributor to uncertainty is the presence of a burr left from the sectioning process. Whereas highly localised ones are easy enough to spot and avoid (as the example in the left side of Figure G-3), there is no guarantee that each and every one will be so small — or indeed, that a burr region will have been left in each section. Although no direct quantification has been produced, it is possible to estimate the impact from unexpected thickness values,

[xlii] Strictly speaking, the bondline has no single perpendicular vector as its thickness fluctuates; in practice, as the change rate is very small (tens of μm over tens or hundreds of mm), both adherend surfaces are approximated as parallel at any given position.

where there is a sharp variation across the length or cord of a stringer. Based on this, it is estimated that the maximum magnitude of a burr is a rare ±50 μm error in the measured bondline thickness, with more likely ±25 μm occasional deviations. Any additional, pervasive bias seems to be repeatable enough to be accounted for as an error constant.

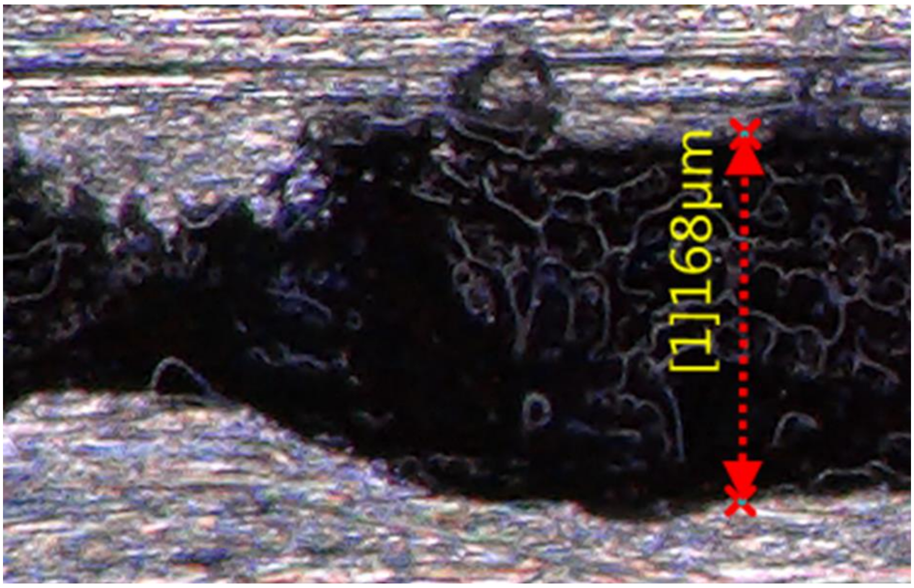

Figure G-3. Bond micrograph with a several-tens-of-microns plasticised zone visible on the left.

Appendix H — Model calibration

H.1 The model calibration paradigm

Computational models require some degree of calibration because of uncertainty around underlying parameters which may not be directly observable (e.g. material properties), as well as limitations of the model itself due to e.g. simplifications of the real physics. Further uncertainty results from lack of total certainty on the prescribed inputs, and from measurement error in any real observations used to calibrate the model. Many of the presumable sources of uncertainty won't be addressed in this work due to sheer lack of resources which prevents thorough physical exploration of a highly multivariate problem[xliii]; however, an attempt will be made to examine the factors of variability, as far as it has been economical do to so.

In their seminal work on model calibration, Kennedy and O'Hagan (Kennedy and O'Hagan, 2001) proposed the following calibration structure:

$$(observed\ value) = \rho \cdot (model\ prediction) + (inadequacy) + (observation\ error) \quad \textbf{(H-1)}$$

where ρ is a regression parameter and the "inadequacy" (i.e. the model error still unexplained after accounting for all calibration parameters) is only dependent on the model inputs. The authors emphasised that the exact structure presented was a pragmatic solution that works, but alternatives should be possible; indeed, "[this equation] is only one possible formulation; equally cogent arguments could probably be evinced in favour of other models". According to this, the exact formulation, and the exact way in which it is implemented, are of no critical concern. Further, the sensible solution may depend on what information is available: for instance, in their case study Kennedy and O'Hagan deliberately simplified the observation error as following a normal distribution of known, fixed mean and variance, with no discussion of the specific observations taken or the

[xliii] Recall that the inputs to the assembly problems herein are the entire geometry (in a discrete grid), compliance matrices, external forces, and adhesive properties/cure parameters. The geometry alone makes for hundreds of correlated independent variables even if the assembly compliance and external forces are considered known and fixed. Evaluating e.g. competing adhesive models of differing complexity would increase the problem dimensionality even further.

method used. Attention was drawn to how modelling parameters as random in a Bayesian fashion (that is, making them dependent on uncertain hyperparameters) may be risky due to lack of knowledge of the hyperparameters, as well as computational cost; proposing instead to “derive plausible estimates of [the hyperparameters] and then to act as if these were fixed”.

Of course, ever-evolving computational power and tools mean that processing cost is less of a concern as time passes; further, some hyperparameters will be shown to be possible to estimate with good certainty from dedicated observations (even though simply deriving Maximum Likelihood Estimations [MLE] from the same data would not materially affect the results).

More recently, in a widely-cited paper, Arendt *et al.* (Arendt, Apley and Chen, 2012) employed the framework above to support model validation, including a provision to ‘close the loop’ by refining the model or generating more calibration observations (Figure H-1). This framework was demonstrated in calibration of FEA for a simple structure, and similar to the seminal paper, used MLE of the hyperparameters rather than modelling them as random. The paper noted that it may be hard to distinguish (“identify”) error due to calibration parameters from intrinsic model inadequacy; further, it was shown that the calibration parameters and various quantifiers of uncertainty/error should not be assumed to be well-known: “Assuming informative priors for the calibration parameters or the inadequacy function is not a satisfying solution to the identifiability problem”. Thus, explicitly acknowledging the uncertainty, and attempting to address it through well-chosen calibration tests, may be less problematic; indeed, “incorporating multiple experimental responses that share a mutual dependence on a common set of parameters can substantially improve identifiability”.

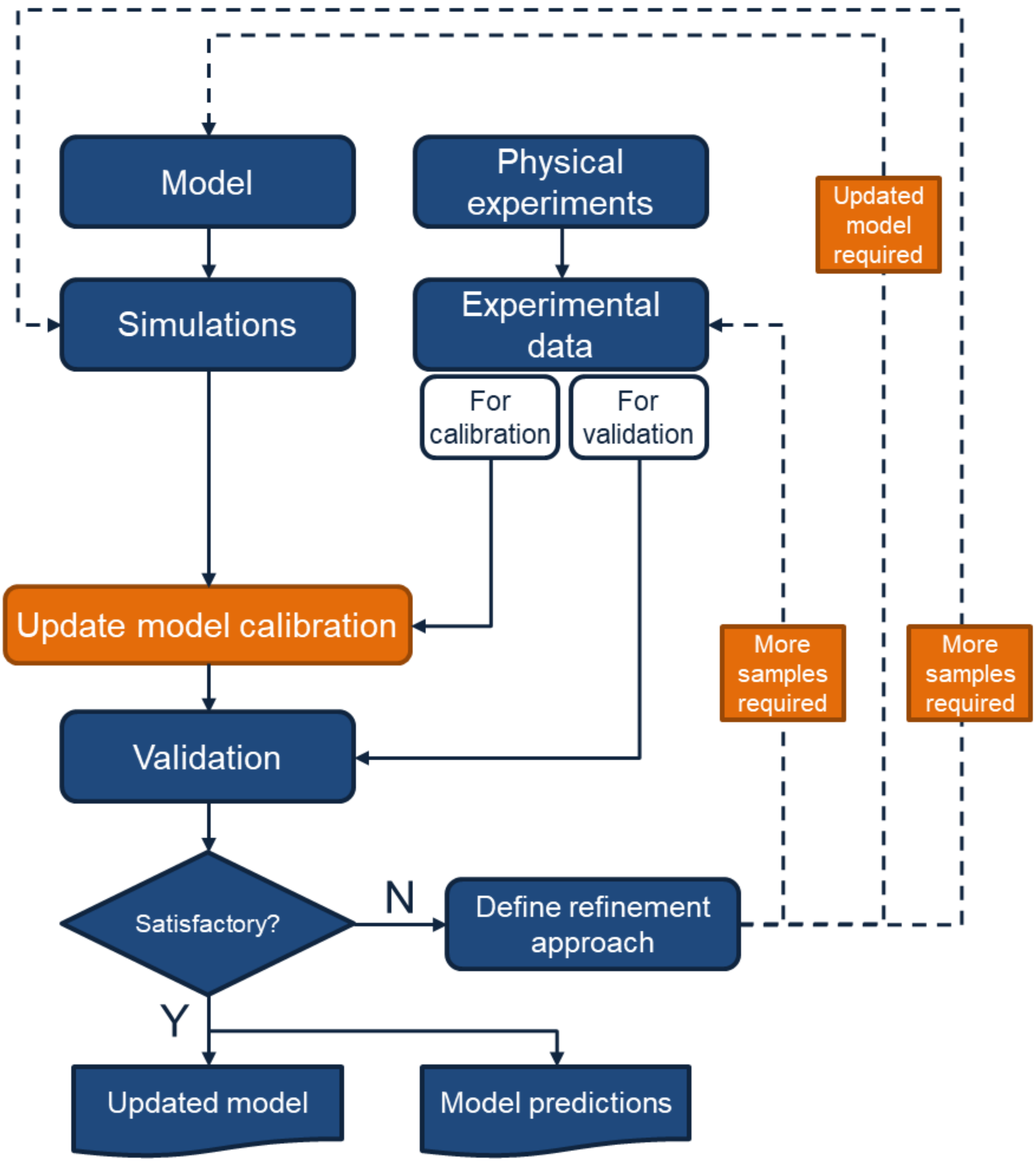

Figure H-1. Framework for model updating/validation/refinement using the model calibration paradigm (based on Arendt, Apley and Chen, 2012).

Both references above used Gaussian Processes, but also drew attention to the potential difficulty of deriving distributions for large numbers of calibration parameters, mentioning the possibility of conducting a Markov Chain Monte Carlo (MCMC) experiment instead. This was indeed the case, for instance, in another widely-cited paper by Qian and Wu (Qian and Wu, 2008), who used hierarchical Bayesian modelling to generate a linear regression between cheap-but-inaccurate and expensive-but-accurate experiments. This regression was demonstrated on two different engineering modelling problems, without considering any internal calibration parameters. By retaining the scaling factor ρ from the original formulation by Kennedy and O'Hagan, and in combination with the "inadequacy" (which provides a displacement-like, or bias, correction), an adjustment model was generated for translation between different experiments that "give different outputs but share similar trends... Most problems in practice fall in [this category]".

In the present application, a single iteration, without closing the loop in Figure H-1, will be presented, using MCMC. Due to time and resource constraints, the loop can not be completely closed (which would require carrying out additional tests); rather, the inadequacy values will be used to support the discussion of potential model improvements and extra tests. Bayesian MCMC is a method for statistical regression and inference based on observed data and probabilistic models of arbitrary complexity. It has become increasingly popular thanks to widely accessible user-friendly front-ends and increasingly cheaper computational resources, and performs particularly well against high-dimensional problems. It is presented below.

H.2 Basics of Bayesian Markov Chain Monte-Carlo (MCMC)

Bayesian statistical analysis differs from typical probabilistic analysis in the epistemic treatment of parameters: while in a probabilistic study values will be fixed, or if calculated, the Maximum Likelihood Estimation (MLE) of a statistic may be used, the Bayesian paradigm treats the observed data as fixed and considers uncertainty for the underlying parameters. This inversion offers the advantage of laying bare any model assumptions, including certainty of initial guesses (prior distributions). By combining priors and likelihoods, it is possible to derive probability distributions from arbitrarily complex relationships between output variables and model (hyper)parameters (henceforth "parameters"). Conversely, by using the actual observed data, the prior distribution of parameters can be updated to take into account the real results of experiments and simulations. It is possible to progressively update a model by adding new observational data; even though some basic random distributions support doing this analytically, it is more often necessary to perform a numerical or stochastic calculation every time the parameters are updated.

Bayesian MCMC is one such way of performing stochastic calculation. Potential parameter combinations are randomly generated based on given priors and already-accepted combinations; they are accepted or rejected depending on how well the candidate parameter values explain observed data when compared to the immediate previous iteration (thus “Markov Chain” as each iteration’s candidate parameter values are correlated with the previous iteration’s). For a large enough number of iterations, the density of parameter combinations will approximate the posterior multidimensional probability (thus “Monte-Carlo”). Many variants exist depending on how the candidate parameter values are sampled; a popular one is the Metropolis-Hastings algorithm with Gibbs sampling (which draws new parameter values one by one using a unidimensional, symmetrical distribution). This was the case in the paper by Qian and Wu referenced above. Gibbs sampling provides a good solution for multidimensional problems, and is quite amiable to general MCMC tools. The general flow of the technique is presented in Figure H-2. A good introduction to Bayesian MCMC, including Gibbs sampling, is presented by Andrieu *et al* (Andrieu et al., 2003). Importantly, thanks to the development of readily available MCMC processing tools, it is not necessary to develop any routines from scratch. In this case, the tool JAGS implemented in R (or, RJAGS), developed by Martyn Plummer[xliv], has been used.

[xliv] Accessible through http://mcmc-jags.sourceforge.net/ (working link last visited 2019-07-13). Version 4.3.0 (released 2017-07-18).

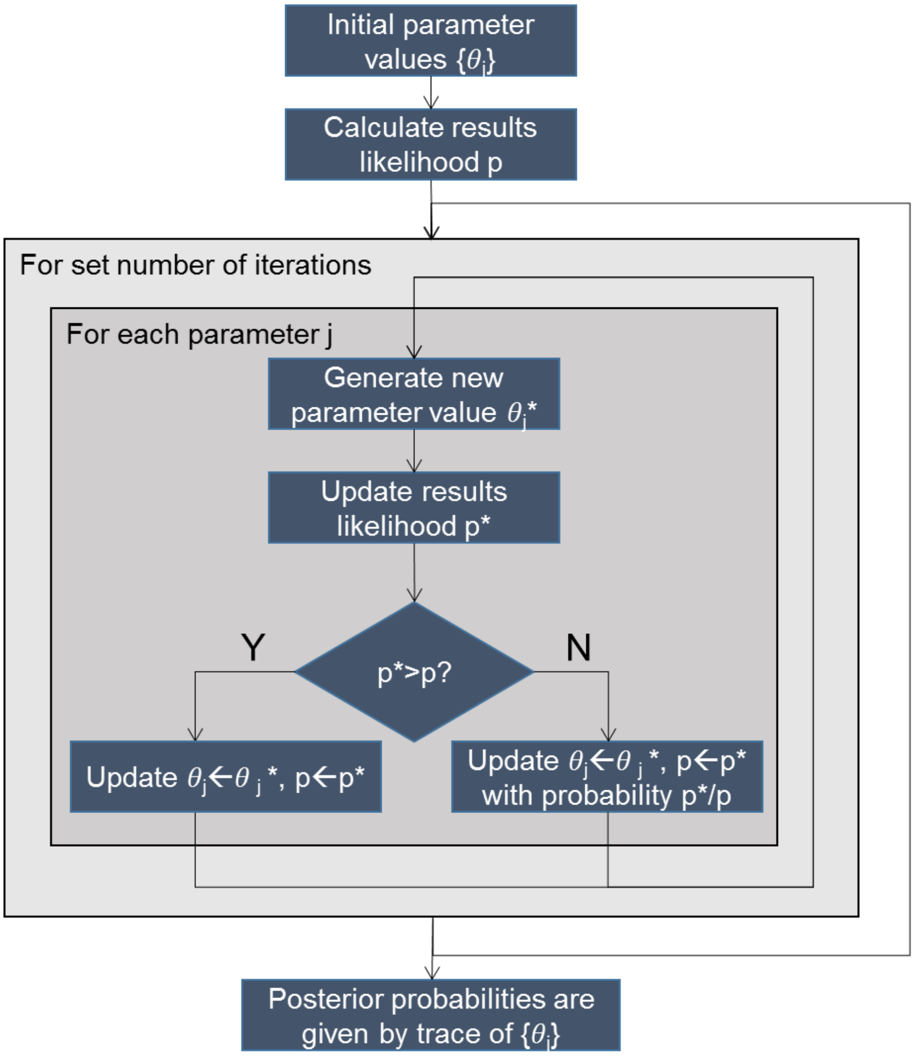

Figure H-2. Overview flow of MCMC Gibbs sampling procedure.

If dealing with multiple, group-dependent sources of uncertainty, this MCMC approach potentially offers stronger analysis than simply segregating results by different criteria and performing regression separately: by creating a hierarchical model, it is possible for the (un)certainty on common parameters to be shared, while still accounting for group differences, and accommodating non-categorical variables. In addition, the observed data can combine arbitrarily variegated sources, e.g. calibration and reference observations, reducing uncertainty as and when such data becomes available (as suggested by Arendt *et al*). This is precisely what will be done in this case.

H.3 Model for simulation/measurement validation

Our assembly problems contain a large number of geometric inputs which, by the nature of the assembly procedure, are highly correlated; the outputs are similarly correlated and additionally show non-linear relationships with the inputs due to the contact restriction. For this reason, a simulation-experiment correlation that tried to account for the whole simulated/inspected point grid would risk being overcomplicated and ridden with many unidentifiable components.

Instead, a category-based, low-dimensional model will be used for the model inadequacy δ_{mod}, accounting for the following[xlv]:

- Location potentially linked with inaccuracy due to squeeze-flow simplification:
  - `xsectpos`: Is the point near the stringer foot middle or near the edge? (middle[1] or edge[2])
  - `contact`: Is the point at a designated gap area, or is hard contact expected from the beginning of assembly? (gap[1] or no gap[2])
- Boundary conditions which result in different degree of part deflection:
  - `BC_skin`: Single- or Double-sided pressure (Single[1] or Double[2])
  - `BC_strg`: Degree of skin-deflection interference (8 values, depending on the specific stringer arrangement and particular stringer):
    - [1] One 'bad' stringer — Side stringer (nominally flat);
    - [2] One 'bad' stringer — Middle stringer (added profile variation)
    - [3] No defect interference — Any stringer
    - [4] Large defect interference — Side stringer
    - [5] Large defect interference — Middle stringer
    - [6] Some defect interference — Side stringer (not flipped)
    - [7] Some defect interference — Middle stringer (not flipped)
    - [8] Some defect interference — Side stringer (flipped)

[xlv] Numbers in brackets are used to indicate the subgroup for each categorical input considered.

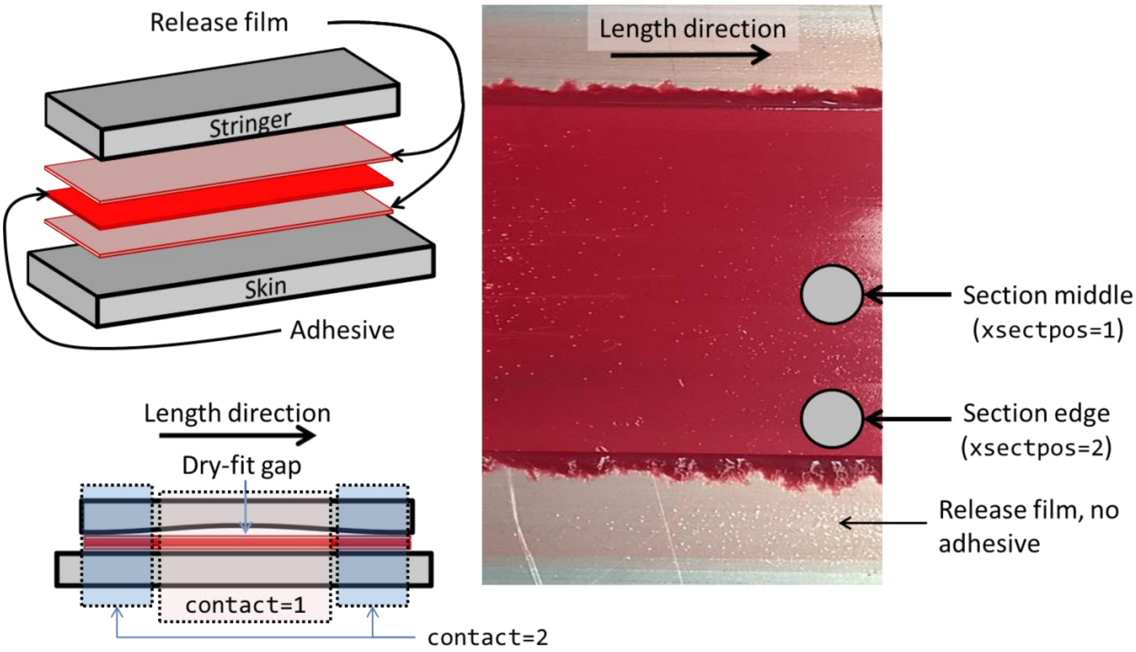

Figure H-3. Formation of the bond and location-related groups.

The factors above correspond to known inputs of the experimental assessment, and will be modelled hierarchically such that there may be a linear correction between any two different categories.

The factors relating to boundary conditions are expected to reflect as part of a proportionality factor ρ, since they affect the overall ability to close a gap by deflection. Meanwhile, the location factors are translated as additive terms since they relate to modelling inaccuracies in an additive element of the bondline geometry model.

In addition, the observation deviation ε depends on the particular method:

- Verifilm and contact measurement:
  - Additional thickness from two layers of release film;
  - Micrometre measurement error.
- Bonding and optical measurement of sections:
  - Optical measurement error;
  - Unremoved metal burr near the bondline.

Any unexplained deviation left after these adjustments is expressed by a further random component of inadequacy ς. Ideally, the dispersion of this component will be small compared to that of other corrections and to typical engineering tolerances; in such a case, the logical conclusion would be that the simulation results can be reliably translated into the measured test values (even if only for the tiny subset of the overall design space that has been explored).

The base model for translation of the simulation into an observed thickness value, then, is

$$b_{obs} = (\rho \times b_{sim} + \delta_{mod} + \varepsilon_{meas}) + \varsigma \tag{H-2}$$

or alternatively, separating the minimum adhesive thickness $b_{min,sim}$ and thickness variation in each stringer $b_{var,sim}$,

$$\begin{aligned} b_{obs} &= \left(\rho \times b_{var,sim} + b_{min,sim} + \delta_{mod} + \varepsilon_{meas}\right) + \varsigma \\ b_{var,sim} &= b_{sim} - b_{min,sim} \end{aligned} \tag{H-3}$$

These alternatives will be referred to by their equation numbers; respectively, as (H-2) and (H-3).

In both cases, the regression coefficient ρ and inadequacy δ_{mod} are defined as:

$$\begin{aligned} \rho &= \left(\rho_{general} + \zeta_{BC,skin} \times \xi_{BC,strg}\right) \\ \delta_{mod} &= (\alpha_{xsectpos} + \beta_{contact}) \end{aligned} \tag{H-4}$$

Meanwhile, ε_{meas} is the measurement error (which has been discussed in Appendix F and Appendix G), and ς is the calibration model uncertainty.

The prior distributions for these variables are fairly non-informative (i.e. their dispersion is higher than that expected, reflecting the lack of prior information):

$$\begin{aligned} &\rho_{general} \sim \mathrm{N}\,(1, 0.1) \\ &\alpha_{xsectpos} \sim \mathrm{N}\,(1, 0.1) \\ &\beta_{contact} \sim \mathrm{N}\,(1, 0.1) \\ &\zeta_{BC,skin} \sim \mathrm{N}\,(1, 0.1) \quad | \quad \zeta_{\mathrm{BC,skin}} > 0 \text{ [amplifies effect of stringer position]} \\ &\xi_{BC,strg} \sim \mathrm{N}\,(1, 0.1) \end{aligned} \tag{H-5}$$

$\varsigma \sim \mathrm{N}\,(0, 0.\sigma_\varsigma)$ | $1/\sigma_\varsigma^2 \sim \Gamma(5, 0.04)$ [so the expected value of $1/\sigma_\varsigma^2$ is $1/0.1^2$]

In the case of the measurement-related uncertainties, initial uncertainty calculations were made in previous appendices:

For verifilm: $\varepsilon_{meas} \sim \mathrm{N}(\mu_{rf}, \sigma_{micrometre})$
$\mu_{rf} \sim \mathrm{N}\,(0.05, 0.005)$
$1/\sigma^2_{micrometre} \sim \Gamma(5, 0.0004)$ [so the expected value of $1/\sigma^2_{micrometre}$ is $1/0.01^2$]
(H-6)
For bonded micrograph: $\varepsilon_{meas} \sim \mathrm{N}(\mu_{burr}, \sigma_{micrograph})$
$\mu_{burr} \sim \mathrm{N}\,(-0.04, 0.01)$ [the burr reduces measured thickness]
$1/\sigma^2_{micrograph} \sim \Gamma(5, 0.0004)$ [so the expected value of $1/\sigma^2_{micrograph}$ is $1/0.01^2$]

In the definitions above, $\mathrm{N}\,(\mu, \sigma)$ is the normal distribution with mean μ and variance σ^2; and $\Gamma\,(k, \theta)$ is the gamma distribution with shape k and scale θ. These distributions are widely used and we will not linger in them.

H.4 MCMC regression: simulated – measured results

The MCMC regression was performed according to both models (H-2) and (H-3) using the priors in (H-5) and (H-6). Micrometre measurements of the release film alone were included in the analysis dataset to support calibration of the contact measurements. Five chains and 10^5 iterations were used. As a reference, a similar regression was performed using only 10^4 iterations; the results only varied by thousandths, which indicates convergence of the Markov chain. The resulting fit of the explanatory variables is shown on Table H-1 (note: units are omitted from the following discussion; the table indicates which variables are dimensional). Several key aspects stand out[xlvi]:

- The infuence of position along the cross-section isn't accounted for much better with the edge/middle correction ($\mathrm{Exp}[\alpha_{middle} - \alpha_{edge}] < 0.006$).In contrast, accounting for location under a high pressure zone with an extra corrective term yields a larger effect ($\mathrm{Exp}[\beta_{gap} - \beta_{no\ gap}] \approx 0.020$; i.e. high

[xlvi] Part of the discussion that follows uses the expected value, denoted as $\mathrm{Exp}[variable]$. In addition, the suffix p% is used to indicate the value for which a variable's cumulative probability achieves p%. This is estimated through the percentiles of the distributions obtained by MCMC.

contact areas are comparatively thinner than simulated). These values do not change between both models used.

- The uncalibrated simulation results, according to the MCMC adjustment, tended to overestimate the bondline thickness ($\mathrm{Exp}[\rho_{general}] = 0.815$ for model (H-2) and $\mathrm{Exp}[\rho_{general}] = 0.940$ for model (H-3)). Since in model (H-3) only the bondline variation (from the dry component of the simulation) is multiplied, the higher value of $\rho_{general}$ does not necessarily result in a larger predicted thickness.
- All measurement-related uncertainties are small contributors to the overall variability. The means for both burr and release-film thickness are well within the bounds indicated by the priors, and show minimal dispersion; similarly, the uncertainty from micrograph and micrometre assessments are very small ($\sigma_{micrograph,97.5\%} = 0.008$; $\sigma_{micrometre,97.5\%} = 0.006$)
- The residual prediction error (measured by standard deviation σ_{ς}) is satisfactorily small ($\sigma_{\varsigma,97.5\%} > 0.025$; this is comparable to typical shopfloor-based measurement systems, and reasonably small compared to a notional bondline thickness tolerance of 0.250 mm).

Note the additive corrections a, b have a very high dispersion because they are able to drift together during the random walk. However, they are highly correlated: $\alpha_{middle} - \alpha_{edge}$, $\beta_{gap} - \beta_{no\ gap}$, and $\alpha - \beta$ show a much lesser degree of scatter. Indeed, the 95% equal-tailed confidence interval for the value of $\alpha_{middle} + \beta_{gap}$ is only 0.013 mm wide, and the differences between location categories are even less dispersed, as shown in the blue-shaded rows at the top of Table H-1,

Table H-2. A similar effect is observed for the components of ρ, as evidenced by the comparatively minor uncertainty of $\rho_{general} + \zeta_{Single} \times \xi_{[1]}$ included in the tables.

Examination of the expected values, for different boundary conditions, of ρ, $\mathrm{Exp}[\rho] \approx \mathrm{Exp}[\rho_{general}] + \mathrm{Exp}[\zeta_{(BC,skin)}] \times \mathrm{Exp}[\xi_{BC,strg}]$ (Figure H-4, Figure H-5) also highlights the cases where the assembly simulations produced a particularly inaccurate outcome. Specifically, stringer boundary condition [7] “Some defect interference — Middle stringer (not flipped)” had predicted thickness values that were comparatively much larger than the measurements (thus resulting in lower final ρ values). This is most prominent in the results for model (H-3) as the bondline thickness variation was small for this case. More widely, the values of $\mathrm{Exp}[\rho]$ for stringer boundary conditions [1], [5], [6], [7] were the farthest from a value of $\rho = 1$ (which would have meant a 1:1 correlation between simulations and test results). These four boundary conditions correspond to assembly cases with some twist associated with deflection of the skin (and of the bonding table) resulting in lateral deflection which may not be fully captured by the simplified adhesive flow assumptions and foot flange discretisation.

Table H-1. Model correction variable values obtained with MCMC fit model (H-2).

variable	percentile, p 2.5%	25%	50%	75%	97.5%	mean	95% CI width
$\alpha_{middle} - \alpha_{edge}$ (mm)	0.004	0.006	0.006	0.007	0.008	**0.006**	**0.004**
$\beta_{gap} - \beta_{no\ gap}$ (mm)	0.019	0.020	0.020	0.021	0.022	**0.020**	**0.003**
$\alpha_{middle} + \beta_{gap}$ (mm)	0.030	0.035	0.037	0.039	0.043	**0.037**	**0.013**
α_{middle} (mm)	-0.075	-0.022	0.020	0.057	0.118	0.019	
α_{edge} (mm)	-0.081	-0.028	0.014	0.051	0.112	0.013	
β_{gap} (mm)	-0.081	-0.020	0.016	0.058	0.112	0.018	
$\beta_{contact}$ (mm)	-0.101	-0.040	-0.004	0.038	0.091	-0.003	
ζ_{Single}	0.147	0.226	0.274	0.318	0.397	0.272	
ζ_{Double}	0.102	0.156	0.189	0.229	0.317	0.195	
$\xi_{[1]}$	-0.199	-0.143	-0.113	-0.077	0.008	-0.108	
$\xi_{[2]}$	-0.145	-0.082	-0.051	-0.019	0.043	-0.051	
$\xi_{[3]}$	-0.075	-0.022	0.010	0.047	0.120	0.014	
$\xi_{[4]}$	0.041	0.100	0.145	0.215	0.341	0.162	
$\xi_{[5]}$	-0.109	-0.050	-0.018	0.017	0.090	-0.016	
$\xi_{[6]}$	-0.206	-0.138	-0.100	-0.060	0.020	-0.098	
$\xi_{[7]}$	-0.441	-0.356	-0.307	-0.243	-0.101	-0.295	
$\xi_{[8]}$	-0.020	0.049	0.093	0.145	0.239	0.099	
σ_{ς} (mm)	0.023	0.023	0.023	0.023	0.024	**0.023**	**0.001**
$\rho_{general}$	0.763	0.799	0.816	0.831	0.863	**0.815**	**0.100**
$\rho_{general} + \zeta_{Single} \times \xi_{[1]}$	0.739	0.768	0.784	0.799	0.829	**0.784**	**0.090**
μ_{burr} (mm)	0.011	0.013	0.014	0.014	0.016	**0.014**	**0.005**
$\sigma_{micrograph}$ (mm)	0.005	0.006	0.006	0.007	0.008	**0.006**	**0.003**
μ_{rf} (mm)	0.049	0.050	0.051	0.051	0.052	**0.051**	**0.003**
$\sigma_{micrometre}$ (mm)	0.004	0.005	0.005	0.005	0.006	**0.005**	**0.002**

Table H-2. Model correction variable values obtained with MCMC fit model (H-3).

variable	percentile, p 2.5%	25%	50%	75%	97.5%	mean	95% CI width
$\alpha_{middle} - \alpha_{edge}$ (mm)	0.004	0.005	0.005	0.006	0.007	**0.005**	**0.003**
$\beta_{gap} - \beta_{no\ gap}$ (mm)	0.018	0.019	0.020	0.020	0.021	**0.020**	**0.003**
$\alpha_{middle} + \beta_{gap}$ (mm)	0.008	0.010	0.010	0.011	0.013	**0.010**	**0.005**
α_{middle} (mm)	-0.052	-0.008	0.018	0.033	0.076	0.013	
α_{edge} (mm)	-0.057	-0.013	0.013	0.028	0.071	0.008	
β_{gap} (mm)	-0.065	-0.023	-0.008	0.018	0.062	-0.003	
$\beta_{contact}$ (mm)	-0.085	-0.042	-0.027	-0.002	0.043	-0.023	
ζ_{Single}	0.555	0.630	0.671	0.712	0.793	0.672	
ζ_{Double}	0.158	0.251	0.298	0.346	0.437	0.298	
$\xi_{[1]}$	-0.335	-0.214	-0.151	-0.088	0.033	-0.151	
$\xi_{[2]}$	-0.065	0.030	0.080	0.130	0.228	0.080	
$\xi_{[3]}$	-0.105	-0.016	0.031	0.078	0.170	0.031	
$\xi_{[4]}$	0.120	0.210	0.259	0.308	0.406	0.260	
$\xi_{[5]}$	-0.367	-0.289	-0.249	-0.208	-0.131	-0.249	
$\xi_{[6]}$	-0.242	-0.132	-0.075	-0.018	0.092	-0.075	
$\xi_{[7]}$	-0.739	-0.658	-0.615	-0.573	-0.492	-0.616	
$\xi_{[8]}$	-0.025	0.081	0.136	0.191	0.295	0.136	
σ_{ς} (mm)	0.022	0.023	0.023	0.023	0.024	**0.023**	**0.001**
$\rho_{general}$	0.883	0.920	0.939	0.959	0.996	**0.940**	**0.113**
$\rho_{general} + \zeta_{Single} \times \xi_{[1]}$	0.702	0.792	0.838	0.883	0.971	**0.837**	**0.269**
μ_{burr} (mm)	0.012	0.013	0.014	0.015	0.017	**0.014**	**0.005**
$\sigma_{micrograph}$ (mm)	0.005	0.006	0.006	0.007	0.008	**0.006**	**0.003**
μ_{rf} (mm)	0.049	0.050	0.051	0.051	0.052	**0.051**	**0.003**
$\sigma_{micrometre}$ (mm)	0.004	0.005	0.005	0.005	0.006	**0.005**	**0.002**

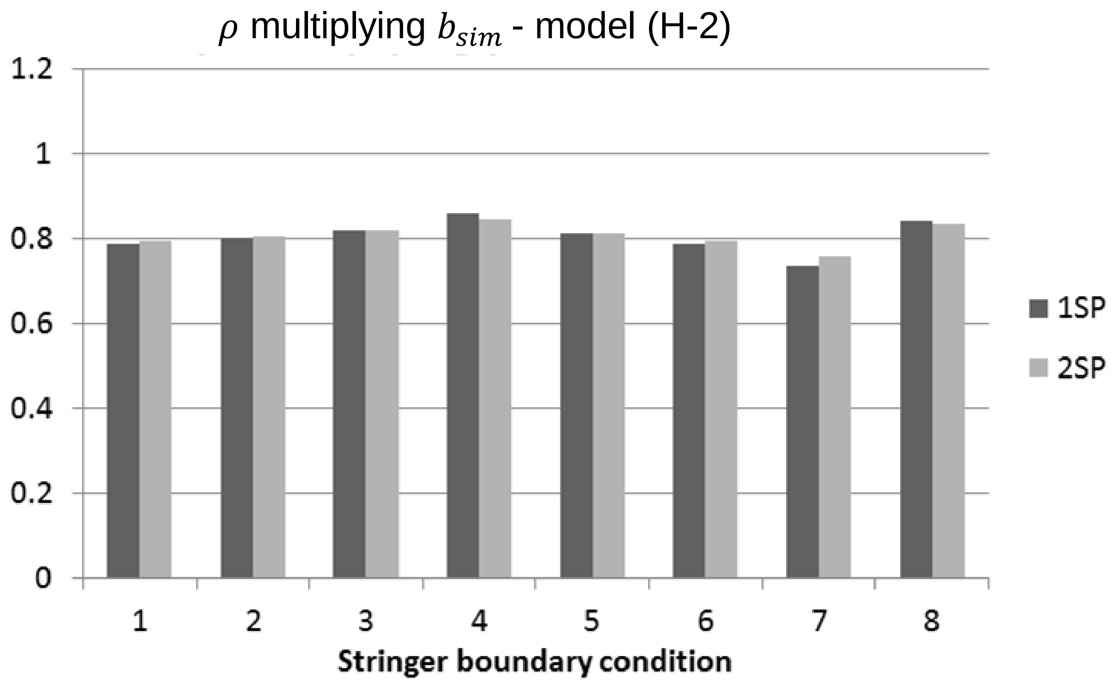

Figure H-4. Expected values of ρ for model (H-2), for all combinations of skin (1SP/2SP) and stringer (1-8) boundary conditions.

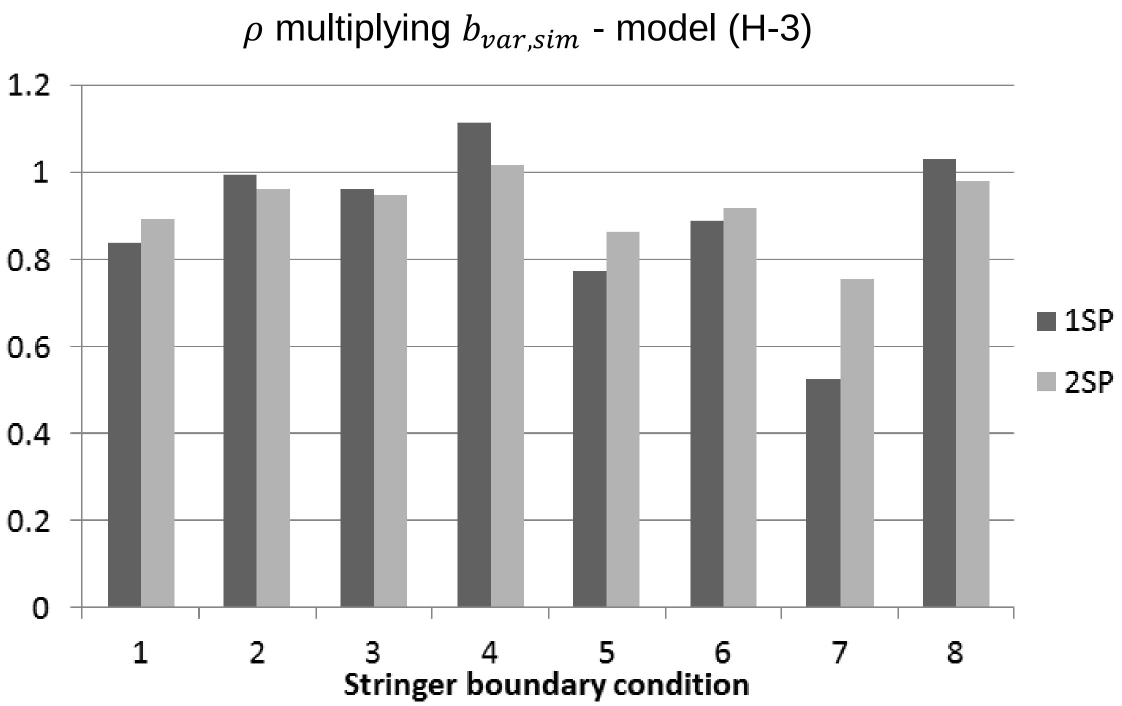

Figure H-5. Expected values of ρ for model (H-3), for all combinations of skin (1SP/2SP) and stringer (1-8) boundary conditions.

Appendix I — Test of the spectral pressure score

I.1 Introductory considerations

As outlined in prior discussion, spectral analysis is *a priori* an attractive way of quantifying viability of an assembly. It has also been outlined, however, how the analysis is not without shortcomings.

In order to ascertain viability of the technique, the analysis has been applied to all the assemblies studied. Spectral pressure scores will be considered viable if they correlate with the pressures actually applied; that is, if, upon deflection of a stringer under a pressure P, its pressure score similarly decreases by P.

The formal relation that describes this pressure score reduction/improvement is

$$\left(\sum_{j=0}^{k} P_j\right)_0 - \left(\sum_{j=0}^{k} P_j\right)_P = P \qquad \textbf{(I-1)}$$

where P_j designates the calculated closure pressure for the corresponding single wavelength $\lambda_j = 1/f_j$; the subscripts 0 and P indicate the unpressed and pressed status respectively; and k corresponds to a cutoff variation wavelength which should be consistent across cases of the same assembly.

Henceforth, f_k^* will be used to refer to the first (lowest) spatial frequency for which equation (I-1) holds[xlvii], whereas f_k will be any cutoff frequency for which the pressure score improvement is calculated (even if it does not match the pressure applied).

The two main aspects to be explored are:

I. How does the pressure score improvement behave for changing assembly conditions and for more frequencies analysed? i.e. what is the general behaviour of the left-hand term of equation (I-1)?

[xlvii] In practice, given the discrete nature of the spectral analysis, it will be the lowest value of f_k for which the pressure score improvement is equal to or greater than the pressure applied.

II. When/how is equation (I-1) fulfilled? Is f_k^* consistent across different variants of an assembly scenario, and how does it relate to the residual variation still present?

These aspects will be explored in the following two subsections. It will be shown that while there is a qualitative correspondence between the pressure score and the gap geometry, quantitative insights are limited.

I.2 General trend in pressure score improvement

The behaviour of the assemblies studied will be visualised with a spectral plot as shown in Figure I-1. The horizontal axis corresponds to the maximum spectral frequency (or minimum wavelength) analysed. The vertical axis corresponds to the left hand term in equation (I-1)). A horizontal line marks the pressure actually applied (i.e. the right hand term in the equation). An arrow marks the value of $1/f_k^*$ where equation (I-1) is met.

Given the logarithmic scale, negative values (i.e. *increases* in the score) are conspicuously absent. For Figure I-1, this is the case for the longer wavelengths $1/f_k$ ≥777 mm, as well as around $1/f_k$ ≥104 mm. In addition, all spectra have been truncated to 0.01 mm precision; this is expressed as a small plateau at the very right of Figure I-1.

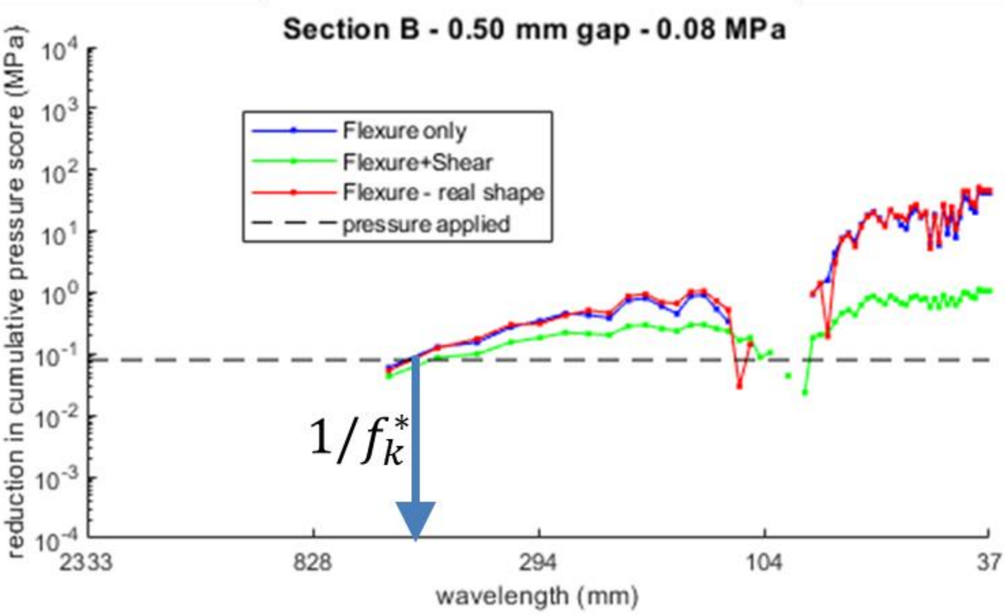

Figure I-1. Pressure score improvement plot example (flat thin stringer, deflecting on 0.50 mm shims under 0.08 MPa). The highest wavelength $1/f_k^*$ that meets equation (I-1) is marked.

I.2.1 Flat assembly scenarios

For the first set of tests conducted with flat stringers and shims, the results for all pressures tested are presented for both stringer cross-sections. Only the results for the smallest and biggest gap simulated (0.2 mm and 0.8 mm, respectively) are presented; the 0.5 mm gap assemblies did not behave any differently. The three spectral analysis approaches have been used — flexural-only, flexural-and-shear, and deflection-shape decomposition. All three behave very similarly, with no substantial divergence until very high spatial frequencies ($1/f_k < 104$ mm) which are in the order of magnitude of the stringer cross-section, and where the slender beam assumption does not hold. Importantly, although the exact shape of the mode (sine or polynomial) has little bearing on the overall behaviour of the calculated, it is true that the polynomial-based spectral analysis consistently yields slightly higher improvements in the calculated pressure score.

An important observation is that, whenever the gap closure is most incomplete (due to the large initial gaps, low bonding pressure or stiff part), the pressure score shows a large number of spurious increases. This is most noticeable when comparing the cases of the 'Thick' stringer A under 0.08 MPa with an 0.80 mm gap (Figure I-2, bottom right) against the 'Thin' stringer A under 0.60 MPa with an 0.20 mm gap (Figure I-5, top left): the former is jagged and fragmentary, while the latter shows a steady climb with only a slight dip around $1/f_k = 104$ mm. Such behaviour is consistent with the appearance of artefacts due to local deflection: as local gaps become smaller, their spectral expression gets confined to the highest-frequency harmonics, and the longer wavelengths are less affected by them.

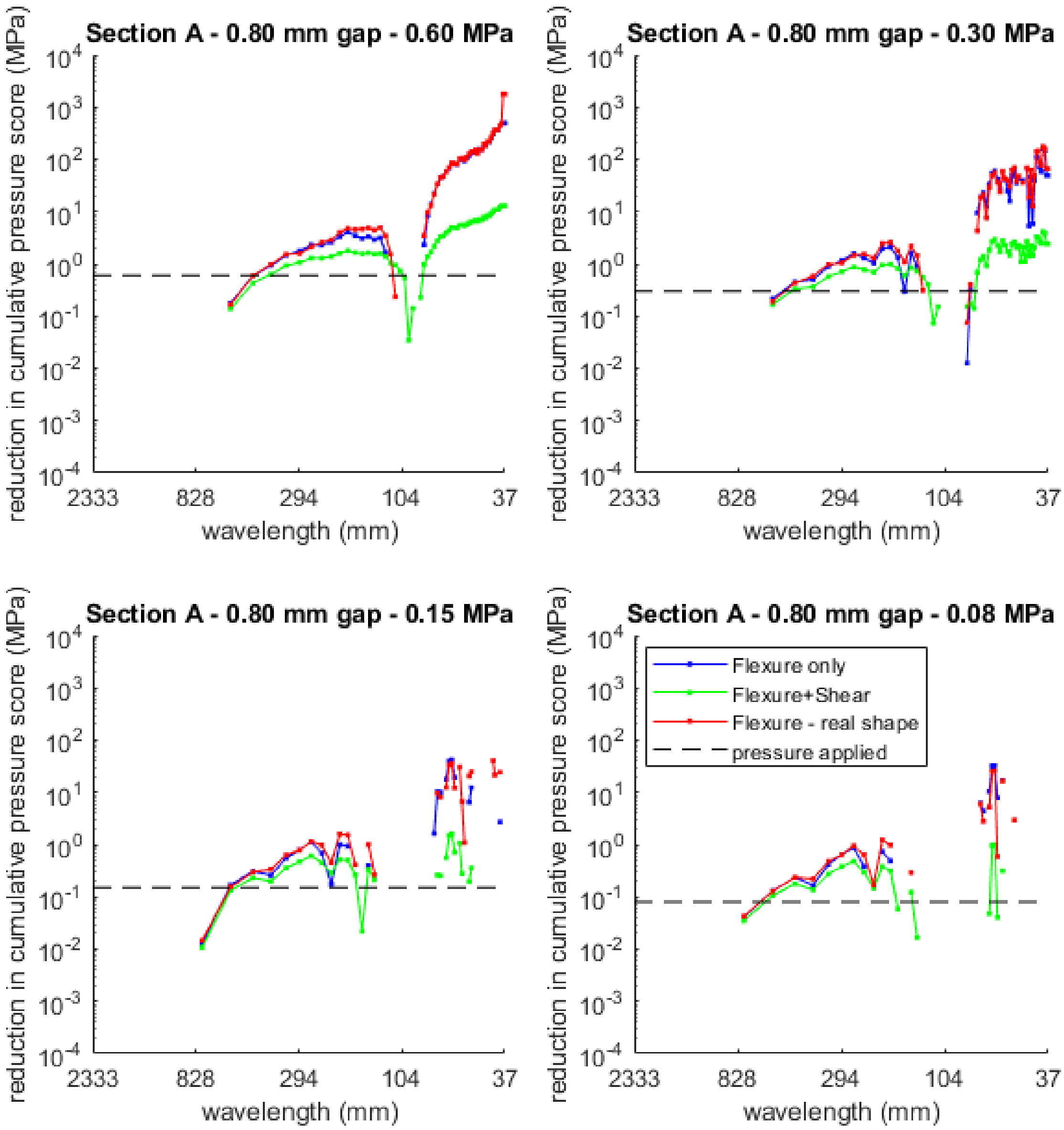

Figure I-2. Pressure score improvement for the flat thick stringer assemblies (largest gap studied) according to all three spectral scoring criteria advanced.

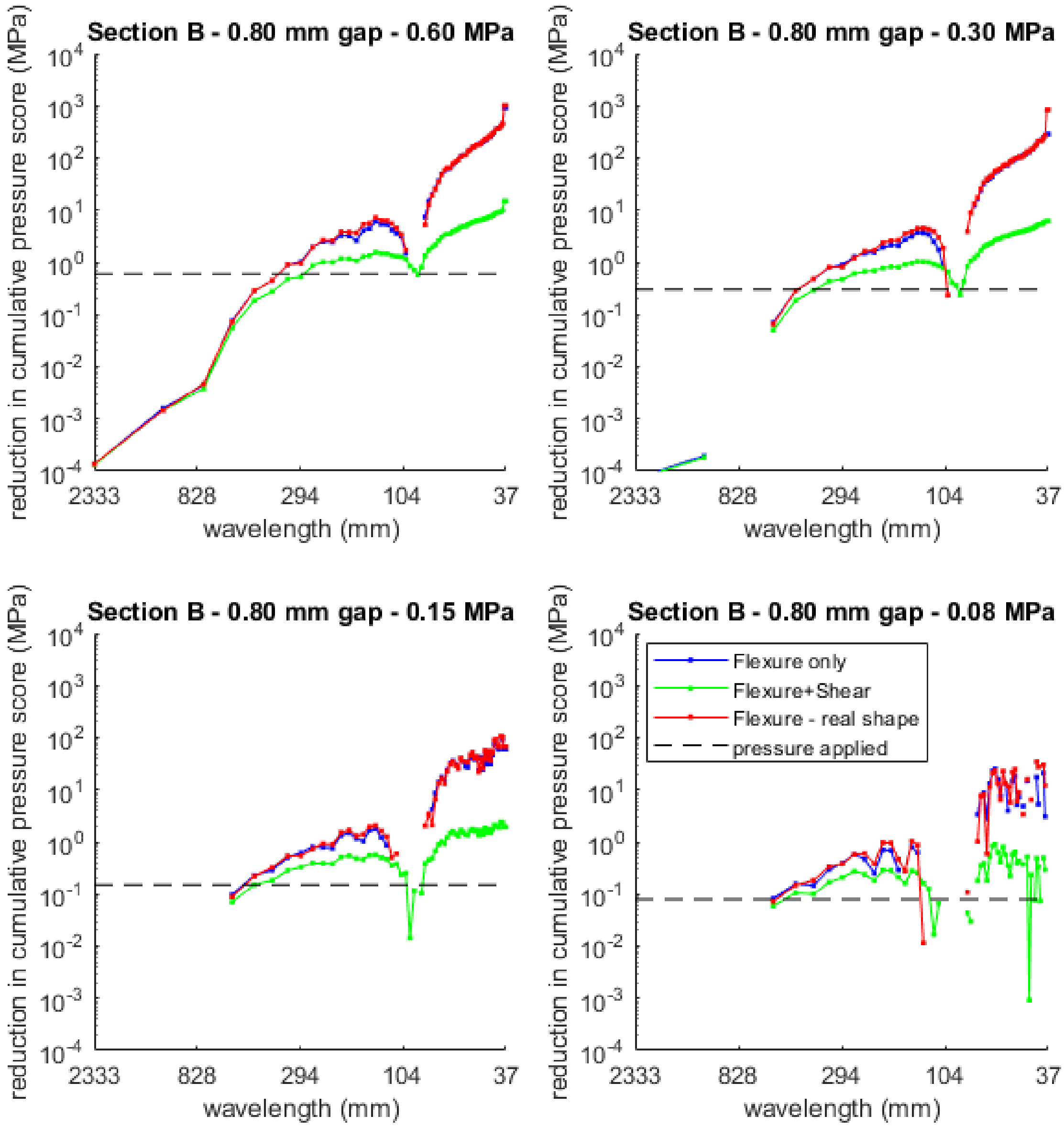

Figure I-3. Pressure score improvement for the flat thin stringer assemblies (largest gap studied) according to all three spectral scoring criteria advanced.

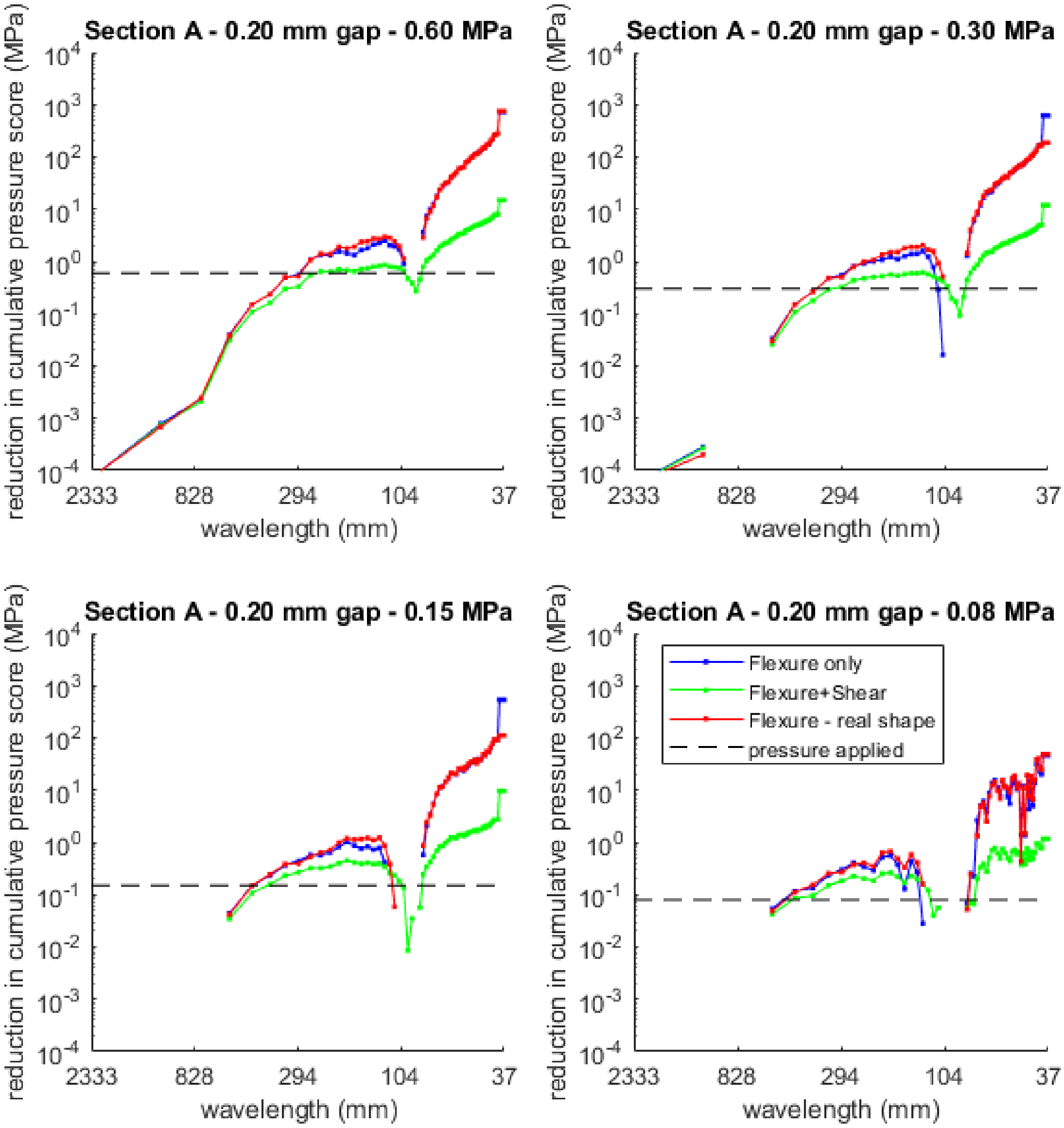

Figure I-4. Pressure score improvement for the flat thick stringer assemblies (smallest gap studied) according to all three spectral scoring criteria advanced.

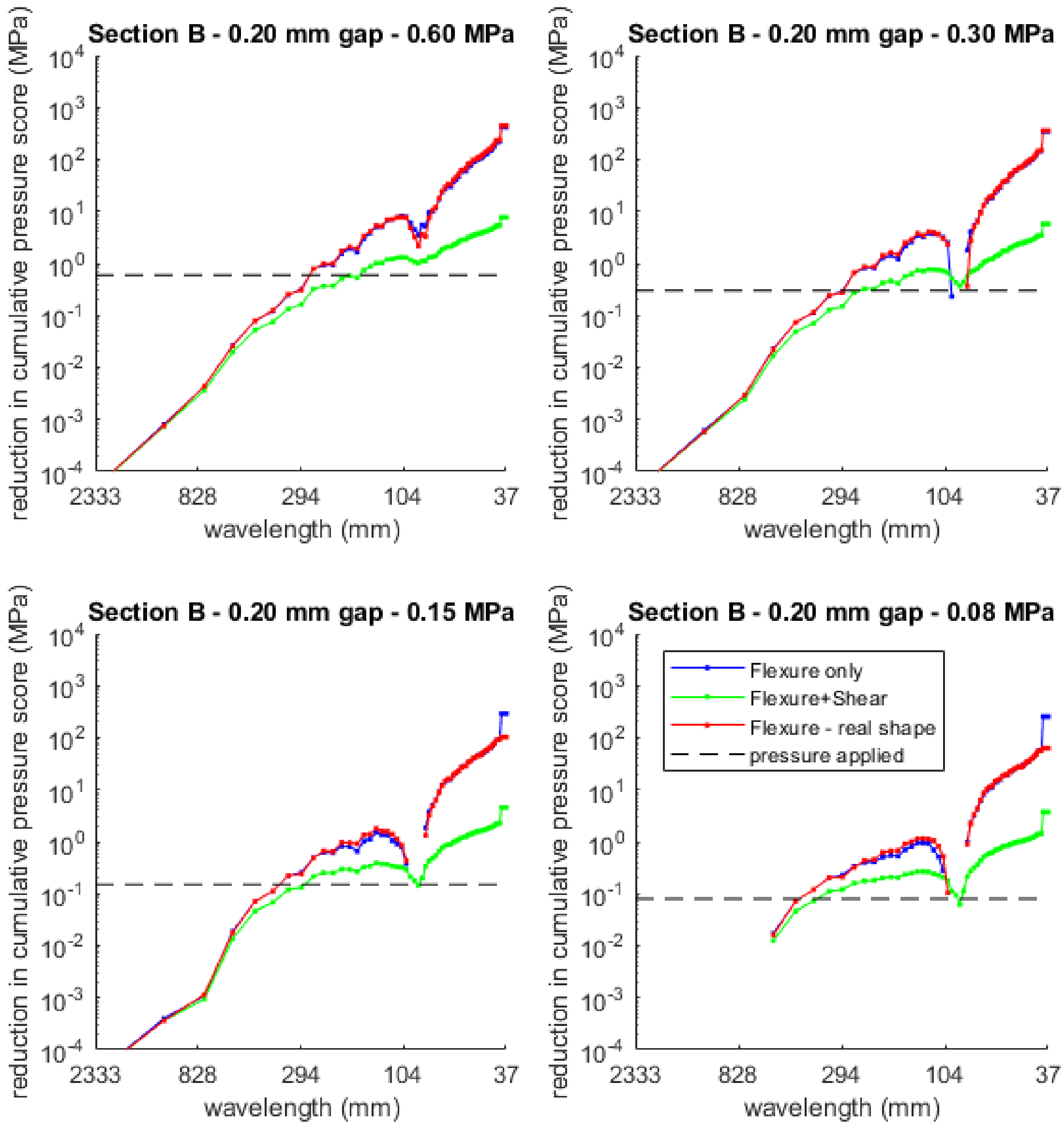

Figure I-5. Pressure score improvement for the flat thin stringer assemblies (smallest gap studied) according to all three spectral scoring criteria advanced.

I.2.2 Curved assembly trials

The curved assembly trials are closer to the scenario one could find in operation: limited sharp steps with local variation of relative smoothness. A benefit of these trials is the availability of fairly dense real dimensional data, which allows to explore another aspect of the problem: are the numerical model's inadequacies reflected in spectral analysis?

The results for these trials are visualised with the same plot used above, but in this case *both* simulation and measured test results are shown. As all assemblies were carried out under 0.60 MPa, the pressure is not indicated in individual charts.

The first assembly ('Legacy') displays a behaviour very similar to that encountered in the flat assembly simulations: the expected improvement of 0.60 MPa is much exceeded; some high spatial frequencies display a worsening of the score (dips around $1/f_k = 140\ mm$), and the contribution of shear becomes substantial at high frequencies. Very conspicuously, no datapoints for the spectra from measured results is visible; this is because the score became worse when basing it off the measured assembly results. This is suspected to be caused by poor measurement quality, rather than the bond geometry itself.

The second assembly ('Alternative') behaves in a very similar manner; however, in this case the measured values correlate nicely with those from simulation. This is not surprising as this assembly was designed for, and achieved, a very good skin-stringer fit — thus both the simulation and assembly reached a bondline with minimal variability.

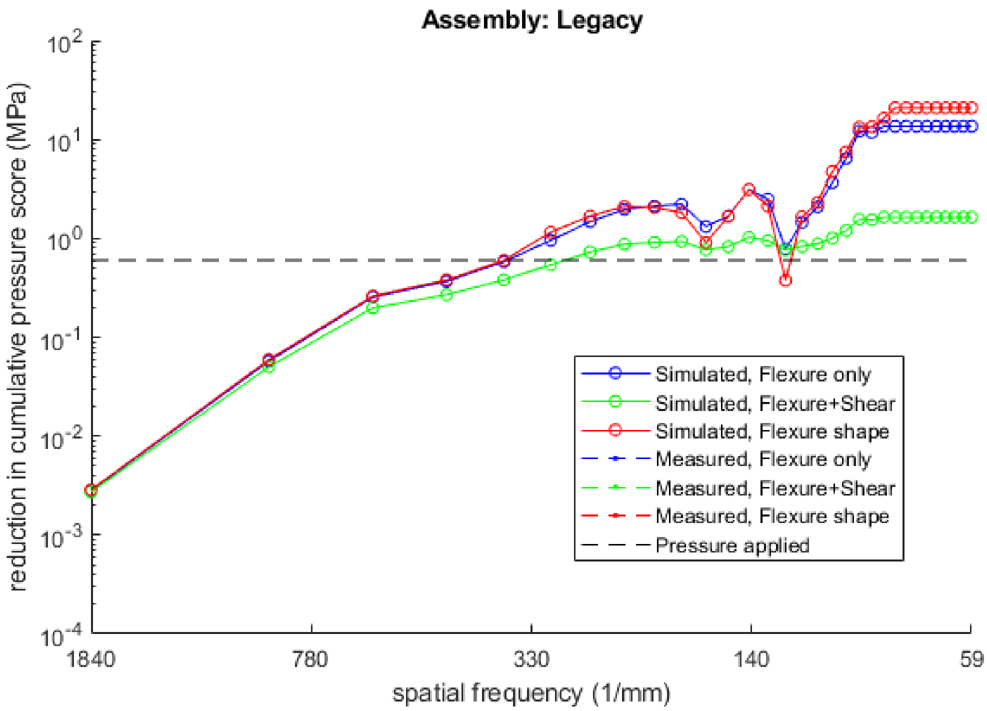

Figure I-6. Improvement in the pressure score for the 'Legacy' (baseline stringer with facetted skin) curved assembly. Note the absence of any values for the measured geometry.

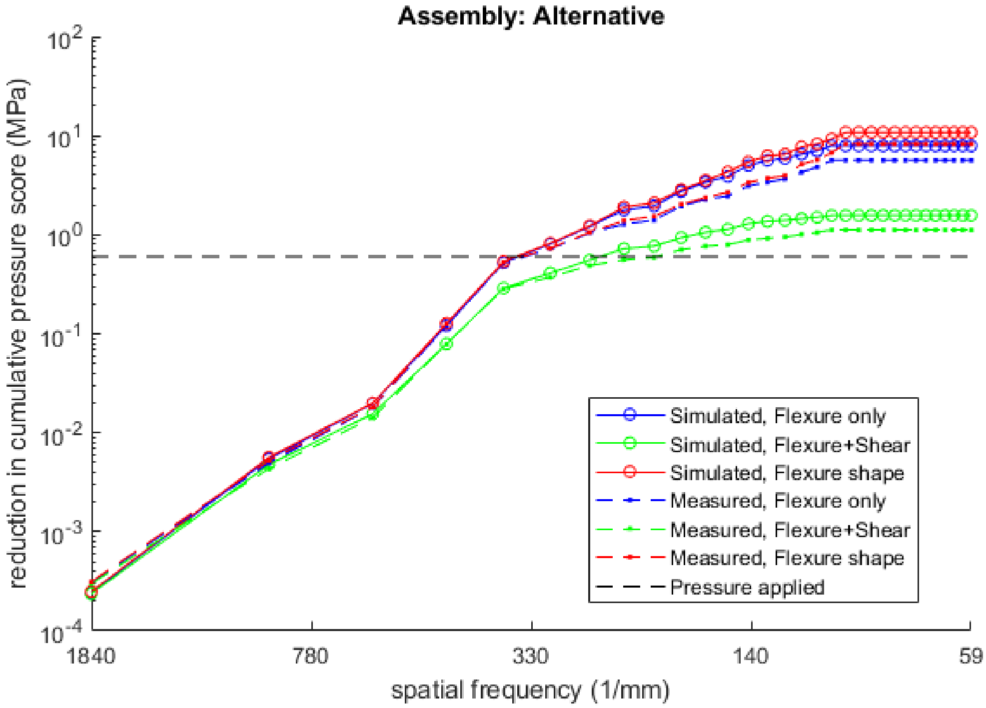

Figure I-7. Improvement in the pressure score for the 'Alternative' (baseline stringer with facet-less skin) curved assembly.

The two assemblies with thinner stringers exhibit highly diverging spectra depending on whether the simulation or measurement results are analysed (Figure I-8, Figure I-9). Such divergence is consistent with how the geometry prediction was far from perfect. The pressure scores from measured results show improvements within about 50% of the calculated value from simulation, but quickly become worse for higher spatial frequencies ($1/f_k \lesssim 330$ mm); the 'Padup' assembly's score never improves by more than ~0.1 MPa (atmospheric pressure), while the 'FML' concept reaches a score improvement of P before suddenly becoming negative. This evolution is reflective of the multiple localised (i.e. high spatial frequency) bumps which appear due to complex adhesive flow. Note that the 'FML' assembly was analysed in terms of the gap between the stringer and the topmost doubler.

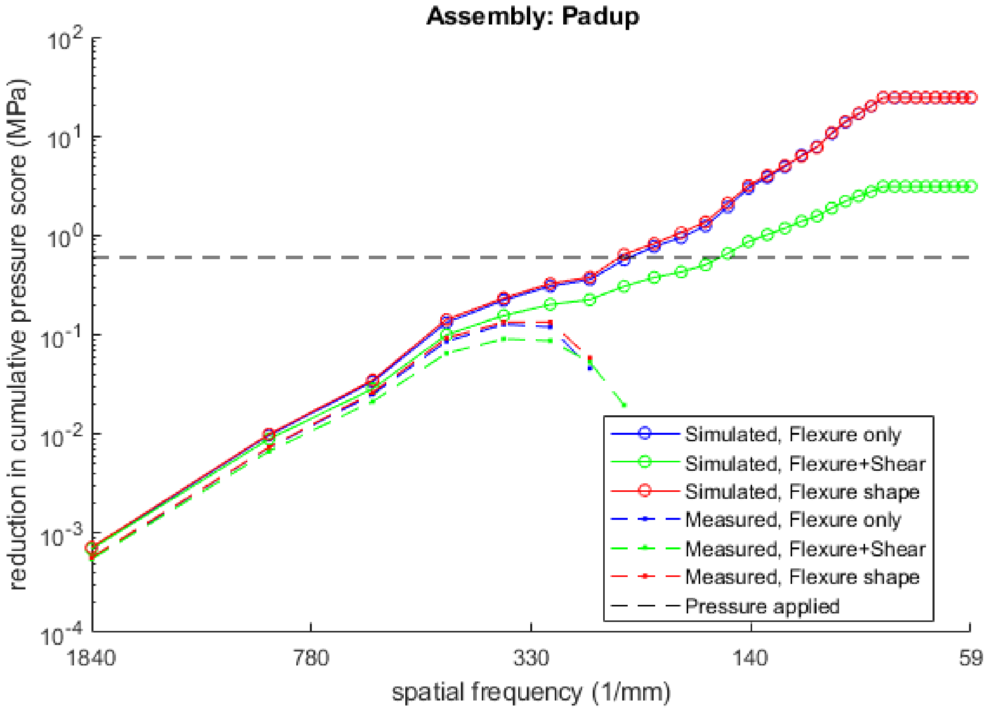

Figure I-8. Improvement in the pressure score for the 'Padup' (thin foot stringer with thicker facet-less skin) curved assembly.

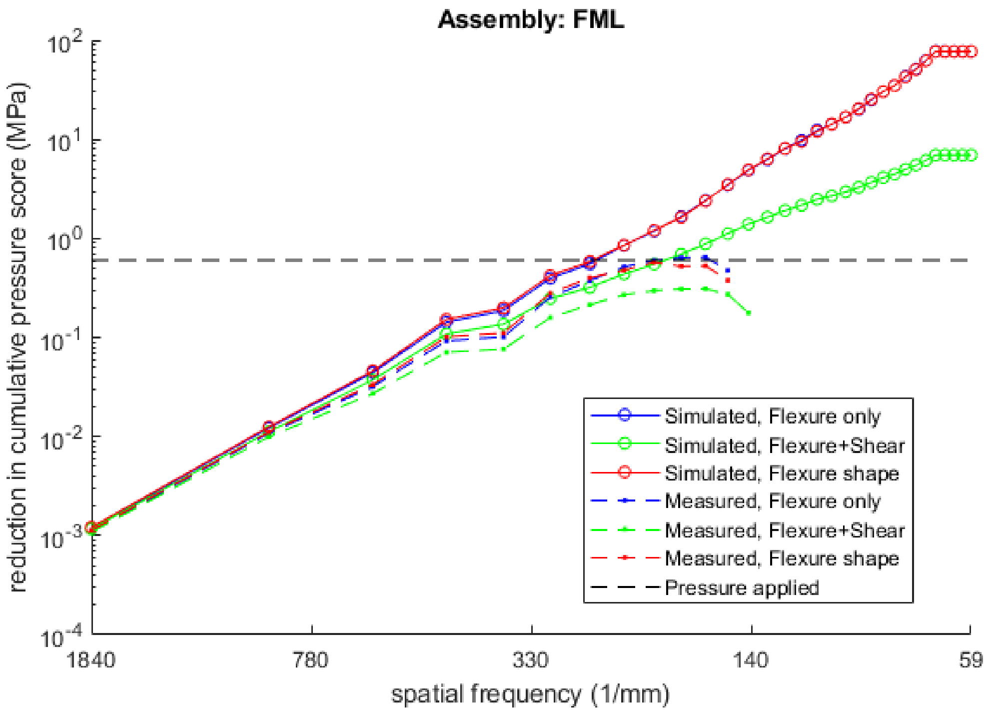

Figure I-9. Improvement in the pressure score for the 'FML' (thin foot stringer with doublers and facet-less skin) curved assembly.

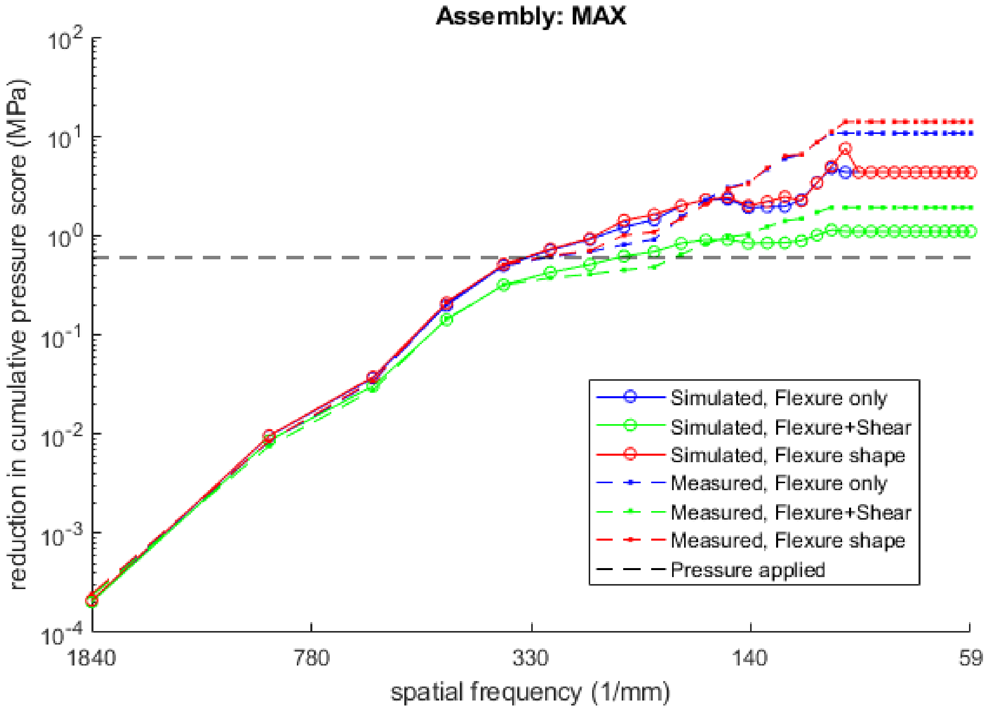

Figure I-10. Improvement in the pressure score for the 'MAX' (thick stringer with facet-less skin) curved assembly.

I.2.3 Multi-stringer flat panels

For the multi-stringer assembly tests, only one of the scores — that corresponding to senoidal components considering flexural and shear deflection — has been used. This is merely to preserve clarity and avoid clutter due to excessive volumes of data; the three scores considered in the sections above have been found to behave very similarly, and thus the discussion will be no less valid.

It should be noted that half of the assemblies were realised in a two-side pressure condition, and therefore in violation of one of the basic assumptions (as in those cases, the stringer would not be the sole part deflecting and contributing to gap closure). They are nevertheless presented for completeness. Additionally, note the truncation to 0.01 mm takes effect for relatively long wavelengths ($1/f_k$ <151 mm), suggesting that the variation is overall 'smoother' (i.e. smaller contribution from high frequencies) than for the other cases studied.

Some common, easily-explained patterns appear:

- Analysis of assemblies A, E, H, L (where only the middle stringer was deliberately warped) shows a different behaviour in the middle stringer, which shows higher improvement at low spatial frequencies than the lateral ones (simply because it had more room to deflect) but then experiences a worsening score as the adhesive flow and residual gap combine to form highly localised bumps.
- The assemblies with no stringer interference (B, F, J) show a marked improvement in the pressure score, well beyond the applied pressure; this is especially the case in the two-side-pressure scenario (assembly F). In this case, as the skin is very to deform, there is a marked further decrease in bondline thickness variation, with no prominent punctual worsening of the pressure score. The close evolution of the measured and simulated results also are consistent with this setup's ability to mitigate interface variation.
- The panels with strong stringer interference (C, G, K), where gap-closing ability was minimised even in the face of the bonding table's deflection, show a characteristic behaviour where middle frequencies (around the range $1/f_k$ =151 mm~356 mm) are associated with worsening pressure scores. This matches the range of the bumps that appear due to residual variation and adhesive flow (in the fashion of assembly A's middle stringer), which are exacerbated by the practically absolute inability of the skin to deflect.

The multiplicity of effects that contribute to variation are thus captured by the spectral analysis — though not in the scale that would lead to meeting equation (I-1): the relatively long-range variation introduced into the stringer profile is pushed out; the residual gap generates sharp mid-high-frequency peaks due to bumpy adhesive distribution; and unimpeded skin deflection creates a smooth bondline by helping redistribute pressure.

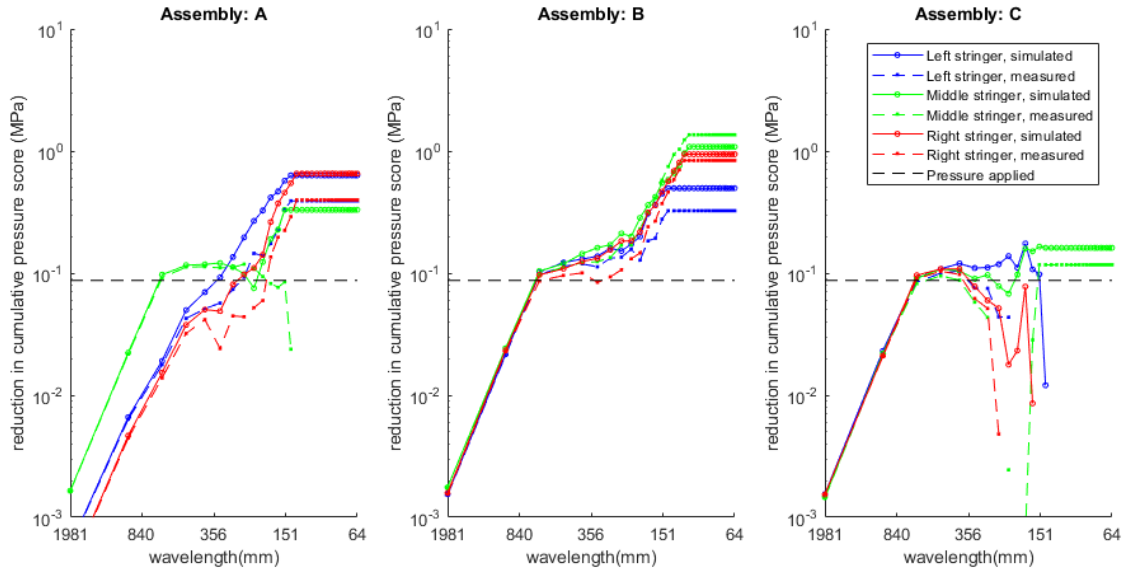

Figure I-11. Pressure score improvement (flexure and shear) for multi-stringer flat panels A, B, C.

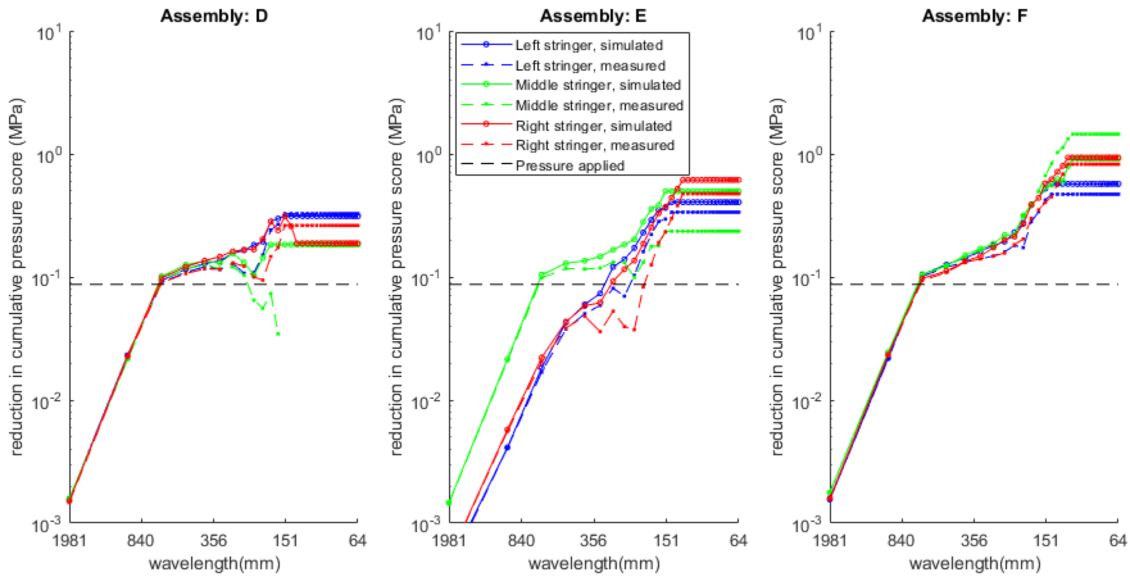

Figure I-12. Pressure score improvement (flexure and shear) for multi-stringer flat panels D, E, F.

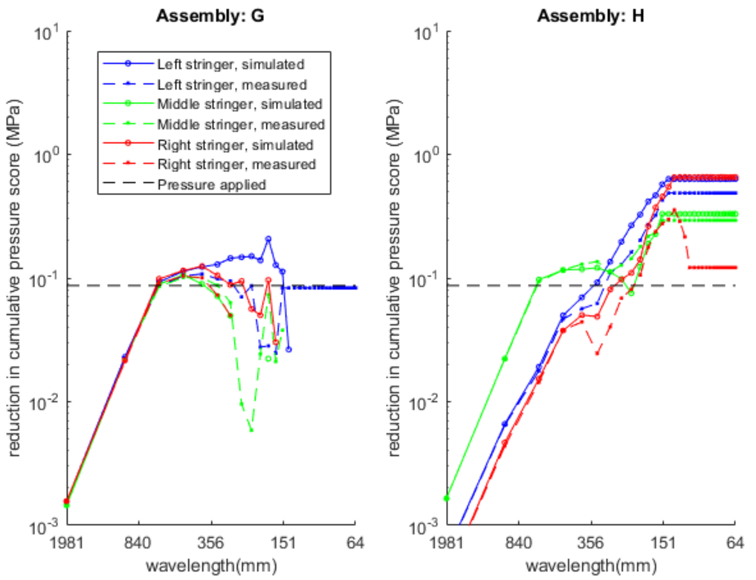

Figure I-13. Pressure score improvement (flexure and shear) for multi-stringer flat panels G, H, I.

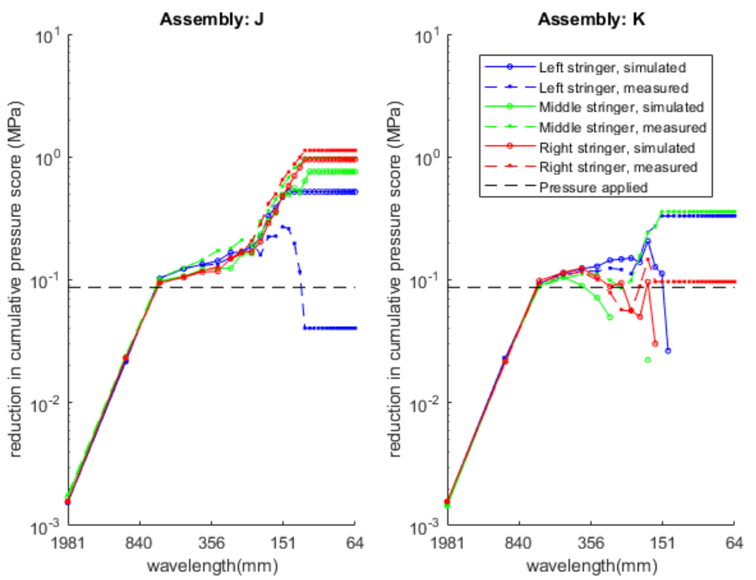

Figure I-14. Pressure score improvement (flexure and shear) for multi-stringer flat panels J, K, L.

I.2.4 Subscale panel scenarios

The large number of assembly instances simulated for the subscale panel design will provide a good reference of how consistent the spectral analysis would be. The expectation would be for all scenarios to display roughly the same decrease in pressure score. This is actually not the case. In fact, as it can be seen from Figure I-15 and Figure I-16, there is a substantial degree of scatter, as well as behaviours consistent with artefacts such as *increases* in the pressure score (i.e. the pressure score improvement sometimes goes down and even becomes negative).

As a point of comparison, the pressure score variations are also shown for one of the two-side pressure bonding scenarios (Figure I-17). The pressure score as calculated bears limited sense, as the envelope-bag situation clearly violates the assumption that only the stringer is free to deflect. In spite of this, no drastic differences can be seen between such a boundary-condition-violating scenario, and the single-side-pressure equivalent in Figure I-15.

As a qualitative descriptor, however, the spectral analysis still conveys meaningful information on residual mating gaps, even when violating the boundary condition: while in many assembly instances the pressure score improvement became negative around $1/f_k \approx 400$ mm in the single-side pressure scenario, the double-side pressure results in better closure of the shorter-range gaps, which is reflected in positive pressure score improvements for most stringers. This is especially noticeable for Stringer 2.

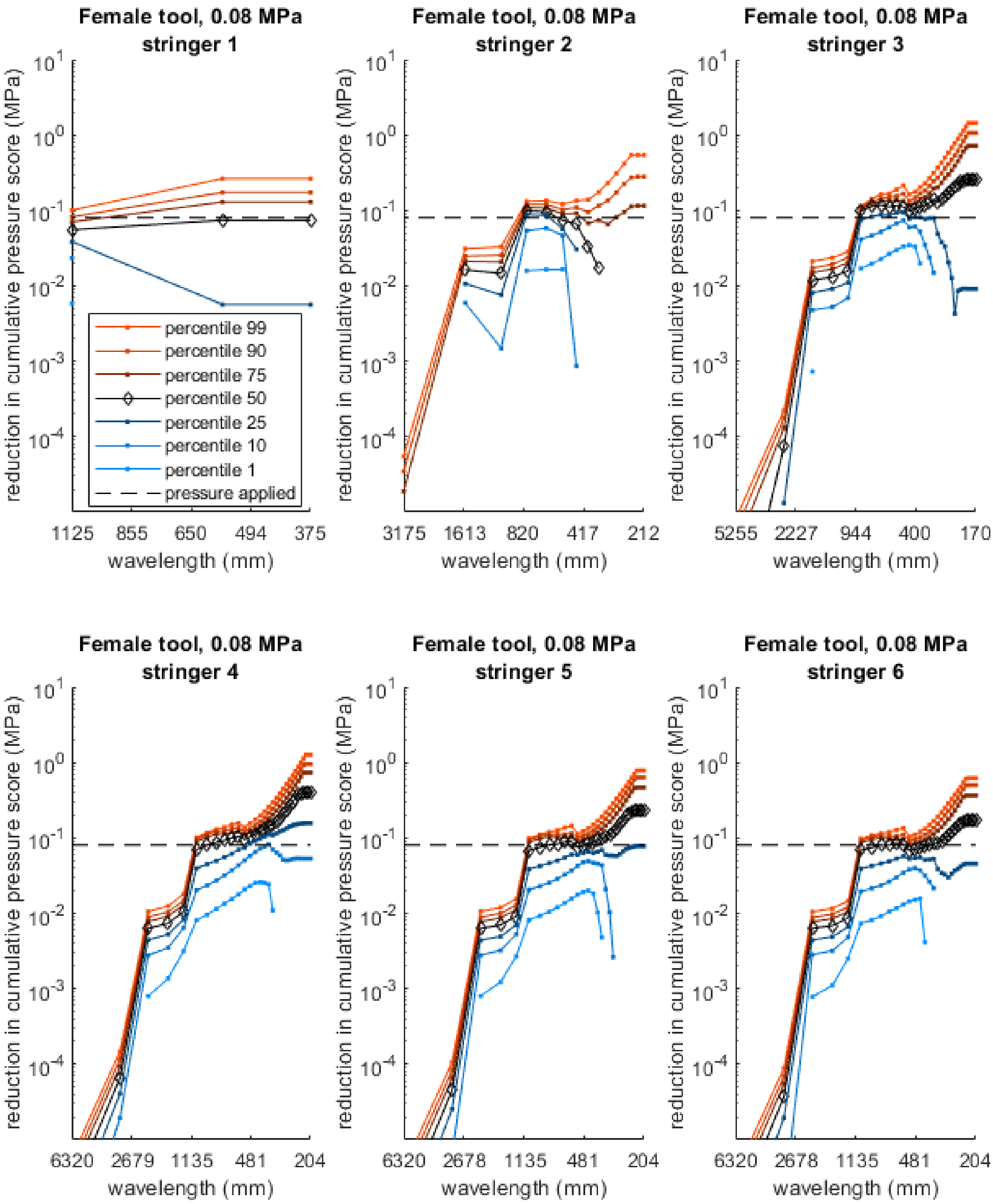

Figure I-15. Improvement in spectral pressure score for the subscale assembly in single-side pressure bonding, under representative out-of-autoclave pressure. (Scores calculated based on flexure and shear.) Note that all lines plateau towards the right of the horizontal axis, due to the truncation to 0.01 mm precision.

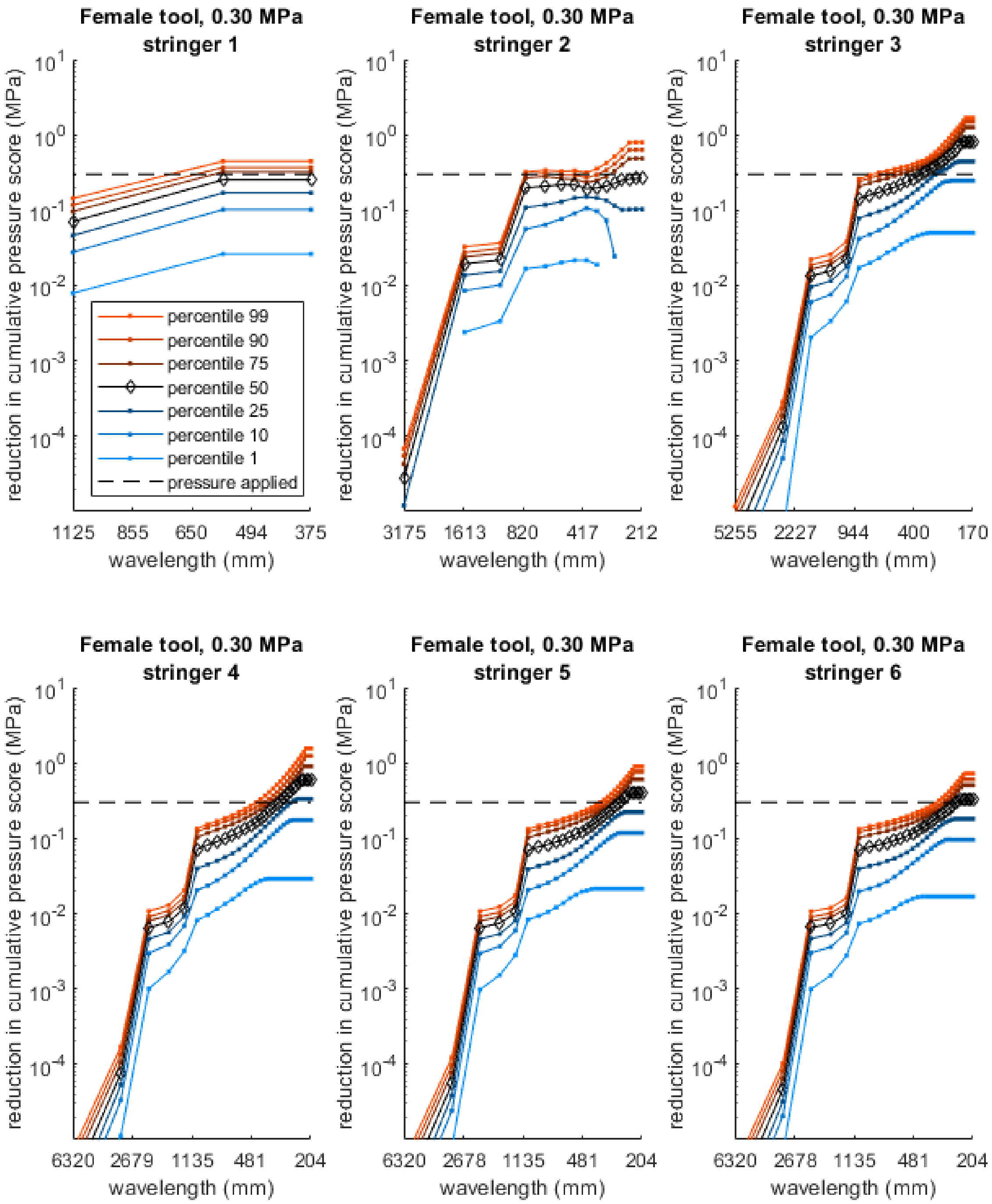

Figure I-16. Improvement in spectral pressure score for the subscale assembly in single-side pressure bonding, under representative light autoclave pressure. (Scores calculated based on flexure and shear.)

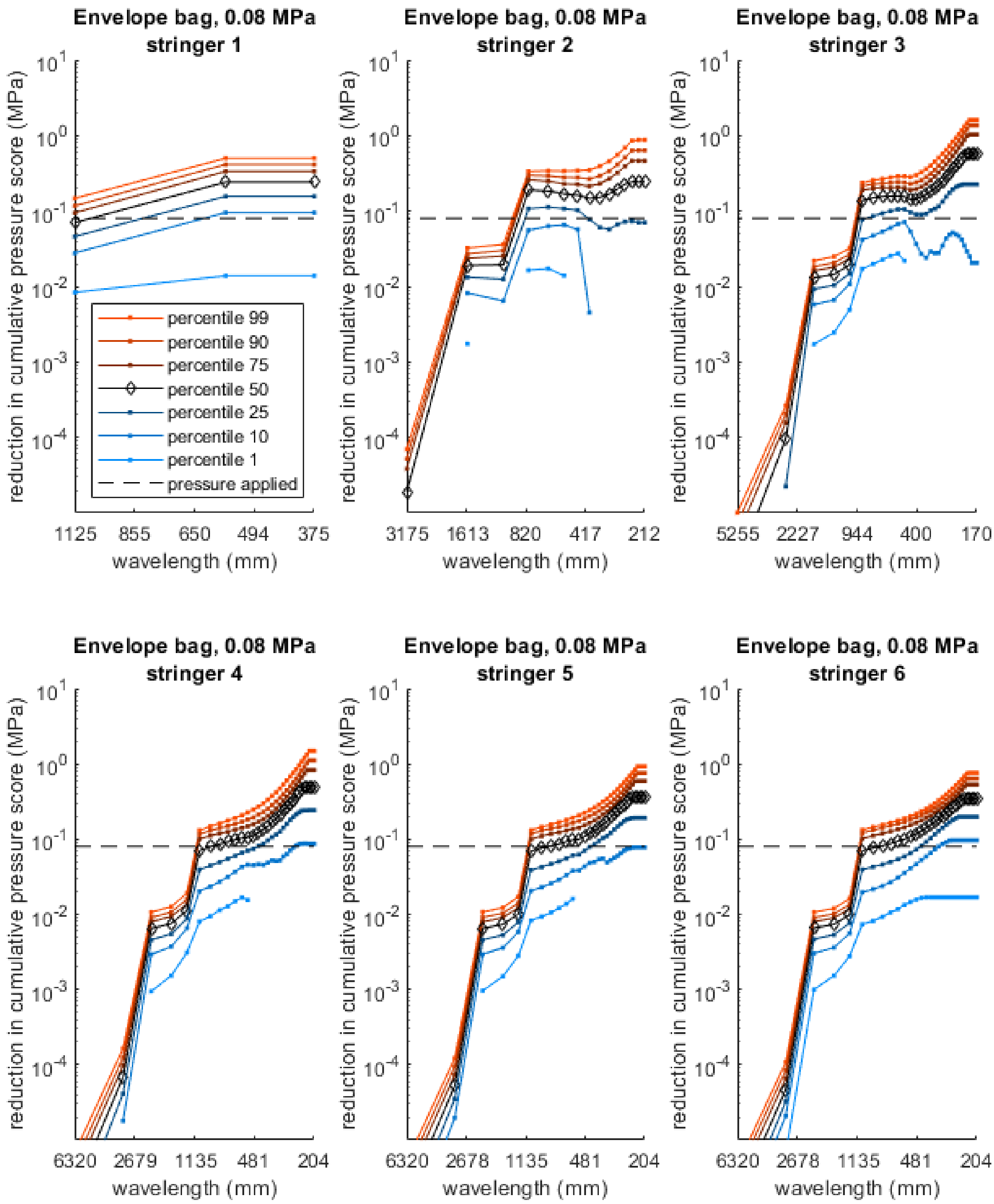

Figure I-17. Improvement in spectral pressure score for the subscale assembly in two-side pressure bonding, under representative out-of-autoclave pressure. (Scores calculated based on flexure and shear.)

I.3 Frequency f_k^* that meets the expected improvement

The prior sub-section has shown a general trend whereby application of a bonding pressure P to a stringer causes its spectrally-calculated gap-closure pressure to improve (i.e. drop). The general trend is that, as shorter wavelengths (that is, higher spatial frequencies) are added to the analysis, the expected improvement P is met (as per equation (I-1)) at a wavelength $1/f_k$ in the 100 mm order of magnitude. When even shorter wavelengths ($f_k > f_k^*$) are added, the score behaves somewhat erratically, sometimes dropping further, sometimes increasing dramatically, and seems to have little quantitative meaning, though still can be interpreted qualitatively (e.g. in terms of residual local variation).

Such partially erratic behaviour is in spite of the fact that a truncation has been applied based on typical measurement uncertainties and bonding tolerances. It is, further, insensitive to whether the analysis includes shear-related deflection or accounts for the geometrical shape of the deflecting stringer. These observations heavily suggest that the spectral-analysis-based assembly-force estimation presented in this work is unsuitable for real geometries. Such limitation would be in agreement with Stricher's observation that mode-specific model corrections are scarcely linearly additive (Stricher, 2013). It also explains the apparent scarcity (or outright nonexistence) of published assembly work where variation modes are a key input/output.

It is, however, also possible that one of the limiting factors is the excessive simplification of the deflection behaviour of each mode. Indeed, it was shown, during discussion on the shear deflection, that the flexure-only simplification resulted in heavily inflated pressure scores at mid-short wavelengths (e.g. $1/f_k \lesssim$500 mm). If this is the case, it stands to reason that the constant-cross-section and no-torsion assumptions, hitherto left unaddressed, would also contribute to grossly misquantifying stringer behaviour at even shorter wavelengths (e.g. for $1/f_k < 5w$).

As these potential sources of inaccuracy are all associated to high spatial frequencies, the score's behaviour at *lower* spatial frequencies should be fairly consistent. (It mostly is, as shown by the reliable score improvement in this lower-frequency range). If the stringer behaviour is consistent for spatial frequencies below f_k^*, then it still may be possible to use the spectral analysis quantitatively.

The subsections below show how this is hardly the case, or at least not with a meaningfully short variation range.

I.3.1 Flat assembly scenarios

Figure I-18 shows the substantial variation range for f_k^* (presented as the inverse $1/f_k^*$ for clearer physical meaning). Higher applied pressure, lower stringer stiffness, and smaller initial variation correlate with lower values of $1/f_k^*$ (i.e. higher values of f_k^*). The upper limit of the $1/f_k^*$ values observed is 583.3 mm, while the lower limit is 233.3 mm — corresponding to an over 100% increase in f_k^*. These wavelength values are equivalent to only a few times the stringer width, and thus are in the interval where shear deflection becomes relevant.

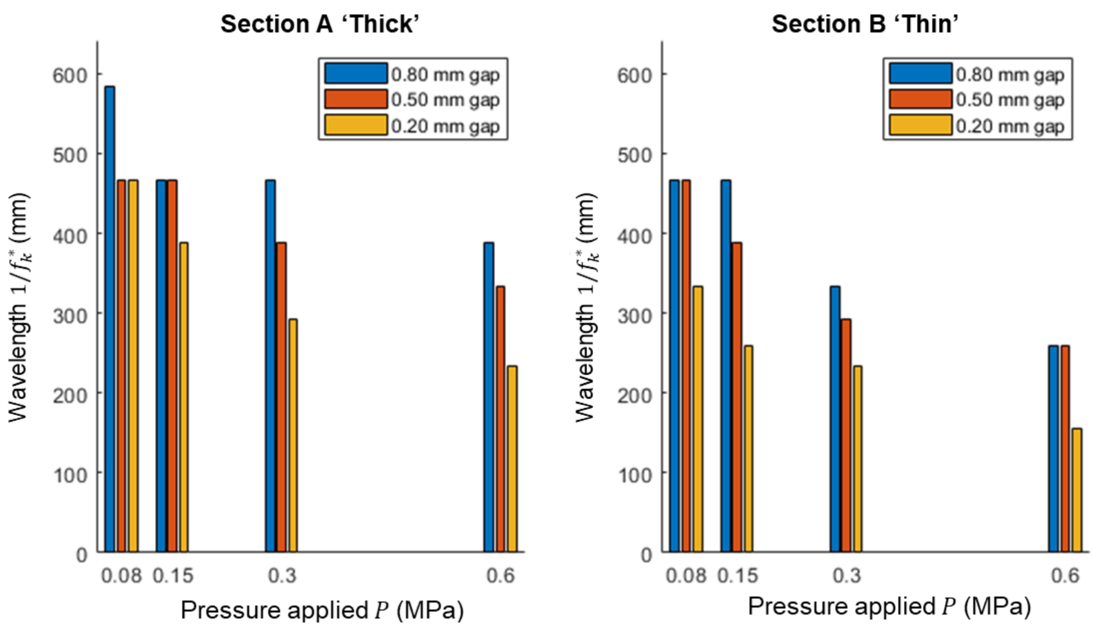

Figure I-18. Wavelengths $1/f_k^*$ at which the pressure score (flexure and shear deflection) achieves an improvement of P for the flat assembly scenarios.

I.3.2 Curved assembly trials

The single-stringer curved panels show (Figure I-19) substantially less variation in $1/f_k^*$ than the flat assembly scenarios above. This is easily explained by the fact that only one bonding pressure has been used, and stringer variations weren't so different in scale (meanwhile, the flat assembly scenarios had a 300% increase in gap size between the smallest and largest case). The wavelengths are, again, in the order of a few stringer widths, and squarely in the range where shear becomes relevant.

For these trials, the difference between the simulated and measured behaviour becomes even more obvious when focusing only on f_k^* than when looking at the pressure score as a whole: three of the assemblies have no experimental f_k^*, as the pressure score worsens (i.e. increases) before ever achieving an improvement P. The reasons have been discussed when presenting the general trend.

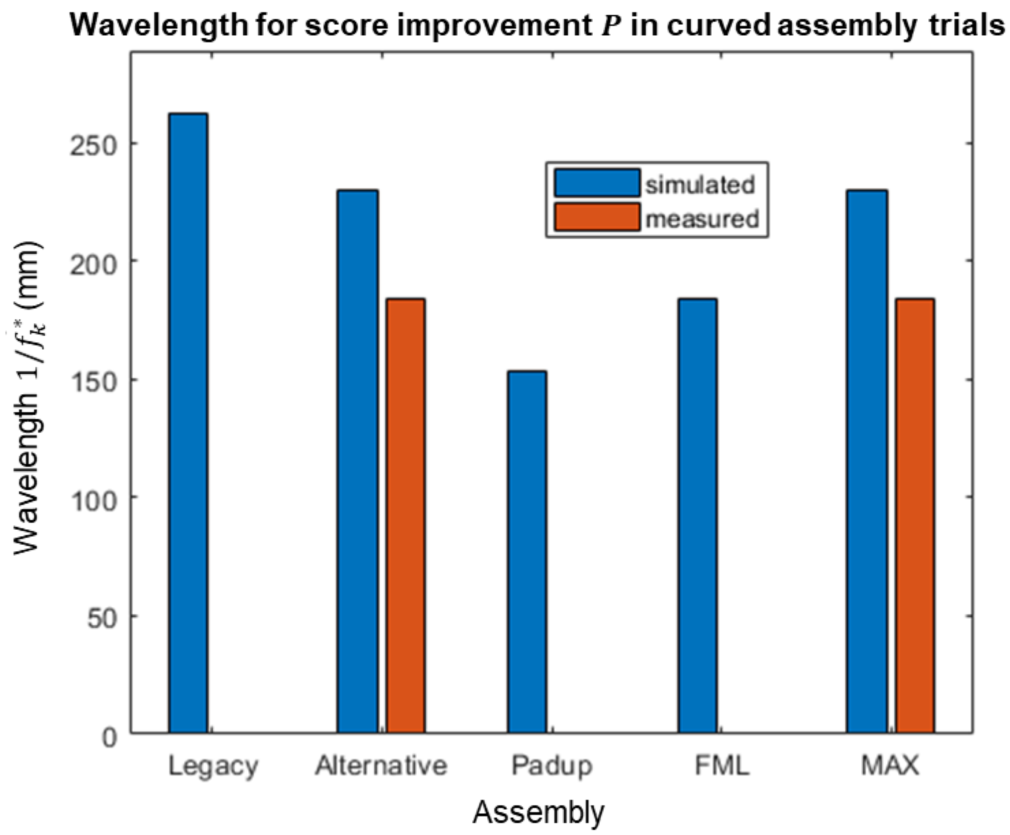

Figure I-19. Wavelengths $1/f_k^*$ at which the pressure score (flexure and shear deflection) achieves an improvement of 0.60 MPa for the curved assembly trials. Note some bars absent for measured results (improvement not achieved).

I.3.3 Multi-stringer flat panels

In contrast with the results found above, the multi-stringer flat panels show fairly good consistency with regards to the value of f_k^* (Figure I-20). Bar one slight deviant (Middle stringer in the assembly C simulation), all pre-deformed stringers achieved pressure score reduction P at $1/f_k^* = 660.3$ mm (about 9 times the foot width); the nominally-flat ones did the same at higher spatial frequencies, around $1/f_k^* = 200$ mm (about 3 times the foot width). In addition, there is considerable agreement between the results from measurements and simulations, with only minor discrepancies between the measured and simulated f_k^* for the nominally-flat stringers.

The seemingly neat results, however, do not support the validity of the spectral analysis, for four reasons: (i) differences depending on variation magnitude; (ii) poor correspondence with variation wavelength; (iii) insensitivity to boundary-condition assumption violation; (iv) poor reflection of discrepancies in residual variation.

(i) The large difference in f_k^* values between the two types of stringer variation show that the technique can't be readily translated between variabilities of different magnitude within an assembly.

(ii) The value of $1/f_k^*$ for the pre-deformed stringers is too high compared to the ranges of variation present: the shortest profile wave was about 450 mm long prior to assembly, and its height was reduced under pressure. Thus, the pressure score improvement of P should not have been achieved without these shorter wavelengths.

(iii) The value of $1/f_k^*$ does not change for two-side-pressure bonded panels, which generally enjoy a greater gap-closure capability (and indeed were shown to substantially smoothen gaps in some cases). In this regard, there is no difference in f_k^* values between panels with different levels of stringer interference: skin deflection, and the bondline variation reduction it results in, are simply not reflected at all.

(iv) The different deflection between simulations and physical tests close to high-adhesive-pressure areas (where the simulations underestimated residual variation) should have been accordingly reflected in the pressure score. However, the value of f_k^* is almost a perfect match between simulated and measured results.

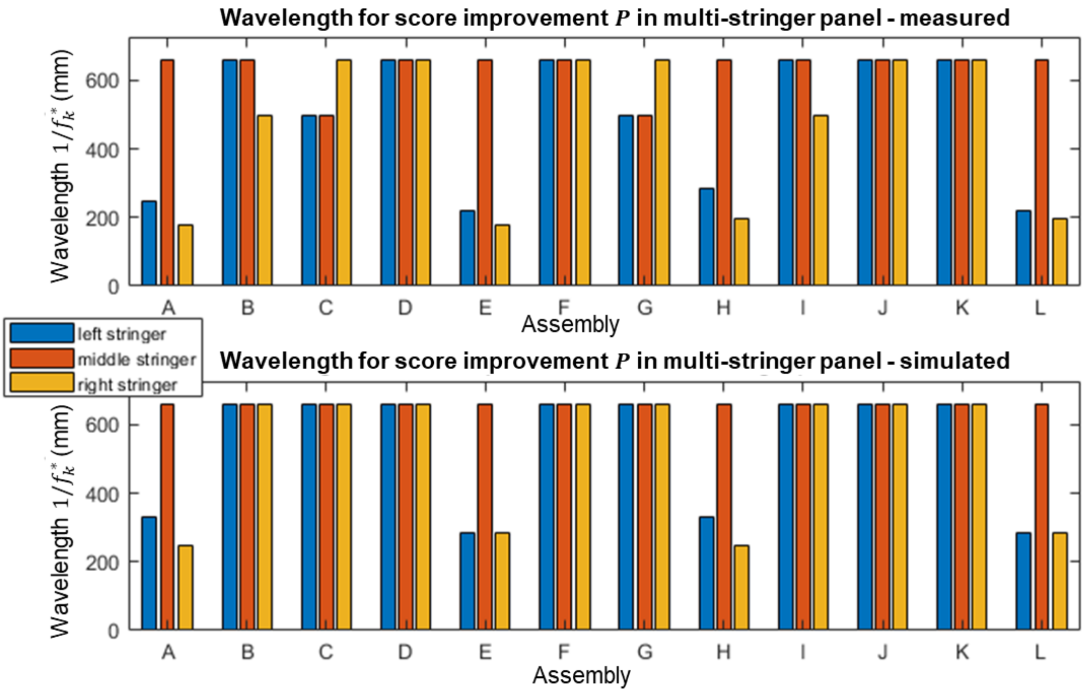

Figure I-20. Wavelength $1/f_k^*$ that achieves a pressure improvement 0.087 MPa for each of the multi-stringer flat panels.

I.3.4 Subscale panel scenarios

The values of f_k^* for the subscale panel show substantial variability among repeats (Figure I-21). This is little surprise, as it matches the dispersion of the whole evolution of the pressure score, presented in the prior subsection: the value of f_k^* is seen to vary by a factor of more than 2. Note that in Figure I-21, whenever a point falls on the horizontal line designating the minimum $1/f_k$ value, it means that a pressure improvement P was never achieved.

Increasing pressure applied causes an increase in f_k^*, that is, a decrease in $1/f_k^*$ (compare top and bottom row in Figure I-21), with several percents of the stringers never reaching a pressure score improvement of 0.30 MPa. This is justified by how the variation of these stringers is made up of a small number of variation modes; when the variation from a longer mode is completely eliminated, the wavelength corresponding to the next, shorter mode must be included in the analysis.

Conversely, when applying double-sided pressure (thus violating the boundary conditions set to justify the spectral score calculation), longer frequencies are enough. Some stringers which never achieved a 0.30 MPa pressure improvement with one-side pressure do achieve this target improvement when the skin is allowed to move.

This confirms that there was residual variation which the skin was able to mitigate, but which was not properly accounted for by the pressure score.

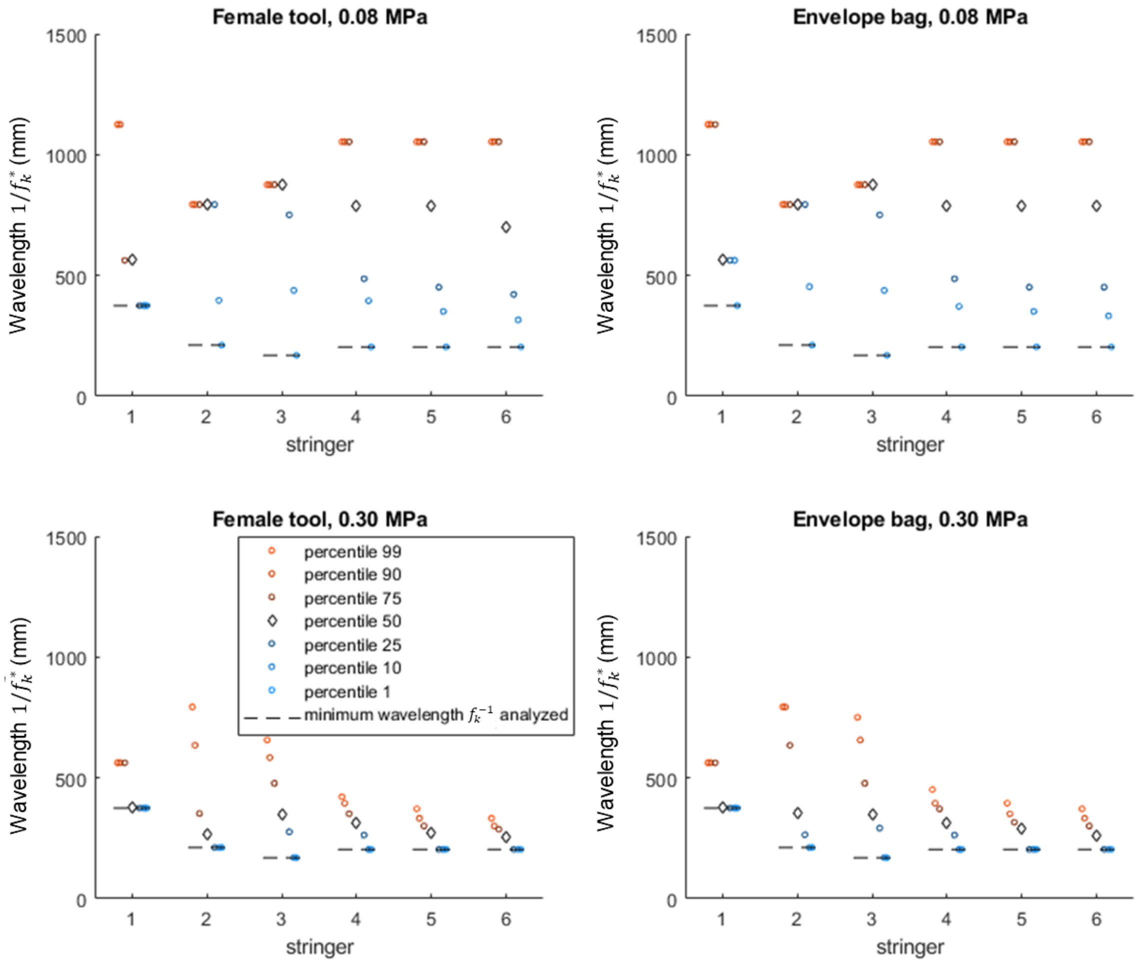

Figure I-21. Values of $1/f_k^*$ for the subscale panels simulated. A point at the height of the minimum $1/f_k$ value (horizontal line) implies the target pressure score was not reached.

I.4 Conclusion

An attempt has been made at making a correlation between the spectral “pressure score” advanced herein, and the behaviour of stringers under bonding pressure in a variety of representative scenarios. This has been done through a general “score improvement” metric presented in equation (I-1).

In spite of the usefulness of the spectral pressure score as a qualitative descriptor, it has proven a bad predictor of the part behaviour under pressure. Its limited value becomes obvious when comparing scenarios that differ in terms of variation magnitude and pressure applied: the results vary wildly and fail to reflect features of residual variation which stand out in the spatial domain. These inaccuracies and inconsistencies cannot even be blamed on the limitations of a slender-beam model assumption, as the failings appear at fairly long wavelengths for some of the assembly scenarios studied.

This failure to provide quantitative insight is, as already pointed out during discussion of the literature and results, in line with the scarce explicit observations offered by prior art on the subject of modal analysis for assemblies.

Appendix J — Journal paper “Enhanced bondline thickness analysis for non-rigid airframe structural assemblies”

Appended is the published version of the paper “Enhanced bondline thickness analysis for non-rigid airframe structural assemblies”, by the author of this thesis and the extended supervisory team. It was published in Aerospace Science and Technology (volume 91, August 2019, pp. 343-441) and is accessible through:

https://doi.org/10.1016/j.ast.2019.05.024

(last accessed 2020-07-27)

The paper is open access (Gold) and subject to a Creative Commons licence (CC BY 4.0). It can be shared freely on commercial and non-commercial platforms provided the original is properly cited. More information is available at:

https://creativecommons.org/licenses/by/4.0/

(last accessed 2020-07-27)

Additional information on the publisher’s conditions for article sharing is available on the following web address:

https://www.elsevier.com/authors/journal-authors/submit-your-paper/sharing-and-promoting-your-article

(last accessed 2020-07-27)

Note that the variable naming convention and references are kept separate from the rest of this thesis.

Aerospace Science and Technology 91 (2019) 434–441

Contents lists available at ScienceDirect

Aerospace Science and Technology

www.elsevier.com/locate/aescte

Enhanced bondline thickness analysis for non-rigid airframe structural assemblies

Pablo Coladas Mato [a], Philip Webb [a,*], Yigeng Xu [a], Daniel Graham [b], Andrew Portsmore [c], Edward Preston [b]

[a] School of Aerospace, Transport and Manufacturing, Cranfield University, College Road, Cranfield, Bedfordshire, MK43 0AL, UK
[b] GKN Aerospace UK, Golf Course Lane, Filton, Bristol, BS34 7QQ, UK
[c] GKN Aerospace UK, Falcon Yard, Ferry Road, Isle of Wight, PO32 6RA, UK

ARTICLE INFO

Article history:
Received 7 January 2019
Received in revised form 8 April 2019
Accepted 9 May 2019
Available online 13 May 2019

Keywords:
Non-rigid assembly
Bonded airframe structure
Bondline thickness
Adhesive flow
Direct linearization method
Quadratic programming

ABSTRACT

Adhesive bonding is a proven alternative to mechanical fasteners for structural assembly, offering lighter and thus more fuel efficient aircraft and cost-effective manufacturing processes. The effective application of bonded structural assemblies is however limited by the tight fit-up requirement, which is with sub-mm tolerance and can be a challenge for the industry to meet considering the variability of current part manufacturing methods and the conservative nature of the conventional tolerance stack-up analysis method. Such a challenge can discourage effective exploitation of bonding technologies, or lead to development of overengineered solutions for assurance. This paper addresses this challenge by presenting an enhanced bondline thickness variation analysis accounting for part deflection of a bonded skin-stringer assembly representing a typical non-rigid airframe structure. A semi-analytical model accounting for unilateral contact and simplified 1D adhesive flow has been developed to predict bondline thickness variation of the assembly under two typical curing conditions: namely autoclave curing and out-of-autoclave curing. The effects of component stiffness and manufacturing variations on bondline thickness are investigated by incorporating stringers of different stiffness, as well as shims of different thicknesses in-between the skin and stringer, in the stringer-skin assembly. A small-scale bonding demonstrator has been built and the physical results are in good agreement with the model prediction. It has been demonstrated that the part deflections need to be accounted for regarding fit-up requirement of bonded non-rigid structural assembly. The semi-analytical model offers more reliable and realistic prediction of bondline thickness when compared to a rigid tolerance stack-up. The analysis method presented can be a major technology enabler for faster, more economical development of the aircraft of the future, as well as of any analogue structures with high aspect ratios where weight savings and fatigue performance may be key objectives.

1. Introduction

The global aviation industry is experiencing steep growth; the UK's Aerospace Technology Institute, for example, forecasts a doubling in the number of commercial and business aircraft within the next two decades, with an associated asset value of several US$ trillion. This high-growth environment results in strong competition for market share and positioning; it creates a substantial incentive for technology improvements that may lead to improvements in manufacturing rate and efficiency, as well as increased energy efficiency or new functionalities [1].

Aircraft are manufactured as an assembly of a large number of parts, which are typically joined by means of mechanical fasteners such as rivets. With thousands of fasteners in each aircraft, this translates to a large weight added, as well as manufacture costs due to drilling and fastener insertion operations. It also leads to concerns over structural integrity due to stress concentration.

Adhesive bonding is a proven alternative to mechanical fastening which has found successful applications in the aerospace industry for decades. It can substantially cut manufacturing time and joint weight, in addition to other benefits such as preservation of the aerodynamic profile, improved mechanical and corrosion performance, and applicability to a multitude of different materials without needing large process changes. However, its industrial-

* Corresponding author.
E-mail addresses: p.coladas.mato@gmail.com (P. Coladas Mato), p.f.webb@cranfield.ac.uk (P. Webb), yigeng.xu@cranfield.ac.uk (Y. Xu), dan.graham@gknaerospace.com (D. Graham), andrew.portsmore@gknaerospace.com (A. Portsmore), ed.preston@gknaerospace.com (E. Preston).

https://doi.org/10.1016/j.ast.2019.05.024

ization has sometimes been limited due to difficulty in meeting quality requirements. Among these, bondline dimensional control is perceived as one important limiting factor which affects load distribution and joint strength [2,3].

Interface gap values resulting from tolerance stack-ups and dry-fit inspection typically exceed the maximum acceptable bondline thickness and permissible variation [4]. However, aircraft structural subcomponents are in most cases flexible (non-rigid); that is, assembly forces can cause deflections comparable to the geometrical tolerance values [5]. Thus, part flexibility can be capitalized on to mitigate manufacturing variation. This needs to be accounted for in the assembly tolerance analysis and requirement definition, as tolerances will otherwise be unnecessarily pessimistic. If a joining technology is perceived as too stringent, it may be wrongly discarded early during a development program, and the benefits and drawbacks of different manufacture and assembly concepts will not be properly assessed. This does not just apply to bonding, but also to greener alternatives to autoclave curing (AC) for application of the curing forces. For instance, out-of-autoclave (OoA) curing, which is less energy- and tooling-demanding than AC [6,7], also naturally offers less control over the final bondline geometry given the smaller forces applied; as a result, OoA may be sidelined early during bonding manufacturing development due to quality concerns, ultimately resulting in a more costly manufacture solution which may or may not be justified.

This observation on the relevance of part deflections for assembly tolerancing is not new: the effect has been known and utilized for decades in the aerospace [8–11] and automotive [12,13] sectors. It also has been incorporated into various inspection approaches [14–16] and commercial stochastic tolerancing software [17,18]. However, publicly available studies of the implications for bonding are strictly empirical [10]; meanwhile, Computer Aided Tolerancing (CAT) applications have focused largely on fastener- and spotweld-based assemblies. Quantitative study of the effect of part flexibility on bonding outcomes is, thus, left wanting for a reliable prediction tool accounting for continuous contact and adhesive flow characteristics.

This paper presents an enhanced bondline thickness variation analysis accounting for part deflection of a bonded skin-stringer assembly representing a typical non-rigid airframe structure. The background of the research is introduced in this section. The second section provides an overview of key aspects associated with the assembly variability management. The third section concerns the model setup, including an efficient algorithm solving the contact problem and simplified adhesive modeling. The fourth section presents a demonstrator assembly used for model verification. Results are compared to a FE model for in- and out-of-autoclave pressures, with varying component stiffness and in-built gap dimensions. General applicability of the model is discussed. The last section summarizes the main findings of the research and a way forward for further work.

2. Key aspects with assembly variability management

2.1. Recorded aerostructural bonding issues

The problem of achieving a good adherend fit is well documented; for example, industry communications in the 1950s to 1970s highlighted the need for appropriate tooling to push parts together, with stringent tolerances which may not be met by hard tooling [9,19,20]. The Primary Adhesively Bonded Structures Technology (PABST) program, undertaken by McDonnell Douglas during the 1970s, highlighted how not even autoclave and flexible bags may enable a proper fit, and how tooling concepts can make all the difference by facilitating deflection of different adherends [10]. Later reflections on this programme, and application of its learnings to Fokker and SAAB products, emphasized the need to account for deflection of the adherends and how the parts themselves, rather than the tooling, determine the final geometry [11,21]. Although geometric tolerances were quoted following the PABST development, no calculation method, nor any systematic testing approach to ascertain the geometric capability of the bonding process, were reported.

2.2. Modeling of adhesive flow

Though it may be tempting to assume hot-setting adhesives flow freely and fully accommodate any part deflection, this is not strictly true. This is for two reasons: first, adhesives will usually contain a medium, such as a carrier film or glass beads, which effectively behaves as incompressible, thus limiting the minimum distance between adherends. Secondly, viscous resistance to flow increases sharply as the adhesive layer is squeezed and becomes thinner; thus, even under large pressures, adhesive flow is limited and the bondline thickness becomes stable before the cure is complete. This slow flow of the viscous adhesive under pressure is known as squeeze flow.

Squeeze flow modeling in planar bondlines has not been widely documented for dominantly-viscous materials. Industry reports tend to characterize the bondline geometry empirically or neglect adhesive flow mechanics when discussing tolerances [9,10,19,20,22]. It has received some limited attention to assess how different parameters help control bondline thickness [23], although without any consideration for adherend behavior. Squeeze flow also has been studied in cases where the focus was not bondline thickness, but other quality criteria such as void formation [24]. The packaging industry has seen more recent study to support process parameter optimization [25], though with a focus on excess material and cycle time. In all three cases referenced, a one-dimensional viscous flow model was used, justified by the high aspect ratio of the bonded joint, achieving good agreement with experimental results.

2.3. Non-rigid assembly modeling

Although knowledge of the impact of part deflections has been formalized at least for 4 decades [12], it is only close to the new millennium that this is actively studied and incorporated into models, driven by an increasing push for manufacturing efficiency and expanding computational capacity. The Association for the Development of Computer-Aided Tolerancing Systems (ADCATS) research group developed simplified approaches to modeling of part variation and part compliance using superelements and spectral decomposition, and showed their application to fastened assemblies assuming perfect fit at joined nodes [26,27]. The Stream-of-Variation method, incorporated considerations of how assembled parts are deformed to fit each other and mitigate location errors [28], though without further considerations of part contact outside joined spots or deflection due to tooling variation [29]. The Method of Influence Coefficients (MIC) was developed as a linear expansion of variation accounting for part deformation within a PCFR cycle (Position-Clamp-Fasten-Release), by considering only the joined nodes and thus reducing computation time dramatically. The RDnT software for stochastic assembly tolerancing was expanded with a non-rigid module [17], including the potential to account for contact, as was the similar 3DCS [18,30]. The effect of contact between non-joined points was also incorporated to the MIC-based calculation, showing considerable influence in the final simulation results, and highlighting difficulties with modeling and prediction of friction-based interactions [31–34].

These methods have been primarily applied to automotive assemblies or generic sheet metal. However, in the past decade aerospace-type assemblies have also been studied, for example, with application and second-order expansion of MIC for fastened fuselage frames [35]; use of 3DCS for analysis of wing spar-panel fastening [36]; and optimization of fuselage panel skin-stringer temporary fastener positioning, using iterative compliance matrix updating without [8] and with contact considerations [37].

It has been noted that most studies of assembly variation do not dwell on the joint formation itself. In most cases, two nodes are simply joined by a fastener or spot weld. In some work, the thickness of a weld nugget [38], the dimensions of a hole and rivet [35], and the deformation caused by the fastener insertion [39], have been added into the assembly model, although in these cases the part clearance was always assumed to be zero at the joined spot.

Study of fillet welding [40,41] showed that not only can the joint formation mechanics be a contributor to variability, but also that variation of the individual parts assembled can amplify the variation substantially even when dealing with simple geometries. Thus, formation of the joint and variation of the assembly details should be studied together. It is worth underscoring that these welded joints were not assumed to have zero thickness; indeed, variation was implemented as a change in the joint geometry. This rings close to the case of an adhesively bonded joint where no two points can be assumed to be brought in contact, and the bondline thickness is likely to vary throughout.

3. Model setup

3.1. Basic features of the model

Before enunciating the technical detail of the modeling approach, it is worth highlighting the basic features of the model, which are different to the ones commonly found in the literature.

First, the external forces applied are known as the assembly in the current study is vacuum bagged and oven or autoclave cured; the clamping or fastening forces for the joints in literature would be a product of the part deviation from nominal and are normally unknown beforehand.

Second, the focus in this study is not the assembly deformation after release of the assembly forces due to part deformations and internal stresses. Rather, it is the joint geometry (namely, the bondline thickness) that is key. This would typically be prescribed as zero in fastening or spotwelding applications, and as a product of the initial deviations in fillet welding. Meanwhile, in the current model it is an unknown. In addition, since the joint geometry is the quantity of interest, the calculation finishes at the joint formation (adhesive cure) step and therefore the springback is not considered.

Fig. 1 illustrates the formation of the bondline thickness of uncured bonded joint. The bondline thickness of the joint will be determined by two separate mechanisms: the ability of adhesive to flow, and the deflection of the adherends. Both of which are driven by the external pressure. Since the adhesive's flow resistance is highest when the bondline is thinnest, the external pressure will be reacted where the adherends are brought closest together. Thus, the bondline thickness is separated into two components: a wet component for minimum bondline thickness and a dry component for adherend separation left after discounting the wet component.

The interaction between adherends prior to the formation of the bonded joint, which consists of the transmission of pressure through the uncured adhesive, is approximated as a contact interaction at the regions of lowest adhesive thickness, since these are where the adhesive resists flow the most and becomes highly pressurized. Thus, the "dry" component is approximated as the clearance between the adherends when pushed against each other as shown in Fig. 1.

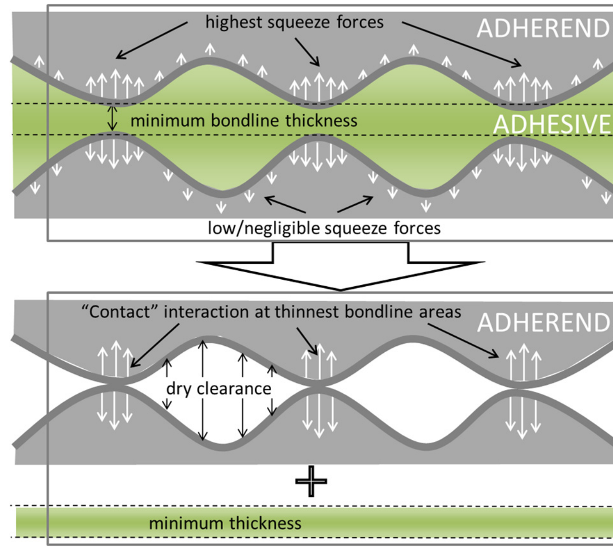

Fig. 1. Separation of the uncured bonded joint into dry and wet components.

3.2. Wet component: minimum bondline thickness

Flow of the adhesive at the thinnest bondlines was modeled as one-dimensional squeeze flow (1DSF), as in references [23–25].

The basic assumptions are:

(a) The uncured adhesive behaves as a Newtonian fluid.

(b) Each layer of fabric acts as a solid boundary and the layers of adhesive under and above it act as different flow domains.

(c) Both adherends can be approximated as flat and parallel for flow purposes.

(d) The problem is quasi-steady, and thus effects of inertia and accelerations are negligible (quasi-static force equilibrium applies).

(e) Flow only takes place in the cross-section plane without any longitudinal component.

(f) Adhesive flows freely once squeezed out from the space between adherends.

The general concept and dimensions are captured in Fig. 2. Thickness of a single squeezed bondline can be idealized [23] as

$$b_{1t}\left(t, Z_0\right) = \frac{1}{\sqrt{\left(\int_0^t \eta^{-1}\mathrm{d}t\right)\frac{2P}{w^2} + \frac{1}{Z_0^2}}} \tag{1}$$

where η is the adhesive kinematic viscosity, $P = P_{external} - P_0$ the manometric pressure applied, $Z_0 = b_{1t}$ $(t = 0)$ the initial bondline thickness, and w the bond width. The width of the bondline is assumed to remain constant and equal to w at all times.

The total bondline thickness for n layers of film adhesive with carrier will thus be

$$b_{bond} = \sum_{j=1}^{j=n+1} b_{1t}\left(t, Z_{0_j}\right) + \sum_{k=1}^{k=n} b_{carrier_k} \tag{2}$$

The only term dependent on the adhesive properties, as seen in Eq. (1), is $\left(\int_0^t \eta^{-1}\mathrm{d}t\right)$ which is a function of the rheology curve for the specific temperature cycle encountered. The evolution of the viscosity with time is highly dependent on the heat rate [42], which can be difficult to predict and control for industrial equipment and large assemblies, and even idealized test data is not always provided by suppliers. For the current study, this information is estimated based on the data in literature and experimentally observed minimum bond thickness.

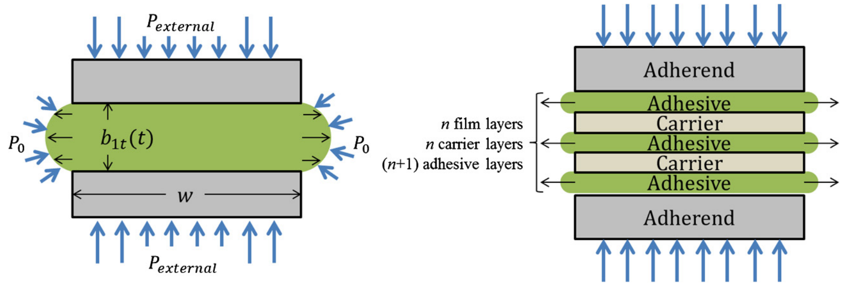

Fig. 2. Squeeze-flow with a single domain (left) and multiple domains (right).

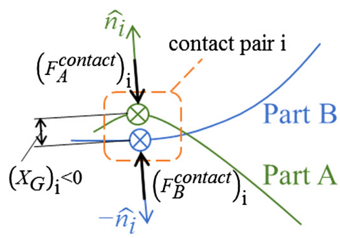

Fig. 3. Part interaction based on node pairs with normal reactions only.

3.3. Dry component: clearance from part shape mismatch

The dry assembly has been modeled by part linearization and modeling of the hard contact into a quadratic equation. The contact solution follows the prior art in [43], with the node interactions reframed to better reflect the assumptions of the bonding problem. The solution is reformulated below for the reader's benefit. Solution of the contact problem starts with the following simplifications:

1. The individual assembly parts satisfy the small deformations hypothesis, which justifies the application of the principle of superposition;
2. External forces are applied normal to the nominal surface at each position;
3. Adhesive behavior has been accounted for in the wet component (as presented in Fig. 1) and will be ignored for the determination of the dry component of the bondline thickness. The adhesive will however transmit the reaction forces and act as a lubricant which eliminates any friction between parts from tangential displacements.

Based on the assumptions above, only the interactions normal to the nominal mating surface (that is, only normal forces and displacements) are considered, as represented in Fig. 3. Thus at node i,

$$\boldsymbol{F_i} = (F_{i,x}, F_{i,y}, F_{i,z}) \cdot \hat{n}_i \tag{3}$$

$$\boldsymbol{X_i} = (X_{i,x}, X_{i,y}, X_{i,z}) \cdot \hat{n}_i \tag{4}$$

A linear model is constructed based on the compliance matrix:

$$\Delta X = \begin{bmatrix} \Delta X_1 \\ \vdots \\ \Delta X_N \end{bmatrix} = \begin{bmatrix} U_1 & \cdots & U_{1N} \\ \vdots & \ddots & \vdots \\ U_{N1} & \cdots & U_{NN} \end{bmatrix} \begin{bmatrix} F_1 \\ \vdots \\ F_N \end{bmatrix} = \boldsymbol{U} F \tag{5}$$

The problem only needs to concern itself with the nodes at interfaces; thus, the compliance matrix is obtained by applying a unit force in a finite element mesh and recording the deflections at each point of interest.

The contact problem is formulated by considering the points interfacing between two linearized bodies A, B. The gap between them is also linearized, and a single normal $\hat{n}_i$ is picked at each contact pair such that $(X_G)_i = (X_B^A - X_A^B)_i > 0$ when there is clearance.

$$\Delta X_G = \Delta X_B^A - \Delta X_A^B = \boldsymbol{U_B^A} F_B - \boldsymbol{U_A^B} F_A \tag{6}$$

Consider deflection due to internal forces that arise due to contact, these will be applied on both parts, due to action-reaction:

$$\left(F_B^{contact}\right)_i = -\left(F_A^{contact}\right)_i = \left(F^{contact}\right)_i \cdot \hat{n}_i \tag{7}$$

$$\Delta X_G = \Delta X_B^A - \Delta X_A^B = \boldsymbol{U_B^A} F_B^{external} - \boldsymbol{U_A^B} F_A^{external} + \left(\boldsymbol{U_B^A} + \boldsymbol{U_A^B}\right) F^{contact} \tag{8}$$

Considering computational implementation, this effectively means that the forces are being applied sequentially, as $F^{contact}$ is initially unknown:

$$\Delta X_G = \left[\left(\Delta X_B^{initial} - \Delta X_A^{initial}\right) + \boldsymbol{U_B^A} a F_B^{external} - \boldsymbol{U_A^B} F_A^{external}\right] + \left(\boldsymbol{U_B^A} + \boldsymbol{U_A^B}\right) F^{contact} = X_G^{no\ contact} + \boldsymbol{U_G} F^{contact} \tag{9}$$

The unilateral contact condition is enforced by quadratic programming, by solving a problem resulting from the Hertz-Signorini-Moureau criteria [43,44].

$$1.\ (X_G)_i \geq 0, \quad \forall i \text{ – no penetration} \tag{10}$$

$$2.\ \left(F^{contact}\right)_i \geq 0, \quad \forall i \text{ – no “pull” reaction during cure} \tag{11}$$

From Eqs. (10), (11) and as X_G, $F^{contact}$ are column vectors of positive values,

$$(X_G)^{\mathrm{T}} F^{contact} \geq 0 \tag{12}$$

The definition of X_G in Eq. (9) is substituted in Eq. (12):

$$\left(X_G^{no\ contact}\right)^{\mathrm{T}} F^{contact} + \left(F^{contact}\right)^{\mathrm{T}} \boldsymbol{U_G} F^{contact} \geq 0 \tag{13}$$

Further, either the contact force or the gap will be zero at each contact pair, which is expressed by the third Hertz-Signorini-Moureau criterion:

$$3.\ (X_G)_i \left(F^{contact}\right)_i = 0, \quad \forall i \tag{14}$$

Thus, the quadratic inequation (13) can be turned into a convex minimization problem which looks for

$$\operatorname{argmin}(f) = \operatorname{argmin}\left(\left(X_G^{no\ contact}\right)^{\mathrm{T}} F^{contact} + \left(F^{contact}\right)^{\mathrm{T}} \boldsymbol{U_G} F^{contact}\right) \tag{15}$$

where $F^{contact}$ is the N-dimensional dependent variable.

In this implementation, the problem has been solved using MATLAB's quadprog (QP) function, which offers pre- and post-processing for increased efficiency, algorithm selection, and convergence parameter control with little user effort.

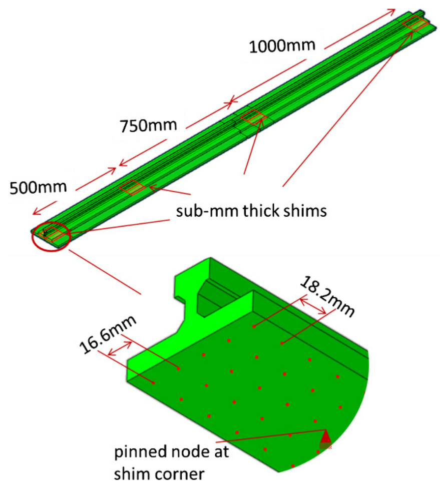

Fig. 4. Assembly and subset of nodes considered for verification against FEA.

The problem is reformulated for input to the function as

$$f = \frac{1}{2}\left(F^{contact}\right)^{\mathrm{T}} 2\boldsymbol{U}_{\boldsymbol{G}} F^{contact} + \left(X_G^{no\ contact}\right)^{\mathrm{T}} F^{contact},$$
$$\begin{cases} -\boldsymbol{U}_{\boldsymbol{G}} F^{contact} \leq X_G^{no\ contact} \\ (0)_{N\times 1} \leq F^{contact} \end{cases} \tag{16}$$

And the input to MATLAB is (with each variable/parameter appearing in the same order):

```
F_contact = quadprog (2*U_G, X_G_nocontact, -U_G,
X_G_nocontact, [],[],zeros(N,1),[])
```

with the `[]` empty square brackets denoting lack of equality constraints or upper bounds.

The algorithm used to determine the contact force of the problem was quadprog's default interior-point convex optimization algorithm.

From the resulting value of $F^{contact}$, it is straightforward to calculate the individual part positions, as well as X_G which is the parameter of most interest in this study.

4. Results and discussion

4.1. Stringer-skin assembly for model validation

The model proposed in Section 3 will first be validated against the FEA results of a stringer-skin assembly. A bonding scenario with variation occurring over multiple ranges has been used for validation. This consists of a thin (5 mm) flat skin plate, and flat stringers bonded on top of it. Stringer profile variation was emulated by introducing shims of controlled thickness at variable intervals (Fig. 4).

A physical assembly demonstrator has been manufactured for this study. The skin plates were gap checked against the table prior to bonding using a 0.05 mm feeler gauge, with no gaps detected. Given the skin flatness and high stiffness of the bonding table used, the skin was modeled as an encastred plate, and the shims as padups integral to it.

The stringer is of a constant cross-section and both parts were made of representative aluminum alloy ($E = 72000$ MPa, $\nu = 0.30$). Two cross-sections were considered: 'Thick' ($I_z \approx 275000$ mm^4 with a 12 mm-thick foot flange) and 'Thin' ($I_z \approx 120000$ mm^4 with a 4 mm-thick foot flange).

4.2. Dry model validation against FEA results

As a first verification of the semi-analytical model, comparison was established with results from conventional Finite Element Analysis (FEA) with Abaqus. No adhesive was considered in this case as the focus of the verification was on part deflection and contact enforcement (dry part). This also had the effect of increasing the maximum deflection achievable, and thus improving detectability of deviations.

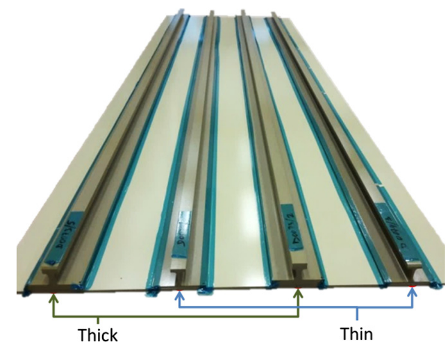

Fig. 5. Test panel with both 'Thick' and 'Thin' stringers.

Results for deflection were obtained for two models in each case: FEA with a fine solid mesh (C3D8 elements), and the proposed QP-based method using a stringer compliance matrix obtained from the same mesh.

For the QP model, each stringer was reduced to $128 \times 5 = 640$ nodes equidistant on the foot (Fig. 4), with matching nodes on the skin and shims. By assuming the skin panel to be perfectly flat and the table infinitely stiff, the need to model the assembly jointly (including skin-tool contact and impact of one stringer on the rest of the panel) was effectively removed. Thus, each stringer's deflection was modeled separately. This resulted in much smaller matrices and faster calculation times.

The results were extracted for nodes in the middle of the stringer flange and 1/10 the flange width from the edge. A small subset of the results (0.5 mm shim with the highest and lowest pressures) is shown in Fig. 6; there is very good agreement between the FEA and QP results (solid and dashed lines), except for moderate deviations in the deflection achieved where there is no adherend contact in a span between shims, as well as for the foot flange edge (red lines) of the 'Thin' stringers.

The root-mean-square (RMS) difference between the QP and FEA results generally stay below 5% of the initial gap as shown in Fig. 5. The only substantial divergence was when dealing with a thin foot flange; in this case, the failure of the coarse node grid to properly account for the stringer edges resulted in inaccurate modeling of the contact interactions, and flange deflection was overestimated ("edge" red lines in Fig. 7). This can be easily improved by adding more nodes in the width of the stringer flange, demonstrating the validity of the proposed semi-analytical model.

4.3. Physical test results and reliability of flow modeling assumption

The dry component simulation of the proposed model has shown good agreement with FEA results. The remaining work is to verify that the adhesive flow assumptions hold satisfactorily, which will be tested with the physical assembly demonstrator shown in Fig. 4. The intention of this test is not to verify the exact minimum-bondline-thickness achieved. Rather, the objective is to validate the model simplification presented in Section 3, where adhesive behavior is only relevant for calculation of a minimum bondline thickness (wet component). If this is the case, it is reasonable to use 1DSF, and ($\int_0^t \eta^{-1} dt$), along with the other film parameters, can then be calculated through material characterization (e.g. using a rheometer as in [42]), or the expected minimum-bondline-thickness can be determined though process-specific tests that replicate the pressure and thermal cycle. In

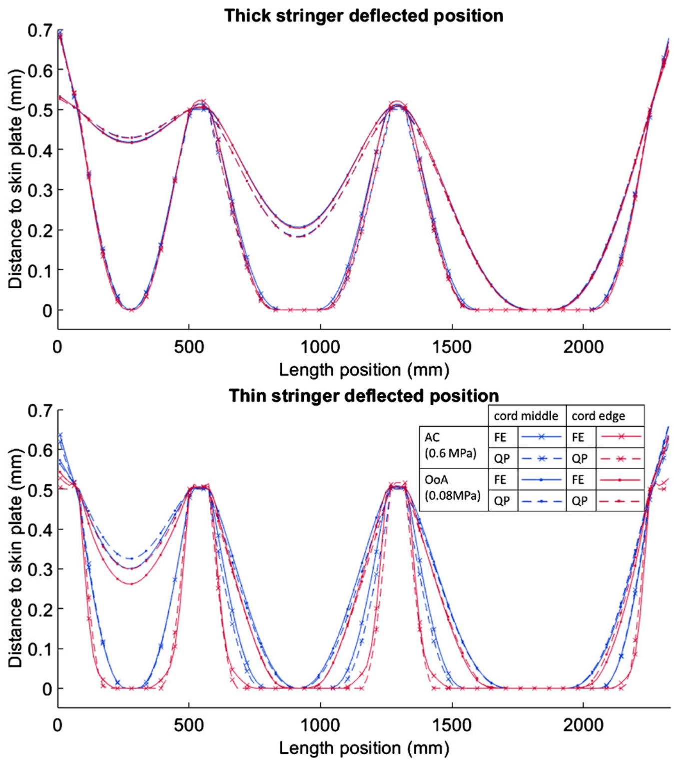

Fig. 6. Part deflections as obtained by FEA and by the proposed method, for 0.5 mm gaps with no adhesive, under the maximum and minimum pressures considered. (For interpretation of the colors in the figure(s), the reader is referred to the web version of this article.)

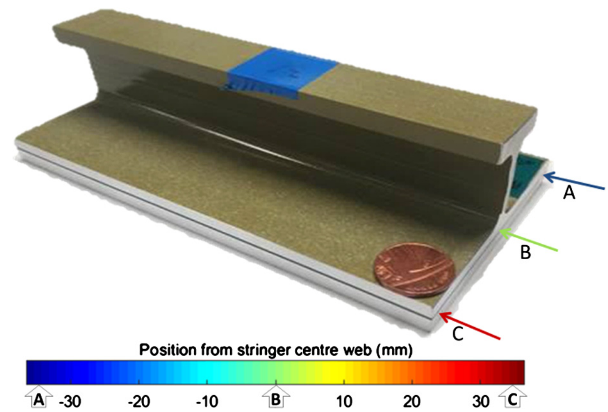

Fig. 8. Section taken from a 'Thin' stringer, with microscopy locations marked and a penny for scale.

either case, one should confirm the actual thermal cycle in the joint, especially in large assemblies where the part and tooling's thermal mass may result in large deviations across the structure and from the nominal. Usual industry practice includes attachment of multiple thermocouples to ensure the structure has undergone the correct treatment. Closer scrutiny of the adhesive model and properties may be in order if other outcomes, such as spew fillet volume and void formation, are also of concern.

The tests used the same skin-shims-stringers arrangement presented above, but incorporating adhesive outside the shimmed areas. Trials were conducted with 1 and 2 adhesive film layers.

The bonded assemblies were simulated with the QP model as described above. For the minimum bondline thickness, constant viscosity $\eta = 50$ Pa s, total squeeze time $t = 1200$ s, initial per-layer thickness $Z_0 = 0.1$ mm, and carrier thickness $b_{carrier} = 0.050$ mm was assumed. With $X_0 = 83$ mm, this results in minimum thickness values in the 0.081 mm and 0.146 mm for 1 and 2 layers, respectively.

The assembly comprised a skin plate with two 'thick' and two 'thin' stringers, one of each with 0.2 mm shims (1 film layer) and other with 0.3 mm shims (2 film layers). The number of layers is the maximum that would not overfill the artificial gaps according to manufacturing best practice, based on a nominal cured layer thickness of 0.125 mm. The parts were bonded using an epoxy adhesive with scrim carrier (Cytec FM94-0.06K). The assembly was encapsulated in a vacuum bag and cured at a representative autoclave pressure of 0.6 MPa. The heat cycle comprised heating at a 2 °C/min rate, holding at 120 °C for an hour.

The stringers were machined to a tight profile tolerance of 0.2 mm in the bonding surface. Simulation of assembly for parts with such small variation were found yield minimal (<25 µm) deviations from nominal, so the results from assembling nominally-flat stringers were used instead of individual part inspection values.

The cured assemblies were sectioned into ∼200 mm segments at regular intervals between the shims, at locations adjacent to the shims and where minimum bondline thickness was expected. The bondline thickness was assessed via optical microscopy, with three spots measured at each cross-section (Fig. 8). The longitudinal section distribution is presented in Fig. 9, along with example results (simulated and measured for 'Thick' stringers).

The results show consistent behavior of the adhesive under each stringer at high pressures, with small variability among the measured thicknesses, with standard deviations below 0.020 mm and numerical results in the range of the 1DSF preliminary sizing (Table 1). However, there exist divergences between stringers which are likely not fully explained by slight differences in effective heat rates, with the thin stringers obtaining more variable bondlines.

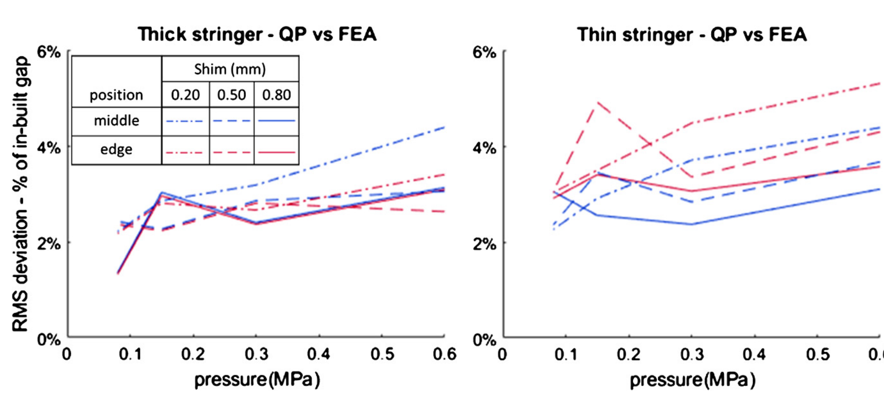

Fig. 7. RMS deviation between all QP and FEA simulations performed (dry component only).

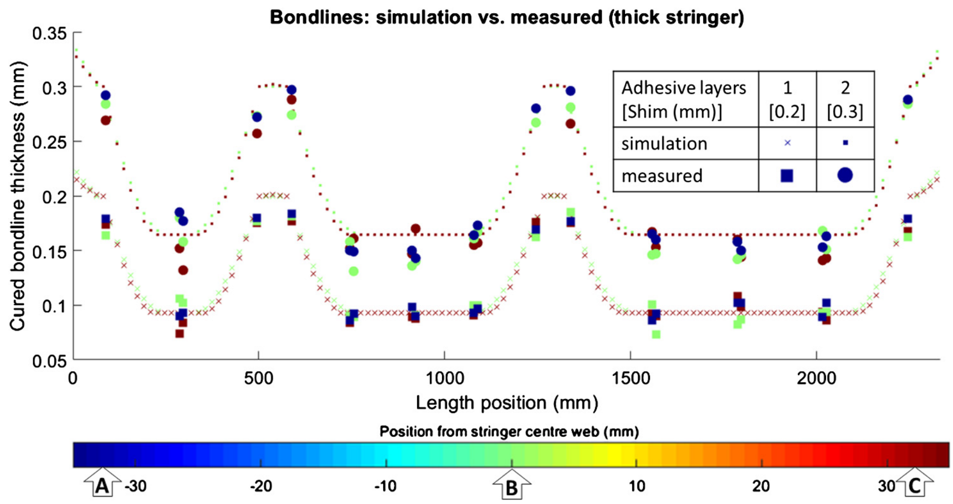

Fig. 9. Predicted and measured (small and large markers, respectively) bondline thicknesses for the 'Thick' stringers under 0.6 MPa. The section measurements show good agreement with the predicted results.

Table 1
Measured minimum bondline thicknesses: standard deviation and root mean square (RMS) difference to the 1DSF prediction.

Adhesive layers [Shim (mm)]	'Thick' stringer		'Thin' stringer	
	σ (mm)	RMS (mm)	σ (mm)	RMS (mm)
1 [0.2]	0.007	0.008	0.012	0.024
2 [0.3]	0.012	0.016	0.018	0.023

5. Conclusions

The model provides a good approximation of the demonstrator stringer behavior for a representative scenario, when compared with a more resource-intensive FEA simulation from a commercial package. The Matlab-based solution provides a better understanding of the development of bondline geometries and is easily shared across an organization. It allows easy integration and experimentation with multiple data sources or additional post-treatment. This solution should also be possible to integrate in existing CAT packages that calculate parts' elastic behavior with contact, provided surface-based force application and variable-size joint elements (for representation of the adhesive joint) are supported; such integration would also benefit from the ability to input part shape variation, monitor distances between surfaces at multiple points, and measure initial surface dimensions such that a potential violation of the adhesive flow assumptions may be flagged up.

The proposed method offers considerable advantages against a simple tolerance stack for non-rigid simple assemblies, owing to its ability to achieve less conservative bondline predictions by accounting for part deflection and adhesive flow. The implementation has been found to offer satisfactory predictive capability, taking into account typical product tolerances and measurement uncertainties. With this tool, it is possible to evaluate diverse assembly concepts and make better-informed tolerance-allocation decisions for bonded assemblies of monolithic parts.

The importance of adhesive contribution to geometrical variation, and the potentially-critical role of the bonding procedure, has been highlighted both with model and physical test article results. Furthermore, the simulations carried out highlight the interaction of thin stringer flanges with interface steps, resulting in deformations where stringer cross-sections experience changes in shape. The experimental work also points out to a natural limitation of the dry-wet separation which manifests itself when adherends are thin enough; the cross-section deforms under the external and adhesive forces, changing the shape of the adhesive flow domain. This effect can place an inherent limitation on modeling accuracy for assemblies of sheet stringers or doublers. Inaccuracies (not observed here) may likewise arise in assemblies where part twist is significant, making the flow asymmetrical in each cross-section; or when gaps are locally large enough that some flow may happen through the length of the stringer. In this light, laminate or doubly-curved structures may especially benefit from method refinement.

The next stage of development will be the study of bonded assemblies where the part itself causes the bondline variability, as well as physical OoA rather than AC curing, testing different boundary conditions, and removing the assumption of perfect, stiff skins.

Further development should also look at applicability to larger, more-representative assemblies. This includes factors such as doubly-curved geometries and large (several mm) deformations which may be unsuitable for linear modeling. The scope of applicability will need to be fully explored before it is possible to make a leap to wide industrialization; however, the initial results show encouraging capability for simple geometries. The semi-analytical model presented herein offers more reliable and realistic prediction of bondline thickness; as such, it can be a major technology enabler for lighter and more cost-effective development of high-performance structures. The scope of applicability is likely to extend beyond aerospace; additional opportunities for application may be found in other stiffened thin-walled structures, such as marine or automotive, which stand to benefit substantially from the weight savings, performance improvements, and corrosion resistance offered by adhesive bonding. Some of the modeling assumptions, especially around adhesive flow and force application, may need to be examined for these cases. For now, the technique presented offers tempting possibilities to support development of airframes of the near future.

Declaration of Competing Interest

There is no competing interest.

References

[1] ATI, Raising Ambition: Technology Strategy and Portfolio Update 2016, https://www.ati.org.uk/wp-content/uploads/2017/10/Raising-Ambition-ATI-Technology-Strategy-Portfolio-Update-2016.pdf, 2016. (Accessed 18 December 2018).
[2] J. Tomblin, K. Strole, G. Dodosh, L. Ilcewicz, Assessment of Industry Practices for Aircraft Bonded Joints and Structures, FAA report DOT/FAA/

AR-05/13, 2005, http://www.tc.faa.gov/its/worldpac/techrpt/ar0513.pdf. (Accessed 2 March 2016).

[3] L.J. Hart-Smith, Adhesive Layer Thickness and Porosity Criteria for Bonded Joints, USAF contract report AFWAL-TR-82-4172, Long Beach, California, https://apps.dtic.mil/dtic/tr/fulltext/u2/a129817.pdf, 1982. (Accessed 2 March 2016).

[4] L.J. Hart-Smith, Adhesively bonded joints in aircraft structures, in: L.F.M. da Silva, A. Öchsner, R.D. Adams (Eds.), Handb. Adhes. Technol., Heidelberg, 2011, pp. 1104–1147.

[5] G.N. Abenhaim, A. Desrochers, A. Tahan, Nonrigid parts' specification and inspection methods: notions, challenges, and recent advancements, Int. J. Adv. Manuf. Technol. 63 (2012) 741–752, https://doi.org/10.1007/s00170-012-3929-2.

[6] H. Nobis, W. Roeglin, O. Bischoff, A. Schroeder, Method for autoclave-free adhesive bonding of components for aircraft, 2010, Patent EP1984241 (B1).

[7] T. Centea, L.K. Grunenfelder, S.R. Nutt, A review of out-of-autoclave prepregs – material properties, process phenomena, and manufacturing considerations, Composites, Part A 70 (2015) 132–154, https://doi.org/10.1016/j.compositesa.2014.09.029.

[8] G. Liu, W. Tang, Y.-L. Ke, Q.-L. Chen, Y. Bi, Modeling of fast pre-joining processes optimization for skin-stringer panels, Assem. Autom. 34 (2014) 323–332, https://doi.org/10.1108/AA-05-2014-036.

[9] Conference on bonded aircraft structures, Aircr. Eng. Aerosp. Technol. 29 (1957) 139–142, https://doi.org/10.1108/eb032825.

[10] K.L. Land, F.B. Lennert, Primary Adhesively Bonded Structure Technology (PABST). Phase III: Tooling, Fabrication and Quality Assurance, USAF report AFFDL-TR-79-3154, 1979.

[11] L.J. Hart-Smith, G. Strindberg, Developments in adhesively bonding the wings of the SAAB 340 and 2000 aircraft, Proc. Inst. Mech. Eng., G J. Aerosp. Eng. 211 (1997) 133–156, https://doi.org/10.1243/0954410971532578.

[12] N. Takezawa, An improved method for establishing the process-wise quality standard, JUSE Reports Stat. Appl. Res. 27 (1980) 63–76.

[13] S.C. Liu, S.J. Hu, Variation simulation for deformable sheet metal assemblies using finite element methods, J. Manuf. Sci. Eng. 119 (1997) 368–374.

[14] P. Hammett, J. Baron, D. Smith, Automotive Body Measurement System Capability, Auto/Steel Partnership report, Southfield, http://www-personal.umich.edu/~phammett/Papers/asp-meas-rept.PDF, 1999. (Accessed 5 May 2016).

[15] H. Radvar-Esfahlan, S.-A. Tahan, Nonrigid geometric metrology using generalized numerical inspection fixtures, Precis. Eng. 36 (2012) 1–9, https://doi.org/10.1016/j.precisioneng.2011.07.002.

[16] F. Thiébaut, C. Lacroix, C. Lartigue, L. Andolfatto, Evaluation of the shape deviation of non rigid parts from optical measurements, Int. J. Adv. Manuf. Technol. 88 (2017) 1937–1944, https://doi.org/10.1007/s00170-016-8899-3.

[17] R. Söderberg, L. Lindkvist, S. Dahlström, Computer-aided robustness analysis for compliant assemblies, J. Eng. Des. 17 (2006) 411–428, https://doi.org/10.1080/09544820500275800.

[18] DCS, 3DCS Mechanical Solutions, https://www.cenit.com/fileadmin/dam/3DS-PLM/PDFs/3DCS_Mechanical_Variation_Analyst.pdf, 2013.

[19] W.E. Goff, Methods of airframe production, Flight Int. (1973) 873–874.

[20] E.J. Catchpole, Development of synthetic resin adhesives: a review of the background to adhesives for metal-to-metal bonding and honeycomb sandwich construction and their current scale of application, Aircr. Eng. Aerosp. Technol. 35 (1963) 7–19, https://doi.org/10.1108/eb033669.

[21] L.J. Hart-Smith, Adhesive bonding of aircraft primary structures, SAE Transact. 89 (1980) 3718–3782, https://doi.org/10.4271/801209.

[22] P. Hubert, A. Poursartip, A review of flow and compaction modelling relevant to thermoset matrix laminate processing, J. Reinf. Plast. Compos. 17 (1998) 286–318.

[23] A.J. Smiley, M. Chao, J.W. Gillespie Jr., Influence and control of bondline thickness in fusion bonded joints of thermoplastic composites, Compos. Struct. 2 (1991) 223–232.

[24] R.J. Chester, J.D. Roberts, Void minimization in adhesive joints, Int. J. Adhes. Adhes. 9 (1989) 129–138.

[25] B.A. Morris, J.M. Scherer, Modeling and experimental analysis of squeeze flow of sealant during hot bar sealing and methods of preventing squeeze-out, J. Plast. Film Sheeting 32 (2016) 34–55, https://doi.org/10.1177/8756087915578183.

[26] K.G. Merkley, Tolerance Analysis of Compliant Assemblies, PhD Thesis, Brigham Young University, 1998.

[27] B.F. Bihlmaier, Tolerance Analysis of Flexible Assemblies Using Finite Element and Spectral Analysis, MSc Thesis, Brigham Young University, 1999.

[28] S.J. Hu, Stream-of-variation theory for automotive body assembly, CIRP Ann. 46 (1997).

[29] J.V. Abellán Nebot, Prediction and Improvement of Part Quality in Multi-Station Machining Systems Applying the Stream of Variation Model, PhD Thesis, Universitat Jaume I, 2011.

[30] DCS, 3DCS FEA Compliant Modeler, www.plmmarketplace.com/upload/3DCS_FEA_Compliant_Modeler_Overview_2.ppt, 2007. (Accessed 10 October 2016).

[31] S. Dahlström, L. Lindkvist, Variation simulation of sheet metal assemblies using the method of influence coefficients with contact modeling, J. Manuf. Sci. Eng. 129 (2007) 615–622, https://doi.org/10.1115/1.2714570.

[32] L. Lindkvist, K. Wärmefjord, R. Söderberg, Tolerance simulation of compliant sheet metal assemblies using automatic node-based contact detection, in: Proc. IMECE2008 2008 ASME Int. Mech. Eng. Congr. Expo., Oct. 31-November 6, 2008, Boston, Massachusetts, USA, 2008.

[33] X. Liao, G.G. Wang, Non-linear dimensional variation analysis for sheet metal assemblies by contact modeling, Finite Elem. Anal. Des. 44 (2007) 34–44, https://doi.org/10.1016/j.finel.2007.08.009.

[34] B. Lindau, K. Wärmefjord, L. Lindkvist, R. Söderberg, Aspects of fixture clamp modeling in non-rigid variation simulation of sheet metal assemblies, in: Proc. ASME 2013 Int. Mech. Eng. Congr. Expo., San Diego, California, USA, 2013.

[35] A. Stricher, Tolérancement flexible d'assemblages de grandes structures aéronautiques, PhD Thesis, École normale supérieure de Cachan, 2013, https://tel.archives-ouvertes.fr/tel-00824579.

[36] P.G. Maropoulos, P. Vichare, O. Martin, J. Muelaner, M.D. Summers, A. Kayani, Early design verification of complex assembly variability using a Hybrid – Model Based and Physical Testing – Methodology, CIRP Ann. - Manuf. Technol. 60 (2011) 207–210, https://doi.org/10.1016/j.cirp.2011.03.097.

[37] G. Liu, W. Tang, Y. Ke, Q. Chen, X. Chen, Pre-joining process planning model for a batch of skin – stringer panels based on statistical clearances, Int. J. Adv. Manuf. Technol. 78 (2015) 41–51, https://doi.org/10.1007/s00170-014-6629-2.

[38] K. Xie, J.A. Camelio, L.E. Izquierdo, Part-by-part dimensional error compensation in compliant sheet metal assembly processes, J. Manuf. Syst. 31 (2012) 152–161, https://doi.org/10.1016/j.jmsy.2011.07.005.

[39] G. Liu, H. Huan, Y. Ke, Study on analysis and prediction of riveting assembly variation of aircraft fuselage panel, Int. J. Adv. Manuf. Technol. 75 (2014) 991–1003, https://doi.org/10.1007/s00170-014-6113-z.

[40] A. Pahkamaa, L. Karlsson, J. Pavasson, M. Karlberg, M. Näsström, J. Goldak, A method to improve efficiency in welding simulations for simulation driven design, in: Proc. ASME 2010 Int. Des. Eng. Tech. Conf. Comput. Inf. Eng. Conf., ASME, Montreal, 2010, pp. 1–10.

[41] A. Pahkamaa, K. Wärmefjord, L. Karlsson, R. Söderberg, J. Goldak, Combining variation simulation with welding simulation for prediction of deformation and variation of a final assembly, J. Comput. Inf. Sci. Eng. 12 (2012) 1–6, https://doi.org/10.1115/1.4005720.

[42] M. Préau, P. Hubert, Bonded repairs of composite structures: void formation mechanisms in an adhesive film, in: 17th Eur. Conf. Compos. Mater., Munich, 2016, pp. 26–30.

[43] B. Lindau, S. Lorin, L. Lindkvist, R. Söderberg, Efficient contact modeling in nonrigid variation simulation, J. Comput. Inf. Sci. Eng. 16 (2016) 1–7, https://doi.org/10.1115/1.4032077.

[44] P. Wriggers, Computational Contact Mechanics, second ed., Springer-Verlag, Heidelberg, 2006, pp. 70–71.